Universidade de Aveiro
2015

Departamento de Física

Joana Catarina Ferreira Rodrigues

Nanoestruturas baseadas em ZnO e GaN para aplicações optoeletrónicas: síntese e caracterização

ZnO and GaN nanostructures for optoelectronic applications: synthesis and characterization

Universidade de Aveiro
2015

Departamento de Física

Joana Catarina Ferreira Rodrigues

Nanoestruturas baseadas em ZnO e GaN para aplicações optoeletrónicas: síntese e caracterização

ZnO and GaN nanostructures for optoelectronic applications: synthesis and characterization

Tese apresentada à Universidade de Aveiro para cumprimento dos requisitos necessários à obtenção do grau de Doutor em Nanociências e Nanotecnologia, realizada sob a orientação científica da Doutora Florinda Costa, Professora associada e da Doutora Teresa Monteiro, Professora associada com agregação do Departamento de Física da Universidade de Aveiro.

Apoio financeiro da FCT através da bolsa de Doutoramento SFRH/ BD/76300/2011.

Dedico este trabalho aos meus pais.

o júri

presidente

Prof. Doutor António Manuel Rosa Pereira Caetano
Professor Catedrático, Universidade de Aveiro.

vogais

Profª. Doutora Elvira Maria Correia Fortunato
Professora Catedrática, Faculdade de Ciências e Tecnologias, Universidade Nova de Lisboa

Prof. Doutor Armando José Trindade das Neves
Professor Associado, Universidade de Aveiro

Profª. Doutora Florinda Mendes da Costa
Professora Associada, Universidade de Aveiro **(orientadora)**

Prof. Doutor João Pedro dos Santos Hall Agorreta de Alpuim
Professor Auxiliar, Universidade do Minho

Profª. Doutora Katharina Lorenz
Investigadora Auxiliar, Instituto Tecnológico Nuclear, Instituto Superior Técnico, Universidade de Lisboa

agradecimentos

Esta tese é o resultado da participação e colaboração de várias pessoas e instituições, as quais foram fundamentais para a realização do trabalho aqui apresentado. Em particular, gostaria de começar por agradecer às minhas orientadoras, Professoras Florinda Costa e Teresa Monteiro, por todo o apoio e disponibilidade, por acreditarem em mim e nas minhas capacidades, por me terem desafiado a mais esta etapa, por todos os conhecimentos transmitidos e sobretudo por toda a amizade que sempre demonstraram. Muito obrigada!

À Professora Katharina Lorenz pelo importante contributo no trabalho relacionado com os materiais baseados em GaN. Agradeço toda ajuda e disponibilidade.

À Professora Rosário Correia por toda a amizade, ensinamentos, por todas as discussões e conversas sobre Física (e não só) e por me incentivar a ir sempre um pouco mais além.

A todos os meus colegas e amigos do grupo de Espectroscopia, por toda ajuda, apoio, boa disposição, disponibilidade, paciência... Em especial à Nabiha, à Rosa, ao Cláudio, ao Zé, ao Miguel, ao Marco Peres, à Teresa, ao Tiago Holz, ao Nuno Santos, ao Nuno Ferreira, ao Ricardo, ao Diogo, ao Alexandre e ao Tozé.

Aos Professores Luís Rino e Jorge Soares por todo o apoio no laboratório e disponibilidade para esclarecer dúvidas.

Ao *Laboratório de Aceleradores e Tecnologias da Radiação* do CTN/IST pela colaboração fundamental para a realização desta tese, nomeadamente ao grupo do Professor Eduardo Alves e da Professora Katharina Lorenz, com um agradecimento especial à Maria, ao Sérgio, e ao Andrés.

Ao grupo do Professor Bruno Daudin (Univ. Grenoble Alpes, CEA/CNRS) pela produção de todas as nanoestruturas de GaN analisadas nesta tese.

Ao CENIMAT/I3N, em particular ao grupo da Professora Elvira Fortunado, pela colaboração que foi estabelicida e pela ajuda na caracterização de algumas das amostras aqui estudadas. Agradeço especialmente à Ana Pimentel pela sua enorme disponibilidade.

À Universidade de Cádiz e ao grupo da Professora Teresa Ben por toda a caracterização de TEM realizada nas estruturas de ZnO.

À Doutora Rosário Soares pela análise de difracção de raios-X em algumas das amostras aqui estudadas.

Ao Professor Rui Silva e ao Ricardo Silva pela deposição de ZnO por ALD em algumas das amostras usadas na produção de células fotovoltaicas e pelo fornecimento de algumas das florestas de CNTs utilizadas.

Ao Professor António Cunha, ao Mário Lima, à Marta, à Ana e ao João por toda a ajuda no desenvolvimento de protótipos para as células solares.

À Professora Bianchi Méndez e ao Doutor Emilio Nogales da Universidade Complutense de Madrid pela colaboração na caracterização ótica de algumas das nanoestruturas de GaN.

agradecimentos

Ao Departamento de Física e à Universidade de Aveiro, bem como a todos os docentes que me acompanharam ao longo de todo o meu percurso académico.

À unidade de investigação FSCOSD/I3N por me ter acolhido durante a realização deste trabalho e por disponibilizar todos os equipamentos necessários à realização do mesmo.

A todos os meus amigos por, mesmo longe, estarem sempre presentes e me apoiarem sempre, *I get by with a little help from my friends*.

Ao Bruno por toda a entropia que veio trazer à minha vida e por tantas vezes me salvar de mim própria e da minha obsessão pelo trabalho. Por estar sempre presente com todo o amor e paciência e por fazer de mim uma pessoa melhor! Obrigada por estares aqui!

Por fim, mais importante que tudo, aos meus pais. Não há palavras suficientes para vos agradecer! É mesmo amor incondicional...

Este trabalho foi realizado no âmbito dos projetos UID/CTM/50025/2013, RECI/FIS-NAN/0183/2012 (FCOMP-01-0124-FEDER-027479), PTDC/CTM-NAN/2156/2012 e PTDC/FIS-NAN/0973/2012.

FCT Fundação para a Ciência e a Tecnologia

MINISTÉRIO DA EDUCAÇÃO E CIÊNCIA

palavras-chave ZnO, GaN, $Al_xGa_{1-x}N$, CNTs, $Cd_xZn_{1-x}O$, iões terras raras, deposição de fluxo assistida por laser (LAFD), fotoluminescência, fotovoltaicos, fotocatálise

resumo

Os semicondutores de elevado hiato energético, como é o caso do GaN e do ZnO, são materiais com aplicações em diversas áreas tecnológicas, que incluem, por exemplo, iluminação, eletrónica transparente, sensores, catalisadores ou fotovoltaicos.

Esta tese é dedicada ao estudo de materiais baseados em GaN e ZnO, sendo dada ênfase à incorporação de iões terras-raras (RE) nas matrizes de nitretos, com a finalidade de contribuir para o desenvolvimento de dispositivos de iluminação de estado sólido. O uso dos iões RE é motivado pelas suas emissões intraiónicas abrangendo uma ampla gama espectral (do ultravioleta ao infravermelho próximo), quando estão no seu estado de carga trivalente. A implantação iónica surge como uma alternativa para a dopagem destes materiais, uma vez que permite a introdução de dopantes de uma forma controlada e independente dos limites de solubilidade dos iões nas matrizes. Amostras de GaN com diferentes dimensionalidades foram analisadas e a sua influência nas propriedades luminescentes dos RE^{3+} foi investigada. Medidas de fotoluminescência (PL) revelaram que, depois de um tratamento térmico, a ativação ótica dos iões foi bem-sucedida para as amostras implantadas com os diferentes iões. Uma análise espectroscópica detalhada das transições luminescentes dos RE^{3+} foi realizada usando técnicas como a PL em estado estacionário e transiente e excitação da fotoluminescência.

Outro objetivo desta tese foi o crescimento e caracterização de micro e nanoestruturas de ZnO, recorrendo a uma nova técnica de crescimento designada por deposição de fluxo assistida por laser (LAFD). Este é um método com elevado rendimento, baseado num mecanismo sólido-vapor, que permite o crescimento de ZnO com diferentes morfologias (nanopartíclulas, tetrapodes e microfios). A sua análise estrutural pôs em evidência a excelente qualidade cristalina do ZnO produzido por esta técnica. As propriedades óticas foram também investigadas através de fotoluminescência, revelando a sua elevada qualidade ótica. Para além dos cristais não dopados intencionalmente, foram ainda preparados compósitos com prata e nanotubos de carbono (CNTs). No primeiro caso, foram observadas partículas esféricas de prata distribuídas de uma forma não uniforme na superfície dos microfios, mostrando uma tendência para se acumularem no topo destes e promovendo a sua renucleação. No caso dos compósitos ZnO/CNTs, foram usadas duas abordagens: i) deposição de partículas de ZnO diretamente no topo dos CNTs alinhados verticalmente, sem a utilização de nenhum catalisador adicional, e ii) produção de ZnO/CNTs *buckypapers*. No primeiro caso, a técnica de LAFD provou manter o alinhamento dos CNTs, evitando o seu colapso, sendo esta uma vantagem do método usado. Adicionalmente, tendo em consideração a importância do controlo do hiato energético dos materiais a ser aplicados em dispositivos optoelectrónicos, foram também estudadas as propriedades óticas da liga $Cd_xZn_{1-x}O$. Devido ao aumento da fração molar de CdO na liga ternária observou-se um desvio do hiato do ZnO para a região visível do espetro eletromagnético.

Finalmente, as estruturas de ZnO crescidas por LAFD foram testadas em dispositivos fotovoltaicos e em estudos de fotocatálise.

keywords

ZnO, GaN, $Al_xGa_{1-x}N$, CNTs, $Cd_xZn_{1-x}O$, rare-earth ions, laser assisted flow deposition (LAFD), photoluminescence, photovoltaic, photocatalysis

abstract

Wide bandgap semiconductors, such as GaN and ZnO, are materials with a wide range of applications in several important technological areas including lighting, transparent electronics, sensors, catalysis or photovoltaics.
This thesis focuses on the study of GaN and ZnO, including related compounds. In the first case, the emphasis is given to the incorporation of rare-earth (RE) ions ($4f^n$) into the nitride hosts envisaging to contribute for the development of “all-nitride” solid state lighting devices. GaN and related III-nitrides ternary alloys appear as excellent hosts for the incorporation of these ions. The use of RE ions is motivated by the electromagnetic widespread spectral range (from the ultraviolet to the near infrared) covered by the intraionic radiative relaxation of the trivalent charged ions. Ion implantation appears as an alternative approach to doping since it allows the introduction of impurities in a controlled way and without solubility limits. GaN samples with different dimensionalities were analysed and their influence in the luminescence properties of the RE^{3+} was investigated. Photoluminescence (PL) measurements revealed that after thermal annealing a successful optical activation of the RE^{3+} was achieved for the samples implanted with the different RE^{3+}. A detailed spectroscopic analysis of RE^{3+} luminescent tarnsitions is presented by using temperature dependent steady-state PL, room temperature PL excitation and time resolved PL.
This thesis also aims to the growth and characterization of ZnO micro and nanostructures, through a new growth technique designated by laser assisted flow deposition (LAFD). LAFD is a very high yield method based on a vapour-solid mechanism that enables the growth of ZnO crystals in a very short timescale. LAFD was used in the growth of wurtzite micro/nanocrystalline ZnO with different morphologies (nanoparticles, tetrapods and microrods) as revealed by the extensive morphological characterization. Moreover, structural analysis evidenced the high crystalline quality of the produced crystals. The optical properties of the as-grown ZnO crystals were fully investigated by luminescence techniques, which revealed a high optical quality of the LAFD produced ZnO. In addition to the unintentionally doped micro/nanocrystals, ZnO/Ag and ZnO/carbon nanotubes (CNT) composite structures were also synthesized by LAFD. Silver-related spherical particles were found to be inhomogeneously distributed at the microrods surface, accumulating at the rods tips and promoting the ZnO nanorods re-nucleation. For the case of the ZnO/CNT composites two main approaches were adopted: i) a direct deposition of ZnO particles on the surface of vertically aligned multi-walled carbon nanotubes (VACNTs) forests without employing any additional catalyst and ii) ZnO/CNT buckypaper nanocomposites. It was found that the use of the LAFD technique carried out in framework of the first approach preserves the CNTs structure, their alignment, and avoids the collapse of the VACNTs array, which is a major advantage of this method.
Additionally, taking into account that a crucial step in designing modern optoelectronic devices is to accomplish bandgap engineering, the optical properties of $Cd_xZn_{1-x}O$ alloy were also evaluated. A tuning of the ZnO bandgap towards the visible spectral region was accomplished by alloying this semiconductor with CdO.
Finally, the potential application of the LAFD produced ZnO structures in the photocatalysis and photovoltaic fields was tested.

List of abbreviations and symbols

A^-	Ionized acceptor
A^0	Neutral acceptor
a_B	Bohr exciton radius
ALD	Atomic layer deposition
AM	Air mass
A_{nm}	Einstein coefficient for the spontaneous emission
AX	Acceptor-bound exciton
A^0X	Neutral acceptor-bound exciton
B	Bulk modulus
BL	Blue luminescence
B_{mn}	Einstein coefficient for absorption
B_{nm}	Einstein coefficient for stimulated emission
BX	Bound exciton
CB	Conduction band
C_N	Substitutional carbon on nitrogen sites
CL	Cathodoluminescence
CNT	Carbon nanotube
CVD	Chemical vapour deposition
D^-	Ionized donor
D^0	Neutral donor
DAP	Donor-acceptor pair
DX	Donor-bound exciton
DFT	Density-functional theory
DOS	Density of states
DSSC	Dye-sensitized solar cell
D^0X	Neutral donor-bound exciton
D^+X	Ionized donor-bound exciton
e-A	Free-to-bound (transition)
E_a	Activation energy
E_A	Acceptor binding energy
E_D	Donor binding energy
EDS	Energy dispersive spectroscopy
E_f	Fermi energy
E_{fm}	Fermi energy of the metal
E_{fs}	Fermi energy of the semiconductor
E_g	Bandgap energy
e-h	Electron-hole pair
EL	Electroluminescence
E_{loc}	Exciton localization energy
EPM	Empirical pseudopotential method
EPR	Electron paramagnetic resonance
EQE	External quantum efficiency
E_{xb}	Exciton binding energy
FF	Fill factor
FFT	Fast Fourier transform
FTO	Fluorine-doped tin oxide
FWHM	Full-width at half maximum
FX	Free exciton

GGA	Generalized-gradient approximation	m_e	Electron mass
GL	Green luminescence	m_e^*	Electron effective mass
h	Planck's constant	m_h	Hole mass
HAADF	High angle annular dark field	m_h^*	Hole effective mass
hcp	Hexagonal-close-packed	**MOCVD**	Metal-organic chemical vapour deposition
HOMO	Highest occupied molecular orbital	**MOVPE**	Metal-organic vapour-phase epitaxy
HRTEM	High resolution transmission electron microscopy	m_R	Reduced effective mass
HS	High spin	**MR**	Microrod
HVPE	Hydride vapour phase epitaxy	**MWCNT**	Multi-walled carbon nanotubes
IL	Ionoluminescence	N_A	Acceptor concentration
IPCE	Incident photon to current conversion efficiency	**NBE**	Near band edge
IQE	Internal quantum efficiency	N_D	Donor concentration
IR	Infrared	**ND**	Neutral density (filters)
I_s	Saturation current	**NIR**	Near infrared
I_{sc}	Short-circuit current	N_i	Interstitial nitrogen
J_s	Saturation current density	**NP**	Nanoparticle
J_{sc}	Short-circuit current density	**NW**	Nanowire
k	Wavevector	$\tilde{n}(\omega)$	Complex refraction index
k_B	Boltzmann's constant	O_i	Interstitial oxygen
LA	Longitudinal acoustic (phonon mode)	O_N	Substitutional nitrogen in oxygen sites
LAFD	Laser assisted flow deposition	**PAMBE**	Plasma-assisted molecular beam epitaxy
LATR	*Laboratório de Aceleradores e Tecnologias da Radiação*	***p***	Linear momentum
LD	Laser diode	**PIXE**	Particle-induced X-ray emission
LED	Light emitting diode	**PL**	Photoluminescence
LO	Longitudinal optical (phonon mode)	**PLD**	Pulsed laser deposition
LS	Low spin	**PLE**	Photoluminescence excitation
LT	Low temperature	**PMT**	Photomultiplier tube
LUMO	Lowest unoccupied molecular orbital	**PVD**	Physical vapour deposition
MB	Methylene blue	**QD**	Quantum dot
MBE	Molecular beam epitaxy	**QCSE**	Quantum confined stark effect

QW	Quantum well	V_{Ga}	Gallium vacancy
RB	Rose Bengal (dye)	V_H	Hall voltage
RBS	Rutherford backscattering spectrometry	V_N	Nitrogen vacancy
RBC/C	Rutherford backscattering spectrometry/ Channelling	V_O	Oxygen vacancy
RE	Rare-earth	V_{oc}	Open-circuit voltage
REI	Rare-earth isovalent (trap)	V_{Zn}	Zinc vacancy
RF	Radio-frequency	**VPE**	Vapour phase epitaxy
R_H	Rydberg constant	**VS**	Vapour-solid (growth mechanism)
RHEED	Reflection high energy electron diffraction	**XPS**	X-ray photoelectric spectroscopy
RL	Red luminescence	**XRD**	X-ray diffraction
R_S	Series resistance	**WZ**	Wurzite
RS	Rocksalt	**YL**	Yellow luminescence
R_{SH}	Shunt resistance	**Z**	Atomic number
RT	Room temperature	**ZB**	Zinc-blende
RTA	Rapid thermal annealing	Zn_i	Interstitial zinc
SAED	Selected area electron diffraction	Zn_O	Substitutional oxygen in zinc sites (Zn antisites)
SEM	Scanning electron microscopy	ε	Dielectric constant
Si_{Ga}	Substitutional silicon on gallium sites	$\varepsilon (\omega)$	Dielectric function
SK	Stranski-Krastanov (growth mode)	κ	Extinction coefficient
SL	Superlattice	λ	Wavelength
SX	Surface exciton	η	Efficiency
TA	Transversal acoustic (phonon mode)	μ_e	Electron mobility
TEM	Transmission electron microscopy	μ_h	Hole mobility
TES	Two electron satellite	μ_H	Hall mobility
TO	Transversal optical (phonon mode)	ρ	Resistivity
TRPL	Time-resolved photoluminescence	τ	Lifetime/decay time
UHV	Ultrahigh-vacuum	τ_n	Electron lifetime
UV	Ultraviolet	τ_p	Hole lifetime
VACNTS	Vertically aligned carbon nanotubes	τ_{nrad}	Nonradiative recombination lifetime
VB	Valence band	τ_{rad}	Radiative recombination lifetime

υ	Frequency
χ	Electrical susceptibility
ω	Angular frequency

Table of contents

Introduction **1**

I. Historical overview, motivation and objectives 1

II. Thesis organization 7

III. References 4

Chapter 1. Materials **11**

1.1. Crystalline structure 11

1.2. Electronic band structure 15

1.3. Lattice dynamics 19

1.4. Bandgap dependence with temperature 21

1.5. Bandgap dependence with composition 23

1.6. GaN and related nitrides 23

1.6.1. Impurities and native defects: *n*- and *p*-type GaN 27

1.6.2. Rare-earth doped nitrides 28

1.7. ZnO-based oxides 29

1.7.1. *n*- and *p*-type ZnO 31

1.7.2. ZnO common alloys 31

1.8. From bulk to nanostructures 33

1.9. References 36

Chapter 2. Growth techniques and samples **43**

2.1. Description of the samples 43

2.1.1. GaN and related nitrides 43

2.1.2. ZnO based oxides 49

2.1.2.1. ZnO 49

2.1.2.2. ZnO/CNTs composites 52

2.1.2.3. $Cd_xZn_{1-x}O/Mg_yZn_{1-y}O$ heterostructures 55
2.2. Growth methods 56
2.2.1. Laser assisted flow deposition (LAFD) 56
2.2.2. Epitaxial techniques 63
2.2.2.1. Molecular beam epitaxy (MBE) 63
2.2.2.2. Hydride vapour phase epitaxy (HVPE) 66
2.3. Doping 69
2.3.1. Ion implantation 69
2.4. References 72

Chapter 3. Morphological, structural and electrical characterization 77
3.1. Electron microscopy 77
3.1.1. Transmission electron microscopy (TEM) 78
3.1.2. Scanning electron microscopy (SEM) 84
3.2. X-ray diffraction (XRD) 86
3.3. Rutherford backscattering spectrometry (RBS) 88
3.4. Particle-induced X-ray emission (PIXE) 94
3.5. Raman spectroscopy 95
3.6. Hall Effect measurements 100
3.7. References 102

Chapter 4. Optical characterization 105
4.1. Transmittance, absorbance and diffuse reflectance 105
4.1.1. Theoretical background 105
4.1.2. Experimental setup 109
4.2. Photoluminescence spectroscopy 110
4.2.1. Theoretical background 110
4.2.2. PL excitation, time-resolved PL and lifetime measurements 117
4.2.3. Luminescence in GaN and ZnO 119
4.2.3.1. GaN 119
4.2.3.1. ZnO 120
4.2.4. Luminescent activators: RE^{3+} 122
4.2.4.1. Electronic States and Coupling Scheme 123
4.2.4.2. Crystal-field interaction and selection rules 127

4.2.4.3. Judd-Ofelt theory and transition probabilities 129
4.2.4.4. Excitation mechanisms in RE^{3+} doped semiconductors 130
4.2.4.4.1. Isovalent trap model 130
4.2.4.4.2. Dorenbos' model (charge transfer) 132
4.2.5. Experimental setup 137
4.3. References 141

Chapter 5. GaN and related nitrides: in pursuit of solid state lighting 147
5.1. Bulk GaN 147
5.2. Intentionally induced yellow luminescence in GaN nanowires 151
5.3. GaN nanowires implanted with Eu^{3+} 161
5.3.1. Low temperature PL 164
5.3.1.1. UV-Vis-NIR spectral range 164
5.3.1.2. Intra-4f^6 Eu^{3+} luminescence 166
5.3.2. Temperature dependency of the intraionic Eu^{3+} luminescence 171
5.3.3. RT luminescence studies 171
5.3.3.1. PLE and excitation energy dependent PL 171
5.3.3.2. Time resolved photoluminescence 174
5.4. GaN nanostructures implanted with Pr^{3+} 176
5.5. GaN and AlN layers co-implanted with Eu^{3+} and Pr^{3+} 186
5.6. $Al_xGa_{1-x}N$ layers implanted with Tb^{3+} and Tm^{3+} 193
5.6.1. Tb^{3+} 193
5.6.1.1. Structural characterization 194
5.6.1.1.1. Raman Spectroscopy 194
5.6.1.1.2. RBS/C measurements 195
5.6.1.2. Optical characterization 196
5.6.1.2.1. Low temperature PL 196
5.6.1.2.2. Temperature-dependent PL 200
5.6.1.2.3. RT PLE studies 205
5.6.1.2.4. Excitation model 206
5.6.1.2.5. RT kinetics: time resolved spectra and decay profiles 209
5.6.2. Tm^{3+} 211
5.6.2.1. Structural characterization 211
5.6.2.2. Photoluminescence studies 213

5.7. Conclusions 220
5.8. References 221

Chapter 6. Zinc oxide-based materials 229
6.1. ZnO produced by laser assisted flow deposition 229
6.1.1. Tetrapods and nanoparticles 230
6.1.2. ZnO microrods 246
6.2. ZnO grown in the presence of silver 260
6.3. ZnO/CNTs composites 267
6.3.1 VACNTs decorated with ZnO 268
6.3.2 ZnO/CNTs buckypapers 273
6.4. $Cd_xZn_{1-x}O/Mg_yZn_{1-y}O$ heterostructures 280
6.5. Conclusions 290
6.6. References 291

Chapter 7. Applications of LAFD grown ZnO 299
7.1. Solar cells 299
7.1.1. Theoretical principles of an ideal solar cell 300
7.1.2. Dye-sensitized solar cells (DSSC) 303
7.1.3. ZnO-based DSSCs fabrication 305
7.2. Photocatalysis 313
7.3. Conclusions 321
7.4. References 322

Conclusions and future work 325

Introduction

I. Historical overview, motivation and objectives

The invention of the first semiconductor transistor by the scientists of Bell Laboratories, in 1947, paved the way for the incredible development of the semiconductor industry, which has been growing at an unimaginable pace ever since, and fabricating faster, smaller, more powerful devices while manufacturing in larger volume and with lower costs [1,2]. Even though the very first semiconductor transistor was made from germanium (Ge), silicon (Si) rapidly established itself as the basis of the (micro-)electronic industry, mostly due to the presence of a natural oxide availability and electrical properties [1].

In addition to Si, gallium nitride (GaN) and zinc oxide (ZnO), including related compounds, are amongst the most studied semiconductors over the last decades. These materials constitute a novel class of semiconductors with unique characteristics in terms of crystallography, crystal growth, optical, electrical and magnetic properties, and so forth [3]. Moreover, these semiconductors have been under the spotlight for a long time because of the vast field of applications in materials science and industry, such as piezoelectric transducers, optical waveguides, gas sensors, photovoltaic devices, transparent conductive electrodes, and other optoelectronic applications [4–9]. Even though these semiconductors are considered "old", and are known to possess such unique properties for more than three decades, the interest was renewed due to the more advanced technology to fabricate novel electronic and optical devices, and the possibility to explore their new properties when produced at the nanoscale.

GaN was first synthesized in 1932 by Jonhson, and later by Juza and Hahn in 1938, motivated by the study of its crystal structure as part of a systematic study of many compounds. By that time, only small needles and platelets were produced [10,11]. It was only in 1969 that Maruska and Titjen [12] succeeded in growing GaN on sapphire substrates by chemical vapour deposition (CVD), and produced the first GaN epitaxial layers [10,11,13,14]. Their work was followed by pioneering growths of GaN by means of metalorganic vapour phase epitaxy (MOVPE) and molecular beam epitaxy (MBE), carried out by Manasevit *et al.* [15] in 1971 and by Yoshida *et al.* [16] in 1975, respectively [14]. However, it took more than 40 years to achieve a structural perfection sufficient to enable the production of efficient light-emitting devices [17]. The GaN samples fabricated at that time exhibited a poor crystal quality and a high *n*-type conductivity, although not intentionally doped [14]. Along this period it became clear that crystals with a high structural quality and with precise control of the

dopants concentration are required to enable both the investigation of the fundamental physical processes as well as for the development of efficient devices [17,18]. Nevertheless, early works using zinc-compensated samples led to the first demonstrations of blue, green, yellow and red metal-insulating-*n*-type GaN light emitting diodes (LEDs) [13,19].

By the end of the 1980s, two significant milestones led to the breakthrough for GaN technology: the introduction of AlN and GaN buffer layers deposited at low temperatures, which resulted in a significant reduction of the lattice mismatch problems, and the crucial demonstration of *p*-type conductivity [13,20,21]. The introduction of an intermediated AlN buffer layer was proposed by Amano *et al.* [22], aiming to improve the GaN crystal quality and obtain 2D layers as smooth as possible. The introduction of the buffer layer also resulted in a significant reduction of the background *n*-type carrier density in unintentionally doped GaN films [13,22,23]. It was the same team, Akasaki and Amano [23], that in 1989 achieved the first *p*-doped GaN using magnesium (Mg) as an acceptor impurity [13,14]. The III-nitride semiconductor family also triggered the interest of the scientific community due to the fact that these materials formed the first semiconductor system in which extended defects do not severely affect the optical properties of devices [13].

The research advances observed in the III-nitride materials and devices led to an "exponential" increase in activity directed towards electronic and optoelectronic applications [13]. Presently, GaN-based light emitters are widely used in optoelectronics and revolutionized the field of solid-state lighting [17,24,25]. The fabrication of highly efficient blue and green LEDs and laser diodes (LDs) boosted the development of GaN technology. Surprisingly, the robust and versatile properties of GaN have also made it a suitable candidate for high speed and high power electronics, cold cathode emitters, solar-blind ultraviolet (UV) light detectors, and microwave power electronics, thereby powering the expansion of GaN applications [21,26]. Furthermore, semiconductor nanowires (NWs) have opened a new era both in material research and device development, as their limited interfacial area with the substrate overcome the most fundamental limitation in epitaxy, *i.e.*, finding a suitable substrate for epitaxial film growth [17]. The development of GaN NWs started with the observation of the tendency of GaN to grow as coalesced columnar crystals [27], during the demand for the ideal film growth conditions [14]. After this discovery, the groups of Kishino [28] and Calleja [29] observed that GaN could form as nano-sized well separated columns under specific MBE growth conditions; this was the first demonstration of the production of self-assembled GaN NWs. However, it took 10 years after this discovery to awaken the interest of the research community in such nanostructures [14].

Although these III–V compounds already found their place in the field of light-emitting semiconductor devices like LEDs or LDs, GaN and the related group III-nitrides still face some problems, namely in what concerns the technology for large scale integration/growth and the costs of the raw materials. Therefore, there is a tendency to look for alternative materials. An obvious choice is the II–VI semiconductor ZnO, which has been extensively investigated for many decades [2]. In fact, ZnO has been commonly used in its polycrystalline form for more than a hundred years in a wide range of applications, like facial powders, sunscreens, catalysts, lubricant additives or paint pigmentation, and later as piezoelectric transducers or varistors [1,30–32]. The first reports on its characterization go back to 1935 [33]. In 1957, the New

Jersey Zinc Company published a book entitled “Zinc Oxide Rediscovered’’ to promote the material’s “frontier’’ properties (luminescent, catalytic, photoconductive, and photochemical properties) and gather illustrative applications [1]. The research in this semiconductor had its highpoint around the end of the 1970s and the beginning of the 1980s. The interest then faded away, mostly due to the difficulty in attain both *n*- and *p*-type conductivity, which is indispensable for the application of ZnO in the optoelectronic field [34].

The reawakening of the ZnO research started in the mid-1990s, with the appearance of a large number of publications and books, and a great number of conferences being held [4,34]. ZnO was rapidly emerging as a class of promising wide bandgap semiconductors, which, together with GaN and related nitrides, were revolutionizing an increasing number of applications and bringing significant contributes to vast areas of development [3]. The interest in ZnO was powered by its prospects in optoelectronics applications owing to its direct wide bandgap (3.3 eV at 300 K) [33]. Even with some optoelectronic applications overlapping with that of GaN, ZnO presented several advantages, namely the availability of fairly high-quality bulk single crystals, much simpler crystal-growth technology, resulting in a potentially lower cost for ZnO-based devices. Additionally, it is much less poisonous (in fact, it has been used as additive to human and animal food), it is cheaper, and vastly produced (more than 100 thousand tons per year) [2,33]. Other favourable aspects of ZnO include its broad chemistry, leading to many opportunities for wet chemical etching, its high energy radiation stability, and biocompatibility [1,33]. Moreover, ZnO has a similar crystal structure and close lattice parameters to that of GaN, making it a good candidate to be used as a substrate for epitaxial growth of high-quality GaN films [33,35,36]. Nevertheless, GaN possess a much more mature technology in terms of devices (viable *p*-type conductivity), as GaN-based high-performance electronic and optical devices are already commercialized [37,38].

The emphasis of this new active period of ZnO research was essentially promoted by topics that include the possibility to grow epitaxial layers, quantum wells, quantum dots, novel nanostructures with different shapes, ranging from nanowires to nanobelts and even nanosprings, new growth and doping techniques, with a special focus on application-related aspects [34,39]. The topic of *p*-doping remains the main drawback of this material. Despite all the progress that has been made, and incessant investigation driven by many groups, it is still extremely difficult to obtain high quality, stable, and reproducible *p*-type doping [2,33,39]. A better understanding of physical processes in ZnO is necessary in order to overcome this bottleneck, specifically regarding the nature of the residual *n*-type conductivity in undoped ZnO [33]. While stable ZnO *p*–*n* homojunctions are still difficult to attain, the advantages of ZnO are being explored and exploited by alternative methods such as heteroepitaxy, in which *p*–*n* heterostructures can be obtained by using *n*-type ZnO and other *p*-type materials, such as Si, GaN, aluminium gallium nitride (AlGaN), silicon carbide (SiC), gallium arsenide (GaAs), etc., while still using ZnO as the active layer [33,37]. The first ZnO-based hybrid heterostructure LED was fabricated in 1987 by Drapak [40], using copper oxide (Cu_2O) as *p*-type layer, and more works followed, even though with very low efficiencies and stability [37]. A decade ago, D. C. Look and co-authors [38] reported a compilation of several light emitting devices based on ZnO, predicting a good future for this semiconductor in the lighting industry. Though, the mismatch between the lattice parameters has limited the growth of heterostructures free of

defects, even when materials with similar lattice parameters are used, as is the case of *p*-GaN and 4H *p*-SiC [37]. Thus, there are still a number of important issues that need to be addressed, which require further investigation before ZnO can be used in commercial competitive applications. The nanostructures offer a path to a new generation of devices, providing research material to "feed" the ZnO investigation.

As mentioned, one of the most important applications of these semiconductors (GaN and ZnO) is related with the fabrication of solid-state lighting devices. In the last few decades, there has been a great demand to find visible light sources with high efficiency and low energy consumption and the progress in the field of LEDs has been, citing Schubert [41], *breathtaking*. Even so, this progress did not stop yet, great technological advances are still happening and there is much room for improvement. State-of-the-art LEDs are reliable, bright and efficient, which contrast enormously with other types of light source [41]. They appear as a more efficient and cheaper alternative to lighting based on incandescent and fluorescent lamps. Unlike the conventional light sources, these LED devices provide a direct transfer of electrical energy into light with minor losses [42]. In the vast ocean of energy consumption, a 100 W incandescent lamp might not be a key target for energy savings. However, lighting constitutes about 15% of all the energy consumed [43]. Not only does lighting consume a significant amount of energy, but it is also extremely inefficient. For instance, incandescent lights convert close to 5% of the electricity used into visible light, while fluorescent lamps are only around 20% efficient [24]. LEDs constitute a key component in nowadays technology. Indeed, LEDs have a tremendous impact in human life, residential and industrial sectors [44]. There are countless places where LEDs can be found, from small indicators in various household appliances to street lighting or traffic lights, passing through computer screens, mobile phones, mp3 players, among many others places. Furthermore, these devices are currently being used both for indoor and outdoor lighting. Not only LEDs are capable of higher efficiencies but they also last longer [45]. The average lifetime of a LED is greater than 30000 h, higher than the lifetimes of fluorescent (~ 12000 h) and incandescent (~ 1000 h) lamps, making them very attractive in the market [43,46].

The first LED emitting in the visible spectral region was based on a compound semiconductor alloy, gallium phosphorus arsenide (GaPAs), and exhibited a red emission with an extremely low external efficiency (< 1.0%) [47–49]. Years after, the development of aluminium gallium arsenide (AlGaAs) LEDs grown on GaAs substrates allowed these early red LEDs to exceed the luminous efficiency of a red-filtered incandescent lamp [47]. Today, the external efficiencies of red LEDs based on aluminium gallium indium phosphide (AlGaInP) are higher than 50%. Moreover, this alloy is also capable to emit in the orange, amber, and yellow spectral regions, although with lower efficiency [48]. These red LEDs are mainly used as indicator lights [50]. It took several decades to achieve efficient blue-emitting semiconductor material that could meet the requirements for illumination purposes, allowing a high output power. A great number of research was dedicated to semiconductors containing group II and VI elements, *e.g.*, zinc sulphide selenide (ZnSSe) or zinc telluride (ZnTe), in order to obtain blue LEDs, however the easy formation of structural defects diminished their lifetimes and their potential usefulness for commercial applications [50,51]. Finally, in 1993, Nakamura achieved the breakthrough for solid-state lighting by proving the successful use of indium gallium nitride

(InGaN) as a material in LEDs, providing bright emission from the green to the near-UV range [50–52]. The rapid progress of nitride semiconductor devices was astonishing in comparison with other conventional III-V compound semiconductor devices, as is the case of the ones made of AlGaAs, indium gallium arsenide phosphide (InGaAsP), or aluminium indium gallium phosphide (AlInGaP). For instance, the first InGaN-based high-brightness blue LED appear in the market in 1993, while InGaN-based quantum well structure high-brightness blue and green LEDs were introduced in 1995. As soon as 1999, these InGaN-based green and blue LEDs were already used in many applications, such as LED full-colour displays, traffic lights, and even white lighting sources [21]. Thus, GaN-based LEDs are already well established in the market [5], however some issues remain to be addressed, namely the efficient tuning of the electron-hole recombination through the whole visible spectrum with comparable emission intensities. Additionally, the demand for bright and stable white emitting LEDs has increased. Nowadays, white light generation is accomplished mainly by colour conversion of blue LEDs using yellow phosphors (typically YAG:Ce^{3+}), near-UV emitting LEDs plus red, green and blue phosphors, or by externally mixing the light from red, green and blue (RGB) LED chips, resulting in a perceived white emission [24,44,50]. The first two types are called phosphor-converted LEDs (pc-LEDs) and the white light is obtained using a two-step process where the emission from the LED excites the phosphors, given rise to the phosphor luminescence. The combination from the different emissions results in the observed white light. In addition to heating effects, phosphor-based white light emitters suffer from Stokes losses, non-radiative and optical losses, which constitute an important drawback of this technology [44,53,54]. The combination of RGB chips also presents some limitations, essentially due to the different efficiencies of the three colours and different degradation of the emitting materials over time [24]. Therefore, new solutions are still being pursuit in order to attain efficient and reliable white emitters without the use of phosphor converters or the combination of different materials, namely by the incorporation of different luminescence activators, as is the case of the rare-earth (RE) ions, in the same GaN-based LED structure. The combination of red, green and blue activators may offer an alternative strategy to achieve white light emission [55–57]. However, further testing and development are required.

Besides the demand for low energy consumption devices, new solutions for clean and renewable energy production are of paramount importance. The world is facing an energy crisis. Humanity continues to increase in number and, even though major efforts towards improving the efficiency of energy consumption have been employed, the overall *per capita* use of energy continues to increase, especially due to increasing economic growth rates, particularly in developing countries [58–60]. Consequently, the natural fossil fuel sources are becoming scarce and gradually more expensive. Thus, to mitigate the depletion of fossil fuels in the near future, as well as its hazardous influence in the environment (as is the case of global warming), renewable clean energy sources are inevitable and undoubtedly the answer to the upcoming times [59,61,62]. Solar power is clean and endlessly abundant. The total amount of solar radiation on Earth exceeds by a factor of 10 thousand, the entire global energy consumption [61]. In fact, the energy from sunlight striking the earth in one hour can meet the annual global energy consumption [58,62]. However, in order to effectively use this energy easy storage and transport is required, so it is necessary that the solar energy could be easily

transformed into electrical energy [58]. It is in this context that photovoltaic devices appear as fuel-free energy sources.

The photovoltaic effect was first recognized by E. Becquerel in 1839. Still, the first scientific paper on photovoltage using a semiconductor (selenium) was published only in 1877 [58]. The first demonstration of practical conversion of solar radiation into electric energy by use of a *p-n* junction type solar cell was reported in 1954 by researchers at the Bell Telephone Laboratories, evidencing an efficiency of 6% [58,63,64]. Up to now, the photovoltaic field has been dominated by solid-state junction devices, usually made of Si, benefiting from the well-established silicon technology and material availability resulting from the research and semiconductor industry [65]. However, the emergence of a third generation of cells, based for example on nanocrystalline materials, is now challenging this dominance [65]. Nevertheless, these new devices will only be sustainable if their production is not too expensive and if the materials required for their fabrication are abundant and environmentally safe [66]. In this sense, it is required the use of non-toxic and low cost material, as is the case of ZnO, which is a fairly abundant material and not harmful to the environment. Nowadays, the efficiency of the photovoltaic devices constitutes a crucial point. To overcome this limitation it is mandatory to have an effective control of all the properties (structural, electrical and optical) of the materials that composed the different parts of the devices [67,68]. In the research for new innovative photovoltaics technologies the use of nanostructured semiconductor materials has become a hot topic within science and engineering, bringing some potential benefits over traditional wafer or thin film based devices related mainly to cost, stronger light absorption and new charge separation mechanisms [62,67–70].

In the framework of the above historical contextualization, the present work can be divided into two major objectives. The first one is to contribute for the development of high efficient solid-state lighting devices, based on GaN and related nitrides, that can cover all the visible range. To date, III-nitride low dimensional structures are capable of light emission from the UV to the red; however green and red emission still suffer from low efficiencies [44,55]. One approach to overcome this limitation is the incorporation of efficient luminescent activators emitting in the desired spectral regions. In this sense, part of the present work is devoted to the optical study of different nitride structures intentionally implanted with trivalent RE ions, capable of tune the luminescent emission from the UV to the near-infrared by an adequate choice of the RE ion. The second objective is focused on the growth and characterization of ZnO micro/nanostructures, together with the development of a new growth technique designated by laser assisted flow deposition (LAFD). The control of the physical properties, together with reproducibility is a critical point when one seeks to incorporate these materials into devices. Thus, all samples were subject to morphological, structural and optical characterization, in order to establish a correlation between the physical properties and the growth parameters (*e.g.* laser power, the substrate nature, growth atmosphere, and growth time), as well as the influence of heat treatments in the nanosized structures. Furthermore, the final goal foresees the evaluation of the potential applications of the produced ZnO structures, namely in the fields of photocatalysis and photovoltaic devices.

II. Thesis organization

This thesis is organized in nine chapters, including introduction (the present one) and the one devoted to conclusions and future work. In the introduction part, the main objectives of this work were pointed out and the work was contextualized in the framework of the nowadays technological demands. **Chapter 1** is dedicated to the fundamental properties of the GaN and ZnO semiconductors, highlighting the similarity of these two semiconductors in a great number of fundamental aspects. Besides these semiconductors, also their common alloys were reviewed. This chapter ends with a brief reference to the differences that may occur in the material's properties between bulk and low dimensional samples. **Chapter 2** comprises a description of all the samples that were analysed during this work and the growth techniques that were employed to produce them. Among these techniques, relevance is given to the newly developed LAFD technique, with an especial attention to the growth mechanisms. **Chapter 3** is concerned with the experimental techniques used in the morphological, structural and electrical characterization of the samples. A short explanation of each of the used techniques is provided, together with the basic theoretical concepts involved. **Chapter 4** is devoted to the optical characterization, which constitutes the central core of this work. In this chapter, a detailed revision of the fundamental theoretical concepts regarding absorption and luminescence processes, together with the main optical centres frequently reported for the mentioned semiconductors is presented. Moreover, an especial emphasis is given to the trivalent RE ions' optical properties and excitation mechanisms when incorporated in nitride matrixes. The main results are reported in Chapters 5, 6 and 7. While the GaN and related nitrides are analysed in Chapter 5, Chapters 6 and 7 are dedicated to ZnO-based samples. Regarding the nitride samples, **Chapter 5** starts with the study of a GaN bulk sample, followed by the analysis of the induced/enhanced yellow luminescence in GaN NWs. The next sections focused on the evaluation of optical properties of the nitrides doped with trivalent RE ions. **Chapter 6** begins with the description of the properties of the ZnO structures grown by LAFD. It was the analysis presented in this chapter that allowed to understand the basic phenomena involved in the crystal's growth by LAFD, and consequently to develop the technique. Chapter 6 also includes the study of ZnO samples grown in the presence of silver, as well as ZnO/carbon nanotubes composites. The chapter ends with a brief study of the optical properties of the ZnO alloy with CdO, discussing bandgap engineering as a mean to tune the ZnO emission towards the visible range. Applications of the produced LAFD ZnO structures are reported in **Chapter 7**, showing the potential of this material to be employed in photocatalysis and in the fabrication of photovoltaic devices. Finally, the last part of this thesis covers the main conclusions of the present work and points out some prospects as future research lines.

III. References

1. C. Jagadish and S. J. Pearton, *Zinc Oxide Bulk, Thin Films and Nanostructures: Processing, Properties and Applications* (Elsevier, 2006).

2. C. F. Klingshirn, A. Waag, A. Hoffmann, and J. Geurts, *Zinc Oxide: From Fundamental Properties Towards Novel Applications* (Springer, 2010).

3. T. Yao and S.-K. Hong, *Oxide and Nitride Semiconductors* (Springer, 2009).

4. Z. C. Feng, *Handbook of Zinc Oxide and Related Materials: Volume Two, Devices and Nano-Engineering* (CRC Press, 2012).

5. U. Özgür, Huiyong Liu, Xing Li, Xianfeng Ni, and H. Morkoç, Proc. IEEE **98**, 1180 (2010).

6. U. Özgür, D. Hofstetter, and H. Morkoç, Proc. IEEE **98**, 1255 (2010).

7. N. O. V. Plank, I. Howard, A. Rao, M. W. B. Wilson, C. Ducati, R. S. Mane, J. S. Bendall, R. R. M. Louca, N. C. Greenham, H. Miura, R. H. Friend, H. J. Snaith, and M. E. Welland, J. Phys. Chem. C **113**, 18515 (2009).

8. B. Tian, T. J. Kempa, and C. M. Lieber, Chem. Soc. Rev. **38**, 16 (2008).

9. Y. Huang, X. Duan, Y. Cui, and C. M. Lieber, Nano Lett. **2**, 101 (2002).

10. H. Morkoç, *Nitride Semiconductors and Devices* (Springer, 1999).

11. J. I. Pankove and T. D. Moustakas, *Gallium-Nitride (GaN) I - Seminductores and Semimetals, Volume 50* (Academic Press, 1998).

12. H. P. Maruska, Appl. Phys. Lett. **15**, 327 (1969).

13. M. O. Manasreh, *III-Nitride Semiconductors: Electrical, Structural and Defects Properties: Electrical, Structural and Defects Properties* (Elsevier, 2000).

14. K. Hestroffer, Croissance et Caractérisation de Nanofils de GaN et D'hétérostructures Filaires de GaN/AlN, PhD thesis, Université de Grenoble, 2013.

15. H. Manasevit, J. Electrochem. Soc. **118**, 1971 (1971).

16. S. Yoshida, S. Misawa, and A. Itoh, Appl. Phys. Lett. **26**, 461 (1975).

17. C. Hauswald, Dynamics of Free and Bound Excitons in GaN Nanowires: Origin of the Nonradiative Recombination Channel, PhD thesis, Humboldt-Universität zu Berlin, 2014.

18. B. Shklovskii and A. Efros, *Electronic Properties of Doped Semiconductors, Volume 45 of Solid-State Sciences* (Springer Verlag, 1984).

19. J. I. Pankove, J. Lumin. **7**, 114 (1973).

20. Z. C. Feng, *III-Nitride Devices and Nanoengineering* (Imperial College Press, 2008).

21. J. H. Edgar, *Properties, Processing and Applications of Gallium Nitride and Related Semiconductors* (EMIS Datareviews Series, n°23, An INSPEC publication, 1999).

22. H. Amano, N. Sawaki, I. Akasaki, and Y. Toyoda, Appl. Phys. Lett. **48**, 353 (1986).

23. H. Amano, M. Kito, K. Hiramatsu, and I. Akasaki, Jpn. J. Appl. Phys. **28**, L2112 (1989).

24. C. J. Humphreys, MRS Bull **33**, 459 (2008).

25. S. Pimputkar, J. S. Speck, S. P. DenBaars, and S. Nakamura, Nat. Photonics **3**, 180 (2009).

26. S. J. Pearton, C. R. Abernathy, and F. Ren, *Gallium Nitride Processing for Electronics, Sensors and Spintronics* (Springer Verlag, 2006).

27. K. Hiramatsu, S. Itoh, H. Amano, I. Akasaki, N. Kuwano, T. Shiraishi, and K. Oki, J. Cryst. Growth **115**, 628 (1991).

28. M. Yoshizawa, A. Kikuchi, M. Mori, N. Fujita, and K. Kishino, Jpn. J. Appl. Phys. **36**, L459 (1997).

29. M. A. Sanchez-Garcia, E. Calleja, E. Monroy, F. J. Sanchez, F. Calle, E. Muñoz, and R. Beresford, J. Cryst. Growth **183**, 23 (1998).

30. M. Michio, *Non-Linear Resistor, US3503029 A* (United States Patent Office, 1970).

31. D. C. Look, Mater. Sci. Eng. B **80**, 383 (2001).

32. T. Shiosaki, Appl. Phys. Lett. **25**, 10 (1974).

33. U. Özgür, Y. I. Alivov, C. Liu, A. Teke, M. A. Reshchikov, S. Doğan, V. Avrutin, S.-J. Cho, and H. Morkoç, J. Appl. Phys. **98**, 041301 (2005).

34. C. Klingshirn, Phys. Status Solidi **244**, 3027 (2007).

35. X. Gu, M. A. Reshchikov, A. Teke, D. Johnstone, H. Morkoç, B. Nemeth, and J. Nause, Appl. Phys. Lett. **84**, 2268 (2004).

36. F. Hamdani, M. Yeadon, D. J. Smith, H. Tang, W. Kim, A. Salvador, A. E. Botchkarev, J. M. Gibson, A. Y. Polyakov, M. Skowronski, and H. Morkoç, J. Appl. Phys. **83**, 983 (1998).

37. U. Özgür, D. Hofstetter, and H. Morkoç, Proc. IEEE **98**, 1255 (2010).

38. D. Look, B. Claflin, Y. Alivov, and S. Park, Phys. Status Solidi **201**, 2203 (2004).

39. L. Schmidt-Mende and J. L. MacManus-Driscoll, Mater. Today **10**, 40 (2007).

40. I. T. Drapak, Semiconductors **2**, 624 (1968).

41. E. F. Schubert, *Light-Emitting Diodes* (Cambridge University Press, 2006).

42. M. R. Krames, O. B. Shchekin, R. Mueller-Mach, G. O. Mueller, Ling Zhou, G. Harbers, and M. G. Craford, J. Disp. Technol. **3**, 160 (2007).

43. G. Zissis and P. Bertoldi, *JRC Science and Policy Reports- 2014 Update on the Status of LED Market* (2014).

44. N. Ben Sedrine, T. C. Esteves, J. Rodrigues, L. Rino, M. R. Correia, M. C. Sequeira, A. J. Neves, E. Alves, M. Bockowski, P. R. Edwards, K. P. O'Donnell, K. Lorenz, and T. Monteiro, Sci. Rep. **5**, 13739 (2015).

45. P. Patel, MRS Bull. **36**, 678 (2011).

46. K. Müllen and U. Scherf, *Organic Light-Emitting Devices: Synthesis, Properties, and Applications* (Wiley-VCH, 2006).

47. D. A. Steigerwald, J. C. Bhat, D. Collins, R. M. Fletcher, M. O. Holcomb, M. J. Ludowise, P. S. Martin, and S. L. Rudaz, IEEE J. Sel. Top. Quantum Electron. **8**, 310 (2002).

48. E. F. Schubert, T. Gessmann, and J. K. Kim, in *Kirk-Othmer Encycl. Chem. Technol.* (John Wiley & Sons, Inc., 2005).

49. N. Holonyak Jr and S. Bevacqua, Appl. Phys. Lett. **1**, 82 (1962).

50. C. R. Ronda, *Luminescence: From Theory to Applications* (Wiley-VCH, 2008).

51. F. A. Ponce and D. P. Bour, Nature **386**, 351 (1997).

52. S. Nakamura, S. J. Pearton, and G. Fasol, *The Blue Laser Diode: The Complete Story* (Springer Verlag, 2000).

53. M. Huang and L. Yang, Photonics Technol. Lett. IEEE **25**, 1317 (2013).

54. T. Tamura, T. Setomoto, and T. Taguchi, J. Lumin. **87-89**, 1180 (2000).

55. K. P. O'Donnell, M. Auf der Maur, A. Di Carlo, K. Lorenz, and the SORBET consortium, Phys. Status Solidi - Rapid Res. Lett. **6**, 49 (2012).

56. A. J. Steckl, J. C. Heikenfeld, M. J. Garter, C. C. Baker, and R. Jones, IEEE J. Sel. Top. Quantum Electron. **8**, 749 (2002).

57. K. P. O'Donnell, *Rare-Earth Doped III-Nitrides for Optoelectronic and Spintronic Applications* (Springer, 2009).

58. R. C. Neville, *Solar Energy Conversion: The Solar Cell* (Elsevier Scientific Publishing Co., 1978).

59. P. Newell, J. Phillips, and D. Mulvaney, *Human Development Research Papers, Pursuing Clean Energy Equitably* (United Nations Development Programme, 2011).

60. IPCC 2007, *Contribution of Working Group III to the Fourth Assessment Report of the Intergovernmental Panel on Climate Change, 2007* (Cambridge University Press, 2007).

61. M. Toivola, J. Halme, K. Miettunen, K. Aitola, and P. D. Lund, Int. J. Energy Res. **33**, 1145 (2009).

62. K.-Q. Peng and S.-T. Lee, Adv. Mater. **23**, 198 (2011).

63. D. Chapin, C. Fuller, and G. Pearson, J. Appl. Phys. **25**, 67 (1954).

64. B. Li, L. Wang, B. Kang, P. Wang, and Y. Qiu, Sol. Energy Mater. Sol. Cells **90**, 549 (2006).

65. M. Grätzel and G. Michael, J. Photochem. Photobiol. C Photochem. Rev. **4**, 145 (2003).

66. F. Vasilis, Renew. Sustain. Energy Rev. **13**, 2746 (2009).

67. Grätzel M, Curr. Opin. Colloid Interface Sci. **4**, 314 (1999).

68. A. Hagfeldt, G. Boschloo, L. Sun, L. Kloo, and H. Pettersson, Chem. Rev. **110**, 6595 (2010).

69. J. Zhu and Y. Cui, Nat. Mater. **9**, 183 (2010).

70. A. I. Hochbaum and P. Yang, Chem. Rev. **110**, 527 (2010).

Chapter 1. Materials

It is well known that Si-based electronic devices cannot tolerate very high temperatures and chemically aggressive environments. Consequently, the research on new materials that could easily work in those conditions is of extreme importance [1]. Materials like ZnO or GaN and their alloys became the subject of intense investigation due to their potential properties, highlighting their large bandgap, high electron mobility and high breakdown field strength, making them suitable for high power, high temperature electronic devices and short wavelength optoelectronics [2,3]. Moreover, these semiconductors have ideal bandgaps for optical applications, specifically for solid state lighting [4]. The growing need for higher-density optical storage and full colour display technologies led to an important development of these materials [1].

Before the incorporation of these materials in any technologies it is important to have an adequate knowledge of their fundamental properties. ZnO and GaN share a number of important characteristics, namely direct bandgap, crystalline structure, electron mobility, radiation resistance, high exciton binding energy, amongst others [2]. A revision of the most important properties of the above mentioned materials is given in the following sections.

1.1. Crystalline structure

ZnO, GaN, and the other group III nitrides [*e.g.* aluminium nitride (AlN) and indium nitride (InN)], are most commonly found in the hexagonal wurtzite (WZ) structure, which belongs to the $P6_3mc$ (C^4_{6v}) spatial group. These materials can also be found in other crystalline structures like zinc-blende (ZB) [$F\bar{4}3M$ (T^2_d) spatial group] or rocksalt (RS) [$Fm3M$ (O^5_h) spatial group], although these structures are less common [3,5,6]. The schematic representation of these structures is depicted in Figure 1-1.

The WZ stacking of {0001} planes is AaBbAaBb... along [0001] direction, while in ZB the stacking sequence of {001} planes is AaBcCcAaBbCc... along the [111] axis. The [111] direction of the ZB structure coincides with the WZ [0001] direction (see Figure 1-1a and b). While the WZ structure primitive cell includes two cation-anion pairs, the ZB contains only one, but in both cases the cation atom is tetrahedrally surrounded by four anion atoms and vice-versa (coordination number 4) [5,7]. Due to the tetrahedral coordination both WZ and ZB structures show virtually identical short range order. If slight deviations from ideal spherical closed packing

were neglected in WZ, each atom would be tetrahedrally surrounded by four nearest neighbours with the same bond distance as in ZB structure. Also, the twelve next-nearest neighbours are at the same distance in both structures. The significant differences appear only for the third next-nearest neighbours [8]. A fault in the stacking sequence can convert one structure into the other [8].

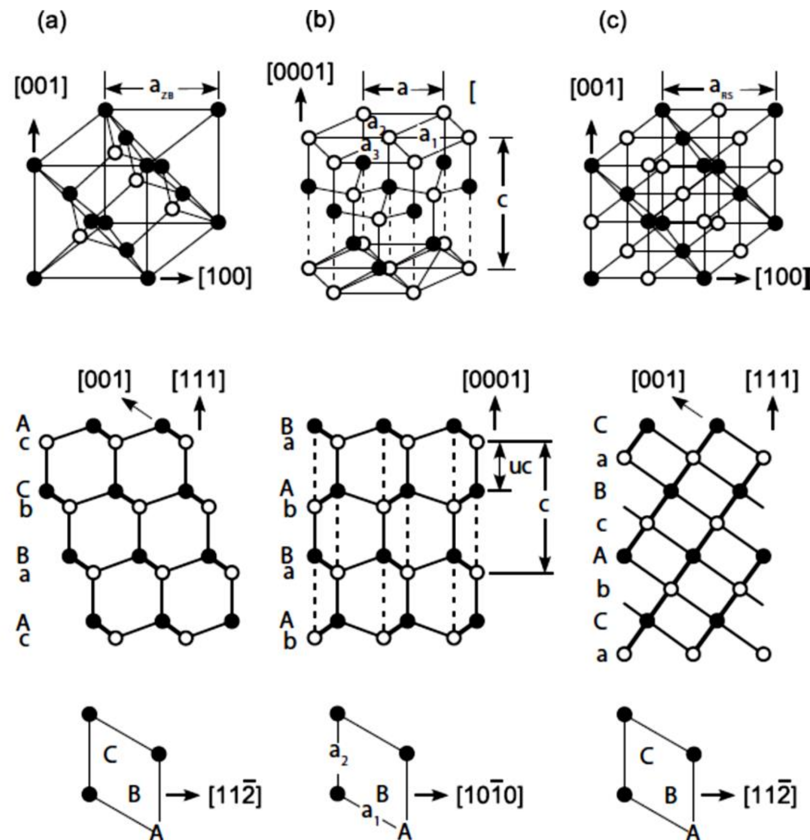

Figure 1-1 – Crystalline structures of (a) ZB, (b) WZ and (c) RS structures. The closed circles represent the cation, while the open ones correspond to the anions and the solid lines indicate the projection of two bonds. Reproduced from reference [3].

The ideal WZ structure has a hexagonal unit cell with two lattice parameters, *a* and *c*, and the relation between them is given by $c/a=\sqrt{8/3}$ =1.633. It is comprised by two interpenetrating hexagonal-close-packed (hcp) sub-lattices, each consisting of one type of atom displaced with respect to each other (in the case of the binary compounds) along the threefold *c*-axis by the amount of *u* (*u*=3/8=0.375), being *u* an internal parameter (in ideal wurtzite structure). *uc* corresponds to the length of the bonds parallel to [0001] and *u* is given in units of *c* [3,7]. The internal parameter *u* can be seen as a measure of the amount by which each atom is displaced with respect to the next, along the *c*-axis [2]. The dash lines that are present in Figure 1-1b for the WZ structure connect pairs of cations and anions along the [0001] direction. These pairs are attracted to each other by the electrostatic force. It is believed that this electrostatic force is responsible for the higher stability of the WZ structure over the ZB [3]. In real crystals, the length of these bonds (in the WZ structure) tends to be shorter than the ideal value and the ratio *c/a* is smaller than 1.633. In fact, it is easier to shorten the interlayer distances A-b and B-a than that of A-a and B-b, by introducing a deformation angle between the bond pairs [3]. The ideal

arrangement of the WZ structure can be modified in two ways: changing the *c/a* ratio or the *u* value [9]. There is a strong correlation between this *u* parameter and the ratio *c/a*: decreasing the later, the first one increases. Owing to this relationship, the four tetrahedral distances are kept nearly constant through a distortion of the tetrahedral angles, due to long-range polar interactions [7]. The bond lengths would be equal if $u=(1/3)(a^2/c^2)+1/4$ [9]. The differences of the electronegativities are correlated with *c/a* ratio values. The compounds that exhibit higher differences in the electronegativities of their constituents are the ones that show a larger deviation from the ideal *c/a* ratio. Only the WZ structures with value of *c/a* lower than the ideal one are stable [9]. Values for the lattice parameters, *c/a* ratios and the internal parameter *u* for some crystals are displayed in Table 1-1. In the case of GaN, the value of the *c/a* ratio is very close to the ideal one. Thus, all four Ga-N distances possess nearly equal length and bond angles, in very good agreement with the expected values for a regular tetrahedron [9].

Table 1-1 – Lattice constants *a, c* and internal parameter *u* of the WZ structure. Lattice constants a_{ZB} and a_{RS} for the ZB and RS structures, respectively, are also listed. All the units are given in Å [3].

Semiconductor	a	c	u	c/a	a_{ZB}	a_{RS}
ZnO	3.250	5.204	0.382	1.601	4.60	4.271
CdO	3.660	5.860	0.350	1.601		4.770
AlN	3.112	4.982	0.380	1.601	4.38	
GaN	3.189	5.185	0.376	1.626	4.50	
InN	3.545	5.703	0.377	1.609	4.98	

The RS structure (Figure 1-1c) is the least frequent of the three structures and can be obtained when high pressures are applied [6,7]. It is a cubic structure and each atom has six nearest neighbours positioned at the corners of an octahedron (coordination number 6). The structure consists of two interpenetrating face centred cubic (fcc) sub-lattices, each with one type of atom, displaced along the cube edge by $a_c/2$, with a_c being the cubic lattice parameter [6].

None of the mentioned structures have a centre of inversion, which means that describing an atom's position on a closed packed plane with coordinates (*x*,*y*,*z*) it is not the same position as (-*x*,-*y*,-*z*). The absence of inversion symmetry leads to crystallographic polarity in the crystal [8]. Like so, these structures show polar crystal planes, i.e., planes with either all group II/III atoms or all oxygen/nitrogen atoms. These polar faces are generally perpendicular to the *c*-axis (which is the most common crystallographic growth orientation for these materials) and are known to possess different chemical and physical properties [2,6,9]. For the cubic structures (ZB and RS) the closed-packed {111} and $\{\bar{1}\bar{1}\bar{1}\}$ planes are the main polar planes, whereas in the case of WZ, major polar planes corresponds to the basal or {0001} and $\{000\bar{1}\}$ planes [6,8]. There are other secondary polar planes that are not frequently referred since they are not exposed in macroscopic faceting of crystallites [8]. For instance, in GaN, a basal surface should be either Ga- or N-faced (Figure 1-2). It is commonly accepted that the N-face is chemically active, while the Ga-face is inert [9,10]. Ga-faced stands for Ga on the top position of the {0001} bilayer, corresponding to [0001] polarity [10]. As mentioned before, the (0001) and $(000\bar{1})$ surfaces of GaN are inequivalent

(the [0001] direction it is assumed to be given by a vector pointing from a Ga atom to a nearest-neighbour N atom) [10]. A similar feature is found in ZnO where the two polar faces correspond to Zn-face (0001) and O-face ($10\bar{1}0$) oriented along the *c*-axis [2].

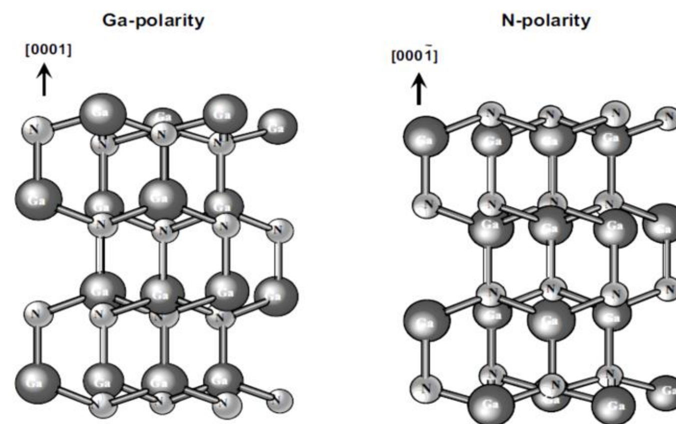

Figure 1-2 – Representation of the different polarities of WZ GaN, showing Ga and N- faces [11].

The polar orientation determines the direction of the spontaneous polarization vector as well as the type of charge induced at the surface of the crystal or its interface with other materials. Since the spontaneous polarization constitutes a non-zero dipole moment per unit volume in the crystal, an internal electrical field is present [12]. Several properties of the material exhibit polarity dependence, like the growth, etching, defect generation and piezoelectricity. For instance, WZ layers epitaxially grown on hexagonal (0001) substrates show piezoelectric properties when subjected to residual (thermal) stress [8]. The large piezoelectric polarization present in strained crystals combined with the spontaneous polarization are expected, among others, to have a strong influence in the electric behaviour of a device and are crucial parameters to take into account during the device fabrication [12]. Figure 1-3 depicts the spontaneous polarization versus the molar fraction in the three ternary nitride alloys [11].

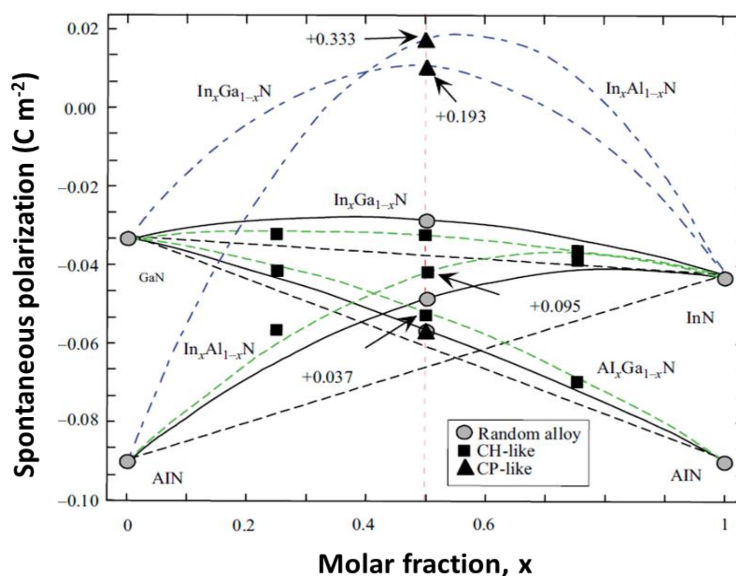

Figure 1-3 – Spontaneous polarization versus molar fraction in the three ternary nitride alloys. The black dashed lines represent the data calculated using Vegard's law. CH denotes chalcopyrite-like structures and CP corresponds to the CuPt structure. Adapted from reference [11].

1.2. Electronic band structure

Direct bandgap semiconductors possess the maximum of the valence band (VB) and the minimum of the conduction band (CB) at the same **k** value of the reciprocal space (or k-space), where **k** is the wavevector of the plane wave. The extremes of both bands are considered to be at **k**=0, which corresponds to the Γ point of the first Brillouin zone [13]. The electrons in the CB tend to settle at its minimum energy which is at **k**=0. Similarly, holes in the VB tend to gather at the uppermost VB energy [14]. This constitutes a very important feature, since a direct optical transition can be drawn vertically between the two allowed bands with conservation of the crystal momentum (or **k**) [13–15]. This direct absorption process involves the absorption of a photon by the crystal and a subsequent creation of an electron and a hole. The two charged carriers may then recombine radiatively without the creation or annihilation of a phonon [15]. This type of recombination has a higher probability transition in comparison with the one occurring in indirect semiconductors (phonon mediated transitions to warranty the conservation laws) making the direct bandgap semiconductors more suitable for applications in optoelectronic devices like is the case of LEDs or lasers [14].

The first Brillouin zone of a crystal with the WZ structure is a hexagonal prism with a height of *2π/c* [3]. Figure 1-4 shows a schematic representation of this Brillouin zone with the high symmetry points that are commonly used to describe the electronic band structure of semiconductors, E(**k**). The electronic band structure of WZ ZnO, GaN and AlN are displayed in Figure 1-5, and Figure 1-6a and b, respectively. In these diagrams the zero energy corresponds to the VB maximum. In the case of ZnO the band structure was obtained using density-functional theory (DFT) calculations within the generalized-gradient (GGA) approximation including self-interaction corrections into the GGA exchange correlation potentials (GGA+U). For AlN and GaN, the band structure was calculated using the empirical pseudopotential method (EPM). In both cases the spin-orbit interactions were neglected.

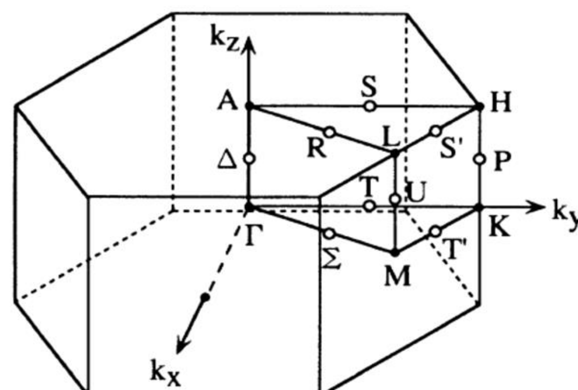

Figure 1-4 – Representation of the first Brillouin zone for the WZ-type structure [16].

In ZnO, GaN and AlN, the degeneracy of CB and VB are rather analogous. The CB is nondegenerate and the VB is split by the combination of crystal field and spin-orbit interactions [2,17]. The lowest CB band consists mainly of *s*-like states, while the vicinity of the VB maximum is essentially comprised by *p*-like states [2,18]. Each perturbation (crystal field and spin-orbit) leads

to degeneracy lifting. The spin-orbit coupling is proportional to $\boldsymbol{l.s} = (\boldsymbol{j}^2\text{-}\boldsymbol{l}^2\text{-}\boldsymbol{s}^2)/2$ and splits the energy levels according to the total angular momentum $\boldsymbol{j}$, where $\boldsymbol{l}$ and $\boldsymbol{s}$ are the total orbital and spin angular momenta, respectively, and $\boldsymbol{j}=\boldsymbol{l}+\boldsymbol{s}$ [3,19]. The eigenvalue of the square of the total angular momentum, $\boldsymbol{j}^2$, is given by $j(j+1)$, where for a given l, $j=l\pm1/2$ [19]. $\boldsymbol{l}$ and $\boldsymbol{s}$ are not separately conserved but the total angular momentum $\boldsymbol{j}$ is [20]. The crystal field is induced by the hexagonal symmetry of the WZ structure [16]. A schematic representation of the influence of these components in the splitting of the VB is depicted in Figure 1-7.

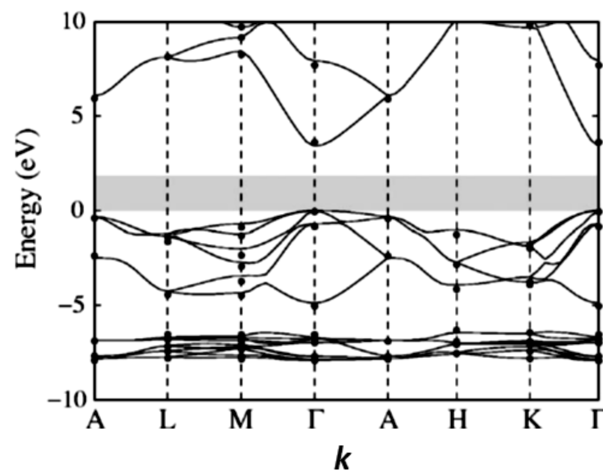

Figure 1-5 – Electronic band structure of WZ ZnO obtained from DFT calculations within the GGA+U method. Spin-orbit interaction was neglected in the calculations. Reprinted from reference [21].

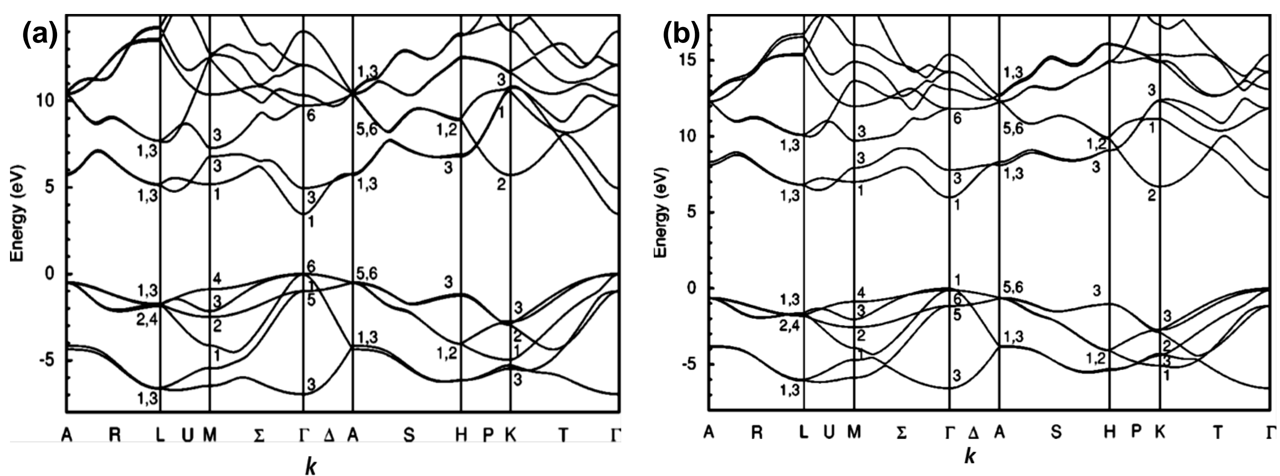

Figure 1-6 – Band structure of WZ (a) GaN and (b) AlN obtained from EPM. Spin-orbit interaction was neglected in the calculations. The small numbers that appear in the diagrams correspond to the symmetry of the bands in the respective high-symmetry points. Reprinted from reference [22].

In the case of ZnO, the first two CB states are strongly Zn localized and match to empty *s* states. The VB is *p*-like and their highest states correspond to $2p^6$ bonding states of the oxygen atoms in the ZnO lattice, which are constructed out of appropriate linear combinations of products of *p*-like (p_x, p_y and p_z -like) orbitals with spin functions [2,23–25]. When the crystal field interaction is considered, the VB is splitted into a nondegenerate band with Γ_1 symmetry and a doublet Γ_5 band [26]. The Γ_1 singlet is fundamentally p_z-like and the double degenerate band with Γ_5 symmetry is a p_x, p_y-like state [26]. *x* and *y* correspond to the directions perpendicular to the

hexagonal *c*-axis and *z* to the *c* direction [27]. The doublet corresponds to the upper sub-band and the singlet to the lower one. The first study on the fine structure nature of the VB maximum in ZnO was performed by D.G. Thomas in 1960 [27]. This author assumed that the crystal field splitting was large when compared with the splitting due to the spin-orbit interaction. When the spin-orbit interaction is introduced and combined with the action of the crystal field, the CB, which is nondegenerate, exhibits Γ_7 symmetry whereas the degeneracy of the VB at the Γ point is reduced into three sub-bands denominated *A*, *B* and *C* (independently of their symmetry character), as can be seen in Figure 1-8 [23,24]. *A* is the top valence band, followed by *B,* and *C* the lower one [2,23]. It has been assumed in a great number of reports [23,28,29] that, for ZnO, the upper VB has Γ_9 symmetry while the remaining ones exhibit Γ_7 symmetry. However, the symmetry of the top VB has been subject of intense discussion over the years and there is no unanimity in the literature. Recent works of Wagner *et al.* [24] and Lambrecht *et al.* [26] provided strong evidence that the upper VB shows, in fact, Γ_7 symmetry. These results are in agreement with those reported by Thomas [27]. In his paper, the symmetry of the *A*, *B* and *C* bands is reported to be Γ_7, Γ_9 and Γ_7, respectively (Figure 1-8). Reflection measurements at low temperatures performed by this author revealed three sharp peaks that arise from direct exciton transitions at **k**=0, corresponding to radiative recombination of an electron and a hole from each VB, and thus denominated free excitons (FX) *A*, *B* and *C*.

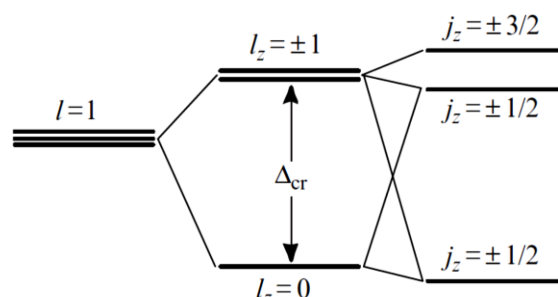

Figure 1-7 – Schematic energy diagram of a possible splitting of the upper VB of the WZ structure. The crystal field and the spin-orbit interactions are considered as small perturbations to the perfect crystal Hamiltonian. Adapted from reference [3].

Since the minimum of the CB exhibits *s*-like character and top VB shows *p*-like, the angular momentum changes by unity at **k**=0, resulting in allowed transitions. The exciton transitions are dependent of the light polarization. Transitions from *A* and *B* appear with light polarized perpendicularly to the *c*-axis (E⊥*c*), while C can be seen with parallel polarization (E∥*c*) [27]. When the spin-orbit effect is added, a mixing of the three sub-bands is observed, however with a weak strength, since the crystal field action dominates. Therefore, explaining why, in reflection measurements, peaks from *A* and *B* appear only for E⊥*c* and the *C* peak is the one visible for E∥*c*. Nevertheless, absorption experiments showed that the weak mixing of excitons *A* and *C*, leads to a faintly observation of exciton *A* in E∥*c* configuration, since it acquires a slight mixture of p_z-like character. Thus, following group theory considerations, exciton *B* should only occur for E⊥*c*, meaning that the correspondent band remains purely p_x, p_y-like, leading to the Γ_9 assignment for band *B* and Γ_7 for band *A* [26,27]. Theoretical calculations gave rise to a negative spin-orbit splitting for the upper VBs, coming from the contribution of Zn *3d* bands. The maximum of the VB is an antibonding combination of anion *p*-like states and cation *d*-like states, resulting in a

negative contribution of the atomic *d*-orbit to the effective spin-orbit splitting [26]. By inspection of the wavefunctions using first-principles calculations, Lambrecht *et al.* [26] found that the highest VB (*A*) contains p_z and *s* components, corroborating the attributions of the Γ_7 symmetry, while the second state (*B*) does not exhibit any contribution from p_z or *s* components, only pure p_x, p_y, as reported by Thomas [27].

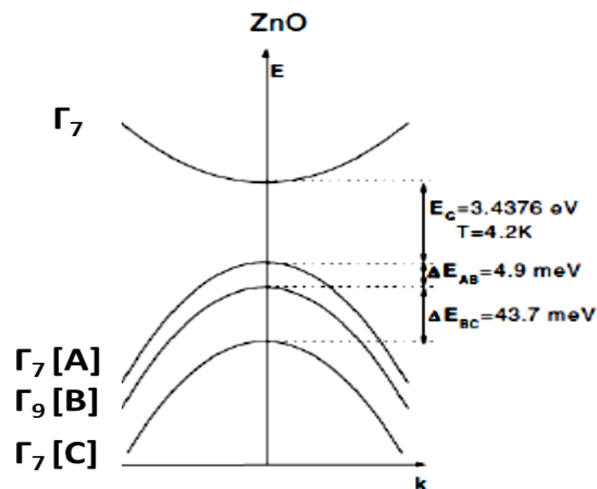

Figure 1-8 – Schematic diagram of the band structure near the high-symmetry Γ point (k=0) for ZnO. The crystal field and spin-orbit interaction lead to the splitting of the VB in three sub-bands. The values present for the energy difference between the sub-band were obtained at 4.2 K. Adapted from reference [2].

According to the selection rules, $\Gamma_7 \rightarrow \Gamma_9$ transitions are allowed when light is oriented in a way that $E \perp c$ while the $\Gamma_7 \rightarrow \Gamma_7$ transitions are permitted for both polarizations (perpendicular and parallel) [23].

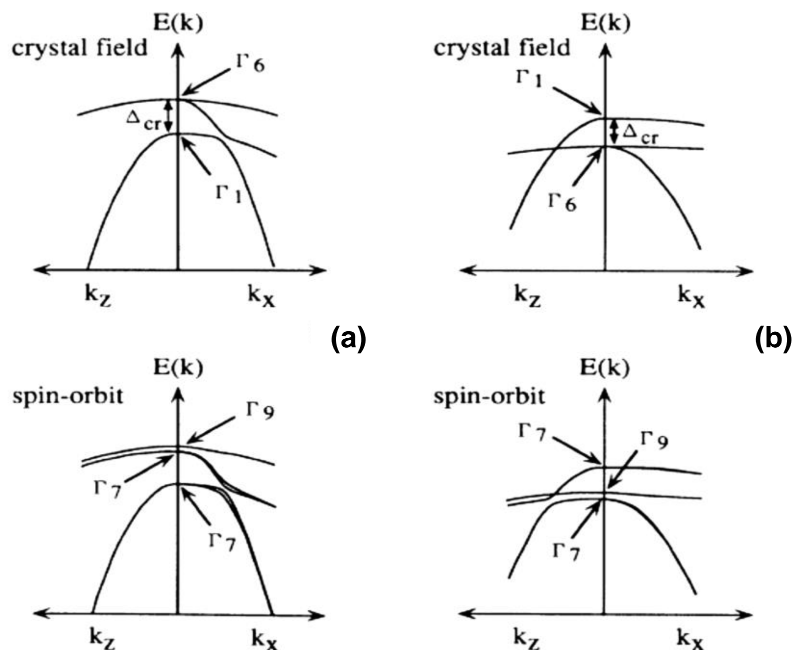

Figure 1-9 – Schematic band structures near the high-symmetry Γ point (a) GaN and (b) AlN under the action of only crystal field (upper images) and under the action of both crystal field and spin-orbit interactions (lower images) [16].

Figure 1-9 illustrates the VB splitting under the action of crystal field and spin-orbit interaction for GaN (Figure 1-9a) and AlN (Figure 1-9b). In GaN, the VB arises from N *2s*, *2p* and Ga *4s* and *4p* states. In the neighbourhood of the VB maximum the contribution is made almost exclusively from the N *2p* states [16]. Like in the case of ZnO, the VB splits into three sub-bands *A*, *B* and *C* (from the top to the bottom) due to the combined effect of the crystal field spin-orbit coupling. The main features in this energy region are very similar in GaN and AlN, though, the levels order around the VB maximum are different (Figure 1-6 and Figure 1-9). The difference resides in the irreducible representations for each band. For GaN, considering just the crystal field, the upper band is twofold-degenerated with a Γ_6 symmetry and the lowest energy band is nondegenerated and labelled Γ_1 (like in ZnO). An opposite order of the bands is observed for AlN where $\Gamma_1 > \Gamma_6$ (Figure 1-9) [16]. The wavefunctions of Γ_6 also transform like p_x and p_y-like states. The introduction of the spin-orbit contribution requires the use of the double group notation, so that Γ_1 becomes Γ_7 and Γ_6 splits into Γ_9 and Γ_7 (by this order) [16,30]. As seen in Figure 1-9, the hole effective masses of the three uppermost VBs are strongly dependent of the **k** wavevector [30].

1.3. Lattice dynamics

As mentioned before, WZ structure exhibit four atoms (or two formula units) per primitive cell, with all atoms occupying C_{3v} sites [31]. The number of atoms in the unit cell, N = 4, leads to 3N = 12 vibration eigenmodes [32]. Thus, twelve phonon modes at the zone centre **k** ~ 0 (Γ-point) are expected: one longitudinal acoustic (LA), two transverse acoustic (TA), three longitudinal optical (LO), and six transverse optical (TO) [2,33,34]. The classifications of the phonons into transverse (T) or longitudinal (L) depend on their displacements regarding the direction of the wavevector: T modes are perpendicular while L modes are parallel to the wavevector [35]. Since the WZ crystal structure belongs to the C^4_{6v} spatial group, the group theory predicts eight sets of phonon modes with irreducible representation $\Gamma = \Gamma_{ac} + \Gamma_{opt} = 2A_1 + 2E_1 + 2B_1 + 2E_2$, where Γ_{ac} and Γ_{opt} stand for acoustic and optical modes, respectively [5,34,36]. A_1 and B_1 are nondegenerate modes while E_1 and E_2 are doubly degenerated [34]. One set of A_1 and E_1 modes correspond to acoustic phonons, whereas the remaining ones are optical modes, $\Gamma_{opt} = A_1 + E_1 + 2B_1 + 2E_2$ [5,6]. Among these vibrational modes, only the A_1, E_1 and E_2 are Raman active. A_1 and E_1 are also infrared (IR) active and B_1 are neither Raman or IR active and are called silent modes [5,6].

Figure 1-10 illustrates the atomic displacement of the optical modes present in the WZ structure. B_1 and E_2 modes are labelled with a superscript H or L meaning that they belong to the higher or lower frequency branch of the phonon dispersion curves. The phonon dispersion curves of ZnO, GaN and AlN are shown in Figure 1-11 and Figure 1-12. A_1 and B_1 modes give atomic displacements along the *c*-axis, while perpendicular atomic displacements are accounted for the E_1 and E_2 modes [5]. The A_1 mode consists of an oscillation of the rigid sub-lattices, cation vs. anion. Since this is a polar bond, the sub-lattice displacement leads to an oscillating polarization. In the case of the B_1 modes, it is possible to consider that one sub-lattice is at rest and in the other one the neighbouring atoms move opposite to each other. However the B_1 modes do not induce polarization, since the displacements of the ions within each sub-lattice sum up to zero [32]. The

E_1 mode is an oscillation of rigid sub-lattices and an oscillating polarization is induced. On the other hand, the E_2 modes are non-polar due to the mutual compensation of the displacement vectors within each sub-lattice [32].

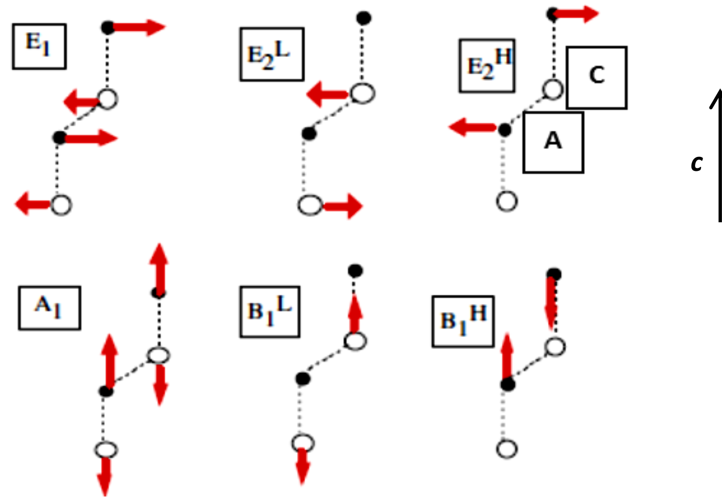

Figure 1-10 – Atomic displacement of optical phonon modes in WZ structure. C and A stand for cation and anion, respectively, while the H and the L superscripts correspond to high and low frequency modes, respectively. Adapted from reference [5].

Since the WZ structure is an anisotropic noncentrosymmetric crystal, the crystal field leads to the polarity-induced splitting of the optical E_1 mode at Γ into TO and LO branches due to the macroscopic electric field [34]. A similar effect happens for the optical A_1 mode, showing different frequencies near the Γ-point, which depend on the symmetry direction [34]. Thus, the A_1 and E_2 polar modes exhibit different energies for the LO and TO polarizations [6]. In both cases, the LO phonon frequency exceeds that of the TO mode. Due to this frequency split of polar modes into LO and TO, a higher number of eigenfrequency values occurs in comparison to those predicted by group theory [32].

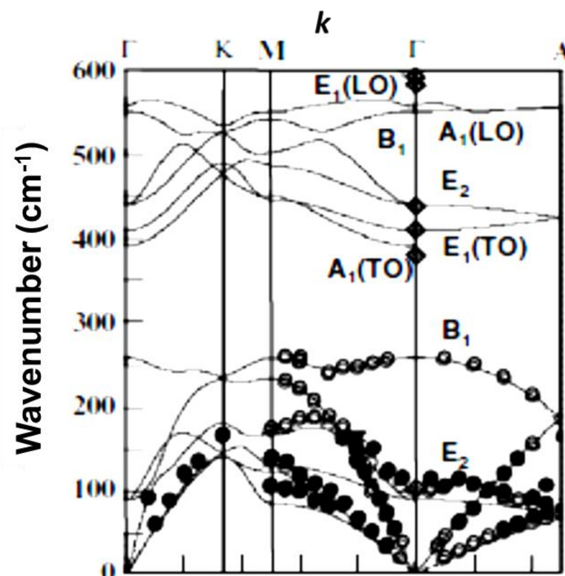

Figure 1-11 – Phonon dispersion curves for WZ ZnO [32].

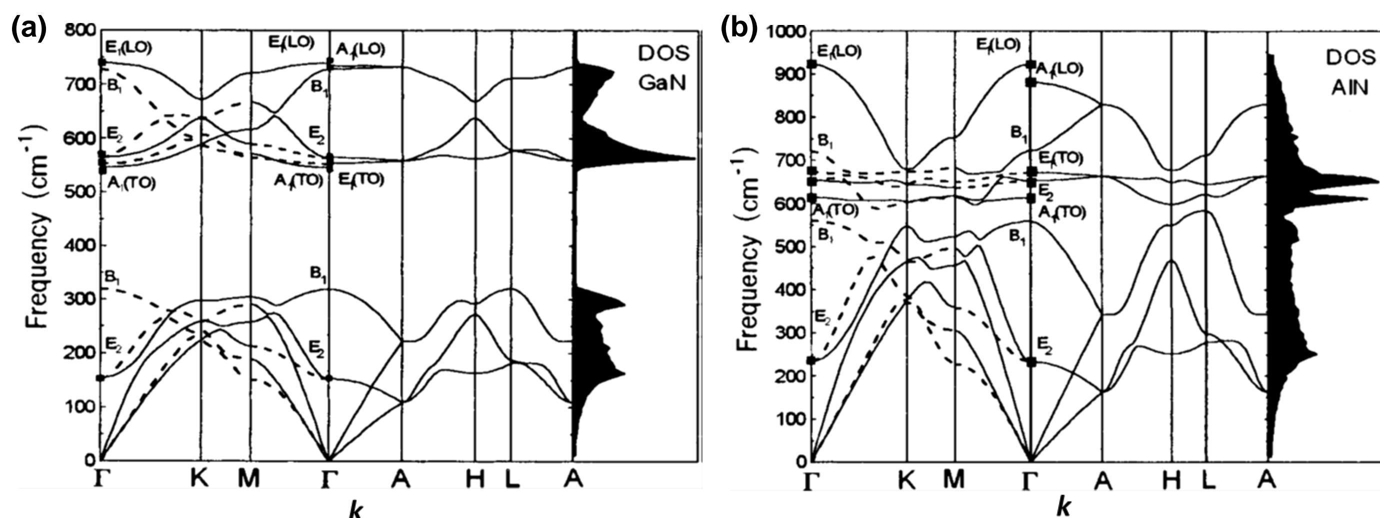

Figure 1-12 – Phonon dispersion curves and correspondent density of states for WZ GaN (a) and AlN (b), respectively [36].

In the case of ideal alloys, namely in the $Al_xGa_{1-x}N$ ($0 \leq x \leq 1$) alloy, N atoms are estimated to occupy all the anion sites, while Al and Ga atoms share the cation sites in a random way. This randomness leads to a broadening of the phonon spectral resonances, since the Raman spectra are sensitive to the lattice disorder. Moreover, relaxation of the Raman selection rules may occur, resulting in the observation of additional unexpected peaks. Furthermore, a shift in the phonon frequency with the change in the AlN/GaN molar fraction is expected to take place due to the change of the average reduced mass of the anion and cation pairs. Two types of characteristic behaviour are often observed. One in which the phonon frequency at $k \sim 0$ varies continuously from the mode frequency of one binary compound to that of the other one and appears with approximately constant strength, called one-mode-type behaviour. The so-called two-mode type behaviour corresponds to the one where, for an intermediate alloy, two sets of phonon frequencies are observed at frequencies close to those of the binary material and the strength of each mode is almost proportional to the percentage of each component [5].

Up to now, only the first-order Raman scattering was discussed. In this case, wavevector conservation limits the phonons involved in first-order Raman scattering to those with $\mathbf{k} \sim 0$, however phonons from the entire Brillouin zone participate in second-order Raman scattering. Consequently, second-order spectra can exhibit feature-rich structures, determined by the phonon density of states (DOS) and by the selection rules of the two-phonon scattering processes [37]. Details about these processes can be found in references [37,38].

1.4. Bandgap dependence with temperature

Along the years, there has been a constant seeking for an accurate physical model to fit the experimental results obtained for the bandgap energy (E_g) behaviour with increasing temperature observed for the majority of semiconductor materials.

Most semiconductors exhibits E_g temperature dependence up to room temperature (RT) and higher temperatures due to the cumulative effects of thermal lattice expansion and electron-phonon interaction [39–41]. The first contribution can be accounted for combining the volume dependence of band energies with the thermal-expansion coefficients [41]. This temperature dependence is frequently given by an empirical expression, called "Varshni formula" [42]

$$E_g(T) = E_g(T=0) - \frac{\alpha T^2}{T+\beta}, \qquad \textbf{Eq. 1-1}$$

where α and β are the Varshni parameters characteristic of each material, which can be obtained from fittings of experimental data [43]. α is given in meV/K units and β in K [3]. The α parameter is related with the gap entropy in the limit T→∞ and β is assumed to be comparable with the Debye temperature, Θ_D, for a given material [40]. Despite the reasonable fits obtained with this formula for the temperature shrinkage of the semiconductor gaps, some issues have been raised in the literature regarding this purely empirical relation, since it lacks any theoretical foundation and fails for the high and low temperature limits [40,44]. For instance, when temperatures approach to zero a quadratic temperature dependence is assumed while theory requires a T^4 dependence, as stated by Cardona [43,45], taking into account the Debye's model of the asymptotic behaviour of the specific heat, which is exact in the limit T→0 [45,46]. Thus, a modification of the Varshni equation can be written as [43,47]

$$E_g(T) = E_g(T=0) - \frac{\alpha T^4}{(T+\beta)^3}, \qquad \textbf{Eq. 1-2}$$

which reproduces the correct low and high temperature behaviours of the gap, meaning that the gap energy is proportional to T^4 for T→0 and proportional to T for T→∞ [43]. Fernández *et al.* [47] stated that the tendency is proportional to T^4 for temperatures below 80 K due to the electron-phonon scattering, while for higher temperatures the trend is dominated by the lattice thermal expansion, leading to a linear behaviour. However, it is worth to mention that there is no consistent connection between the parameter β and a feature that describes the electron-phonon interaction or the Debye temperature [40,44].

Viña *et al.* [41] proposed a semi-empirical model based on the Bose-Einstein statistics that provides a good fitting of the temperature dependence of E_g and the estimation of the Debye temperature, Θ_D [39,40]. This model was then adapted by Pässler *et al.* [40,44] who suggested the following expression:

$$E_g(T) = E_g(T=0) - \frac{\alpha \Theta}{\exp(\Theta/T) - 1}, \qquad \textbf{Eq. 1-3}$$

where Θ is the effective phonon temperature and $\Theta_D = 3/2\Theta$ [39,40]. Yet, this equation fails to accurately describe the behaviour with temperature in the cryogenic region [40]. More complex models to describe the bandgap behaviour with the temperature over a wide range of temperatures were proposed by Pässler [40,44,48] and Cardona [43].

1.5. Bandgap dependence with composition

The bandgap of ideal alloys (solid solutions) has been estimated by using an empirical rule, known as "Vegard's law". According to this expression, at a constant temperature, there is a linear relationship between the crystal lattice constants and the concentration of each component [49,50]. However, a great number of metallic alloys was found not to obey to this rule [49]. Usually, the deviations can be overcome considering a simple parabolic function of the composition [51]. The bandgap energy of an alloy $A_xB_{1-x}C$ can be well described by a quadratic function of *x*, given by [3]

$$E_g(x) = (1-x)E_g^{BC} + xE_g^{AC} - bx(1-x), \quad \textbf{Eq. 1-4}$$

where *b* is the coefficient of the parabolic term in the phenomenological expression, designated as bowing parameter [52]. The bowing parameters depend on the difference in electronegativities of the binaries [53]. The bowing parameters for the III-nitride ternary alloys are listed in Table 1-2.

Table 1-2 – Bowing parameters for the III-nitride ternary alloys [3].

Alloy	*b*
$In_xGa_{1-x}N$	1.6 ± 0.2
$Al_xGa_{1-x}N$	0.7 ± 0.1
$In_xAl_{1-x}N$	3.4 x ± 1.2

1.6. GaN and related nitrides

The group-III nitrides, including GaN, AlN, InN and their alloys, establish an important family of compounds for technological applications, being considered some of the most important semiconductors, in addition to Si [11]. The alloying of these materials enables the coverage of bandgap energies in the spectral range from UV to infrared (IR), with unique properties particularly suitable for modern electronic and optoelectronic applications [54]. The combination of these elements constitutes important components to be used in LED structures, LDs and detectors [55]. Extraordinary breakthroughs have been attained in the latest years in the field of high-power and high-brightness blue-green-white LEDs [9]. The importance of these materials to the lighting industry was confirmed by the attribution of 2014 Physics Nobel Prize to Isamu Akasaki, Hiroshi Amano and Shuji Nakamura for the development of efficient blue LEDs.

InN possesses a bandgap energy of ~ 0.7 eV [56], emitting in the IR spectral region, while GaN has a bandgap energy of ~ 3.4 eV [57] and emits in the near-UV range, at the other end of the visible spectrum. By mixing these two binaries, in theory, it is possible to produce luminescent emission at any colour in the visible spectrum, as well as IR and near-UV [58]. The colour tuning from near-UV to IR can be achieved by increasing the In content in the $In_xGa_{1-x}N$ alloy [59]. For instance, blue and green light can be produced with InN molar fractions of 0.1 and 0.2, respectively. However, in practice, it is found that the efficiency of the light emission from

$In_xGa_{1-x}N$ alloy is low for high indium contents, mainly due to problems related with In segregation. This means that, although $In_xGa_{1-x}N$ emits a strong blue light, its green light emission is less intense, and its red light emission is weaker [58]. On the other hand, $Al_xGa_{1-x}N$ compounds offer the possibility to tune the E_g between 3.4 and 6.2 eV, with increasing AlN molar fraction [60]. Therefore, these group-III nitrides can be applied in the fabrication of optical devices that are active at wavelengths ranging from the IR to deep UV [30]. The bandgap variation as a function of the lattice constant for the ternary and quaternary alloys of these semiconductors is depicted in Figure 1-13.

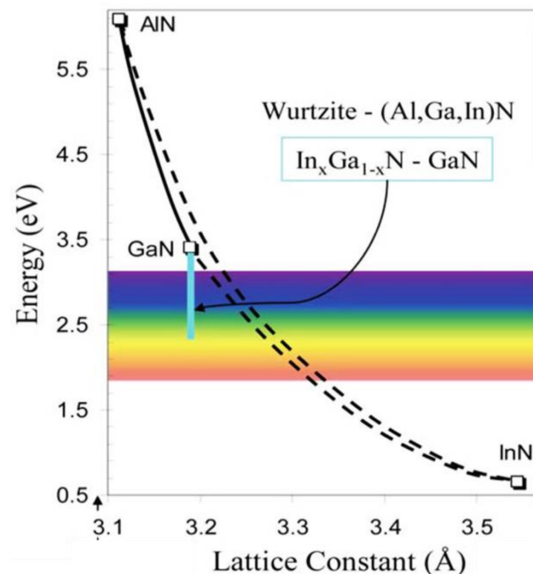

Figure 1-13 – Energy bandgap versus lattice constant for wurtzite III-nitride systems. Adapted from [61].

Besides the wide bandgap, one of the main advantages of the nitrides over other wide bandgap semiconductors is the strength of their chemical bonds. This makes these materials extremely stable and resistant to degradation under severe conditions, as in the case of high electric currents and intense light illumination, like the one encountered in the active regions of the LED devices. Due to their chemical inertia, III-nitrides also possess large avalanche breakdown fields, high thermal conductivities and large high-field electron drift velocities [62]. The strong chemical bonds are also responsible for the difficulty in introducing dislocations once the material is grown, which represents a benefit regarding other materials, since these defects constitute one of the main mechanisms of device degradation [63]. However, the lack of adequate substrates for the nitrides growth makes the fabrication of reproducible and reliable samples very challenging [64]. This low availability of appropriate substrates is mostly driven by the necessary high growth temperatures, and only substrates that are stable at such elevated temperatures can be used [63]. The two most used substrates are sapphire and SiC. Due to differences in the materials lattice parameters and in their linear thermal expansion rates, the growth often requires the use of buffer layers to accommodate the structure, minimizing the lattice mismatch and reducing the strain in the growing sample.

The lattice constants, binding energy and decomposition temperatures of group III-nitrides have a strong influence in the thermal stability of nitride-based devices [10]. For instance, these nitrides are known to thermally dissociate well below their melting point with the loss of nitrogen.

The most stable of the three is AlN, while InN is the least stable, thermally dissociating at temperatures higher than 600 °C [62]. For GaN, nitrogen diffusion out of the sample was observed at ~ 800 °C [65]. Even though the decomposition mechanisms are not well understood, the thermal stability of these materials is critical for its applications which may use high-power or high-temperature, as well as high-temperature processing [30].

GaN has been studied far more extensively than the other group III-nitrides. One of the most significant properties of this semiconductor is its luminescence. Luminescence spectra of GaN frequently exhibit a well-structured and defined near band-edge (NBE) emission, sometimes followed by broad visible bands due to deep defect levels whose origin is still not very clear nowadays. Details regarding these important luminescent features of GaN will be briefly discussed in Chapter 4. Some of the GaN main important properties (for bulk crystals) are displayed in Table 1-3. It is important to mention that most of the properties also depend on the growth method and quality of the samples. For instance, the thermal properties depend, to a considerable extent, on the growth conditions, stoichiometry, free carriers, strains and on the concentration and type of impurities and/or defects present [10,11]. This fact compromises a good assessment to the sample's characteristics. Nevertheless, due to the crystal structure anisotropy the thermal expansion is greatly dependent on the crystalline growth direction. The linear expansion coefficients for both *c* and *a* directions, assuming that this quantity remains the same for different temperatures, are listed in Table 1-3. However, this is not entirely true and a temperature dependence of the thermal expansion with temperature was observed, as is illustrated in Figure 1-14 [11]. In the case of the epitaxial layers, it is important to keep in mind that the lattice parameter dependence with temperature is also affected by the substrates nature, since the materials show different thermal expansion coefficients [11].

Table 1-3 – Properties of WZ GaN (bulk) [66,67]**.**

Property	**Value**
Volumetric density	6.15 g cm^{-3}
Stable crystalline phase at RT	wurtzite
Melting point	> 2500 °C
Thermal conductivity	> 2.1 W m^{-1} K^{-1}
Linear expansion coefficient	a_0 = 5.59x10^{-6} °C^{-1} c_0 =3.17x10^{-6} °C^{-1}
Static dielectric constant	8.9-9.5
Bandgap at RT	3.4 eV (direct)
Exciton binding energy	25 meV
Electron effective mass	0.20 m_0
Electron Hall mobility at RT for low *n*-type conductivity	~ 1000 cm^2 V^{-1}s^{-1}
Hole effective mass	0.59 m_0
Hole Hall mobility at RT for low *p*-type conductivity	≤ 200 cm^2 V^{-1}s^{-1}

The bulk modulus (*B*), inverse of compressibility, is an important parameter to evaluate the mechanical properties of the material. In the case of WZ GaN values around 245 GPa have been predicted and experimentally measured [6,11,68]. The Young's modulus was estimated to be ~ 150 GPa [6,11,69].

In 1994, Chin *et al.* [70] performed an accurate prediction of the carrier concentration dependence of the bulk mobility [71], still used nowadays. The electron mobility was calculated by the variational principle for different carrier concentrations and compensation ratios, over a wide range of temperatures. It was found that the maximum electron mobility was obtained between 100 K and 200 K. A value higher than 6000 $cm^2 V^{-1}s^{-1}$ was estimated for 77 K, while at 300 K, and taking into account the low electron concentration (~ 10^{16} cm^{-3}), an electron mobility of 1000 $cm^2 V^{-1}s^{-1}$ was calculated. The increase of the electron concentration or the compensation level results in a reduction of the mobility [70]. A larger number of experimental measurements of mobility have been carried out since then, and different values have been reported [6,72–74], mainly due to differences in the quality of the grown materials. In 2003, Mnatsakanov *et al.* [75] developed a semi-empirical analytical model to describe the carrier mobility behaviour in a wide range of temperatures (50 to 1000 K) and for electron concentrations between 10^{14} e 10^{19} cm^{-3}, resulting in a very adequate model to fit the experimental values. Calculations using this model led to an electron mobility concentration value, at RT, similar to the one obtained by Chin *et al.*, while a value of 170 $cm^2 V^{-1}s^{-1}$ was estimated for the hole mobility.

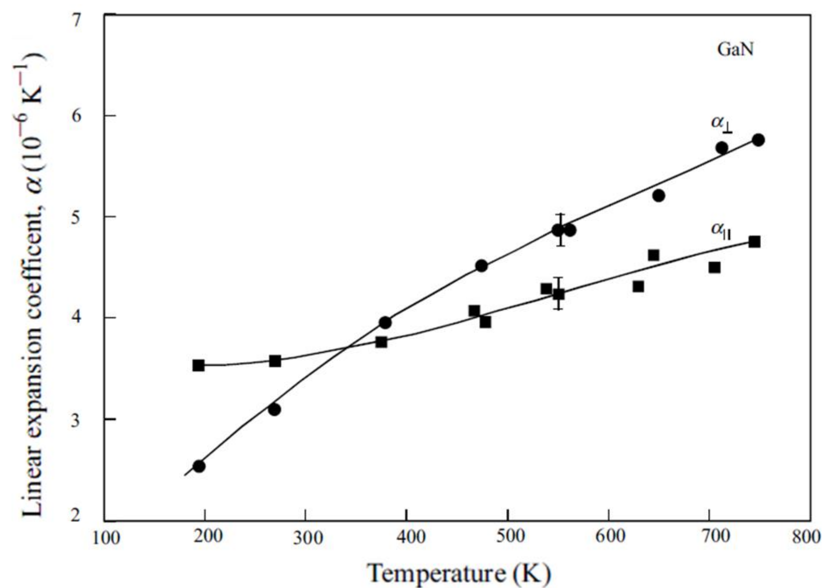

Figure 1-14 – Temperature dependence of the thermal linear expansion coefficient for basal plane (α‖), corresponding to the *a* parameter, and out of the basal plane (α⊥), corresponding to c parameter, directions, for GaN [11].

Dielectric properties measurements of the WZ GaN have been reported since the 60's. For instance, the refractive index has been studied in the visible and IR spectral range (from 370 to ~ 2000 nm), where the imaginary part of dielectric function is assumed to be negligible and can be disregarded [6]. Due to the anisotropy of the WZ structure, GaN possesses a uniaxial birefringence, which is reflected in the existence of two different refractive indices for

polarization parallel and perpendicular to the *c* axis. The difference in the refractive indices for E⊥*c* and E∥*c* was found to be about 1.5 % at 500 nm [6,76]. In 1971, Ejder [76] determined the refractive index from transmission and reflexion measurements, at 300 K, for different energies: values of 2.67 at 3.38 eV and 2.33 at 1.0 eV were found when E⊥*c*.

1.6.1. Impurities and native defects: *n*- and *p*-type GaN

A precise knowledge of the impurities and native defects present in the materials is of paramount importance when electronic and/or optoelectronic applications are in mind. Namely, for the fabrication of bipolar devices, like in the case of LEDs, *n*- and *p*-type samples are needed, while pure undoped materials with high mobility are required for various transistor and detector structures [77]. Shallow dopants are intentionally introduced to control the type (i.e., *n*- vs *p*-type) and magnitude of the electrical conductivity [78]. Impurities and native defects are known to affect the electrical conductivity of semiconductors. Most of the nominal undoped GaN samples present *n*-type conductivity, which is frequently attributed to unintentional incorporation of dopant impurities, as it is the case of residual oxygen introduced during the growth process, or nitrogen vacancies (V_N) [18,77,79–81]. However, some experiments suggested that the background electron concentration could not be due to V_N, since this defect forms a level at ~ 64 meV below the CB edge [81], while the thermal activation energy of electrons from the donor levels to the CB edge in unintentionally doped GaN is typically around 25 - 35 meV [77,78,81]. Look *et al.* [81] showed, for the first time, the presence of interstitial nitrogen (N_I) as an acceptor. Conductivity engineering in GaN can be accomplished by the introduction of donor species such as Si, O and Ge or with acceptors such as Mg, Zn and Be [77]. Si is the most common specimen used for *n*-type doping in III-nitrides [78], which makes the phenomena that rule the Si incorporation in GaN and its properties well understood. This element incorporates effectively on substitutional Ga sites of GaN, leading to the formation of a shallow donor with activation energies between 12 and 16 meV, depending on Si concentration and the concentration of the compensating acceptors (if present) [77,78]. Si-doped samples often exhibit higher electron concentrations and lower electron mobility than the non-intentionally doped ones [78]. For instance, values of about 250 $cm^2V^{-1}s^{-1}$ at RT were reported for Si-doped samples [77]. The achievement of *p*-type doping has been a demanding task, mostly due to the difficulty in growing high quality samples and to compensate the background *n*-type character. It was only in 1989 that Amano *et al.* [82], and later in 1992 Nakamura *et al.* [83], accomplished the *p*-type of GaN with Mg [78]. As in the case of the Si, the Mg is introduced in Ga substitutional sites [78]. One of the problems with Mg-doping lies in the fact that Mg forms a “quasi-shallow” acceptor level, located nearly 165 - 200 meV above the VB edge, which results in a poor acceptor ionization at RT [77,78,84]. Since the hole concentration that can be achieved at RT are usually at least two orders of magnitude below the acceptor concentration, high Mg concentrations are required to produce *p*-type samples to be used in optoelectronic devices, like LEDs [77,78].

Among the native defects, gallium and nitrogen vacancies (V_{Ga} and V_N) are the dominant ones, depending on growth conditions, namely the richness of N and Ga [11]. The V_{Ga} exhibits a low formation energy when the Fermi level is close to the bottom of the CB, thus being favoured in

n-type GaN [11]. These vacancies are mobile in a wide range of temperatures (including the ones of growth and annealing) and can form complexes with donor impurities, particularly with oxygen in N sites ($V_{Ga}O_N$) or V_N ($V_{Ga}V_N$) [11,18].

1.6.2. Rare-earth doped nitrides

RE-doped semiconductors have been widely investigated as a class of materials with promising properties, especially in the optoelectronic field. Their main advantage resides on the remarkable atomic-like intra-$4f^n$ transitions of the trivalent charged ions [85–87]. GaN and its alloys together with the other III-nitrides have been widely used as a host for the incorporation of luminescent activators such as the RE ions. As evidenced by Favennec *et al.* [88], there is a direct correlation between the bandgap of the host material and the optical efficiency of the RE^{3+} emission, in a way that the luminescence thermal quenching decreases with increasing bandgap energy, making wide bandgap materials appropriate for the RE^{3+} optical activation [89,90]. Among the main advantages of GaN as a host for RE ions, the high transparency makes it suitable for the incorporation of ladder-like RE^{3+} electronic energy levels, which promotes the optical activation of the ion with reduced luminescence thermal quenching [86,91,92]. Furthermore, the trivalent charge state is easily achieved since RE are preferentially located on the isovalent Ga-site [93]. The ion lattice location is very important because the local symmetry in which the ion is placed dictates the features of the ion-related emission, *e.g.* spectral shape and luminescence intensity. Thus, the lattice location engineering can be used as a way to maximise the RE emission intensity [94]. In the case of WZ GaN, and as referred above, the RE ions tend to be located on Ga sites where the lack of inversion symmetry gives rise to strong ligand fields, increasing the probability of the $4f \rightarrow 4f$ intraionic transitions and resulting in the optical activation of the ions [65,95–98]. This substitutional incorporation coupled with the strong bonds of the GaN lattice, allows high doping levels (up to ~ 3-5 at%) with preservation of the optically active RE dopants [95]. Though, care must be taken regarding the doping doses, since these ions show some tendency to agglomerate for high dopant concentrations [94]. In the revision work of O'Donnell and Hourahine [94] on RE incorporation in GaN, the authors state that site location of the ions in the lattice seems to be independent of the doping method. Moreover, they showed that although the Ga substitutional site (or slightly displaced) is the more frequent lattice site for RE incorporation, site multiplicity is very common for RE-doped GaN samples.

Considerable research efforts have been devoted to this field in the last decades [87,96,99–104]. The initial works were focused on optical communications and were conducted on Er-doped GaN emitting at 1.54 µm [77]. Despite Er ions were the first RE^{3+} implanted in GaN in 1976 [105], the Er-related 1.54 µm luminescence was only reported after 1994 [106,107]. Latter, a great number of reports concerning samples doped with other RE ions, such as Eu^{3+} [108], Tm^{3+} [109] or Pr^{3+} [110], demonstrated the tunability of the emission to the visible spectra range [77]. For instance, recently, an efficient red LED based on Eu-doped GaN host was reported [111]. Another example is the work of Hommerich *et al.* [112] where GaN samples were grown by molecular beam epitaxy and doped *in-situ* with trivalent Er, Eu and Tm ions. Intraionic transitions in the red, green and blue were observed using above bandgap excitation for the samples doped with Eu^{3+},

Er^{3+} and Tm^{3+}, respectively, which constitutes an important step towards the production of white perceived luminescence through the co-doping with RE. Further details about the properties of the RE ions will be given in Chapter 4.

1.7. ZnO-based oxides

ZnO can offer some advantages over GaN. Perhaps the most important ones are its larger free exciton binding energy (~ 60 meV against the ~ 25 meV of GaN), which enables the enhancement of the luminescence efficiency [2], and the simpler crystal-growth technology which may lead to lower costs in the fabrication of ZnO-based devices [7]. Moreover, this semiconductor exhibits low power threshold for optical pumping, radiation hardness and biocompatibility [2]. The RT electron Hall mobility found for single crystal ZnO is ~ 200 cm^2 $V^{-1}s^{-1}$, lower than the value reported for GaN (~ 1000 cm^2 $V^{-1}s^{-1}$) [2]. Some of ZnO properties are listed in Table 1-4. It is important to bear in mind that, as in the case of GaN, an uncertainty still exists in some of the values mentioned, namely the hole mobility and effective mass. These results are still under debate due to the lack of reliable reports for *p*-type ZnO [113]. In addition, the strong dependence of the electrical properties on the growth process and quality of the samples has been hampering their accurate quantification, as significant variations from sample to sample have been observed. Nevertheless, it is assumed that the background carrier concentration is usually ~ 10^{16} cm^{-3} [2].

Table 1-4 – Properties of WZ ZnO (bulk). Adapted from [113].

Property	Value
Volumetric density	5.606 g cm^{-3}
Stable crystalline phase at RT	wurtzite
Melting point	1977 ^oC
Thermal conductivity	0.6; 1-1.2 W m^{-1} K^{-1}
Linear expansion coefficient	a_0 = 6.5x10^{-6} $^oC^{-1}$ c_0 =3.0x10^{-6} $^oC^{-1}$
Static dielectric constant	8.656
Refractive index (~ 575 nm)	n_o =2.008; n_e =2.029
Bandgap at RT	3.37 eV (direct)
Intrinsic carrier concentration	< 10^6 cm^{-3} (max *n*-type doping > 10^{20} cm^{-3} electrons); max *p*-type doping < 10^{17} cm^{-3} holes
Exciton binding energy	60 meV
Electron effective mass	0.24 m_0
Electron Hall mobility at RT for low *n*-type conductivity	200 cm^2 $V^{-1}s^{-1}$
Hole effective mass	0.59 m_0
Hole Hall mobility at RT for low *p*-type conductivity	5 - 50 cm^2 $V^{-1}s^{-1}$

From the mechanical point of view, ZnO is a relatively soft material. In the bulk form, grown along the *c*-axis, this semiconductor has a hardness of ~ 5 GPa, at a plastic penetration depth of 300 nm, and a Young's modulus of ~ 111 GPa [2]. There are some indications that the mechanical properties of WZ ZnO depend on the crystal orientation. For instance, in an *a*-axis oriented material the basal plane is perpendicular to the surface, which makes the material more predisposed to slip, leading to a reduction of the hardness value. Also, for *c*-oriented epitaxial grown ZnO, some differences have been identified and a higher hardness value found [2]. Another interesting characteristic of ZnO is its piezoelectric properties, which are a reflection of the strong bond polarity and WZ structure. For ZnO, this piezoelectric effect is extremely prominent, being one of the most pronounced among all tetrahedrally coordinated semiconductors [32].

As in GaN, the thermal properties of WZ ZnO reflect the anisotropy of its crystal structure and dependence on stoichiometry, presence of extended defects, and free-carrier concentration [7]. The thermal expansion is strongly direction-dependent [33], as it is the thermal conductivity. Thermal conductivity is an extremely important property that must be taken into account in high-power/high temperature applications [2,7]. Since ZnO presents a great number of points defects, which have a substantial influence on the thermal conductivity, the values reported in the literature often vary from sample to sample [2]. The values for both thermal expansion and thermal conductivity are listed in Table 1-4. In the case of the specific heat, very few reports are available for this semiconductor.

The optical properties of ZnO, including its refractive index and dielectric constant, have been widely studied over several decades [2,7,33,114]. Since the most stable structure for ZnO is the WZ one, this material possesses anisotropic optical properties (uniaxial) that lead to an uniaxial birefringence (as in the case of GaN) [7,114]. The refractive index dispersion curves for polarizations parallel and perpendicular to the *c*-axis are depicted in Figure 1-15. The luminescence properties are summarized in Chapter 4.

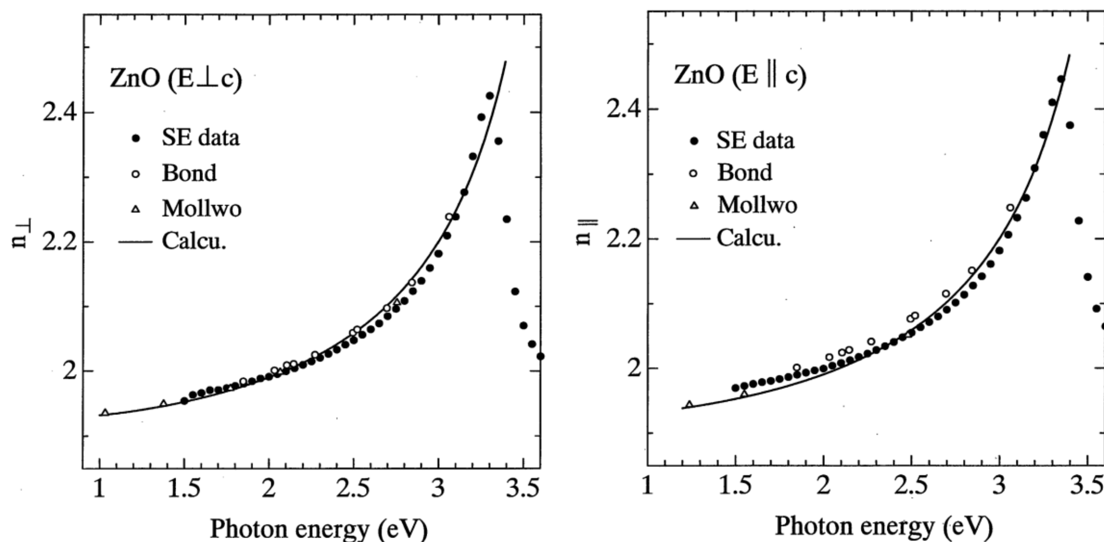

Figure 1-15 – Refractive index dispersion of ZnO for E⊥*c* (left) and E∥*c* (rigth) for energies below the absorption edge. The symbols represent experimental data obtained by spectroscopic ellipsometry while the solid line corresponds to calculated data [2,114].

1.7.1. *n*- and *p*-type ZnO

To foresee any type of device application based on ZnO, it is vital to have and adequate control over the concentration of the intentionally introduced impurities responsible for the electrical properties [53], as referred previously in section 1.6.1. In the case of nominally undoped ZnO, intrinsic *n*-type conductivity is generally associated to deviations from stoichiometry, with the presence of Zn interstitials (Zn_i) or oxygen vacancies (V_O). These intrinsic defect levels that lead to *n*-conductivity are often located approximately 0.01–0.05 eV below the CB. The ZnO *n*-type character can easily be improved by the introduction of dopants, such as Al, Ga, In or even H. In fact, H is a common donor found in ZnO, that is easily ionized and has a low formation energy. According to the literature, it is well accepted that the H shallow donor can contribute significantly to ZnO *n*-conductivity [2]. Group-VII elements, like Cl and I, can act as substitutional elements for O, thus a significant research has been devoted to the use of these element as *n*-type dopants [7,113]. As mentioned previously, one of the main questions that still remains subject of intense investigation concerns *p*-type doping. One reason for the difficulty in the *p*-type achievement is related with the inherent *n*-type ZnO, requiring the compensation of the defects responsible for electron doping. Additionally, the low solubility of dopants within ZnO can play a significant role in this matter [2]. The elements that are mostly believed to form acceptors in ZnO include group-I elements, such as Li, Na, K, Cu and Ag, substituting for Zn. Group-V elements, substituting for O, as N, P and As have also been considered [2,7]. However, most of these elements give rise to deep acceptors and do not contribute significantly to *p*-type conductivity [7]. It is accepted that group-I elements should be better *p*-type dopants than group-V, regarding the shallowness of the introduced acceptor levels, however they tend to occupy interstitial sites, which leads to the formation of donor levels instead. Even when incorporated in substitutional sites, a bond length larger than the normal Zn-O is formed, thereby introducing lattice strain. The strain effect contributes to the increase of defects such as vacancies, resulting in a compensation of the introduced dopants [7]. Thus, there are still questions to overcome in order to attain reliable *p*-type doping in ZnO.

1.7.2. ZnO common alloys

The bandgap energy of ZnO can be tuned by divalent substitution on the cation site to form alloys, namely with magnesium oxide (MgO) and cadmium oxide (CdO). Alloying ZnO with MgO ($E_g \sim 7.7$ eV), i.e., $Mg_xZn_{1-x}O$, results in a increasing of the energy bandgap. $Cd_xZn_{1-x}O$ alloy would be a good candidate for accomplishing narrower bandgaps because of the small direct bandgap of CdO ($E_g \sim 2.3$ eV) [33]. Smaller bandgap energies are desirable for wavelength tunability in the visible spectrum. Figure 1-16 shows how the bandgap can be engineered by alloying the mentioned compounds. E_g close to 3.0 eV can be easily accomplished by Cd^{2+} incorporation, while the addition of Mg^{2+} results in the increase of the bandgap energy up to 4.0 eV, maintaining the WZ structure [2,113].

MgO and CdO are ionic crystals with a cubic RS structure and the triangular lattice structure in the (111) plane is close to the hexagonal (0001) plane. Consequently, WZ $Mg_xZn_{1-x}O$ and $Cd_xZn_{1-x}O$ do not tend to form for values of x close to unity [3]. The maximum percentage reported for alloy

incorporation while maintaining the WZ structure is around 45% for MgO [115] and ~ 69% for CdO [33,116]. One of the most important intrinsic limitations for its applications in the visible range resides on the low solubility of the Cd in ZnO [117]. In fact, there is a lack of a consistent binary CdO-ZnO phase diagram in the literature [118]. Compositional limits for the growth of WZ $Cd_xZn_{1-x}O$ are strongly dependent on the growth method and conditions, and, consequently are not clearly established [116–119]. A number of works reporting the synthesis of $Cd_xZn_{1-x}O$ alloy using different methods, including metal-organic vapour-phase epitaxy (MOVPE) [120], molecular beam epitaxy (MBE) [121], and pulsed laser deposition (PLD) [122], showed the difficulties in maintaining a single WZ phase [118]. A recent work reporting $Cd_xZn_{1-x}O$ alloy grown by MOCVD showed RS inclusions for $0.32 < x < 0.60$ and also ZB phases for $0.07 < x < 0.17$ [118]. Phase separation is therefore a meaningful drawback that has to be overcome. Also the spontaneous misorientation with increasing Cd content needs to be fully understood [118]. The $Mg_xZn_{1-x}O$ alloy faces similar problems; however, the closer ionic radii make the problem less severe than that of Cd alloys [117]. Phase separation can also occur within the same crystallographic structure because of lateral and in-depth variations in the composition, which is often associated with strain relaxation processes [119,123]. However, the strain can play different roles depending on the growth conditions and the materials involved. Strain can either restrict the amount of material to be incorporated or can be a consequence of compositional variations or segregation during the growth [124,125]. Nonetheless, usually the strain relaxation takes place without any relationship with composition [126]. Due to the different role of strain in these alloys, it is usually difficult to determine whether some compositional phase separation is present or not. Furthermore, due to the lack of consensus in the physical properties of WZ CdO and MgO binaries, the accurate characterization of strain and composition in ZnO-based compounds is even more challenging [119]. Alloys with beryllium oxide (BeO) have been also used to increase the bandgap of ZnO [2,3,33]. Unlike the previously mentioned alloys, $Be_xZn_{1-x}O$, adopts the WZ structure throughout the entire compositional range, since WZ is the most stable phase of BeO [33]. Even so, this semiconductor is not yet well known, and thus alloying with MgO remains the most common via to widen the ZnO bandgap.

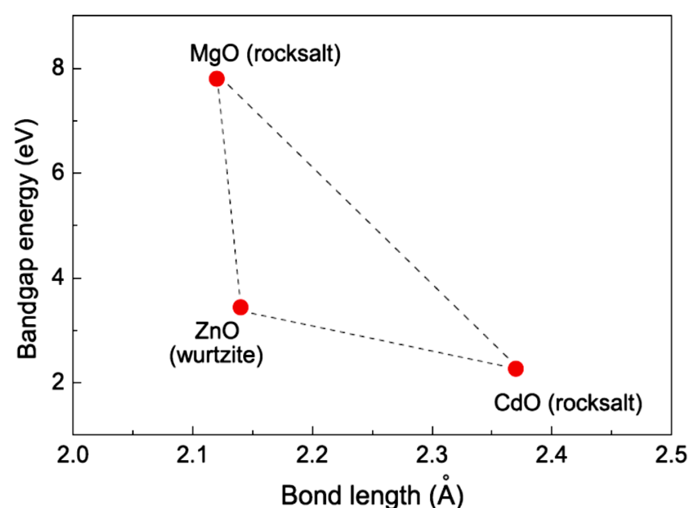

Figure 1-16 – Bandgap energy versus ionic bond length for ZnO, MgO and CdO. Image taken from [117].

Despite the mentioned problems, it is rather clear that the bandgap of ZnO can be increased by alloying with Mg and be reduced by alloying with Cd. Such alloy bandgap engineering, combined for instance with ZnO itself, may result in heterostructures with potential application in advanced devices to be designed [33]. There are already some reports on the literature about the fabrication of $Cd_xZn_{1-x}O$-based heterojunction LEDs on *p*-4H-SiC substrates emitting in the blue, green and red spectral region, showing the viability of the production of light emitting devices in the visible region based in this alloy [127,128].

1.8. From bulk to nanostructures

All the properties described above were found for bulk materials. However, when the dimensionality of the materials is reduced at the nanoscale several changes in their properties may occur. A reduction in the spatial dimension at a particular direction can introduce different effects from the ones of the bulk, which can affect the physical properties of the system. A crystal is considered "nano" if at least one of its dimensions lies below ~100 nm. There are a huge number of different kinds of nanostructures with different morphologies, as well as different ways to fabricate them. One of the most important consequences of the reduction of the crystals' size is the quantum confinement effect. Electronic quantum confinement happens when one or more spatial dimensions fall below the Bohr exciton radius (a_B). The a_B values for ZnO, GaN and AlN are listed in Table 1-5.

Taking as an example a finite crystal where two infinite barriers are place at a distance L ($L < a_B$) in the z direction, these barriers are able to reflect the Bloch waves along that direction and the waves are said to be confined. For a free carrier with effective mass $m*$ confined in the mentioned crystal the allowed wavevectors k_z of the Bloch waves are given by

$$k_{zn} = \frac{2\pi}{\lambda_n} = \frac{n\pi}{L}, n = 1,2,3, \dots \qquad \textbf{Eq. 1-5}$$

where $\lambda_n = 2L/n$. Consequently, the energy of its ground state increases by ΔE, in comparison to the case where confinement effects are absent. This difference can be expressed as

$$\Delta E = \frac{\hbar^2 k_{z1}^2}{2m^*} = \left(\frac{\hbar^2}{2m^*}\right)\left(\frac{\pi^2}{L^2}\right), \qquad \textbf{Eq. 1-6}$$

with $\hbar = h/2\pi$, being h the Plank's constant. This energy increase is referred as the confinement energy. In addition to the energy increase of the ground state of the carrier, confinement also causes quantization of the excited energies [35]. This effect is responsible for significate changes in the material properties, namely in the E_g value or in the dielectric constant.

The nanostructured materials and systems can be classified considering the number of dimensions within the confinement range. Systems where the carries are confined in three dimensions are known as quantum dots (QDs) and can be seen as quasi zero-dimensional (0D) structures, with atom-like energy states with only discrete energy levels allowed, that can be seen as Dirac delta-functions in the density of states distribution. Systems confined in two dimensions

are called quantum wires and correspond to one-dimensional (1D) nanostructures, since the carries can only move freely in one dimension. Here the density of states is known to follow an $E^{-1/2}$ trend. Finally, systems confined in one dimension correspond to quantum wells (QWs) which are two-dimensional (2D) structures, with 2 degrees of freedom for the carriers' motion and constant density of states [35,129,130]. These QWs structures are very common in the fabrication of LED devices. The density of states for all the dimensionalities can be seen in Figure 1-17.

Table 1-5 – Bohr exciton radius, a_B, values for ZnO, GaN and AlN.

Semiconductor	a_B (Å)
ZnO	18-23 [131,132]
GaN	27 [133]
AlN	12 [133]

Even when no confinement effect is observed in the nanostructures, differences can be observed due to the higher surface to volume ratio. With the increase of the surface area over the volume, surface effects tend to dominate the crystal properties and new features may arise. These surface states can be due to dangling bonds, point defects or adsorbed species at the surface. In the presence of surface states, the Fermi level is pinned at the surface which causes a bending of the electronic bands in the proximity of the surface, leading to the capture of charge carriers in that region and the generation of a surface charge [134,135]. The effect on the nanostructure properties caused by the formation of this depletion region will depend on the nanostructures diameter, since it may be comparable or even smaller than the width of the depletion zone, resulting in the depletion region extending over the complete volume of the structure [134]. Taking as an example the optical properties, the formation of this depletion region leads to modifications in the recombination processes, which becomes particularly important for samples with a high surface to volume ratio. If these defects are optically active, new luminescence features may arise, dominating over the bulk luminescence. It is also important to bear in mind that the nature of the surface states can depend on the crystallographic orientation of the surface [134].

The use of low dimensional nitride nanostructures such as QWs, NWs and QDs has gained a great interest for lighting applications. For instance, the use of GaN NWs as potential nanoscale building blocks for future optoelectronic devices offers some advantages over traditional layered structures, mostly due to their ability to be grown in different, cheaper, and highly mismatched substrates, with absence of extended defects and that can efficiently release the strain by surface relaxation [136,137]. For instance, the possibility to grow GaN NWs on a Si substrate enables the compatibility with the existing microelectronic technology, which is a requirement for large mass production. Higher light extraction efficiency is also expected from these low dimensional structures when compared with layered structures due to their non-planar geometry. This geometry is favourable for light extraction due to the decrease in the fraction of photons experiencing total internal reflection (due to the large refractive index of GaN). In addition, the extraction efficiency strongly depends also on the density of the NW array as well as on the

refractive index of the substrate [138]. Other advantages of the NWs include high flexibility and mechanical robustness [139].

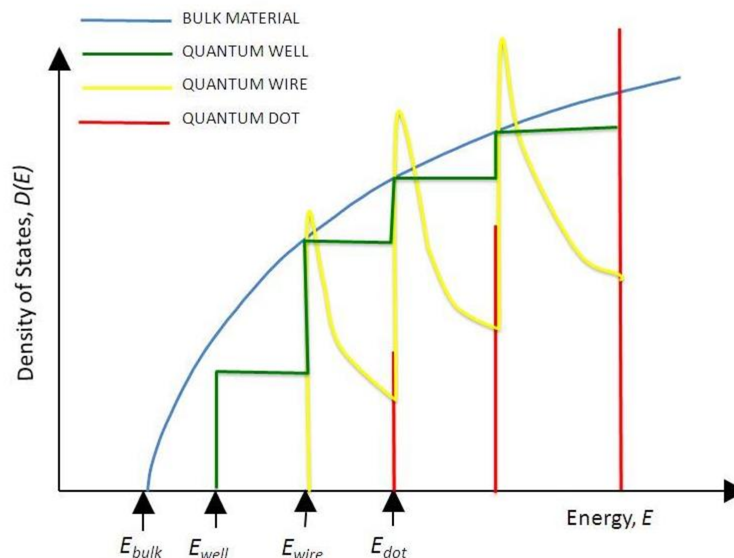

Figure 1-17 – Schematic representation of the electronic density of states of a crystal depending on its dimensionality. Image adapted from [140]**.**

GaN quantum structures like QWs or QDs also offers some benefits due to the spatial confinement effects of the carriers [141,142]. For instance, QDs can capture carriers that will occupy strongly localized states limiting their migration toward the defects that are formed during the growth process [141]. In RE-doped GaN and AlN layers the nonradiative carrier recombination channels strongly limit the intra-4*f* luminescence efficiency. These channels are expected to be reduced with the incorporation of RE^{3+} in GaN quantum structures due to the strong confinement of the carriers in the dots and the expected decrease of the nonradiative decay paths [143], as was already verified for Eu-doped GaN QDs [144,145].

In a similar way, low dimensional ZnO nanostructures with “custom-made” geometries as building blocks are also expected to play a decisive role in the fabrication of nanodevices [146,147]. 1D ZnO nanostructures, namely nanorods and NWs, have been subject to intense research due to their excellent properties, mostly associated to their large surface area/volume ratio [148]. Moreover, tetrapod-like structures have attracted some attention due to their unique electronic transport properties, demonstrating higher electron transfer efficiency when compared with the nanorods and reducing the number of intercrystalline contacts between grain boundaries [149,150]. Furthermore, the branching structure provides a large surface area for sensing purposes and charge separation, while the good interconnection between the branches offers multiple pathways for electron transport [151,152].

1.9. References

1. H. Morkoç, S. Strite, G. B. Gao, M. E. Lin, B. Sverdlov, and M. Burns, J. Appl. Phys. **76**, 1363 (1994).

2. C. Jagadish and S. J. Pearton, *Zinc Oxide Bulk, Thin Films and Nanostructures: Processing, Properties and Applications* (Elsevier, 2006).

3. T. Yao and S.-K. Hong, editors , *Oxide and Nitride Semiconductors* (Springer, 2009).

4. D. Laks, C. Van de Walle, G. Neumark, and S. Pantelides, Phys. Rev. Lett. **66**, 648 (1991).

5. H. Harima, J. Phys. Condens. Matter **14**, R967 (2002).

6. J. H. Edgar, editor , *Properties of Group III Nitrides* (EMIS Datareviews Series, n°11, An INSPEC publication, 1994).

7. U. Özgür, Y. I. Alivov, C. Liu, A. Teke, M. A. Reshchikov, S. Doğan, V. Avrutin, S.-J. Cho, and H. Morkoç, J. Appl. Phys. **98**, 041301 (2005).

8. J. I. Pankove and T. D. Moustakas, editors , *Gallium-Nitride (GaN) I - Seminductores and Semimetals, Volume 50* (Academic Press, 1998).

9. J. H. Edgar, editor , *Properties, Processing and Applications of Gallium Nitride and Related Semiconductors* (EMIS Datareviews Series, n°23, An INSPEC publication, 1999).

10. O. Ambacher, J. Phys. D. Appl. Phys. **31**, 2653 (1998).

11. H. Morkoc, *Handbook of Nitride Semiconductors and Devices, Materials Properties, Physics and Growth* (Wiley-VCH, 2009).

12. R. Collazo and N. Dietz, in *Photoelectrochem. Water Split. Perspect.*, edited by H.-J. Lewerenz and L. M. Peter (RSC Publishing, 2013), pp. 193–222.

13. S. M. Sze, *Physics of Semiconductor Devices* (Wiley, 1981).

14. D. A. Neamen, *Semiconductor Physics and Devices: Basic Principles* (McGraw Hill, 1992).

15. C. Kittel, *Introduction to Solid State Physics* (John Wiley & Sons, 1971).

16. M. Suzuki, T. Uenoyama, and A. Yanase, Phys. Rev. B **52**, 8132 (1995).

17. S. J. Pearton, editor , *GaN and Related Materials II* (CRC Press, 2000).

18. S. Nakamura and S. F. Chichibu, editors , *Introduction to Nitride Semiconductor Blue Lasers and Light Emitting Diodes* (CRC Press, 2000).

19. I. Sobelman, *Atomic Spectra and Radiative Transitions* (Springer Verlag, 1979).

20. S. Blundell, *Magnetism in Condensed Matter* (Oxford University Press, 2001).

21. P. Erhart, K. Albe, and A. Klein, Phys. Rev. B **73**, 205203 (2006).

22. D. Fritsch, H. Schmidt, and M. Grundmann, Phys. Rev. B **67**, 235205 (2003).

23. Y. Park, C. Litton, T. Collins, and D. Reynolds, Phys. Rev. **143**, 512 (1966).

24. M. R. Wagner, J.-H. Schulze, R. Kirste, M. Cobet, A. Hoffmann, A. V. Rodina, B. K. Meyer, U. Röder, and K. Thonke, Phys. Rev. B **80**, 205203 (2009).

25. H. Landolt, R. Börnstein, H. Fischer, O. Madelung, and G. Deuschle, *Landolt-Bornstein: Numerical Data and Functional Relationships in Science and Technology, Volume 17* (Springer Verlag, 1987).

26. W. Lambrecht, A. Rodina, S. Limpijumnong, B. Segall, and B. Meyer, Phys. Rev. B **65**, 075207 (2002).

27. D. G. Thomas, J. Phys. Chem. Solids **15**, 86 (1960).

28. D. C. Reynolds, D. C. Look, B. Jogai, C. W. Litton, G. Cantwell, and W. C. Harsch, Phys. Rev. B **60**, 2340 (1999).

29. A. Teke, Ü. Özgür, S. Doğan, X. Gu, H. Morkoç, B. Nemeth, J. Nause, and H. Everitt, Phys. Rev. B **70**, 195207 (2004).

30. H. Morkoç, *Nitride Semiconductors and Devices* (Springer, 1999).

31. C. Arguello, D. Rousseau, and S. Porto, Phys. Rev. **181**, 1351 (1969).

32. C. F. Klingshirn, A. Waag, A. Hoffmann, and J. Geurts, *Zinc Oxide: From Fundamental Properties Towards Novel Applications* (Springer, 2010).

33. H. Morkoç and Ü. Özgür, *Zinc Oxide: Fundamentals, Materials and Device Technology* (John Wiley & Sons, 2008).

34. J. Serrano, F. J. Manjón, A. H. Romero, A. Ivanov, R. Lauck, M. Cardona, and M. Krisch, Phys. Status Solidi **244**, 1478 (2007).

35. P. Y. Yu and M. Cardona, *Fundamentals of Semiconductors: Physics And Materials Properties, Volume 3* (Springer, 2005).

36. V. Y. Davydov, Y. E. Kitaev, I. N. Goncharuk, A. N. Smirnov, J. Graul, O. Semchinova, D. Uffmann, M. B. Smirnov, A. P. Mirgorodsky, and R. A. Evarestov, Phys. Rev. B **58**, 12899 (1998).

37. R. Cuscó, E. Alarcón-Lladó, J. Ibáñez, L. Artús, J. Jiménez, B. Wang, and M. Callahan, Phys. Rev. B **75**, 165202 (2007).

38. H. Siegle, G. Kaczmarczyk, L. Filippidis, A. P. Litvinchuk, A. Hoffmann, and C. Thomsen, Phys. Rev. B **55**, 7000 (1997).

39. C. Boemare, T. Monteiro, M. J. Soares, J. G. Guilherme, and E. Alves, Phys. B Condens. Matter **308-310**, 985 (2001).

40. R. Pässler, E. Griebl, H. Riepl, G. Lautner, S. Bauer, H. Preis, W. Gebhardt, B. Buda, D. J. As, D. Schikora, K. Lischka, K. Papagelis, and S. Ves, J. Appl. Phys. **86**, 4403 (1999).

41. L. Viña, S. Logothetidis, and M. Cardona, Phys. Rev. B **30**, 1979 (1984).

42. Y. P. Varshni, Physica **34**, 149 (1967).

43. M. Cardona and R. K. Kremer, Thin Solid Films **571**, 680 (2014).

44. R. Pässler, F. Blaschta, E. Griebl, K. Papagelis, B. Haserer, T. Reisinger, S. Ves, and W. Gebhardt, Phys. Status Solidi **204**, 685 (1997).

45. M. Cardona, T. Meyer, and M. Thewalt, Phys. Rev. Lett. **92**, 196403 (2004).

46. R. M. Eisberg and R. Resnick, *Quantum Physics of Atoms, Molecules, Solids, Nuclei, and Particles* (John Wiley & Sons, 1985).

47. M. Fernández, P. Prete, N. Lovergine, A. M. Mancini, R. Cingolani, L. Vasanelli, and M. R. Perrone, Phys. Rev. B **55**, 7660 (1997).

48. R. Pässler, J. Appl. Phys. **89**, 6235 (2001).

49. A. Denton and N. Ashcroft, Phys. Rev. A **43**, 3161 (1991).

50. K. A. Gschneidner and G. H. Vineyard, J. Appl. Phys. **33**, 3444 (1962).

51. V. S. Urusov, J. Struct. Chem. **33**, 68 (1992).

52. F. Yun, M. A. Reshchikov, L. He, T. King, H. Morkoc, S. W. Novak, and L. Wei, J. Appl. Phys. **92**, 4837 (2002).

53. S. J. Pearton and F. Ren, Int. Mater. Rev. **59**, 61 (2014).

54. Z. C. Feng, editor , *III-Nitride Semiconductor Materials* (Imperial College Press, 2006).

55. R. Szweda, editor , *Gallium Nitride and Related Wide Bandgap Materials & Devices. A Market and Technology Overview 1998-2003* (Elsevier Advanced Technology, 2000).

56. V. Y. Davydov, A. A. Klochikhin, R. P. Seisyan, V. V. Emtsev, S. V. Ivanov, F. Bechstedt, J. Furthmüller, H. Harima, A. V. Mudryi, J. Aderhold, O. Semchinova, and J. Graul, Phys. Status Solidi **229**, r1 (2002).

57. T. Suski, P. Perlin, H. Teisseyre, M. Leszczyński, I. Grzegory, J. Jun, M. Boćkowski, S. Porowski, and T. D. Moustakas, Appl. Phys. Lett. **67**, 2188 (1995).

58. C. J. Humphreys, MRS Bull **33**, 459 (2008).

59. W. Shan, W. Walukiewicz, E. E. Haller, B. D. Little, J. J. Song, M. D. McCluskey, N. M. Johnson, Z. C. Feng, M. Schurman, and R. A. Stall, J. Appl. Phys. **84**, 4452 (1998).

60. N. Nepal, S. M. Bedair, N. A. El-Masry, D. S. Lee, A. J. Steckl, and J. M. Zavada, Appl. Phys. Lett. **91**, 222503 (2007).

61. M. R. Krames, O. B. Shchekin, R. Mueller-Mach, G. O. Mueller, Ling Zhou, G. Harbers, and M. G. Craford, J. Disp. Technol. **3**, 160 (2007).

62. D. A. Neumayer and J. G. Ekerdt, Chem. Mater. **8**, 9 (1996).

63. F. A. Ponce and D. P. Bour, Nature **386**, 351 (1997).

64. M. A. Reshchikov and H. Morkoç, J. Appl. Phys. **97**, 061301 (2005).

65. K. P. O'Donnell, *Rare-Earth Doped III-Nitrides for Optoelectronic and Spintronic Applications* (Springer, 2009).

66. M. Shur and R. F. Davis, *GaN-Based Materials and Devices: Growth, Fabrication, Characterization and Performance* (World Scientific, 2004).

67. M. E. Levinshteĭn and S. L. Rumyantsev, *Properties of Advanced Semiconductor Materials: GaN, AlN, InN, BN, SiC, SiGe* (John Wiley & Sons, 2001).

68. P. Perlin, C. Jauberthie-Carillon, J. P. Itie, A. San Miguel, I. Grzegory, and A. Polian, Phys. Rev. B **45**, 83 (1992).

69. V. A. Savastenko and A. U. Sheleg, Phys. Status Solidi **48**, K135 (1978).

70. V. W. L. Chin, T. L. Tansley, and T. Osotchan, J. Appl. Phys. **75**, 7365 (1994).

71. R. Quay, *Gallium Nitride Electronics* (Springer, 2008).

72. S. Strite, J. Vac. Sci. Technol. B Microelectron. Nanom. Struct. **10**, 1237 (1992).

73. S. Nakamura, T. Mukai, and M. Senoh, J. Appl. Phys. **71**, 5543 (1992).

74. W. Götz, N. M. Johnson, C. Chen, H. Liu, C. Kuo, and W. Imler, Appl. Phys. Lett. **68**, 3144 (1996).

75. T. T. Mnatsakanov, M. E. Levinshtein, L. I. Pomortseva, S. N. Yurkov, G. S. Simin, and M. Asif Khan, Solid. State. Electron. **47**, 111 (2003).

76. E. Ejder, Phys. Status Solidi **6**, 445 (1971).

77. M. O. Manasreh, editor , *III-Nitride Semiconductors: Electrical, Structural and Defects Properties: Electrical, Structural and Defects Properties* (Elsevier, 2000).

78. Jacques I. Pankove and T. D. Moustakas, editors , *Gallium-Nitride (GaN) II* (Academic Press, 1998).

79. J. Neugebauer and C. G. Van de Walle, Phys. Rev. B **50**, 8067 (1994).

80. M. Ilegems and H. C. Montgomery, J. Phys. Chem. Solids **34**, 885 (1973).

81. D. C. Look, D. C. Reynolds, J. W. Hemsky, J. R. Sizelove, R. L. Jones, and R. J. Molnar, Phys. Rev. Lett. **79**, 2273 (1997).

82. H. Amano, M. Kito, K. Hiramatsu, and I. Akasaki, Jpn. J. Appl. Phys. **28**, L2112 (1989).

83. S. Nakamura, N. Iwasa, M. Senoh, and T. Mukai, Jpn. J. Appl. Phys. **31**, 1258 (1992).

84. W. Goetz, N. M. Johnson, D. P. Bour, C. Chen, H. Liu, and W. Imler, *Shallow Dopants and the Role of Hydrogen in Epitaxial Layers of Gallium Nitride (GaN)* (Electrochemical Society, Inc., Pennington, NJ (United States), 1996).

85. L. Bodiou, A. Braud, J.-L. Doualan, R. Moncorgé, J. H. Park, C. Munasinghe, A. J. Steckl, K. Lorenz, E. Alves, and B. Daudin, J. Appl. Phys. **105**, 043104 (2009).

86. Z. Fleischman, P. S. Tafon, V. Dierolf, C. Munasinghe, and A. J. Steckl, Phys. Status Solidi **4**, 834 (2007).

87. A. J. KENYON, Prog. Quantum Electron. **26**, 225 (2002).

88. P. Favennec and H. L'haridon, Electron. Lett. Lett. **25**, 718 (1989).

89. M. R. Soares, J. Rodrigues, N. F. Santos, C. Nico, R. G. Carvalho, A. J. S. Fernandes, M. P. Graça, L. Rino, M. J. Soares, A. J. Neves, F. M. Costa, and T. Monteiro, in *SPIE OPTO*, edited by F. H. Teherani, D. C. Look, and D. J. Rogers (International Society for Optics and Photonics, 2013), p. 862607.

90. A. Wakahara, Opt. Mater. (Amst). **28**, 731 (2006).

91. J. Rodrigues, N. Ben Sedrine, M. Felizardo, M. J. Soares, E. Alves, A. J. Neves, V. Fellmann, G. Tourbot, T. Auzelle, B. Daudin, M. Boćkowski, K. Lorenz, and T. Monteiro, RSC Adv. **4**, 62869 (2014).

92. H. Peng, C.-W. Lee, H. O. Everitt, C. Munasinghe, D. S. Lee, and A. J. Steckl, J. Appl. Phys. **102**, 073520 (2007).

93. E. Alves, K. Lorenz, R. Vianden, C. Boemare, M. J. Soares, and T. Monteiro, Mod. Phys. Lett. B **15**, 1281 (2001).

94. K. P. O'Donnell and B. Hourahine, Eur. Phys. J. - Appl. Phys. **36**, 91 (2006).

95. A. J. Steckl, J. C. Heikenfeld, M. J. Garter, C. C. Baker, and R. Jones, IEEE J. Sel. Top. Quantum Electron. **8**, 749 (2002).

96. T. Monteiro, C. Boemare, M. J. Soares, R. A. Sá Ferreira, L. D. Carlos, K. Lorenz, R. Vianden, and E. Alves, Phys. B Condens. Matter **308-310**, 22 (2001).

97. K. Wang, K. O'Donnell, B. Hourahine, R. Martin, I. Watson, K. Lorenz, and E. Alves, Phys. Rev. B **80**, 125206 (2009).

98. K. Lorenz, E. Alves, F. Gloux, P. Ruterana, M. Peres, A. J. Neves, and T. Monteiro, J. Appl. Phys. **107**, 023525 (2010).

99. A. J. J. Steckl, J. Heikenfeld, D. S. S. Lee, and M. Garter, Mater. Sci. Eng. B **81**, 97 (2001).

100. Y. Q. Wang and A. J. Steckl, Appl. Phys. Lett. **82**, 502 (2003).

101. J. Rodrigues, S. M. C. Miranda, N. F. Santos, A. J. Neves, E. Alves, K. Lorenz, and T. Monteiro, Mater. Chem. Phys. **134**, 716 (2012).

102. K. Lorenz, E. Alves, I. S. Roqan, R. W. Martin, C. Trager-Cowan, K. P. O'Donnell, and I. M. Watson, Phys. Status Solidi **205**, 34 (2008).

103. Y. Fujiwara, A. Nishikawa, and Y. Terai, in *Intemational Conf. Compd. Semicond. Manuf. Technol. (CS MANTECH)* (2010), p. 215.

104. M. Fialho, K. Lorenz, S. Magalhães, J. Rodrigues, N. F. Santos, T. Monteiro, and E. Alves, Nucl. Instruments Methods Phys. Res. Sect. B Beam Interact. with Mater. Atoms **307**, 495 (2013).

105. J. I. Pankove and J. A. Hutchby, J. Appl. Phys. **47**, 5387 (1976).

106. R. G. Wilson, R. N. Schwartz, C. R. Abernathy, S. J. Pearton, N. Newman, M. Rubin, T. Fu, and J. M. Zavada, Appl. Phys. Lett. **65**, 992 (1994).

107. C. H. Qiu, M. W. Leksono, J. I. Pankove, J. T. Torvik, R. J. Feuerstein, and F. Namavar, Appl. Phys. Lett. **66**, 562 (1995).

108. J. Heikenfeld, M. Garter, D. S. Lee, R. Birkhahn, and A. J. Steckl, Appl. Phys. Lett. **75**, 1189 (1999).

109. A. J. Steckl, M. Garter, D. S. Lee, J. Heikenfeld, and R. Birkhahn, Appl. Phys. Lett. **75**, 2184 (1999).

110. R. Birkhahn, M. Garter, and A. J. Steckl, Appl. Phys. Lett. **74**, 2161 (1999).

111. A. Nishikawa, T. Kawasaki, N. Furukawa, Y. Terai, and Y. Fujiwara, Appl. Phys. Express **2**, 1004 (2009).

112. U. Hömmerich, E. E. Nyein, D. S. Lee, J. Heikenfeld, A. J. Steckl, and J. M. Zavada, Mater. Sci. Eng. B **105**, 91 (2003).

113. S. J. Pearton, D. P. Norton, K. Ip, Y. W. Heo, and T. D. Steiner, Prog. Mater. Sci. **50**, 293 (2005).

114. H. Yoshikawa and S. Adachi, Jpn. J. Appl. Phys. **36**, 6237 (1997).

115. K. Koike, K. Hama, I. Nakashima, G. Takada, K. Ogata, S. Sasa, M. Inoue, and M. Yano, J. Cryst. Growth **278**, 288 (2005).

116. J. Ishihara, A. Nakamura, S. Shigemori, T. Aoki, and J. Temmyo, Appl. Phys. Lett. **89**, 091914 (2006).

117. S. Kalusniak, S. Sadofev, J. Puls, and F. Henneberger, Laser Photonics Rev. **3**, 233 (2009).

118. V. Venkatachalapathy, A. Galeckas, M. Trunk, T. Zhang, A. Azarov, and A. Y. Kuznetsov, Phys. Rev. B **83**, 125315 (2011).

119. A. Redondo-Cubero, J. Rodrigues, M. Brandt, P. Schäfer, F. Henneberger, M. R. Correia, T. Monteiro, E. Alves, and K. Lorenz, in *SPIE OPTO*, edited by F. H. Teherani, D. C. Look, and D. J. Rogers (International Society for Optics and Photonics, 2013), p. 86260N.

120. T. Gruber, C. Kirchner, R. Kling, F. Reuss, A. Waag, F. Bertram, D. Forster, J. Christen, and M. Schreck, Appl. Phys. Lett. **83**, 3290 (2003).

121. K. Sakurai, T. Takagi, T. Kubo, D. Kajita, T. Tanabe, H. Takasu, S. Fujita, and S. Fujita, J. Cryst. Growth **237-239**, 514 (2002).

122. T. Makino, Y. Segawa, M. Kawasaki, A. Ohtomo, R. Shiroki, K. Tamura, T. Yasuda, and H. Koinuma, Appl. Phys. Lett. **78**, 1237 (2001).

123. A. Wilkinson and A. McNaught, *IUPAC Compendium of Chemical Terminology, (the“ Gold Book”)* (International Union of Pure and Applied Chemistry, 1997).

124. S. Pereira, M. Correia, E. Pereira, K. O’Donnell, C. Trager-Cowan, F. Sweeney, and E. Alves, Phys. Rev. B **64**, 205311 (2001).

125. K. Lorenz, N. Franco, E. Alves, S. Pereira, I. M. Watson, R. W. Martin, and K. P. O’Donnell, J. Cryst. Growth **310**, 4058 (2008).

126. S. Pereira, M. R. Correia, E. Pereira, K. P. O’Donnell, E. Alves, A. D. Sequeira, N. Franco, I. M. Watson, and C. J. Deatcher, Appl. Phys. Lett. **80**, 3913 (2002).

127. K. Yamamoto, A. Nakamura, J. Temmyo, E. Munoz, and A. Hierro, IEEE Photonics Technol. Lett. **23**, 1052 (2011).

128. A. Nakamura, T. Ohashi, K. Yamamoto, J. Ishihara, T. Aoki, J. Temmyo, and H. Gotoh, Appl. Phys. Lett. **90**, 093512 (2007).

129. R. W. Kelsall, I. W. Hamley, and M. Geoghegan, *Nanoscale Science and Technology* (John Wiley and Sons, 2005).

130. G. Schmid, *Nanoparticles: From Theory to Application* (Wiley, 2004).

131. Y. Gu, I. Kuskovsky, M. Yin, S. O'Brien, and G. Neumark, Appl. Phys. Lett. **85**, 3833 (2004).

132. M. Yin, Y. Gu, and I. Kuskovsky, J. Am. Chem. Soc. **126**, 6206 (2004).

133. G. Steude, B. K. Meyer, A. Göldner, A. Hoffmann, F. Bertram, J. Christen, H. Amano, and I. Akasaki, Appl. Phys. Lett. **74**, 2456 (1999).

134. R. Calarco, T. Stoica, O. Brandt, and L. Geelhaar, J. Mater. Res. **26**, 2157 (2011).

135. Z. N. Urgessa, J. R. Botha, M. O. Eriksson, C. M. Mbulanga, S. R. Dobson, S. R. Tankio Djiokap, K. F. Karlsson, V. Khranovskyy, R. Yakimova, and P.-O. Holtz, J. Appl. Phys. **116**, 123506 (2014).

136. S. Li and A. Waag, J. Appl. Phys. **111**, 071101 (2012).

137. F. Glas, Phys. Rev. B **74**, 121302 (2006).

138. A.-L. Henneghien, G. Tourbot, B. Daudin, O. Lartigue, Y. Désières, and J.-M. Gérard, Opt. Express **19**, 527 (2011).

139. P. Yang, R. Yan, and M. Fardy, Nano Lett. **10**, 1529 (2010).

140. nanoHUB-U TE Therm. Energy Nanoscale Sci. Overview, Univ. Purdue (2015).

141. J. Brault, T. Huault, F. Natali, B. Damilano, D. Lefebvre, M. Leroux, M. Korytov, and J. Massies, J. Appl. Phys. **105**, 033519 (2009).

142. M. Peres, S. Magalhães, V. Fellmann, B. Daudin, A. Neves, E. Alves, K. Lorenz, and T. Monteiro, Nanoscale Res. Lett. **6**, 378 (2011).

143. J. M. Gérard, O. Cabrol, and B. Sermage, Appl. Phys. Lett. **68**, 3123 (1996).

144. M. Peres, S. Magalhães, J. Rodrigues, M. J. Soares, V. Fellmann, A. J. Neves, E. Alves, B. Daudin, K. Lorenz, and T. Monteiro, Opt. Mater. (Amst). **33**, 1045 (2011).

145. Y. Hori, X. Biquard, E. Monroy, D. Jalabert, F. Enjalbert, L. S. Dang, M. Tanaka, O. Oda, and B. Daudin, Appl. Phys. Lett. **84**, 206 (2004).

146. J. Rodrigues, D. Mata, A. J. S. Fernandes, M. A. Neto, R. F. Silva, T. Monteiro, and F. M. Costa, Acta Mater. **60**, 5143 (2012).

147. X. Fang, Y. Bando, U. K. Gautam, C. Ye, and D. Golberg, J. Mater. Chem. **18**, 509 (2007).

148. J. G. Lu, P. Chang, and Z. Fan, Mater. Sci. Eng. R Reports **52**, 49 (2006).

149. R. R. Bacsa, J. Dexpert-Ghys, M. Verelst, A. Falqui, B. Machado, W. S. Bacsa, P. Chen, S. M. Zakeeruddin, M. Graetzel, and P. Serp, Adv. Funct. Mater. **19**, 875 (2009).

150. C.-H. Lee, W.-H. Chiu, K.-M. Lee, W.-H. Yen, H.-F. Lin, W.-F. Hsieh, and J.-M. Wu, Electrochim. Acta **55**, 8422 (2010).

151. Y. F. Hsu, Y. Y. Xi, C. T. Yip, A. B. Djurišić, and W. K. Chan, J. Appl. Phys. **103**, 083114 (2008).

152. Q. Zhang and G. Cao, Nano Today **6**, 91 (2011).

Chapter 2. Growth techniques and samples

During the work reported in this thesis several kinds of samples were studied and different growth techniques were employed in their production. In this chapter, a detailed description of all the samples is present, including growth parameters and all the doping conditions. Moreover, all the growth techniques used are briefly discussed, highlighting the newly developed LAFD.

2.1. Description of the samples

The analysed samples can be divided in two major groups: GaN and related nitrides and ZnO-based oxides.

2.1.1. GaN and related nitrides

Bulk, layers and nanostructured (NWs, QWs and QDs) nitride samples were analysed. All samples were kindly provided by the *Material Characterization* group of *Laboratório de Aceleradores e Tecnologias da Radiação (LATR)* in *CTN/IST*. The properties of all these samples are analysed in detail in Chapter 5.

The GaN bulk sample was obtained from *Furukawa Co, Japan* and was grown by hydride vapour phase epitaxy (HVPE). The sample (designated as U245) has a thickness of near 2 mm and dimensions of 15×10 mm^2. One side of the sample is terminated in Ga and the opposite one in N. The Ga-face corresponds to the top surface obtained during the growth, while the N-face was achieved by chemical polishing the face closer to the substrate. The sample exhibits a low background donor concentration $< 5 \times 10^{16}$ cm^{-3} and a density of dislocations around $\sim 10^{6}$ cm^{-2}.

The layers (GaN, $Al_xGa_{1-x}N$ and AlN) were also grown by HVPE on (0001) sapphire substrates and were commercially purchased either from TDI (Oxford Instruments) or Lumilog. Figure 2-1 shows a schematic representation of the samples' structure. The thickness of the layers is about 3.5 μm for GaN and < 1 μm for $Al_xGa_{1-x}N$ (($0 < x \leq 1$), as indicated by the suppliers.

NWs, QWs and QDs were grown by radio frequency plasma-assisted MBE (PAMBE) by the group of Professor B. Daudin, *CEA/CNRS Group, "Nanophysique et Semiconducteurs"* at the *University Grenoble Alpes*.

GaN NWs were grown on (111) Si substrates, as described elsewhere [1]. A thin (2-3 nm) AlN buffer layer was deposited prior to the NWs growth. The AlN buffer is nearly relaxed since the

(0001) of AlN has a coincidence relationship with (111) of Si. During the growth process, there is no use of any metal catalyst. The 3D islands resulting from the Stranski-Krastanow (SK) growth mode of GaN on AlN are the precursors for the growth of the NWs [1]. The typical Ga/N ratio values for NW growth was nearly 0.3. All samples exhibit almost fully relaxed *c*-oriented NWs. The structures grow vertically aligned with only small tilts between them. A schematic representation of the samples' structure is depicted in Figure 2-2.

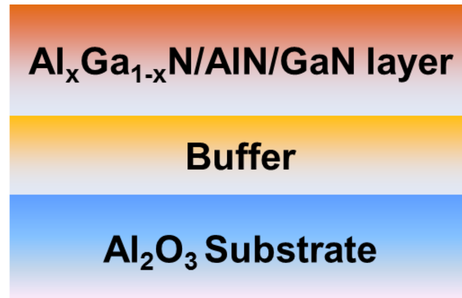

Figure 2-1 – Schematic representation of the layers' structure. This is valid for the all GaN, AlN and $Al_xGa_{1-x}N$ layer samples.

Different NWs wafers were grown for the different studies carried out during this thesis. Consequently, diverse growth conditions were used. In the case of **N1005**, the growth was performed for 2 hours at 880 ^{o}C in nitrogen rich conditions, resulting in NWs with diameters between 20 and 40 nm and an average length of ~ 300-400 nm. **NW1928** were grown during 8 h with a temperature close to 840 ^{o}C. Higher growth time led to longer NWs, with lengths around 1000 nm. Yet, the diameters remained close to the previous ones, around 40-50 nm. It is important to mention that, in the case of this sample, a 2D GaN layer was also present, showing a thickness close 70 nm. The growth of **NW2030** was performed during approximately 13 h at 860 ^{o}C. These NWs displayed diameters of ~ 70 nm and lengths between 1450 and 2300 nm. The **NW2032** sample was grown under similar conditions to the previous ones, resulting, however in slightly wider NWs, with diameters between 90 and 140 nm, while the length was kept nearly the same. It is also worth to note that there is an error associated with the growth temperature, so deviations up to 30 ^{o}C from the referred value can be found. Another important aspect is that the length and diameter of the NWs often vary from the centre to the periphery of the wafer where they are grown. Thus, the values indicated for diameter and lengths correspond to the ones measured in the sample's pieces analysed in the present work.

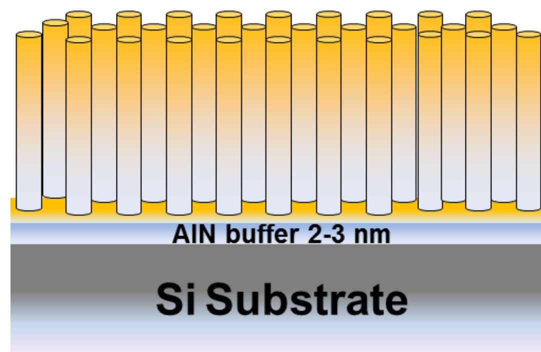

Figure 2-2 – Illustration of the structure of the NWs samples.

GaN QD/AlN and GaN QW/AlN superlattice (SL) samples are composed of 20 periods of QDs or QWs with a height of ~ 2 nm, with an AlN spacer ~ 5 nm thick. A schematic representation of these samples is shown in Figure 2-3. Both samples were grown in AlN buffers deposited on *c*-oriented sapphire substrates, commercially acquired. Nearly the same substrate temperature (720-730 °C) was used to grow both samples. Details about the growth can be found in references [2–5].

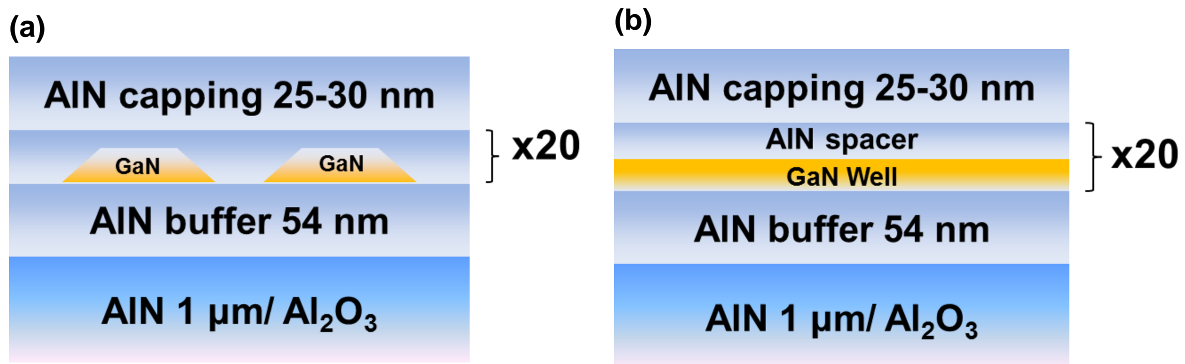

Figure 2-3 – Schematic representation of the (a) GaN QD/AlN and (b) GaN QW/AlN superlattice samples.

Layers, NWs, QDs and QWs were doped with several RE ions by ion implantation at *LATR* in *CTN/IST*. Post-implant thermal annealing was performed to remove implantation damage and optically activate the ions in the different nitride structures. Implantation and annealing conditions for each set of samples are listed in Tables 2-1 to 2-6. Additionally, to gain some insight into the understanding of the yellow luminescence (YL) frequently present in GaN structures, post-growth sample annealing and ion implantation were used to intentionally induce/enhance the YL recombination in GaN NWs. The samples used in this study are displayed in Table 2-1.

Table 2-1 – Implantation and annealing conditions of all the GaN NWs samples used for the study of the yellow luminescence band. Samples studied in section 5.2.

Sample	Ion	Implantation				Annealing	Type of nanostructure
		Fluence (ion.cm^{-2})	Energy (keV)	Tilt (°)	Temperature (°C)		
N1005	-	-	-	-	-	-	NWs
N1005Er	Er	1×10^{13}	150	0	RT	1000 °C, 30 s, N_2 flux	NWs
NW1928	-	-	-	-	-	-	NWs
NW1928a	-	-	-	-	-	1000 °C, 30 s, N_2 flux	NWs
NW1928Er	Er	1×10^{13}	150	0	RT	1000 °C, 30 s, N_2 flux	NWs

To verify the possible influence of surface states in the stability of the luminescence centre identified in these NWs (Table 2-1), different surface treatments were carried out. Hydrogenation was performed in N1005Er and NW1928a samples, during 30 minutes, in a microwave plasma chemical vapour deposition (MPCVD) system (2.45 GHz), ASTeX PDS-18, using H_2 as the only feed gas. Microwave plasmas are well known for their good yield in atomic hydrogen production, as

required for passivation experiments. In order to preserve the samples' integrity, a low temperature, below 100 ^{o}C, was kept in the specimen by water cooling it using a cool dish, on top of which the sample holder was placed. Also, no bias was applied between the plasma and the holder, therefore preventing surface damage by ionic bombardment. The plasma experiments were conducted using the following parameters: 650 W forward power (~ 2 W reflected power), total pressure of 2.13 kPa and 250 $ml.min^{-1}$ of H_2 flow. Other surface treatments were implemented in sample N1928Er. For the hydroxylation process, GaN NWs were immersed in a water solution containing 0.06 M sulfuric acid (H_2SO_4) and 0.26 M nitric acid (HNO_3) during 14 h, at RT. The sample was dried in air. Silica (SiO_2) coating was performed via hydrolysis/condensation reactions in which tetraethyl orthosilicate (TEOS: $Si(OC_2H_5)_4$) was used as precursor. First, a solution containing 5 ml of ethanol (CH_3CH_2OH), 450 µl of deionised water, 75 µl of ammonia (NH_3) and 225 µl of TEOS was prepared at RT. The GaN NWs were then immersed in the ethanolic solution for 2 h. This method produces an amorphous network composed mainly by silica that coats the GaN wires. The sample was then removed from the solution bath, washed with ethanol and dried in air [6].

The remaining sets of samples described in Tables 2-2 to 2-6 were used to evaluate the optical properties of the incorporated RE ions.

Table 2-2 – Implantation and annealing conditions of the GaN NWs and reference layers implanted with Eu ions. All the samples were implanted with 300 keV at RT. Samples studied in section 5.3.

Sample	Ion	Implantation		Annealing	Type of nanostructure
		Fluence ($ion.cm^{-2}$)	Tilt (^{o})		
NW 2030a/Ra	Eu	1×10^{13}	20	1000 ^{o}C, 30 s, N_2 flux	NWs/ Layers (Lumilog)
NW 2030b/Rb	Eu	5×10^{13}	20	1000 ^{o}C, 30 s, N_2 flux	NWs/ Layers (Lumilog)
NW 2030c/Rc	Eu	1×10^{14}	20	1000 ^{o}C, 30 s, N_2 flux	NWs/ Layers (Lumilog)
NW 2030d/Rd	Eu	5×10^{14}	20	1000 ^{o}C, 30 s, N_2 flux	NWs/ Layers (Lumilog)
NW 2030e/Re	Eu	1×10^{15}	20	1000 ^{o}C, 30 s, N_2 flux	NWs/ Layers (Lumilog)
NW 2030f/Rf	Eu	2×10^{15}	20	1000 ^{o}C, 30 s, N_2 flux	NWs/ Layers (Lumilog)
NW 2030g/Rg	Eu	3×10^{15}	20	1000 ^{o}C, 30 s, N_2 flux	NWs/ Layers (Lumilog)
NW 2032a/R2a	Eu	1×10^{15}	30	1000 ^{o}C, 30 s, N_2 flux	NWs/ Layers (Lumilog)
NW 2032b/R2b	Eu	2×10^{15}	30	1000 ^{o}C, 30 s, N_2 flux	NWs/ Layers (Lumilog)
NW 2032c/R2c	Eu	3×10^{15}	30	1000 ^{o}C, 30 s, N_2 flux	NWs/ Layers (Lumilog)

Table 2-3 – Implantation and annealing conditions of the GaN nanostructures implanted with Pr ions. All the samples were implanted with 150 keV at 0 ° and RT. Samples studied in section 5.4.

Sample	Ion	Implantation fluence (ion.cm^{-2})	Annealing	Type of nanostructure
GaNPr07	Pr	1×10^{13}	1000 °C, 30 s, N_2 flux + 1400 °C, 30 min, N_2 (10^4 bar)	Layers (TDI)
GaNPr08	Pr	1×10^{15}	1000 °C, 30 s, N_2 flux + 1400 °C, 30 min, N_2 (10^4 bar)	Layers (TDI)
AlNPr04	Pr	1×10^{13}	1200 °C, 30 s, N_2 flux	Layers (TDI)
AlNPr05	Pr	1×10^{15}	1200 °C, 30 s, N_2 flux	Layers (TDI)
N1005A	Pr	1×10^{13}	1200 °C, 30 s, N_2 flux	NWs
NW2030l	Pr	1×10^{15}	1200 °C, 30 s, N_2 flux	NWs
N1236	Pr	1×10^{13}	1200 °C, 30 s, N_2 flux	QWs
N1236b	Pr	1×10^{15}	1200 °C, 30 s, N_2 flux	QWs
N1223	Pr	1×10^{13}	1200 °C, 30 s, N_2 flux	QDs
N1223b	Pr	1×10^{15}	1200 °C, 30 s, N_2 flux	QDs

Table 2-4 – Implantation and annealing conditions of the GaN layers implanted with Eu and Pr ions. All the samples were implanted with 150 keV at 0 ° and RT. Samples studied in section 5.5.

Sample	Ion	Implantation fluence (ion.cm^{-2})	Annealing	Type of nanostructure
GaN:Eu	Eu	8×10^{14}	1000 °C, 20 min, N_2 flux	Layers (TDI)
AlN:Eu	Eu	8×10^{14}	1000 °C, 20 min, N_2 flux	Layers (TDI)
GaN:Pr	Pr	8×10^{14}	1000 °C, 20 min, N_2 flux	Layers (TDI)
AlN:Pr	Pr	8×10^{14}	1000 °C, 20 min, N_2 flux	Layers (TDI)
GaN:Eu,Pr	Pr+Eu	8×10^{14}	1000 °C, 20 min, N_2 flux	Layers (TDI)
AlN:Eu,Pr	Pr+Eu	8×10^{14}	1000 °C, 20 min, N_2 flux	Layers (TDI)

Table 2-5 – Implantation and annealing conditions of the $Al_xGa_{1-x}N$ ($0 \leq x \leq 1$) samples implanted with Tb ions. The implantation fluence was confirmed by Rutherford backscattering spectrometry (RBS) measurements. All the samples were implanted with 150 keV at 0 ° and RT. Samples studied in subsection 5.6.1.

Sample	Ion	Implantation fluence ($ion.cm^{-2}$)	Annealing	Type of nanostructure
GaNSiTb1a	Tb	5×10^{14}	1200 °C, 120 s, N_2 (1 bar)	Layers (TDI)
GaNSiTb2	Tb	1×10^{13}	1200 °C, 120 s, N_2 (1 bar)	Layers (TDI)
GaNSiTb1	Tb	5×10^{14}	1200 °C, 120 s, N_2 (1 bar) + 1400 °C, 30 min, N_2 (10^4 bar)	Layers (TDI)
$Al_{0.043}GaNTb1$	Tb	5×10^{14}	1200 °C, 120 s, N_2 (1 bar)	Layers (TDI)
$Al_{0.186}GaNTb1$	Tb	5×10^{14}	1200 °C, 120 s, N_2 (1 bar)	Layers (TDI)
$Al_{0.234}GaNTb1$	Tb	5×10^{14}	1200 °C, 120 s, N_2 (1 bar)	Layers (TDI)
$Al_{0.54}GaNTb1$	Tb	5×10^{14}	1200 °C, 120 s, N_2 (1 bar)	Layers (TDI)
$Al_{0.77}GaNTb1$	Tb	5×10^{14}	1200 °C, 120 s, N_2 (1 bar)	Layers (TDI)
AlNTb1	Tb	5×10^{14}	1200 °C, 120 s, N_2 (1 bar)	Layers (TDI)
AlNTb2	Tb	5×10^{14}	1200 °C, 120 s, N_2 (1 bar)	Layers (TDI)

Table 2-6 – Implantation and annealing conditions of the $Al_xGa_{1-x}N$ ($0 \leq x \leq 1$) samples implanted with Tm^{3+} ions. The implantation fluence was confirmed by RBS measurements. All the samples were implanted with 300 keV at RT Samples studied in subsection 5.6.2.

Sample	Ion	Implantation		Annealing	Type of nanostructure
		Fluence ($ion.cm^{-2}$)	Tilt (°)		
GaNTm#119a	Tm	1×10^{15}	0	500 °C, 120 s, N_2 (1 bar)	Layers (TDI)
$Al_{77}GaN$#1	Tm	1×10^{13}	10	1200 °C, 120 s, N_2 (1 bar)	Layers (TDI)
$Al_{77}GaN$#2	Tm	1×10^{14}	10	1200 °C, 120 s, N_2 (1 bar)	Layers (TDI)
$Al_{77}GaN$#3	Tm	4×10^{14}	10	1200 °C, 120 s, N_2 (1 bar)	Layers (TDI)
$Al_{77}GaN$#4	Tm	1×10^{15}	10	1200 °C, 120 s, N_2 (1 bar)	Layers (TDI)
$Al_{77}GaN$#5	Tm	4×10^{15}	10	1200 °C, 120 s, N_2 (1 bar)	Layers (TDI)
$Al_{15}GaN$#1	Tm	1×10^{13}	10	1200 °C, 120 s, N_2 (1 bar)	Layers (TDI)
$Al_{15}GaN$#2	Tm	1×10^{14}	10	1200 °C, 120 s, N_2 (1 bar)	Layers (TDI)
$Al_{15}GaN$#3	Tm	4×10^{14}	10	1200 °C, 120 s, N_2 (1 bar)	Layers (TDI)
$Al_{15}GaN$#4	Tm	1×10^{14}	10	1200 °C, 120 s, N_2 (1 bar)	Layers (TDI)
$Al_{15}GaN$#5	Tm	4×10^{15}	10	1200 °C, 120 s, N_2 (1 bar)	Layers (TDI)
$Al_{15}GaN$#6	Tm	1×10^{14}	0	1200 °C, 120 s, N_2 (1 bar)	Layers (TDI)
$Al_{15}GaN$#7	Tm	1×10^{15}	0	1200 °C, 120 s, N_2 (1 bar)	Layers (TDI)
$Al_{15}GaN$#8	Tm	5×10^{15}	0	1200 °C, 120 s, N_2 (1 bar)	Layers (TDI)
AlN#6	Tm	1×10^{14}	0	1200 °C, 120 s, N_2 (1 bar)	Layers (TDI)
AlN#7	Tm	1×10^{15}	0	1200 °C, 120 s, N_2 (1 bar)	Layers (TDI)
AlN#8	Tm	5×10^{15}	0	1200 °C, 120 s, N_2 (1 bar)	Layers (TDI)

2.1.2. ZnO-based oxides

The ZnO-based oxides samples can be divided into three main sections: ZnO, ZnO/Carbon nanotubes (CNTs) composites and $Cd_xZn_{1-x}O/Mg_yZn_{1-y}O$ heterostructures. These samples are analysed in detail in Chapter 6.

2.1.2.1. ZnO

ZnO samples were produced by the LAFD technique in the *Department of Physics* from the *University of Aveiro*. This method allows the production of ZnO structures with different morphologies, depending on the employed growth parameters and the different local conditions inside the growth chamber, as will be explained in detail in sub-section 2.2.1. Using LAFD technique, three types of ZnO samples with different morphologies were produced: microrods (MRs), tetrapods (TPs) and nanoparticles (NPs).

Aiming at the understanding and control of the TPs and NPs growth, parameters like laser power, growth time, distance between the sample holder and the top of the precursor, as well as growth atmosphere were evaluated. This study allowed to establish the ideal growth conditions for each morphology and to gain some insight about the growth mechanisms involved in the formation of the mentioned ZnO nano/microstructures. It is worth to mention that, besides the growth conditions, one of the first approaches was the test of the substrates where the ZnO was deposited. The samples were grown in silicon, sapphire, glass and aluminium substrates. Since no significant differences were found, further tests were performed using only silicon substrates. The details associated with each sample are listed in Table 2-7.

Table 2-7 – Growth parameters of the ZnO nanostructures (TPs and NPs) prepared by LAFD. Samples studied in section 6.1.1.

Sample	Laser power (W)	Precursor-holder distance (mm)	Atmosphere	Growth time	Thermal annealing treatment
ZnO_1	20	6	Air (1 atm)	3 min	
ZnO_2	23			3 min	
ZnO_3	25			3 min	
ZnO_4	20			6 min	
ZnO_5	23			6 min	
ZnO_6	20			12 min	
ZnO_7	20			3 min	
ZnO_8	20	12	Air (1 atm)	3 min	
ZnO_9	20	30			
ZnO_10	20	6	Air (1 atm)	1 min	
ZnO_11				30 s	
ZnO_12				10 s	
ZnO_13				10 s	
ZnO_14	40	6	Air (1 atm)	3 min	
ZnO_15	50				
ZnO_16	60				
ZnO_17	80				

ZnO_LP1	17	6	Air (1 atm)	6 min	
ZnO_LP2	18				
ZnO_LP3	19				
ZnO_LP4	20				
ZnO_LP5	20			3 min	
ZnO_T1	25	6	Air (1 atm)	4 depositions of 20 s with an interval of 1 min	
ZnO_T2				4 depositions of 20 s with an interval of 1 min	
ZnO_T3				4 depositions of 10 s with an interval of 1 min	
ZnO_T4				4 depositions of 5 s with an interval of 1 min	
ZnO_TT0	25	6	Air (1 atm)	3 min	
ZnO_TT500_1					500 ^oC / 2 h in air
ZnO_TT600					600 ^oC / 2 h in air
ZnO_TT700					700 ^oC / 2 h in air
ZnO_TT500_2					500 ^oC / 10 h in air
ZnO_TT500_3	20				500 ^oC / 10 h in air
ZnOAir20	20	6	Air (1 atm)	3 min	
ZnOAir25	25				
ZnOAir30	30				
ZnOAir35	35				
ZnOAir40	40				
ZnON20	20	6	N_2 (1 atm)	3 min	
ZnON25	25				
ZnON30	30				
ZnON35	35				
ZnON40	40				
ZnON25_TT500	25				500 ^oC / 2 h in air
ZnOPN20	20	6	N_2 (2 atm)	3 min	
ZnOPN25	25				
ZnOPN30	30				
ZnOPN35	35				
ZnOPN40	40				

ZnOArg20	20	6	Argon (1 atm)	3 min	
ZnOArg25	25				
ZnOArg35	35				
ZnOArg40	40				

For the MRs the main parameter tested was the laser power. The studied growth conditions are depicted in Table 2-8.

Table 2-8 – Growth parameters of the ZnO MRs prepared by LAFD. Samples studied in subsection 6.1.2.

Sample	Laser power (W)	Atmosphere	Growth time (min)
ZnO_R_25	25	Air (1 atm)	3
ZnO_R_35	35		
ZnO_R_40	40		
ZnO_R_50	50		
ZnO_R_60	60		
ZnO_R_35_N_2	35	N_2 (2 atm)	3

In order to study the relationship between some of the observed optical centres in ZnO MRs and the presence of surface defects, surface treatments were conducted. Hydrogen plasma treatments were performed during 30 minutes in a commercial microwave MPCVD system (previously described), using H_2 as the only feed gas. Two sets of parameters were employed: 1500 W of microwave power, total pressure of 70 Torr and H_2 flow of 250 ml.min^{-1}, and 2000 W of power and 80 Torr of pressure, keeping the same flow value. The sample hydrogenated in the conditions of the first set (MR_sample#2, as characterized in Table 2-9) was then thermally annealed at 700 ^{o}C during 5 h (in air atmosphere). Nitrogen plasma treatments were conducted using the same MPCVD reactor. The treatment was performed during 15 minutes with a N_2 flow of 100 ml.min^{-1}. As in the case of the hydrogenation, two sets of parameters were employed. In the first set of experiments a microwave power of 900 W and a total pressure of 20 Torr were used, while in the second set the power was fixed at 1000 W and the total pressure was raised to 40 Torr. The sample characteristics are listed in Table 2-9.

The feasibility of the LAFD method for the growth of hybrid or composite structures without the need of several time-consuming steps was tested with the system ZnO/Ag. It is known that the ZnO potential for some applications can be improved by forming composite structures. Therefore, the synergetic combination with other materials have been intensively investigated due to the possibility of modulation of their properties [7]. The addition of Ag to the ZnO precursors has as main aim the study of the morphology, since this property has a great influence on possible applications, namely in photocatalysis and/or toxicity studies. Another goal was the determination of the Ag incorporation in the ZnO host as a potential acceptor element. For this, different amounts of $AgNO_3$ were added to the precursor rods. The samples were grown in air atmosphere at two different laser powers. All the growth parameters are depicted in

Table 2-10. Even though both MR and TPs have been produced in each growth, the main focus of this study was given to the MR.

Table 2-9 – Growth, plasma treatment and annealing conditions of the ZnO MRs. Samples studied in subsection 6.1.2.

Sample	Laser power (W)	Atmosphere	Growth time (min)	MPCVD plasma treatment			Thermal annealing treatment
				Power (W)	Pressure (Torr)	Gas flow ($ml.min^{-1}$)	
MR_Sample#1	40	Air (1 atm)	3	-	-	-	as-grown
MR_Sample#2				1500	70	H_2 250	-
MR_Sample#3				2000	80	H_2 250	-
MR_Sample#4				1500	70	H_2 250	700 ^oC / 5 h in air
MR_Sample#5				900	20	N_2 100	-
MR_Sample#6				1000	40	N_2 100	-

Table 2-10 – ZnO samples grown in the presence of Ag. Samples studied in section 6.2.

Sample	Laser power (W)	Atmosphere	Ag content (mol %)	Growth time (min)
ZnO_0_25	25	Air (1 atm)	0	3
ZnO_0_35	35			
ZnO_0.1Ag_25	25		0.1	
ZnO_0.1Ag_35	35			
ZnO_0.5Ag_25	25		0.5	
ZnO_0.5Ag_35	35			
ZnO_0.8Ag_25	25		0.8	
ZnO_0.8Ag_35	35			
ZnO_1Ag_25	25		1.0	
ZnO_1Ag_35	35			
ZnO_2Ag_25	25		2.0	
ZnO_2Ag_35	35			
ZnO_3Ag_25	25		3.0	
ZnO_3Ag_35	35			
ZnO_5Ag_25	25		5.0	
ZnO_5Ag_35	35			

2.1.2.2. *ZnO/CNTs composites*

Two types of ZnO/CNTs composites were prepared: vertically aligned CNTs (VACNTs) decorated with ZnO and ZnO/CNTs buckypapers. VACNTs were provided by *CICECO* laboratory from *University of Aveiro*. The VACNTs arrays were synthesized by an optimized catalyst-supported chemical vapour deposition (CVD) technique. Prior to the synthesis step, the 2 inch diameter *p*-type Si/SiO_2 wafer (Siegert Consulting) substrates for the CNT growth were coated with a bilayer of Al_2O_3 (10 nm)/Fe (1 nm), by magnetron sputtering. Then, the Fe film was converted into nano-sized particles (~ 20 nm) with a round shape morphology and a uniform density (~ 10^{10} particles.m^{-2}) by means of *in-situ* annealing inside the CVD reactor at 770°C, under a reductive gas flow of H_2/Ar (500/200 sccm). Subsequently, the H_2 and Ar flows were adjusted to

400 and 100 sccm respectively, and a C_2H_2 flow (10 sccm) was added for 15 min to yield the Fe-catalysed growth of VACNTs with diameter and length sizes of ~ 15 nm and ~ 1.5 mm, respectively, on large areas [8,9]. The VACNTs were then used as substrates for the growth of ZnO by LAFD. In this sense, different laser powers were applied to grow the ZnO structures directly on top of the VACNTs array, as detailed in Table 2-11. During the growth of each sample, a silicon substrate was also attached to the sample holder in order to have a ZnO reference sample with exactly the same growth conditions. Figure 2-4 exhibits a schematic representation of the structure of these ZnO/VACNTs samples.

Table 2-11 – Deposition parameters of the VACNTS decorated with ZnO nanostructures grown by the LAFD method. Samples studied in section 6.3.1.

Sample	Laser power (W)	Precursor-holder distance (mm)	Atmosphere	Growth time (min)
ZnO_CNTs_1	35			
ZnO_CNTs_2	35			
ZnO_CNTs_3	20			
ZnO_CNTs_4	35	6	Air (1 atm)	3
ZnO_CNTs_5	25			
ZnO_CNTs_6	25			

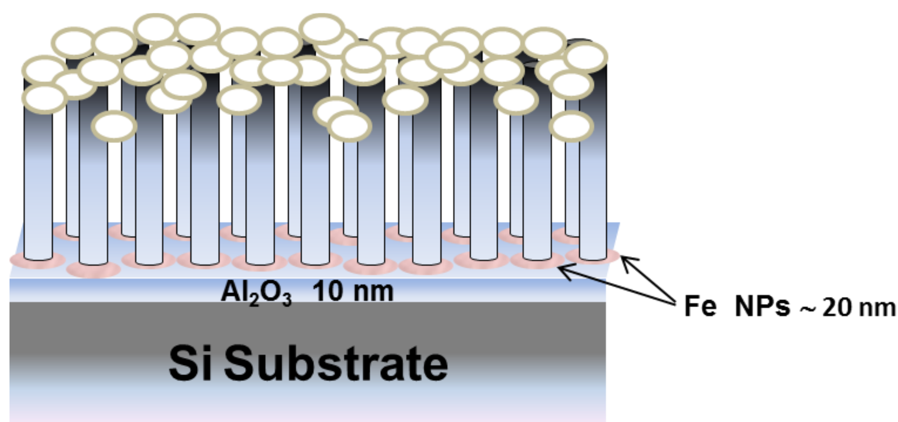

Figure 2-4 – Schematic representation of the VACNTs arrays decorated with ZnO structures produced by LAFD technique.

Functionalized multi-walled CNTs (NC3101-Nanocyl) were used to prepare the ZnO/CNT composites. The CNTs had an average length and diameter sizes of 1.5 µm and 9.5 nm, respectively, with a purity level of 95 wt.% and a 4 wt.% content of covalently bonded carboxylic groups (-COOH). ZnO/CNTs composites with a weight ratio of 4:1 were prepared in isopropyl alcohol (IPA, ≥ 99.8%). The preparation procedure comprised essentially five steps: (1) CNT suspensions of 0.1 g.l^{-1} started to be processed by high-speed shearing for 15 min (IKA T25-Ultra-Turrax, working at 20500 rpm) with a shearing force of 96 Pa to eliminate big CNTs agglomerates; (2) afterwards, the CNT suspension was sonicated (working at 60 kHz, 200 W) for 60 min to yield mixtures of individualized CNTs and small sized agglomerates (< 3 µm) [10]. At the same time, both the suspensions of ZnO TPs and NPs, with a fixed concentration of 1 g l^{-1}, each were

sonicated in the same conditions of those of the CNTs suspension to de-agglomerate possible ZnO clusters. (3) Next, the suspensions were mixed together and sonicated during 15 min to promote interactions of individual ZnO particles with CNTs. (4) The ZnO/CNT suspension was then dropped into a cylindrical mould of 10 mm of diameter placed onto a 0.22 µm pore size filter (hydrophobic PTEF) to produce the buckypapers of ZnO and CNTs by vacuum filtration [11]. This was accomplished by coupling a rotary vacuum pump to a filter-Büchner funnel-Kitasato flask setting. A scheme of the experimental apparatus is illustrated in Figure 2-5. Each membrane is comprised by 6 layers, as represented in Figure 2-6a, each one with approximately 3 ml of suspension. The first and the last two layers are composed by a ZnO/CNT mixture, while the two middle ones include only CNTs and were added in order to reinforce the mechanical stability of the membranes. (5) Finally, the membranes were dried in an oven at 80 ^{o}C for 15 min. The final samples can be seen in Figure 2-6b. Each ZnO/CNT membrane has 10 mm of diameter and the thickness is around 100 µm. The ZnO TPs used were prepared by the LAFD technique, while the NPs where obtained by colloidal synthesis. The details of the prepared samples are displayed in Table 2-12.

Table 2-12 – Preparation conditions for the ZnO/CNTs buckypaper composites. Samples studied in section 6.3.2.

Sample	Laser power for the growth of ZnO (W)	ZnO:CNTs proportion	Type of ZnO nanostructures
BP_CNTs			
BP_CNTs_ZnO_TPs	35	4:1	TPs
BP_CNTs_ZnO_NPs	-		NPs

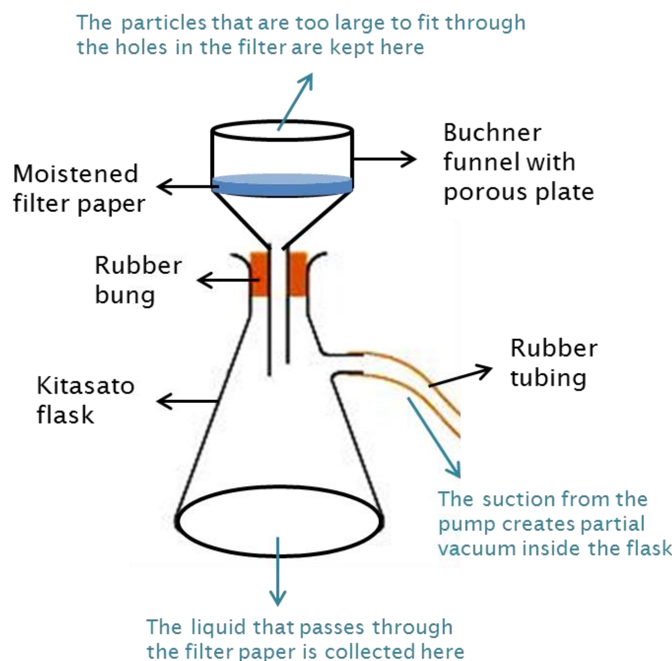

Figure 2-5 – Sketch of the experimental apparatus for the ZnO/CNTs buckypaper filtration.

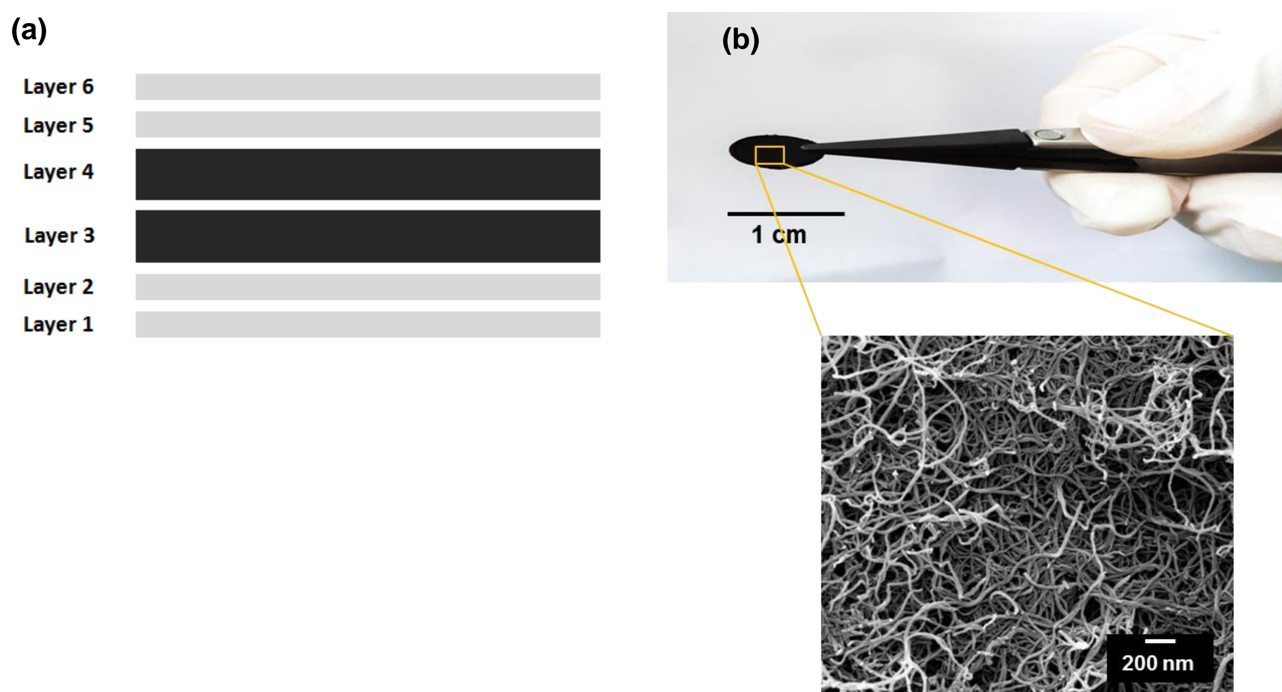

Figure 2-6 – (a) Schematic representation of the structure of the buckypaper samples. The middle layers (3 and 4) are only composed by CNTs while the outer layers (1, 2, 5 and 6) are composed by a mixture of CNTs and ZnO nanostructures. (b) Macroscopic and microscopic images of the produced buckypapers.

2.1.2.3. $Cd_xZn_{1-x}O/Mg_yZn_{1-y}O$ heterostructures

The $Cd_xZn_{1-x}O/Mg_yZn_{1-y}O$ heterostructures (Figure 2-7) were grown by MBE in *Institut für Physik, Humboldt-University of Berlin* and were kindly provided to us by our partners of the *IPFN* group in *CTN/IST*, as in the case of the nitride samples. A DCA-450MBE system was used to grow the $Cd_xZn_{1-x}O/Mg_yZn_{1-y}O$ heterostructures. Zn, Mg and Cd were evaporated from conventional effusion cells while atomic O was added through an Addon RF plasma source [12]. The alloys were grown on an *a*-plane sapphire (Al_2O_3) substrate using $Mg_yZn_{1-y}O$ as buffer layer. An illustration of the samples' structure can be seen in Figure 2-8. For the $Mg_yZn_{1-y}O$ alloy the nominal magnesium content was kept at 0.08, while for the $Cd_xZn_{1-x}O$ the CdO molar fraction was varied between 0 and 0.31 ($0 \leq x \leq 0.31$). The buffer layer was used in order to reduce the lattice and thermal expansion mismatch between the substrate and the $Cd_xZn_{1-x}O$ layer. By doing so, it is possible to minimize the propagation of the defects from the sapphire interface. The buffer layer with a thickness of ~ 500 nm was grown at 380 ^oC, while a temperature of 130 ^oC was used to grow the $Cd_xZn_{1-x}O$ layer with ~ 200 nm of thickness. A post-growth annealing in air was performed at 400 ^oC. A summary of the samples' characteristics is displayed in Table 2-13. Details of the growth process of these samples can be found in references [13,14].

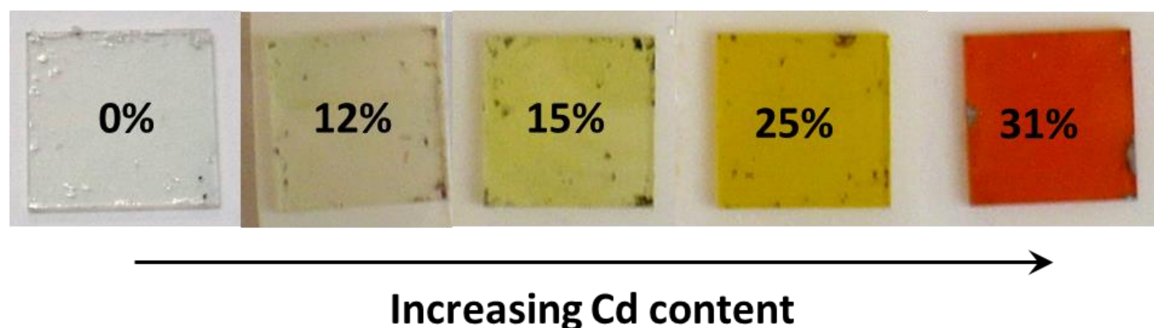

Figure 2-7 – Pictures of the $Cd_xZn_{1-x}O/Mg_yZn_{1-y}O$ samples with different Cd content. A change in the colour of the samples is observed with increasing Cd amount.

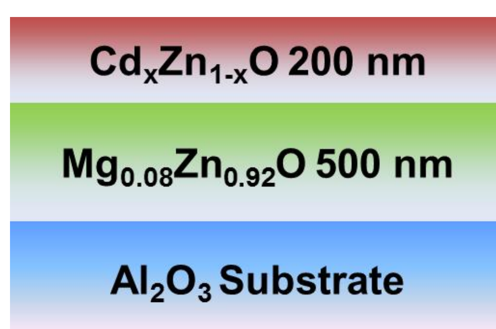

Figure 2-8 – Schematic representation $Cd_xZn_{1-x}O/Mg_yZn_{1-y}O$ heterostructures.

Table 2-13 – Main parameters of the $Cd_xZn_{1-x}O$/ $Mg_yZn_{1-y}O$ samples. Samples studied in section 6.4.

Sample	Thickness	Cd content	Mg content	Annealing (air)
ZnO/MgZnO 934	200 nm/ 500 nm	0	0.08	400 °C
CdZnO/MgZnO 935a	200 nm/ 500 nm	0.12	0.08	400 °C
CdZnO/MgZnO 936	200 nm/ 500 nm	0.15	0.08	400 °C
CdZnO/MgZnO 937	200 nm/ 500 nm	0.25	0.08	400 °C
CdZnO/MgZnO 938	200 nm/ 500 nm	0.31	0.08	400 °C

2.2. Growth methods

2.2.1. Laser assisted flow deposition (LAFD)

ZnO is a versatile material that can be grown by a large number of techniques, which include colloidal synthesis [15], CVD [16], PLD [17], MBE [18], thermal evaporation [19], among others. It is also one of the richest materials regarding the ability to be grown with different morphologies. Its different nanostructures includes tetrapods, nanorods, nanoribbons, nanocombs, nanoparticles, nanorings and so on [19,20]. Some of the mentioned morphologies can be seen in Figure 2-9.

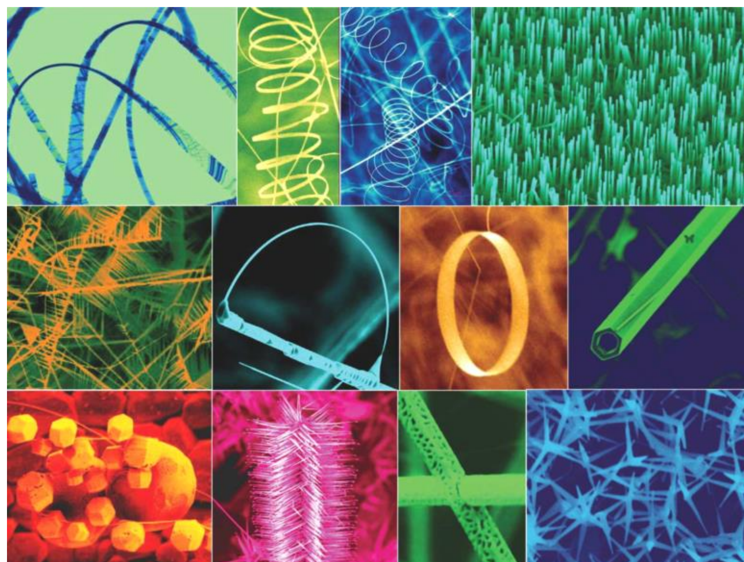

Figure 2-9 – Different ZnO morphologies produced by thermal evaporation. Image reprinted from [19].

Due to its high vapour pressure and the fact that ZnO does not melt, instead decomposes into its atomic components at the temperature of 1977 ^{o}C (at atmospheric pressure), the flux methods have been extensively studied [21]. The method used to grow the ZnO samples during this work can be fitted within this framework. The technique proved to be a very efficient method to grow ZnO samples with high crystallinity and optical quality [22–25].

The LAFD method is based on the laser floating zone (LFZ) technique [26–28]. The growth system comprises a CO_2 laser with a 10.6 µm line and a maximum power of 200 W as heating source, coupled to a reflective optical set-up producing a circular crown-shaped laser incidence. Figure 2-10 shows a picture of the growth system apparatus and a schematic representation of the process is depicted in Figure 2-11. The motors near to the planar and the parabolic mirrors are responsible for the translational and rotational movements of the feed rod precursor and the substrate holder. The precursors are moulded into the shape of cylindrical rods in order to be attached to the downer spindle of the system. These precursors are prepared by mixing the ZnO powders with a ligand (polyvinyl alcohol - PVA) to keep the powders aggregated and then processed by cold extrusion. To collect the material that evaporates from the precursor, substrates are placed on a sample holder attached to the upper spindle of the LFZ system, above the feed rod (Figure 2-11). The laser beam hits radially the tip of the precursor causing the decomposition of ZnO from the rod and the material is deposited on the substrate. The precursor rod must be well aligned with the centre of the substrate to improve the homogeneity of the deposition. Both the precursor and the sample holder are kept under rotation during the growth process for the same reason. Differences in the alignment can result in the necessity to adjust the growth parameters.

This process combines local heating generated by the high power laser focused on the precursor with the thermal decomposition of ZnO at its melting temperature. The generated gases are transferred to the lower temperature regions, after the reaction of the zinc with the atmospheric oxygen to form ZnO products. Different ZnO morphologies (mainly MRs, NPs and TPs) can be obtained for the as-grown samples as a result of different kinetics/thermodynamics

local conditions verified in different regions of the growth chamber [9,23]. The growth of crystals with dimensions on the micrometer scale (MRs) is promoted in the high temperature regions, close to the precursor tip, where there is a permanent air convection. The TPs and NPs are formed in the holder region, where the temperature is lower. These structures exhibit smaller dimensions than those formed on the top of precursor rod, some of them at the nanoscale. This growth process presents the advantage of being catalyst-free, it is highly versatile to grow ZnO nano/microstructures at relatively high synthesis rates (depending on the applied laser power), avoiding time consuming operations and thus being easily up scalable to large area deposition [23]. Furthermore, this is a simple single-step method that prevents contamination, since no crucibles or additional reagents are used to synthetize the ZnO structures.

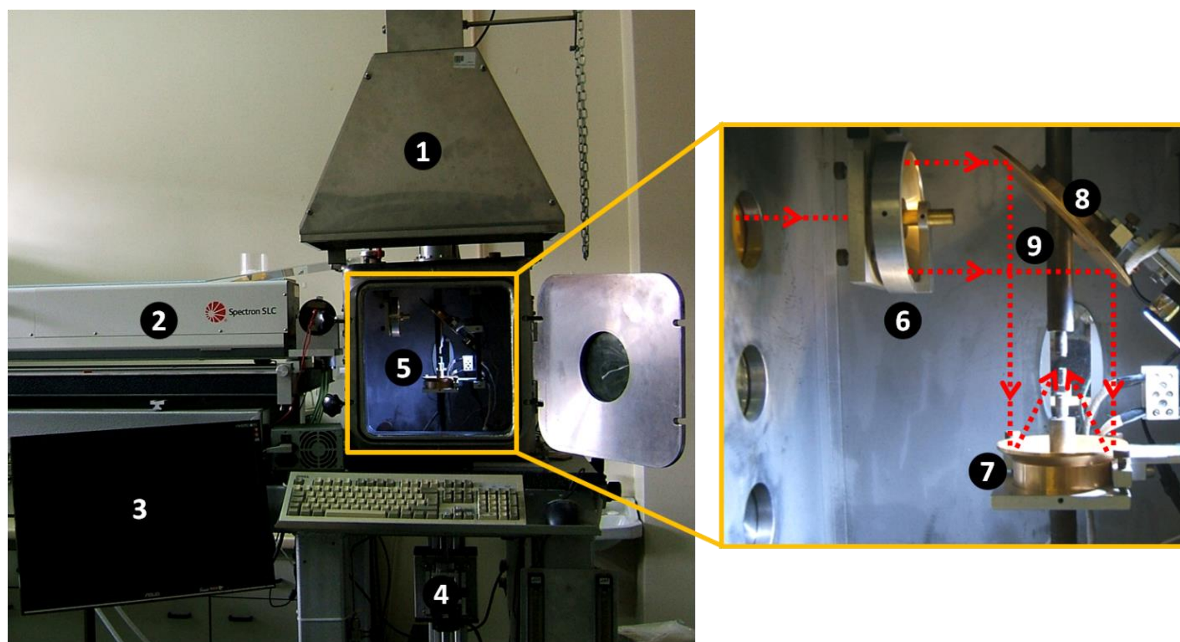

Figure 2-10 – LAFD apparatus comprising a ventilation system (1), a CO_2 laser (2) as heating source, the software control system (3), motors (4) and the growth chamber (5). A magnification of the growth chamber is depicted showing a scheme of the laser path. The chamber is constituted by a reflexicone (6), a parabolic (7) and a planar (8) mirrors and the motors (9), two for translational and two for rotational movements.

The morphologies can be controlled by an adequate combination of laser power, distance between precursor rod and sample holder and growth atmosphere. For laser powers higher than ~ 25 W, mostly TPs are produced, although some NPs can also be found in the same run of growth due to the initial heating stage, hampering the production of only TPs. The ratio TPs/NPs can, however, be increased by using high heating powers during the growth. High laser power results also in an increase of the growth yield. Even though TPs cannot be obtained separately, it is possible to produce only NPs. In this case, lower laser powers, close to 20-22 W, must be used. Under these conditions, a strong reduction of the growth yield is verified and a smaller amount of ZnO is produced, when compared with the use of higher powers.

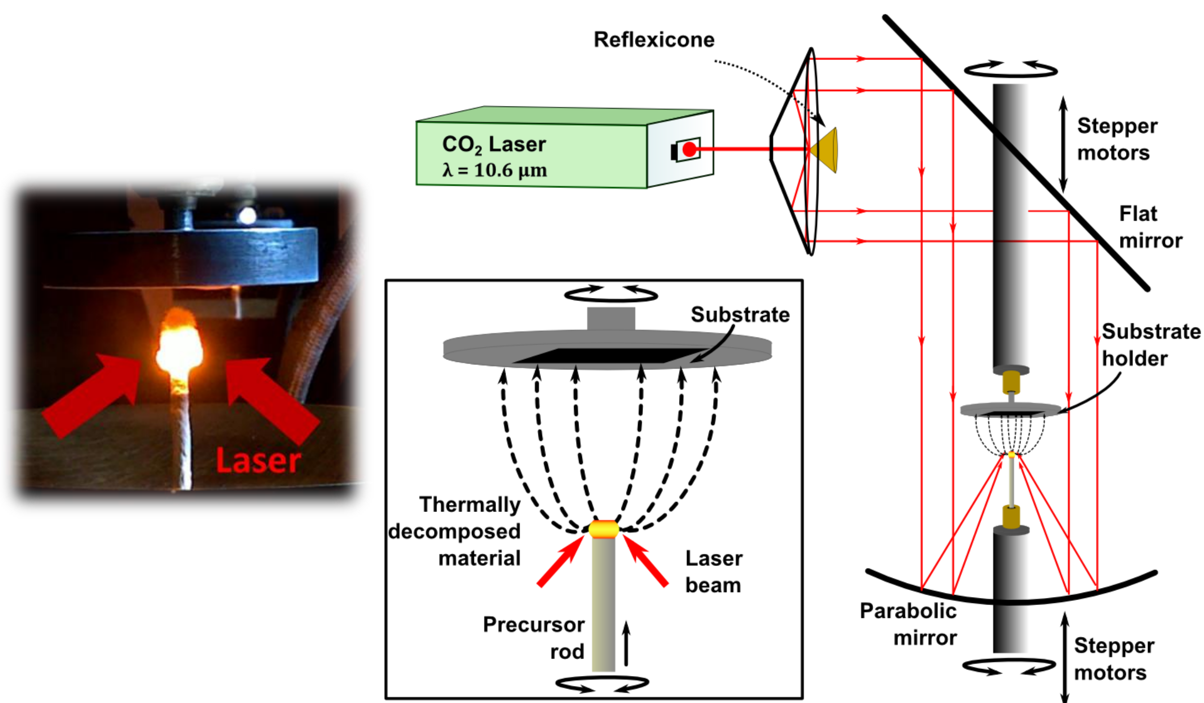

Figure 2-11 –Schematic representation of the LAFD process. The inset corresponds to a close-up of the growth region with the laser incidence area being clearly shown and indicated by the red arrows.

The growth atmosphere is also an import parameter in the control of the morphology. For instance, an oxygen-poor atmosphere leads to the production of NPs with laser powers up to 30 W, corresponding to a higher growth yield. A thermal evaporation process is very sensitive to the concentration of oxygen in the growth chamber since it will influence the volatility of the source materials and the stoichiometry of the vapour phase, as well as the formation of the products [29]. Under oxygen-poor atmospheres the production of MRs is strongly reduced.

A significant temperature gradient is present inside the growth chamber, with a high temperature drop with increasing distance from the position of the precursor tip, thus resulting in the mentioned different kinetics/thermodynamics local conditions. However, an accurate determination of the temperature present in holder and at the top of the precursor rod is not an easy task, due to the growth apparatus (rotating system and laser path). Therefore, it was not possible to measure the temperature at which each morphology is produced.

It is important to note that while the NPs and TPs are grown in the vapour phase and do not depend on the substrate used to collect the produced material, the MRs grow directly on the precursor rod and are attached to it (inset in Figure 2-11). So, the precursor rod can be seen as the substrate for the MRs growth. These structures are, generally, grown with laser powers between 30 W and ~ 50 W. For higher laser powers, decomposition of the produced MRs starts to take place, which will contribute for the TPs growth and the reduction of the MRs.

According to reference [30], this method can be included in the physical vapour deposition (PVD) category. PVD methods are characterized by a material flux direction always from hot to cold regions and a nonconformal and highly directional deposition. There is no need of a transport

(carrier) gas since the vapour is obtained from the sublimation of a solid source. The pressure of the system is usually kept under 1 atm. The LAFD method is founded on a vapour-solid (VS) mechanism that can be seen as a variation of the typical thermal evaporation technique. In this technique, condensed or solid (usually powder) sources are vaporized at elevated temperatures and then the resultant vapour phases condense under specific conditions, namely temperature, pressure or atmosphere, to form the desired products. The temperature applied to the source material depends mainly on the volatility of the material and it is slightly lower that the melting point of the source material [29].

The VS mechanism rules the growth of many metal oxide nanomaterials when no metal catalysts are used [31]. The crystal's growth is determined by the combination of external conditions such as temperature, supersaturation, reaction time or additives, and structurally related factors, like surface energy, anisotropy, intermolecular bonds or dislocations [30,32–34]. There are three basic steps involved in the formation of a crystal in an initially disordered phase: supersaturation of the liquid or gas phase, nucleation and growth of the nuclei into a crystal [30]. When the crystal's growth starts, in the present case from a supersaturated vapour phase, the material tend to condensate and form small nuclei that will continuously attach material until it develops to a "seed" for the crystal's formation. As time proceeds and the external conditions approach the "equilibrium" conditions, the growth process starts to be conducted by the surface energy of the formed crystal's faces [35]. The shape of the crystal is governed by the difference of relative growth rates at various crystal´s faces [34]. The growing surface would assume the shape for which the surface energy is the lowest [30]. Therefore, in general, the surface area of a crystal's face decreases with increasing surface energy and the facet with highest surface energy usually exhibits the smallest area, while lower energy facets are larger [29,35]. The planes with higher growth rates tend to disappear first, and consequently the planes with slower growth rates dominate the morphology of the crystal [33,34]. The bonds in the structure also play a significant role in its shape. The crystals have a tendency to elongate into the direction of the strongest bonds [35]. Since the interaction among the charges is governed by their distribution, the crystalline structure is arranged in order to minimize the electrostatic energy and usually the polar surfaces possess the highest surface energy [29].

In the case of WZ ZnO, its structure is described as a stacking of alternating planes comprised by tetrahedrally coordinated Zn^{2+} and O^{2-} along the *c*-axis, as shown in the first Chapter. This anisotropic structure leads to differences in the surface energy of the crystal's faces and a strong anisotropy in their growth rate [33,36]. ZnO exhibits a wide range of morphologies that can be produced by tuning the growth rates along the different crystal´s faces. The kinetic parameters for the different crystal's planes can be controlled by an appropriate choice of the growth conditions [37]. One of the more common morphologies for ZnO are the 1D structures, specifically wires or rods. In this case, due to the chemically active polar surfaces with electrostatic charges, the rods with the WZ structure frequently show a hexagonal morphology oriented along the polar growth direction, in order to minimize the total surface energy and giving rise to a uniaxial polarization along the *c*-axis [32,33]. A conceptual scheme of the growth of a WZ ZnO rod is displayed in Figure 2-12. The highest growth rate is observed along the *c*-axis, with the extremities of the rod being

composed by the polar (0001) and $(000\bar{1})$ planes and the large lateral facets corresponding to the nonpolar $\{01\bar{1}0\}$ and $\{2\bar{1}\bar{1}0\}$ family of planes, which have lower surface energy (Figure 2-13).

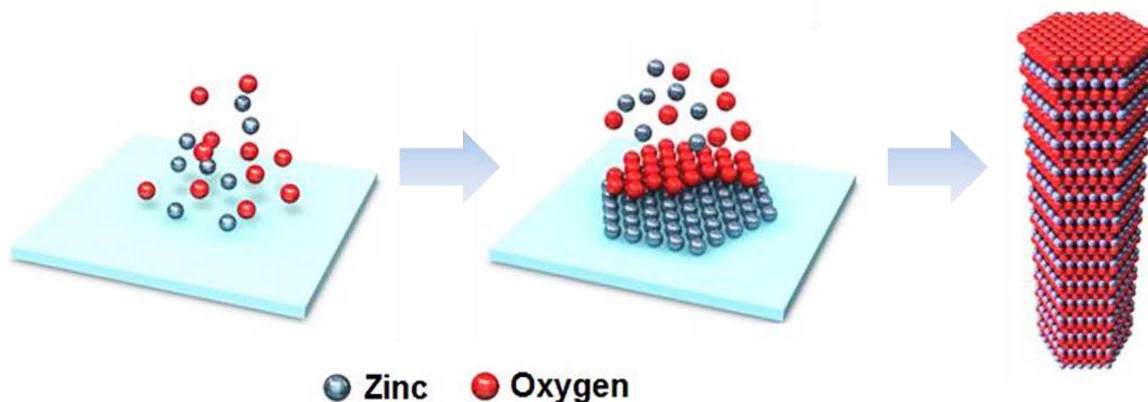

Figure 2-12 – Schematic representation of the growth mode and structural model for the growth of ZnO rods without the use of any catalyst. Adapted from reference [32].

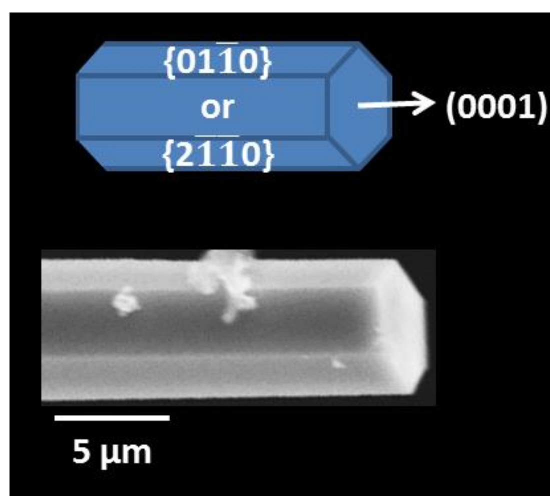

Figure 2-13 – Typical morphology of the LAFD produced ZnO MRs and the schematic representation of the corresponding facets. The indexation was made in accordance with the TEM results (Chapter 6) and reference [37].

ZnO TP structures have been studied by different researchers [38–43] with the aim of clarifying their growth mechanism. It is accepted that the formation of ZnO TPs has two steps: nucleation and growth. Several growth models have been proposed [38–43], among which the more cited are the ones of Shiojiri *et al*. [39] and Iwanaga *et al.* [40,41]. In the first one, the core from which the nucleation takes place are octahedral shaped nanocrystals of zinc blend structure with four {111} facets consisting of zinc and other four of oxygen. Afterwards, WZ ZnO crystals grow faster along the normal directions to the zinc surfaces, resulting in a TP morphology [39]. Iwanaga [40,41] introduced the so-called "octa-twin model" in which the process begins with the formation of octahedral multiple twin nuclei. During the growth, some of the twin-boundaries crack to release a large misfit strain and the crack openings are filled up by ZnO during further growth of the particle. Then branches grow preferentially oriented in perpendicular direction to the (0001) surfaces. Thus, a tetrapod-shaped particle is formed with the inter-branch angles

deviating from the regular tetrahedral relation due to the cracking of the octa-twin nucleus [41]. This model is adopted by many authors due to the correct description of the crystal geometric structure, although none of the experiments showed that the centre core contains an octahedral seed crystal [43].

More recently, Ronning *et al.* [43] suggested another growth model that comprises a first step with the formation of tiny ZnO clusters. These clusters may become unstable by further condensation of Zn and O atoms, collapsing into a tetrahedron-shape crystal that includes four ZnO grains (Figure 2-14a). These grains develop into the four branches of a TP, due to the faster growth rate along the *c*-axis direction of each of the four crystals. The dimensions and the shape of the particles depend on the growth conditions, namely on the temperature. This is the model that best applies to the synthesis of the present ZnO structures, since NPs always constitute the first layer, which transforms into microcrystalline TPs on the top layers. The first step occurs during the initial heating stage when the laser power starts to be applied. The NPs then collapse into TPs with further increase of the power, attaining the local temperature conditions for transformation. The growth steps should be similar to the ones reported by Chen *et al.* [44]. After decomposition of the ZnO precursor into Zn and oxygen vapours, both are transported to the lower temperature regions, above the laser incidence. Part of the Zn reacts with the oxygen and form small ZnO particles. These particles act as nucleating points for the TP growth. Since these particles are polyhedral with WZ structure, the four legs of TPs can thus grow further out from the nucleus crystal simultaneously via a VS mechanism with continuous condensation and diffusion of Zn and oxygen, provided that the growth conditions are favourable for the process to carry on [44]. As stated before, the polar surfaces have the highest surface energies for the WZ ZnO and thus, a morphology that tends to supress these surfaces is favourable. According to Ronning *et al.* [43], the four ZnO grains located at each apex of the tetrahedron, shown in Figure 2-14a, are oriented with the *c*-axis parallel to the apexes and the three pyramidal facets are composed by $\{11\bar{2}1\}$ planes. This geometry is energetically favourable, minimizing the ratio between the grain-boundary areas and surface areas. The presence of four single crystals, constituting the branches of the TPs, was observed by TEM, as will be shown in Chapter 6. The shape of the resulting TPs is given by the anisotropy of the respective growth rates in the different directions, which depends essentially on the temperature. If the growth rate along the *c*-axis is considerably larger than on $(11\bar{2}1)$ surfaces, the TPs branches will show a high aspect ratio. Alternatively, if the growth rates are similar, the TPs will have a bulkier structure [43].

Besides the crystal surface energies, the growth can also be affected by the presence of defects such as screw-dislocations. The presence of defects promotes the sticking of material species and nucleation [31]. Burton *et al.* [45] proposed that, at low supersaturation conditions, screw dislocations in the crystal surface could act as nucleation points and promote crystal's growth [30]. These authors suggested that, at low supersaturation, the growth can only proceed if new surface steps are formed and the growth rate is enhanced by the presence of defects as dislocations or twins [31]. A representation of a screw-dislocation growth can be seen in Figure 2-14b. Frank [46] showed that when the crystal is growing under supersaturated conditions it forms successive turns of steps in a spiral way (Figure 2-14b) that can form pyramids or cones [45]. Screw dislocations closely spaced lead to the formation of a smoothly advancing surface,

while a single dislocation forms a growth cone [47]. The influence of this type of growth cannot be discarded in the case of the TPs branches.

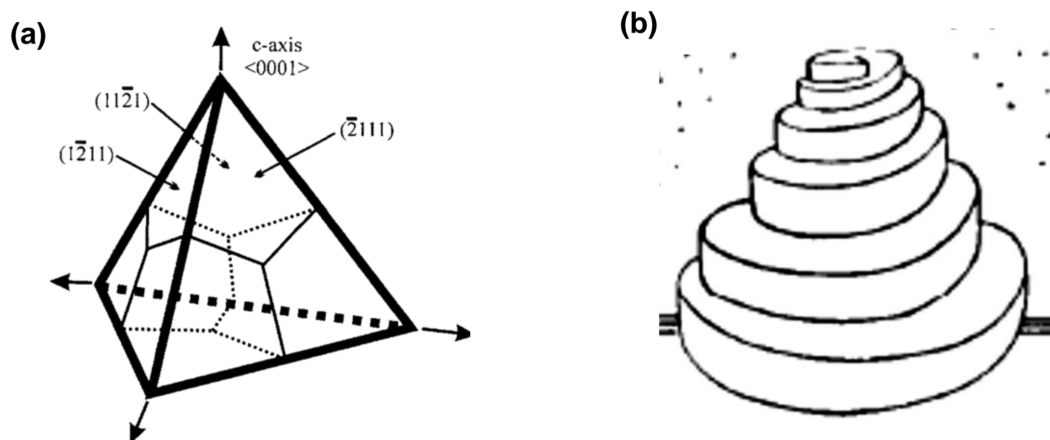

Figure 2-14 – (a) Illustrated view of the nucleus of the TP formation proposed by Ronning *et al.* [43], showing the four hexagonal single-crystalline grains of tetrahedral shape. (b) Growth cone formed by a screw dislocation. Image reprinted from [47].

2.2.2. Epitaxial techniques

The advances in epitaxial techniques to grow different kind of structures like films, NWs or quantum heterostructures have played a major role in device processing [48,49]. A great deal of importance is attributed to the control over composition, doping and interface definition, that can be achieved by the different experimental methodologies [48]. The term "epitaxial" means that the crystalline structure of the grown material follows the one of the underlying substrate [49]. Nowadays, with this kind of techniques an atomic-scale control of planar interfaces is possible. The control over interface definition together with the doping profiles, which allow obtaining high purity materials as well as materials with the desired concentration of optically or electrically active impurities, constitutes an essential testing ground for new ideas in condensed matter physics [48,49]. Specialized device structures can be grown by the deposition of sequences of different epitaxial layers, avoiding the need of post-growth processing steps and the diffusion of the dopant species [49].

Several epitaxy methods can be employed to grow a wide variety of materials, namely vapour phase epitaxy, molecular beam epitaxy and liquid phase epitaxy [48,49].

2.2.2.1. Molecular beam epitaxy (MBE)

MBE is conceptually one of the simplest ways for epitaxial growth, despite the required sophisticated technology [48,50]. This technique can be considered as a refined case of evaporation, using highly controlled evaporation of a variety of sources in ultrahigh-vacuum (UHV) conditions, with values typically lower than $\sim 10^{-10}$ torr [50,51]. It can be seen as a material deposition technique with the ability of yielding material with low impurity levels in a

reproducible and controlled way, allowing the exceptional control over the materials' composition, thickness and tailored doping [50,52]. By definition, the aim of MBE is to grow perfect single-crystal structure with morphology and lattice spacing exactly matching those of the substrate material [53]. A low growth rate is one of the characteristic features of the MBE method. Keeping the growth rate low guarantees sufficient surface diffusion and relaxation, in order to limit the formation of crystalline defects to a minimum, in addition to a well-controlled growth at the monoatomic layer level. The typical growth rates are in the order of 1 μm/h [51].

A scheme of a common MBE growth chamber can be seen in Figure 2-15. The chamber is composed by source cells (or ovens) radially aligned with the substrates, beam shutters and respective control mechanism, *in-situ* characterization tools, substrate heater, a mechanism to place and handle the samples, separate beam fluxes monitor and a system to cool down the chamber walls, in order to remove unused beam flux [49]. Moreover, a cooling system is mounted around the source ovens to reduce radiative heating of the chamber [49].

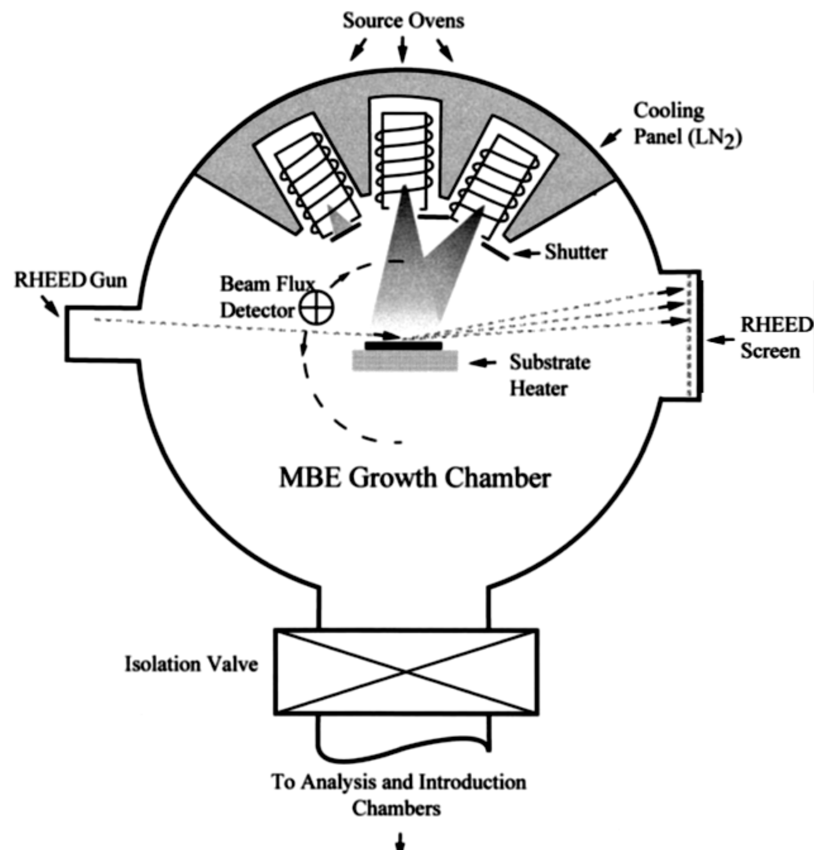

Figure 2-15 – Top view representation of a common MBE chamber showing the essential components: growth sources, shutters, beam flux detector and the reflection high energy electron diffraction (RHEED) system, which allows the monitoring of the structure during growth. Imagen taken from [49].

A MBE apparatus usually comprises an array of multiple sources, with mechanical shutters in front of them, which can be shuttered as desired [53]. As the shutters can be switched almost instantly (in comparison to the rate at which the material is deposited), it is possible to grow very thin layers exhibiting very sharp interfaces and change the composition of the material in an abrupt way [49,53]. Even though some gaseous sources are used in this method (often termed

chemical beam epitaxy), most of the source beams result from the heating of solid materials placed in source cells [51]. The cells are heated to the temperature at which the materials that are placed there evaporate, being then collimated into beams and directed towards the substrate [48,53]. The individual controlling of the evaporation of the sources leads to a precise control of chemical composition of the deposited material, at any specific time [51].

The substrate is placed on a rotating holder with its face oriented towards the material sources. The rotation is maintained in order to improve the homogeneity of the growth over the substrate surface [53]. The substrate is heated at a moderated temperature, providing enough thermal energy for the atoms of the beams to travel over the surface, but at the same time inhibiting diffusion between the interfaces [51]. The different source beams attain the substrate face and the material is deposited atomic layer by atomic layer (~ 0.2 - 0.3 nm) [49,53]. The surface migration plays an important role in the crystalline quality of the epitaxially grown samples. If the temperature is too low, the mobility of the species may not be sufficient to accomplish a thermodynamically stable structure. In this sense, some authors have studied the use of surfactant materials to improve the surface mobility by weakening the bonding of the atoms that reach the substrate. These surfactants are seen as impurities and are almost rejected from the growing structure [49]. The migration of the species defines the morphology of the growing material, which depends on several parameters, as deposition rate, surface temperature, surface material and its crystallographic orientation [48].

In order to produce structures with the crystalline lattice matching the one of the substrate, a substrate with lattice constants and thermal expansion coefficients similar to the ones of the deposited material must be chosen, otherwise dislocations will form. In some cases, a suitable substrate is difficult to find, so an initial layer is deposited to serve as a “virtual” substrate and “accommodate” the lattice parameters between the substrate and material that is being deposited. As previously mentioned, this layer is called buffer layer [53].

Under the low UHV pressure conditions, the interaction between the evaporated atoms (or molecules) in the vapour phase is suppressed, travelling in a nearly collision-free path, until arriving to the substrate or at the cooled walls of the chamber. When the source material attains these walls, it condenses and is removed from the system [49,51]. Thus, only the beam fluxes (that behave ballistically) and the surface reaction with the substrate influence the growth, providing remarkable control and reproducibility [50]. Due to the existence of cooled walls surrounding the source cells and the substrate holder, the beams make basically a single pass through the chamber before condensing on the walls, keeping a low background pressure in the system, which preserves the purity of the samples [49].

Other advantages associated with the use of UHV is the compatibility with *in-situ* analytical techniques, making possible real-time structural and chemical characterization, which are very important to understand the kinetics of the surface reactions and to monitor and refine the growth [50,51,53]. Some of these techniques include RHEED or X-ray photoelectric spectroscopy (XPS) [49–51,54]. It is also possible to attach other analytic instruments to the growth chamber or to a separate one, where the as-grown samples can be transferred to and from the growth chamber without ambient exposure [51].

In conclusion, the combination of extremely clean environment, slow growth rate, and the independent control of the evaporation of individual sources enable the precise fabrication of nanostructures and nanomaterials at a single atomic layer by MBE [51].

A special case of MBE that has been widely used in the growth of nitride samples is the so called plasma-assisted MBE (PAMBE). In this case, plasma-induced nitrogen radicals are combined with the evaporated metal atoms from source cells [55,56].

When considering the growth of heteroepitaxial samples, with substrates of a different material from the one that is being deposited, essentially three morphology growth modes can be considered: Frank-van der Merwe, Volmer-Weber and Stranski-Krastanov [48], as illustrated in Figure 2-16. For the purposes of the present work, only the last one will be briefly addressed, since is the one relevant in the growth of the studied nitride quantum structures. In this case, 3D islands are formed on the top of a thin layer that completely covers the substrate. This kind of morphology is frequently identified in systems where a considerable lattice mismatch between the epilayer and the substrate occurs [48]. The growth is initiated by the formation of a thin layer only with a few monolayers, denominated “wetting” layer, followed by the elastic relaxation of the strain formed due to the lattice mismatch between the substrate and the growing material, which leads to the formation of 3D islands. The subsequent morphology of the deposited structures is found to be strongly dependent on the heating temperature of the substrate, being possible to tailor (up to some extent) the morphology of the growing material [2,57].

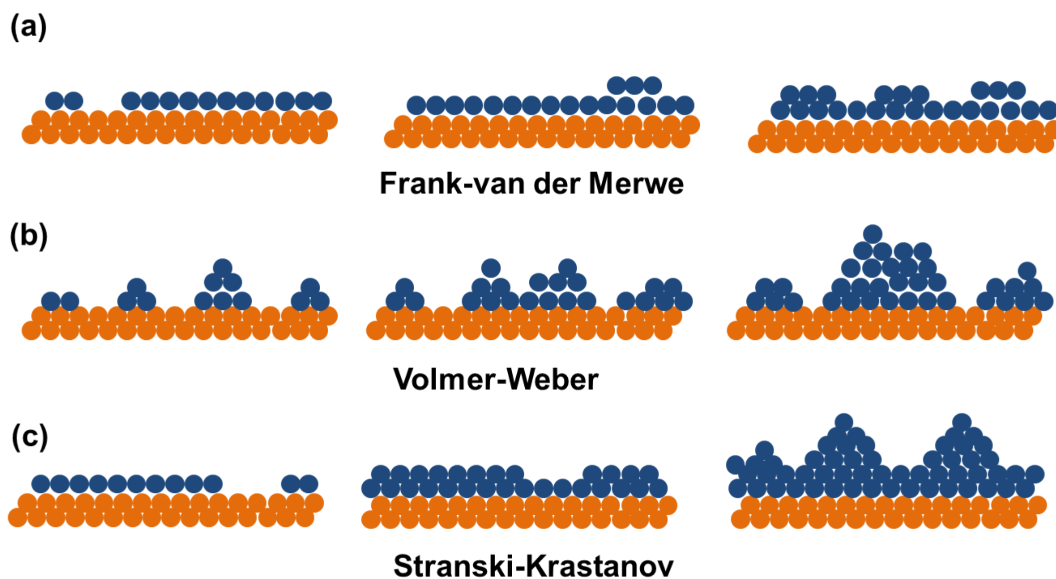

Figure 2-16 – Illustration of the three MBE growth modes for heteroepitaxial growth morphologies: (a) Frank-van der Merwe, (b) Volmer-Weber and (c) Stranski-Krastanov. Image based on [48].

2.2.2.2. Hydride vapour phase epitaxy (HVPE)

Besides the deposition by molecular beams, epitaxial growth can also be made by the hydrodynamic transport of material from gas sources to the substrate, being denominated by vapour phase epitaxy (VPE) [48]. Several advantages are associated to the use of gas sources,

namely the possibility of being used at RT, consequently with less contamination than higher-temperature sources, and a simple reactor design, allowing a more uniform flux of material when compared to MBE. The main drawback of the VPE growth is related with the used gas sources that are frequently toxic [48].

Hydride vapour phase epitaxy (HVPE) is a well-known epitaxial technique that has been widely employed in the production of III-nitride materials, mainly due to its high growth rates (few tens of µm per hour), the production of crack-free, high-quality epitaxial layers with low defect concentrations and its lack of carbon incorporation into the product material, which constitutes a common contaminant in metalorganic process [55,58]. It is an epitaxy process that operates near thermodynamic equilibrium, involving thermo-chemical reactions at atmospheric pressure [59]. Due to the pressures used, the flow of the gas is viscous and the chemicals reach the substrate by diffusion. The transport of the material to the substrate comprises a gas phase and surface chemical reactions, along with mass transport within the gaseous precursors as they flow through the reactor [48]. At the crystal surface, the species experience a sequence of chemical reactions leading to an extension of the substrate crystal lattice and formation of products that must be removed from the neighbourhood region for the process to continue [30]. The main steps of the process are summarized in Figure 2-17.

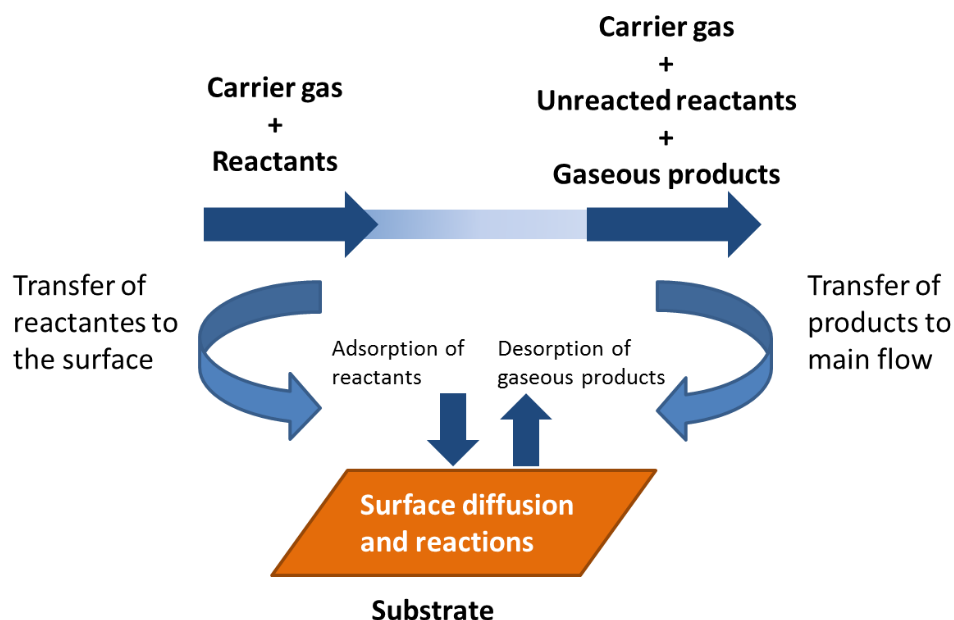

Figure 2-17 – Scheme of the HVPE process. Based on reference [30].

This technique provides selective area growth and lattice-matched growth surfaces and thick, strain-relieved buffer layers [55,59]. Owing to its high growth rate, HVPE allows the growth of very thick films, offering the possibility of substrate removal to obtain substrate-free bulk samples [55].

Figure 2-18 depicts a schematic representation of a HVPE reactor. In this process a hot wall reactor, working at a total pressure close to the atmospheric one (1 atm), is commonly used [54,59]. This reactor is placed in a multiple zone furnace that allows the optimum control of

source and substrate temperatures, as well as the delivery of all reactants. In this way, the temperatures for the reactions and for the deposition can be independently controlled [59].

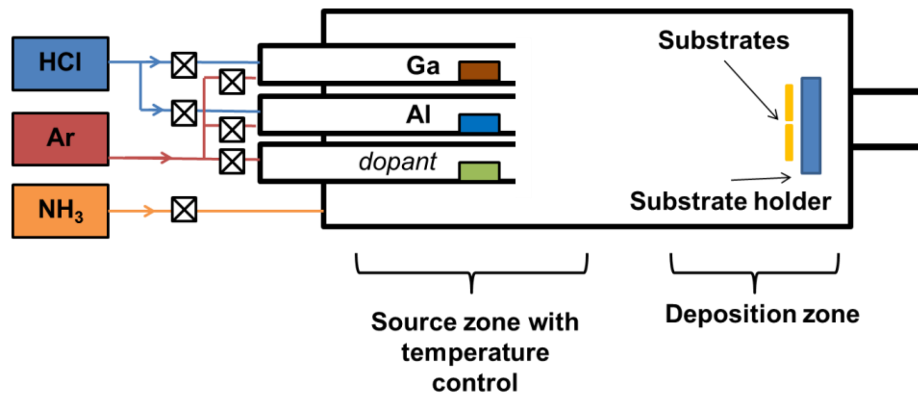

Figure 2-18 – Schematic representation of a common HVPE reactor. Scheme inspired in the one of TDI suppliers website [58].

An important feature of the HVPE technique is that, in the case of the III-V materials' growth, the group-III precursors are synthesized within the reactor vessel, upstream from the substrate, by either the reaction of a halide containing gas, such as hydrogen chloride (HCl), with a group III metal (usually kept at high temperature) or by the reaction of a group V chloride *(e.g.*, $AsCl_3$) with either a group III metal or III-V bulk compound [54]. Carrier gases commonly used include ammonia (NH_3), hydrogen (H_2) and various chlorides or halides [54,55]. The reaction products are determined by the halide and carrier gases flowing through the reactors, the materials inside the reactor, and the temperature at the point of the reaction [59]. The final reaction leads to the deposition of the desired material onto the substrate. The substrate is often kept under rotation in order to achieve a high uniformity of the synthesised material, as in the case of MBE [59]. The growth process is mainly controlled by parameters like the total pressure inside the chamber, the partial pressures of reaction species, the input ratio of V/III and the growth temperature, which can be precisely controlled [30,59].

The main reason to use heated walls on the growth reactor is the relatively low vapour pressures exhibited by the metal chlorides at RT, causing the condensation of these molecules on unheated surface. The *in-situ* synthesis of the metal chlorides and halides constitutes an important advantage, avoiding the need of complex vapour delivery systems and preserving the source integrity during the growth process, which otherwise would be compromised by the hydroscopic and corrosive nature of the halides [54].

The growth of III-nitrides can be seen as a two-step, thermodynamic-driven, chemical reaction between metallic sources of the metal ions (Ga, Al, and In), HCl and NH_3, at temperatures of 1000 - 1100 ^{o}C and atmospheric pressure [58]. For instance and described in a simple way, the heated HCl gas passes through the Ga source, forming gallium chloride (GaCl) that then reacts with NH_3, producing solid GaN (deposited on the substrate) and gaseous H_2 [59]. The substrate is placed on a *susceptor* perpendicular to the main stream of reaction gases. This *susceptor*, which corresponds to a holder made with a material with the ability to absorb electromagnetic radiation

and convert it into heat, is rotated during the growth [59]. The final reaction can be described as [30]:

$$GaCl + NH_3 \rightarrow GaN + HCl + H_2,$$

$$GaCl_3 + NH_3 \rightarrow GaN + 3\ HCl.$$

An important factor to take into account during the growth of these nitrides is the relatively inactive disassociation of NH_3, avoiding the formation of stable N_2 molecules, which are essentially unreactive at the temperatures of interest. The uniform and effective transport of reactive nitrogen to the growth surface is crucial to obtain stoichiometric, homogeneous films over large areas, inhibiting the growth of metal-rich films [54]. Furthermore, the use of corrosive halogen species contributes to the removal of excess metallic species from the growth surface, also preventing the formation of metal-rich material or phase-separated Ga droplets. This effect is designated by self-stabilization and also allows the growth of high quality GaN samples under Ga-rich conditions, requiring lower ammonia flow for stoichiometric growth [54]. Additionally, the use of gaseous HCl also provides an impurity "self-cleaning" effect, resulting in the growth of epitaxial layers with low background impurities [58].

2.3. Doping

As mentioned before, RE-doped nitride samples were studied in order to get some insights about their possible applications in solid state lighting devices. In the last years, several nitride systems have been doped with these ions either *in-situ* or by *ex-situ* methods. In the first case, the ions are introduced into the host during the growth. By doing so, it is possible to avoid the damage of the crystal lattice induced by the *ex-situ* procedures and produce high crystal quality samples with a wide range of doping concentrations [60]. For *in-situ* doping, a good understanding and control of all the growth processes is of crucial importance, as well a deep knowledge about the interactions between the dopant flux and the main V/III fluxes. Only with all these issues addressed, an adequate control of the RE concentration over many orders of magnitude could me obtained, together with an uniform doping [61]. However, some concerns still remain, namely due to diffusion, solubility limits, accumulation of the dopants at the surface or even phase segregation [62].

For the *ex-situ* methods, the highlight is given to ion implantation, which offers many advantages over the *in-situ* processes, since it is a method where the control of the doping concentration can be achieved regardless the growth conditions of the samples, even allowing for optical selective-area doping [61,63].

2.3.1. Ion implantation

Ion implantation is a non-equilibrium method that has been widely used for changing the material properties and modifying the near-surface composition of a sample. This technique constitutes a standard method for controllably introducing dopant species into different hosts,

namely semiconductors for integrated circuits fabrication [64,65]. The ion beam modification of the materials is made by the interactions between the energetic ions and the inter atomic potentials of the bombarded hosts [66]. The presence of these foreign atoms leads to changes in the mechanical, electrical, optical, magnetic, and superconducting properties of the materials [65]. In this sense, this method appears as a convenient way to incorporate RE ions in several matrixes, with an especial emphasis on III-nitrides [62]. The ions can be introduced independently of thermodynamic and solubility factors, therefore allow obtaining dopant concentrations and distributions almost as desired, which, in many cases, would not otherwise be possible [65]. Other advantages of this technique include the short times of the process, the possibility to obtain homogeneity in the ion amount over large areas, adjustable and reproducible doping profiles even with multiple implantations, which is extremely difficult to accomplish by diffusion techniques [66].

Figure 2-19a shows a schematic drawing of an ion beam system. For common applications, an ion beam of the desired dopant is accelerated through a potential in the range of 10 - 100 kV. The basic constituents of this kind of system comprise the dopant source, an acceleration column, a mass-separator and the target chamber [65]. The dopant atoms are volatilized, ionized, accelerated, separated by mass-to-charge ratios, and targeted to the host material [66]. The nature of the interaction between the ions and the host depends mostly on the ion dopant (charge and mass), on the chemical composition and structure of the host material, on the energy of the beam and the temperature of the target [57,66]. All these parameters will define the dominant interactions inside the host target during the ion trajectory. Throughout their path inside the host, some of the ions' energy is transferred to the electrons of the host atoms, leading to their ionization. This transfer results in a loss of energy by the accelerated ions, while their trajectory is practically preserved [57]. Beside the collisions with the electrons, the incident ions suffer nuclear collisions with atoms of the host, causing the displacement of many atoms from their normal locations (Figure 2-19b). These atoms can recoil and collide between themselves inducing additional displacements and producing a collision cascade. All these collisions lead to strong loss of energy by the incident ions, which eventually stop within the crystal. Depending on the target material and ion energy, the penetration depth can go from < 10 nm to 10 μm [57,64–66]. In the case of GaN layers the penetration depth is close to $\sim$ 100 nm (for the implantation energies used in this work) [62]. The amount of ions accelerated in the beam is generally denominated by ion dose or fluence and is defined as the number of ions per cm^2 implanted into the sample, being expressed in units of ions.cm^{-2} [65]. The ion fluence depends on the desired application and is usually in the range from 10^{11} to 10^{18} ions.cm^{-2} [66]. The lattice damage is strongly influenced by this parameter, being probably the most critical one [62].

The major drawback of this technique is related with the mentioned collisions, which conducts to a great damage on the crystal lattice of the host material, since many atoms are displaced from their lattice sites. These events produce a highly disordered region around the path of the ions. If the implantation dose is sufficiently high, an overlap of these different regions can occur, leading to the amorphisation of the implanted region [65]. In order to recover the crystallinity of the lattice, post-implantation thermal annealing treatments at high temperatures are employed [62]. It is assumed, as an empirical rule based on experimental data, that an annealing temperature

about 2/3 of the host's melting temperature (measured in Kelvin) should be used to efficiently remove the damage caused by implantation [62,66,67]. Since this is a ballistic process, damage production is nearly unaffected by the chemical properties of both host and implanted ions and so, the annealing processes are similar for the different ions [62]. However, semiconductors with high melting points but with rather low dissociation temperatures, like is the case of GaN, lack an effective method to address the damage formation. Taking into account the mentioned empirical rule, for GaN, temperatures close to 1600 ^{o}C are the ideal ones for the post-implantation annealing. Yet, at ~ 800 ^{o}C some nitrogen diffusion out of the sample starts to occur. Thus, in order to use higher annealing temperatures, the partial nitrogen pressures must be increased to avoid the surface dissociation. High temperature and high pressure (~ 1GPa) annealing are often performed in III-nitride samples [62]. Implantation at high temperatures can also be used to minimize the damage formation during the process. For instance, GaN evidences a strong dynamic annealing during the implantation, meaning that a portion of the defects, like interstitials or vacancies, created by the high energetic ion beam recombine during the process, even at low temperatures [62]. High temperatures lead to higher defect mobility resulting in a higher defect annihilation. Thus, it is expected that high implantation temperatures will enhance the dynamic annealing effect, improving the structural and optical properties [60,62]. For example, a comparison between implanted nitride samples, with the same fluence of Eu ions, either at RT and 500 ^{o}C revealed that, for the highest temperature, the defect concentration was significantly decreased [62,68].

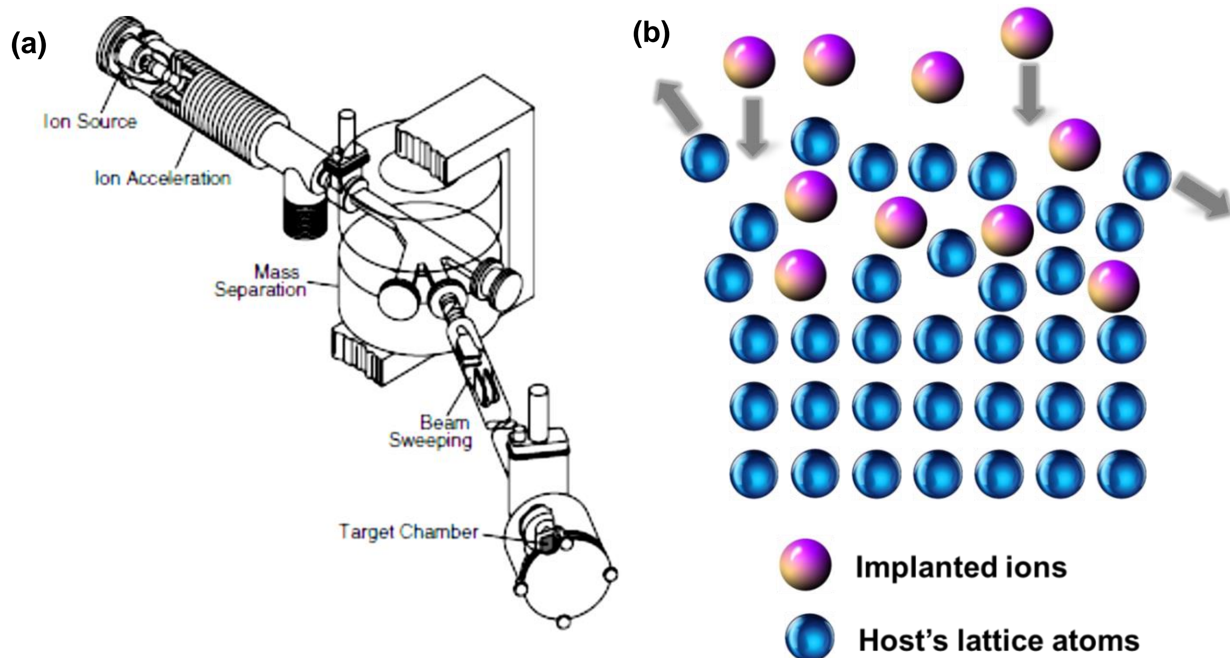

Figure 2-19 – (a) Illustration of an ion implantation system [65]. (b) Schematic representation of the damage created in the lattice of the host during the implantation process.

Taking into account all the mentioned considerations, the most important parameters to consider during an ion implantation experiment are the fluence, the beam energy, the implantation temperature and also the implantation geometry. Generally the samples are tilted

off-axis (7-10°) in order to avoid the channelling effect and also to achieve a more well-define implantation profile [62]. The channelling effect occurs when the beam is aligned with one axis or crystallographic plane of the implanted sample.

For the RE-doped III-nitrides, beside the lattice recovery, the post-implantation thermal annealing is used as a means to optically activate the ions. For these ions, relatively high fluences are needed. Since the interest resides in obtaining strong light emission, a large number of RE ion centres must be introduced in the nitride templates. The optimum doping level is around 1 at%, which can only be attained using high ion fluences [62]. With such high ion fluences, a high level of lattice damage needs to be overcome. It is known that, in general, samples implanted at RT do not exhibit RE-related luminescence without a post-implantation annealing treatment. This can be related to the formation of defects during the implantation process that can constitute nonradiative recombination centres, which can only be reduced after the annealing. Another role of the annealing is to promote the RE ions diffusion into specific lattice sites where their luminescence can be enhanced [60].

Despite the considerable problems in achieving complete lattice damage removal after the implantation process, ion implantation has proved to be an efficient way to incorporate RE ions into nitride hosts, exhibiting efficient luminescence emission in the different regions of the electromagnetic spectrum [63,69–71].

2.4. References

1. O. Landré, C. Bougerol, H. Renevier, and B. Daudin, Nanotechnology **20**, 415602 (2009).

2. B. Daudin, F. Widmann, G. Feuillet, Y. Samson, M. Arlery, and J. Rouvière, Phys. Rev. B **56**, R7069 (1997).

3. M. Arlery, J. L. Rouvière, F. Widmann, B. Daudin, G. Feuillet, and H. Mariette, Appl. Phys. Lett. **74**, 3287 (1999).

4. V. Chamard, T. Schülli, M. Sztucki, T. Metzger, E. Sarigiannidou, J.-L. Rouvière, M. Tolan, C. Adelmann, and B. Daudin, Phys. Rev. B **69**, 125327 (2004).

5. N. Gogneau, D. Jalabert, E. Monroy, T. Shibata, M. Tanaka, and B. Daudin, J. Appl. Phys. **94**, 2254 (2003).

6. J. Rodrigues, S. M. C. Miranda, A. J. S. Fernandes, E. Nogales, L. C. Alves, E. Alves, G. Tourbot, T. Auzelle, B. Daudin, B. Méndez, T. Trindade, K. Lorenz, F. M. Costa, and T. Monteiro, Phys. Status Solidi **10**, 667 (2013).

7. Y. Zheng, L. Zheng, Y. Zhan, X. Lin, Q. Zheng, and K. Wei, Inorg. Chem. **46**, 6980 (2007).

8. D. Mata, R. M. R. F. Silva, A. J. S. Fernandes, F. J. Oliveira, P. M. F. J. Costa, and R. M. R. F. Silva, Carbon **50**, 3585 (2012).

9. J. Rodrigues, A. J. S. Fernandes, D. Mata, T. Holz, R. G. Carvalho, R. Fath Allah, T. Ben, D. Gonzalez, R. F. Silva, A. F. da Cunha, M. R. Correia, L. C. Alves, K. Lorenz, A. J. Neves, F. M. Costa,

and T. Monteiro, in *SPIE OPTO*, edited by F. H. Teherani, D. C. Look, and D. J. Rogers (International Society for Optics and Photonics, 2014), p. 89871F.

10. D. Mata, F. J. Oliveira, M. Ferro, P. S. Gomes, M. H. Fernandes, M. A. Lopes, and R. F. Silva, J. Biomed. Nanotechnol. **10**, 725 (2014).

11. T. Holz, D. Mata, N. F. Santos, I. Bdikin, A. J. S. Fernandes, and F. M. Costa, ACS Appl. Mater. Interfaces **6**, 22649 (2014).

12. A. Redondo-Cubero, J. Rodrigues, M. Brandt, P. Schäfer, F. Henneberger, M. R. Correia, T. Monteiro, E. Alves, and K. Lorenz, in *SPIE OPTO*, edited by F. H. Teherani, D. C. Look, and D. J. Rogers (International Society for Optics and Photonics, 2013), p. 86260N.

13. S. Kalusniak, S. Sadofev, J. Puls, and F. Henneberger, Laser Photonics Rev. **3**, 233 (2009).

14. S. Sadofev, S. Blumstengel, J. Cui, J. Puls, S. Rogaschewski, P. Schäfer, and F. Henneberger, Appl. Phys. Lett. **89**, 201907 (2006).

15. A. S. Pereira, M. Peres, M. J. Soares, E. Alves, A. Neves, T. Monteiro, and T. Trindade, Nanotechnology **17**, 834 (2006).

16. P.-C. Chang, Z. Fan, D. Wang, W.-Y. Tseng, W.-A. Chiou, J. Hong, and J. G. Lu, Chem. Mater. **16**, 5133 (2004).

17. M. Peres, M. J. Soares, A. J. Neves, T. Monteiro, V. E. Sandana, F. Teherani, and D. J. Rogers, Phys. Status Solidi **247**, 1695 (2010).

18. A. Setiawan, Z. Vashaei, M. W. Cho, T. Yao, H. Kato, M. Sano, K. Miyamoto, I. Yonenaga, and H. J. Ko, J. Appl. Phys. **96**, 3763 (2004).

19. Z. L. Wang, Mater. Today **7**, 26 (2004).

20. L. Schmidt-Mende and J. L. MacManus-Driscoll, Mater. Today **10**, 40 (2007).

21. K. Takahashi, A. Yoshikawa, and A. Sandhu, *Wide Bandgap Semiconductors: Fundamental Properties and Modern Photonic and Electronic Devices* (Springer, 2007).

22. J. Rodrigues, M. R. N. Soares, R. G. Carvalho, A. J. S. Fernandes, M. R. Correia, T. Monteiro, and F. M. Costa, Thin Solid Films **520**, 4717 (2012).

23. J. Rodrigues, M. Peres, M. R. N. Soares, A. J. S. Fernandes, N. Ferreira, M. Ferro, A. J. Neves, T. Monteiro, and F. M. Costa, J. Nano Res. **18-19**, 129 (2012).

24. J. Rodrigues, D. Mata, A. J. S. Fernandes, M. A. Neto, R. F. Silva, T. Monteiro, and F. M. Costa, Acta Mater. **60**, 5143 (2012).

25. J. Rodrigues, T. Holz, R. Fath Allah, D. Gonzalez, T. Ben, M. R. Correira, T. Monteiro, and F. M. Costa, Sci. Rep. **5**, 10783 (2015).

26. F. M. Costa, M. F. Carrasco, R. F. Silva, and J. M. Vieira, *Laser Floating Zone. Perspectives on Superconductivity Research* (Nova Science Publishers, 2005).

27. F. Ritzert, L. Westfall, and L. Center, NASA Tech. Memo. **4732**, (1996).

28. S. M. Koohpayeh, D. Fort, and J. S. Abell, Prog. Cryst. Growth Charact. Mater. **54**, 121 (2008).

29. C. Jagadish and S. J. Pearton, *Zinc Oxide Bulk, Thin Films and Nanostructures: Processing, Properties and Applications* (Elsevier, 2006).

30. G. Dhanaraj, K. Byrappa, V. Prasad, and M. Dudley, *Springer Handbook of Crystal Growth* (Springer, 2010).

31. S. Barth, F. Hernandez-Ramirez, J. D. Holmes, and A. Romano-Rodriguez, Prog. Mater. Sci. **55**, 563 (2010).

32. J. Sohn, W. Hong, S. Lee, and J. Ku, Sci. Rep. **4**, 5680 (2014).

33. A. Pimentel, J. Rodrigues, P. Duarte, D. Nunes, F. M. Costa, T. Monteiro, R. Martins, and E. Fortunato, J. Mater. Sci. **50**, 5777 (2015).

34. W.-J. Li, E.-W. Shi, W.-Z. Zhong, and Z.-W. Yin, J. Cryst. Growth **203**, 186 (1999).

35. P. Hartman and W. G. Perdok, Acta Crystallogr. **8**, 49 (1955).

36. M. R. Alenezi, A. S. Alshammari, K. D. G. I. Jayawardena, M. J. Beliatis, S. J. Henley, and S. R. P. Silva, J. Phys. Chem. C. Nanomater. Interfaces **117**, 17850 (2013).

37. Z. L. Wang, J. Phys. Condens. Matter **16**, R829 (2004).

38. Y. Dai, Y. Zhang, and Z. L. Wang, Solid State Commun. **126**, 629 (2003).

39. M. Shiojiri and C. Kaito, J. Cryst. Growth **52,** 173 (1981).

40. H. Iwanaga, M. Fujii, and S. Takeuchi, J. Cryst. Growth **134**, 275 (1993).

41. H. Iwanaga, M. Fujii, and S. Takeuchi, J. Cryst. Growth **183**, 190 (1998).

42. Y. Ding, Z. L. Wang, T. Sun, and J. Qiu, Appl. Phys. Lett. **90**, 153510 (2007).

43. C. Ronning, N. G. Shang, I. Gerhards, H. Hofsäss, and M. Seibt, J. Appl. Phys. **98**, 034307 (2005).

44. Z. Chen, Z. Shan, M. S. Cao, L. Lu, and S. X. Mao, Nanotechnology **15**, 365 (2004).

45. W. K. Burton, N. Cabrera, and F. C. Frank, Philos. Trans. R. Soc. A Math. Phys. Eng. Sci. **243**, 299 (1951).

46. F. C. Frank, Discuss. Faraday Soc. **5**, 48 (1949).

47. S. Brenner and G. Sears, Acta Metall. **4**, 268 (1956).

48. K. Barnham and D. Vvedensky, *Low-Dimensional Semiconductor Structures: Fundamentals and Device Applications* (Cambridge University Press, 2008).

49. J. R. Arthur, Surf. Sci. **500**, 189 (2002).

50. S. Kasap and P. Capper, *Springer Handbook of Electronic and Photonic Materials* (Springer, 2007).

51. G. Cao, *Nanostructures & Nanomaterials: Synthesis, Properties & Applications* (Imperial College Press, 2004).

52. R. F. C. Farrow, *Molecular Beam Epitaxy: Applications to Key Materials* (Noyes Publications, 2012).

53. R. W. Kelsall, I. W. Hamley, and M. Geoghegan, *Nanoscale Science and Technology* (John Wiley and Sons, 2005).

54. Jacques I. Pankove and T. D. Moustakas, *Gallium-Nitride (GaN) II* (Academic Press, 1998).

55. Z. C. Feng, *III-Nitride Devices and Nanoengineering* (Imperial College Press, 2008).

56. H. Morkoç, *Nitride Semiconductors and Devices* (Springer, 1999).

57. S. Magalhães, Caracterização e Modificação de Heteroestruturas de Nitretos Do Grupo III, PhD thesis, Universidade de Aveiro, 2012.

58. Oxford Instruments, Hydride Vap. Phase Ep. (HVPE by TDI) (2008).

59. T. Yao and S.-K. Hong, *Oxide and Nitride Semiconductors* (Springer, 2009).

60. K. P. O'Donnell and B. Hourahine, Eur. Phys. J. - Appl. Phys. **36**, 91 (2006).

61. A. J. Steckl, J. C. Heikenfeld, M. J. Garter, C. C. Baker, and R. Jones, IEEE J. Sel. Top. Quantum Electron. **8**, 749 (2002).

62. K. P. O'Donnell, *Rare-Earth Doped III-Nitrides for Optoelectronic and Spintronic Applications* (Springer, 2009).

63. E. Alves, K. Lorenz, R. Vianden, C. Boemare, M. J. Soares, and T. Monteiro, Mod. Phys. Lett. B **15**, 1281 (2001).

64. J. S. Williams and J. R. Bird, *Ion Beams for Materials Analysis* (Elsevier, 1989).

65. M. A. Nastasi and J. W. Mayer, *Ion Implantation and Synthesis of Materials* (Springer, 2006).

66. B. Schmidt and K. Wetzig, *Ion Beams in Materials Processing and Analysis* (Springer Science & Business Media, 2012).

67. C. Ronning, C. Borschel, S. Geburt, and R. Niepelt, Mater. Sci. Eng. R Reports **70**, 30 (2010).

68. K. Lorenz, N. P. Barradas, E. Alves, I. S. Roqan, E. Nogales, R. W. Martin, K. P. O'Donnell, F. Gloux, and P. Ruterana, J. Phys. D. Appl. Phys. **42**, 165103 (2009).

69. J. Rodrigues, N. Ben Sedrine, M. Felizardo, M. J. Soares, E. Alves, A. J. Neves, V. Fellmann, G. Tourbot, T. Auzelle, B. Daudin, M. Boćkowski, K. Lorenz, and T. Monteiro, RSC Adv. **4**, 62869 (2014).

70. J. Rodrigues, S. M. C. Miranda, N. F. Santos, A. J. Neves, E. Alves, K. Lorenz, and T. Monteiro, Mater. Chem. Phys. **134**, 716 (2012).

71. H. J. Lozykowski, W. M. Jadwisienczak, A. Bensaoula, and O. Monteiro, Microelectronics J. **36**, 453 (2005).

Chapter 3. Morphological, structural and electrical characterization

An adequate evaluation of the morphological and structural properties of the samples is of paramount importance for any technological application. For instance, characteristics like morphology, structure and crystalline quality are crucial to understand and to improve new growth techniques, as the one developed in the present work. In this sense, this chapter is dedicated to the review of the principal morphological and structural characterization techniques used during this thesis work. Moreover, a brief reference to complementary electrical characterization is also made.

3.1. Electron microscopy

Electron microscopy constitutes one of the key techniques in material science, giving the possibility to assess the morphology and structure of the materials at the nanoscale. Since the wavelength of accelerated electrons is very much smaller than the ones for visible or UV photons used in optical microscopy, electron microscopy exhibits a much greater spatial resolution (~ 1 Å [transmission] *vs* ~ 0.3 µm) [1,2].

The combination of instruments like the scanning electron microscope (SEM) and the transmission electron microscope (TEM) can provide almost all the morphological, structural, phase and crystallographic data that is needed for a full characterization of a material.

Before describing both mentioned techniques, it is important to make a brief reference to the processes involved in the electron-matter interactions that are the background of electron microscopy. In fact, electrons interact strongly with atoms, undergoing either inelastic or elastic scattering with electrons or the nucleus, respectively [3]. The resulting interactions lead to a wide range of secondary signals from the specimen [4]. Collecting these data using adequate detectors enables the combined information on different material characteristics [5]. Figure 3-1a depicts a schematic illustration of the major electron-matter interactions. A representation of the interaction volume and average penetration depths, which give rise to the different signals from thick specimens, is shown in Figure 3-1b. The interaction volume is defined as the region within which 95% of the electrons are brought to rest by scattering, and has a characteristic teardrop shape [1]. This volume dictates the spatial resolution of the image or the analysis and strongly depends on the operation conditions and sample characteristics. Furthermore, materials with a

high atomic number tend to exhibit a reduced electron penetration depth and increased lateral spread, when compared with those of lower atomic number [1].

Among the different signals that result from the electron-matter interactions, the ones that are mostly used in electron microscopy are the secondary, backscattered and transmitted (either undeflected or deflected) electrons [3]. TEM takes advantage of the last ones, while the others are particularly important for SEM analysis.

Among the other phenomena occurring, the emission of characteristic X-rays should be highlighted. These X-rays are characteristics of the chemical elements present in the sample and are produced by the transition of the electrons from higher to lower energy orbitals, after the jumping of an electron from one of the internal layers of the atom. So, the energies of the emitted X-rays depend on the possible transitions between atomic orbitals. Electron dispersive spectroscopy (EDS) is based on this phenomenon. It is important to take into account that this X-ray emission is extremely dependent on the absorption of the signal by the matrix and is accompanied by a secondary, non-desired, fluorescence emission. This emission will induce errors in the quantitative chemical analysis, thus it must be removed using and appropriate software [5].

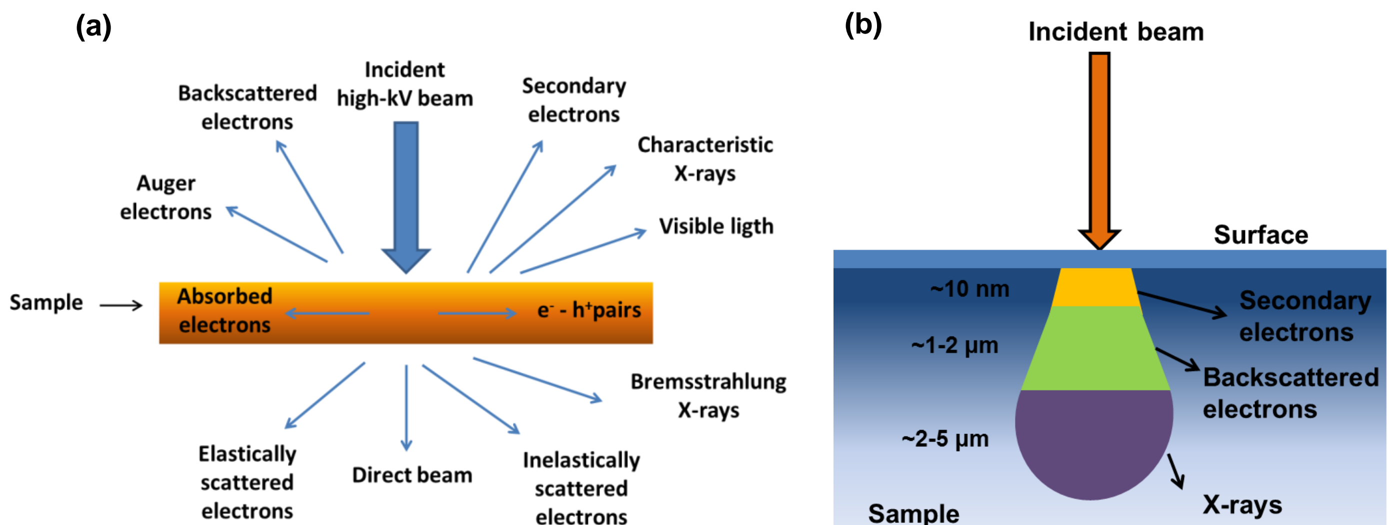

Figure 3-1 – (a) Different type of interactions between electrons and matter and (b) interaction volume and depth penetration of the different signals in a sample. Adapted from [4].

The interaction between the electrons and matter has a strong implication in the design of the electron microscopy systems, implying that all the electron paths must be under vacuum, in order to maintain a coherent and controlled electron beam. The vacuum is also important to keep the microscope clean and control its heating [1,2,4].

3.1.1. Transmission electron microscopy (TEM)

Transmission electron microscopy has emerged as a perfect tool to study the new nanoscale materials, allowing to access atomic-resolution images of the materials, together with spectroscopic data and diffraction patterns from sub-nanometer regions [4]. However, there are

some disadvantages associated with this technique. The first one is related with the use of ionizing radiation, which can damage the sample [2]. The second one is the fact that TEM is a very poor sampling tool, thus the need to use it associated with another technique such as SEM, to have a better knowledge of the sample. Moreover, TEM images have no depth sensitivity, which could induce errors in the interpretation of the results [4]. Finally, and perhaps the major difficulty in TEM measurements is the sample preparation. The sample must be transparent to the electron beam, so it must be thin enough to transmit sufficient electrons, in order that enough intensity falls on the screen. Therefore, sample preparation is frequently a hard task and a limiting factor to obtain adequate TEM information. Powder samples are the easiest to prepare. Usually a diluted and well dispersed suspension of the powders is prepared and then a drop of that suspension is placed onto the surface of a TEM grid, letting the solvent to evaporate [5].

Figure 3-2 shows a picture of a TEM instrument together with a schematic representation of the microscope, highlighting its main components.

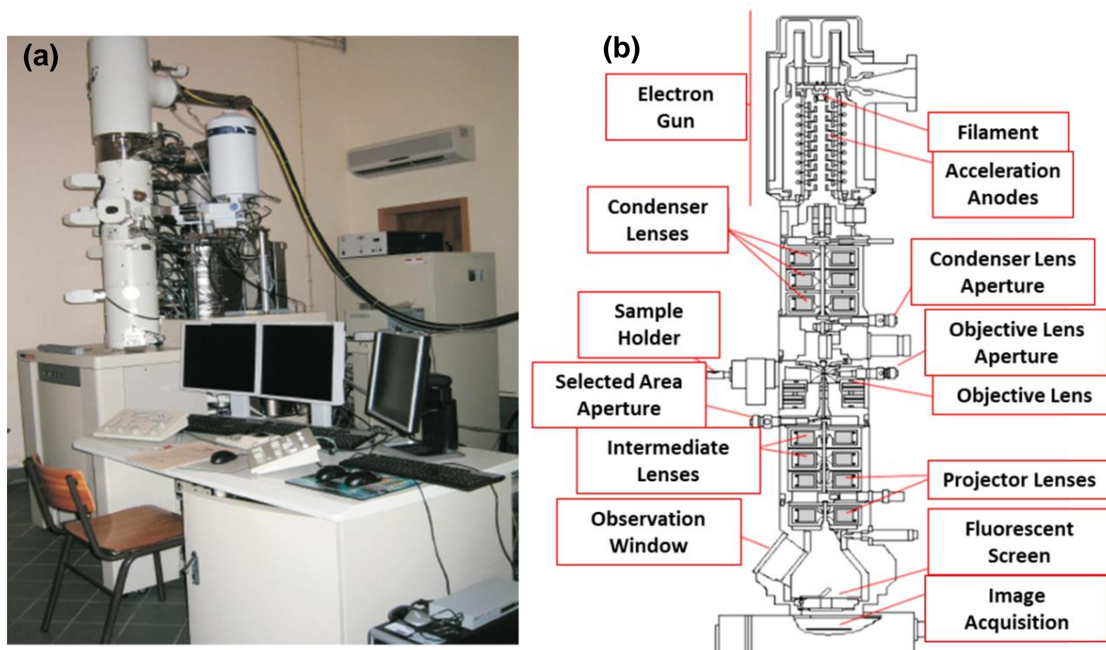

Figure 3-2 – TEM equipment and schematic representation of its main components [6,7].

The TEM equipment comprises an electron-optical system containing an electron gun, which produces the beam of electrons and controls its energy, and several magnetic lenses. The instrument can be divided into three main sections: illumination system, specimen stage and imaging system. The first one includes the electron gun, the acceleration anodes and two or more condenser lenses that focus the electrons onto the sample [2,4]. The specimen stage allows the sample to either be held stationary or intentionally moved, and also inserted or withdrawn from the TEM. Finally, the imaging system contains several lenses that together produce a magnified image (or a diffraction pattern) of the specimen [2]. Electromagnetic lenses are used to change the electron propagation path in a similar way as the glass lenses used in a conventional optical microscope change the path of light. In this case, the change is made by applying an electromagnetic field to the lens [4]. The spatial resolution of the image acquired with a TEM

strongly dependents on the properties of these lenses [2]. Essentially three types of lenses are present in a TEM equipment: condenser, objective and projector. The condenser lens system is responsible for the control of the beam brightness and is used to focus the electron beam on the sample. TEMs are usually equipped with at least two of these lenses [8]. In order to select the diameter of the beam that reaches the sample, this system also includes a set of lenses apertures. These apertures correspond to small holes in a metal diaphragm, located just below the second condenser lens, and allowing the control of the divergence or convergence of the electron paths through the lenses [4]. Objective lenses are the ones closest to the specimen. They control the scattering contrast and create the first image of the sample [2]. This lens takes the electrons emerging from the exit surface of the sample, disperses them to create a diffraction pattern and recombines them to form an image [4]. The image created is then magnified by the projector lenses that are located close to the observation window [4]. The scattering contrast is controlled with the apertures of the objective lenses, which are considered the most important apertures in the TEM [2]. When inserted, its size controls the collection angle, therefore determining the effect of the aberrations and directly influencing the resolution [4]. Besides the set of condenser and objective lenses apertures, there are another set called selected area apertures. These apertures are used to select the area from which the electron diffraction will be performed.

It is well known from quantum mechanics that electrons can behave either like particles or like waves. This wave-like behaviour is characterized by a wavelength

$$\lambda = \frac{h}{p} \qquad \textbf{Eq. 3-1}$$

where h is the Planck constant (6.626 x 10^{-34} J.s) and p represents the linear momentum of the electron. When electrons are accelerated by a potential difference of several kV it is possible to obtained a wavelength with dimensions even smaller than the atomic ones [4]. In TEM measurements, the applied voltages are in the order of some hundred kV so the electron's mass must be corrected to relativistic effects and the wavelength is given by

$$\lambda = \frac{h}{\sqrt{em_0 eV\left(1 + \frac{eV}{2m_0 ec^2}\right)}}. \qquad \textbf{Eq. 3-2}$$

where m_0 is the electron mass at rest (9.109 x 10^{-31} kg), e is the electron charge (1.602 x 10^{-19} C), V is the applied accelerating voltage and c is the speed of light. Electrons accelerated at such voltages exhibit a wavelength comparable to the interatomic distances [2]. For instance, electrons accelerated at 200 kV will have a wavelength of ~ 2.5 pm [4]. Such high energy electrons can penetrate distances of several microns (µm) into a solid. If the solid is crystalline, the electrons are diffracted by atomic planes inside the material, as in the case of X-rays (section 3.2) [2]. Thus, it is possible to form a transmission electron diffraction pattern from electrons that have passed through a thin specimen. Focussing these electrons, the specimen can be imaged with a high spatial resolution (atomic-resolution) [2]. As mentioned above, since electrons have low-mass and are negatively charged particles, they can easily be deflected by passing close to other electrons or the positive nucleus of an atom, leading to scattering interactions. These interactions are the crucial point of the TEM technique [2,4]. The diffraction patterns are the basis of all image

formation in TEM, as well as all crystallographic analysis and defect characterization [4]. A TEM image is a two-dimensional projection of the internal structure of a material [1]. For instance, a high resolution TEM (HRTEM) image is simple a Fast Fourier Transform (FFT) of the diffraction pattern.

Diffraction is a complex phenomenon of scattering and interference originated by the interaction of electromagnetic waves or relativistic particles (as the case of the electron beam in TEM) with the crystal lattice. It is one of the most important properties of the crystals, deriving directly from their periodic structure. It is an extremely powerful tool in the study of the crystalline properties of materials since it is completely dependent of the periodic structure [9]. An electron diffraction pattern is a scaled representation of a section of the reciprocal lattice and contains information about the crystalline structure and crystallographic quality. At all times, the crystallographic information of a diffraction pattern and the analytical information can be related to the image of the studied sample [4].

The elastically scattered incident beam is diffracted by the atomic planes of a crystalline material according to Bragg's law (Eq. 3-3 and Figure 3-3) [10]

$$2d\sin\theta = n\lambda, \qquad \textbf{Eq. 3-3}$$

where d is the spacing between the planes, θ is the angle between the incident beam and the scattering planes, n is an integer that defines de order of the diffraction and λ is the wavelength of the incident electron beam. Only the planes favourably oriented with respect to the incident beam (those where the Bragg condition is met) will interfere in a constructive way, giving rise to interference maxima corresponding to the diffraction spots. From this equation it is easy to see that atomic planes that are closer together give rise to larger scattering angles. Since the wavelengths of beam used in TEM are very small, λ<<d, and taking into consideration the small angle approximation [5], the equation above can be re-written as

$$\lambda \approx 2\theta d. \qquad \textbf{Eq. 3-4}$$

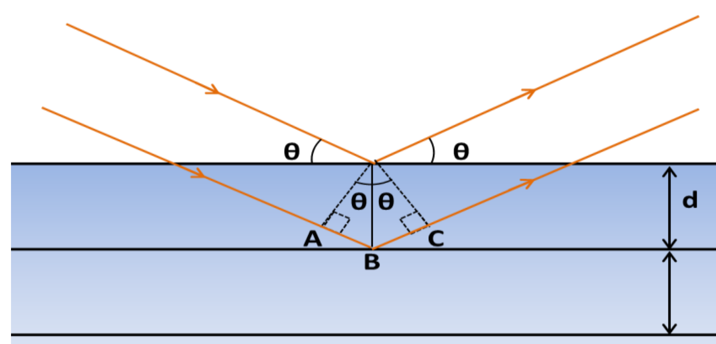

Figure 3-3 – Schematic representation of the Bragg's law. Illustration of the dispersion of an incident beam by a family of lattice planes. Image adapted from [9].

Knowing the value of the used wavelength and measuring the diffraction angle, it is possible to determine the distance between the crystallographic planes by using the reciprocal relationship that θ is proportional to *1/d*. Since θ is small, strong diffraction will only appear when the planes of the atoms are almost parallel to the incident beam. The beam direction corresponds to the

direction of the zone axis, i.e. the direction defined by the intersection of two non-parallel crystallographic planes. Therefore, the angles between the observed diffraction spots will be equal to the angles between the crystal planes [2,4]. Each spot represents a crystallographic plane where the beam was diffracted.

One important aspect when dealing with diffraction is the reciprocal lattice concept, since it plays a fundamental role in most analytic studies of periodic structures. One can consider a set of points **R**, constituting a Bravais lattice, and a plane wave $e^{ik.r}$. For a general **k**, such plane wave will have the same periodicity of the Bravais lattice for certain special choices of the wavevector **k**. Thus, the set of all wavevectors **K** that yield plane waves with the periodicity of a given Bravais lattice is known as the reciprocal lattice. This **K** vector belongs to the reciprocal lattice of a Bravais lattice of **R** points, provided by the relation [11]

$$e^{i\boldsymbol{K}.(\boldsymbol{r}+\boldsymbol{R})} = e^{i\boldsymbol{K}.\boldsymbol{r}} \text{ and } e^{i\boldsymbol{K}.\boldsymbol{R}} = 1. \quad \textbf{Eq. 3-5}$$

The reciprocal lattice is itself a Bravais lattice. The correspondence between reciprocal lattice vectors and families of lattice planes provides a convenient way to specify the orientation of a lattice plane. It is very common to describe the orientation of a plane by giving a vector that is normal to that specific plane. This is done by the Miller indices. The Miller indices of a lattice plane are the coordinates of the shortest reciprocal lattice vector normal to that plane, with respect to a specified set of primitive reciprocal lattice vectors [11]. Thus, a plane with Miller indices *h,k,l* (integers) is normal to the reciprocal lattice vector $h\mathbf{b_1}+k\mathbf{b_2}+l\mathbf{b_3}$. In the reciprocal lattice, sets of parallel (*hkl*) atomic planes are represented by a single point located at a distance $1/d_{hkl}$ from the lattice origin [4].

The Ewald sphere is a geometric construction that operates in a reciprocal space and allows a simple visualization of the diffraction conditions. Figure 3-4a shows a representation of a sphere with radius k (=1/λ) and centred at the origin of an incident wavevector **k,** with the apex on the origin of the reciprocal lattice. For diffraction to occur at least one point of the lattice, in addition to the origin, must lie on the surface of the sphere [9]. In this case, the Bragg condition will be satisfied which will result in the diffraction of the incident beam by a plane from the family of direct lattice planes perpendicular to that reciprocal lattice vector. Through the construction of this sphere it is possible to obtain some experimental information. Rotating the crystal in all the directions with respect to the incident beam, all the points lying inside a sphere of radius *2k* (Figure 3-4b) will cross the surface of the Ewald sphere during the crystal rotation. This second sphere is known as the reflection limit sphere, since it establishes a limit to the data that are accessible in a diffraction experiment (with a fixed wavelength) [9]. Knowing that the radius of the sphere is 1/λ, if the wavelength of the incident beam is changed, the radius of the Ewald sphere will also change, and different crystal planes will diffract. When the electrons are accelerated with a voltage of 100 kV their wavelength is close to 3.7 pm. In this case, the Ewald sphere would have a radius of ~ 270 nm^{-1}. This seems almost planar in comparison with the array of the reciprocal lattice spots. So, the Ewald sphere for electrons can be considered, in first approximation, as a plane that intercepts the reciprocal lattice at (000). In TEM, the Bragg condition is nearly satisfied for a great number of planes, and thus many diffraction spots are observed [4]. Bragg's law

predicts that the diffraction takes place only at defined angles. However, this is only true when the crystal is infinite and perfect.

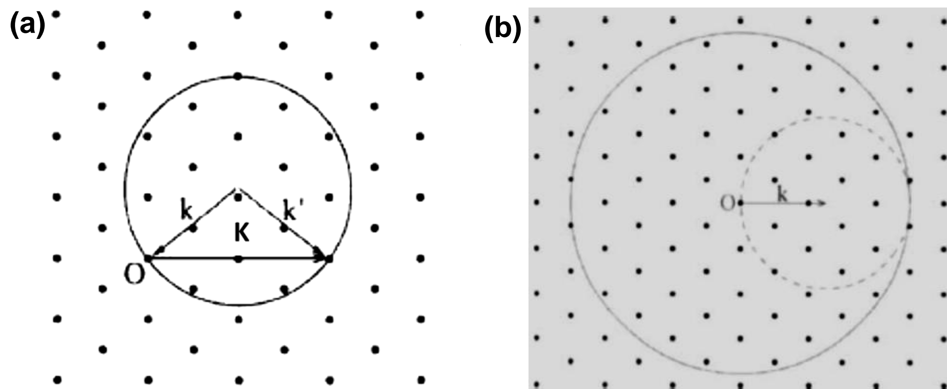

Figure 3-4 – (a) The Ewald sphere and the diffraction conditions and (b) reflection limit sphere and its relation with the Ewald sphere [9]. The vector k' corresponds to the wave vector of the Bragg reflected ray.

The electron diffraction patterns are tremendously helpful in the identification of phases and crystalline structure, determination of the crystal symmetry, growth orientation, as well as for the identification of defects, site occupancy and ordering behaviour of crystalline structures [4,12].

Electron diffraction presents some advantages when compared with X-ray diffraction. For instance, it allows local analysis since the electron beam has a diameter of a few nanometers. It is possible to obtain a precise selection of the area of interest and collect diffraction patterns (the so-called selected area electron diffraction [SAED]) and images of that specific area, accessing the relationships between morphology and crystallography. Moreover, due to the stronger interaction between electrons and matter when compared with X-rays, a higher sensitivity is expected. The disadvantages include the fact that when an electron is diffracted once it can be re-diffracted by different lattice planes. Besides, there are dynamic effects that change the intensity of the diffracted beams and can produce not allowed reflections (double diffraction) [2,4].

Figure 3-5 shows examples of different electron diffraction patterns. As can be seen, the patterns vary for different crystalline structures and also in different zones of the same crystal. Each diffraction spot represents a plane family. A spotted pattern, as the one depicted in Figure 3-5a, accounts for a single crystal, while concentric rings correspond to a polycrystalline sample (Figure 3-5b), being a composition of numerous diffraction spots coming from the different crystals orientation. Figure 3-5c depicts a characteristic pattern of an amorphous material [4].

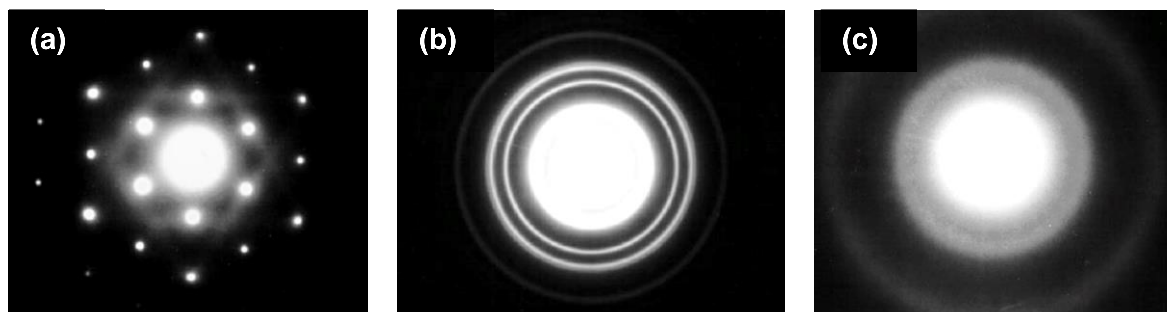

Figure 3-5 – Electron diffraction patterns obtained from different samples: (a) Al single crystal, (b) polycrystalline Au and (c) amorphous carbon [4].

The TEM, HRTEM and high angle annular dark field scanning TEM (HAADF-STEM) measurements performed in this thesis were kindly carried out by the group of Professor Teresa Ben in the *University of Cadiz*. The analysis was conducted using a JEOL 1200 EX and a JEOL 2010F microscopes operating at 120 and 200 kV, respectively. Quantitative compositional analysis was performed by using an Oxford INCA Energy 2000 system for EDS, using a probe size of about 1 nm.

3.1.2. Scanning electron microscopy (SEM)

SEM is one of the most widely used techniques in the characterization of nanomaterials and nanostructures [3]. In a SEM analysis, the surface of a sample is scanned with an electron beam, giving morphological and topographical information about the sample, with a high resolution (few nm) [2,3,13,14]. The image is formed by scanning point-to-point the sample surface with the electron beam, making use of the fact that electrostatic or magnetic fields, applied at right angles to the beam by the lenses, can be used to change its direction of travel, as in the TEM [2]. When combined with the chemical analytical capabilities provided by the EDS, SEM can assess not only morphology and microstructures information, but also detailed information of chemical composition and elemental distribution with a good spatial resolution [3].

In a general way, in a SEM, the maximum accelerating voltage is lower than for a TEM [2]. The electrons are focused into a beam with energy typically ranging from a few hundred eV to 50 keV [3]. Lower voltages are preferred to increase surface detail and avoid sample charging in non-conducting or poorly conducting samples [1].

Figure 3-6 shows a picture of a SEM equipment, as well as a schematic representation of its fundamental components, most of them similar to the ones found in a TEM. However, in this case fewer lenses are used. Moreover, since the energy needed is lower, the electron gun is smaller and requires less insulation [2]. Normally, two or more condenser lenses are used to demagnify the crossover produced by the gun, while the objective lens focuses the electron probe onto the sample, resulting in a small-diameter electron probe (around 2-10 nm) [1–3]. The performance (including aberrations) of the objective lens strongly determines the spatial resolution of the SEM instrument, in a similar way with what happens in the TEM [2]. The objective aperture controls the angular spread of the electrons and the deflection coils are responsible for rastering the beam over the surface of the sample [1,3]. The focused beam is scanned across the specimen surface in

a two-dimensional square or rectangular area of the sample (called raster), with the beam passing through the optic axis at the objective lens. An image of this area can be formed by collecting the electron signal from each point on the sample [1,2]. During this process, an appropriate detector monitors the out coming signals [1]. As mentioned above, as the electrons strike and penetrate the surface of the material several interactions take place, resulting in the emission of both electrons and photons from the sample. SEM images are produced by collecting the emitted electrons (secondary and backscattered) [3]. The intensity of each pixel on the collecting monitor is controlled by the amplified output of the selected detector. Thus, the intensity of the produced image is directly related to the emission intensity of the selected interaction, at the corresponding point of the sample's surface [1]. It is possible to divide the output signals into three major types (although other interactions may be also recorded with the appropriate detector): secondary electron images, backscattered electron images and elemental X-ray maps [3].

In an inelastic collision between an electron from the incident beam and another one from the sample, the incident electron transfers part of its energy to the other electron. If the energy transferred is large enough, the other electron will be emitted from the sample [3]. These electrons are called secondary and only originate from the top few nanometres of the samples' surface, giving a topographical contrast image [1,2]. They are easily absorbed by the sample and only the ones that are able to escape the surface can be collected by the detector. Their energy is typically less than 50 keV. The lateral resolution in secondary electron images is in the order of 1 - 5 nm for typical samples, although it can be varied with probe size and signal-to-noise considerations. The depth resolution is a function of the accelerating voltage. Secondary electron imaging is the most useful signal for imaging nanostructures in the SEM, since it offers a high signal level combined with high lateral and depth resolution [1]. The secondary and backscattered electrons can be distinguished by their kinetic energy [2]. Backscattered electrons correspond to the high energy electrons that are elastically scattered and, thus, exhibit the same energy as the beam electrons. Contrarily to the previous case, the backscattered electron yield is almost independent of accelerating voltage and is small compared with the secondary electron yield. Increasing the atomic number of the elements that composed the sample leads to an increase of the backscattering probability, making it possible to obtain an useful contrast between regions of the sample that differ widely in atomic number, Z, acquiring information about the material chemical composition [3]. For this purpose, a well-polished sample is preferred, in order to minimize topographic effects [1]. The resolution of these images is in the range of 25-100 nm, which is considerably lower than the one found for secondary electron images. This is caused by the larger penetration depth (Figure 3-1b), that conduct to an increase in the sampling volume [1].

In this thesis, the samples' morphology was characterized by SEM using both Hitachi SU-70 and TESCAN Vega3 SBH SEM microscopes.

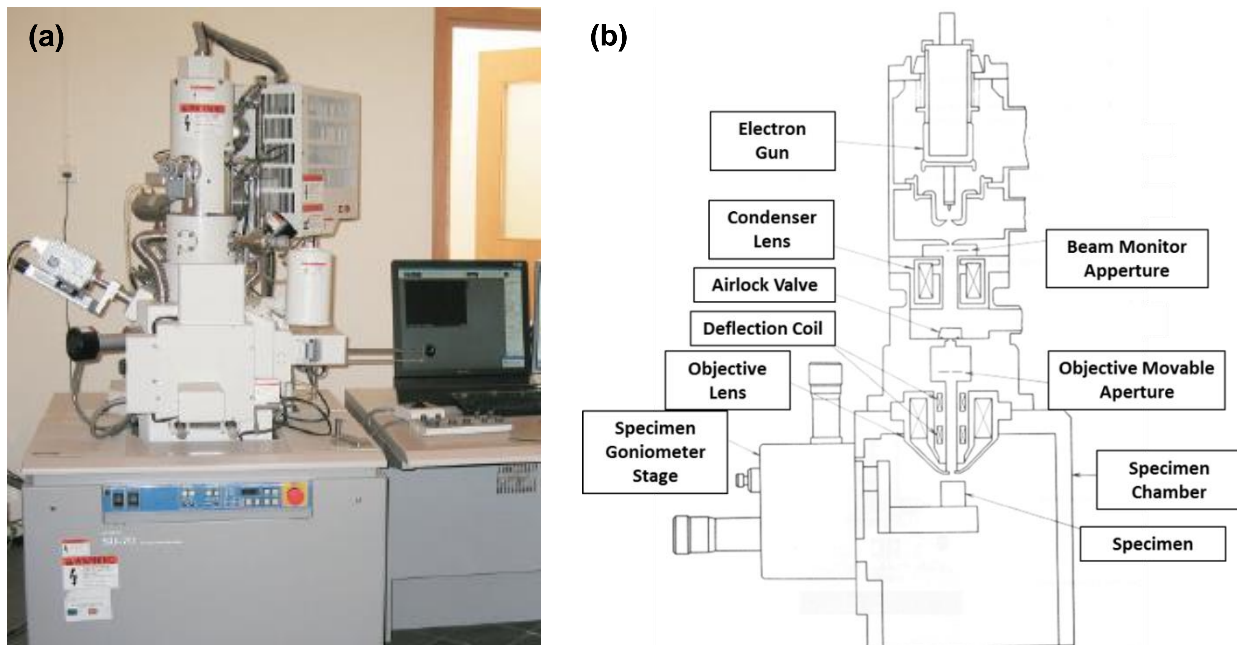

Figure 3-6 – (a) SEM equipment photograph and (b) schematic representation of its fundamental components [7,15].

3.2. X-ray diffraction (XRD)

Diffraction experiments are crucial tools to determine the structural quality and properties of crystalline materials [16]. X-ray diffraction (XRD) appears as a technique of paramount importance in the study of the composition of the samples, together with their crystalline structures [1]. This is a non-destructive technique that does not require a previous and elaborated preparation of the samples (contrarily to the TEM). X-rays are high energetic electromagnetic radiation, with wavelengths on the order of the atomic spacings of crystals. Like so, when the X-ray beam impinges on a material, a portion of this beam will be scattered in all directions by the electrons associated with each atom or ion that lies within the beam's path [13].

The concepts of diffraction and reciprocal lattice were already introduced in sub-section 1.1 for electron diffraction. In an XRD experiment, a collimated beam of X-rays, with a wavelength typically ranging from 0.7 to 2 Å, strikes the sample and is diffracted according to Bragg's law (Eq. 3-3). The intensity of the diffracted X-rays is measured as a function of the diffraction angle 2θ and the sample's orientation [3]. The monochromatic beam is accomplished either by the use of monochromators or filters, allowing only to pass the strong characteristic K_α components of the whole spectrum from an X-ray tube, or by monochromatized radiation from a synchrotron source, allowing the tuning of the wavelength [1]. Figure 3-7 shows a representation of the classic geometry used in an XRD powder diffractometer. In this case, the sample is mounted on a support substrate that does not give rise to interfering reflections. The detector is set to receive reflections at an angle θ, which is varied over the angular range of interest or by keeping the sample fixed and rotating the incident beam and detector in opposite directions. The reflected

beams are only recorded from the planes which lie parallel, or nearly parallel, to the sample surface. To measure reflections from planes that are at an angle to the sample's surface, tilt or rotation of the sample is required [1]. In the resultant diffractometer, the angles (and consequently the *d* spacings) and intensities of the reflected beams act as a "fingerprint" for the crystal structure of a specific material [7].

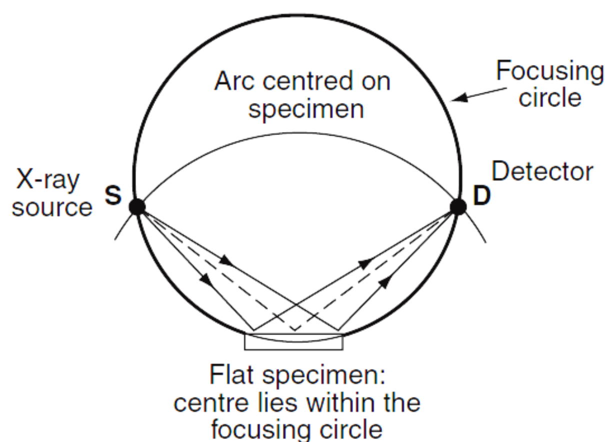

Figure 3-7 – Schematic diagram of the typical geometry used in an XRD powder diffractometer. Image taken from reference [1].

The lattice parameters of a structure can be calculated knowing the spacing between planes, *d*, and the Miller indices (*hkl*) of those planes. For instance, in the case of the hexagonal system, this correlation is given by the expression

$$\frac{1}{d^2} = \frac{4}{3a^2}(h^2 + hk + k^2) + \frac{1}{c^2}l^2. \qquad \textbf{Eq. 3-6}$$

Two non-parallel planes are enough to determine the lattice parameters *a=b* and *c* for a sample with hexagonal structure, as is the case of ZnO or GaN.

In the hexagonal system it is frequent to use a slightly different plane indexation where four indices, (*hkil*), are used, being designated by Miller-Bravais indices. The additional index denoted by *i* is dependent of the values of *h* and *k* by the relation *h+k=-i* [17].

The XRD technique can be used in different types of samples, including nanocrystalline solids, powders, single-crystal, thin films or multilayers. Besides the typical determination of their crystalline structures and their lattice parameters by the analysis of the directions and intensities of diffracted beams, it is also possible to extract information regarding crystallite size, orientation of single crystals, preferred orientation of polycrystals, defects, stresses, strains, dislocation content and, in the case of films, lattice mismatch, total thicknesses and texture [1,3,16]. The major information is obtained by careful examination of the shape, intensity and position of the diffraction maxima in the XRD pattern. Homogeneous or uniform elastic strain leads to a shift in the diffraction peak position, allowing assessing the change in *d*-spacing resulting from the slight change in the lattice constants under strain. On the other hand, inhomogeneous strains may vary from crystallite to crystallite or even within a single crystallite, causing a broadening in the diffraction peaks, which increases with *sin* θ. However, it is important to note that the peak broadening is also observed due to the finite size of the crystallites, but in this case it is independent of *sin* θ. Therefore, a careful analysis of peak shapes and positions is required when

both contributions are present [3]. For the layered structures, an analysis of low-angle Bragg peaks gives information on the total thicknesses and the texture is inferred from an analysis of pole figures or orientation distribution functions [1]. A detailed description of the theoretical concepts and applications of the XRD technique can be found in reference [18].

As mentioned in the discussion of the electron diffraction, one of the disadvantages of XRD is the low intensity of diffracted X-rays, particularly for materials with low atomic number. Thereby, a large amount of sample is frequently necessary and the information acquired is an average over a large amount of material [3].

In the present work the crystal structure of the ZnO nano/microstructures was investigated by measuring θ-2θ XRD scans using a PANalytical X'Pert PRO diffractometer (Cu K_{α} radiation, λ = 1.54056 Å).

3.3. Rutherford backscattering spectrometry (RBS)

Rutherford backscattering spectrometry is a technique that allows the determination of the structure and the chemical composition of a given material. This technique is very useful, for instance, to measure the thickness of a known sample and to access its crystalline quality. In the specific case of samples doped by ion implantation, it is essential to know the distribution of the dopants, their location in the crystal lattice, as well as their concentration. Since ion implantation tends to cause great damage in the samples, the determination of the damage level and the evaluation of the reproducibility of the structural properties are crucial. All this information can be obtained by RBS, which makes it a powerful technique for material characterization.

In an RBS experiment, high-energy light ion beams, generally H^+ or $^4He^+$ ions, are accelerated with energies in the range of 1-4 MeV, to serve as probes. When a sample is irradiated with such beams nearly all the ions penetrate inside the sample, up to almost 10 µm, until they lose all their kinetic energy [19]. The loss of the kinetic energy is mainly due to the collisions with the electrons of the sample [20]. Some ions collide with the target atoms and undergo an elastic Coulomb scattering, also called Rutherford scattering, and may be backscattered from the sample. The backscattered ions are detected by semiconductor sensors and the output of this detector is proportional to the energy of the detected ion. The kinematics of the collisions does not depend on the type of the chemical bonds, so the backscattering measurements are independent of the electronic configuration or chemical bond within the target sample. Therefore, the energy of the ions that are backscattered depends on the ratio between the mass of the target atoms and the mass of the beam particles, the energy of the incident beam and where the collision occurred, since particles lose some of their energy during their path inside the sample. All these factors allow quantitative determination of the composition and depth profiling of individual elements [21,22]. A quantitative analysis of elements (except hydrogen) can be done with a good depth resolution of the order of a few nanometers (around 10 nm), which can be increased using a grazing-angle incidence [19]. Another advantage of this technique is the fact that the analysis is based on absolute calculations and there is no need of standards for quantification. There is a great sensitivity for heavy elements, about 100 ppm, which allow a very good detection in such

case. However, this technique encounters severe limitations in the sensitivity of detection for light elements [19,22]. Another constraint resides in the lack of specificity of the signal, making it extremely difficult to distinguish between elements with similar mass. Also, if the elements are present in low concentrations, the sensitivity of the RBS technique is low. These limitations usually require the combinations of other analytical tools like Auger electron spectrometry or secondary ion mass spectroscopy [22].

The basic principles of the RBS technique are schematized in Figure 3-8. As mentioned previously, a target is placed in a monoenergetic ion beam, α-particles ($^4He^+$) for instance, that are accelerated up to some MeV by an ion accelerator [22]. These α-particles interact with the sample and some of the ions are elastically scattered by the surface atoms, whereas others go through the sample, losing some energy, and are backscattered at a certain depth [20]. Since there is a conservation of energy and momentum (elastic collision) it is possible to obtain the velocity and the energy of the particles through the angles of scattering (θ) and recoil (φ). The backscattering spectrum corresponds to the number of backscattering α-particles as a function of their energy. This spectrum contains the information about the nature of the elements present in the target and their depth distributions [19,20]. There are four basic physical concepts that must be taken into account in a RBS experiment [22]: the energy transfer from the beam particles to the target sample can be understood as an elastic two-body collision, which leads to the concept of *kinematic factor* and the mass sensitivity; the probability of these collisions are directly correlated with the *scattering cross-section*, which allows the quantitative analysis of atomic composition; the average energy loss by a particle moving inside a dense medium conducts to the notion of *stopping cross-section*, which gives the ability of depth perception; and finally, the statistical fluctuations in this energy loss leads to *energy straggling*, which is the main cause of the limitation in mass and depth resolution.

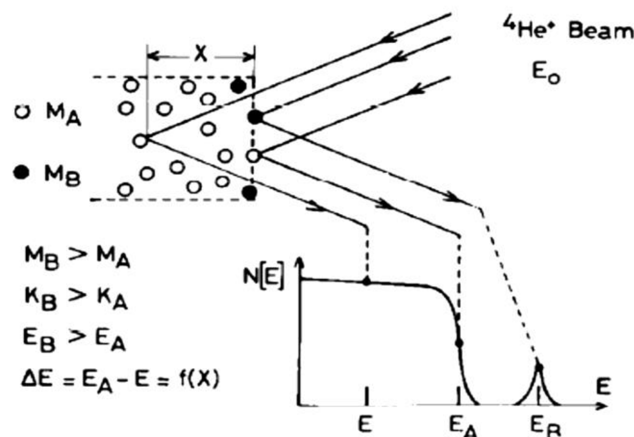

Figure 3-8 – Schematic representation of the basic principles of the RBS analysis [20].

Considering two particles, one of them being the incident ion and the other one the nuclei of an atom of the sample, the collision process can be schematically represent as shown in Figure 3-9a. Here, the first particle has mass M_1, velocity *v* and energy $E_0 = \frac{1}{2}M_1v^2$ and the second one has mass M_2 and $v_2=0$. After the collision, the energies $E_1 = \frac{1}{2}M_1v_1^2$ and $E_2 = \frac{1}{2}M_2v_2^2$, and the

velocities, v_1 and v_2, will be determined by θ and φ. Using the laws for the conservation of energy and momentum, the following expression is obtained [19]

$$K = \frac{E_1}{E_0} = \left[\frac{(M_2^2 - M_1^2 \sin^2\theta)^{\frac{1}{2}} + M_1\cos\theta}{M_1 + M_2}\right]^2. \quad \textbf{Eq. 3-7}$$

This equation is based in two assumptions [22]: the energy E_0 is much larger than the binding energy of the atoms and nuclear reactions, and resonances are absent. In fact, these effects are negligibly small in collisions between ions with energy in the range of MeV and target atoms [19]. K is called the kinematic factor and is clearly determined by the mass ratio M_2/M_1 and the scattering angle θ. Once E_0 is fixed, the energy of backscattered particles ($K.E_0$) depends only on the nature of the atoms in the sample. Thus, the energy scale can be used as a mass scale [20]. Accessing the energy of the backscattered particles allows the determination of the chemical nature of the element present in the target, since the only unknown variable is the mass of the target atoms.

For the direct backscattering, θ=180 °, the ratio between E_1 and E_0 has a minimum value [22]

$$\frac{E_1}{E_0} = \left(\frac{M_1 - M_2}{M_1 + M_2}\right)^2, \quad \textbf{Eq. 3-8}$$

While for θ=90 °, the ratio is given by

$$\frac{E_1}{E_0} = \left(\frac{M_2 - M_1}{M_1 + M_2}\right), \quad \textbf{Eq. 3-9}$$

So when θ=180 °, the energy transferred to the target atom, E_2, reaches its maximum value

$$\frac{E_2}{E_0} = \frac{4M_1M_2}{(M_1 + M_2)^2}, \quad \textbf{Eq. 3-10}$$

and the general expression is written as

$$\frac{E_2}{E_0} = \frac{4M_1M_2}{(M_1 + M_2)^2}\cos^2\varphi. \quad \textbf{Eq. 3-11}$$

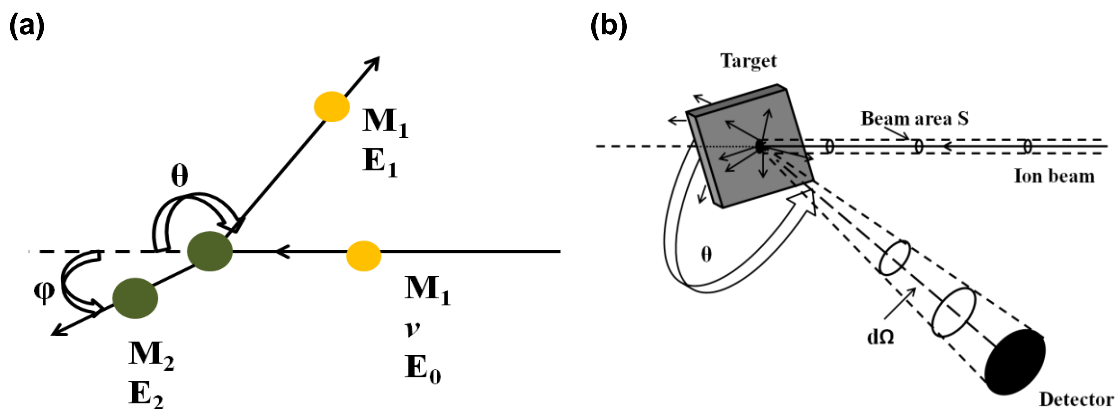

Figure 3-9 –Schemes of the (a) collision between two particles and (b) scattering cross-section. Adapted from [22].

In practise, if the target contains atoms with a small difference in the mass ΔM_2, the experimental geometry is adjusted in order to maximize the ΔE_1 energy after the collision. The mass resolution ΔM_2 is connected with the energy resolution ΔE_1. If ΔE_1 falls below the resolution of the detection system the distinction between two masses is not possible. So, to obtain an adequate mass resolution, the ΔM_2 must be as large as possible. This can be achieved by increasing the primary energy E_0, increasing M_1 and measure at scattering angles close to 180° [22].

The number of atoms in the target per unit area is determined by the probability of the collision between the incident particle and the target atoms. This quantity is measured by the total number of particles detected, Q_D, for a given number of incident particles Q. The Q value is determined by the integration time of charged particles current that hit the target. The total number of incident particles must be high, in order that the ratio dQ/Q has a well known value [22]. The differential effective cross-section $dS/d\Omega$ that describes the probability of a target atom to scatter an incident particle, with an angle θ, within a differential solid angle $d\Omega$ (Figure 3-9b) around θ, is given by

$$\frac{dS(\theta)}{d\Omega} \cdot d\Omega \cdot N_s = \frac{n^{\underline{o}}\ of\ particles\ scattered\ inside\ d\Omega}{total\ n^{\underline{o}}\ of\ incident\ particles}, \qquad \textbf{Eq. 3-12}$$

where N_s is the number of target atoms per cm^2. N_s is usually related with Q_D by the expression

$$Q_D = \sigma(\theta) \cdot \Omega \cdot Q \cdot N_s. \qquad \textbf{Eq. 3-13}$$

Since in the backscattering spectroscopy the solid angle of the detector is small (~ 10^{-2} sterad), an average effective cross-section $\sigma(\theta)$, also known as scattering effective cross-section, can be defined as [22]

$$\sigma(\theta) = \frac{1}{\Omega}\int_{\Omega} \frac{dS}{d\Omega} d\Omega. \qquad \textbf{Eq. 3-14}$$

This scattering effective cross-section can also be written as

$$\sigma(\theta) = -\frac{dS}{d\Omega}. \qquad \textbf{Eq. 3-15}$$

In a simple way, the scattering is caused by a central force which conserves the kinetic energy and the momentum of the particles. A positively charged particle Z_1e approaches a target nucleus, with charge Z_2e, and the first particle is subject to a repulsive force, changing its path from the initial one. This repulsive force can be seen as a Coulomb force operating at a distance r. With some mathematical manipulation one gets the analytical formula to the differential cross-section, called Rutherford formula [22]

$$-\frac{dS}{d\Omega} = \sigma(\theta) = \left(\frac{Z_1 Z_2 e^2}{16\pi\varepsilon_0 E}\right)^2 \frac{1}{\sin^4\frac{\theta}{2}}. \qquad \textbf{Eq. 3-16}$$

The dependence on the inverse square of the energy leads to an increase of the backscattering yield when the energy of the incident ions decreases (depth increases) and the square of atomic number of the target atoms dependence shows why the sensitivity is strongly enhanced for

heavier elements [20]. With the information on the cross-section it is possible to determine the concentration of the target atoms.

In addition to the elastic scattering, the beam particles also lose part of their energy when penetrating the target. The energy losses are essentially owed to interactions with the electrons of the medium [20]. As a particle enters inside the sample, it slows down, reducing its kinetic energy. The amount of energy ΔE lost per distance Δx crossed depends on the identity of the beam particle, on the density and composition of the target sample and on its velocity itself [22]. Energy loss during the penetration process is directly proportional to the thickness of the sample and a depth scale can be quantitatively attributed to the energy spectra of the detected backscattered particles [22]. The rate of the energy loss per unit path length, dE/dx, is called stopping power. The inelastic collisions can be divided into fast and slow, depending on the velocity of the incident particle and the average orbital velocity of the electrons of the target sample. If the velocity of the incident particle is much higher than the orbital velocity of the electrons (fast collisions), the influence of the incident particle in the target atom is considered a small perturbation. The effective stopping section decreases as the velocity increases, since the particle spends less time in the proximity of the atom. For slow collisions, the stopping power is proportional to the velocity. At a given depth x the beam particles have an energy that is a function of the stopping power of the medium. In the fast collision regime and for a fixed velocity

$$\frac{dE}{dx} \propto Z_1^2. \qquad \textbf{Eq. 3-17}$$

where Z_1 is the atomic number of the incident particle. Taking into consideration the first order perturbation theory, the stopping power can be expressed by [19]

$$\frac{dE}{dx} = \frac{4\pi Z_1^2 Z_2 N e^4}{m_e v^2} ln\left(\frac{m_e v^2}{I}\right), \qquad \textbf{Eq. 3-18}$$

being m_e the electron mass, v the velocity of the ion and I the mean excitation energy of the target electrons. This equation is called the Bethe-Bloch formula and is used as a guide for semi-empirical fitting of stopping power data [19]. A quantity called stopping cross-section is often used to calculate the stopping power and is defined as [19]

$$\varepsilon = \frac{1}{N}\left(\frac{dE}{dx}\right). \qquad \textbf{Eq. 3-19}$$

The depth location x of the atoms can be related to the measured energy difference ΔE between the theoretical position ($K.E_0$) and the detected energy E of beam particles backscattered by the atoms at depth x by the expression [20]

$$\Delta E = x\left[K\varepsilon(\bar{E}_{in}) + \left(\frac{1}{\cos\theta}\right)\varepsilon(\bar{E}_{out})\right], \qquad \textbf{Eq. 3-20}$$

where $\varepsilon(\bar{E}_{in})$ and $\varepsilon(\bar{E}_{out})$ correspond to the stopping cross-sections in the incoming and outgoing path, respectively. $\bar{E}_{in}$ and $\bar{E}_{out}$ are the average incoming and outgoing energy of the beam particles, respectively. These stopping cross-sections must be taken into account for the construction of a depth scale. The depth resolution is dependent on the overall energy resolution, the stopping power and the geometry. One can consider mainly three contributions for the

intrinsic energy resolution [19]: the energy spread of the incident beam δE_{in}, the detector resolution δE_d and the energy loss straggling δE_s:

$$(\delta E)^2 = (\delta E_{in})^2 + (\delta E_d)^2 + (\delta E_s)^2. \quad \textbf{Eq. 3-21}$$

The energy straggling is essential in the interpretation of the RBS results, and corresponds to the energy spreading during the slowing down of the ions, due to statistical fluctuations of energy transfer in the collision process [21]. For long path length, the energy distribution approaches a Gaussian distribution [19]. The contribution of the energy-loss straggling to the energy resolution can be described in accordance to the Bohr's theory as [19]

$$(\delta E_s)^2 = 8ln2(K^2\Omega_{in}^2 + \Omega_{out}^2), \quad \textbf{Eq. 3-22}$$

with *8ln2* being a conversion factor from the standard deviation to the full width at half maximum and Ω_{in}^2 and Ω_{out}^2 are the straggling during inward and outward paths, respectively.

With the RBS technique it is also possible to gain information about the crystalline structure of a sample using ion channelling configuration. Information about crystal damage, defect concentrations or crystal alignment can be obtained. The channelling configuration allows a large sensitivity for atoms displaced from the regular sites in the lattice. This phenomenon happens when an ion beam is aligned with a major crystallographic axis or plane of the sample. With this geometry, the backscattering yield is very much higher for the first surface layers than in the bulk, due to the formation of a shadow cone for the incident beam by the first atomic plane and by atoms which are displaced from crystallographic sites [20]. The backscattering probability inside the crystal is much reduced since the beam will only "see" the atoms that are displaced from the lattice sites. Information on the disorder can be obtained comparing aligned and random spectra [19]. Moreover, it is also possible to assess the lattice sites of the foreign ions, in the case of doped samples.

It is important to note that the irradiation of the sample with the RBS ion beam can cause some damage in the sample and even the incorporation of some beam particles. These particles can generate recombination centres which will affect some of the features of the original sample, namely optical and electrical properties.

Figure 3-10 shows a schematization of a RBS apparatus. This equipment is essentially composed by an ion source, a linear particle accelerator and a detector. As mentioned before, in most of the times α-particles with energies between 1 and 4 MeV are used, but other particles can be employed. For example, when the analysis of deeper regions is needed, H^+ ions can be used, although these particles have poorer mass and depth resolutions than the α-particles. The ions generated by the ion source are accelerated by an electric field and analysed by a magnet, in order to eliminate contaminant ion species and to select the ion energy. In the next step, the ion beam is collimated by apertures and is introduced to a scattering chamber where the target is mounted. The detector is installed inside the chamber to measure the energy spectrum of the scattered ions. Then, the signal from the detector is amplified and sent to an analyser [19]. The signals obtained by the electronics of the detector are electric impulses with amplitude

proportional to the energy of the incident particle. These impulses are recorded in the channels of a multichannel analyser. The channel number, which is related to the ion energy, can be calibrated in terms of depth for a given atomic number of the target atoms.

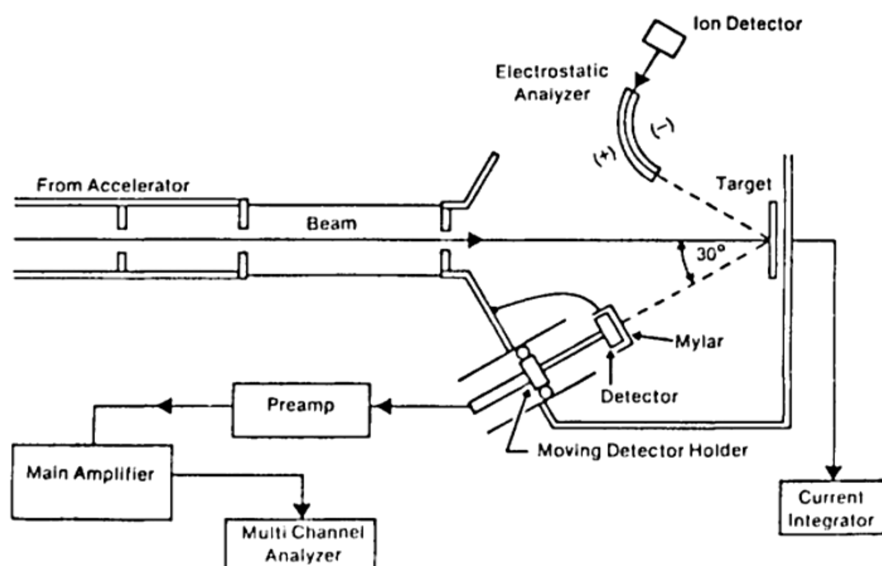

Figure 3-10 – Schematic diagram of a Rutherford backscattering spectrometer [23].

In this work, RBS/C studies were performed *at LATR* in *CTN/IST*, using a 1 mm diameter collimated beam of 2 MeV He ions, produced by a Van de Graaff accelerator. The backscattered particles were detected at 165° with respect to the incoming beam direction using a pin-diode detector.

3.4. Particle-induced X-ray emission (PIXE)

Particle-induced X-ray emission (PIXE) is an ion beam multielemental analysis method that takes advantage of the characteristic X-rays produced via ion beam interactions with the electron cloud of the sample's atoms [24,25]. From experimental point of view, this technique is very similar to RBS, however a different output is recorded. The principle of PIXE is similar to that of EDS, though in PIXE the primary particles are light ions instead of electrons [24]. A PIXE experiment comprises a few stages. Firstly, a beam of light ions, typically protons, is accelerated to an energy of a few MeV, and directed to impinge the target sample. The ions collide with the atoms and create vacancies in the electron shells of the target's atoms, which are subsequently filled by outer shell electrons. In a similar way to the above described EDS technique, this process leads to the emission of the characteristic X-rays. The probability of emission of the characteristic X-rays from the atoms ionized along the particle path is given by the X-ray production cross-section σ, that depends on the velocity of the ion and on the square of the ion's atomic number Z [24–26]. Due to the absence of electron induced bremsstrahlung, the sensitivity of PIXE is enhanced by a factor of almost 100 compared to EDS. Consequently, PIXE is able to detect concentrations of the order of 1-100 ppm, depending on the sample's constituents (their Z) and also the sample's characteristics [24]. This technique is particularly sensitive to elements between

aluminium and uranium. Another feature of PIXE is its ability to probe deep inside the target sample (from ~ 10 μm up to tens of millimetres), because the high-energetic particles produce high-energy X-rays that are weakly absorbed along the path. Even so, the X-rays emerging from the point of emission are slightly attenuated inside the material, with an attenuation factor μ which is dependent on the material. PIXE is often used with raster imaging, focusing the beam to an area of some μm^2 (microprobe). This is called micro-PIXE and allows to acquire an elemental map of the sample [24].

In this thesis, micro-PIXE was performed at *LATR* in *CTN/IST* using an Oxford Microbeams OM150 type scanning microprobe. This allowed to focus a 2.0 MeV proton beam down to 3 - 4 μm^2 using a 100 pA beam current. The produced X-rays were collected by a 80 mm^2 Si(Li) detector with a resolution of 145 eV positioned at 135° with the beam direction. The operation and basic data manipulation, including elemental distribution mapping, was achieved through the OMDAQ software code, and the quantitative analysis was done using the DAN32 application [27].

3.5. Raman spectroscopy

Another important technique based on scattering is the Raman spectroscopy. When light (UV-visible-NIR) travels through a medium, besides the most common absorption or transmission phenomena, the photons that interact with the matter also undergo scattering processes [28,29]. The scattering can either be elastic or inelastic. The former process is the dominant one and the frequency of the light is unchanged [30–32]. This process is denominated by Rayleigh scattering and is represented in Figure 3-11a. Inelastic scattering takes place when the incident photons interact with the acoustic or optical phonons of the crystal lattice. In the first case it is called Brillouin scattering and the latter corresponds to the Raman scattering [31,33]. Optical phonons show higher energies than the acoustic ones, thus larger energy shifts are verified for the former, as illustrated in Figure 3-11b [31].

Typically, in these scattering processes, the incident photon gives part of its energy $\hbar\omega_i$ to the lattice in the form of a phonon of energy $\hbar\omega_0$, resulting in the emission of a lower energy photon $\hbar\omega_s = \hbar\omega_i - \hbar\omega_0$. This is called Stokes-shifted scattering (Figure 3-11a) [31,33]. This phenomenon can also be seen as an excitation of a phonon. As represented in the Figure 3-11a, when the incident photons interacted with the phonon, the phonon is excited from the ground vibrational state *m* to a virtual state (which is not a real energy state of the crystal), the phonon is then left in a higher energy excited vibrational state *n*, emitting the remaining energy of the incident photon [29,33]. The energy difference between these levels corresponds to the phonon energy $\hbar\omega_0$, which is a characteristic of the material that is being analysed. If the lattice of the crystal is already in an excited vibrational state (*n*), which means that the crystal already has a considerable density of phonons, the scattering process may result in the emission of a more energetic photon upon returning to the ground state, with energy $\hbar\omega_s = \hbar\omega_i + \hbar\omega_0$ (Figure 3-11a). The up-converted frequency shifts are designated by anti-Stokes shifted scattering mode [33]. The anti-Stokes modes are much weaker than the Stokes ones (Figure 3-11b), since usually there are fewer phonons to be absorbed than to be emitted [33]. In other words, the population

of the phonon excited states is inferior to the ground state by a factor of exp($-\hbar\omega_0/k_BT$) and thus, the probability for absorption is lower than for emission [33,34]. Moreover, the probability for anti-Stokes scattering decreases when the temperature is lowered [30]. Therefore, it is the Stokes shift that is most frequently monitored [31]. Stokes and anti-Stokes lines are always at frequency positions that are symmetrically to both side of the Rayleigh line [34]. In either case, the resulting photon of energy $\hbar\omega_s$ may interact with the lattice to produce a second photon of still lower energy, and the process can be repeated m times, emitting $\hbar\omega_s = \hbar\omega_i - m\hbar\omega_0$. However, the intensity of these interactions decreases as the order of the process increases [33]. When instead of virtual states the sample is excited to real electronic states the process is called resonant Raman, resulting in a strong enhancement of the Raman signal originating in the particular electronic transition [32].

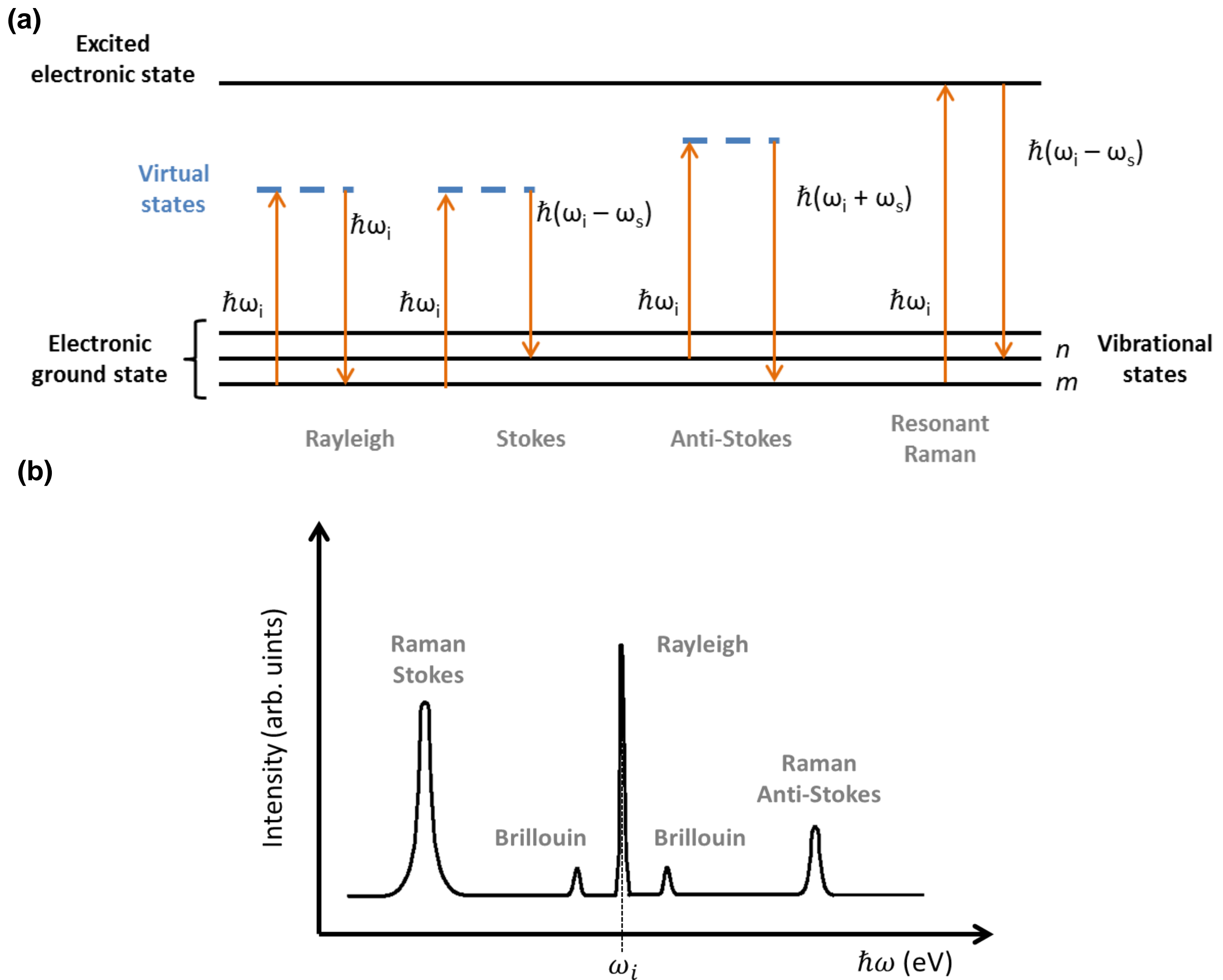

Figure 3-11 – (a) Diagram of the Rayleigh and Raman scattering processes. The lowest energy vibrational state is labelled with a *m*. Adapted from [29]. (b) Energy distribution of the scattered light, showing the different types of scattering. Adapted from [31].

Besides the conservation of energy, also the momentum must be conserved during the mentioned processes [33].

Following a simple classical model, it is possible to understand the Raman effect. When a crystal is irradiated with electromagnetic radiation by an oscillating electrical field

$$\boldsymbol{E} = \boldsymbol{E}_0 e^{i\omega_i t}, \quad \textbf{Eq. 3-23}$$

the crystal becomes polarized and the induced electric polarization in any specific direction can be approximated to [34]

$$P_j = \chi_{jk}\, E_k, \quad \textbf{Eq. 3-24}$$

being χ_{jk} the susceptibility tensor. The electrical susceptibility should be a second rank tensor, although in here, for simplicity, it is assumed that the medium is isotropic in order to represent χ as a scalar [28]. The susceptibility becomes altered due to the periodical vibration of the atoms in the solid around the equilibrium positions [34]. For a specific phonon at frequency ω_0, each component of the susceptibility tensor can be written as [34]

$$\chi_{jk} = \chi_{jk}^{(0)} + \frac{\chi_{jk}^{(0)}}{\partial Q} Q + \cdots \quad \textbf{Eq. 3-25}$$

with

$$Q = Q_0 e^{\pm i\omega_0 t} \quad \textbf{Eq. 3-26}$$

representing a normal coordinate measured from the equilibrium position, indicated by the superscript (0) in Eq. 3-25. $\chi_{jk}^{(0)}$ denotes the electric susceptibility of the medium without fluctuations [28]. The induced polarization can be expressed as [34]

$$P_j = \chi_{jk}\, E_k = \chi_{jk}^{(0)} E_{0k} e^{i\omega_i t} + Q_0 E_{0k} \frac{\chi_{jk}^{(0)}}{\partial Q} e^{i\omega_s t} + \cdots, \quad \textbf{Eq. 3-27}$$

where $\omega_s = \omega_i \pm \omega_0$. This expression describes oscillating dipoles re-radiating light with frequencies ω_i (Rayleigh), $\omega_i - \omega_0$ (Stokes Raman) and $\omega_i + \omega_0$ (anti-Stokes Raman). Moreover, the radiated intensity of these oscillating dipoles is also proportional to $|d^2\mathbf{P}/dt^2|$ and

$$I \propto \omega_i^4 \left(\chi_{jk}^{(0)} E_{0k}\right)^2 + \omega_s^4 \left(Q_0 E_{0k} \frac{\chi_{jk}^{(0)}}{\partial Q}\right)^2 + \cdots. \quad \textbf{Eq. 3-28}$$

The first term on the right side of the equation is related to the Rayleigh scattering intensity, while the second accounts for the Raman scattering intensity. Typically, for visible light $\omega_i^4 \approx \omega_s^4$, meaning that the intensity of the scattered lines is proportional to ω_i^4 [34]. To be Raman active, the lattice vibration must cause a change in the susceptibility (or polarizability), which means [34]

$$\left(\frac{\partial \chi}{\partial Q}\right)_0 \neq 0. \quad \textbf{Eq. 3-29}$$

The model described above considers only one-phonon Raman scattering, which probes only the first Brillouin zone-centre phonons. Expanding Eq. 3-25 to second order terms results in induced polarizations whose frequencies are shifted from the incident one by the amount $\pm\omega_a \pm \omega_b$ (where ω_a and ω_b are the frequencies of the two phonons involved) and give rise to two-phonon Raman scattering. Peaks with Raman frequencies $\omega_a + \omega_b$ or $\omega_a - \omega_b$ are referred as combination or difference modes, respectively. If the two phonons are identical, the resultant peak is denominated an overtone [28].

Taking advantage of all these phenomena, Raman spectroscopy became an important and accurate tool for studying semiconductors, giving information on the vibrational modes of the solids, as well as their crystallinity [31,33,34]. Since the lattice vibrational modes and their energy position are characteristic of each material, the Raman spectrum can work as a “fingerprint” of the material [34]. Thus, several properties of a sample can be assessed using this technique, for instance, its composition, the strain state (evaluating the shift of the peaks) of a crystal or the crystallographic orientation (taking advantage of the polar modes under polarized conditions) [31]. It is also possible to evaluate the damage created by processes like ion implantation. Using two-phonon Raman scattering, the phonon density of states can also be estimated [28]. Moreover, polarization studies may also provide information about disorder and directionally varying strain, and are useful to assign vibration modes (based on their polarity) and determine relative values of Raman tensor elements [35].

Since the Raman signal is rather weak, laser sources are generally used to produce a sizeable scattering rate [30,34]. Using lasers with different wavelength, and therefore different penetration depths, it is possible to profile the sample in depth [31]. Furthermore, as Raman peaks are sharper than the peaks usually detected in the visible region by absorbance and emission, and are measured as a shift from the energy of the excitation source, a monochromatic source is required [29]. The typically small efficiency of the Raman process requires the optimization of every component of the measuring system [28]. The basic components of a Raman spectroscopy measuring system are: a collimated and monochromatic source of light, an efficient optical system to collect the weak scattered radiation, a spectrometer to analyse the scattered signal and a highly sensitive detector [28]. Figure 3-12 shows a schematic representation of a typical Raman apparatus (Figure 3-12a) as well as picture of the system used in the present work (Figure 3-12b). In a simple way, during a Raman experiment, a laser beam illuminates the sample, then the scattered light is collected and focused onto the entrance slit of a spectrometer and the Raman-shifted wavelengths/frequencies are detected by a photodetector [30,31]. Filters are frequently used to avoid the detection of the Rayleigh scattering. The number of photons emitted at a particular wavelength is recorded and stored in a computer for analysis [30]. In many cases, the Raman equipment is coupled to a microscope, as an integral part of the spectrometer. The microscope has many advantages, including the possibility to look at extremely small samples and detect very small amounts of material, as well as to map the sample and look for differences in the crystalline phases, composition, strain, etc. [29]. Since the Raman signal is 4 to 6 orders of magnitude weaker than the Rayleigh signal and the difference in frequency between the Raman peaks’ position and the incident light is very small (about 1% of the laser frequency), the spectrometer must satisfy a number of rigorous conditions. These conditions include a high spectral resolving power and an excellent stray light rejection ratio (ratio between the background light and the signal). The resolving power of modern Raman spectrometers is $\lambda/\Delta\lambda > 10^4$ (for visible light), which can be easily obtained using diffraction gratings. Double monochromators are frequently used to minimize the detection of stray background light.

Raman spectroscopy is a non-destructive technique and requires minimum sample handling and preparation. In most cases the sample can be directly placed in a microscope lamella to be analysed [29]. Its major limitation is the interference caused by other signals like luminescence,

either from impurities or the sample itself. This can be minimized by using nonresonant illumination, in order that the Raman spectrum does not appear masked by the luminescence signal [31,34].

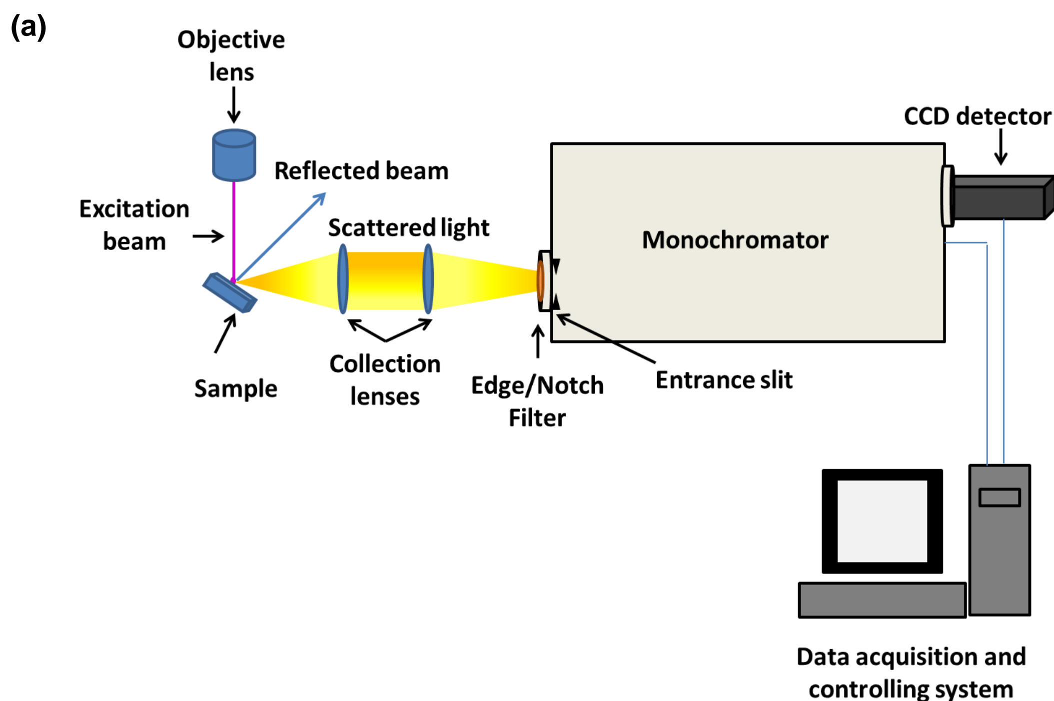

Figure 3-12 – (a) Schematic illustration of a Raman measuring system. Adapted from [30]. (b) Photograph of the Raman system used in this work.

For the samples studied in this thesis, the Raman spectra were performed at RT on a Horiba Jobin Yvon HR800 spectrometer, under the incidence of the 325 nm or 442 nm He-Cd (Kimmon IK Series) laser lines, and also the 532 nm (Ventus-LP-50085, Material Laser Quantum) and 632.8 nm laser excitation. The backscattering geometry $x(y,\cdot)\bar{x}$ was used to minimize the signal from substrate (when present).

3.6. Hall Effect measurements

The evaluation of the electrical properties of the materials is very important for the fully material characterization, especially when device applications are in mind.

According to Ohm's law, the current *I* passing through a material is proportional to the applied voltage *V* [11,13]

$$V = RI, \qquad \textbf{Eq. 3-30}$$

where *R* is the resistance of the material through which the current is passing. *R* is also dependent on the material's shape and dimensions. In order to eliminate this dependence, the concept of resistivity (ρ) was introduced and is described as

$$\rho = \frac{RA}{l}. \qquad \textbf{Eq. 3-31}$$

Here, l is the distance between the two points at which the voltage is measured, and *A* is the cross-sectional area perpendicular to the direction of the current [13]. The resistivity is defined as the proportionality constant between the electrical field ***E*** and the current density ***J*** that it induces. In this sense, for electrons in the relaxation-time approximation, the resistivity can also be expressed as [11]

$$\rho = \frac{ne^2\tau}{m^*}, \qquad \textbf{Eq. 3-32}$$

Where *n* is the number of electrons, τ is the relaxation time between electron collisions and m^* is the carrier effective mass. This result can be stated in terms of the inverse of the resistivity, the conductivity σ=1/ ρ [11,13]. For electrons, this quantity can also be defined by

$$\sigma = ne\mu_e, \qquad \textbf{Eq. 3-33}$$

where μ_e is called the electron mobility, which is a measure of the frequency of electrons' scattering events by imperfections in the crystal lattice, including impurity atoms, vacancies, interstitial atoms, dislocations, and even the thermal vibrations of the atoms themselves. This scattering events lead to the loss of kinetic energy by an electron and changes in its direction of motion [13,36]. In the presence of both electrons and holes [36]

$$\sigma = e(n\mu_e + n\mu_h), \qquad \textbf{Eq. 3-34}$$

being μ_h the hole mobility.

Simple electrical conductivity measurements are not enough to determine the majority charge carrier type, concentration, or the carriers' mobility of a given material. In this case, Hall effect experiments are more adequate [13]. The Hall effect is a consequence of the forces that are exerted on moving charges by electric and magnetic fields [37]. Taking advantage of this effect it is possible to distinguish whether a semiconductor is *n* or *p*-type [37].

When a semiconductor sample is placed under the influence of a magnetic field ***B*** and an electric field ***E***, a current component I_H, perpendicular to both fields arises [38]. Figure 3-13 illustrates an example of an Hall effect geometry. In such geometry, in response to an externally applied electric field the electrons and/or holes will move in the *x* direction, giving rise to a

current I_x. The addition of the magnetic field in the positive z direction, B_z, leads to a force exerted on the charge carriers, deflecting them in the *y* direction, depending on their charge [13]. This force is expressed by [37]

$$\mathbf{F} = e[\boldsymbol{E} + \boldsymbol{v} \times \boldsymbol{B}], \qquad \textbf{Eq. 3-35}$$

where v is the charge carriers velocity. Since this force results in a charge separation to opposite sides of the sample, a voltage, called Hall voltage V_H, will be established in the same direction of the force [13]. The magnitude of V_H depends on the induced current, the magnetic field and the sample's thickness *d* and can be written as [13]

$$V_H = \frac{R_H\, IB}{d}. \qquad \textbf{Eq. 3-36}$$

Here, R_H refers to the Hall coefficient, which is constant for a given material and is defined as [11]

$$R_H = -\frac{1}{nec}. \qquad \textbf{Eq. 3-37}$$

Thus, taking into consideration Eq.3-33, the carrier Hall mobility μ_H is given by

$$\mu_H = |R_H|\sigma c. \qquad \textbf{Eq. 3-38}$$

Therefore, the Hall mobility can be determined if the conductivity is accurately known. This quantity can be determined using either a four-point probe or van der Pauw measurement technique [39].

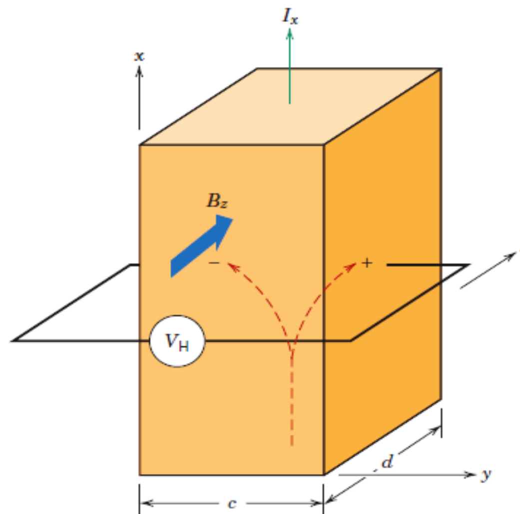

Figure 3-13 – Example of the sample geometry for performing Hall effect measurements. Image reprinted from reference [13].

One frequent limitation of Hall effect measurements is the shape of the sample [28]. This limitation is typically overcome using the van der Pauw geometry. In this geometry, an arbitrarily shaped thin sample is attached to four ohmic contacts placed on the periphery of the sample (Figure 3-14) [39]. Van der Pauw showed that R_H can be obtained by [28]

$$R_H = \frac{[V_{12}(B) - V_{12}(0)]d}{I_{34}B} = \frac{[V_{12}(B) - V_{12}(-B)]d}{2I_{34}B}, \qquad \textbf{Eq. 3-39}$$

where $V_{12}(\mp B)$ is the Hall voltage measured across the contacts 1 and 2, when the magnetic field is applied, and $V_{12}(0)$ corresponds to the voltage with no magnetic field. I_{34} is the current flowing from contact 3 to contact 4.

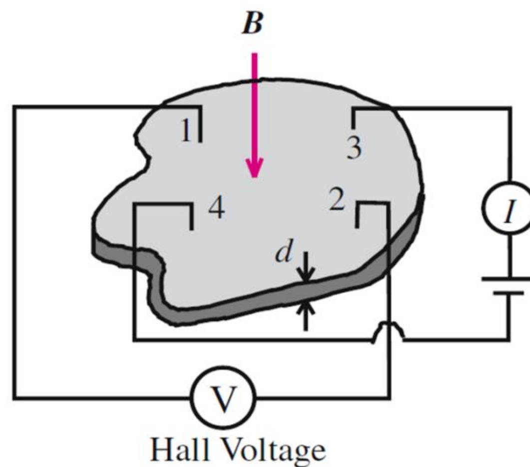

Figure 3-14 – Example of a configuration for the van der Pauw measurements. Image adapted from [28].

The electrical resistivity and Hall mobility of the samples analysed in this thesis were determined from Hall Effect measurements in the van der Pauw geometry using silver contacts, with a Biorad model HL5500 at a constant magnetic field of 0.5 T. These measurements were carried out in *CENIMAT/I3N*.

It should be also emphasized that additional electrical measurements were realized in this work, namely those related with the *J-V* characteristics of the solar cells described in Chapter 7. The analysis of such light to electricity conversion devices will be discussed later followed by the description of the corresponding experimental technique.

3.7. References

1. R. W. Kelsall, I. W. Hamley, and M. Geoghegan, *Nanoscale Science and Technology* (John Wiley and Sons, 2005).

2. R. Egerton, *Physical Principles of Electron Microscopy: An Introduction to TEM, SEM, and AEM* (Springer, 2006).

3. G. Cao, *Nanostructures & Nanomaterials: Synthesis, Properties & Applications* (Imperial College Press, 2004).

4. D. Williams and C. Carter, *Transmission Electron Microscopy: A Text Book for Materials Science* (Springer, 2009).

5. J. Ayache, L. Beaunier, J. Boumendil, G. Ehret, and D. Laub, *Sample Preparation Handbook for Transmission Electron Microscopy: Techniques* (Springer, 2010).

6. Hitachi, *Instruction Manual for Model H-9000NA Electron Microscope* (1989).

7. RNME-UA-National Netw. Electron Microsc. Pole Univ. Aveiro (2015).

8. L. Reimer, *Transmission Electron Microscopy: Physics of Image Formation and Microanalysis* (Springer-Verlag, 1984).

9. P. W. Hawkes, *Advances in Imaging and Electron Physics: Advances in Electron Microscopy and Diffraction* (Academic Press, 2002).

10. C. Kittel, *Introduction to Solid State Physics* (John Wiley & Sons, 1971).

11. N. W. Ashcroft and N. D. Mermin, *Solid State Physics* (Thomson Learning, 1979).

12. P. J. Goodhew, J. Humphreys, and R. Beanland, *Electron Microscopy and Analysis* (Taylor & Francis, 2000).

13. W. D. Callister, *Materials Science And Engineering: An Introduction* (John Wiley & Sons, 2007).

14. B. Bhushan, *Springer Handbook of Nanotechnology* (Springer Science & Business Media, 2007).

15. Hitachi, *Instruction Manueal for Model S-4100 Field Emission Scanning Electron Microscope* (1991).

16. J. Singh, *Electronic and Optoelectronic Properties of Semiconductor Structures* (Cambridge University Press, 2003).

17. B. D. Cullity and S. R. Stock, *Elements of X-Ray Diffraction* (Addison-Wesley Publishing Company, Inc., 1956).

18. S. K. Chatterjee, *X-Ray Diffraction: Its Theory and Applications* (PHI Learning Pvt. Ltd., 2010).

19. K. Kimura, in *Encycl. Anal. Chem. Theory Instrum.*, edited by R. A. Meyers (John Wiley & Sons, Ltd, 2000).

20. P. Jaques, Vacuum **37**, 429 (1987).

21. M. Mayer, in *Lect. given Work. Nucl. Data Sci. Technol. Mater. Anal. Trieste* (Workshop on Nuclear Data for Science and Technology: Materials Analysis, 2003).

22. W.-K. Chu, J. W. Mayer, and M.-A. Nicolet, *Backscattering Spectrometry* (Academic Press, 1978).

23. G. E. McGuire, *Semiconductor Materials and Process Technology Handbook for Very Large Scale Integration(VLSI) and Ultra Large Scale Integration(ULSI)* (Noyes Data Corporation, Noyes Publications, 1988).

24. B. Schmidt and K. Wetzig, *Ion Beams in Materials Processing and Analysis* (Springer Science & Business Media, 2012).

25. S. A. E. Johansson, J. L. Campbell, and K. G. Malmqvist, *Particle-Induced X-Ray Emission Spectrometry (PIXE)* (John Wiley & Sons, Inc., 1995).

26. J. S. Williams and J. R. Bird, *Ion Beams for Materials Analysis* (Elsevier, 1989).

27. G. Moschini, V. Valkovic, and G. W. Grime, Nucl. Instruments Methods Phys. Res. Sect. B Beam Interact. with Mater. Atoms **109**, 170 (1996).

28. P. Y. Yu and M. Cardona, *Fundamentals of Semiconductors: Physics And Materials Properties, Volume 3* (Springer, 2005).

29. E. Smith and G. Dent, *Modern Raman Spectroscopy: A Practical Approach* (Wiley, 2013).

30. A. M. Fox, *Optical Properties of Solids* (Oxford University Press, 2010).

31. D. K. Schroder, *Semiconductor Material and Device Characterization* (John Wiley & Sons, 2006).

32. J. R. Ferraro, K. Nakamoto, and C. W. Brown, *Introductory Raman Spectroscopy*, 2nd editio (Elsevier, 2003).

33. J. I. Pankove, *Optical Processes in Semiconductors* (Dover Publication, Inc., 1971).

34. J. Solé, L. Bausa, and D. Jaque, *An Introduction to the Optical Spectroscopy of Inorganic Solids* (John Wiley & Sons, 2005).

35. D. Tuschel, *Applied Polarized Raman Spectroscopy Webinar* (Horiba Scientific, 2013).

36. M. Grundmann, *The Physics of Semiconductors: An Introduction Including Devices and Nanophysics* (Springer Science & Business Media, 2006).

37. D. A. Neamen, *Semiconductor Physics and Devices: Basic Principles* (1992).

38. R. Enderlein and N. J. M. Horing, *Fundamentals of Semiconductor Physics and Devices* (World Scientific, 1997).

39. R. Green, *Hall Effect Measurements in Materials Characterization* (Keithley Instruments, Inc., 2011).

Chapter 4. Optical characterization

The basis of all optoelectronic technology resides in the interaction between electrons and photons in semiconductors [1]. Therefore, an adequate knowledge of some of the most important phenomena occurring in the semiconductors upon photon illumination, as well as the underlying theoretical concepts, is needed in order to explain and understand the experimental results. This chapter is devoted to the review of these concepts and the optical characterization techniques with relevance for the present work.

4.1. Transmittance, absorbance and diffuse reflectance

4.1.1. Theoretical background

Perhaps the most simple and direct method to assess the electronic band structure of a semiconductor is by measuring its absorption spectrum. Absorption occurs when the incident photon, with energy $\hbar\omega$, is absorbed by an electron, leaving it in an excited state (with higher energy).

In order to understand the absorption phenomenon in semiconductors, it is important to briefly review the concepts of direct and indirect bandgap. While in the case of the atoms the energy level diagram consist on a series of states with discrete energies, the energy diagram of semiconductor materials is more complex, with the formation of bands with their delocalized states [2]. The distinction between the two types of semiconductors is made with respect to the relative positions of the CB minimum and the VB maximum in the Brillouin zone. In a direct bandgap semiconductor the minimum of the CB and the maximum of the VB are at the same *k* position, while in the indirect case the extremes of the bands appear in different *k* positions, as represented in Figure 4-1. This has very important consequences for the optical properties. In a typical semiconductor, interband optical absorption between the VB and the CB is only possible when the photon energy is equal or higher than the energy difference between the maximum of the VB and the minimum of the CB, creating a hole in the initial state and an electron in the final state, and forming an electron-hole (e-h) pair. For indirect semiconductors, since the minimum of the CB and the bottom of the VB are not in the same *k* position, the transition must involve a phonon to obey the conservation of momentum of the electron wavevector. This diverges from the direct case where no phonons are involved in the absorption process [2].

Since there is a continuous range of energy states within the upper and lower bands, the interband transitions can take place in a continuous range of energies, where the minimum value is E_g, thus $\hbar\omega \geq E_g$. Interband transitions originate a continuous absorption spectrum from the low energy threshold (E_g) to a superior value that is defined by the extreme limits of the bands that may be participating in the absorption process, contrasting with the discrete lines observed in atomic absorption spectra [2]. Other absorption processes, besides the interband transition between the VB and the CB, may take place in a semiconductor, for instance involving discrete levels caused by impurities or dopants.

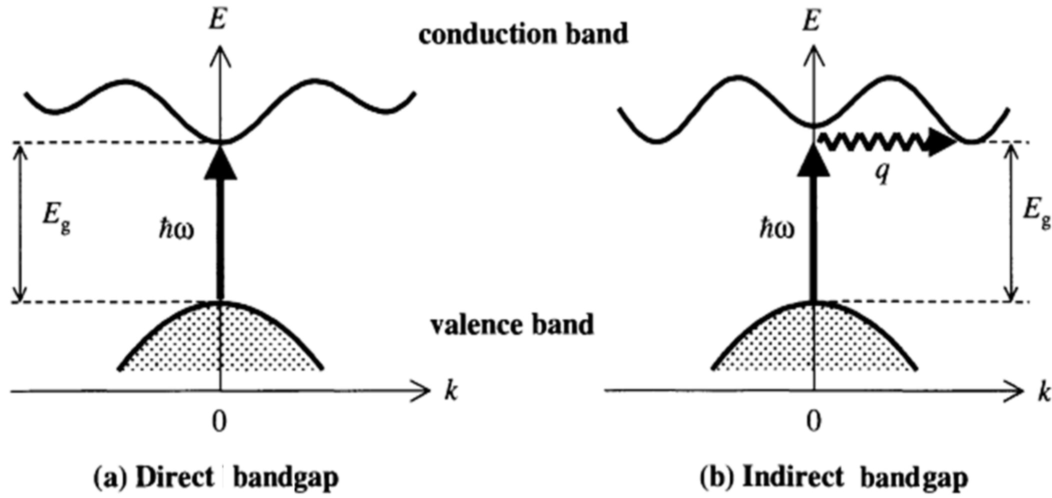

Figure 4-1 – Interband absorption transitions in direct (a) and indirect (b) bandgap semiconductors. The vertical arrow denotes the photon absorption process and the curved arrow corresponds absorption or emission of a phonon [2].

Taking into account the above mentioned phenomena, the transmission of a light beam through a material can be described by the *Beer-Lambert law* [3]

$$I_{out} = I_{in}e^{-\alpha L}, \qquad \textbf{Eq. 4-1}$$

where I_{out} is the beam intensity after transmission through the sample, I_{in} corresponds to the incident beam intensity (incident intensity minus the reflection losses at the surface), L is the thickness of the material (corresponding to the light path) and α is the absorption coefficient, which is a characteristic of the material. The optical absorption coefficient can be determined from the transition probability rate $W_{i\rightarrow f}$ of the electron excitation from the state Ψ_i to Ψ_f, which is promoted by the absorption of a photon with frequency ω. Ψ_i and Ψ_f are the eigenfunctions of the ground and excited states, and are described by Bloch functions [2,3]. The transition probability rate is given by Fermi's golden rule and can be written as [2]

$$W_{i\rightarrow f} = \frac{2\pi}{\hbar}|M|^2 g(\hbar\omega), \qquad \textbf{Eq. 4-2}$$

where M is the matrix element $\left|\langle\Psi_f|H_p|\Psi_i\rangle\right|$ that describes the external perturbation effect on the electrons due to the incident light wave (H_p is the perturbation Hamiltonian), and $g(\hbar\omega)$ is the joint density of states (DOS) [2,3]. Under the description of photons as electromagnetic waves, the perturbation Hamiltonian, H_p, is defined as [2]

$$H_p = -\boldsymbol{p}_e \cdot \boldsymbol{\varepsilon}_{photon} \qquad \text{Eq. 4-3}$$

and

$$\boldsymbol{\varepsilon}_{photon}(\boldsymbol{r}) = \boldsymbol{\varepsilon}_0 e^{\pm i\boldsymbol{k}\cdot\boldsymbol{r}}, \qquad \text{Eq. 4-4}$$

where $\boldsymbol{p}_e = e\boldsymbol{r}$ is the electric dipole moment of the electron, and $\boldsymbol{r}$ is its position vector. The sign in the expression depends on the direction of the wave propagation. The conservation of momentum requires that the change in the crystal momentum of the electron must be equal to the momentum of the photon. Since the wavevector of the electron is much larger than the photon one, the photon momentum can be neglected. A direct optical transition leads, therefore, to a negligible change in the wavevector of the electron. This is why the optical absorption is represented by a vertical arrow (Figure 4-1) [2].

The joint DOS function $g(\hbar\omega)$ describes the distribution of the states in the bands of the semiconductor and takes into consideration the fact that both the initial and final electron states are within continuous bands. Taking as approximation parabolic bands, for a bulk material, $g(\hbar\omega)$ can be written as [2]

$$g(\hbar\omega) = \begin{cases} \frac{1}{2\pi^2}\left(\frac{2m_R}{\hbar^2}\right)^{\frac{2}{3}}\left(\hbar\omega - E_g\right)^{\frac{1}{2}}, & \hbar\omega \geq E_g \\ 0, & \hbar\omega < E_g \end{cases} \qquad \text{Eq. 4-5}$$

where

$$\frac{1}{m_R} = \frac{1}{m_e^*} + \frac{1}{m_h^*}, \qquad \text{Eq. 4-6}$$

is the reduced electron-hole mass and m_e^* and m_h^* are the electron and hole effective masses, respectively. Thus, in direct bandgap bulk materials, the behaviour of the absorption coefficient as a function of the frequency can be predicted as follows [2]

$$\begin{aligned} \alpha(\hbar\omega) &\propto \left(\hbar\omega - E_g\right)^{\frac{1}{2}}, \quad \hbar\omega \geq E_g \\ \alpha(\hbar\omega) &= 0, \qquad \hbar\omega < E_g. \end{aligned} \qquad \text{Eq. 4-7}$$

For indirect bandgap semiconductors the previous relationship becomes

$$\alpha(\hbar\omega) \propto \left(\hbar\omega - E_g \mp \hbar\Omega\right)^2, \qquad \text{Eq. 4-8}$$

where the difference $\mp\hbar\Omega$ accounts for whether a phonon is absorbed or emitted. The Eqs. 4-7 and 4-8 can be used to estimate the bandgap of a material from which the absorption coefficient is known. However, it is important to keep in mind some of the approximations made:

i. the Coulomb interaction between the electron and the hole was neglected;
ii. no impurity or defect's states within the bandgap were considered;
iii. the parabolic band approximation is only valid near *k = 0*. Increasing photon energy above the bandgap, the derived joint DOS will no longer obey the conditions depicted in Eq. 4-7.

The first approximation works well at RT, though, for lower energies, the Coulomb attraction can enhance the absorption rate and lead to the formation of excitons, especially at cryogenic

temperatures. On the other hand, the presence of defect states inside the bandgap may lead to the absorption of photons with energies lower than E_g [2].

The dielectric function $\varepsilon(\omega)=\varepsilon_r(\omega)+i\varepsilon_i(\omega)$ accounts for the interaction between the electromagnetic radiation and the material. The complex refraction index is related with the dielectric function by

$$\tilde{n}(\omega) = \sqrt{\varepsilon(\omega)} = n + i\kappa.$$ **Eq. 4-9**

where n is the real part of refraction index and κ is designated by extinction coefficient. The first term of Eq. 4-9 is connected with the refraction properties of the medium, while the imaginary part is related with the absorption properties and [4]

$$\alpha = \frac{2\omega\kappa}{c}.$$ **Eq. 4-10**

Experimentally, an absorption spectrum is typically measured as absorbance (A) or transmittance (T), which can be defined returning to the *Beer-Lambert law* in Eq. 4-1

$$I_{out} = I_{in}T,$$ **Eq. 4-11**

and so

$$T = \frac{I_{out}}{I_{in}} = e^{-\alpha x},$$ **Eq. 4-12**

The absorbance is written as (neglecting reflection processes) [3]

$$A = 1 - \frac{I_{in}}{I_{out}} = log\left(\frac{I_{in}}{I_{out}}\right) = -\log(T).$$ **Eq. 4-13**

Both transmittance and absorbance depend not only on the type of material, but also on the amount or thickness of the analysed material. However, they are frequently used to obtain the experimental absorption coefficient at a specific wavelength λ, using the expression

$$\alpha_\lambda = \frac{1}{L} ln\left(\frac{I_{in}}{I_{out}}\right)_\lambda = \frac{1}{L} ln\left(\frac{1}{T}\right)_\lambda.$$ **Eq. 4-14**

In the above considerations the reflection processes were neglected, nevertheless, they can play a role in the optical characterization. Reflectance spectra provide similar and complementary information to the absorbance or transmittance measurements. This type of measurements is frequently used in bulk samples or powders. Similarly to absorbance and transmittance, reflectance, R, is defined as [3]

$$R = \frac{I_r}{I_{in}},$$ **Eq. 4-15**

where I_r corresponds to the intensity of the reflected light. Thus, from Eqs. 4-11, 4-13 and 4-15 it readily follows that $R=1-A-T$. If the incidence is normal to the sample's surface, reflectance can be written as [5]

$$R = \frac{(n_0 - n_1)^2 + \kappa_1^2}{(n_0 + n_1)^2 + \kappa_1^2},$$ **Eq. 4-16**

where n_0 is the refractive index of the ambient (usually air), while the refractive index of the sample's material is ($n_1+i\kappa_1$). The real part of the refraction index can be obtained through the

Kramers-Kronig relations, which is an analytic method that connects the real and imaginary parts of the refractive index [6–9]. Using these relations, it is only necessary to determine experimentally the imaginary part of the refraction index to determine mathematically the real part (and vice-versa), usually with the help of computational methods [4,6,7].

As mentioned, a perfect semiconductor (without defects or impurities) is transparent for photon energies lower than E_g. In this sense, the transmittance can be obtained through reflectance by [5]

$$T = \frac{1-R}{1+R}. \qquad \text{Eq. 4-17}$$

Adding the absorption, the expression above becomes

$$T = \frac{(1-R)^2 e^{-\alpha L}}{1-R^2 e^{-2\alpha L}}, \qquad \text{Eq. 4-18}$$

and

$$\alpha_\lambda = \frac{1}{L} ln\left(\frac{\sqrt{(1-R)^4 + 4T^2R^2} - (1-R)^2}{2TR^2}\right)_\lambda. \qquad \text{Eq. 4-19}$$

Two types of reflectivity can be recorded: direct or specular reflectivity and diffuse reflectivity. The former case is used in well-polished samples while, the latter is used for rough samples or powders. Diffuse reflectance measurements require the use of an integrated sphere since the light is reflected in all directions, as represented in Figure 4-2.

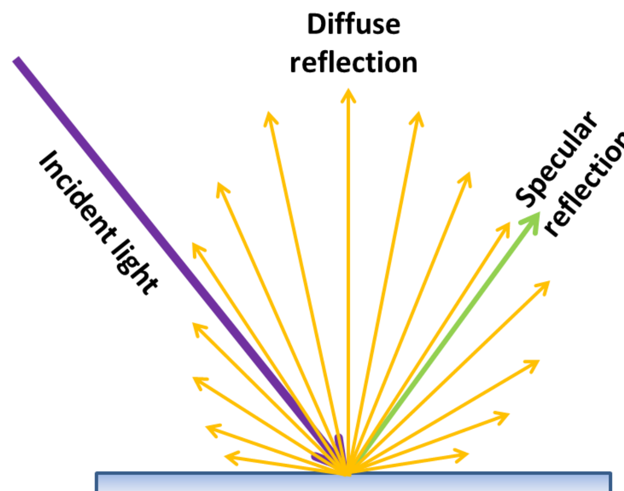

Figure 4-2 – Schematic illustration of the diffuse reflection process, which is characterized by light reflection in all directions. This process is typical in powders or samples with rough surfaces. In used approximation of the ray-model also the specular reflection is shown.

4.1.2. Experimental setup

From the experimental point of view, a piece of a semiconductor is placed in front of an excitation source coupled to a monochromator, and the transmitted signal is analysed taking into

account the changes regarding the excitation profile. This allows to obtain information about the transitions that can take place in the sample, as well as the distribution of electronic states [4].

In this thesis, RT absorbance/transmittance measurements were performed in a double-beam Shimadzu UV1000 spectrometer in transmission mode in a wavelength range from 200 to 850 nm (~ 6.2 eV to 1.5 eV). RT diffuse reflectance measurements were carried out in an *Avantes Avasphere-50-REFL* integrated sphere, using a 450 W Xe lamp as excitation source. The light was conducted from the lamp to the sphere via a FC-UV600-1 (*Avantes*) optical fibre and the signal was processed in an Ocean Optics USB4000 UV-VIS spectrometer (from 200 to 850 nm).

4.2. Photoluminescence spectroscopy

After the absorption process described in the previous section, the system can return to the ground state by the emission of photons and it is this de-excitation process that is called luminescence or radiative recombination [3]. When the carriers' generation is made with light (photons), as in the case of this thesis work, the process is denominated by photoluminescence (PL). Similarly, if the excitation source is an electron beam instead of a photon beam, it is called cathodoluminescence (CL). While PL allows selective excitation of a particular emission process, CL allows depth-resolution information by the variation of the electron beam energy. Another widely used luminescence technique is electroluminescence (EL), where the excitation is made by carriers' electric injection through the material. This process is particularly important in the development of LED devices. In the present work, the main focus is given to the PL technique.

Luminescence constitutes a powerful tool that enables the optical characterization of semiconductors and insulators. Luminescence measurements can provide information on different types of impurities at the same time, based on their distinct radiative recombination processes [5]. Defects or impurities are commonly found in semiconductors, either intentionally or un-intentionally incorporated. They introduce electronic energy levels within the bandgap of the material that can give rise to the appearance of optical transitions at energies lower than E_g. These defects/impurities are then called optically active centres and exhibit a variety of interesting optical properties [3].

4.2.1. Theoretical background

The physics behind PL is more complex than that involving the absorption phenomena, since the generation of light is closely related with energy relaxation mechanisms in the semiconductors. Additionally, the shape of a luminescence spectrum is affected by the thermal distribution of the electrons and holes within the bands and defect states. Therefore, all these phenomena must be taken into consideration in the analysis of the PL output [2]. During a PL experiment, the generation of e-h pairs through optical absorption leads to a non-equilibrium distribution of the pairs. In most cases, the electrons and holes thermalize among themselves and reach a quasi-thermal equilibrium in a time scale shorter than the one that it takes for their recombination. It is possible that these electrons and holes show different quasi-equilibrium

distributions. After the thermalization, the e-h pairs recombine radiatively, producing spontaneous emission. Since the luminescence is produced by thermalized e-h pairs, the emitted photons have no correlation with the excitation process [10]. In summary, a typical band-to-band PL process may be described by three main steps [2,10]:

1. *Excitation*: e-h pairs are generated by the excitation source. An excited electron is injected in the CB by the photon absorption and a hole is created in the VB.
2. *Thermalization*: the excited e-h pairs relax towards quasi-equilibrium distributions. This means that generated electrons and holes relax very rapidly to the lowest energy states within their respective bands by emitting phonons. Thus, the electrons accumulate at the bottom of the CB and the holes at the top of the VB.
3. *Recombination*: the thermalized pairs recombine radiatively emitting photons.

It is important to introduce here the concept of configurational coordinate diagram since it is useful in explaining the phonon-assisted process that may accompany several radiative transitions [4]. At its equilibrium position, the ground and the excited states frequently have their minimum potential at different positions, as is illustrated in Figure 4-3. Thus, when an electron is excited from the ground state (at A) to the excited state at B, the system rapidly relaxes to condition C and the excited electron loses some of its energy in the process. This loss energy is dissipated in the form of an atomic displacement, i.e., as a phonon. In the emission process, the electron returns to the ground state at D, and a new phonon is emitted in order to return to the minimum potential (A). Due to the phonon emission, the energy of the photon emitted in the transition C→D is lower than the energy absorbed in the transition A→B [4]. These steps follow the Franck-Condon principle, which states that the electronic transitions occur so rapidly that the nuclei of the atoms do not move significantly during the transition (according to the Born-Oppenheimer approximation). This is why the optical transitions are represented by vertical arrows in the configurational coordinate diagram [2].

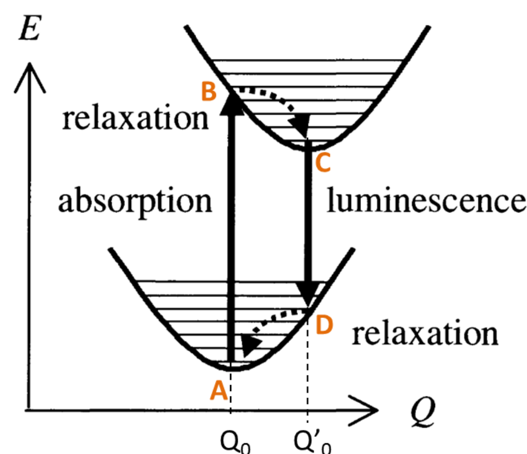

Figure 4-3 – Configurational coordinate diagram for the ground state and first electronic excited state of an optical centre. Adapted from [2].

The spontaneous emission rate for a radiative transition between the levels *n* and *m* can be determined by the Einstein coefficient A_{nm}. This coefficient is proportional to the *B* coefficient, which is related to the absorption probability [2,10]

$$A_{nm} = \frac{8\pi h \upsilon^3 n_r^3}{c^3} B_{nm}, \ \ (B_{nm} = B_{mn}) \quad \textbf{Eq. 4-20}$$

where $h = 2\pi\hbar$, υ is the excitation photon frequency $\upsilon = \omega/2\pi$, n_r is the refractive index of the medium and *c* is the velocity of light in vacuum [10]. The relationship implies that transitions with large absorption coefficients also have high emission probabilities and short radiative lifetimes [2]. If the stimulated emission processes were neglected, the radiative emission rate is given by [2]

$$\left(\frac{dN}{dt}\right)_{rad} = -A_{nm}N, \quad \textbf{Eq. 4-21}$$

for the upper level *n* with population *N* at time *t*. Thus, the number of photons emitted in a specific time is proportional not only to the Einstein coefficient A_{nm}, but also to the population of the excited level *n*. Taking into account the populations of the involved levels, the rate equation can be defined as

$$N(t) = N(0)e^{-A_{nm}t} = N(0)e^{-t/\tau_{rad}}, \quad \textbf{Eq. 4-22}$$

which means that $\tau_{rad}=1/A_{nm}$ is the radiative recombination lifetime.

Considering that a beam with intensity I_{in} enters the material and an intensity I_{out} passes through it, the intensity of the emitted light I_{em} should be proportional to the absorbed intensity. The relationship can be expressed as [3]

$$I_{em} = \eta(I_{in} - I_{out}). \quad \textbf{Eq. 4-23}$$

Here, η is the internal luminescence efficiency or internal quantum efficiency (IQE) and can be written as [5]

$$\eta = \int_0^L \frac{\Delta n}{\tau_{rad}} e^{-\alpha x} dx \ , \quad \textbf{Eq. 4-24}$$

where Δn is the excess minority carrier density. The exponential term describes the absorption of the light that is generated by the sample itself. Δn depends on the photon flux density and on the recombination mechanisms. It is also important to take into account that, in most of the luminescence experiments, only a fraction of the emitted light is collected, depending on the experimental parameters like focusing system and geometrical characteristics of the detector. Assuming that all the emitted light is collected, an efficiency $\eta < 1$ indicates that a fraction of the absorbed light is lost by nonradiative processes [3].

Given that an excited centre is not at thermodynamic equilibrium, it will return to its ground state after a certain relaxation time. The return to the ground state can be either radiative (with the emission of a photon) or nonradiative (in the form of lattice vibrations or energy transfer to impurities or defects called “traps” [2]). In the first case, the photon is emitted after a mean lifetime τ_{rad}, as expressed above. For the latter, the relaxation is ruled by a nonradiative recombination time (nonradiative lifetime), τ_{nrad}. The inversed values of these two lifetimes represent the probability of the correspondent transition per unit of time, i.e., the recombination rate. Thus, the total probability of a transition from the excited to the ground state can be expressed as [11]

$$\frac{1}{\tau} = \frac{1}{\tau_{rad}} + \frac{1}{\tau_{nrad}}, \qquad \text{Eq. 4-25}$$

and the IQE can be re-written as the ratio between the radiative recombination and the total recombination rates [11]

$$\eta = \frac{\frac{1}{\tau_{rad}}}{\frac{1}{\tau_{rad}} + \frac{1}{\tau_{nrad}}} \leq 1. \qquad \text{Eq. 4-26}$$

If τ_{rad} << τ_{nrad}, η becomes close to the unity and the maximum possible amount of light is emitted. Alternatively, when τ_{rad} >> τ_{nrad}, η is very small and the light emission is inefficient. Thus, a high luminescence efficiency is obtained when the nonradiative processes are minimized and the radiative lifetime is much shorter than the nonradiative one [2].

Both radiative and nonradiative recombination rates can be accounted for a classical model. The nonradiative transition probability constitutes a thermally activated pathway for the depletion of the emitting state, which can be classically described by an activation energy, E_a [11]

$$\frac{1}{\tau_{nrad}} \propto e^{-\frac{E_a}{k_B T}}. \qquad \text{Eq. 4-27}$$

Following this approach, the IQE value can be estimated by the ratio between the integrated emission at RT, I_{PL}(RT), and low temperature, I_{PL}(LT), assuming that the nonradiative processes are negligible at low temperature (~ 14 K). Consequently, the IQE in a photoluminescence experiment is estimated as

$$IQE \sim \frac{I_{PL}(RT)}{I_{PL}(LT)}. \qquad \text{Eq. 4-28}$$

Within the proposed classical model and considering that the probability of a radiative transition, ${\tau_{rad}}^{-1}$, is temperature independent, the evolution with temperature of the PL integrated intensity can be described according to

$$\frac{I(T)}{I_0} = [1 + C\ e^{-E_a/k_B T}\ ]^{-1}, \qquad \text{Eq. 4-29}$$

where T is the absolute temperature, I_0 the PL intensity at low temperature, C corresponds to the ratio of the electronic levels' effective degeneracies and k_B is the Boltzmann constant. Therefore, a frequent decrease of $I(T)/I_0$ with increasing temperature is observed, and this effect is called thermal quenching of the luminescence [11].

Figure 4-4 shows a schematic representation of the main recombination processes involving radiative transitions occurring in a semiconductor upon above bandgap photon excitation [1,5]. The first one is band-to-band recombination, where electrons from the CB recombine directly with holes in the VB. Thus, interband luminescence corresponds to the annihilation of an e-h pair. This will result in the emission of a photon with energy close to E_g [2]. This type of optical transitions take an important role at higher temperatures where all the shallow impurities are typically ionized, as well as in less pure or less perfect crystals where local fields created by the defects tend to dissociate the exciton into free carriers [4,5,10]. When an e-h pair is created the carriers may be attracted to each other by Coulombic interaction, forming the so-called free exciton. Electron and hole remain bound to each other in a hydrogen-like state mediated by the

dielectric constant of the materials [5]. Typically, this elementary excitation can be seen as the excited state of a pure crystal, with the recombination processes likely to be observed at cryogenic temperatures in low defective semiconductor samples. The excitons can be either free (FX) or be bounded to defect or impurity states (BX). As mentioned, FXs often form in a sufficiently pure material and the energy of their recombination is slight less than E_g. In a direct bandgap semiconductor, the energy of the emitted photon is given by [5,9]

$$\hbar\omega = E_g - E_{xb} - n\hbar\omega_{LO}, \quad \text{Eq. 4-30}$$

where E_{xb} is the exciton binding energy corresponding to the energy required to the exciton dissociation and $n\hbar\omega_{LO}$ corresponds to the optical phonons assisting the transition, which are designated by vibronic replicas [12]. For indirect bandgap semiconductors, the phonon energy should be considered, due to the conservation of momentum of the electron wavevector, and subtracted to the above expression. When the semiconductor contains a small number of donors or acceptors in their neutral or ionized states (which are common at low temperature), the excitons “feel” their local field and can be attracted to these impurities or defects via Coulomb or van der Walls interactions. This attraction decreases the exciton energy by bounding the excitons to the impurity/defect states and forming a BX. Each BX is associated with a specific defect that can be a neutral or ionized donor (DX) or acceptor (AX), as well as other types of defects, giving rise to a specific BX spectrum, showing, in several cases, well defined sharp lines that are easily identified for each particular BX [13,14]. As a consequence of its localization, the photon emitted in the recombination of a BX shows an energy [10]

$$\hbar\omega = E_g - E_{xb} - E_{loc} - n\hbar\omega_{LO}, \quad \text{Eq. 4-31}$$

where E_{loc} corresponds to the localization energy of the exciton in the impurity/defect. Therefore, BXs constitute major optical signatures of the presence of impurities in the crystal, making them of great importance in the semiconductor characterization [13]. BX transitions and donor-VB transitions frequently appear in the same spectral region, so, in order to distinguish between these two types of transitions, their linewidths should be examined. The full width at half maximum (FWHM) for BX transitions are usually ≤ $k_BT/2$, with a shape similar to a broadened delta function, while donor-VB transitions are found to be wider than k_BT [5].

The presence of both donors and acceptors in a semiconductor is very frequent. In this case the semiconductor is said to be compensated, since, under equilibrium conditions, some electrons of the donors will be captured by the acceptors. So, both ionized donors (D^+) and acceptors (A^-) are present. When carriers are trapped by donors/acceptors, these centres became neutral (D^0, A^0) [10]. An electron on a D^0 can recombine with a hole in an A^0, leading to a donor-acceptor pair (DAP) transition. The emission resulting from the DAP recombination has an energy of [5]

$$\hbar\omega = E_g - (E_A + E_D) + \frac{e^2}{4\pi\varepsilon_0\varepsilon_r r} - n\hbar\omega_{LO}, \quad \text{Eq. 4-32}$$

where E_A and E_D are the acceptor and donor binding energies, respectively. The last term in Eq. 4-32 describes the Coulombic interaction between donors and acceptors, with r being the

distance between the donor and the acceptor, e is the electron charge, ε_0 is the permittivity of free space and ε_r is the semiconductor dielectric constant.

DAP recombination shows a well-defined behaviour, namely in its excitation density and temporal dependences. Appling low excitation densities leads to the excitation of only a fraction of the donors and acceptors. Therefore, only the distant pairs will recombine. When high enough excitation density is applied, all the donors and acceptors become excited (saturation condition), leading to an additional contribution from the closer pairs to the recombination spectra. Hence, one characteristic of the DAP recombination if the shift of the emission spectra to higher energy with the increase of the excitation density. Moreover, the DAP recombination also shows time dependence after excitation by a short pulse. When all the donors and acceptors are excited, the probability transition of recombination is faster for closer pairs as an higher overlap degree of the carriers wavefunctions occur. On the other hand, distant pairs show a low overlap of the carriers' wavefunctions, resulting in lower probability transitions and longer lifetimes. Therefore, the recombination spectra show a shift towards lower energies with increasing time delays, resulting in a redshift of the emission and a non-exponential time decay [10].

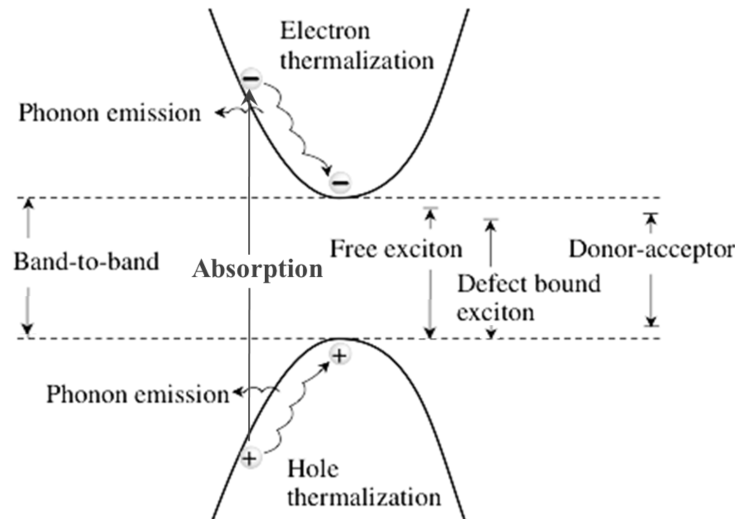

Figure 4-4 – Schematic representation showing thermalization of electrons and holes, as well as the main radiative transitions observed in PL. Adapted from [1].

Besides the above mention recombination mechanisms present in Figure 4-4, other transitions may take place, as is the case of free-to-bound (e-A) transitions, as well as recombination between deep defect levels and intraionic recombination of luminescent activators present in a semiconductor sample. In the first case, free electrons can recombine radiatively with holes trapped in acceptors. In the free-to-bound recombination the energy of the emitted photon is given by [10]

$$\hbar\omega = E_g - E_A - n\hbar\omega_{LO}. \quad \textbf{Eq. 4-33}$$

This emission constitutes a simple way of measuring impurity binding energies. Wavevector conservation in e-A transitions is relaxed since the translational symmetry of the crystal is broken by the impurities/defects. Thus, a carrier in the CB can recombine with another carrier of opposite charge bound to the defect/impurity regardless of its wavevector [10].

According to T. Schmidt *et al.* [15], the PL intensity as a function of the excitation density can be well fitted to a power law,

$$I \propto P^m, \qquad \text{Eq. 4-34}$$

where I is the luminescence intensity, P is the excitation power and m is a parameter that represents the slope in a log-log representation of I and P. This relationship gives information regarding the type of transition involved. When $m < 1$, and according with the rate equations, it is proposed that the nature of the radiative transitions involves DAPs or free-to-bound carrier recombination, while when $1 < m < 2$ exciton-like transition should be involved.

Excitons have been the subject of intensive research in the semiconductor field, especially in the case of wide bandgap semiconductors, as GaN or ZnO. Excitons may play an important role in light emitting devices based on these materials (even at RT), due to their large free exciton binding energy [13].

As mentioned above, when an e-h pair is formed, the carriers can interact with each other by mutual Coulomb attraction and become bound, creating an exciton. An exciton can be seen as a small hydrogenic system [2], no longer representing two independent quasi-particles. Therefore, an exciton can be viewed as a quasi-particle that moves freely through the crystal and transports energy without contributing to electron conductivity. Since the electron and the hole are bound, excitons create discrete electronic levels of energies just slightly below the CB, resulting in the excitonic transitions observed near the bandgap energy [3,11]. Stable excitons can only be formed when the attractive potential is enough to maintain the e-h pair bound, even in the presence of collisions with phonons. Taking into account that the maximum energy of a thermally excited phonon at temperature T is $\sim k_BT$, this condition is satisfied if the exciton binding energy is higher than k_BT [2].

Generally, two types of excitons can be found in crystalline materials: *Wannier-Mott excitons*, called FXs, and *Frenkel excitons* [2,3,10]. FXs exhibit a large radius (in the order of few nm) when compared with the interatomic distances and originate delocalized states that can move freely through the crystal (thus the term “free” excitons) [2,3]. Due to the large e-h separation, FXs are “weakly” bounded. In this case, it is possible to consider both particles to be moving in a uniform dielectric material, with dielectric constant ε_r. A system like this can be approximated to a hydrogen atom, replacing the electron mass by the reduced effective mass, m_R, of the e-h system (Eq. 4-6). In this approach, the energy levels, measured from the ionization level (0 eV), can be given by [2–4]

$$E_x(n) = -\frac{m_R e^4}{2h^2 \varepsilon n^2} = -\frac{m_R R_H}{m_e \varepsilon_r^2 n^2}, \qquad (n \geq 1), \qquad \text{Eq. 4-35}$$

where R_H is the Rydberg constant of the hydrogen atom (13.6 eV), m_e is the electron mass and n is the principal quantum number. For n = 1 the exciton is in its ground state, so the energy that is necessary to ionize it is

$$E_{xb} = \frac{m_R R_H}{m_e \varepsilon_r^2}, \qquad \text{Eq. 4-36}$$

which corresponds to the aforementioned *exciton binding energy*. In most semiconductors, the exciton binding energy is in the meV range [3]. Considering the ionization level at the bottom of the CB, the exciton energy levels can be defined as [2,3]

$$E_n = E_g - \frac{m_R R_H}{m_e \varepsilon_r^2 n^2}. \qquad \textbf{Eq. 4-37}$$

As a result, discrete energy levels near the CB of the semiconductor can originate a number of absorption peaks near the band edge spectral region, for n = 1, 2, 3 and so on. The ground state is the one that shows the highest binding energy, as well as the shortest e-h radius. For n>1, the pair is less strongly bound and has a larger radius [2].

The second type of excitons, the *Frenkel excitons* have a much smaller radius than that of the FXs, in the same size range as the units cell, which makes them localized states tightly bounded to a defect/impurity. Consequently, their mobility is lower than that of FXs and they move through the crystal by hopping from one atom site to another [2]. The energy levels of *Frenkel excitons* are not described by the effective mass theory as those of the FXs, since the *Frenkel excitons* are localized in close proximity with a single atom and the medium cannot be considered uniform, as in the case of FXs. Due to the strong coupling between excitons and the crystalline lattice, a more refined and complicated theoretical treatment is needed [2,3]. Regarding their binding energies, they are larger than the ones found for FXs and vary from 0.1 eV to several eV [2]. This type of excitons commonly occurs in insulators rather than in semiconductors.

4.2.2. PL excitation, time-resolved PL and lifetime measurements

PL excitation (PLE) spectroscopy is a very useful technique to assess the preferential pathways for excitation of the optical centres. In order to acquire an excitation spectrum, the intensity of a specific luminescence line, I_{lum}, is monitored while continuously changing the energy of the exciting light, $\hbar\omega_{exc}$, at a constant incident intensity or photon flux. Thus, a PLE spectrum results from the curve $I_{lum} = f(\hbar\omega_{exc})$ [9,16]. The peaks/bands observed in a PLE spectrum give information about the processes involved in the excitation of a specific transition, as well as the optimum conditions for its excitation. In this way, PLE provides complementary information to the one obtained in absorption measurements [1].

Time-resolved PL (TRPL) can provide important knowledge about the temporal behaviour of the luminescence signal, namely the shape of the luminescence decay curve after the excitation is turned off, contributing to the identification of the recombination processes and, sometimes, for the deconvolution of overlapped emitting centres that show different time dependence [11]. The temporal evolution of the PL signal is recorded by controlling the delay time after a pulse [1,9,17]. In a lifetime measurement, the time-dependent intensity of a chosen emission is measured following the excitation pulse. The decay time, τ, is calculated from the slope of a plot *log I(t)* as a function of time, *t*, or from the time at which the intensity decreases *1/e* of the value at *t = 0* [18]. The radiative lifetime of a specific transition corresponds to the average time the excited state of the optical centre remains populated, following excitation, before the electrons return to the ground state emitting photons [18]. The lifetime of a transition can be extremely different,

varying from ps to ms, according to the spin multiplicity of the states involved, i.e, depending on the transition probability of the emitting states. Transitions between states with the same multiplicity are fast (~ 10^{-9} to 10^{-7} s), while transitions between states with different spin multiplicity are slower (~ 10^{-4} to 10^{1} s). In the first case, the emission is generally referred as fluorescence, while the second case is called phosphorescence.

In the simplest case, the lifetime of the radiative recombination, τ_{rad}, can be obtained from Eq. 4-22, following a simple exponential decay. Experimentally, it is advantageous to re-write Eq. 4-22 in the form

$$I(t) = I_0 e^{-t/\tau_{rad}}, \quad \textbf{Eq. 4-38}$$

where $I(t)$ is the intensity measured as a function of time, and I_0 is the intensity of the monitored emission at $t = 0$. It must be noted that the measured emissions frequently show multiexponential decays, i.e., complex decays. In that case, distinct optical centres or transitions may be contributing for the emission observed at the same spectral position. Therefore, a more general expression should be considered [18]

$$I(t) = \sum_{i=1}^{n} \alpha_i e^{-t/\tau_i}, \quad \textbf{Eq. 4-39}$$

with α_i representing the amplitude of each centre/transition at $t = 0$. τ_i accounts for the decay times and n is the number of decay times involved. The physical meaning of the parameters α_i and τ_i depends on the system in study [18]. For instance, α_i may correspond to the percentage of centres contributing for the transition with lifetime τ_i.

In some cases, the emission decay follows a slightly different lifetime distribution, denominated by stretched exponential, which can be described by

$$I(t) = I_0 e^{(-t/\tau_{rad})^{\beta}}, \quad \textbf{Eq. 4-40}$$

where β ($0 < \beta < 1$) is the stretching parameter, also known as the dispersion factor. The stretched exponential decay behaviour is often encountered in systems with lattice disorder and is considered to be a result of diffusion of excited carriers [18–21].

The excitation source used in this type of measurements is of paramount importance, so it is worth to discuss some of its characteristics. The most important parameters of the excitation source are the pulse duration, the pulse energy and the repetition rate [1]. The pulse duration determines the time resolution of the measurement, while the pulse energy determines which electronic levels are assessed during the experiment. An excitation source must be modulated in time with a pulse shorter or at least comparable with the decay time to be measured [9]. The repetition rate controls how fast the data can be acquired. This rate should be slow enough that the system is still disturbed before the next pulse comes in [1]. Generally, in order to achieve a good output signal, and to improve the signal-to-noise ratio, the signal measured from the detector must be sampled at equally spaced time intervals after each excitation pulse, and the output result corresponds to an average of those signals. Moreover, the excitation source should exhibit an extremely reproducible profile [17].

4.2.3. Luminescence in GaN and ZnO

As presented in Chapter 1, GaN and ZnO share a significant number of properties, including analogous luminescent features. Thus, a brief description of the main optical transitions in these semiconductors is given bellow.

4.2.3.1. GaN

As mentioned, GaN is a direct bandgap material with fundamental optical transitions at the Γ-point (*k = 0*) of the first Brillouin zone [22]. These optical transitions involve the recombination of an electron from the CB minimum with a hole from each one of the three uppermost VB states, labelled A, B and C, as shown in Chapter 1 [13,22,23]. The excitons arising from the bands A, B and C are FXs, and are labelled FX_A, FX_B and FX_C, accordingly. Studies carried out at 2 K in bulk samples revealed energy spectral positions at 3.478 eV, 3.484 eV and 3.502 eV for each FX, respectively [24]. In the case of the epilayers, the spectral position is strongly dependent on the strain state of the samples [24]. In addition to the FXs, bound excitons (DX and AX) are often present. The most common DX in GaN are associated either with the recombination of an A exciton to a neutral O_N donor or a neutral Si donor on the Ga site (Si_{Ga}). These transitions can be identified at 3.4714 eV and 3.4723 eV, respectively [13]. The emission resulting from the DX_A excited states appear in the higher energy side and are normally overlapped with the transition related with the B exciton and the broad emission of an A exciton-polariton, peaked at 3.478 eV [13]. In the lower energy side, transitions designated by two electron satellite (TES) are also observed [13,14]. A TES transition corresponds to a radiative recombination of a DX which leaves the donor in an excited state, thus leading to a transition with lower energy than the one of the DX, by an amount equal to the energy difference between the first excited state and the ground state of the donor [25]. Additionally, a transition at ~ 3.466 eV and several phonon replicas of the main transitions (FX and/or DX) below 3.41 eV were identified [14]. The transition at 3.466 eV is commonly ascribed to an exciton bound to a neutral acceptor (A^0X), since it is frequently observed in Mg-doped samples. This assignment was corroborated by magneto-optical measurements [26], even though some doubts remain about its nature [13]. The Mg impurity assumes an important role on the development of GaN-based devices. The control of the *p*-type conductivity in this host predominantly *n*-type was achieved by the deliberated introduction Mg into GaN, resulting in a shallow energy level (~200 meV) above the VB, allowing a controlled and reproducible way to produce *p*-type GaN [27–30].

Other AX transitions have been reported for excitons bound to Zn and Cd impurities [31]. DAP recombination is also a common feature in the GaN emission spectra. These transitions have been found at energies between 3.268 eV and 3.264 eV, associated to acceptor impurities like Mg, Zn or Cd, with 2 or 3 phonon replicas towards lower energies [24,31]. The donors involved in the recombination have been pointed out as oxygen and silicon, as in the case of the DXs [14].

Concerning the deep defect recombination, a special attention should be paid to broad emission bands that are well-known to occur in GaN samples due to different defect natures [14,32–38]. Early works claimed the involvement of the broad yellow luminescence (YL), that is typically observed in GaN samples, with Si_{Ga}, while others debated the possible involvement of carbon on nitrogen site, C_N [36,39,40]. It is well established nowadays that undoped and doped

GaN layers typically exhibit the broad YL described by DAP (involving a shallow donor) or e-A transitions [14,36–38,41–43]. Currently, it is commonly believed that the YL is associated with the presence of native defects, namely V_{Ga} and their $V_{Ga}O_N$ complexes in the 2-/- charge states [14,36–39,41–43]. First principles calculations, positron annihilation, doping experiments and detailed analysis of the emission spectra strongly suggest that both the YL band and the 1.23 eV emission line in GaN samples are related to a common deep centre, probably the $(V_{Ga}O_N)^{2-/-}$ [39]. On the other hand, besides the YL, annealed GaN layers and Ga-face terminated bulk samples frequently exhibit a broad green luminescence (GL) that can be ascribed to the -/0 states of the same defect [42,43]. In the same spectral region, different types of defects can be found, for instance Reshchikov and co-workers [34] reported a study where they propose that a GL band peaked at 2.35 eV (~ 528 nm), denominated GL2, was associated with the presence of V_N. The same author also reported the involvement of the C_N defects in the broad band luminescence observed in high-purity GaN samples grown by the HVPE technique [44]. The work described in [44] claims that the GL band with a maximum at 2.4 eV that is observed in this type of samples is attributed to transitions of electrons from the CB to the 0/+ level of the C_N defect. In the case of the *n*-type GaN grown by HVPE, the YL band with a maximum at 2.1 eV is caused by a recombination of free electrons with holes at the −/0 level of C_N at low excitation intensities, and it is replaced by the GL band at high excitation intensity, in a similar way with what was reported earlier by the same author considering the $V_{Ga}O_N$ complex [42]. Carbon impurities forming complexes with oxygen (C_NO_N) may also be accounted for a YL band at 2.2 eV [44].

Another common centre in this material corresponds to the blue luminescence (BL), usually peaked at ~ 2.9 eV and varying from 2.7 eV to 3.0 eV. A lot of research has been devoted to the study of this BL, in part due to the controversial assignment of its origin. It is important to bear in mind the distinct origin of this band and the one related with Mg-doping, exhibiting very distinctive features. The BL is attributed to transitions from the shallow donors to a relatively deep acceptor, with an ionization energy around 0.34 - 0.40 eV [14]. Finally, the red luminescence (RL) band, emitting in the 1.5 - 2.0 eV range is the less studied and less common of the bands observed in GaN. Thus, the nature of the optical centres involved in this luminescence remains unclear [14].

4.2.3.2. ZnO

The optical properties of ZnO have been widely studied by different techniques like absorption, transmission, reflection, PL, CL, among others [25,45–47]. The interest in its remarkable emission, either in the near band edge (NBE) or in the visible spectral regions, has motivated a great number of PL investigations. Numerous reports showed that, in high quality bulk crystals, the luminescence linewidth of excitonic recombination is as narrow as 40 μeV. Moreover, many fine spectroscopic details have been distinguished in this semiconductor [46]. The sharp lines that dominate the NBE spectral region are attributed to various DXs recombination. The DXs recombination transitions are usually followed by LO phonon replicas with an energy separation of ~ 72 meV [48]. The related FXs emission is originated from the transitions between the CB and the three VBs, A, B and C, as discussed previously [47]. At low temperatures, the DXs related transitions dominate the radiative channels, while for higher

temperatures the FX emission becomes dominant [46]. For bulk ZnO, an emission line located at ~ 3.377 eV (higher energy than the DXs) is usually associated with FX transitions from the A-VB (FX_A) [25,48]. The emission at 3.367 eV is normally attributed to ionised donor bound excitons (D^+X), whereas the neutral DX (D^0X) emission is observed between 3.3628 eV and 3.359 eV [46]. In the energy range from 3.34 - 3.31 eV, another feature appears, which is typically attributed to TES transitions. Between 3.4 eV and 3.1 eV, the phonon-assisted transitions of the DXs can be observed. It is also in this spectral range that the DAPs are expected (that can also be followed by phonon replicas) [25,49]. These DAP transitions usually appear at ~ 3.22 eV. However, due to the superposition with the LO replicas of the D^0X transitions, these emissions are sometimes difficult to distinguish [25]. Moreover, a prominent transition at 3.333 eV is frequently observed. This line is commonly labelled Y-transition and was tentatively assigned to excitonic recombination related with structural defects [49]. Figure 4-5 shows a scheme with the energy ranges for the mentioned optical transitions. The scheme shows that $E(D^+X) > E(D^0X) > E(A^0X)$ [25]. Although several (up to eleven) excitonic recombinations due to bound excitons have been identified, the chemical nature of the donor and/or acceptor species is still not completely clear [46]. Nevertheless, excitons bound to elements like H, Al, In and Ga were already reported in the literature. A complete review of the optical properties of exciton related transitions and DAP recombination can be found in the work of B. K. Meyer *et al*. [46].

Another common emission that has been extensively studied in bulk [50], thin films [51] and nanostructures [52], is the 3.31 eV emission line. This line has been associated to distinct recombination mechanisms. Among them, the most accepted hypotheses for the nature of the centres involved are the surface excitonic contribution [52,53] or structural defects-related transitions [51,54–56].

Regarding the visible spectral region, and similarly with what was observed for GaN, an important feature in the PL spectra of ZnO is the presence of broad bands. The most common is the well-known green luminescence [25], although other emission bands in the blue, yellow and orange/red spectral region have also been reported [57–59]. However, there is still some controversy regarding the nature of different defect emissions and different hypotheses have been proposed to explain them. It is known that different types of defects are responsible for the emissions in the different spectral ranges, but the association between these defects and the observed luminescence have not been yet conclusively established [57]. The defect-related luminescence in the green region is frequently ascribed to intrinsic defects in the ZnO matrix, namely oxygen/zinc vacancies (V_O/V_{Zn}), Zn antisites (Zn_O), interstitial Zn atoms, transitions from Zn interstitials to Zn vacancies and also extrinsic impurities, as is the case of Cu [60,61]. On the other hand, some reports presented convincing evidence that defects located at the surface may give rise to luminescence bands also in this spectral region [57]. The GL often exhibits different spectral shapes depending on the type of samples and their growth methods. In some cases, a structured GL is observed and this is the one attributed to Cu related-defects. This band is known since the 60's and was extensively studied by Dingle [61]. Nonetheless, a structureless band reported at nearly the same position as the structured one is often associated with other defects, namely V_O or V_{Zn} [47]. Thus, in spite having similar peak positions and width, the origin of the observed GL may be rather different from sample to sample [25,47].

The YL and RL have been less discussed. Nonetheless, it was proposed that these emissions arise from similar deep levels but with different initial states, for instance, between CB or shallow donors and deep acceptors [57,59]. The YL was attributed to and Li acceptor, as well as oxygen interstitial (O_i) defects [25,57]. The latter was also pointed out as the defect responsible for the RL since this emission in commonly associated with the presence of excess oxygen. Other hypotheses include surface dislocations or Zn_i [57].

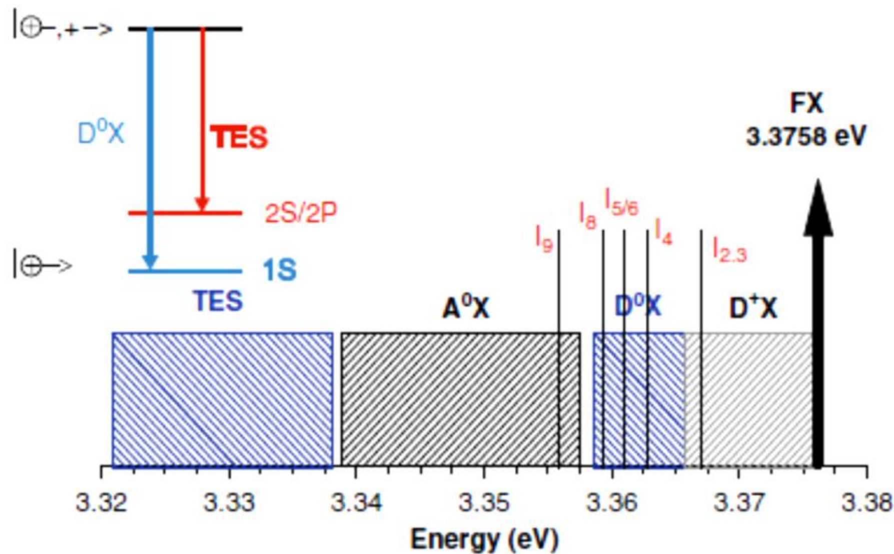

Figure 4-5 – Schematic representation of the energy ranges where the various ZnO NBE transitions are usually observed. The level scheme for TES transitions of the D^0X with the neutral donor in the 1s ground and 2s/2p excited states is also depicted. Image reproduced from reference [49].

4.2.4. Luminescent activators: RE^{3+}

In Chapter 1 the importance of the RE ions' incorporation into nitride hosts was highlighted. In this section a brief description of the RE properties will be given.

Rare earth elements, including both lanthanide and actinide groups, are characterized by the progressive filling of the 4*f* and 5*f*-shells of their electronic configuration [62]. Even though both of these groups are designated by rare-earths, in this work by REs only the lanthanide group is intended. The neutral REs show a core electronic structure common to the one of Xenon (Xe) atoms, [Xe]→ $1s^2 2s^2 2p^6 3s^2 3p^6 3d^{10} 4s^2 4p^6 4d^{10} 5s^2 5p^6$, with two or three outer electrons ($6s^2$ or $5d^1 6s^2$) [62]. When incorporated into compounds, the RE ions are frequently found in their divalent or trivalent charge states, being this last one the most important for the lighting applications. These charge states are achieved by the successive removal of electrons. The first two steps comprise the consecutive removal of the 6s-electrons (Lutetium is an exception), whereas in the last step all the electrons from the 6s and 5d shells are removed, leaving a $4f^n$ configuration. Consequently, the electronic configuration of the ground state of RE^{3+} ions is [Xe]$4f^n$, with $1 \leq n \leq 14$ from Cerium (Ce-$4f^1$) to Lutetium (Lu-$4f^{14}$) [62,63].

These ions exhibit especial luminescent properties owning to their partial filled inner shell (4*f*) that is shielded from the surrounding ambient by the filled outer orbitals (5*s* and 5*p*) [64]. Since

the *f*-eigenfunctions cannot penetrate appreciably into the ion environment, any strong interactions between the 4*f*-electrons and its surroundings is prevented [62]. As a result, the influence of the lattice host in the 4*f* core shell states is very small, although being extremely important [65]. The energy levels of these ions are almost insensitive to the environment in which they are placed, and the positions of their electronic levels are influenced much more by spin–orbit interactions than by the applied crystal field [66]. Therefore, the spectral position of the RE^{3+} emission lines is determined almost entirely by the energy of the transitions between the 4*f* states [67]. Nevertheless, the host plays a crucial role on the radiative transition probability, which is reflected in the intensity of the intraionic luminescence [67]. In theory, the intra-4*f* transitions of these ions are parity forbidden by the Laporte's selection rule, which states that for a free ion, transitions between states with the same parity are forbidden. However, if the ion is placed in the crystal field of the host, this selection rule relaxes due to the admixture of the wavefunctions, resulting in an increase of the transition probability. The crystal field acts strongly in the spectral fine structure of these ions, lifting the degeneracy of the ground and excited states [68]. REs ions incorporated into a partially ionic solid usually favour substitutional occupation of the cation site, which must provide an uneven ligand crystal field in order to cause the relaxation of the selection rule. Since the transitions remain not completely allowed, the emission of the RE^{3+} is generally characterized by long lifetimes (µs - ms) [67].

4.2.4.1. Electronic States and Coupling Scheme

The nonrelativistic Hamiltonian (in c.g.s. units) of a free ion with *n* electrons and a nuclear charge *Ze* can be defined, assuming the nuclear mass to be infinite and, therefore, the nucleus as being fixed (Born–Oppenheimer approximation), as [62,63,69]:

$$H_F = H_0 + H_c + H_{so} = \left[-\frac{\hbar^2}{2m}\sum_{i=1}^{n}\nabla_i^2 - \sum_{i=1}^{n}\frac{Ze^2}{r_i}\right] + \sum_{i<j}^{n}\frac{e^2}{r_{ij}} + \sum_{i}^{n}\varepsilon(r_i)\boldsymbol{l}_i\cdot\boldsymbol{S}_i. \quad \textbf{Eq. 4-41}$$

Here, the first term on the right side corresponds to the sum of the kinetic energy of all electrons, the second term represents the potential energy of all electrons in the field of the nucleus, the third is the repulsive Coulomb potential energy of the interaction between pairs of electrons, and the last term describes the spin-orbit interactions, which can be understood as magnetic dipole-dipole interactions between the spin and angular moment of the electrons. r_i and r_{ij}, refers to the distances from each electron to the nucleus and between the *i* and *j* electrons, respectively. The spin-orbit coupling constant, $\varepsilon(r_i)$, is defined as a function of r_i. $\boldsymbol{l}_i$ and $\boldsymbol{S}_i$ are the angular and spin operators [62,69]. A conventional approach to solve the Schrödinger equation for an atom with *n*-electron is to use the central field approximation [69]. In this approximation, the movement of each electron is assumed to be independent of the field of the nucleus and the central field that is created by spherically averaged potential fields of each of the other electrons. The quantum mechanical solution for this case is the same as the one for a hydrogen atom with a single electron. Each electron is assumed to move in a spherically symmetry potential, $U(r_i)/e$. This one-electron operator is a good approximation to the real potential energy of an electron *i* in the field of the nucleus and the others *n-1* electrons [62,69]. The non-spherical part of the electronic

interactions is then treated as a perturbation to this spherically potential [69]. Thus, (in c.g.s. units) the central field Hamiltonian, H_{CF}, can be written as [62,69]:

$$H_{CF} = \sum_{i=1}^{n} \left[-\frac{\hbar^2}{2m} \nabla_i^2 + U(r_i) \right], \qquad \textbf{Eq. 4-42}$$

where

$$U(r_i) = -\sum_{i=1}^{n} \frac{Ze^2}{r_i} + \langle \sum_{i<j}^{n} \frac{e^2}{r_{ij}} \rangle. \qquad \textbf{Eq. 4-43}$$

The second term of the right side of Eq. 4-43 describes the average of the electron repulsion over the sphere, which is independent of the angular coordinates. Taking into account that most of the inter-electron repulsion is already included in the H_{CF}, H_c becomes [69]:

$$H'_c = \sum_{i<j}^{n} \frac{e^2}{r_{ij}} + \langle \sum_{i<j}^{n} \frac{e^2}{r_{ij}} \rangle, \qquad \textbf{Eq. 4-44}$$

which has a little effect on the RE^{3+} ion and can be treated as a perturbation along the spin-orbit coupling.

The eigenfunctions of H_{CF} for a *n*-electron ion are obtained by a linear combination of one-electron wavefunctions that satisfy the Pauli's exclusion principle[1] and that are subject to the orthonormality condition [69]. In this framework, the wavefunction of each electron is described as a product of radial and angular functions of the spherical harmonics multiplied by a spin function [62,63,69]

$$\Psi_{nlm_lm_s}(\boldsymbol{r}, m_s) = r^{-1} R_{nl}(r) Y_{lm_l}(\theta, \varphi) \sigma(m_s), \qquad \textbf{Eq. 4-45}$$

where the radial function $R_{nl}(r)$ is dependent of the central field potential, which is responsible for the radial charge distribution functions. The spherical harmonic function $Y_{lm_l}(\theta, \varphi)$ is characterized by the four quantum numbers *n*, *l*, m_l and m_s, which define an unique state of an electron in an atom [69]. *n is* the principal quantum number and is an integer (1, 2, 3, and so on) that represents the radial expansion of the orbital. The angular quantum number *l* varies from 0 to *n*-1 and characterizes the shape of the orbital. m_l is the magnetic quantum number and accounts for the projection of the vector ***l*** onto the *z* axis, and is related to the orientation of the orbital in space ($m_l = -l, -l+1, \ldots, l$). Finally, m_s corresponds to the projection of the vector ***s***, and can assume values of ±1/2, according to Pauli's principle.

An electronic shell consists in all electrons having the same quantum number *n*. A sub-shell regroups electrons with same *n* and *l* numbers, having (2*l*+1) orbitals, that may contain a maximum of (4*l*+2) electrons [63]. In the case of a 4*f* configuration, *n* = 4 and *l* = 3. Each of the *n* electrons of the $4f^n$ configuration is associated with one of the seven 4*f* wavefunctions. There are a number of ways of associating the *n* electrons with the 4*f* orbitals, taking the spin into

[1] Pauli's principle states that two electrons of the same atom can only be in the same orbital if they possess opposite spin, since the electrons have to differ in at least one of the quantum numbers.

consideration. This number corresponds to the multiplicity, or degeneracy, of the configuration and is given by the following combinatorial expression [63]:

$$\frac{(4l+2)!}{n!\,(4l+2-n)!} = \frac{14!}{n!\,(14-n)!}, \quad (l=3). \qquad \textbf{Eq. 4-46}$$

In order to obtain the wavefunctions of a system with *n*-independent electrons through the central field approximation, it is necessary to define a set of basis states in a well-defined coupling scheme of momentum [62,69]. There are two coupling schemes that are frequently used in atomic spectroscopy: the Russell-Saunders or LS coupling and the j-j coupling. The former is essentially used for lighter atoms when the spin-orbit interactions are smaller than the electrostatic interactions between electrons. In this coupling scheme L and S are considered good quantum numbers. L and S are the total angular orbital and total spin momentum operators [69], respectively, and are defined as:

$$\boldsymbol{L} = \sum_{i=1}^{n} \boldsymbol{l}_i \qquad \textbf{Eq. 4-47}$$

and

$$\boldsymbol{S} = \sum_{i=1}^{n} \boldsymbol{s}_i. \qquad \textbf{Eq. 4-48}$$

In the LS coupling case, the total angular momentum operator is given by

$$\boldsymbol{J} = \boldsymbol{L} + \boldsymbol{S}, \qquad \textbf{Eq. 4-49}$$

and has $2J+1$ eigenstates, with J = L+S, L+S-1,…,|L-S|, represented by the magnetic quantum number $M = -J, -J+1, \ldots, J$ [69,70].

For atoms with a high atomic weight, the electrostatic interactions decrease and the spin-orbit interactions become dominant. So, in heavy atoms, the spin-orbit interactions are much stronger than the Coulomb interactions and the second type of coupling should be considered. For the REs, the two interactions (Coulomb and spin-orbit) have the same order of magnitude. Therefore, none of the previous coupling schemes are appropriate. Calculations for energy levels of these ions are mathematically more complicated and are performed in a scheme called intermediate coupling, that can be developed from the LS scheme, followed by a simultaneous diagonalization of the perturbation Hamiltonians H'_c and H_{so} [62,69]. However, for the sake of simplicity, the LS treatment will be considered to describe electronic states of a RE ion. In such a simplified scenario, the electronic states of the RE ions can be represented by the angular and spin momentum quantum numbers (*L* and *S*), using the notation $^{2S+1}L_J$. $^{2S+1}L_J$ is called the spectroscopic term [63]. Here, *2S+1* accounts for the spin multiplicity (i.e., the number of possible orientations of the total spin of the ion, *S*) and *J* is the total angular momentum, determined by the LS coupling. Each $^{2S+1}L_J$ term corresponds to a degenerate group or a multiplet with $2J+1$ states that, when the ions are incorporated into a crystalline matrix, are split into Stark levels by the action of the local crystal-field. The number of splittings depends on the local field symmetry, with a maximum number of $2J+1$ for *J* integer and *J+1/2* for *J* half-integer (see sub-section 4.2.4.2). *L* is usually represented by a capital letter (S, P, D, F, G...) corresponding to the values of *L* (0, 1, 2, 3, 4...) [63,70]. The Hund's rules can be applied to find the ground state term. First rule states that

the term with the largest spin multiplicity (*2S+1*) has the lowest energy, while rule number two states that, for the same *S* value, the term with lowest energy is the one with largest orbital multiplicity (*L*). Finally, the third rule defines that when the shell in less than half filled the term with lowest energy is the one with lowest *J*, while for a more than a half filled shell, the lowest energy term has the highest *J* [63]. It is important to note that these are empirical "rules" that are used mostly to determine the ground state term of multi-electron atoms. Figure 4-6 shows a diagram of the energy levels of the $4f^n$ configuration for all the RE^{3+} ions, from Ce (n = 1) to Ytterbium (Yb, n = 13).

Even though the description based on the LS coupling accounts for the major features of REs, it is very important to take into account that when spin-orbit, spin-spin and similar interactions are included, *L* and *S* are no longer considered good quantum numbers, since states of different *L* and *S* will be mixed. *J* and *M* remain good quantum numbers since $\boldsymbol{J}^2$ and $\boldsymbol{M}$ commute with the spin-orbit Hamiltonian H_{so} [62,69]:

$$[H_{SO}, \boldsymbol{L}] \neq 0,\ [H_{SO}, \boldsymbol{S}] \neq 0 \text{ and } \left[H_{SO}, \boldsymbol{J}^2\right] = 0. \quad \textbf{Eq. 4-50}$$

A detailed discussion about the coupling schemes for RE ions can be found in reference [62] by Wybourne.

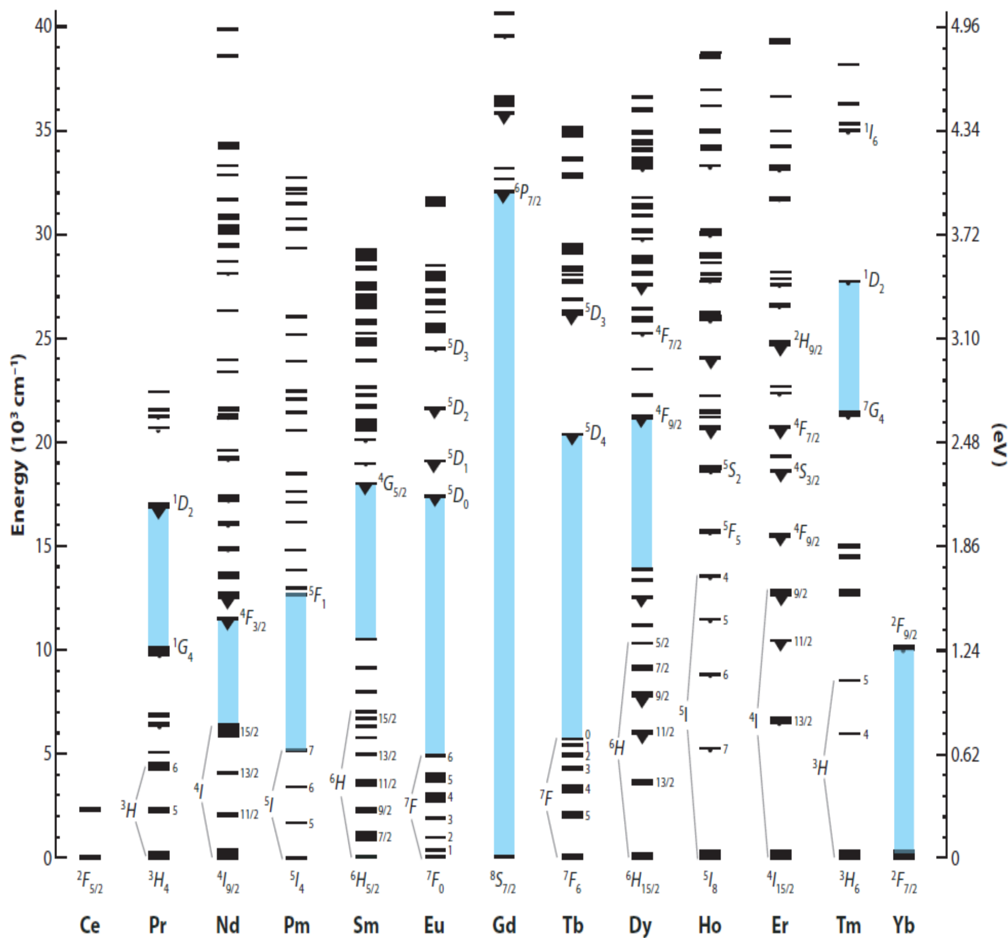

Figure 4-6 – Dieke energy diagram for the $4f^n$ configuration of RE^{3+} ions. The width of the bars represent the order of magnitude of the crystal field splitting and the blue shading between levels marks the largest energy gap. Image reproduced from [71].

4.2.4.2. Crystal-field interaction and selection rules

When the RE ions are incorporated in a crystal, the interaction with charged particles or dipoles will create a perturbing field that will destroy the spherical symmetry of its electronic structure, which will split the degenerate *J*-levels under the influence of the electric field produced by the crystalline environment [63,69,72]. The degeneracy lifting of the ion levels by the action of the crystal-field is called Stark effect. The *2J+1* degeneracy of the ion spectroscopic levels is partly lifted, depending on the exact symmetry of the ion site [63]. Table 4-1 shows the number of Stark splittings for each *J* value depending on the site symmetry where the ion is placed. The number of splittings increases with the decreasing of the local symmetry in the ion surroundings. Lowering the symmetry implies a decreasing on the number of equivalent direction and the charge distribution around the ion becomes further away from the spherical one of the free ion [73].

Table 4-1 – Number of Stark levels versus the value of quantum number *J* depending on the site symmetry [63].

Symmetry	Site symmetry	***J* integer**								
		0	1	2	3	4	5	6	7	8
Cubic	T, T_d, T_h, O, O_h	1	1	2	3	4	4	6	6	7
Hexagonal Trigonal	C_{3h}, D_{3h}, C_6, C_{6h}, C_{6v}, D_6, D_{6h} C_3, S_6, C_{3v}, D_3, D_{3d}	1	2	3	5	6	7	9	10	11
Tetragonal	C_4, S_4, C_{4h}, C_{4v}, D_4, D_{2d}, D_{4h}	1	2	4	5	7	8	10	11	13
Low	C_1, C_S, C_2, C_{2h}, C_{2v}, D_2, D_{2h}	1	3	5	7	9	11	13	15	17

Symmetry	Site symmetry	***J* half-integer**								
		1/2	3/2	5/2	7/2	9/2	11/2	13/2	15/2	17/2
Cubic	T, T_d, T_h, O, O_h	1	1	2	3	3	4	5	6	6
All others[2]	See above	1	2	3	4	5	6	7	8	9

Whereas in the case of the transition metal ions (d^n) the strength of the crystal-field is in the order of 10 000 cm^{-1}, for RE ions ($4f^n$) it is much smaller, up to few hundreds of cm^{-1} [65]. This means, as stated above, that the crystal-field action on these ions is small and can be treated as a perturbation [63,69]. Since this effect is much smaller than the spin-orbit effect, when one is dealing with the crystal field effects by perturbation theory, it is important to apply the spin-orbit interaction first [2]. Therefore the Hamiltonian that describes the local field of the ion in a crystal host, H_{LF}, is given by [62,63,69,72]:

$$H_{LF} = H_F + V_C, \quad \textbf{Eq. 4-51}$$

[2] All Stark sublevels are doubly degenerate [63].

where, H_F is the Hamiltonian from Eq. 4-41 and V_c is the crystal potential acting on the ion. This potential can be generally expressed as a power series in spherical harmonics and is written as follows:

$$V_c = \sum_{k,q,i} B_q^k C_q^{(k)}(i), \quad \text{Eq. 4-52}$$

where the summation involving i is of all the 4f electrons, B_q^k correspond to crystal-field parameters and $C_q^{(k)}$ are the components of tensor operators $\boldsymbol{C}^{(k)}$ which transform like the spherical harmonics used for the analytical form of the 4f wavefunctions:

$$\boldsymbol{C}^{(k)} = \sqrt{\frac{4\pi}{2k+1}}\, \boldsymbol{Y}^{(k)}. \quad \text{Eq. 4-53}$$

k and q are running numbers. k should be a number even and smaller than 2l and the q values must be $|q| \leq k$. These numbers are limited by the point group symmetry into which the RE ion is inserted [63,69]. The further evaluation of the matrix elements is frequently made by the tensor operator methods proposed by Racah [62,74]. Since the $C_q^{(k)}$ operators do not involve spin, only the orbital part of $\boldsymbol{J}$ is considered. Attending to the commutation relations between $C_q^{(k)}$ and J_z and $J_{\mp}$ components of the $\boldsymbol{J}$ tensor operator, the matrix element of $C_q^{(k)}$ between two states can be written using the Wigner-Eckart theorem [62,75]. The non-vanishing matrix elements of $\boldsymbol{C}^{(k)}$ correspond to the c^k parameters of Condon and Shortley [76]. Racah expressed these matrix elements using the Legendre polynomials, which limit the number of nonzero c^k integrals due to the orthogonality properties of the Legendre polynomials [74,75]. This formalism can be consulted in detail in the references [62,74]. Nevertheless, it is important to mention that Racah introduced new parameters, E^k (k = 0, 1, 2, 3,...), for the f^n configurations that became commonly used to express the term energies of the RE ions. The matrix elements are normally written as a linear combination of Slater radial integrals, F^k (k even) [62,74,75].

A simpler way to compare the crystal-field strengths in different compounds was proposed by Auzel [77] as an "average" total crystal-field effect [63,69]:

$$N_v = \left[\frac{1}{4\pi} \sum_{k,q,} \frac{\left(B_q^k\right)^2}{(2k+1)}\right]^{1/2}. \quad \text{Eq. 4-54}$$

Although the crystal-field interaction makes only a minor contribution to the energy of the RE system, its effect on the dynamical processes is profound. The crystal-field is accountable for the radiative transitions between 4f states, and also influences the nonradiative processes that allow for energy to be exchanged between the ion and the host [16].

The interactions with the crystal-field lead to the introduction of selection rules for the ion transitions. According to the Laporte's rule, electric dipole transitions between the 4f levels are forbidden since the parity of the states is the same [63,78]. However, the parity prohibition can be lifted by the influence of the crystalline lattice. Noncentrosymmetric interactions allow the mixing of electronic states of opposite parity into the 4f wavefunctions, relaxing the selection rules and making the transition partially allowed. Such a transition is called induced or forced

electric dipole transition [63]. When the ion is placed in a site that is a centre of symmetry in the crystal lattice, the parity prohibition cannot be lifted. However, even a small deviation from the inversion symmetry causes the transitions to appear, sometimes dominantly, in the emission spectra [79].

Magnetic dipole transitions are possible even in a perfect centrosymmetric site, since the magnetic dipole operator possesses even transformation properties under an inversion [78,79]. These transitions can be understood as a rotational displacement of charge having even parity [79]. The intensity of this type of transitions is generally weak, even though they often show intensities comparable to the induced electric dipole transitions in a 4*f*-4*f* emission spectrum [63]. Typically, the intensity of the magnetic dipole assisted transitions is nearly insensitive to the ion environment, whereas the intensity of the transitions induced by electric-dipole is quite sensitive [80], being frequently designated by hypersensitive. Hypersensitive transitions often exhibit $\Delta J \leq 2$ [72].

Another type of transitions is the one allowed by electric quadrupole. In this case, transitions between states with the same parity are also allowed. These transitions are much weaker than the ones allowed by magnetic dipole, and so they are rarely observed, even though they can also be considered hypersensitive [63].

For an electric dipole induced transition, the selection rules state that $|\Delta L| \leq 2l$ and $|\Delta J| \leq 2l$. Moreover, the transition $J = 0 \rightarrow J' = 0$, is forbidden; $J = 0 \rightarrow J'$ odd are weak and $J = 0 \rightarrow J'$ even should be strong [79]. In the case of a magnetic dipole allowed transition, the selection rules are given by $\Delta L = 0$ and $\Delta J = 0, \pm 1$, except for $J = 0 \rightarrow J = 0$, which is forbidden [78,79]. Finally for the electric quadrupole transitions, excluding the parity, the remaining selection rules are similar to the ones described for the electric dipole [79].

For the mentioned transitions (electric dipole, magnetic dipole and electric quadrupole) it was shown that $\Delta S = 0$ in all the cases [63]. The spin-orbit coupling can lift the spin selection rule, by the admixture of different spin states [78,79].

The selection rules are nor restrict rules, thus terms like “forbidden” and “allowed” transitions are not accurate, meaning that a forbidden transition is a transition with a low probability and an allowed transition has a high probability to occur [63].

4.2.4.3. Judd-Ofelt theory and transition probabilities

The intensity of the spectral transitions also reflect the interaction between the REs ions and their environment [79]. Judd-Ofelt theory [81,82] has been constructed within the frame of the crystal-field concept and gives a simple model to predict the intensities of the *f-f* transitions [63]. An expression for the oscillator strength between two states of the $4f^n$ configuration was found [82]. The expression obtained for pure-electronic electric dipole transition probability involves matrix elements of an even-order unit tensor between two $4f^n$ states [81]. In this theory the inter-configurational $4f^n$–$4f^{n-1}5d^1$ interactions are neglected [63]. Induced electric dipole transitions between the *J* manifolds can be described as [63,83]:

$$S(aJ,bJ') = e^2 \sum_{t=2,4,6} \Omega_t \left| \langle \Psi \left\| \boldsymbol{U}^{(t)} \right\| \Psi' \rangle \right|^2, \quad \text{Eq. 4-55}$$

where Ψ and Ψ' are the initial and final state wavefunctions, $\boldsymbol{U}^{(t)}$ corresponds to the irreducible tensor form of the operator connecting the $4f$ states and Ω_t is a phenomenological intensity parameter, also known as Judd-Ofelt parameter. The Ω_t parameters are characteristic for a given ion-host and with a sufficiently large set of identified transitions between different multiplets, the Judd-Ofelt and spin-orbit parameters, as well as the surrounding crystal-field can be determined [68,83]. The validity of the Judd-Ofelt treatment was tested for most of the trivalent REs in both crystals and solutions [83]. One of the most important features of the Judd-Ofelt approach is that once all the intensity parameters are determined (for a given ion and host), these parameters can be used to calculate the probability of transitions between any $4f^n$ levels of that RE ion [83]. Although, it is important to bear in mind that calculations of transition probabilities using this theory are usually made under the assumption that all Stark sublevels within the ground level are equally populated and that the material under investigation is optically isotropic, which, of course, it is not always the case [63].

4.2.4.4. Excitation mechanisms in RE^{3+} doped semiconductors

Different excitation mechanisms have been proposed for the RE ions incorporated in semiconductor matrixes. The excitation mechanism can be divided essentially into two types: direct and indirect. In the first case, the excitation is resonant with the high energetic levels of the RE inner $4f$ shell, while the indirect mechanisms are non-resonant and occur by nonradiative energy or charge transfer from the host [84,85]. The recombination of e-h pairs in the host leads to a release of energy that can be transferred nonradiatively to the RE ion, with its subsequent excitation. Furthermore, the RE ions may capture an electron, changing its charge state from trivalent to divalent (3+ → 2+), followed by a capture of a hole. In this case, the determination of the position of the $4f$ levels, regarding the CB and VB of the host, is of paramount importance [84–89].

Mainly two theoretical models to describe the optical activity of RE in the III-nitride compounds are discussed in the literature [85]: one supported by Lozykowski and co-workers [79,85,87] were the REs are treated as isoelectronic impurities and energy transfer mechanisms take place in the RE excitation, and other extensively developed by Dorenbos [86,88–91], to determine and predict the $4f$-level location regarding the CB and VB of the semiconductor host. In the latter the behaviour of the RE ions is explained by the change in the ions' valence charge [85]. These two models are discussed below.

4.2.4.4.1. Isovalent trap model

RBS measurements shown that in nitrides most of the RE^{3+} ions tend to occupy the cation substitutional sites with trigonal C_{3V} symmetry [67,85,92–94]. The outer electron configuration of these ions ($5s^2\ 5p^6$) shows a similar electron configuration as for Ga^{3+} and Al^{3+} cations. In this case, the RE ions are isovalent (or isoelectronic) regarding the ions that they replace. Thus, it is

commonly accepted that RE create isovalent (REI) traps in III-V semiconductors [85,87,95,96]. An isovalent centre can form bound states due to a short-range potential. According to the theory of isoelectronic traps from Balderachi [97], the impurity potential is caused by the combining effects of the difference in the atomic pseudopotentials, electronegativity, spin-orbit contributions and the relaxation of the host lattice around the impurity, which generally exhibits a different size. The ionic radii of the trivalent REs are bigger than the ones of the cations in the III-nitrides hosts, leading to an expansion of the lattice in its surroundings. The displacement of the adjacent host atoms contributes to the increase of the isovalent potential strength for carrier trap [85]. Only very small or very large atoms produce isovalent traps precisely because of the large distortions that are introduced in the lattice by the substituting ions [87]. Balderachi [97] stated that hole traps are expected when larger atoms are introduced in the host. Furthermore, for a given isoelectronic sequence, the electronegativity decreases for heavier atoms, which means that Pauling's electronegativity is smaller in the REs than in the cations that they substitute [85,87,97]. Thus, if a heavier atom replaces a lighter atom, as it is the present case, the potential created by this impurity will attract holes (the opposite is valid for electrons) [85]. Therefore, it is fair to assume that the RE creates a hole trap (above the VB edge), as represented in Figure 4-7.

The formation of bound excitons and their subsequent recombination with energy transfer to the RE ions is one of the most discussed excitation mechanism for RE-doped III-nitrides. The bound exciton formation is comprised by two steps: first a hole becomes bound in a strongly localized state by the short-range potential of the REI trap, leaving the trap positively charged; the second step involves the capture of an electron by Coulomb interaction, creating a bound exciton [85,87]. The positioning of the 4*f* levels below the VB in semiconductors, as defended by Lozykowski [85] and other authors [98], was suggested based on photoemission studies in different hosts [99–101]. Even though these considerations were made assuming a hole trap, similar phenomena are valid for electron traps.

The REI traps are different from the "simple" impurity isoelectronic traps since, while the latter introduce effective-mass-like states inside the bandgap of the matrix, the first possess unfilled $4f^n$ core shells and the luminescence arises from the intraionic 4*f* - 4*f* transitions in the core of the RE ion [85,95]. The creation of the bound exciton by photon excitation gives rise to excitation bands responsible for the excitation of the $4f^n$ core electrons of the REI trap. The excitation bands become broadened due to electron-phonon coupling [85]. The energy of recombining excitons will be the energy responsible for the excitation of the $4f^n$ core electrons (Figure 4-7). The probability for this energy transfer is high due to the close proximity of the interacting systems, since the exciton is bounded to the RE ion [85]. One of the main characteristics of the excitons bound to REI traps is the long luminescence decay time (higher than hundreds of nanoseconds) [85,87,95]. The REI are not necessary "pure" substitutional centres [87], besides the substitutional sites, the RE ions in III-nitrides frequently occupy displaced sites and can create more complex centres involving other impurities or native defects [84,95]. Moreover, the RE^{3+} ions can form pairs and higher clusters, either with the other RE ions or other impurities present in the crystal, resulting in a possible energy-relaxation processes between these centres, namely cross-relaxation phenomena [85].

Figure 4-7 schematizes possible mechanism of energy transfer involving a REI trap. These mechanisms include [79,85,87,95]: (i) energy transfer from excitons bound to the REI centres to the RE ion core electrons; (ii) energy transfer from the recombination of a hole in the REI centre and free electrons in the CB or from a remote donor; and (iii) energy transfer in which the energy of a FX (or other weakly localized host states) near the REI trap is transferred to the localized 4*f*-core excited states. A detailed description of the kinetic models of the RE excitation considering the formation of REI traps can be found in reference [87].

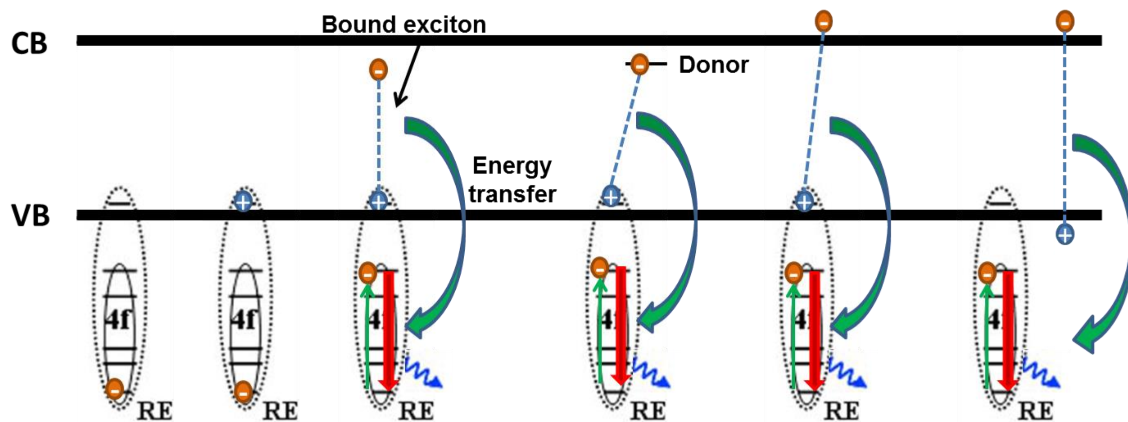

Figure 4-7 – Schematic energy-level diagram for an isovalent trap formed by the RE^{3+} ion, together with the representation of the excitation via energy transfer from the recombination of a bound exciton, an electron in a remote donor or in the CB with a hole trapped in the RE impurity or a FX. Adapted from [85]. The straight red arrow represents the photon emission while the blue curved arrow represents nonradiative processes that may also take place.

The main parameters to take into account in nonradiative energy transfer processes are the spatial proximity between the donor energy state (generally denominated by sensitizer) and the energy acceptor state (called activator) and the spectral overlap between the sensitizer emission spectrum and the activator absorption spectrum [84]. In each case, if the transferred energy does not match the difference between the initial and the final states, the remaining energy is distributed, for instance, by phonon emission or absorption. The energy transfer is more efficient if the phonon coupling to the lattice phonons is higher. However, for an efficient radiative recombination, the phonon coupling must not be very strong, otherwise core de-excitation by nonradiative multiphonon emission can take place [87,95]. The Huang-Rhys factor, S_0, gives an indication on the strength of the electron-lattice coupling. In the case of the RE ions, where the valence charge density shields the electrons in the 4*f*-shell from the charges of the neighbouring atoms rather than from the charge of the central nucleus, typically S_0 values around 0.01 are shown, which means that the zero-phonon lines (defined as the energy transition between the lower vibrational levels of the initial and final electronic states) correspond to 99% of the intensity of the optical spectral, and only 1% accounts for the single-phonon sidebands. That is why RE spectra are characterized by very sharp emission lines. For instance, the aforementioned broad emission bands as well as intraionic transitions with transition metal ions (d^n configuration) can have a S_0 value close to 10 [102].

4.2.4.4.2. Dorenbos' model (charge transfer)

Up to now, only energy transfer processes have been discussed, however, excitation mechanisms involving a change on the RE ion charge have also been proposed [84]. The location of the RE energy levels relative to the CB and VB in inorganic compounds is extremely important in this case, since the levels' positioning will determine the ability of the RE ions to trap an electron from the CB or a hole from the VB. The levels' position is also crucial to understand luminescence, charge trapping and charge donating phenomena [89,90]. Therefore, it is important to take into account the fact that the 4*f*-shell of a trivalent RE ion may donate or accept electrons to or from the energy bands of the III-nitrides, undergoing a valence change $RE^{3+} \rightarrow RE^{4+}$ or $RE^{3+} \rightarrow RE^{2+}$, as it is known to happen in the case of oxides or fluoride compounds [86]. The position of the RE ions ground state regarding the VB of the host can be obtained by photoemission spectroscopy [84,103].

Detailed information about the Dorenbos' model can be found in references [89,91,104–106]. Here, only a simple description will be given. The construction of this phenomenological model is based on the data collected from the 5*d*-4*f* transitions of all the RE ions, in both divalent and trivalent states, for a great number of compounds (which include nitrides). A systematic behaviour for the energy positioning of the RE was observed [91]. It was found that when a RE ion is incorporated in a host the energy lowering of the 5*d* state, regarding the one observed for the free ion, is, in first approximation, independent on the type of RE ion, depending only on the host. It is independent of the ion since the $4f^n$ electrons are almost completely shielded from the crystal field and the interaction between the 5*d* electrons and the remaining 4*f* electrons is identical for all the ions [91,107]. The host dependence is accounted by the strong interaction between unshielded 5*d*-electron with the neighbour anions [108]. In this sense, a parameter called redshift was introduced in the model, corresponding to the first spin and dipole allowed transition from the $4f^n$ ground state to the $4f^{n-1}5d^1$ excited state of the RE ions in a specific compound, which is constant over all RE [88,91,108].

Another assumption of the this model is that the binding energy of the lowest $4f^n$ state of a RE^{q+} ion, where *q+* denotes the ionic charge, always exhibits a characteristic pattern along the RE-series, with increasing *n*, as shown in Figure 4-8 [86,90]. This pattern can be used to construct level diagrams [109]. A similar behaviour is found both for trivalent and divalent RE ions, with the main difference being a stronger binding energy (18 - 19 eV) for the trivalent ions, due to its higher ionic charge [86]. The characteristic shape of the double zigzag curve for the divalent RE ions was known already in the 70's, while the trivalent zigzag curve was only established latter using information obtained by photoelectron spectroscopy on pure RE metals and RE doped compounds [103,110,111].

The parameters to place the levels for the divalent RE ions are not completely independent from those to place the trivalent ones. For instance, the energy difference between the 4*f* ground state of Eu^{2+} and the 4*f* ground state of Eu^{3+} appears relatively constant. This difference is denoted by ΔE(Eu) and can be used to describe the dependence of the binding energy on the RE charge. This difference is assumed to slightly depend on the type of anions in the compound. A value of ΔE(Eu) ~ 5.7 ± 0.3 eV was found to be similar for sulphide, iodide and nitride compounds, while

ΔE(Eu) ~ 6.7 ± 0.3 eV was established for fluorides and oxides [88]. Thus, the present model comprises three host dependent parameters: the bandgap of the semiconductor host, the charge transfer energy for Eu^{3+} and the redshift of the *f-d* transition in a specific host [89]. This model has been developed through the years and some reassignments of the parameters have been performed, though the basis of the model remains the same [104,105]. It is also worth to mention that this model does not take into consideration the effect of the lattice distortion due to the differences in the covalent radii between the RE dopants and the host. When ions with very different radii are introduced, some perturbation of the electronic structure of the host is expected. Moreover, the number of valence electrons and electronegativity may differ from the host and may lead to additional contributions in the levels positioning [85].

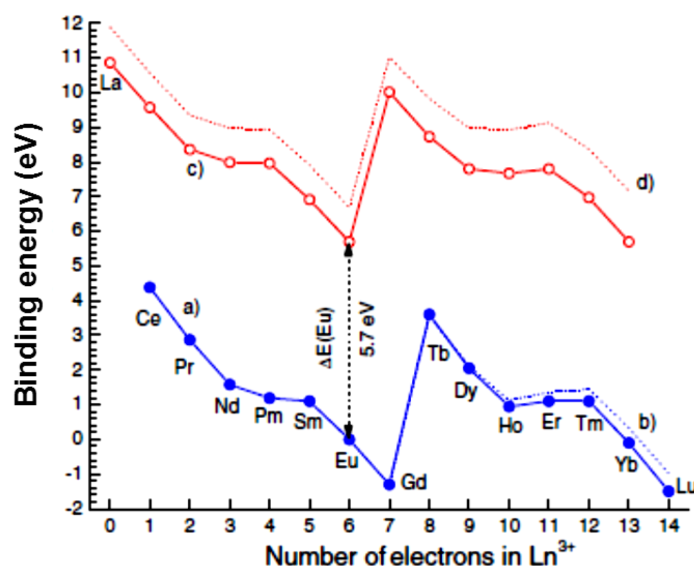

Figure 4-8 – Behaviour of the 4*f*-electron binding energies of trivalent (a) and divalent (c) RE ions for semiconductors, assuming ΔE (Eu) ~ 5.7 eV for sulphide, iodide and nitride compounds. For fluoride and oxide compounds curves (b) and (d) should be followed. In the latter case ΔE (Eu) ~ 6.7 eV [86,88,90].

The levels' scheme constructed for GaN and AlN are depicted in Figure 4-9. In both cases, a value of 5.7 eV was used for the energy difference ΔE(Eu) [86,88,90]. To place the top of the VB the information regarding the energy of charge transfer from this band to the Eu^{3+} ion (arrow 1 in Figure 4-9) was used. In the case of GaN, a value of 3.15 eV was used. This value was obtained from the excitation spectrum of the emission peaked at 622 nm for the $^5D_0 \rightarrow {}^7F_2$ transition of the Eu^{3+} ion in a GaN host [88,90]. It is assumed that charge transfer starts from the top of the VB and the final state corresponds to the ground state of the ion [89].

Figure 4-9a shows the energy levels of some trivalent RE ions. For this positioning the experimental value (8 meV) reported in the literature [112] for the activation energy of the $^5D_4$ excited level of the Tb^{3+} ion was used, considering that this value corresponds to the phonon assisted ionization of the $^5D_4$ electron to the CB. This value was assumed to correspond to the difference between the $^5D_4$ excited level and the CB [86]. From that location all the $4f^n$ ground states of the other RE were determined. Figure 4-9a also shows some of the relevant optical transitions of the different RE ions in the GaN host. Similar considerations were used taking into account the information available on the luminescence of RE in the AlN host, as shown in Figure

4-9b. A careful analysis of the two schemes reveal that the location of the RE ions is quite similar in both GaN and AlN host, differing mainly in the higher energy (almost 3 eV) of the CB in AlN [86]. This fact allowed the construction of the scheme of a RE ion in the $Al_xGa_{1-x}N$ host as a function of the Al molar fraction, *x*, using "Vegard's law" (Eq. 1-4) to determine the position of the CB [86,88]. An example of this diagram created for the Tb^{3+} ion is shown in Figure 4-10. This positioning of the RE levels can predict and explain electron transfer phenomena between a RE ion state and host states and from one RE to another, as well as the expected luminescence transitions [106].

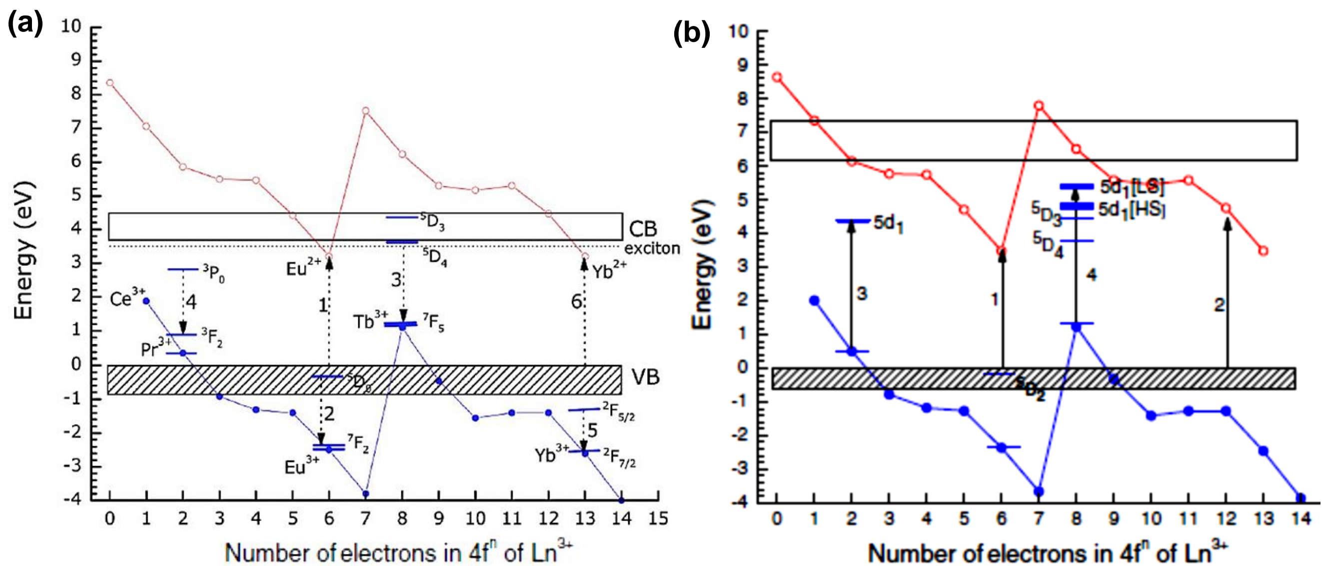

Figure 4-9 – Location of the lowest $4f^n$ states of trivalent and divalent RE ions, as proposed by Dorenbos [86,90]: (a) GaN and (b) AlN. The top of the VB is placed at 0 eV. Arrow 1 indicates charge transfer from the VB to Eu^{3+} in both (a) and (b). (a): arrow 2 indicates the $^5D_0 \rightarrow {}^7F_2$ emission of the Eu^{3+} ion; arrow 3 corresponds to the $^5D_4 \rightarrow {}^7F_5$ emission of the Tb^{3+} ion; arrow 4 represents the $^3P_0 \rightarrow {}^3F_2$ emission of the Pr^{3+} ion and arrows 5 and 6 indicate the emission from the $^2F_{5/2} \rightarrow {}^2F_7/_2$ transition of the Yb^{3+} ion and the charge transfer VB → Yb^{3+}, respectively. (b): arrow 2 represents a charge transfer to Tm^{3+} also from the VB; arrow 3 corresponds to the energy of the first 4*f*-5*d* transition of Pr^{3+} and arrow 4 indicates the energy of the first dipole and spin allowed transition of Tb^{3+}.

The energy level scheme for AlN and GaN predict that the 4*f* shell of a RE ion can be active in trapping charge carriers depending on their location with respect to the VB and CB. Whenever the ground state of a divalent RE ions is located below the bottom of the CB, the corresponding trivalent ion is able to trap an electron from that band. Accordingly, for GaN this can only happen for Eu^{3+} and Yb^{3+} ions. Increasing the bandgap with the increase of the AlN molar fraction, the CB moves further upwards relative to the RE levels, and also Sm^{3+} and Tm^{3+} can become active electron traps. In AlN, even Nd^{3+}, Pm^{3+}, Dy^{3+}, Er^{3+} and Ho^{3+} can form shallow electron traps with < 0.8 eV [86].

If the ground state of a divalent RE ion is placed in the CB it will not be stable, since the electron will quickly autoionize in the CB. However, this model cannot explain why similar features to the ones observed for Eu-doped GaN were identified in other RE for which the divalent ground states were found to be located in the CB [84].

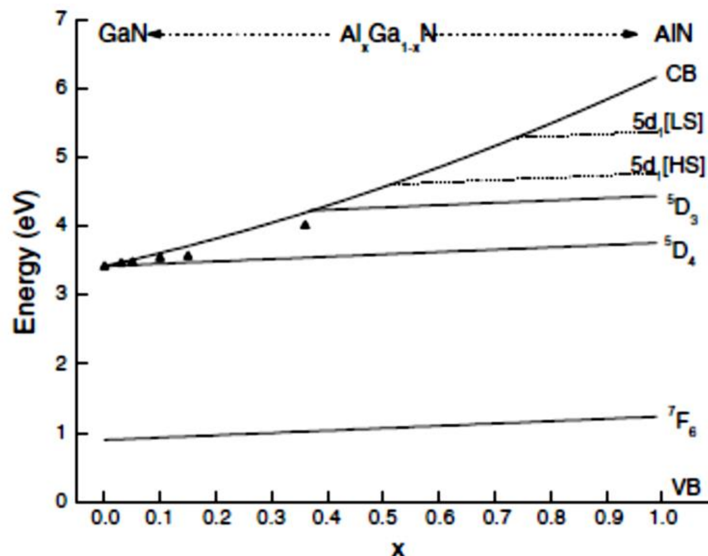

Figure 4-10 – Position of the Tb energy levels relatively to the CB bottom and VB top, as function of the Al content in $Al_xGa_{1-x}N$. The data points correspond to the location of the $^5D_4$ state obtained from experimental techniques [86,88].

The excitation mechanism where a change in the RE charge state occurs usually involve two steps: first, a charge transfer from the host to the ion following an optical excitation, and then the excitation process takes place if the charge transfer state is close in energy to the 4*f* energy levels. If so, a fast intersystem crossing between the 4*f* states occurs and can be followed by an intra 4*f*-4*f* emission, as it is showed in Figure 4-11. When an electron is promoted from the VB to the RE ion the ion's valence changes in a way that RE^{3+}→RE^{2+}+*h*, where *h* corresponds to a hole that, although delocalized, is bound to the RE core. So, RE^{2+}+*h* constitutes the charge transfer state [84]. It is worth to point out that this process is not the same as the one discussed for the bound exciton formation in REI traps. The electron binding energy in these two cases is very different. In a charge transfer state the electron binding energy is stronger [84].

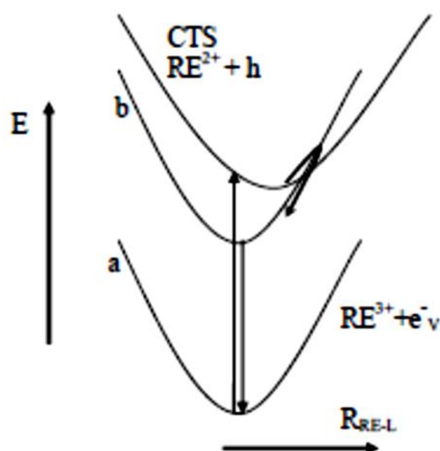

Figure 4-11 – Configuration coordinate diagram showing a charge transfer process. Initially, the RE^{3+} ion is in its ground state with an electron in the VB (parable a). After excitation into the charge transfer state (RE^{2+}+h), a crossover to an excited state of RE^{3+} (parable b) occurs leading to a 4*f*→4*f* emission [84].

Additionally, Wang *et al*. [113] applied an excitation model that formally equates both charge transfer and REI trap with a bound exciton formation models to RE-doped $Al_xGa_{1-x}N$ alloy. These authors ascribe all the Eu^{3+} sharp line emissions to the annihilation of excitons at the Eu ion. Similar experimental findings were obtained for other RE-doped samples, namely with Dy, Tm and Pr, suggesting that excitonic processes strongly assisted the optical processes of RE-doped nitrides [113]. The inspection of the presence of a bound exciton mediating the excitation process is made by the evaluation of the linewidths of the components lines of a chosen transition. An asymmetrical variation of the linewidth as a function of the composition is expected when an exciton is involved, resembling what is observed for the behaviour of the bound excitons in semiconductor alloys [114,115]. This model is based on the one introduced by Schubert *et al.* [114], which consider that the broadening in the linewidth of the transition in alloys is caused by a statistical occupation of the cation places Ga by Al, and the alloy disorder is felt by the exciton. This model takes into account the exciton volume (resulting from the hydrogen model), as well as its Bohr radius [114,116]. The model assumes that Al and Ga atoms are distributed randomly on the group III sites, not taking into account macroscopic inhomogeneity due to inferior crystal quality, defects or alloy clustering [114]. In elemental or binary III-V or II-VI semiconductors, the linewidth of a bound exciton is smaller than kT, considering that this exciton has no kinetic energy. Therefore, its theoretical line shape can be approximated by a Lorentzian function. However, in ternary alloys statistical effects must also be considered [114] and thus the behaviour can be fitted using the following equation [113,115]:

$$\sigma(x) = \sigma_0 + \frac{dE_g(x)}{dx}\sqrt{\frac{8\ln(2)x(1-x)}{(4\pi/3)R_{ex}^3 K}}, \quad \textbf{Eq. 4-56}$$

where σ_0 is the residual linewidth, K is the cation/anion number density, R_{ex} is the mean exciton radius and $E_g(x)$ can be obtained using Vegard's law. K is given by $\sqrt{2/a_0^3}$, with a_0 being the average a-plane wurtzite lattice constant [113,114]. In this model, an excited electron from a neighbouring cation can be transferred to the RE ion, for instance to the 5d shell, leading to the formation of an exciton. The excess energy produced by that exciton can be transferred to the 4f core states, giving rise to the observed ion-related luminescence features [113]. The UV excitation bands frequently observed in the PLE spectra of a given intra-shell transition are likely to be related with the population paths of such recombination excitons, as was proposed by Wang *et al.* [113].

4.2.5. Experimental setup

In a typical PL experiment, an excitation source, frequently with energies higher than the bandgap energy of the semiconductor, is used to create e-h pairs, that then recombine and emit light [1]. The sample is sometimes placed in a cryostat and cooled to temperatures that can go to the liquid helium temperature, since low temperature measurements allow assessing the fullest spectroscopic information by minimizing thermally activated nonradiative recombination processes and also thermal line broadening [5]. The emission of the samples is then recorded with a suitable detector.

In this work, steady state PL measurements were performed using the 325 nm light from a cw He-Cd laser with a beam spot of ~ 1 mm and an excitation power density less than 0.6 $W.cm^{-2}$. The samples were mounted in a cold finger of a closed-cycle helium cryostat and the sample temperature was controlled in a range from 14 K to RT. This temperature variation was accomplished using a heating resistance placed near the cold finger controlled by a temperature controller coupled to a thermo-couple. The inside of the cryostat is kept under vacuum (~ 10^{-5} Torr), using a vacuum system composed by a primary (rotatory) and a secondary (diffusion) pump. The luminescence was measured using a dispersive system SPEX 1704 *Czerny-Turner* monochromator (1 m, 1200 $gr.mm^{-1}$) fitted with a cooled Hamamatsu R928 photomultiplier tube (PMT). The measured spectra were corrected to the optics of the system and to the detector response. For the excitation density PL dependence, neutral density filters were used. Figure 4-12 shows a representation of the PL system apparatus (Figure 4-12a) as well as the schematic illustration of the collection of the emitted light (Figure 4-12b). The optics of the system was projected in order to assure the maximum light collection. After excitation from the light source, the emitted light is collected under a 90° geometry. The emission is focused on the entrance slit of the monochromator by a set of lenses. After passing by the dispersive system, the light is collected by the photomultiplier detector and processed by the analysis software.

For the infrared spectral region, the PL measurements were performed with a Bruker 66V Fourier transform spectrometer (FTIR). The signal was detected with a North-Coast EO-817 liquid nitrogen cooled germanium detector. The samples were inserted in a helium gas flow cryostat that allowed varying the temperature in the range 7 - 300 K. The same cw He-Cd laser was used as excitation source.

The RT PLE was assessed in a Fluorolog-3 Horiba Scientific modular equipment with a double additive grating scanning monochromator (2×180 mm, 1200 $gr.mm^{-1}$) in the excitation and a triple grating iHR550 spectrometer in the emission (550 mm, 1200 $gr.mm^{-1}$). A 450 W Xe lamp was used as excitation source. The PLE was assessed by monitoring the wavelength of the maxima of the PL emission lines and the excitation was scanned to higher wavelengths. The measurements were performed using front face acquisition geometry, and the presented spectra were corrected to the optical components, PMT detector and to the Xe lamp spectral responses. Figure 4-13a shows an image of the Fluorolog-3 equipment, while Figure 4-13b depicts a scheme of the mentioned system as well as the representation of the light path inside the measurement apparatus.

For the TRPL measurements two systems were used. RT TRPL spectra were acquired with the same Fluorolog-3 system using a pulsed Xe lamp coupled to a monochromator. This equipment also allows the measurement of lifetime decays. For this, both excitation and emission wavelength were fixed and the time decay of the emission was assessed. In both cases an initial delay of 0.05 ms was defined in order to avoid the direct light from the lamp. The experimental parameters to take into account are the flash counts, sample window and maximum delay. These input parameters depend on the characteristics of the sample, namely the intensity of the emission and the expected lifetime. Additionally, TRPL measurements were conducted using a Surelite II/10 pulsed Nd:YAG laser (1064 nm, 10 Hz repetition rate) coupled to a fourth harmonic generator crystal (Surelite SLD-II and SLF) in order to achieve 266 nm pulsed excitation with a ~ 5 ns pulse width and 60 mJ of energy. Detection was performed by diffracting the collected

emission in an ORIEL MS-125 monochromator, with a 400 gr.mm^{-1} grating and acquired in an ANDOR iccd (model DH-520, P46 phosphor coated).

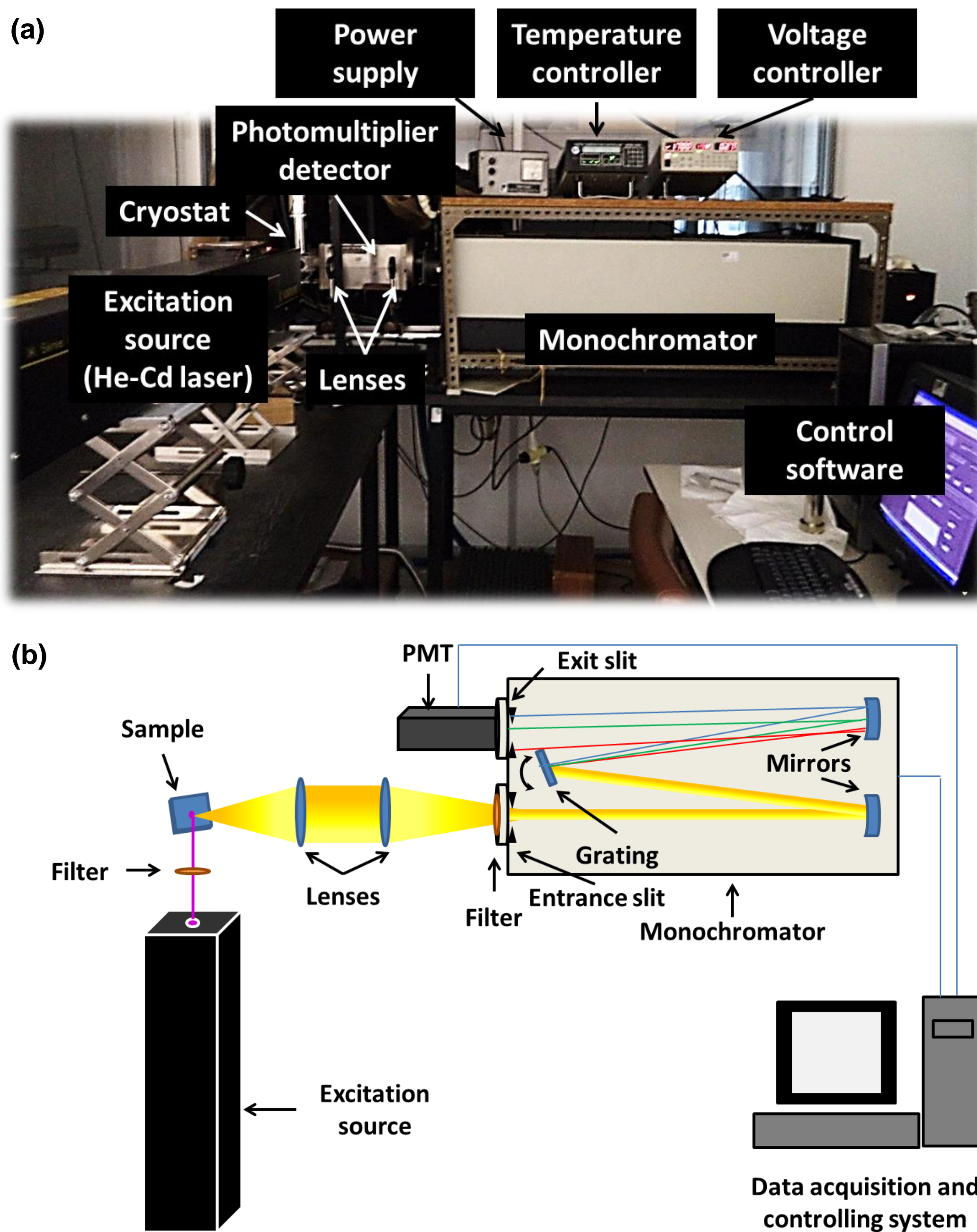

Figure 4-12 – (a) PL system apparatus and (b) schematic representation of the PL measurements.

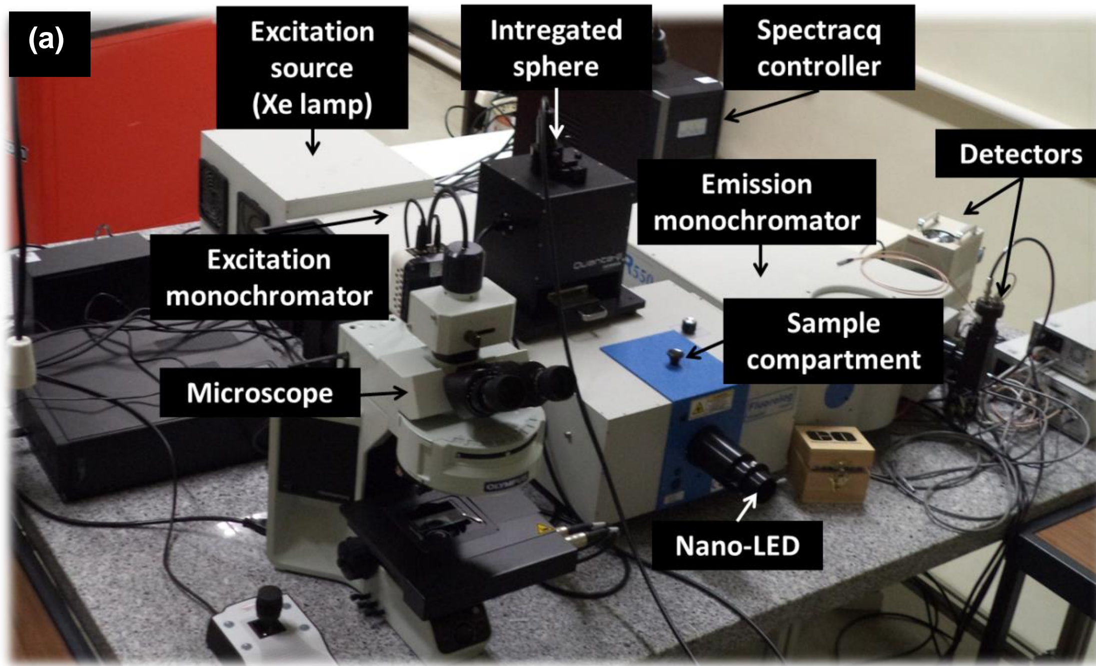

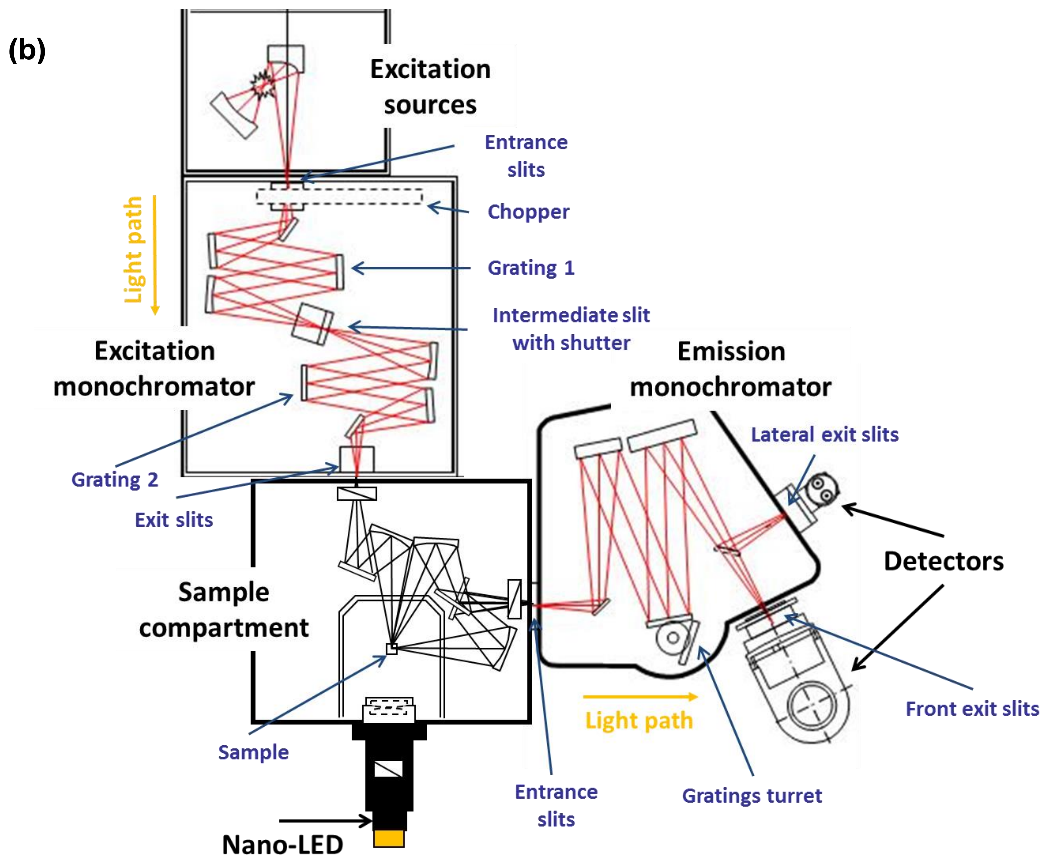

Figure 4-13 – (a) Picture of the Fluorolog-3 system for the PLE and TRPL measurements. (b) Schematic representation of the system components adapted from Horiba manual.

4.3. References

1. J. Singh, *Electronic and Optoelectronic Properties of Semiconductor Structures* (Cambridge University Press, 2003).

2. A. M. Fox, *Optical Properties of Solids* (Oxford University Press, 2010).

3. J. Solé, L. Bausa, and D. Jaque, *An Introduction to the Optical Spectroscopy of Inorganic Solids* (John Wiley & Sons, 2005).

4. J. I. Pankove, *Optical Processes in Semiconductors* (Dover Publication, Inc., 1971).

5. D. K. Schroder, *Semiconductor Material and Device Characterization* (John Wiley & Sons, 2006).

6. V. Lucarini, J. J. Saarinen, K.-E. Peiponen, and E. M. Vartiainen, *Kramers-Kronig Relations in Optical Materials Research* (Springer, 2006).

7. F. Stern, R. F. Guertin, R. E. Morrison, and N. O. L. W. O. M.D., *Elementary Theory of the Optical Properties of Solids* (Defense Technical Information Center, 1962).

8. D. M. Roessler, Br. J. Appl. Phys. **16**, 1119 (1965).

9. C. F. Klingshirn, *Semiconductor Optics* (Springer, 2007).

10. P. Y. Yu and M. Cardona, *Fundamentals of Semiconductors: Physics And Materials Properties, Volume 3* (Springer, 2005).

11. I. Pelant and J. Valenta, *Luminescence Spectroscopy of Semiconductors* (OUP Oxford, 2012).

12. M. Peres, Estudo de Defeitos Em Filmes Finos de ZnO Depositados Por Rf-Sputtering, PhD thesis, Universidade de Aveiro, 2014.

13. B. Monemar, P. P. Paskov, J. P. Bergman, A. A. Toropov, T. V. Shubina, T. Malinauskas, and A. Usui, Phys. Status Solidi **245**, 1723 (2008).

14. M. A. Reshchikov and H. Morkoç, J. Appl. Phys. **97**, 061301 (2005).

15. T. Schmidt, K. Lischka, and W. Zulehner, Phys. Rev. B **45**, 8989 (1992).

16. D. R. Vij, *Handbook of Applied Solid State Spectroscopy* (Springer Science & Business Media, 2007).

17. B. Henderson and G. F. Imbusch, *Optical Spectroscopy of Inorganic Solids* (Oxford University Press, 2006).

18. J. Lackowicz, *Principles of Fluorescence Spectroscopy* (Plenum Press, 1983).

19. M. A. Sousa, T. C. Esteves, N. Ben Sedrine, J. Rodrigues, M. B. Lourenço, A. Redondo-Cubero, E. Alves, K. P. O'Donnell, M. Bockowski, C. Wetzel, M. R. Correia, K. Lorenz, and T. Monteiro, Sci. Rep. **5**, 9703 (2015).

20. M. Pophristic, F. H. Long, C. Tran, I. T. Ferguson, and R. F. Karlicek, J. Appl. Phys. **86**, 1114 (1999).

21. X. Chen, B. Henderson, and K. P. O'Donnell, Appl. Phys. Lett. **60**, 2672 (1992).

22. S. Nakamura, S. J. Pearton, and G. Fasol, *The Blue Laser Diode: The Complete Story* (Springer Verlag, 2000).

23. B. Monemar, Phys. Rev. B **10**, 676 (1974).

24. S. J. Pearton, *GaN and Related Materials II* (CRC Press, 2000).

25. C. Jagadish and S. J. Pearton, *Zinc Oxide Bulk, Thin Films and Nanostructures: Processing, Properties and Applications* (Elsevier, 2006).

26. B. Monemar, P. Paskov, T. Paskova, J. Bergman, G. Pozina, W. Chen, P. Hai, I. Buyanova, H. Amano, and I. Akasaki, Mater. Sci. Eng. B **93**, 112 (2002).

27. H. Amano, M. Kito, K. Hiramatsu, and I. Akasaki, Jpn. J. Appl. Phys. **28**, L2112 (1989).

28. M. O. Manasreh, *III-Nitride Semiconductors: Electrical, Structural and Defects Properties: Electrical, Structural and Defects Properties* (Elsevier, 2000).

29. Jacques I. Pankove and T. D. Moustakas, *Gallium-Nitride (GaN) II* (Academic Press, 1998).

30. W. Goetz, N. M. Johnson, D. P. Bour, C. Chen, H. Liu, and W. Imler, *Shallow Dopants and the Role of Hydrogen in Epitaxial Layers of Gallium Nitride (GaN)* (Electrochemical Society, Inc., 1996).

31. J. H. Edgar, *Properties of Group III Nitrides* (EMIS Datareviews Series, n°11, An INSPEC publication, 1994).

32. Q. Yan, A. Janotti, M. Scheffler, and C. G. Van de Walle, Appl. Phys. Lett. **100**, 142110 (2012).

33. D. O. Demchenko and M. A. Reshchikov, Phys. Rev. B **88**, 115204 (2013).

34. M. A. Reshchikov, D. O. Demchenko, J. D. McNamara, S. Fernández-Garrido, and R. Calarco, Phys. Rev. B **90**, 035207 (2014).

35. T. Suski, P. Perlin, H. Teisseyre, M. Leszczyński, I. Grzegory, J. Jun, M. Boćkowski, S. Porowski, and T. D. Moustakas, Appl. Phys. Lett. **67**, 2188 (1995).

36. T. Ogino and M. Aoki, Jpn. J. Appl. Phys. **19**, 2395 (1980).

37. J. Neugebauer and C. G. Van de Walle, Appl. Phys. Lett. **69**, 503 (1996).

38. M. A. Reshchikov, H. Morkoç, S. S. Park, and K. Y. Lee, Appl. Phys. Lett. **78**, 2882 (2001).

39. A. Sedhain, J. Li, J. Y. Lin, and H. X. Jiang, Appl. Phys. Lett. **96**, 151902 (2010).

40. T. Mattila and R. M. Nieminen, Phys. Rev. B **55**, 9571 (1997).

41. R. Seitz, C. Gaspar, T. Monteiro, E. Pereira, M. Leroux, B. Beaumont, and P. Gibart, MRS Int. J. Nitride Semicond. Res. **2**, e36 (1997).

42. M. A. Reshchikov, H. Morkoç, S. S. Park, and K. Y. Lee, Appl. Phys. Lett. **81**, 4970 (2002).

43. V. Darakchieva, T. Monteiro, J. Rodrigues, M. T. Son, M.-Y. Xie, N. Ben Sedrine, E. Alves, A. Usui, C. Hemmingson, and B. Monemar, in *Oral Presentation* (ICNS-9, 2011).

44. M. A. Reshchikov, D. O. Demchenko, A. Usikov, H. Helava, and Y. Makarov, Phys. Rev. B **90**, 235203 (2014).

45. D. G. Thomas, J. Phys. Chem. Solids **15**, 86 (1960).

46. B. K. Meyer, H. Alves, D. M. Hofmann, W. Kriegseis, D. Forster, F. Bertram, J. Christen, A. Hoffmann, M. Straßburg, M. Dworzak, U. Haboeck, and A. V. Rodina, Phys. Status Solidi **241**, 231 (2004).

47. Ü. Özgür, Y. I. Alivov, C. Liu, A. Teke, M. A. Reshchikov, S. Doğan, V. Avrutin, S.-J. Cho, and H. Morkoç, J. Appl. Phys. **98**, 041301 (2005).

48. H. Morkoç and Ü. Özgür, *Zinc Oxide: Fundamentals, Materials and Device Technology* (John Wiley & Sons, 2008).

49. C. F. Klingshirn, A. Waag, A. Hoffmann, and J. Geurts, *Zinc Oxide: From Fundamental Properties Towards Novel Applications* (Springer, 2010).

50. M. R. Wagner, P. Zimmer, A. Hoffmann, and C. Thomsen, Phys. Status Solidi – Rapid Res. Lett. **1**, 169 (2007).

51. M. Schirra, R. Schneider, A. Reiser, G. M. Prinz, M. Feneberg, J. Biskupek, U. Kaiser, C. E. Krill, K. Thonke, and R. Sauer, Phys. Rev. B **77**, 125215 (2008).

52. J. Fallert, R. Hauschild, F. Stelzl, A. Urban, M. Wissinger, H. Zhou, C. Klingshirn, and H. Kalt, J. Appl. Phys. **101**, 073506 (2007).

53. S. S. Kurbanov and T. W. Kang, J. Lumin. **130**, 767 (2010).

54. D. Tainoff, B. Masenelli, P. Melinon, A. Belsky, G. Ledoux, D. Amans, C. Dujardin, N. Fedorov, and P. Martin, J. Lumin. **129**, 1798 (2009).

55. K. Thonke, M. Schirra, R. Schneider, A. Reiser, G. M. Prinz, M. Feneberg, J. Biskupek, U. Kaiser, and R. Sauer, Microelectronics J. **40**, 210 (2009).

56. D. Tainoff, B. Masenelli, P. Mélinon, A. Belsky, G. Ledoux, D. Amans, C. Dujardin, N. Fedorov, and P. Martin, Phys. Rev. B **81**, 115304 (2010).

57. A. B. Djurišić, Y. H. Leung, K. H. Tam, Y. F. Hsu, L. Ding, W. K. Ge, Y. C. Zhong, K. S. Wong, W. K. Chan, H. L. Tam, K. W. Cheah, W. M. Kwok, and D. L. Phillips, Nanotechnology **18**, 095702 (2007).

58. A. B. Djurišić, Y. H. Leung, K. H. Tam, L. Ding, W. K. Ge, H. Y. Chen, and S. Gwo, Appl. Phys. Lett. **88**, 103107 (2006).

59. M. A. Reshchikov, H. Morkoç, B. Nemeth, J. Nause, J. Xie, B. Hertog, and A. Osinsky, Phys. B Condens. Matter **401-402**, 358 (2007).

60. A. F. Kohan, G. Ceder, D. Morgan, and C. G. Van De Walle, Phys. Rev. B **61**, 19 (2000).

61. R. Dingle, Phys. Rev. Lett. **23**, 579 (1969).

62. B. G. Wybourne, *Spectroscopic Properties of Rare Earths* (Interscience Publishers, Jonh Wiley & Sons Inc., 1965).

63. P. Hanninen and H. Harma, *Lanthanide Luminescence: Photophysical, Analytical and Biological Aspects* (Springer Science & Business Media, 2011).

64. A. Steckl, J. Heikenfeld, M. Garter, R. Birkhahn, and D. Lee, Compd. Semicond **6**, 48 (2000).

65. G. Blasse and B. C. Grabmaier, *Luminescent Materials* (Springer, 1994).

66. A. J. Kenyon, Prog. Quantum Electron. **26**, 225 (2002).

67. A. J. Steckl, J. C. Heikenfeld, M. J. Garter, C. C. Baker, and R. Jones, IEEE J. Sel. Top. Quantum Electron. **8**, 749 (2002).

68. K. P. O'Donnell and B. Hourahine, Eur. Phys. J. - Appl. Phys. **36**, 91 (2006).

69. G. Liu and B. Jacquier, *Spectroscopic Properties of Rare Earths in Optical Materials* (Springer, 2006).

70. P. A. Tipler and R. Llewellyn, *Modern Physics* (W. H. Freeman and Company, New York, 2003).

71. M. D. Chambers and D. R. Clarke, Annu. Rev. Mater. Res. **39**, 325 (2009).

72. B. Di Bartolo, V. Goldberg, and D. Pacheco, *Luminescence of Inorganic Solids* (Plenum Press, 1978).

73. R. A. Sá Ferreira, Estrutura e Luminescência de Materiais Híbridos Orgânicos-Inorgânicos Modificados Por Iões Lantanídeos, PhD thesis, Universitdade de Aveiro, 2002.

74. G. Racah, Phys. Rev **62**, 438 (1942).

75. R. C. Powell, *Physics of Solid-State Laser Materials* (Springer Science & Business Media, 1998).

76. E. U. Condon and G. H. Shortley, *The Theory of Atomic Spectra* (Cambridge University Press, 1951).

77. F. Auzel and O. L. Malta, J. Phys. **44**, 201 (1983).

78. G. Blasse, in *Handb. Phys. Chem. Rare Earths, Vol. 4*, edited by K. A. Gschneidner Jr and L. Eyring (Elsevier Science, North-Holland Physics, 1979).

79. W. M. Jadwisienczak, The Luminescence Properties of the Wide Bandgap Nitrides Doped with Rare Earth Ions and Gallium Nitride Doped with Conventional Isoelectronic Impurities, PhD thesis, Ohio University, 2001.

80. Michael Gaft, R. Reisfeld, and G. Panczer, *Modern Luminescence Spectroscopy of Minerals and Materials* (Springer-Verlag, 2005).

81. G. S. Ofelt, J. Chem. Phys. **37**, 511 (1962).

82. B. Judd, Phys. Rev. **127**, 750 (1962).

83. M. J. Weber, in *Handb. Phys. Chem. Rare Earths, Vol. 4*, edited by K. A. Gschneidner Jr and L. Eyring (Elsevier Science, North-Holland Physics, 1979).

84. K. P. O'Donnell, *Rare-Earth Doped III-Nitrides for Optoelectronic and Spintronic Applications* (Springer, 2009).

85. H. J. Lozykowski and W. M. Jadwisienczak, Phys. Status Solidi **244**, 2109 (2007).

86. P. Dorenbos and E. van der Kolk, Opt. Mater. (Amst). **30**, 1052 (2008).

87. H. Lozykowski, Phys. Rev. B **48**, 17758 (1993).

88. P. Dorenbos and E. van der Kolk, in *Proc. SPIE 6473, Gall. Nitride Mater. Devices II*, edited by H. Morkoc and C. W. Litton (International Society for Optics and Photonics, 2007), pp. 647313–647313–10.

89. P. Dorenbos, J. Phys. Condens. Matter **15**, 8417 (2003).

90. P. Dorenbos and E. Van der Kolk, Appl. Phys. Lett. **89**, 061122 (2006).

91. P. Dorenbos, J. Lumin. **108**, 301 (2004).

92. E. Alves, K. Lorenz, R. Vianden, C. Boemare, M. J. Soares, and T. Monteiro, Mod. Phys. Lett. B **15**, 1281 (2001).

93. M. Fialho, K. Lorenz, S. Magalhães, J. Rodrigues, N. F. Santos, T. Monteiro, and E. Alves, Nucl. Instruments Methods Phys. Res. Sect. B Beam Interact. with Mater. Atoms **307**, 495 (2013).

94. J. Rodrigues, S. M. C. Miranda, N. F. Santos, A. J. Neves, E. Alves, K. Lorenz, and T. Monteiro, Mater. Chem. Phys. **134**, 716 (2012).

95. H. J. Lozykowski, W. M. Jadwisienczak, and I. Brown, J. Appl. Phys. **88**, 210 (2000).

96. U. Hommerich, E. Nyein, and D. Lee, Appl. Phys. Lett. **82**, 4556 (2003).

97. A. Baldereschi, J. Lumin. **7**, 79 (1973).

98. I. Yassievich, M. Bresler, and O. Gusev, J. Non. Cryst. Solids **226**, 192 (1998).

99. W. Lenth, F. Lutz, J. Barth, G. Kalkoffen, and C. Kunz, Phys. Rev. Lett. **41**, 1185 (1978).

100. T. Tiedje, K. M. Colbow, Y. Gao, J. R. Dahn, J. N. Reimers, and D. C. Houghton, Appl. Phys. Lett. **61**, 1296 (1992).

101. E. Guziewicz, B. A. Orlowski, B. J. Kowalski, I. A. Kowalik, A. Reszka, L. Wachnicki, S. Gieraltowska, M. Godlewski, and R. L. Johnson, Appl. Surf. Sci. **282**, 326 (2013).

102. B. Henderson and R. H. Bartram, *Crystal-Field Engineering of Solid-State Laser Materials* (Cambridge University Press, 2005).

103. C. W. Thiel, H. Cruguel, H. Wu, Y. Sun, G. J. Lapeyre, R. L. Cone, R. W. Equall, and R. M. Macfarlane, Phys. Rev. B **64**, 085107 (2001).

104. P. Dorenbos, ECS J. Solid State Sci. Technol. **2**, R3001 (2012).

105. P. Dorenbos, A. H. Krumpel, E. van der Kolk, P. Boutinaud, M. Bettinelli, and E. Cavalli, Opt. Mater. (Amst). **32**, 1681 (2010).

106. P. Dorenbos, Phys. Rev. B **87**, 035118 (2013).

107. P. Dorenbos, J. Lumin. **111**, 89 (2005).

108. P. Dorenbos, J. Alloys Compd. **341**, 156 (2002).

109. P. Dorenbos, J. Lumin. **122-123**, 315 (2007).

110. P. Dorenbos, J. Mater. Chem. **22**, 22344 (2012).

111. C. W. Thiel, H. Cruguel, Y. Sun, G. J. Lapeyre, R. M. Macfarlane, R. W. Equall, and R. L. Cone, J. Lumin. **94-95**, 1 (2001).

112. Y. Nakanishi, A. Wakahara, H. Okada, A. Yoshida, T. Ohshima, and H. Itoh, Phys. Status Solidi **240**, 372 (2003).

113. K. Wang, K. P. O'Donnell, B. Hourahine, R. W. Martin, I. M. Watson, K. Lorenz, and E. Alves, Phys. Rev. B **80**, 125206 (2009).

114. E. Schubert, E. Göbel, Y. Horikoshi, K. Ploog, and H. Queisser, Phys. Rev. B **30**, 813 (1984).

115. A. N. Westmeyer, S. Mahajan, K. K. Bajaj, J. Y. Lin, H. X. Jiang, D. D. Koleske, and R. T. Senger, J. Appl. Phys. **99**, 013705 (2006).

116. G. Steude, B. K. Meyer, A. Göldner, A. Hoffmann, F. Bertram, J. Christen, H. Amano, and I. Akasaki, Appl. Phys. Lett. **74**, 2456 (1999).

Chapter 5. GaN and related nitrides: in pursuit of solid state lighting

This chapter is dedicated to the discussion of the main results obtained in the study of GaN samples, as well as its alloy with AlN ($Al_xGa_{1-x}N$). The main focus is given to the RE-doped samples, since one of the aims of this thesis is to give a contribution to the understanding of the RE ions incorporation in nitrides hosts, envisaging the development of “all-nitride” solid state lighting devices. In this sense, different RE ions were introduced in GaN and $Al_xGa_{1-x}N$ layers and nanostructures and their optical properties were assessed by luminescence techniques.

5.1. Bulk GaN

As a starting point, it is worth to make a brief study of the main luminescence properties of GaN bulk before focusing the analysis on GaN nanostructures and RE-doped samples. Although the luminescence properties of bulk GaN are already widely studied in the literature, an adequate knowledge of the bulk properties is of paramount importance for a proper understanding of the optical properties of the nanostructures, being important for the PL discussion in the following sections.

Figure 5-1 shows the 14 K PL spectra obtained for both Ga- and N-faces of a GaN bulk sample, together with the visual appearance of the emission from each face. The spectra show a dominant NBE recombination for both faces. In addition to the UV emission, a broad unstructured band was observed (Figure 5-1a). However, while for the Ga-face a broad green emission was identified near 2.42 eV (~ 512 nm), for the N-face the band maximum is shifted to the yellow spectral region, around ~ 2.23 eV (~ 556 nm). High resolved spectra performed on the high energy region of both faces are shown in Figure 5-1b. Both faces exhibit similar PL transitions in this region, with only slight changes in their relative intensity. In the high energy region, the presence of the FX recombination at 3.485 eV (~ 355.8 nm - FX_B) and 3.481 eV (~ 356.2 nm - FX_A) is clearly identified. Moreover, an intense recombination due to excitons bound to neutral donors was also observed near ~ 3.47 eV (~ 357.3 nm). Actually, two lines at 3.473 (~ 357.0 nm) and 3.474 eV (~ 356.9 nm) could be resolved (inset of Figure 5-1b), suggesting that the A exciton is bound to two shallow donors, most probably O (on nitrogen site) and Si (on the Ga site), that were likely introduced during the growth. As explained in Chapter 4, these are the most common D^0X in GaN and their

reported energies are close to those found in the present sample [1]. Additionally, the exciton B bound to the donors was also identified at 3.477 (~ 356.6 nm) and 3.478 eV (~ 356.5 nm), as can be seen in the inset of Figure 5-1b. The TES recombination close to 3.45 eV can also be observed, as well as the LO phonon assisted transitions for the free and bound excitons (at lower energies/higher wavelengths). No stacking faults transition (~ 3.41 eV /~ 363 nm) was observed. Moreover, no DAP emission was identified near 3.27 eV (~ 379 nm), where these transitions are expected to occur [2,3]. Also no line near 3.46 eV (~ 358 nm) was detected, meaning that it was not possible to identify excitons bound to acceptors in the present sample, which is also compatible with the absence of the DAP transitions. The observation of all these features constitutes an indication of a low background impurity level and a high optical quality of the sample, inferred by the presence of well resolved excitonic transitions.

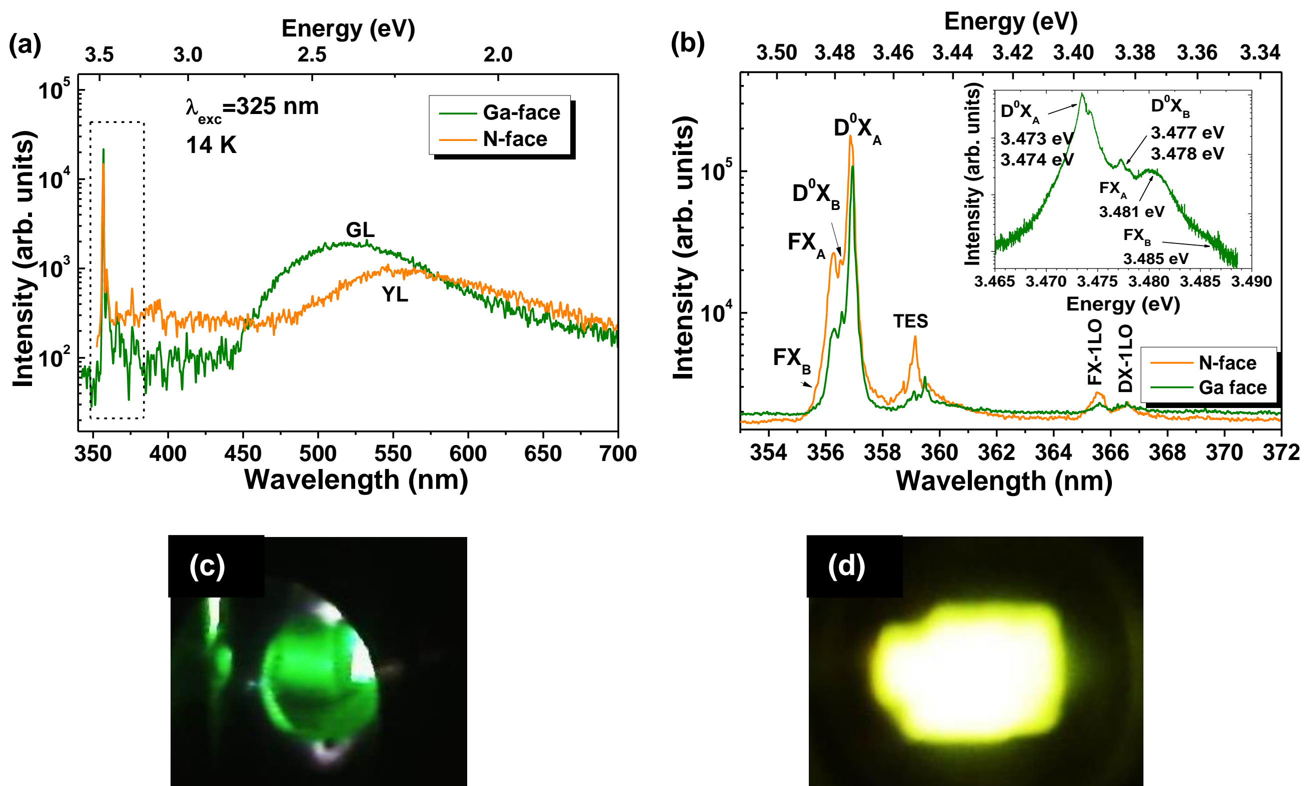

Figure 5-1 – Low temperature spectra of the Ga- and N- faces of GaN bulk sample U245 obtained at 14 K. Figure (b) corresponds to a magnification of the NBE region marked in (a). The inset highlights the well resolved NBE emission. Visual appearance of the emission at low temperature from (c) Ga-face and (d) N-face.

Figure 5-2 shows the temperature dependent PL spectra in the NBE region for both faces, evidencing a similar behaviour. Increasing the temperature a fast decrease of the D^0X transition occurs when compared with the FX region. With the donor ionization, an increase of the FX recombination was observed. For higher temperatures the main emission in this region is due to the FX and LO replicas. At RT, the UV emission is shown to be peaked at ~ 3.42 eV (~ 362 nm). Figure 5-2c depicts the temperature evolution of the energy peak position of the free A exciton. A good fitting of the data was obtained using the model proposed by Pässler *et al.* [4,5] and described by Eq. 1-3 (Chapter 1).

Regarding the broad bands related to deep-level defects, as discussed by Reshchikov *et al.* [6] and already mentioned in Chapter 4, after an intense debate about the origin of the YL band, most researchers settled that it is caused by transitions from the CB or a shallow donor to a deep acceptor [7–9]. The most discussed hypothesis for the deep acceptor is the V_{Ga} and its complex with oxygen ($V_{Ga}O_N$), that are known to be abundantly formed during growth [10,11]. Positron annihilation studies suggested that the dominant point defect in oxygen-rich GaN bulk samples is not the isolated V_{Ga} but the V_{Ga}-containing complex, presumably $V_{Ga}O_N$ [12]. The $V_{Ga}O_N$ complex should act as a double acceptor with its -/2- and 0/- levels that are, respectively, close to the 2-/3- and -/2- levels of the isolated V_{Ga} in GaN [6,10,13]. In *n*-type GaN, the $V_{Ga}O_N$ acceptor is fully occupied with electrons and in equilibrium its charge state is 2-. If the concentration of the these acceptors is very low and the lifetime of the acceptor-related luminescence is long enough, saturation of the -/2- level with photogenerated holes is expected, resulting in the capture of a second hole by the complex, which conducts to its neutral charge state 0/- [6]. Reshchikov and co-workers [6] analysed the Ga-face of a high-purity freestanding GaN template (grown by HPVE) and observed the presence of a broad YL that shifts to higher energies (to the green) with increasing excitation intensity. They concluded that the dominant point defect in undoped GaN is a multiple-charge state acceptor. The YL saturates with increasing excitation density, while the GL becomes dominant, which can be explained by saturation of the 2-/- state of the $V_{Ga}O_N$ acceptor and its transformation into the -/0 state at high excitation levels [6]. Recently, the same group published a work [14] pointing out C_N as the defect responsible for the GL band with a maximum at 2.4 eV in high-purity GaN samples also grown by HVPE. In a similar way with what was described above, the authors claim that, at low excitation intensities, an YL with a maximum at 2.1 eV, due to the recombination of free electrons with holes at the −/0 level of the C_N defects, is replaced with the GL band at high excitation intensity. The GL is attributed to transitions of electrons from the CB to the 0/+ level of the C_N defect. According to first-principles calculations, the C_N defect has two transition levels: the −/0 level at 1.04 eV and the 0/+ level at 0.48 eV above the VB maximum [14]. The intensity of the GL band increases as a square of the excitation intensity, in agreement with the assumption that two holes must be captured by the C_N defect before the GL band can be observed [14]. However, according to Reshchikov and co-authors [14] luminescence from isolated C_N defects can only be observed in HVPE-grown GaN with a low concentration of carbon and oxygen defects. Otherwise, the broad emission is expected to be dominated by C_NO_N complexes.

Power density dependence studies in the bulk sample were also carried out at low temperature by using neutral density filters, as depicted in Figure 5-3a. It is worth to note that the same excitation conditions were used in both sample sides. As mentioned previously, on the N-face the main luminescence arises already from the YL and, in this case, no shift of the band maxima was observed. However, as previously reported by Reshchikov *et al.* [6], a noticed low energy shift to the yellow region was observed for the green band, with the decreasing of the excitation density. This shift was more pronounced for lower excitation densities. Figure 5-3b shows the deconvolution of the broad band, evidencing that the yellow component was already present in the Ga-face, however with a low intensity. This means that different distribution of the charged states defect concentration in the two faces is present. It is clearly seen that an increase of the yellow component occurs for the lowest excitation density. However, even for the lowest

excitation power, the maximum of the broad PL band does not coincide with the one found for the YL in N-face. To reach this value, probably a lower excitation density is needed, in order to achieve a higher intensity of the yellow component over the green one.

This analysis allowed to gain some insight about the GaN luminescent properties, particularly to identify the main optical centres typically present in this semiconductor. Given this brief overview, the next sections will be focused on nitride nanostructures, with especial emphasis on the ones implanted with RE.

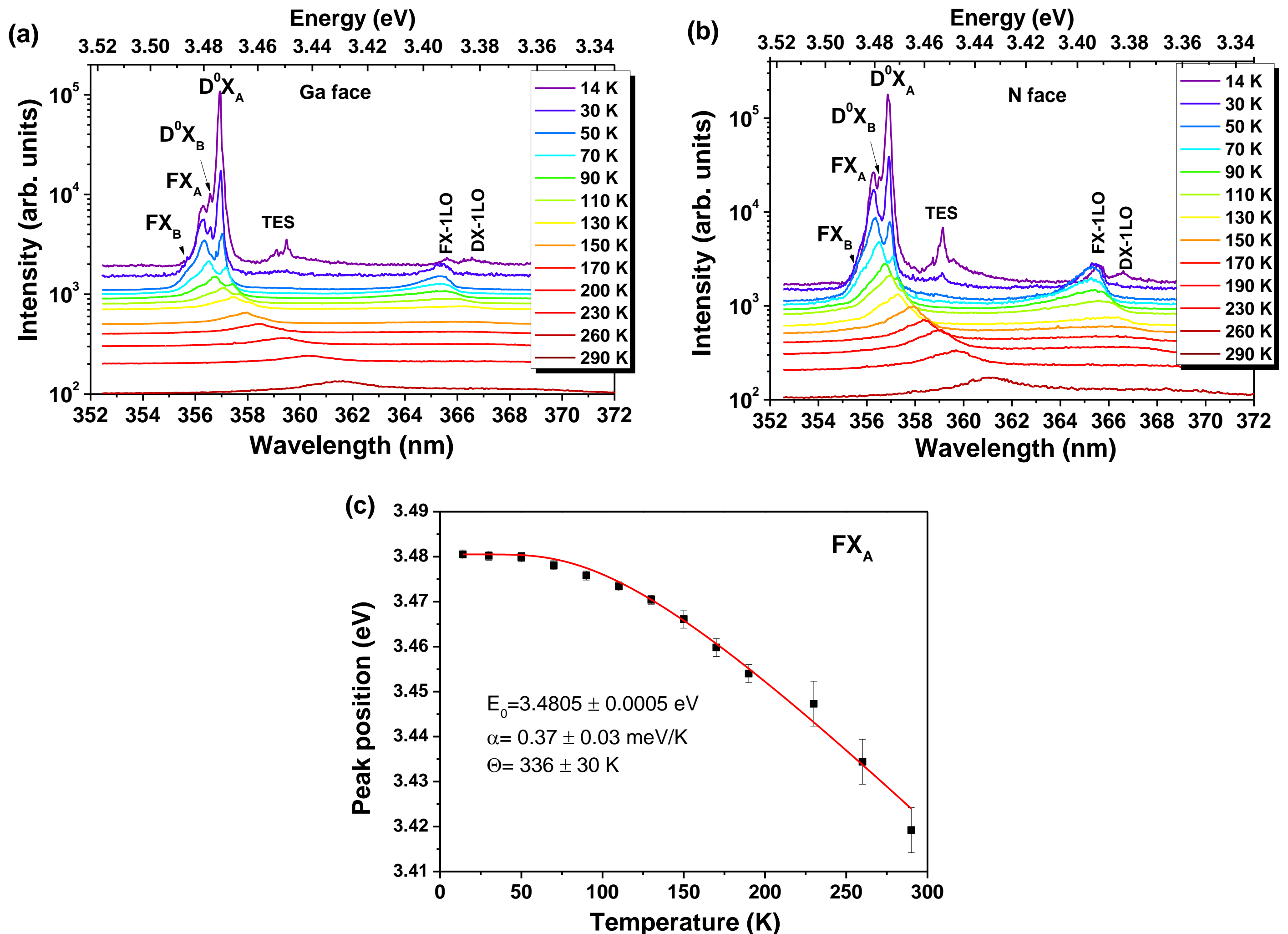

Figure 5-2 – Temperature dependence of the NBE emission from the (a) Ga and (b) N terminated faces for the U245 sample. The spectra were acquired under 325 nm excitation and were vertically shifted for clarity. (c) Evolution of the energy peak position of the A exciton as a function of temperature. The experimental results were well fitted with Eq. 1-3.

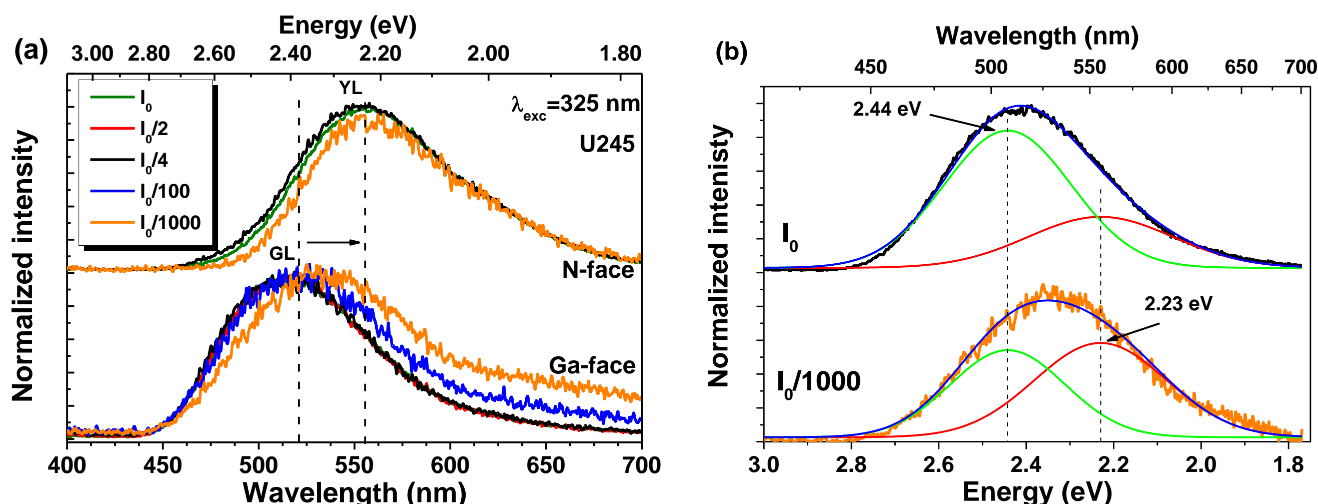

Figure 5-3 – (a) Low temperature PL spectra obtained with 325 nm at different excitation densities for both Ga and N faces of U245 sample. (b) Deconvolution of the GL band into two Gauss components.

5.2. Intentionally induced yellow luminescence in GaN nanowires

NWs are characterized by a large surface to volume ratio which poses additional questions to be addressed in view of a successful application of these nanostructures for electronic and optoelectronic purposes. Devices based on NWs are very sensitive to surface effects, being very attractive for sensing applications [15]. However, the presence of these effects could be detrimental for some devices. Particularly, the presence of a high density of surface states leads to the pinning of the Fermi level at the surface and electronic band bending in the vicinity of the surface, forming a space charge region, which affect the GaN NWs recombination processes and constitute a crucial phenomenon to be controlled for improving the performance of NWs based devices [15–17]. Dangling bonds, point defects and surface adsorbed species lead to charged surface states and were shown to influence the optical and transport properties of NWs [15,18,19]. Recently reports have evidenced the impact of surface states on the charge transport properties of GaN NWs [15,17,19]. For the case of surface sensitive luminescence, most reported studies focused on the surface properties of the GaN NWs NBE recombination and not on the deep defect levels, which is the focus of the analysis presented in this section [20–22].

In the works reported by Calarco *et al.* [15,17] the authors claim that, in the case of unintentionally doped GaN NWs exhibiting a *n*-type behaviour, the Fermi level is assumed to be independent of the dopant concentration and is pinned at the surface at a position close to 0.5 - 0.6 eV below the CB minimum, leading to a upward bending toward the surface, as represented in Figure 5-4. In this sense, the electrons need to overcome a potential barrier to reach the surface (from the bulk), forming an electron depletion region. Figure 5-4 shows a model assuming cylindrically shaped NWs with a uniform distribution of dopants. Different effects can take place depending on the diameter of the NW when compared with the width of the depletion layer. In the case of thicker NWs, it is assumed that the centre of the wire (bulk) preserves the

free electron concentration related to the doping level, while the surface is depleted. However, for thinner NWs the depletion region may spread over the whole volume. The critical diameter at which the NWs are fully depleted is assumed to be around 30 - 40 nm [15], which corresponds to the size of the NWs studied in this section. Unlike the Fermi level pinning, the width of the surface depletion layer depends on the doping concentration and increasing the doping concentration reduces the surface depletion layer thickness [15]. Electrons are likely to reside in the inner part of the wire, whereas holes tend to move to the surface [17]. The surface recombination can be hindered or even supressed due to this spatial separation of the carriers caused by the band bending [16,17]. The photogenerated electrons have to move to the NW lateral surface to recombine with the photogenerated holes that, due to depletion layer field, reside already there [16]. Electrons have to surpass the CB barrier at the surface for recombination to take place [17]. However, as depicted in Figure 5-4, further shrinking of the dimensions leads to a decreasing of the band curvature and therefore a reduction of the barrier for surface e-h pair recombination, which is thus strongly enhanced [16].

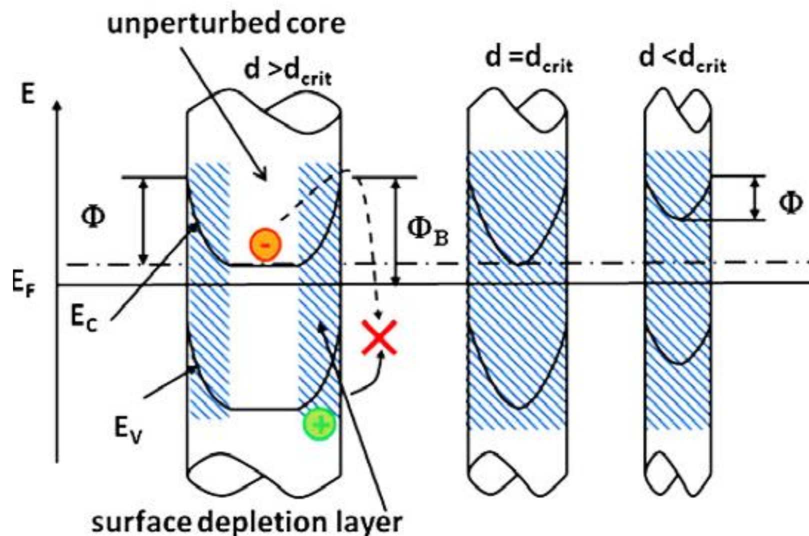

Figure 5-4 – Schematic model of electrical fields in NWs induced by Fermi level pinning at the sidewall surfaces. Different scenarios of the depletion regions (shadowed areas) according to the NWs diameter are considered. Φ corresponds to the barrier for electrons to reach the surface and Φ_B is the Fermi level pinning position at the surface. E_C, E_V, and E_F denote the bottom of CB, the top of VB and Fermi energies, respectively [15]. (The relative energetic location of the different levels is not to scale.)

In this section, the attention is focused on the influence of surface states on the YL in GaN NWs. As mentioned in the previous chapter, the YL corresponds to one of the most studied optically active defects in bulk GaN and GaN layers [12,13] but the chemical nature of the involved defect (*e.g*. V_{Ga}, $V_{Ga}O_N$ and C_N defects [14,15]) is still under debate. Additionally, the type of transition and defect location (in depth or at the surface) are still a matter of discussion [11].

When inspected by PL spectroscopy, the recombination processes of *c*-axis oriented GaN NWs grown by PAMBE are typically dominated by the high energetic transitions in the near bandgap region [17,18]. Nevertheless, the YL in as-grown GaN NWs can be observed under non optimized growth conditions, as reported for the case of NWs ensembles grown on sapphire by Ni catalytic assisted MOCVD [7,8,19]. For GaN NWs, recent theoretical calculations indicate that the most

stable location for the native point defects is in the surface region [30] and the analysis of the spatial distribution of surface defects by panchromatic CL clearly reveals a surface layer with strong YL in thick NWs [29], likely to be associated with the predisposition of the defects/impurities to segregate for the surface [31].

In the present study, YL recombination was intentionally induced/enhanced in PAMBE grown GaN NWs by post-growth sample annealing and ion implantation. In order to investigate the surface interaction effects on the induced YL, the illumination/irradiation time dependence of the RT PL was analysed. Furthermore, the RT YL PL response, performed under continuous UV excitation, was studied in air and vacuum ambiences. The analysis of the photodegraded luminescence is in line with oxygen photoadsorption and photodesorption processes previously reported by others [11,22]. In order to further study the stability of the YL recombination, the GaN NWs were submitted to surface treatments, such as hydrogen plasma etching, wet chemical acid bath and dielectric passivation by using amorphous silica as coating.

Figure 5-5 shows SEM images of the two sets of as-grown GaN NWs used in the current experiments. As observed, the NWs are vertically aligned and are randomly spaced. Both sets of NWs are *c*-oriented, with a length of ~ 0.3 μm in the case of the N1005 set and ~ 1.0 μm long for the NW1928 set. The diameter was similar in both sets (20 - 40 nm). In the case of the NW1928 samples a thin 2D layer could be found in some regions of the NWs array.

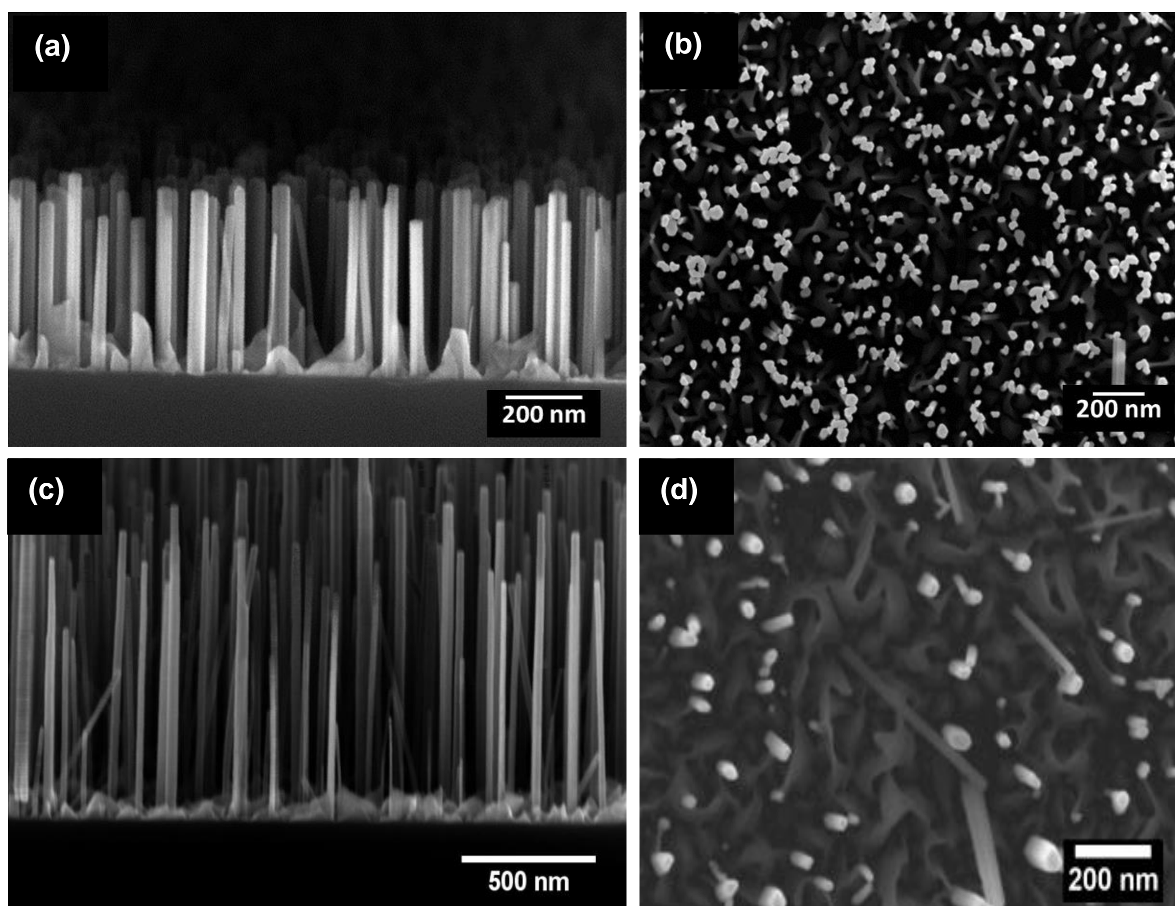

Figure 5-5 – SEM side and top view images of the studied NWs before the implantation and annealing processes: (a) and (b) N1005 and (c) and (d) NW1928.

Low temperature and RT PL spectra for both as-grown samples are present in Figure 5-6. At low temperature it is possible to see a well-defined NBE emission of the GaN NWs, especially in the case of the N1005 sample where both FX and D^0X centres can be well identified. In the case of the NW1928 sample, a broader NBE emission is likely due to a higher dopant concentration introduced unintentionally during the growth process. The RT luminescence is also dominated by the high energy NBE transitions. A total absence of the YL in the case of sample N1005 is evidenced [28]. Importantly, it has to be stressed that the residual vacuum was degraded during the growth of NW1928, which resulted in the presence of a weak YL band. This band was not observed at low temperature due to its weak relative intensity when compared with the NBE emission, but it is visible at RT, though still with a relative intensity much weaker than that of the NBE.

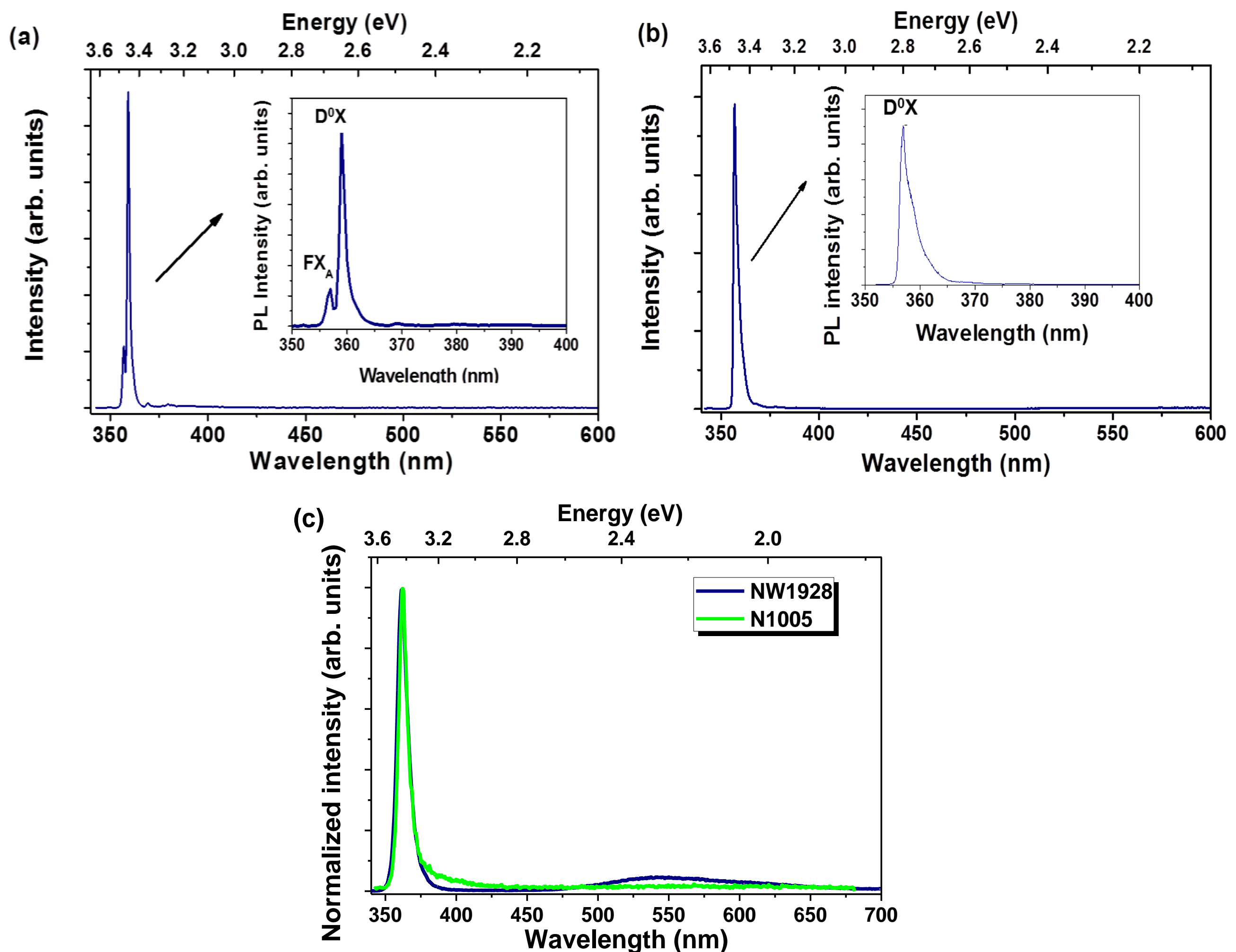

Figure 5-6 – (a) and (b) Low temperature and (c) RT PL spectra observed upon He-Cd excitation of the as-grown GaN NWs (N1005: upper left figure, NW1928: upper right figure). The RT PL spectra were taken in air ambience.

In order to induce/enhance the YL, the GaN NWs were submitted to Er ion implantation and post-implant thermal annealing treatments. SEM analysis revealed that after implantation and annealing the majority of the NWs remain morphologically unchanged and vertically aligned, as shown in Figure 5-7a. For the case of sample NW1928 an additional reference annealed sample

was prepared (NW1928a). As shown in Figure 5-7, the post-growth treatments promote the appearance/increase of the YL intensity. After annealing, the YL of sample NW1928 was seen to increase in intensity by a factor of ~ 2 while a decrease was observed for the NBE recombination by approximately the same factor (Figure 5-7b). When implantation and annealing were performed, the NBE recombination was almost extinguished, and the YL became the dominant recombination (factor of ~ 3) in the NWs (Figure 5-7b). The YL band shows the same spectral shape and position for both samples, as evidenced in Figure 5-7b. PLE measurements on this band revealed that the preferential population pathway is via above bandgap excitation (Figure 5-7c).

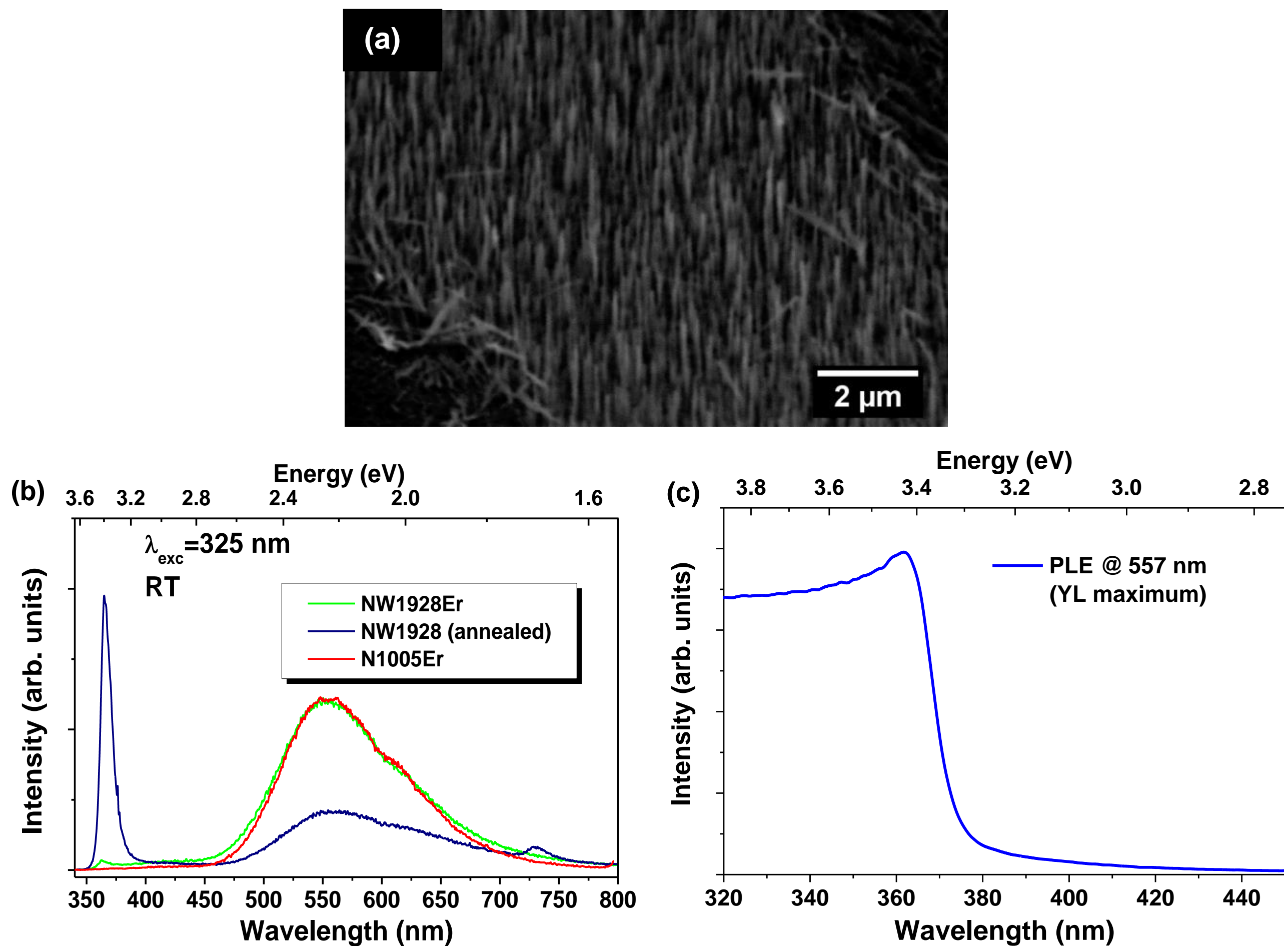

Figure 5-7 – (a) SEM image of Er implanted and annealed sample NW1928Er. The corresponding RT PL observed upon He-Cd excitation is shown on the right side picture (b). The spectra were taken in air ambience. (c) RT PLE spectra monitored on the YL maximum (sample NW1928Er).

The implanted and annealed NWs were characterized by Raman spectroscopy, as indicated in Figure 5-8. Both samples exhibit very similar Raman spectra. As mentioned in Chapter 1 and taking into account the considerations of group theory, it was reported that eight sets of phonon modes are allowed at the Γ point: $2A_1+2E_1+2B_1+2E_2$ [33]. Among these vibrational modes only A_1, E_1 and E_2 are Raman active. Since GaN is a noncentrosymmetric material the A_1 and E_2 modes are split into LO and TO [34]. Figure 5-8 shows typical Raman spectra of the hexagonal GaN NWs where the A_1 TO and LO modes and one of the E_2 modes were identified. These three modes appear at 538, 567 and 734 cm^{-1}, respectively, which is in good agreement with the values found

in literature [33]. Additional modes appear at 521, 673 and 890 cm^{-1}. These modes can be attributed to defect related phonons [35] or to the relaxation of the *k = 0* selection rule due to surface disorder of finite crystalline size, allowing new modes that correspond to *k ≠ 0* phonons, as reported elsewhere [34].

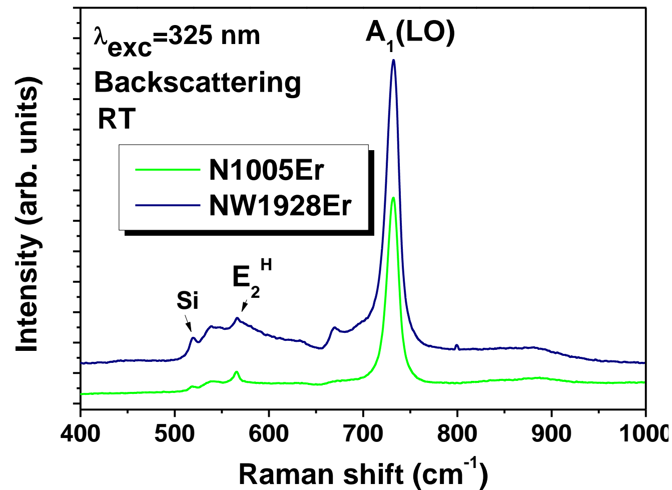

Figure 5-8 – Raman spectra for the NWs implanted and annealed. Similar results were obtained in all samples.

The YL in the implanted and annealed GaN NWs showed that photodegradation of the emitting defect occurs as a function of increasing photon illumination time (Figure 5-9). The normalized broad luminescence intensity as a function of the exposure time is shown in Figure 5-9c. The measurements were performed at RT in two different experimental environments, considering the luminescence evolution in air and vacuum. Under photon illumination, the YL photodegradation is higher in the case of the GaN NWs in air than for the vacuum case. In the first case, the YL peak intensity decreased about 70% in 240 minutes, while in vacuum environment a minimal degradation occurs (PL intensity suffers a decrease of less than 30 % for the same exposure time). This feature contrasts to the one found for the YL in GaN layers (Figure 5-10) where only a slight decrease of the emission intensity was observed and the same behaviour was identified for both air and vacuum conditions.

The formation of lattice defects acting as nonradiative centres, such as aggregates and dislocation loops, have been pointed out as one of the possible mechanisms to explain such luminescence intensity decay in semiconductor nanostructures [36,37]. Dissociation of defect complexes can also be responsible for this behaviour. Since the PL recombination degradation was found to be sensitive to the sample environment other surface mediated processes may also account for the instability of the YL. Nevertheless, this constitutes a strong indication that this band is likely due to surface defects. One of the frequent assignments of the YL is to V_{Ga}. Isolated V_{Ga} were reported to become mobile at 500 - 600 K with estimated migration energy of 1.5 eV. Thus, the surface-related YL may be caused by the diffusion and pilling up of mobile point defects, such as V_{Ga} [29], promoted by implantation and high temperature annealing (1000°C). V_{Ga} may be created during the implantation process and can be further diffused to the surface of the wires. These defects have also be accounted as a possible origin for the pinning of the Fermi level and

the position of the vacancy-related states is in good agreement with the experimental values reported by Calarco *et al.* [15]. As already mentioned, the presence of surface defects creates an electrical field in the NWs. If the strength of this field changes, the PL intensity will be affected [15]. This change can be accomplished by phenomena like photo-promoted adsorption/desorption of chemical species that may form paths for the competing nonradiative recombination. The photodesorption of oxygen from semiconductor surfaces is well known and is caused by charge transfer with photogenerated holes migrating to the surface and neutralizing the negatively charged adsorbed oxygen. A process like this changes the NWs surface potential and may result in the unpinning of the Fermi level [15].

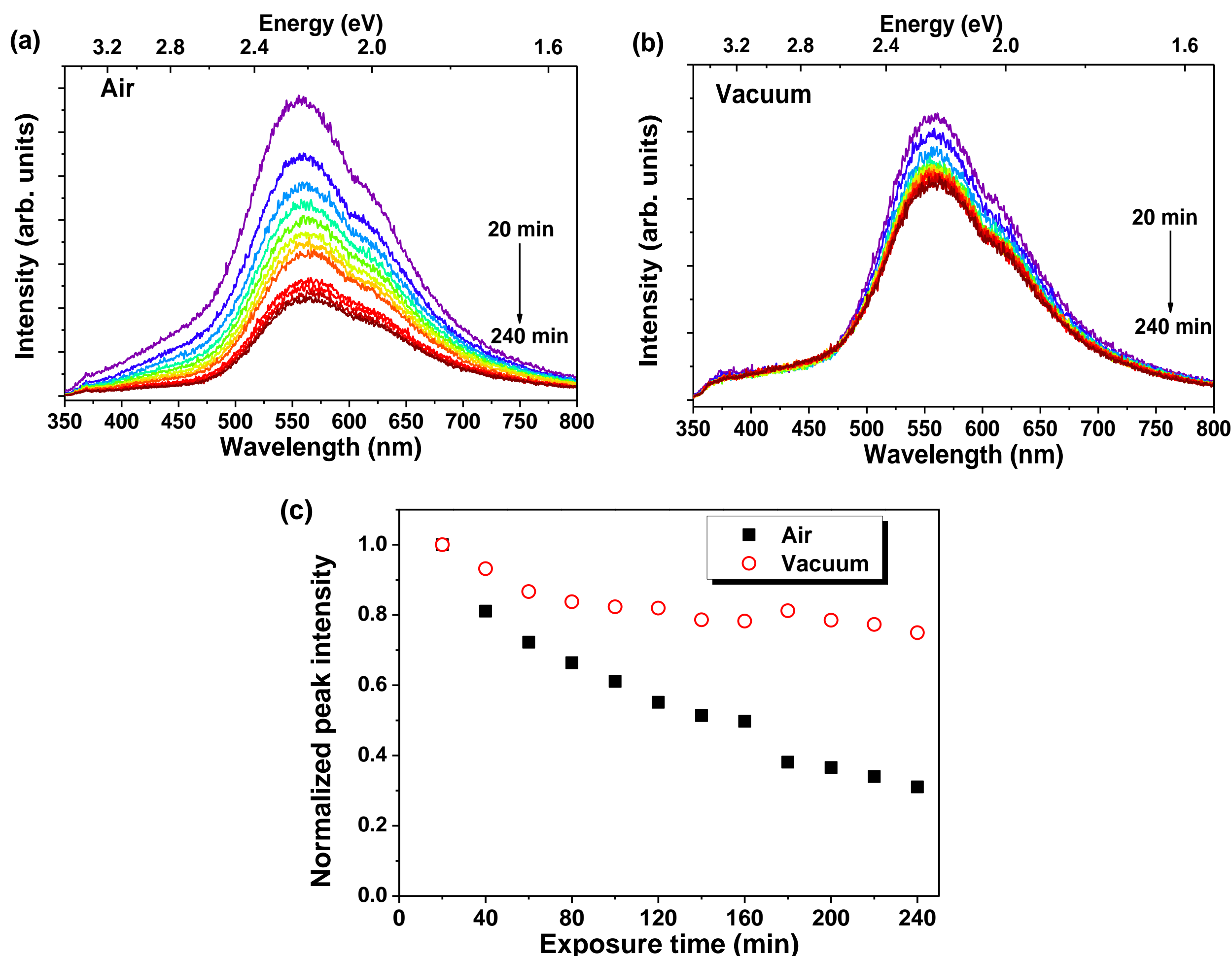

Figure 5-9 – Evolution of the YL spectra with the exposure time measured at RT in (a) air and (b) vacuum for sample N1005Er (implanted and annealed). (c) Maximum peak PL intensity of the YL as a function of the exposition time. Similar behaviour was found for the NW1928Er sample.

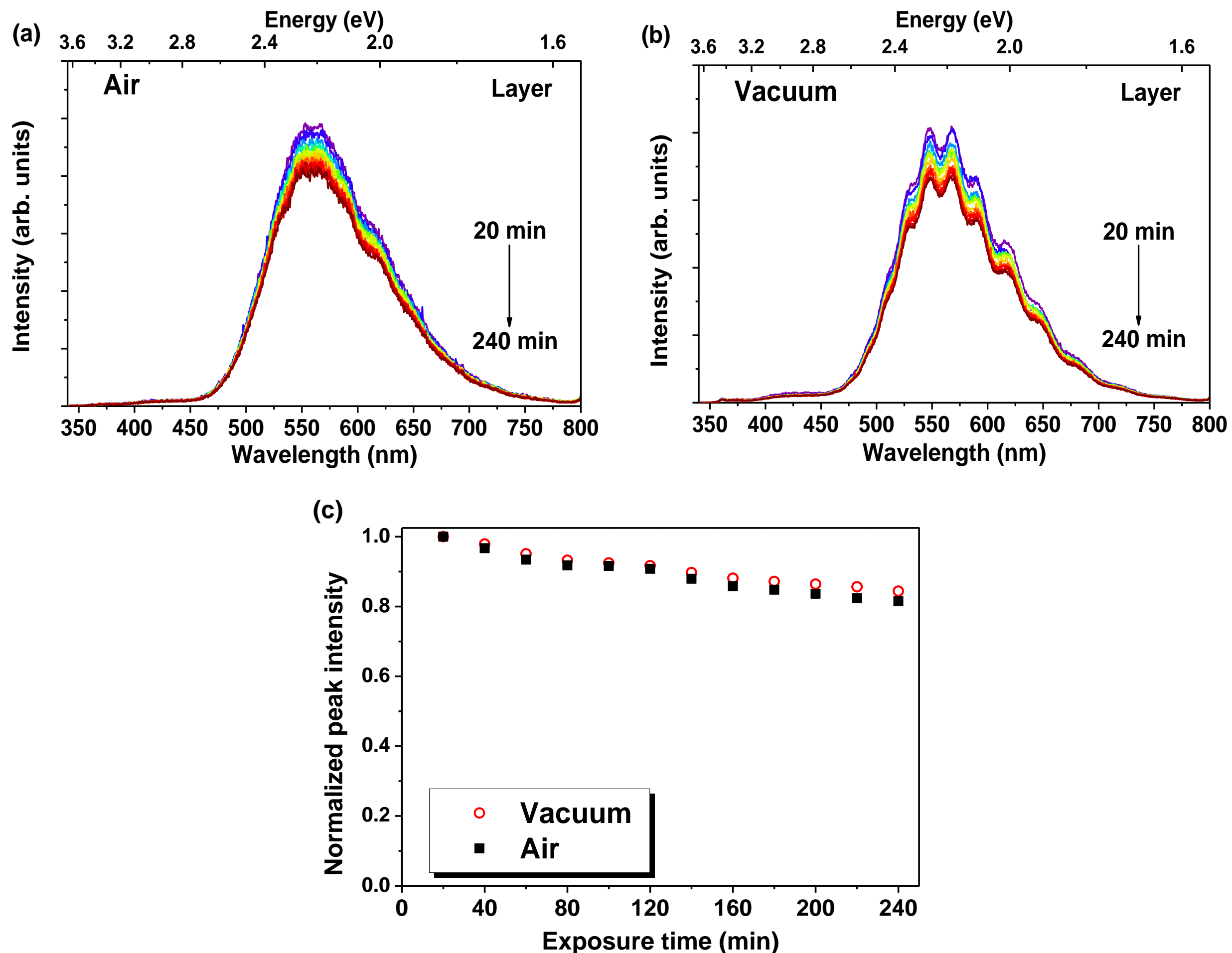

Figure 5-10 – Evolution of the YL spectra with the exposure time measured at RT in (a) air and (b) vacuum for a GaN layer. (c) YL peak intensity as a function of the exposure time.

In order to correlate surface interactions with the YL, distinct surface modifications in the yellow emitting samples were addressed. The samples were submitted to hydrogenation, hydroxylation and silica coating, and the influence of the surface treatments on the YL was studied, as depicted in Figure 5-11 to Figure 5-13.

The different surface treatments led to distinct PL behaviour of the YL intensity, prior and after the surface modification. For the case of the hydrogenated sample, the overall YL was seen to decrease by a factor of ~ 4 after the H_2 plasma treatment (Figure 5-11a) following a similar tendency to the one previously observed in hydrogenated GaN layers [38]. This result is also in line with other reports [39–41], indicating that hydrogenation affects the mid gap level recombination by surface passivation. In contrast, the exposure of the yellow emitting GaN NWs to hydroxylation enhanced the intensity of the YL by a factor of ~ 4.5 when compared with the untreated sample (Figure 5-12a). This behaviour means that either the treatment increases the defect concentration responsible for the YL or it passivates nonradiative defect centres favouring the decay via YL. For the case of the SiO_2 treated sample, no significant difference in the YL intensity was found before and after the treatment (Figure 5-13a).

In the case of the hydroxylated sample (Figure 5-12b), the performed treatment resulted in a detachment of the NWs from the substrate. Their surface presents some roughness, probably due

to some surface degradation during the plasma etching. The wires are seen to be random aligned, with the creation of some bundles, as the one represented in Figure 5-12b. The SEM analysis on the silica coated sample (Figure 5-13b) showed that the NWs are completely coated by the silica layer, while their shape remains unchanged. As in the previous case, also a detachment from the substrate was identified. Raman spectra preformed after each treatment still evidence the vibrational modes expected from GaN (Figure 5-11b, Figure 5-12c and Figure 5-13c), assuring that the surface treatments preserved the GaN integrity.

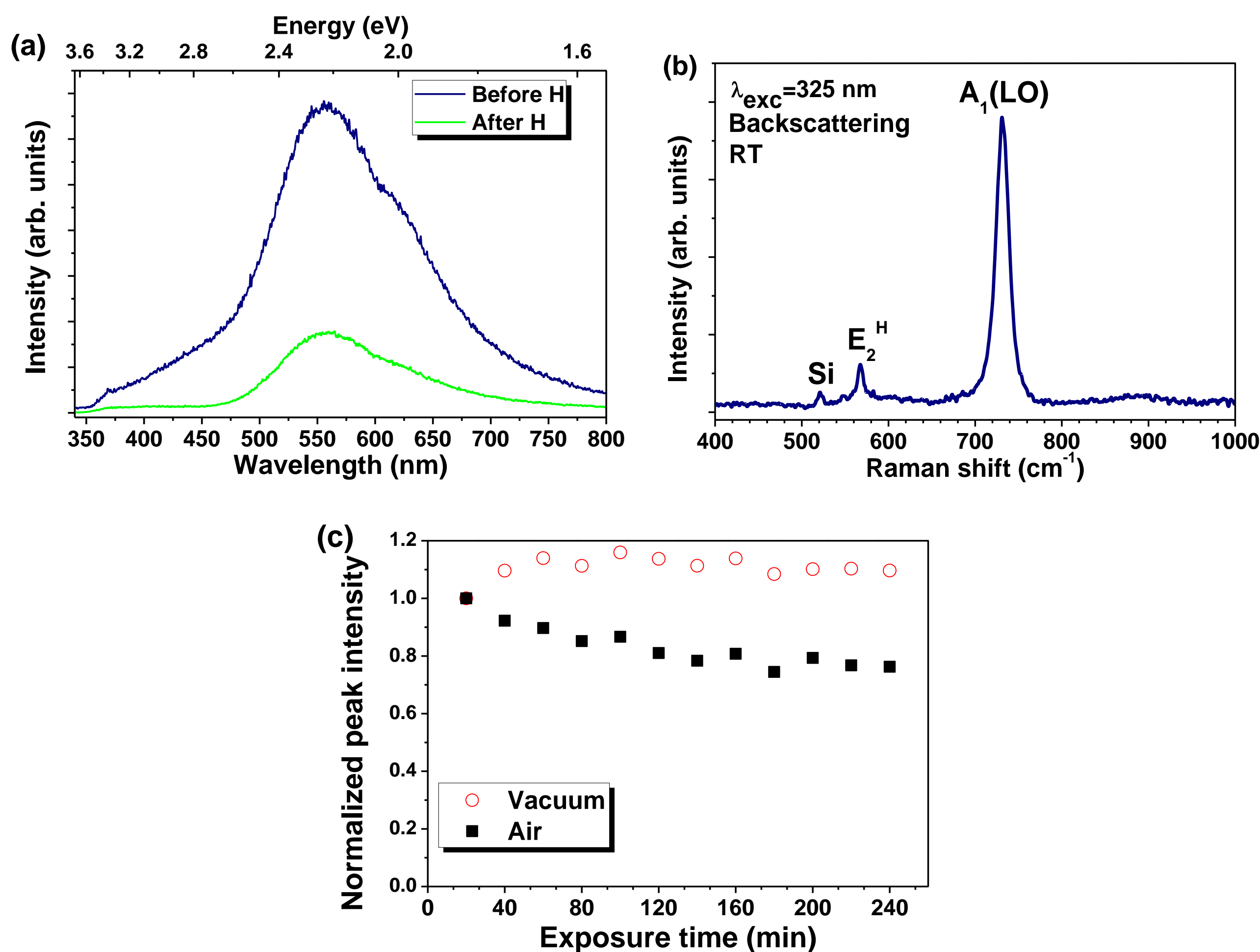

Figure 5-11 – (a) RT PL observed upon He-Cd excitation, (b) Raman spectrum taken with the 325 nm laser line and (c) maximum peak intensity of the YL for the Er implanted and annealed sample passivated with hydrogen (N1005Er).

Besides the RT PL analysis performed in air, the yellow emitting GaN NWs were examined under vacuum conditions. For both environments, the YL stability was observed by PL as a function of the photon illumination time during 4h, like in the case of the untreated samples. All the results evidence that the YL efficiency is sensitive to the measurement ambience and the illumination exposure time. In particular, the nonradiative decay paths which compete with the YL are always superior for samples measured in air than for those measured in vacuum, suggesting phenomena related with oxygen adsorption and desorption, in agreement with the results reported for GaN layers [11,22]. The PL analysis revealed that the YL is nearly stable when

measured in vacuum for all chemical treatments (Figure 5-11c, Figure 5-12d and Figure 5-13d). These data suggest that, for these GaN NWs, the surface treatments and desorbed species promote a higher efficiency of the YL by reducing the nonradiative paths responsible for the photodegration with increasing exposure time. However, despite the surface passivation, photodegradation of the YL is observed under air conditions and with distinct decay rates for the different chemical treatments. In particular, minor photodegradation of the YL intensity in air is seen for the samples passivated with hydrogen (Figure 5-11c), indicating a lower concentration of nonradiative deexcitation routes. In contrast, for samples submitted to hydroxylation, the photodegradation in air is enhanced, counteracting the initial increase of YL intensity after this treatment.

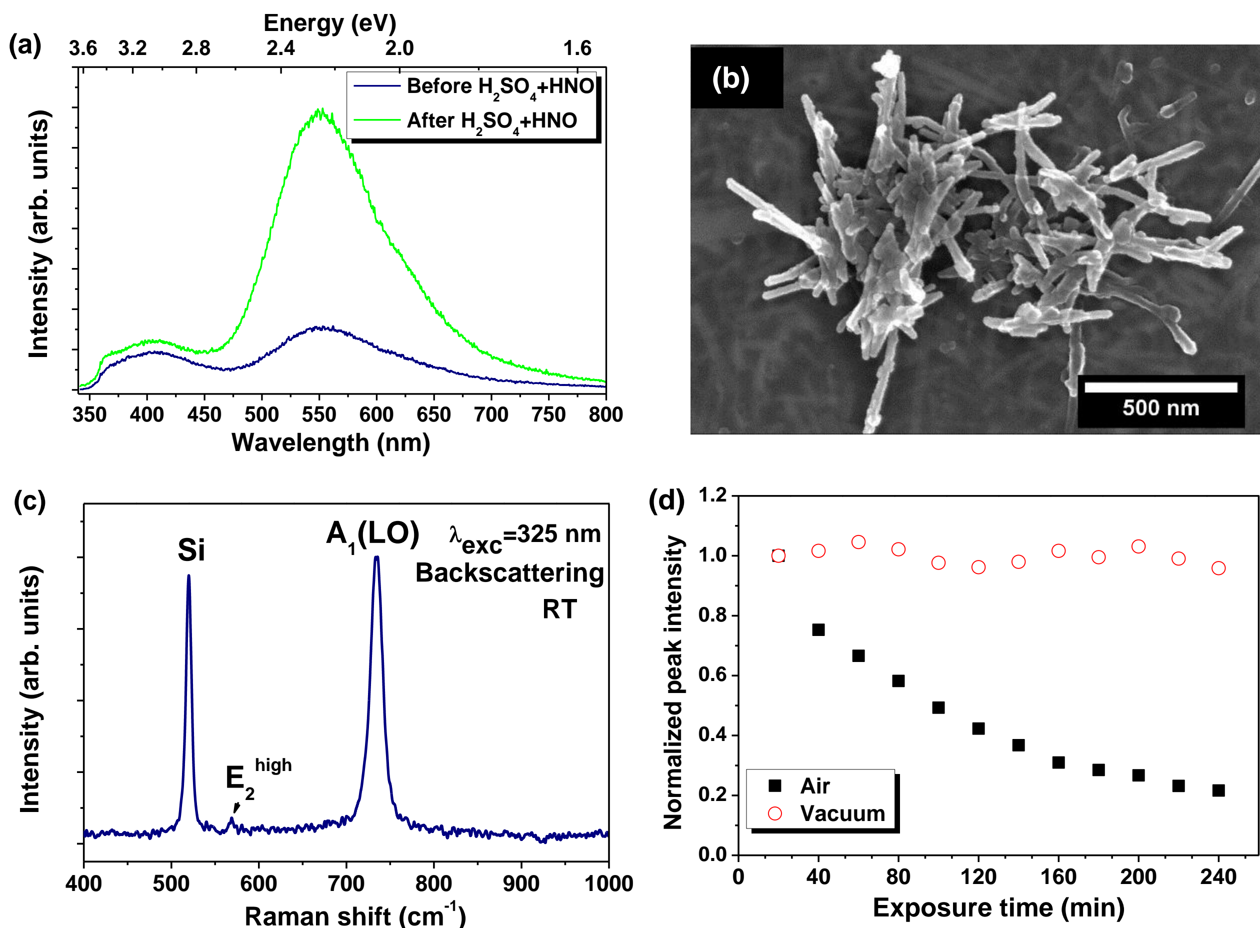

Figure 5-12 – (a) RT PL observed upon He-Cd excitation, (b) SEM top image of the passivated NWs, (c) Raman spectrum taken with the 325 nm laser line, and d) maximum peak intensity of the YL for the Er implanted and annealed sample treated with H_2SO_4+HNO_3 bath (NW1928Er).

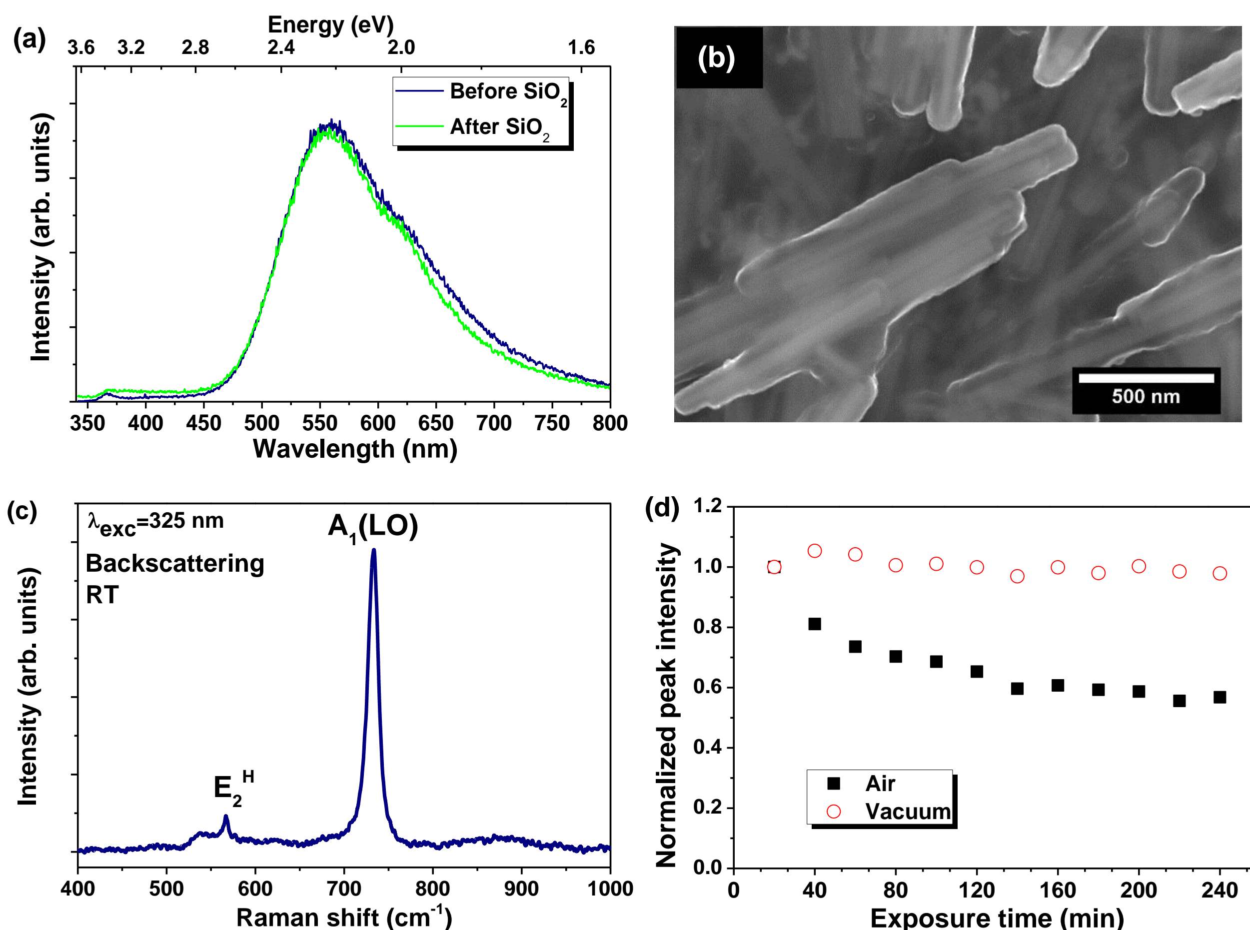

Figure 5-13 – (a) RT PL observed upon He-Cd excitation, (b) SEM top images for the passivated NWs, (c) Raman spectrum taken with the 325 nm laser line, and (d) maximum peak intensity of the YL for the Er implanted and annealed sample coated with SiO_2 (NW1928Er).

The data allowed to conclude that photodegradation mechanisms occur always for samples analysed in air and for the untreated samples analysed in vacuum. For the surface treated samples, a nearly constant YL intensity was found when the samples are probed in vacuum, meaning that under this atmosphere, the nonradiative paths competing with the YL could be suppressed by using surface modification processes. The treatment with hydrogen plasma revealed to be an efficient process to control and improve the YL stability in both environments.

5.3. GaN nanowires implanted with Eu^{3+}

To the best of our knowledge, the optical properties of RE doped GaN NWs were not extensively studied by the scientific community, deserving an in-depth analysis due to their potential application in optoelectronics. Doping NWs is not an easy task due to the low diffusion coefficients of the RE ions, inhibiting *ex-situ* doping by diffusion [42]. The probable segregation of the dopant elements to the surface of the NWs constitutes a challenge when *in-situ* doping is used, as was also reported for other materials [15,31,43]. Considering the *ex-situ* methodology, one approach to dope these nanostructures is by ion implantation [42,44]. As previously

mentioned, this method is a key technology in the semiconductor industry and allows the introduction of dopants in a controlled way and without the limitations of the solubility of the dopant in the matrix [45]. Previous works [46] revealed that it is possible to achieve optical activation of the RE ions in GaN NWs by ion implantation and post-implantation thermal annealing. Trivalent europium (Eu^{3+}) ions are known to be efficient red activators in several wide bandgap hosts. Europium ions are amongst the most studied RE incorporated in nitrides either by *in-situ* or *ex-situ* doping processes. Due to their intra-$4f^{6}$ electronic configuration, the visible emission from Eu^{3+} ions in the orange-red spectral region arises from transitions between the crystal-field split energy levels of the $^5D_0$ and ^7F_J manifolds [47–49].

In this section, it is presented a study carried out on different GaN structures (layers and NWs) doped with Eu^{3+} by ion implantation. The samples were implanted with tilted angles of 20° and 30° relatively to the *c*-axis, in order to evaluate the influence of the implantation angle on the samples optical properties. Post-implantation thermal annealing was performed in the same conditions for all the samples in order to recover the lattice damage and promote the optical activation of Eu^{3+}. The spectroscopic features of the doped structures were studied by means of Raman spectroscopy, PL, PLE and TRPL. All the implanted and annealed samples exhibit the intra-$4f^{6}$ emission from the Eu^{3+} ion along with a broad unstructured YL.

Commercial GaN layers (Lumilog), ~ 3 μm thick, implanted simultaneously with the NWs were used as reference samples. Monte Carlo simulations using the SRIM code [50] were performed to estimate the ion distribution in the samples. For layered GaN samples, these simulations yield values for ion range and straggle of 52.0 nm and 18.6 nm for 20° incidence angle and 48.1 nm and 18.0 nm for 30° incidence angle, respectively. In the case of the NWs, a part of the ions will be implanted into the side facets of the NWs with SRIM estimated values for range/straggle (calculated from the side facet) of 16.5 nm/10.9 nm and 21.8 nm/13.1 nm, respectively, for 20 ^{o} and 30 ^{o} incidence angle. Although the non-planar geometry of the NWs will influence the final distribution of ions inside the NWs [42], these simulations show that most of the ions will come to rest well inside the NW crystal. This assumption is also supported by recent molecular dynamics simulation for Er implantation into GaN NWs using similar parameters as those used in our experiment [51].

Different set of NWs and layer samples implanted with fluences ranging from 1×10^{13} Eu.cm^{-2} to 3×10^{15} Eu.cm^{-2}, as indicated in Table 2-2 (Chapter 2), were measured by PL at low temperature. Since the main features of the PL spectra did not vary significantly, a selection of samples was chosen to study in detail, namely NW2030b, NW2030g and NW2032c and respective reference layers.

Figure 5-14 shows SEM images of the (a) side and (b) top views of the as-grown GaN NWs (NW2032). The NWs are vertically aligned exhibiting lengths between 1500 and 2300 nm and a mean diameter of 140 nm. The density of the NWs was estimated to be higher than 8.4×10^{9} NWs cm^{-2}. No 2D GaN layer between the buffer layer and the NWs was found for the present samples. Some coalescence between the wires is also observed due to the high density of NWs array. Figure 5-15 depicts top view SEM images of the implanted and annealed NWs: NW2030b, NW2030g and NW2032c. As can be inferred by the SEM images of the nanostructures,

the implantation and thermal annealing procedures did not seem to affect significantly the NWs morphology.

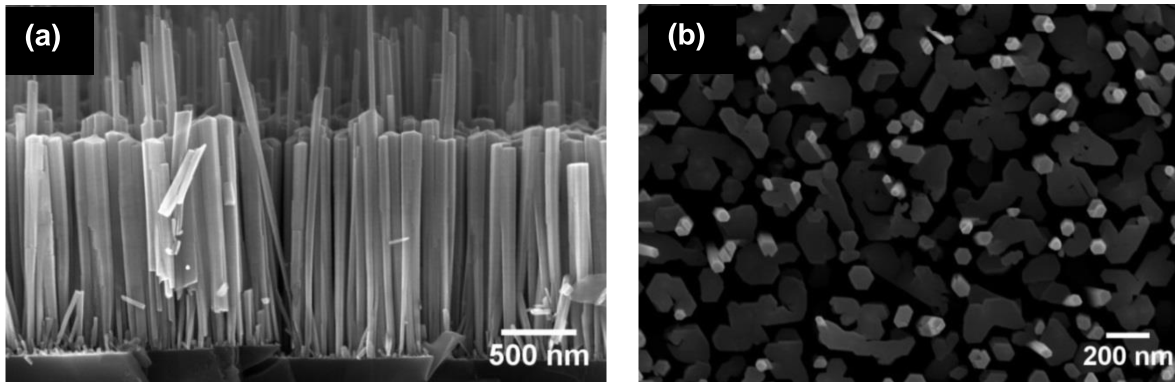

Figure 5-14 – (a) Side view and (b) top view SEM images of the as-grown GaN NWs (NW2032 before ion implantation).

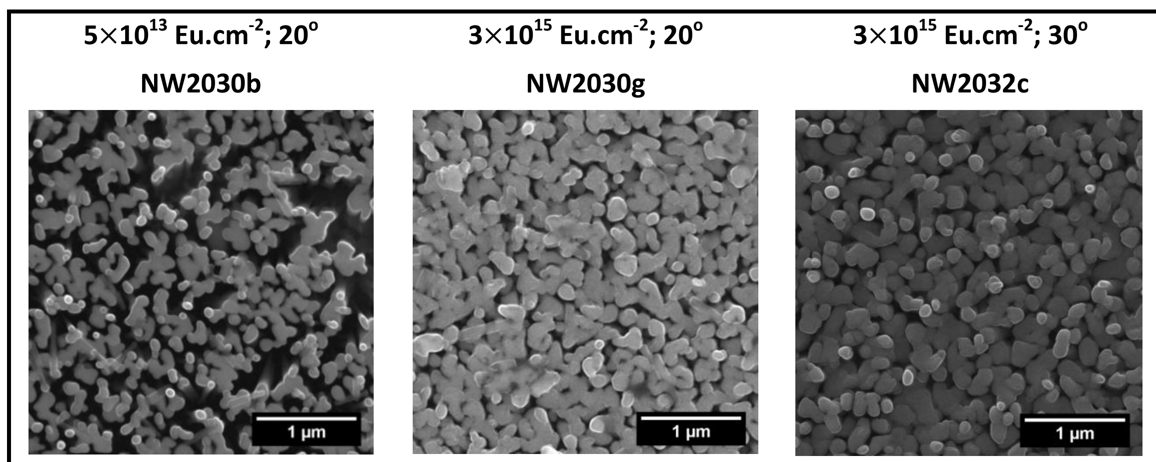

Figure 5-15 – SEM micrographs of the NWs. All the samples were annealed in the same conditions as mentioned in Table 2-2 (Chapter 2).

The structural characterization was evaluated by Raman spectroscopy in the backscattering geometry $x(y,\cdot)\bar{x}$ (see Figure 5-16), in order to minimize the signal from the substrate. The results are shown in Figure 5-17. Raman studies revealed that the E_2^H phonon mode of the as-grown NWs is shifted by 2 cm^{-1} to lower energies relatively to the as-grown GaN layer reference sample, indicating that the NWs are under tensile strain (Figure 5-17a). After implantation, Raman spectroscopy measurements allowed the observation of the phonon DOS activation induced by the damage in the crystalline lattice [52,53] (Figure 5-17 b). After annealing, the Raman spectrum evolved to a spectrum dominated by first-order processes, where the GaN phonon modes of the centre of the first Brillouin zone (E_1(TO); A_1(TO) and E_2), predicted by the selection rules, for $x(y,\cdot)\bar{x}$ scattering geometry, are expected. The measured phonon frequencies coincide with the ones obtained for the as-grown NWs, indicating that the state of strain is the same for as-grown and annealed samples and the recovery of the crystalline lattice was achieved.

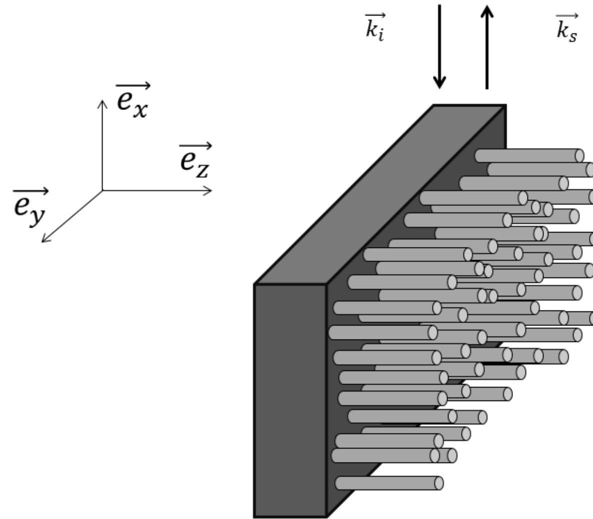

Figure 5-16 – Schematic representation of the scattering configuration used in the Raman measurements.

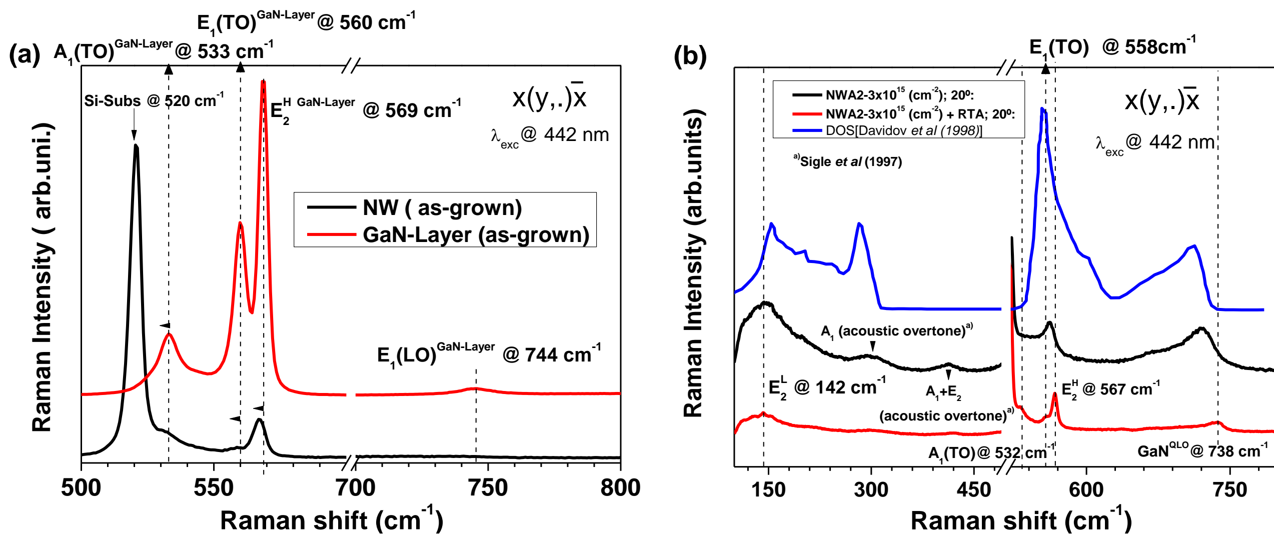

Figure 5-17 – Raman spectra of the (a) as-grown layers and NWs and (b) NWs implanted with 3×10^{15} Eu.cm^{-2} and an angle of 20° before and after the annealing. The theoretical density of states is depicted for comparison.

5.3.1. Low temperature PL

5.3.1.1. UV-Vis-NIR spectral range

Figure 5-18 displays the 14 K PL spectra of the NWs and GaN layers implanted and annealed under the same conditions. The extended PL spectra over the UV, visible and NIR spectral range (Figure 5-18a) were obtained with 325 nm photon excitation, corresponding to an energy above the GaN bandgap. Figure 5-18b depicts high resolution spectra of the Eu^{3+} ion-related emission lines for all the samples. Independently of the implantation angle and fluence, the samples (NWs and layers) exhibit sharp red lines corresponding to the $^5D_0\rightarrow{}^7F_{J\,(1-4)}$ transitions (Figure 5-18b), due to the intra-4$f^{\,6}$ transitions of the Eu^{3+} ion. The schematic energy diagram for the Eu^{3+} levels is

depicted in Figure 5-19. In addition to the intraionic luminescence, other optically active centres, such as D^0X, DAP and broad visible bands can be also identified (Figure 5-18a). The GaN layers show well defined D^0X and DAP transitions, whereas for the NWs only the sample implanted with lower fluence evidences a broad NBE recombination and DAP transitions. The intensity decrease of the NBE emission associated with a strong DAP emission constitutes an indication of a high dopant concentration introduced unintentionally during the growth process, as corroborated by the spectrum of the as-grown NWs sample (Figure 5-18a). An increase of the NBE broadening is further promoted by the implantation and annealing processes. With the exception of the lower fluence NWs, and as a general trend, all the implanted and annealed NWs exhibit higher intensity ratio of the Eu^{3+} emission/NBE when compared with the GaN layers submitted to the same treatments. Notwithstanding, it is important to note that a higher implanted volume fraction is found in the NWs as compared with the layers, so a contribution from the unimplanted deep layers is also present.

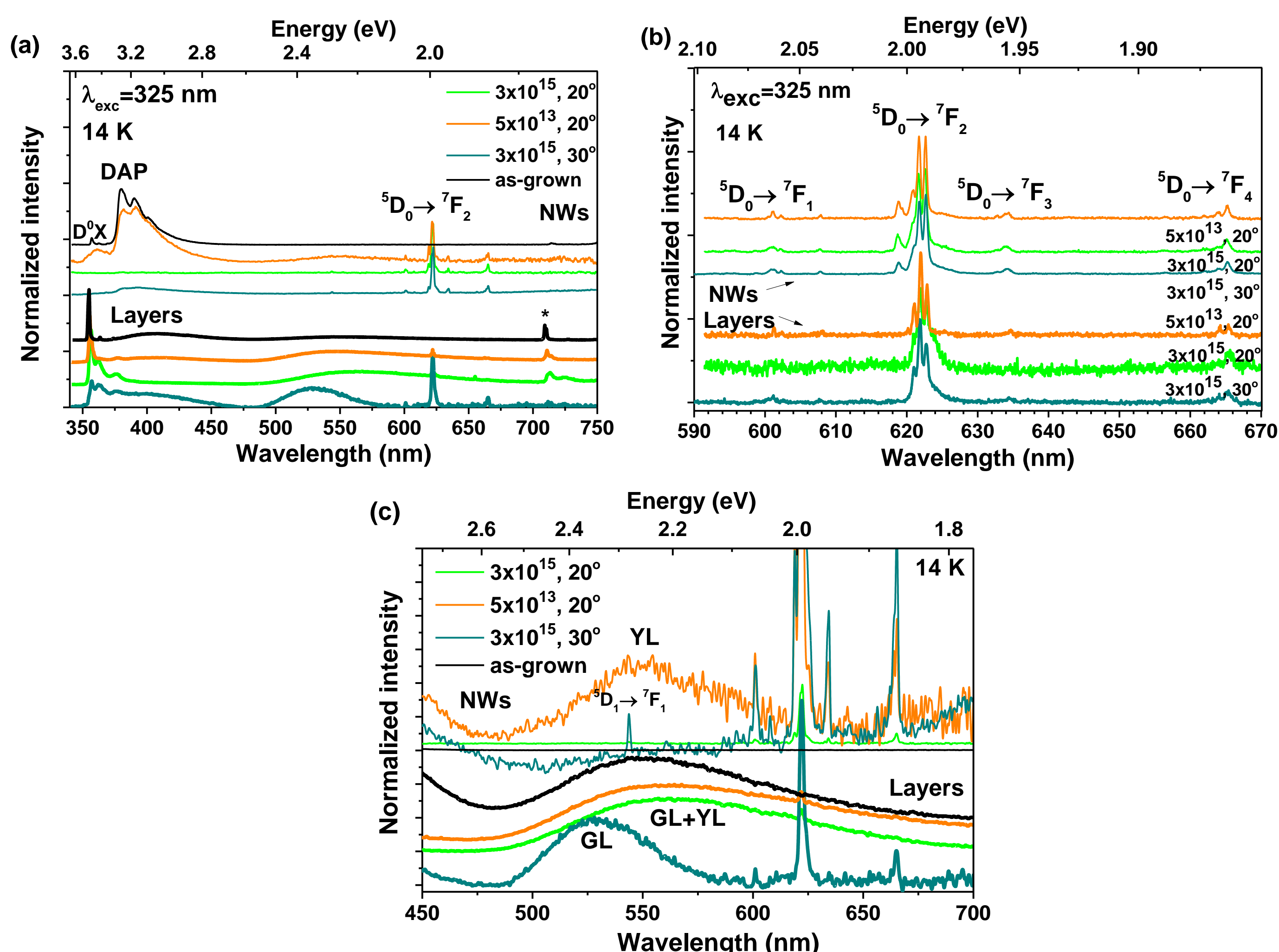

Figure 5-18 – (a), (b) and (c) Low temperature PL spectra of the selected NWs and layers implanted with Eu^{3+} ions, acquired with above bandgap excitation (He-Cd, 325 nm). Figure 3 (b) depict high resolution spectra of the ion-related emission lines while figure (c) displays the PL spectra of the visible spectral region (green/yellow luminescence spectral region).

Concerning the deep defect recombination, a special attention should be paid to the YL identified both in the implanted and annealed NWs and layers (Figure 5-18c). As mentioned in Chapter 4 and in the first section of this chapter, the YL in undoped and doped GaN layers is frequently attributed to DAP (involving a shallow donor) or free-to-bound (e-A) transitions [11,7,10,54,55,6,56] and to V_{Ga} or their $V_{Ga}O_N$ complexes in the 2-/- charge states [6,7,10,11,54–56]. As observed in the GaN bulk sample, the GL also constitutes a frequent feature of the GaN PL spectra. This GL can be ascribed to -/0 states of the same defect where the YL takes place [6,56]. It is known that different defects may result in luminescence bands in the same spectral region, so the presence of other defects cannot be discarded. In the present study, some differences were found for the layers concerning the spectral shape and peak position of the broad bands in the visible region, in a similar way with what was observed for the bulk GaN sample. While for the layer implanted with higher fluence the emission is dominated by the presence of the GL, with the YL showing a negligible intensity when compared with the remaining emissions, for the remaining layers (including the as-grown) both GL and YL appear to be present with comparable intensities. These observations suggest the presence of different defects or the same defects in different charge states. The GL observed in the sample implanted at 30° exhibits a peak position and a spectral shape similar to the one measured by Reshchikov, that was ascribed to the presence of nitrogen vacancies [57]. The different relative intensity of the GL and YL is likely to be due to inhomogeneity of the defects distribution in the layers. In the case of the NWs, the YL is also identified for the implanted and annealed samples, excepting the case of the NW2030g sample, where the YL intensity is negligible when compared with the ion-related emission. It is important to note that, contrary to what was verified in the layers, this band is not present in the as-grown samples, suggesting an induced/enhanced YL recombination in GaN NWs by ion implantation and post-growth annealing, as reported in the previous section [58]. The presence of this YL in the implanted and annealed samples is more clearly observed at RT due to a higher YL/ion emission intensity ratio [not shown here, but present in the RT PL/TRPL spectra (see section 5.3.2.)]. Despite the fact that the emission occurs in the same spectral region of the YL in the layers, its spectral shape and peak position are slightly different. From the work reported in section 5.2, it is assumed that the YL in the NWs is related to a surface mediated recombination process, as suggested by the previous studies [58]. In the case of the NWs studied in this part, the difference between the YL of layers and NWs will be further discussed based on the RT recombination kinetics (section 5.3.2.2).

5.3.1.2. *Intra-4f^{6} Eu^{3+} luminescence*

Enlarged spectra of the 14 K intra-shell Eu^{3+} luminescence for the implanted and annealed NWs and GaN layers are depicted in Figure 5-20a. As currently identified in nitrides, the Eu^{3+} emission is dominated by the electric dipole transition between the $^5D_0$ and $^7F_2$ multiplets [59–62]. The peak position and line assignments of the Eu^{3+} transitions identified in the studied samples are compiled in Table 5-1.

For the hypersensitive $^5D_0 \rightarrow ^7F_2$ transition, the energy peaks are different, depending on where they are observed, whether in NWs or layers. As a general trend, the crystal field split Stark lines

deviate ~ 1 meV to lower energies in the GaN layers when compared with those in NWs. This shift could be attributed to different strain states on the GaN layers and NWs, as suggested by the Raman measurements. A similar effect was obtained for Pr^{3+} doped GaN layers and NWs, as will be presented in the next section [63]. In addition to the shift, the relative intensities between the emission lines from the $^5D_0$ multiplet to the unfolded sublevels of the $^7F_2$ multiplet are dissimilar for NWs and GaN layers. These findings point out that strain induced different transition probabilities between the $^5D_0$ level and the unfolded $^7F_2$ Stark levels, as also noticed for europium doped GaN layers with different thicknesses [64].

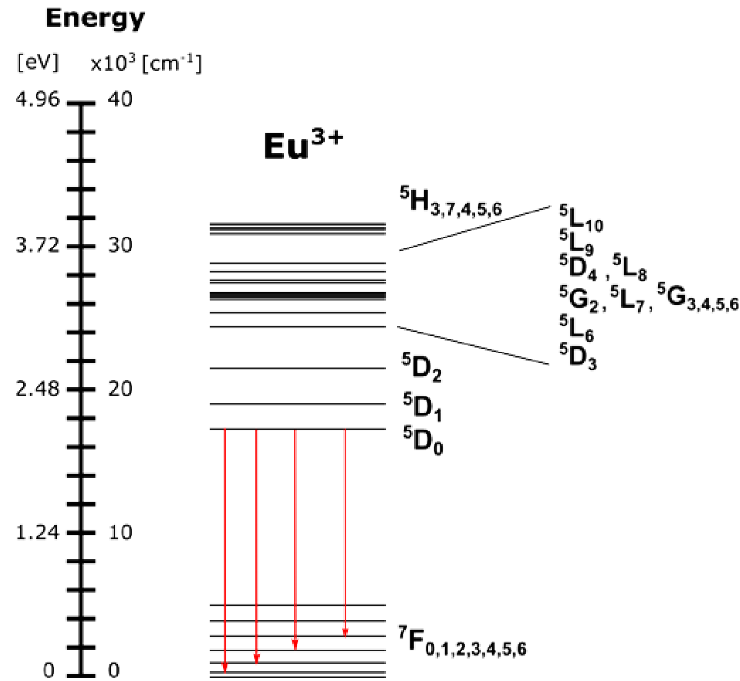

Figure 5-19 – Schematic energy diagram of the Eu^{3+} free ion. The energy levels were constructed based on reference [65]. The arrows indicate the transitions observed in the studied samples.

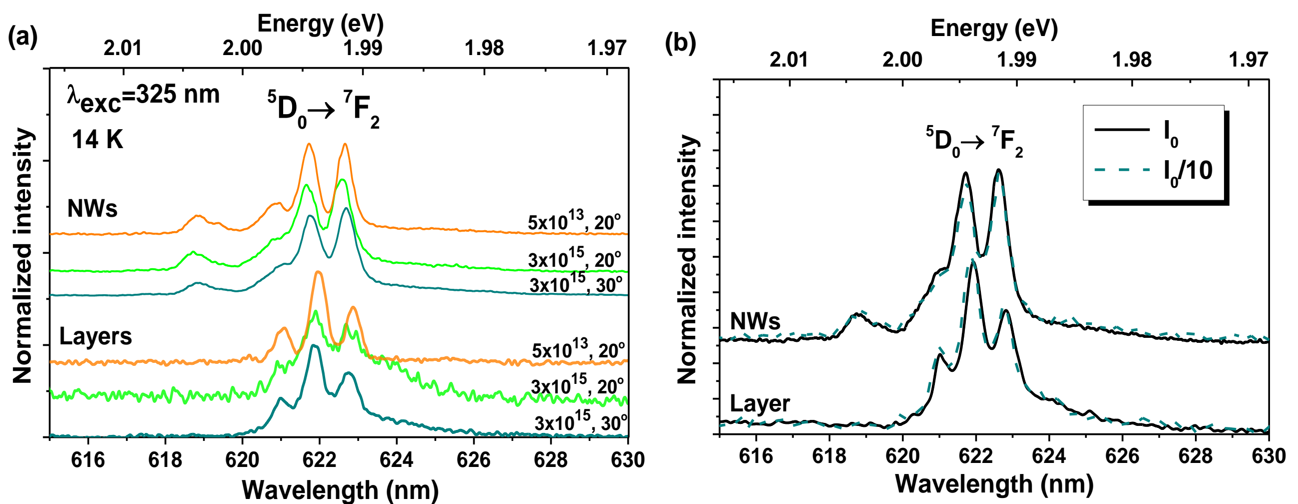

Figure 5-20 – (a) High-resolution spectra of the $^5D_0 \rightarrow ^7F_2$ transition at 14 K. (b) PL spectra recorded at 14 K under above bandgap excitation (325 nm) with two different excitation densities for the layer and (NWs) implanted with with 3×10^{15} Eu.cm^{-2} and an angle of 30°.

Table 5-1 – Assignments and peak position of the Eu^{3+} intra-shell lines for the GaN NWs and layers implanted in the same conditions.

			GaN NWs	GaN Layers
Transitions	**Fluence (ions.cm^{-2})**	**Angle (^{o})**	**Peak positions (± 0.1 nm)**	
$^5D_0 \rightarrow {^7F_1}$	5×10^{13}	20	598.8 600.4 601.1 602.2	600.5 601.2 602.2
	3×10^{15}	20	598.7 601.1 602.2	601.0
		30	598.8 601.1 602.3	598.7 601.1
$^5D_0 \rightarrow {^7F_2}$	5×10^{13}	20	618.8 620.8 621.7 622.6	621.0 622.0 622.9
	3×10^{15}	20	618.7 620.7 621.6 622.6	620.9 621.9 622.8
		30	618.8 619.4 620.9 621.7 622.7	621.0 621.9 622.8
$^5D_0 \rightarrow {^7F_3}$	5×10^{13}	20	632.8 634.1	634.6
	3×10^{15}	20	632.8 634.1	634.8
		30	632.8 634.2	632.8 634.3
$^5D_0 \rightarrow {^7F_4}$	5×10^{13}	20	660.5 662.1 664.0 665.2	662.3 664.3 665.4
	3×10^{15}	20	656.5 660.5 662.1 664.0 665.1	664.0 665.4
		30	656.5 662.1 664.1 665.2	662.2 664.1 665.3

In the case of the NWs, and regardless of the used implantation angle, the most intense PL emission comes from the line peaked at ~ 622.6 nm, while for the layers the line at ~ 621.9 nm is the dominant one. Additionally, differences in the short wavelength region of this transition are identified: one easily notes that for the layers a well-defined line is recognized near 621 nm whereas only a shoulder, slightly shifted to higher energies, is observed in the NWs. Besides the main intense three lines, extra lines at ~ 619 nm are identified in all the NWs. Such transitions are absent in the studied GaN layers.

It is well established that when the ions are placed in a local crystal field environment with low symmetry, a state with *J* = 2, such as the $^7F_2$ multiplet, suffers a maximum fivefold splitting corresponding to the *2J+1* Stark levels of the degenerate state [66–68]. When Eu^{3+} ions are introduced in the hexagonal GaN host they often replace the Ga^{3+} ions occupying substitutional (or near-substitutional) sites with a C_{3v} local symmetry [59,60,67]. In such a case, only three closely spaced lines are expected to be observed for the $^5D_0 \rightarrow {}^7F_2$ transition. Particularly, under this symmetry the degeneracy of a state with *J* = 2 cannot be fully lifted [60,64,67,68] being, however, unfolded in a nondegenerate A level and a two-fold degenerate E level. The fact that more than three splittings are observed for the implanted and annealed NWs implies that either the Eu^{3+} ions could be located in lower site symmetry than the trigonal one or that there are more than one symmetry site/environment resulting in different europium related optically active centres.

In the GaN host, the presence of Eu^{3+} in more than one optically active site was already reported in the literature [59,69–72]. In the work of Dierolf *et al.* [72] at least nine different sites of Eu^{3+} ions were identified in doped GaN layers produced by different methods. In other works [60,70,71,73], involving GaN layers doped by ion implantation and annealed at high temperatures, two major europium luminescence centres, commonly designated by Eu1 and Eu2, emitting in the same spectral region have been found. Their spectral overlap can be lifted using different photon excitation wavelengths, since these centres differ mainly in their preferential excitation pathways [60,69,72]. In order to clarify the different assignments found in the literature, Table 5-2 depicts a summary of the different reported Eu^{3+} optical centres in GaN as well as the results found in the present work. It was reported that the Eu1 centre generally appears at relatively low annealing temperatures and low nitrogen pressures (such as those used in this work) while Eu2 is favoured by high annealing temperatures and nitrogen pressures [60,70,73]. The spectral shape and peak positions of the Eu^{3+} emission lines identified in the GaN layers studied in this work are in very good agreement with previously reported Eu1 centre [69,71–73]. A careful analysis of the spectra reveals also the presence of the minority centre labelled MS8 (Eu_{2l}), whose dominant line is at 621 nm. Another line at 621.9 nm belonging to MS8 centre can be overlapped with Eu1 centre transition. The MS8 centre is commonly found in implanted samples as indicated in Table 5-2 [69,72]. The spectra recorded for the NWs evidence additional features in the spectral region of the $^5D_0 \rightarrow {}^7F_2$ transition, with additional lines in the lower wavelength region (Figure 5-20). Similar to what was observed in the layers, the dominant emission corresponds to the Eu1 centre, while the spectral position of the additional lines suggest the presence of more than one Eu^{3+} optically active minority centres, namely MS4 and MS8. The broad line that appears close to ~ 619 nm can be attributed to the MS4 centre, while the shoulder at 621 nm is in the same position as the

dominant line in the MS8 centre (see Table 5-2). These differences in the spectral signatures of the centres indicate the presence of different local environments for the emitting ion, which could include Eu^{3+} ions in substitutional Ga sites but being perturbed by different nearby defects [72]. This last case is particularly important in the case of the NWs since ions in the same lattice site can experience different strain states depending on the distance with respect to the NWs walls, which constitutes a specific feature of NWs, as was studied in detail by Brandt *et al.* [15,74].

Table 5-2 – Peak positions for the $^5D_0 \rightarrow ^7F_2$ transition lines as well as the Eu^{3+} sites' assignments found in the literature.

Reference		Sites/Peak position (nm)									
Present work	NWs (3×10^{15}, 30°)	621.7 622.7				618.8 619.4				620.9	
	Layers (3×10^{15}, 30°)	621.9 622.8								621.0	
Dierolf *et al.* [72] [1]		621.6 622.6 634.3	624.1	621.0 623.3 630.1	620.4 620.7 633.9	618.9 619.6 632.7	621.1 623.1 631.5	630.0	617.2 623.7 628.9	621.0 621.9	
		Main site	**MS 1**	**MS 2**	**MS 3**	**MS 4**	**MS 5**	**MS 6**	**MS 7**	**MS 8**	
Bodiou *et al.* [69] [2]		622.4 (*m*) 622.6 (*l*)			620.2					620.8	
		$\mathbf{Eu_{1(m/l)}}$			$\mathbf{Eu_{2m}}$					$\mathbf{Eu_{2l}}$	
Peng *et al.* [59] [3]		622.5			620.6	618.8					615.1
		Site I			**Site II**	**Site III**					**Site IV**
O'Donnell *et al.* [62,64,70] [4]		620.8 621.7 622.5				618.7 619.3			617.2	620.8 621.9	
		Eu1				**Eu2**			**Eu2**		

[1] **MS 2**, **3**, **4, 5** and **8** can be excited non-resonantly with visible light; **Main site** and **MS 1** excited with sub-bandgap UV light; **Main site**, **MS 3**, **4** and **5** excited with above bandgap energy;
(**MS 2** and **8** preferentially found in ion-implanted samples, **MS 3** preferentially found in *in-situ* doped samples)

[2] $\mathbf{Eu_{2(m/l)}}$ dominant under low photon flux, $\mathbf{Eu_{1(m/l)}}$ dominant under high photon flux and excited with both above and below bandgap excitation (*m* stands for *in-situ* doped samples and *l* for ion-implanted samples)

[3] **Sites I** and **IV** excited both above and below bandgap; **Site II** excited only above bandgap; **Site III** better observed with below bandgap energy

[4] **Eu1** excited both above and below bandgap; **Eu2** excited only above bandgap

Decreasing the power excitation (Figure 5-20b) by one order of magnitude revealed no changes in the peak position and spectral shape for the Eu^{3+} emission in the NWs and layers. As a general tendency, it is possible to assume that the used implantation angle, fluence and annealing temperature result in a dominant Eu1 centre in the GaN for both layers and NWs, overlapped with different minority centres.

5.3.2. Temperature dependency of the intraionic Eu^{3+} luminescence

Figure 5-21 shows the temperature dependent PL for all the samples, while Figure 5-22 depicts the temperature dependence of the $^5D_0 \rightarrow ^7F_2$ integrated intensity. In all cases, the overall hypersensitive luminescence intensity decreases gradually with increasing temperature due to competitive thermally activated nonradiative processes. The inset in Figure 5-21e reveals slight differences in the temperature behaviour for the dominant lines in the $^5D_0 \rightarrow ^7F_2$ transition of the NWs sample, corroborating the assumption that more than one Eu^{3+} centre are in fact contributing for the luminescent emission. Considering the internal quantum efficiency of the overall luminescence estimated by the ratio $I_{PL}(RT)/I_{PL}$ *(14 K)* [75], the Eu^{3+} emission intensity for the NWs exhibits a slightly higher thermal stability when compared with the GaN layers. At RT ~ 50% of the low temperature intensity is still observed for all the implanted and annealed NWs. Table 5-3 shows the IQE values for the $^5D_0 \rightarrow ^7F_2$ multiplet transitions of the Eu^{3+} ions for all the GaN NWs and layers. The presence of more than one Eu^{3+} site in the same spectral region hampered the evaluation of the activation energies for the $^5D_0 \rightarrow ^7F_2$ emission in the different samples.

Table 5-3 – IQE values for the $^5D_0 \rightarrow ^7F_2$ multiplet transitions of the Eu^{3+} ions in the implanted GaN NWs and layers.

	GaN NWs				GaN layers		
Fluence (ions.cm^{-2})	5×10^{13}	3×10^{15}	3×10^{15}	3×10^{15}	5×10^{13}	3×10^{15}	3×10^{15}
Implantation angle (°)	**20**	**20**	**30**	**40**	**20**	**20**	**30**
IQE (%)	**49**	**45**	**51**	**47**	**35**	**47**	**30**

5.3.3. RT luminescence studies

5.3.3.1. PLE and excitation energy dependent PL

The evaluation of the preferential excitation paths for the intraionic luminescence in both kinds of studied samples was performed at RT via PLE measurements. Figure 5-23a and b displays the PLE spectra for the NWs and layers, respectively, when monitored at the $^5D_0 \rightarrow ^7F_2$ transition. As the emission is spectrally overlapped with the aforementioned YL (Figure 5-18c), the PLE also measures the excitation pathways for the YL recombination. Similar excitation spectral features are observed for all the samples. For the NWs (Figure 5-23a) the preferential population of the

ions' energy levels can be made via a broad subgap excitation band with onset absorption at ~ 425 nm. The band extends to shorter wavelengths overlapping with an unclear GaN band edge absorption. A subgap non-resonant excitation both in the visible and in the UV for the Eu^{3+} emission was previously reported by Dierolf *et al.* [72] and K. Wang *et al.* [62].

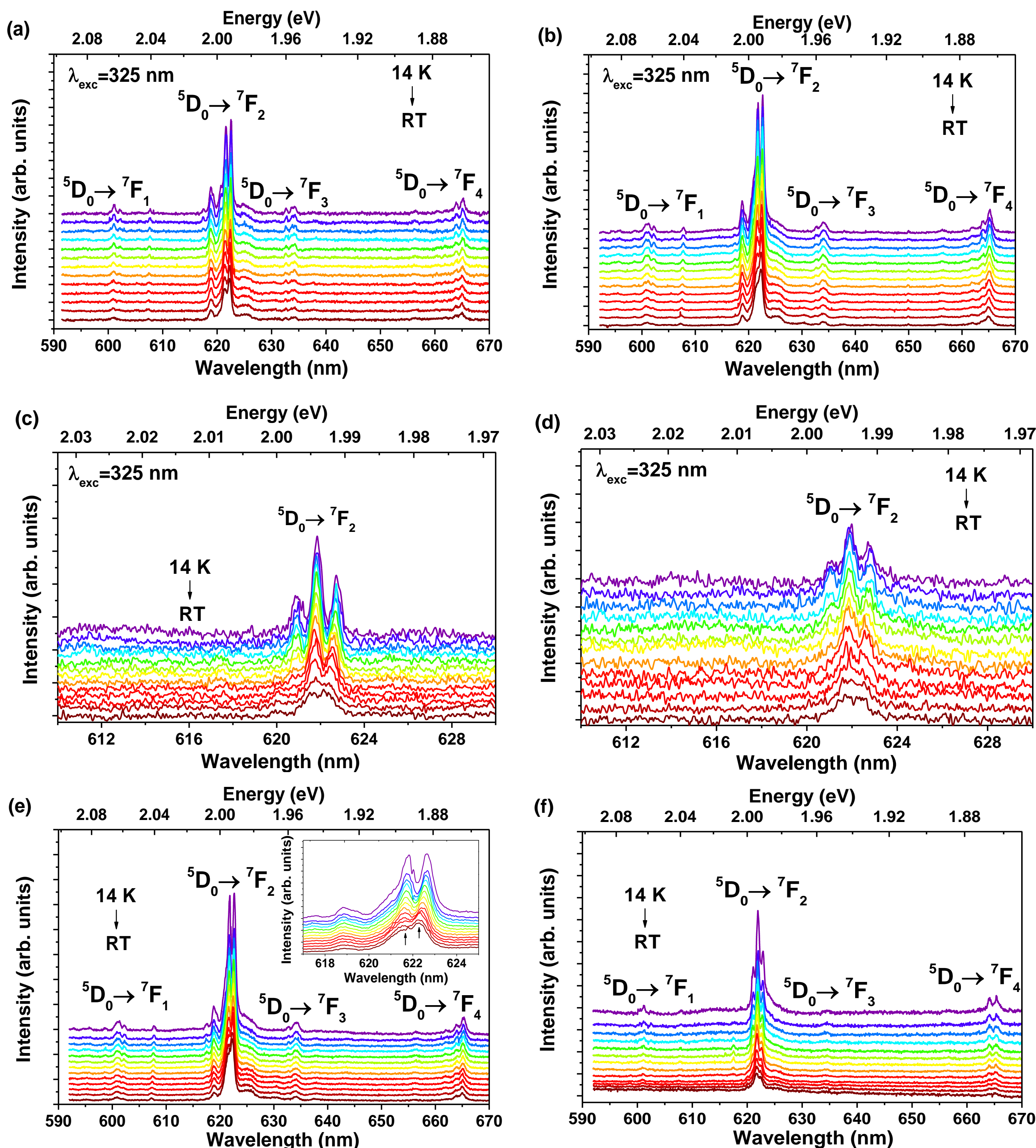

Figure 5-21 – Temperature dependent PL of the Eu^{3+} lines the (a) and (b) NWs and (c) and (d) layers implanted with an angle of 20° and 5×10^{13} Eu.cm^{-2} and 3×10^{15} Eu.cm^{-2}, respectively and (e) NWs and (f) layer samples implanted with 3×10^{15} Eu.cm^{-2} and an angle of 30°. The spectra were obtained upon 325 nm excitation. The spectra were vertically shifted for clarity.

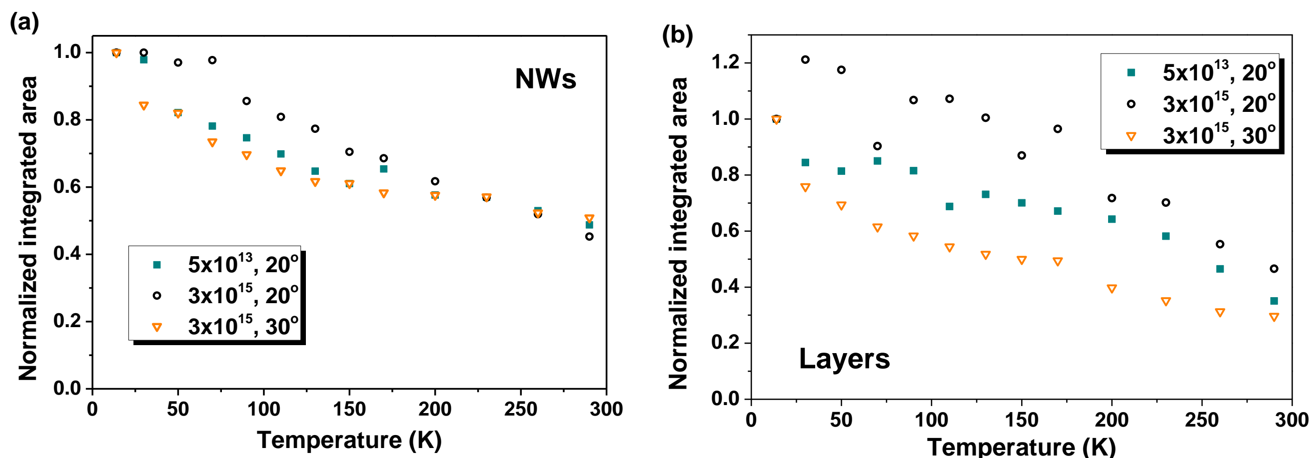

Figure 5-22 – Integrated PL intensity of the $^5D_0 \rightarrow {}^7F_2$ transition as a function of temperature for all the (a) NWs and (b) layers.

In the case of the GaN layers (Figure 5-23b), and despite the presence of a similar subgap excitation band with low intensity, the preferential population mechanism occurs via the well-defined GaN band edge absorption. This behaviour indicates, in both cases, an efficient energy transfer from the GaN host to the Eu^{3+} defects, as reported in the literature [59]. In addition, several lines/shoulders overlapped with the broad excitation band, likely to be associated with the higher energetic levels of the Eu^{3+} ions, can be identified (especially in the case of the NWs). For instance, the maximum at ~ 350 nm could be associated with the $^7F_{0,\,1} \rightarrow {}^5L_{10}$ transition, while the shoulders at ~ 390 nm and ~ 407 nm may correspond to the $^7F_0 \rightarrow {}^5L_6$ and $^7F_{0,1} \rightarrow {}^5D_3$ transitions, respectively. In order to explore this hypothesis, excitation energy dependent PL was performed and the resulting spectra for the samples with the highest RT PL intensity are depicted in Figure 5-23c and d. It is interesting to note that, in the case of the NWs, exciting the samples with an energy equal or above the GaN bandgap promotes, besides the intraionic emission, the observation of the YL. However, the latter becomes almost negligible by pumping the NWs with below bandgap energy. Nevertheless, subgap excitation with wavelength photons of 390 nm and 407 nm clearly promotes the population of the Eu^{3+} emitting levels. Unfortunately, due to the low intensity of the RT emission under Xe lamp excitation (low excitation density) and therefore necessary large width of the slits used in the signal detection, it was not possible to resolve the spectral shape of the intraionic recombination.

For the case of the GaN layers, a strong contribution of the broad emission band was identified for both above and below bandgap excitations, masking the resonant excitation paths via the Eu^{3+} lines. It was observed that with above bandgap excitation by the He-Cd laser (325 nm), the luminescence is dominated by the YL in all the layers. When excited at the bandgap energy (wavelength 366 nm) the strong YL completely dominates the PL spectrum, hindering the observation of the ion-related emission. For the other excitation wavelengths (325, 350, 390 and 407 nm), besides the broad band, it was also possible to identify the ion $^5D_0 \rightarrow {}^7F_2$ transition. When excited with below bandgap excitation, the broad band exhibits a slight shift towards higher energies (~ 10 nm), corroborating the assumption that different luminescence centres emitting in the green/yellow spectral region are present in the GaN layers, as mentioned previously.

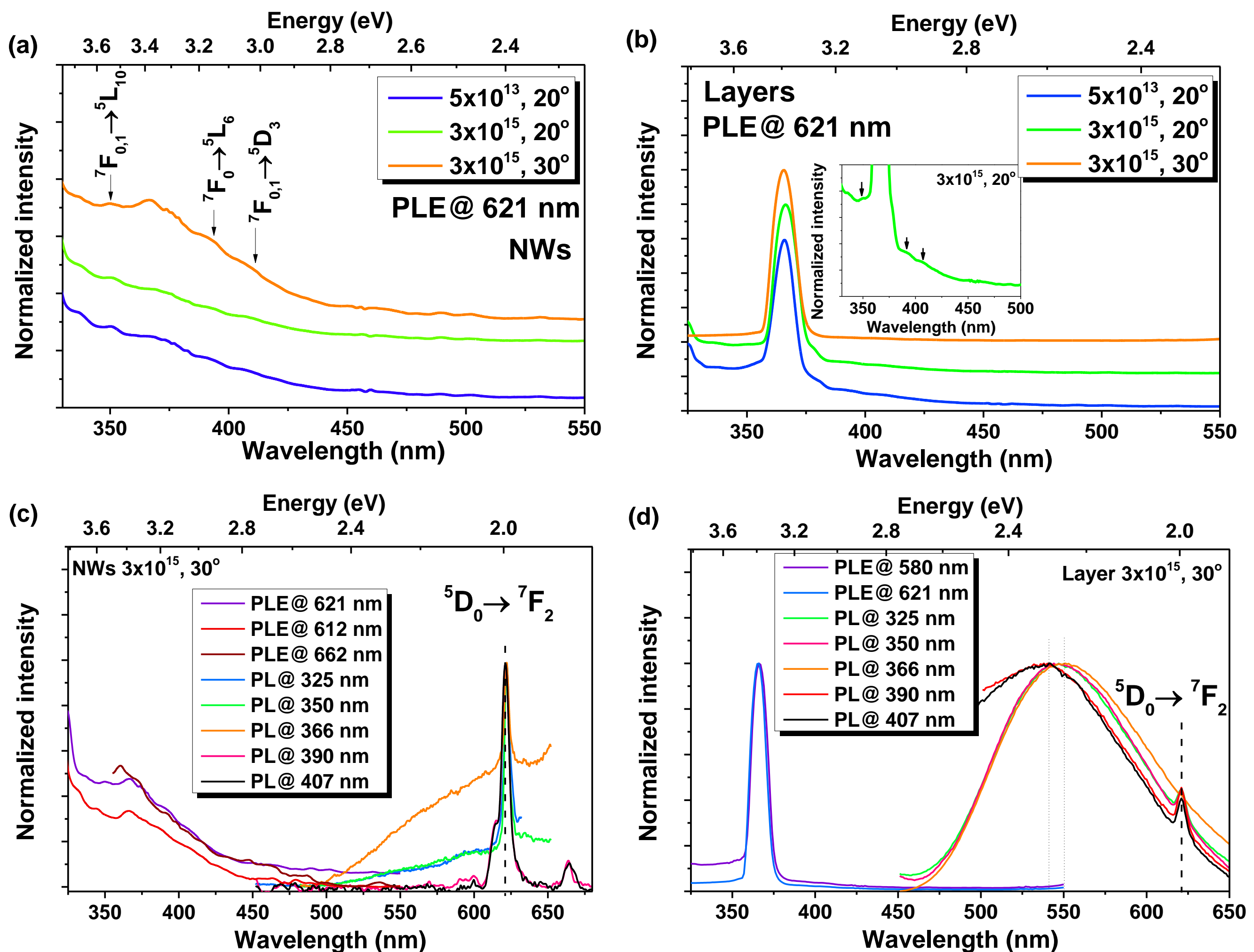

Figure 5-23 – RT PLE spectra for the GaN sample monitored at the $^5D_0 \rightarrow {}^7F_2$ transition of the Eu^{3+} ions: (a) NWs and (b) layers implanted with Eu. RT PL/PLE spectra for the (c) NWs and (d) layers implanted with $3x10^{15}$ $Eu.cm^{-2}$ and 30°. The inset in Figure (b) is a magnified view of the PLE spectrum of one of the layers, showing the broad excitation band as well as the lines/shoulders with the arrows indicating the possible position of the Eu^{3+} ion's energetic levels.

5.3.3.2. Time resolved photoluminescence

Time resolved spectroscopy constitutes a powerful tool to explore the dynamics of the identified optical centres. As such, RT TRPL spectra for the highest fluence implanted NWs and GaN layers are shown in Figure 5-24a to d for different time delays and for above (a and b) and below (c and d) bandgap excitation. The samples were excited with 325 nm and 390 nm photon excitation and the spectra were obtained with different delay times after the pulse of the lamp for a fixed time window of 0.5 ms. In both samples, the intraionic emission and the YL are observed. However, as indicated by the PLE spectra with below bandgap excitation, the intensity of the YL emission is much weaker than the one observed when excited with 325 nm. In all the cases, the spectra clearly evidence that the Eu^{3+} emission vanishes for delays higher than 1 ms, meaning that a shorter lifetime (hundreds of μs) is expected for the $^5D_0 \rightarrow {}^7F_2$ transition for both NWs and layers,

corresponding to the *1/e* decrease of its intensity. The decay is similar in NWs and GaN layers and is in the same order of magnitude of the values reported in the literature for Eu^{3+}-doped layers [60,61,70].

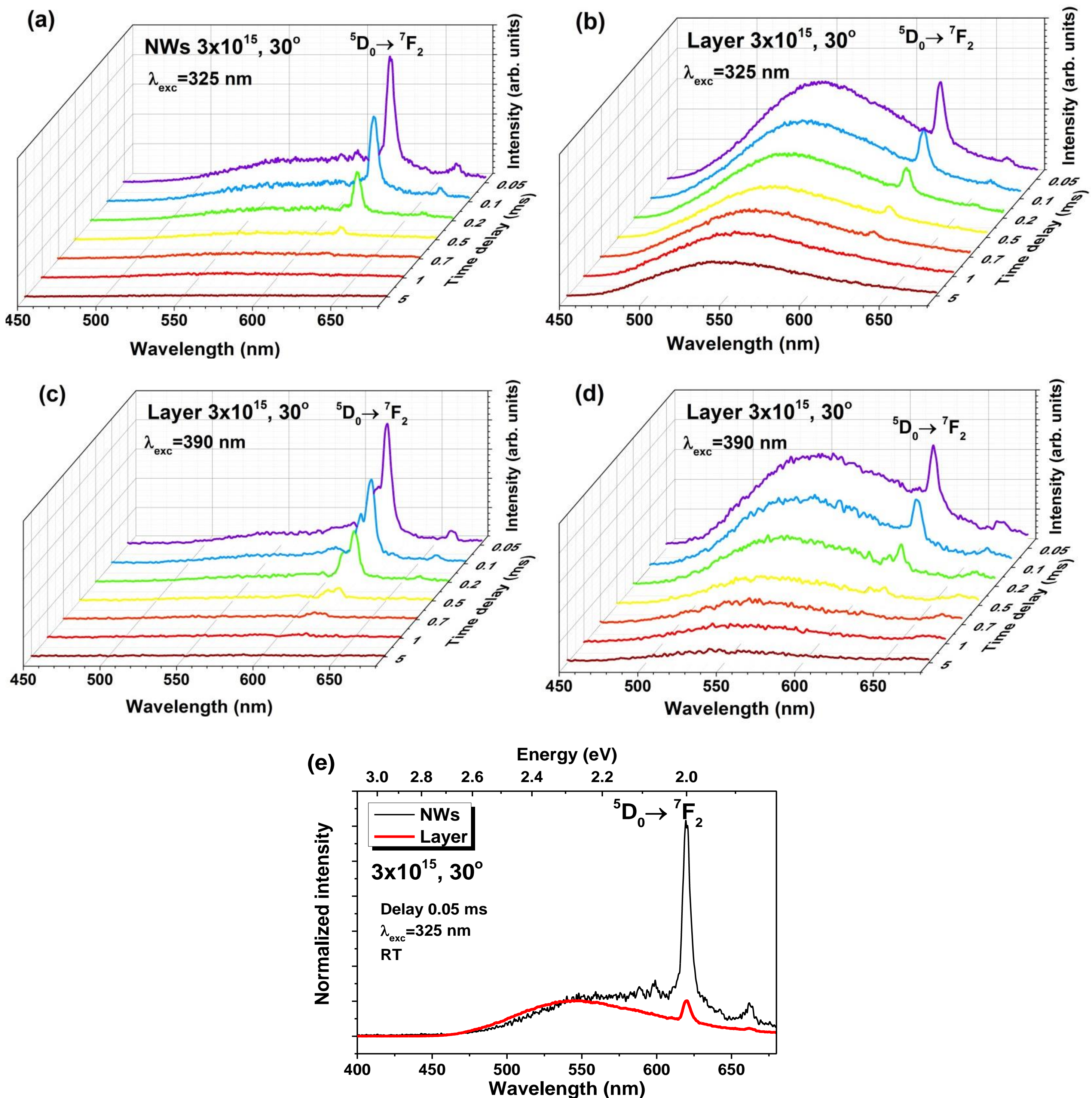

Figure 5-24 – RT TRPL measurements for the (a) and (c) NWs and (b) and (d) layer implanted with 3×10^{15} Eu.cm^{-2} and 30°. The measurements were obtained under (a) and (b) 325 nm (above bandgap excitation) excitation and (c) and (d) 390 nm (below bandgap excitation) of a flash lamp. (e) Normalized RT PL spectra of the NWs and layer implanted with the same conditions, obtained with a time delay of 0.05 ms and above bandgap excitation (325 nm).

The most noticed difference evidenced from the TRPL spectra is related with the kinetics of the YL in NWs and GaN layers. Here, taking into account the results for above bandgap excitation, despite the identification of the luminescence in similar spectral range for NWs and layers (see also Figure 5-18c corresponding to steady state PL at 14 K), the TRPL spectra clearly show that the YL in NWs and layers present different recombination kinetics. As aforementioned, the YL in GaN layers have been ascribed to e-A and/or DAP recombination involving V_{Ga} complexes [7,10,11,54,55]. Such recombination models imply, in the case of DAP transitions, a nonexponential decay dependent on the distance separating shallow donors and deep acceptors in the host. This means that short (long) lived transitions are expected for close (apart) pairs due to the high (low) recombination probability provided by the overlap of the carriers' wave functions. On the other hand, e-A transitions typically exhibit a high transition probability, and therefore a short lifetime. The recombination of an e-A transition involving the same acceptor of a DAP is commonly deviated to shorter wavelengths due to the ionization of the shallow donor involved. Figure 5-24e shows a comparison between the TRPL spectra of GaN NWs and layers for the time delay of 0.05 ms and fixed time window of 0.5 ms obtained with above bandgap excitation. As already observed (see Figure 5-18c), the spectra clearly evidence that the YL in the NWs have a slightly different spectral shape and peak position when compared with those measured for the layers. On the other hand, the emission in the NWs is shifted to longer wavelengths excluding the hypothesis that the measured fast decay could be related with the e-A transition from the same defect identified in the layers. In fact, while the YL in the GaN layers follows the tendency of a DAP recombination as found in the literature [24], the YL in the NWs evidence a very short lifetime, faster than the intraionic emission, in the range of tens/hundreds of microseconds or lower. As such, the kinetics data are consistent with a different recombination model for the YL in the NWs, supporting previous reports which assign the emission to surface states mediated recombination [46,58].

5.4. GaN nanostructures implanted with Pr^{3+}

The trivalent praseodymium (Pr^{3+}) ion has a $4f^2$ configuration with $^3H_4$ ground state and $^3H_{5,6}$, $^3F_{2,3,4}$, $^1G_4$, $^1D_2$, $^3P_{0,1}$, $^1I_6$, $^3P_2$ and $^1S_0$ excited states [76]. This ion has been incorporated in nitride matrixes in order to promote visible emission that arises from transitions between the crystal-field split energy levels of its $^{2S+1}L_J$ manifolds, especially in the red spectral region, due to the intense emission of its $^3P_0 \rightarrow ^3F_2$ transition [49,76–80]. Reported works of Pr^{3+} in different hosts revealed that the emission spectra of Pr^{3+} ions are very complex since they reveal ion-lattice interactions that broaden the pure electronic lines and contribute to a large number of vibronic lines [76,81,82]. In the present section, the analysis of the spectroscopic features of different GaN structures (layers, QWs, NWs and QDs) doped with Pr^{3+} ions by ion implantation is discussed.

SEM images of the NWs evidencing their good vertical alignment were already depicted in Figure 5-5a and b. The *c*-oriented NWs exhibit a length of ~ 300 - 400 nm with a diameter in the 20 - 40 nm range. Both GaN QD/AlN and GaN QW/AlN samples are composed by 20 periods of QDs or QWs with a height of ~ 2 nm and AlN spacer ~ 5 nm thick. Figure 5-25 shows examples of

TEM images for each of these structures reproduced from works previously reported by the growers [83–85]. It was seen that the resulting superlattices exhibit abrupt interfaces [83]. In the case of the QDs, the cross-sectional HRTEM image presented in Figure 5-25a, acquired along the $[2\bar{1}\bar{1}0]$ direction, shows vertically aligned QDs well separated from each other, embedded in the AlN matrix [85]. In reference [85] an analysis of the HRTEM images of different directions combined with atomic force microscopy measurements was performed, revealing that the QDs exhibit a truncated pyramidal shape with walls inclined by ~ 30° from the surface plane. It was also found that tensile strain of about 0.55% was present in the AlN spacer layers, which was attributed to it location between two vertically stacked QDs. For the GaN QDs /AlN system, analytical calculations of the strain tensor in embedded GaN QDs showed a compressive strain close to 0.3 - 0.7 % [85].

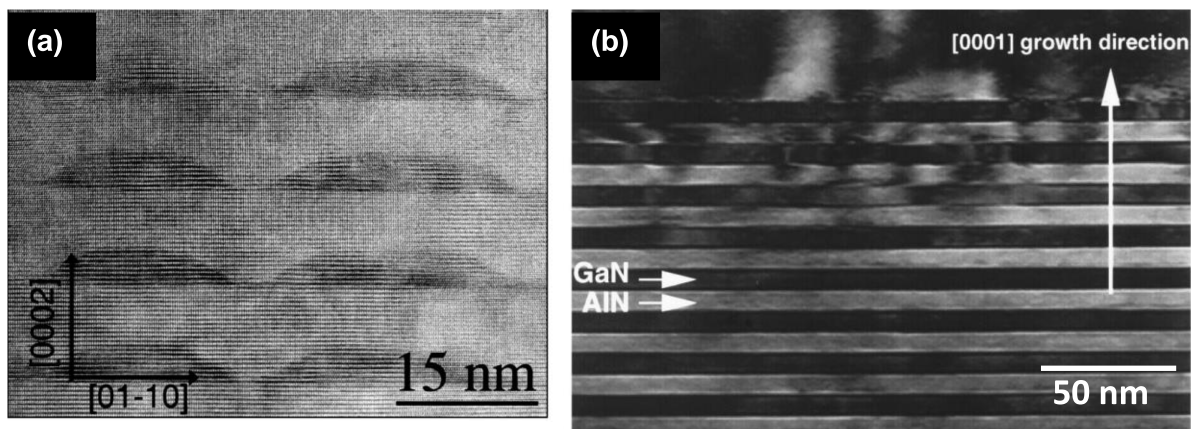

Figure 5-25 – (a) High-resolution TEM image of a QD multilayer sample similar to the ones implanted with Pr^{3+} (from reference [85]). (b) TEM image of a GaN QW/AlN superlattice (from reference [83]).

Figure 5-26 shows the 14 K PL spectra of the GaN:Pr^{3+} layers, NWs, QWs and QDs obtained under 325 nm photon excitation. After implantation and annealing all the analysed samples exhibit the emission lines associated with the intra-4f^2 transitions of the Pr^{3+} ion, from which the most intense is the red transition occurring between the $^3P_0$ and $^3F_2$ multiplets. Besides the intraionic luminescence, other optically active centres are discriminated. Well resolved D^0X and DAP transitions are clearly distinguished for GaN layers and NWs implanted with low fluence. However for the QWs and QDs, the ultraviolet recombination broadens and the peak emission wavelength varies due to the balanced contributions of the spatial carriers confinement and the quantum confined stark effect (QCSE) [86]. As AlN layers are present in the QW and QDs structures, the observed UV recombination could arise from defects in the AlN layers, such as oxygen-related and native defects, as was previously reported [87–89]. In the case of the NWs implanted with higher fluence no NBE emission is observed, probably due to a higher implantation damage. Only a broad band observed in the violet region is identified in the spectral region of the DAP transitions, likely due to defects generated by implantation and annealing. For the samples implanted with high fluence and regardless of the implantation damage recovery after thermal annealing treatments, a suppression of the band edge recombination in GaN layers and QDs is observed. In the longer wavelength region, a broad YL is observed in all the samples.

Once again, despite the similarities in the peak position and spectral shape of the YL, distinct recombination behaviour of the optical centres was measured.

Figure 5-27 depicts enlarged spectra of the intra-shell Pr^{3+} luminescence in the studied samples. As stated above, the most intense luminescence is due to the $^3P_0 \rightarrow ^3F_2$ transition that occurs in the red spectral region. The strongest RT Pr^{3+} luminescence observed in the GaN layer implanted with higher fluence. Figure 5-28 shows a schematic energy diagram of the Pr^{3+} energy levels, showing the transitions that were observed in the studied samples. The peak positions and line assignments of the Pr^{3+} transitions identified in the present samples are compiled in Table 5-4.

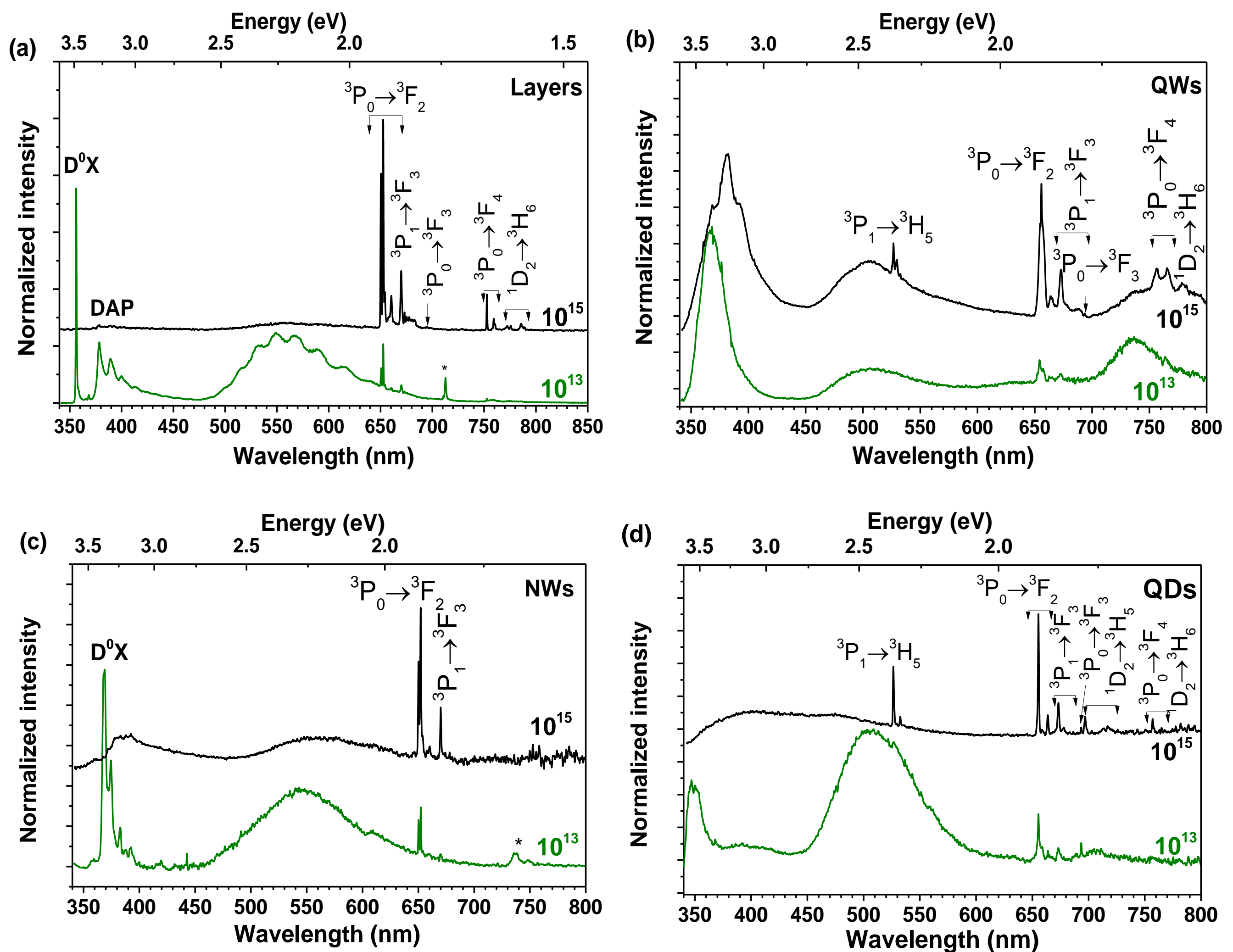

Figure 5-26 – Low temperature PL spectra of the GaN:Pr^{3+} (a) layers, (b) QWs, (c) NWs and (d) QDs. The asterisk denotes the second order of the D^0X emission. All the spectra were acquired at 14 K with an excitation wavelength of 325 nm.

From hereafter, the study will be focused on the transitions between the $^3P_0$ and $^3F_2$ multiplets shown in Figure 5-29. Unambiguous changes occur for the intraionic emission when the ion is incorporated in the different structures. In the case of the GaN layers, the most intense $^3P_0 \rightarrow ^3F_2$ lines obtained with above GaN bandgap excitation were found to occur at ~ 650.3 and 652.4 nm with a full width at half-maximum (FWHM) of ~ 0.2 nm, independently of the used ion fluence.

These findings are in good agreement with previously reported data in praseodymium doped layers [49,76,78]. The $^3P_0\rightarrow^3F_2$ lines in the GaN NWs were found to be similar to those of the layers although slightly displaced to shorter wavelengths. Since the peak position and the spectral shape of this luminescence agrees with those observed in the GaN layers, the possibility that the ion emission originates from Pr^{3+} inside the AlN buffer layers can be discarded, allowing to infer that the ions are effectively incorporated into the GaN NWs and occupy the Ga sites as reported for layers [80]. Additionally, the small wavelength shift in the peak position is likely due to different strain states of the GaN layers and NWs, as was identified for the Eu-implanted samples reported in the previous section.

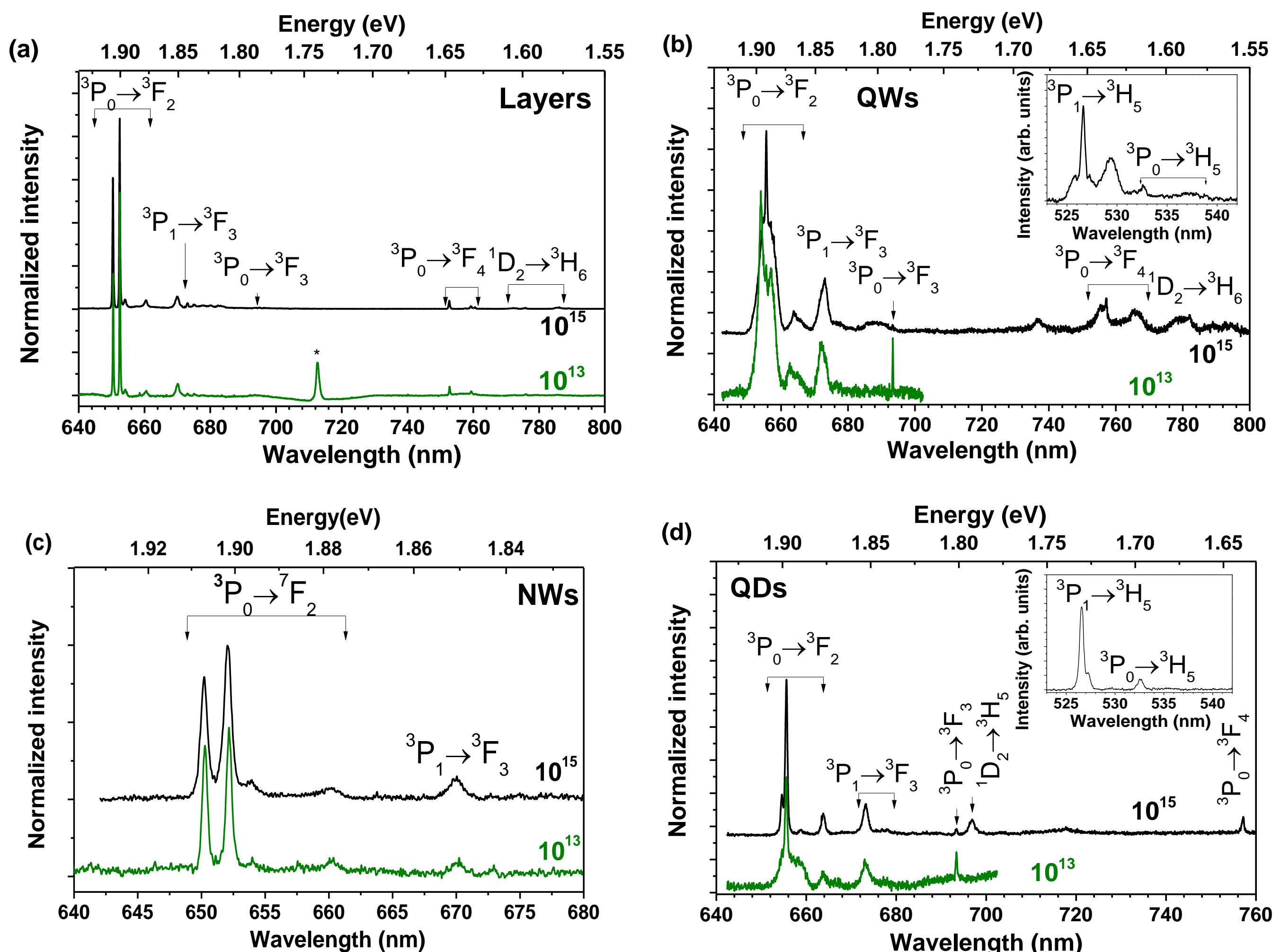

Figure 5-27 – High resolution low temperature PL spectra of the GaN:Pr^{3+} (a) layers, (b) QWs, (c) NWs and (d) QDs recorded on the red-NIR region of the Pr^{3+} emission. The asterisk denotes the second order of the D^0X emission. The insets of figures (b) and (d) correspond to the ion emission on the green region of the electromagnetic spectrum for the samples implanted with higher fluence. All the spectra were acquired at 14 K with an excitation wavelength of 325 nm.

Remarkable changes are noticed in the GaN QWs and QDs embedded in AlN barriers. As a first remark it should be emphasized that in both cases, and for the samples implanted with high fluence, shorter wavelength multiplet transitions from the Pr^{3+} ions were identified in the green spectral region (~ 526 nm) due to the $^3P_1\rightarrow^3H_5$ transition. This emission is usually very weak in

GaN samples [76] and is more commonly observed in AlN layers and $Al_xGa_{1-x}N$ ternary alloys [49,78,90]. Such identification in the analysed QWs and QDs structures suggests that the optically active praseodymium ion in the mentioned samples is probably located inside AlN barriers or in regions where intermixing between QWs/QDs and barriers took place. Particularly, in the case of the QDs, the peak position and relative intensity of the $^3P_0 \rightarrow ^3F_2$ lines at ~ 654.6 nm and 655.6 nm are in fairly good agreement with those observed in Pr^{3+}-doped AlN layers [49]. Therefore, and independently of the used implantation fluence, it is possible to assume that the intraionic luminescence arises mainly from the Pr^{3+} inside the AlN spacers in the SL structure of GaN QDs embedded in the AlN spacers. The shift observed in the peak position is likely to be due to different strain states which are expected between the thin AlN spacers and the fully relaxed thick AlN layer (~ 3 µm). This observation is in contrast with similar GaN QDs implanted with Eu^{3+}, where the dominant Eu^{3+} centre, for low implantation fluences, was suggested to be Eu^{3+} inside QDs [22]. Nevertheless, it agrees well with the fact that the majority of the implanted Pr^{3+} ions are expected to stop in the AlN barriers which account for ~ 90% of the implanted volume.

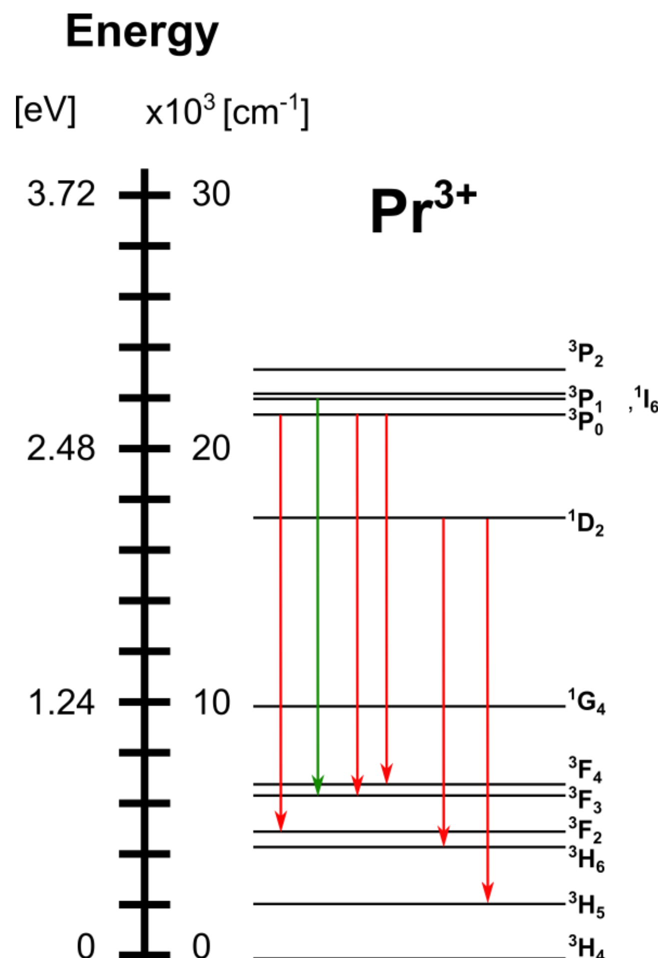

Figure 5-28 – Schematic energy diagram of the Pr^{3+} free ion. The energy levels were constructed based on reference [65]. The arrows indicate the transitions observed in the studied samples.

Table 5-4 – Assignments and peak position of the Pr^{3+} intra-shell lines for the studied samples.

Transitions	Fluence (ions.cm^{-2})	GaN Layers	GaN NWs	AlN/GaN/AlN QWs	AlN/GaN/AlN QDs
		Peak positions (±0.1 nm)			
$^3P_1 \rightarrow {}^3H_5$	1×10^{13}	---	---	---	---
	1×10^{15}	---	---	526.6 529.4	526.6 527.2 529.7
$^3P_0 \rightarrow {}^3H_5$	1×10^{13}	---	---	---	---
	1×10^{15}	---	---	532.6 537.3	532.6
$^3P_0 \rightarrow {}^3F_2$	1×10^{13}	650.3 652.4 654.1 660.4	650.2 652.1 654.0 660.2	653.9 655.4 656.9 663.7	655.5 658.3 663.7
	1×10^{15}	650.3 652.4 654.1 660.4	650.2 652.1 654.0 660.2	655.6 663.7	654.6 655.6 658.7 663.7
$^3P_1 \rightarrow {}^3F_3$	1×10^{13}	670.0 673.0 675.0 677.7	670.0 672.9	672.0	673.0
	1×10^{15}	669.9 672.9 675.0 677.7 680.1 682.5	670.0 672.9	673.1	673.2 678.0
$^3P_0 \rightarrow {}^3F_3$	1×10^{13}	693.4	---	693.4	693.4
	1×10^{15}	693.6	---	693.4	693.4
$^1D_2 \rightarrow {}^3H_5$	1×10^{13}	---	---	---	---
	1×10^{15}	695.1	---		696.9
$^3P_0 \rightarrow {}^3F_4$	1×10^{13}	752.7 759.3 760.5	---	---	---
	1×10^{15}	752.7 757.4 759.3 760.5	---	755.5 757.0 765.7	757.1
$^1D_2 \rightarrow {}^3H_6$	1×10^{13}	772.3 775.8 785.5	---	---	---
	1×10^{15}	772.2 775.8 783.2 785.5 786.1 788.9	---	780.1 788.9	781.9 788.9

An interesting behaviour is seen for the QWs structure. Here, and for the sample implanted with high fluence, Figure 5-29 evidences the $^3P_0 \rightarrow ^3F_2$ main line in a close position as those identified in the AlN layer, in agreement with the fact that part of the optically active Pr^{3+} ions are located in the AlN host. Additionally, the multiplet transitions are overlapped with a broad emission band similar to those previously reported for Pr^{3+} emission in $Al_xGa_{1-x}N$ layers with high aluminium content [78]. This may suggest a promotion of disorder-related effects after the implantation and annealing in the QW structure, generating intermixed AlGaN regions rich in aluminium. Argon implantation in similar GaN/AlN structures was recently shown to promote efficient intermixing, particularly in GaN QD structures [91] while intermixing upon annealing is insignificant at the annealing temperatures used in this study [89,92,93]. However, for the case of the QW sample implanted with low fluence, where intermixing should be low, a similar overlap of emitting centres was found in the $^3P_0 \rightarrow ^3F_2$ spectral region. Moreover, for the case of QDs, where an enhanced ion beam mixing was expected, the broad emission is seen only in the low fluence implanted sample and much weaker than for the QW sample [91]. For the QW sample implanted with low fluence, the observed energy shift of the peak position for the $^3P_0 \rightarrow ^3F_2$ lines is compatible with part of the praseodymium ions being optically active in the GaN QWs. If it is the case, the shift of the dominant Pr^{3+} emission line to longer wavelengths (compared to the Pr^{3+} emission from GaN layers) could be justified by different strain states of the GaN layers and QWs. Yet, similar shifts to low energy of the peak position were found in $Al_xGa_{1-x}N$ layers with low x composition, meaning that one cannot exclude the possibility that the ion luminescence arises from intermixed regions. Site multiplicity involving certain defects may be an alternative explanation.

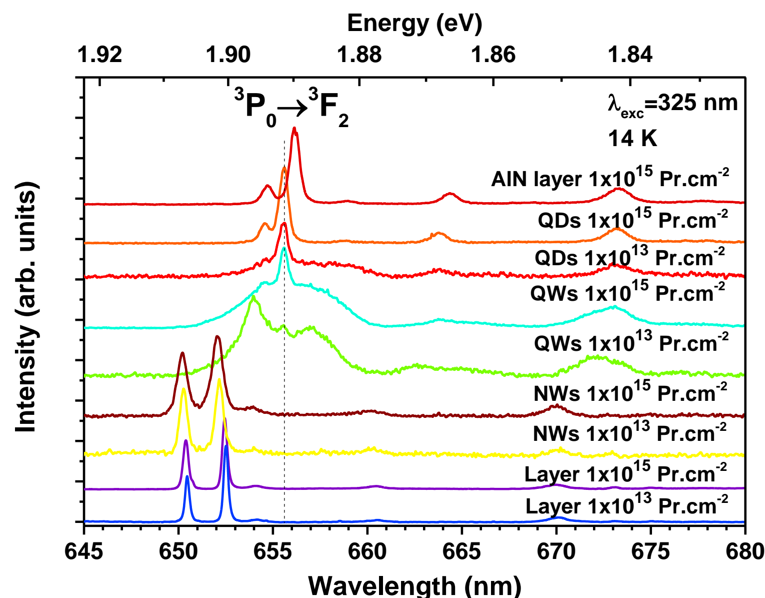

Figure 5-29 – Comparison of the low temperature PL spectra of all the Pr^{3+} implanted samples for the $^3P_0 \rightarrow ^3F_2$ transition.

Figure 5-30 and Figure 5-31 depict the temperature dependence of all the samples and the $^3P_0 \rightarrow ^3F_2$ integrated intensity, respectively. For all studied samples it is shown that the intraionic luminescence decreases gradually with increasing temperature. As mentioned in the previous

section, the IQE can be estimated by the ratio between the integrated ion emission at RT and low temperature, considering that the nonradiative processes are negligible at 14 K. The activation energy for the $^3P_0 \rightarrow ^3F_2$ transition of each sample was obtained using Eq. 4-29. The determined IQE values and activation energies for the ion luminescence in the studied structures are indicated in Table 5-5. For the QWs the IQE value corresponds to the overall integrated intensity in the wavelength range of the $^3P_0 \rightarrow ^3F_2$ transition, which, as aforementioned, corresponds to a region where an overlap of emitting centres is very likely to occur, hampering the calculation of the activation energies for the nonradiative processes of the individual centres. In the case of the NWs, and apart from the two values measured at the highest temperatures (where the integrated intensity calculation has a higher error due to the low signal to noise ratio), the Pr^{3+} emission intensity exhibits a high thermal stability, up to 230 K. At this temperature still ~ 70% of the low temperature ion integrated intensity is observed (for both fluences).

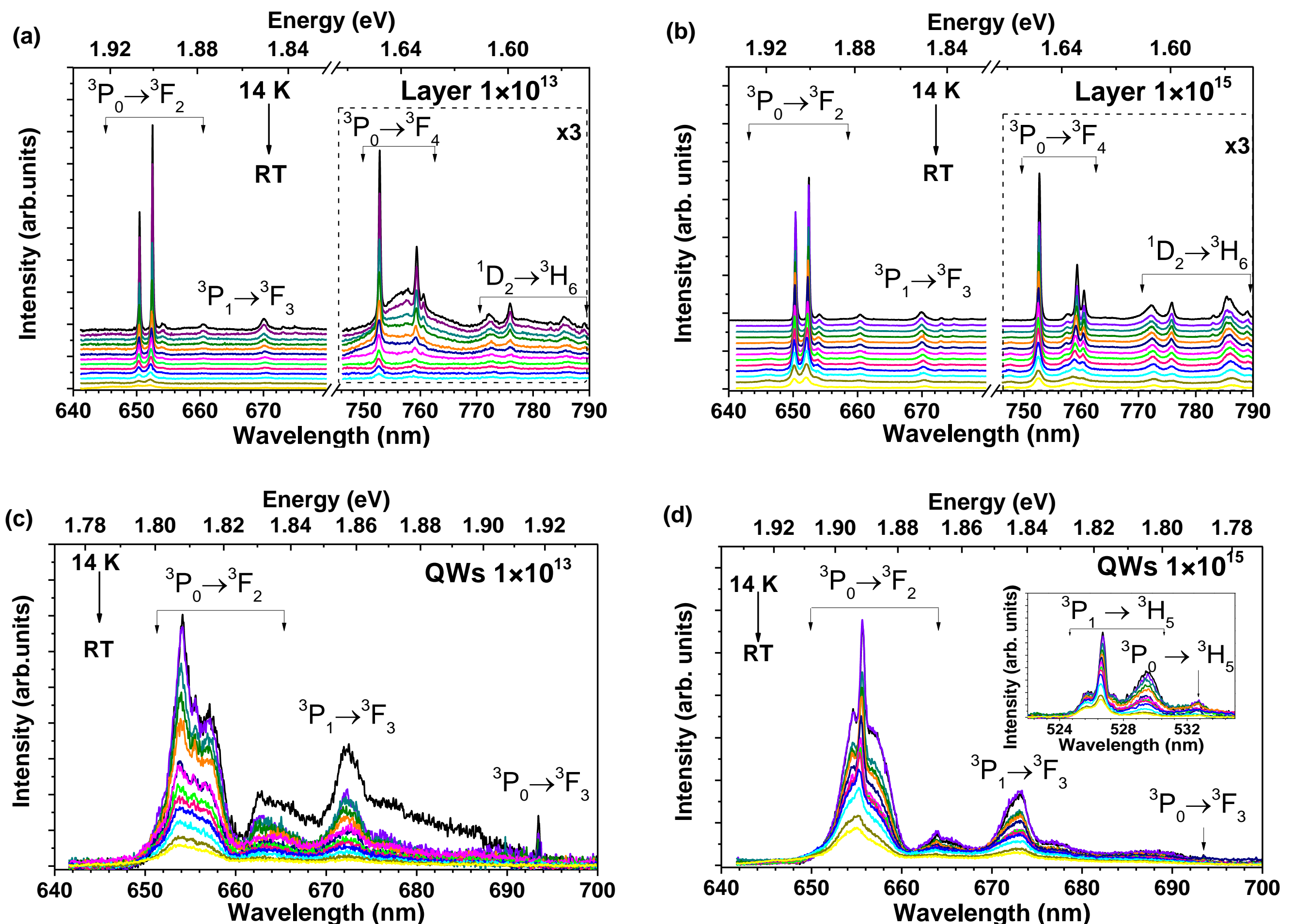

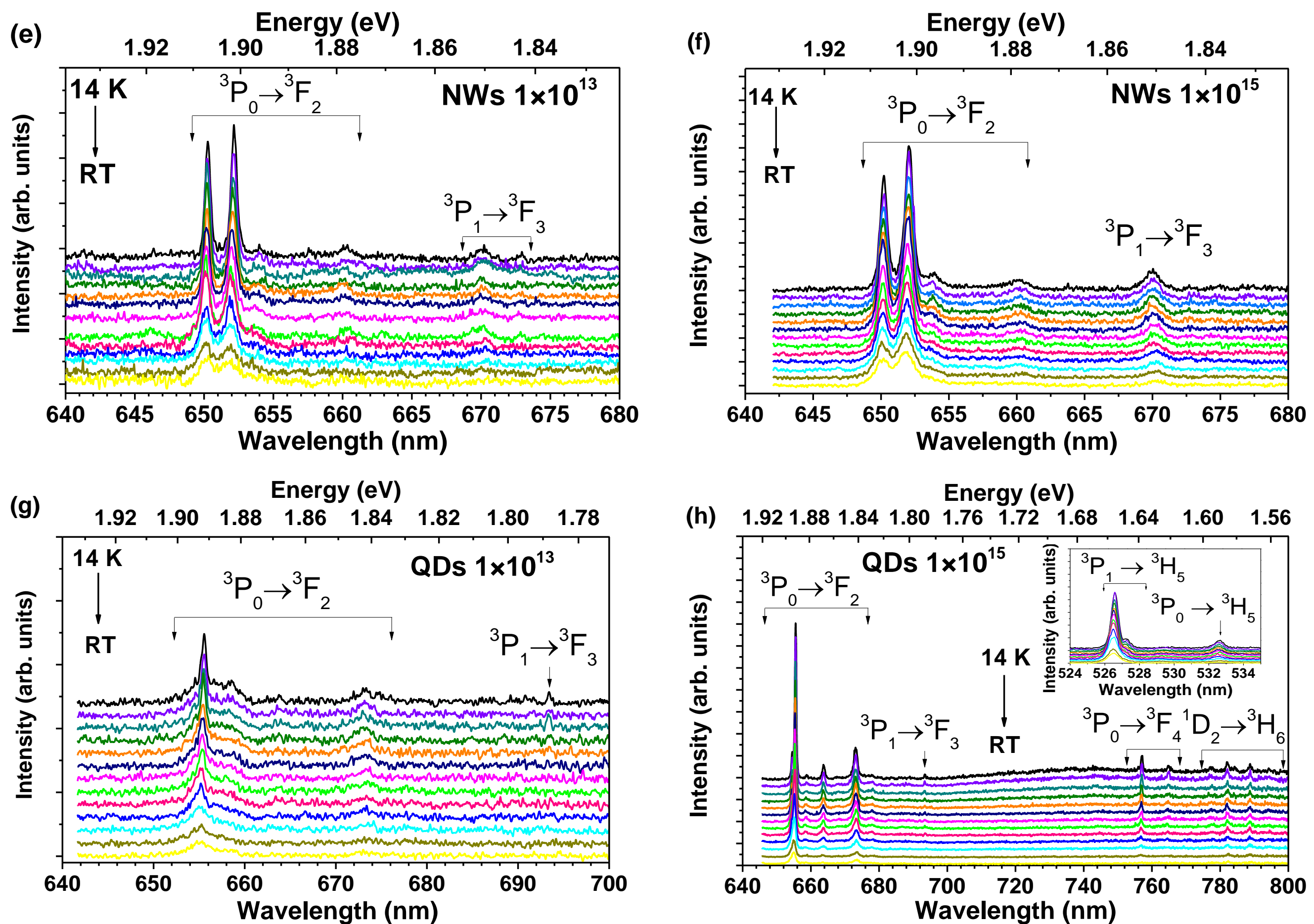

Figure 5-30 – Temperature dependent PL of the Pr^{3+} emission for the layers implanted with 1×10^{13} $Pr.cm^{-2}$ (a) and 1×10^{15} $Pr.cm^{-2}$ (b), QWs implanted with 1×10^{13} $Pr.cm^{-2}$ (c) and 1×10^{15} $Pr.cm^{-2}$ (d), NWs implanted with 1×10^{13} $Pr.cm^{-2}$ (e) and 1×10^{15} $Pr.cm^{-2}$ (f), and QDs implanted with 1×10^{13} $Pr.cm^{-2}$ (g) and 1×10^{15} $Pr.cm^{-2}$ (h). The spectra are vertically shifted for clarity (with the exception of the QWs samples).

A similar behaviour was found for the GaN layer implanted with high fluence, corresponding to the sample displaying the most intense ion luminescence. In this case, ~ 80% of the ion integrated luminescence is still observed at ~ 230 K. The RT visual appearance of the intra-shell Pr^{3+} light emission in this layer is shown in the inset of Figure 5-32a, together with the PLE spectrum, which indicates that, for the GaN layer, the preferential excitation pathway for the Pr^{3+} luminescence is accomplished via above bandgap excitation. The PL decay profile for the $^3P_0 \rightarrow ^3F_2$ transition, measured at RT, for the same sample is shown in Figure 5-32b. The obtained results were well fittet to a single exponential decay with a lifetime of 21.9 µs, as expected for a spin allowed transition. This value is in good agreement with those reported in the literature [76]. The low luminescence intensity of the nanostructures at RT, together with the low power Xe lamp used as excitation source for the PLE and lifetime measurements, hampered the identification of the excitation lines/bands and the PL decay profile for the NWs, QWs and QDs.

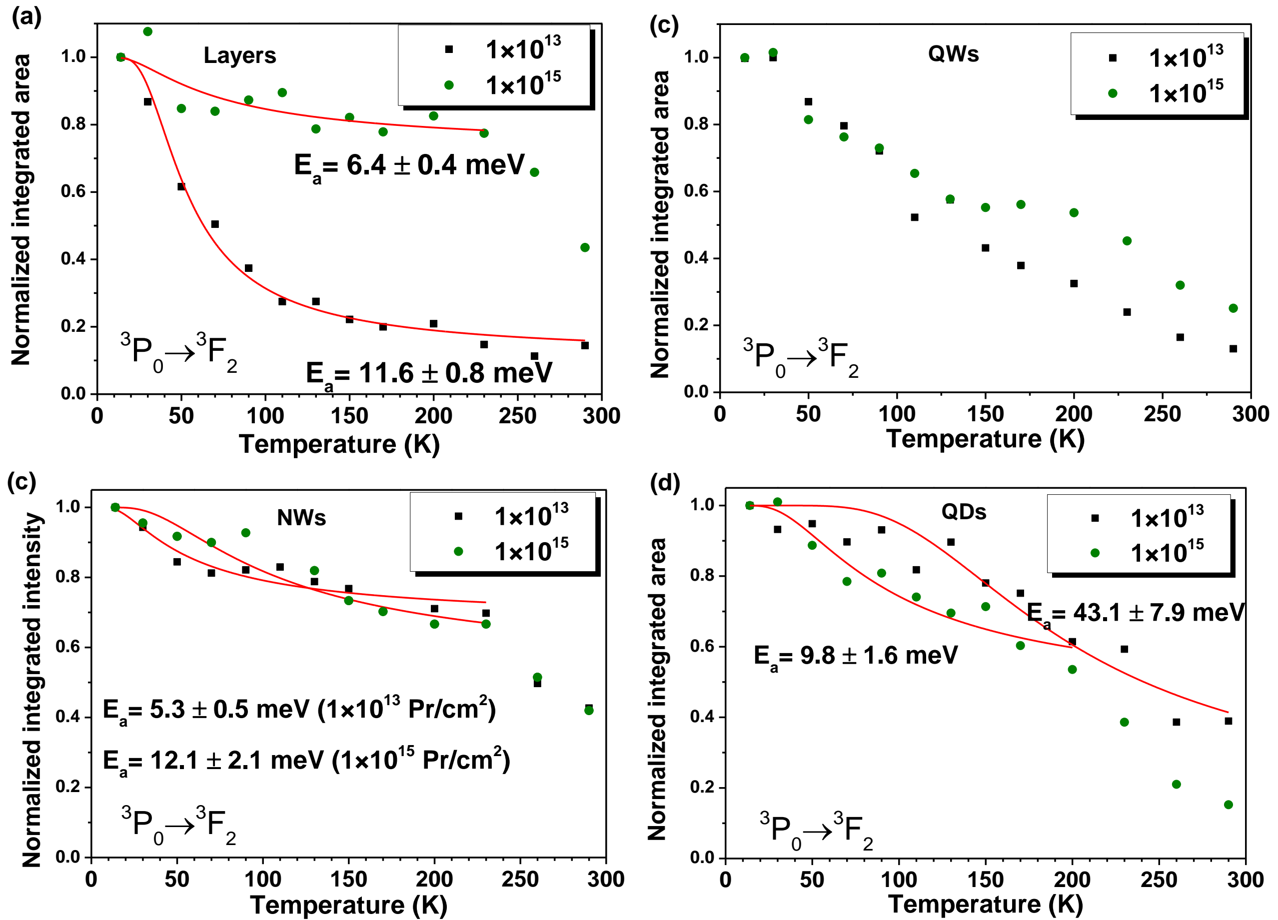

Figure 5-31 –Evolution of the integrated intensity for the GaN (a) layers, (b) QWs (c) NWs and (d) QDs.

Table 5-5 – IQE and E_a values for the $^3P_0 \rightarrow ^3F_2$ multiplet transitions of the Pr^{3+} ions in the studied samples.

	GaN layers		GaN NWs		AlN/GaN/AlN QWs		AlN/GaN/AlN QDs	
Fluence (ions.cm^{-2})	1×10^{13}	1×10^{15}	1×10^{13}	1×10^{15}	1×10^{13}	1×10^{15}	1×10^{13}	1×10^{15}
IQE (%)	14	43	43	42	13	25	39	15
E_a (meV)	11.6 ± 0.8	6.4 ± 0.4	5.3 ± 0.5	12.1 ± 2.1	---	---	43.1 ± 7.9	9.8 ± 1.6

In the case of the layer sample implanted with higher fluence, the high intensity of the intraionic luminescence enabled the observation of additional intra-shell lines in the IR spectral region, as shown in Figure 5-33. For the nanostructures (NWs, QWs and QDs) no emission lines were detected in this spectral region, even at low temperatures, probably due to the reduced visible/IR luminescence intensity.

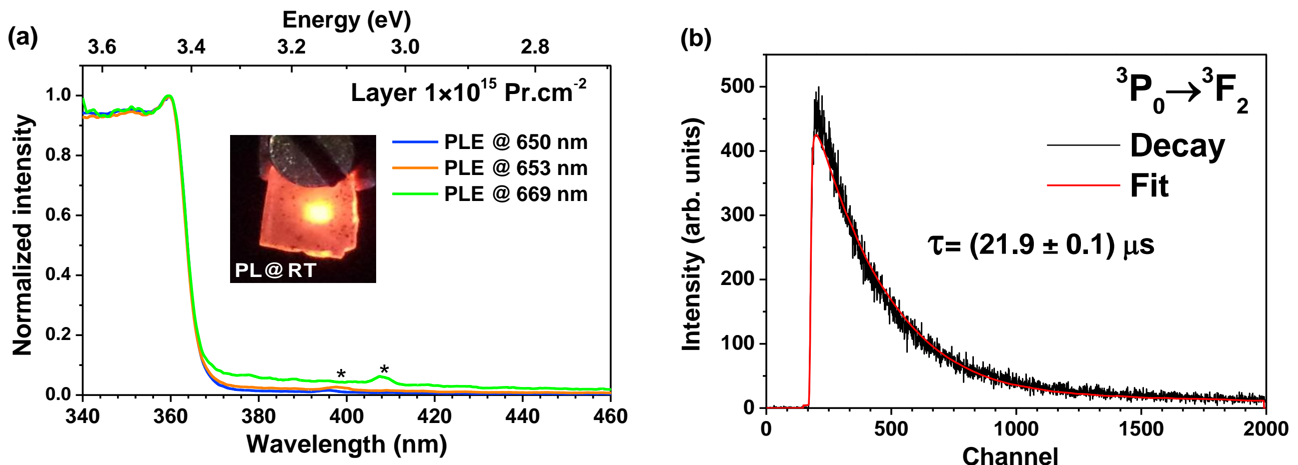

Figure 5-32 – RT PLE spectra of the GaN layer implanted with higher fluence (the asterisks denote artefacts from the system). The inset shows the RT visual appearance of the intra-shell Pr^{3+} light emission in this layer. (b) RT lifetime measurement for the $^3P_0 \rightarrow ^3F_2$ transition for the same sample.

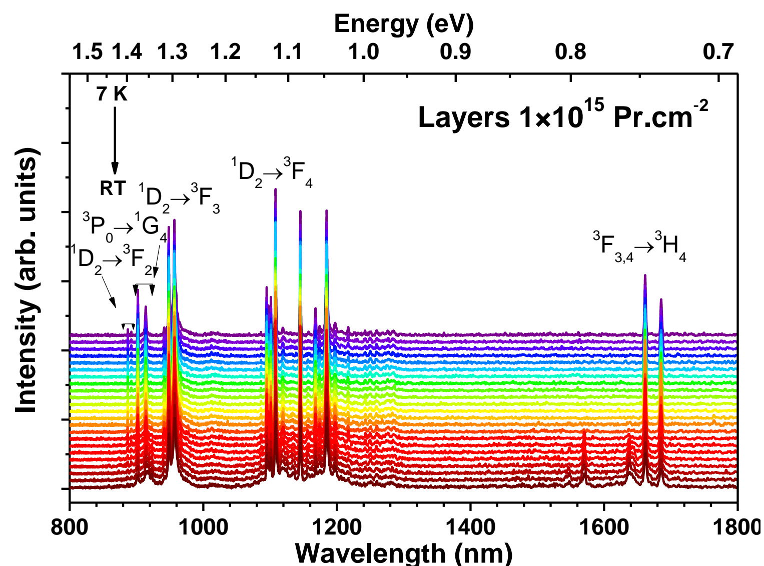

Figure 5-33 – Temperature dependent PL of the Pr^{3+} emission in the infrared region for the GaN layer implanted with 1×10^{15} $Pr.cm^{-2}$. The spectra are vertically shifted for clarity.

5.5. GaN and AlN layers co-implanted with Eu^{3+} and Pr^{3+}

Despite the fact that several works have been published in the literature concerning Eu^{3+} and Pr^{3+} luminescence in nitrides [45,47,67,71,94–96], much less attention has been paid to the co-doping effects with different lanthanide ions in order to improve the potentialities of the RE emitters in the nitride systems. In this section, the optical properties of AlN and GaN layers co-doped with Eu^{3+} and Pr^{3+} ions, both important activators in the red spectral region in several wide bandgap hosts, are discussed. The nitride layers were implanted with both ions, followed by thermal annealing treatments in order to recover the damage and promote the ions optical activation. It was found that the co-doping process leaded to simultaneous Eu^{3+} and Pr^{3+} emission,

widening the contribution of the red spectral range light provided by both ions. The evolution of the ions PL intensity with temperature was analysed for both AlN:Eu,Pr and GaN:Eu,Pr hosts, and compared with the ones of individually doped layers (GaN:Eu, GaN:Pr, AlN:Eu and AlN:Pr).

Figure 5-34a shows the random and aligned RBS/C spectra for as-grown AlN, after implantation with Pr and after co-implantation with Pr and Eu. The RE profiles extracted from the random RBS spectra are shown in Figure 5-34b. In the case of GaN, the maximum RE concentration is found at ~ 20 - 30 nm depth, while the same implantation conditions lead to a wider profile in AlN, with a range of ~ 50 nm. The maximum concentrations in the co-implanted samples are 0.18 at% and 0.1 at% for GaN and AlN, respectively. In both cases, the RE profiles do not change after annealing. Note that it is not possible to distinguish between Eu^{3+} and Pr^{3+} due to their similar mass. The RBS/C spectra in Figure 5-34a reveal the expected increase of backscattering yield from Al within the implanted region due to implantation defects. However, the effect is much stronger for GaN than for AlN (not shown). As a measure for the crystalline quality and level of implantation damage, the minimum yield (yield in the aligned spectrum divided by the yield in the random spectrum) was calculated for Ga and Al within a window comprising the entire implanted region. The minimum yield, χ_{min}, for Al within the implanted area increases from 2% in the as-grown to 5% for the AlN:Pr sample and to 7% for the co-implanted sample. The Ga minimum yield for the as-grown sample is similar to AlN with 2%. However, after Pr implantation χ_{min} increases to 18% and reaches 39% for the co-implanted sample. Annealing recovers the lattice damage only partly resulting in minimum yields of 6% and 30% for AlN and GaN, respectively.

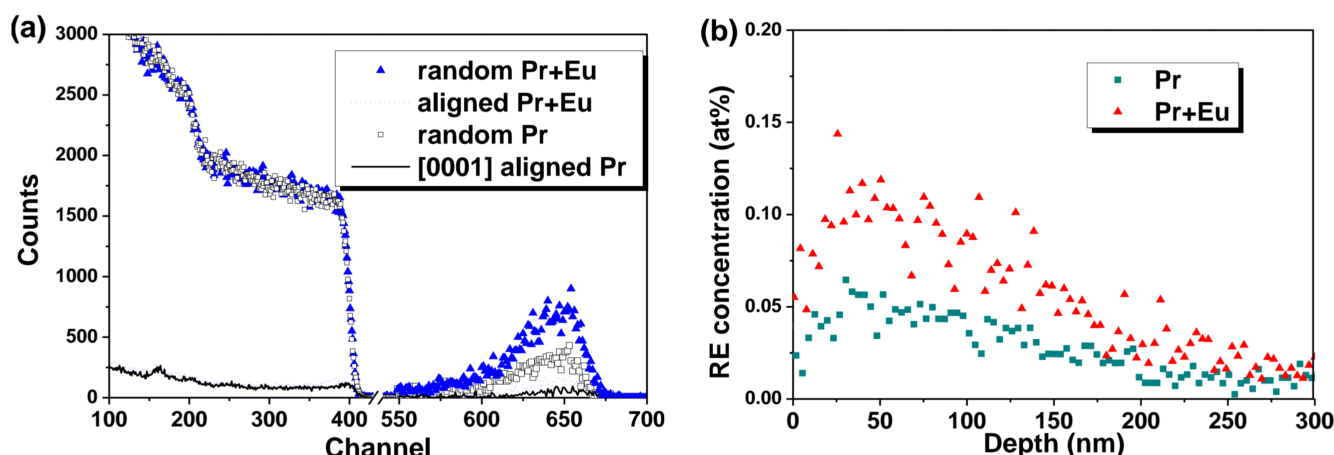

Figure 5-34 – (a) RBS/C random and aligned ([0001]) spectra of the AlN:Pr and AlN:Eu,Pr layers. (b) RE profiles extracted from the spectra in Figure a.

As mentioned previously, it is well established that RE ions in nitride layers are essentially incorporated in substitutional sites or in sites slightly displaced from the substitutional ones [45,67,70,71,78,96]. The fraction of the RE in these near-substitutional sites, f_s, can be estimated by

$$f_s = \frac{1-\chi_{min}^{RE}}{1-\chi_{min}^{Ga\,(Al)}}. \qquad \textbf{Eq. 5-1}$$

Directly after implantation, values of f_s of 87% and 86% were obtained for the AlN:Pr and AlN:Eu,Pr layers, respectively. For GaN the substitutional fraction is estimated to be 89% for simple Pr-implantation, but only 69% for Pr and Eu co-implantation. In both materials the substitutional fraction decreases slightly after annealing, possibly due to the formation of RE-defect clusters.

Figure 5-35 shows the normalized high resolution 14 K PL spectra of the Eu^{3+} and Pr^{3+} co-implanted and annealed GaN and AlN layers in the ions-related emission region (after spectral deconvolution with a broad band present in the GaN sample). The intensity was normalized to the emission maxima of the RE ions and the PL was obtained by above (for the GaN layers) and below (for the AlN layers) bandgap excitation, using the 325 nm line of a He-Cd laser. For comparison purposes the corresponding spectra of the GaN:Eu, GaN:Pr, AlN:Eu and AlN:Pr doped systems were added to Figure 5-35. As can be identified, after implantation and annealing the co-doped GaN:Eu,Pr and AlN:Eu,Pr samples exhibit simultaneously the $^5D_0 \rightarrow {}^7F_2$ and the $^3P_0 \rightarrow {}^3F_2$ transitions, corresponding to the highest intensity transitions of the Eu^{3+} and Pr^{3+} ions in the nitride layers, respectively [67,96]. For the Eu^{3+} luminescence in the GaN:Eu,Pr layer, the $^5D_0 \rightarrow {}^7F_2$ transition is resolved in three main lines with strongest intensity for the 621.6 and 622.5 nm lines. Their spectral shape and relative intensity resembles the ones obtained from the layers studied in section 5.3, attributed to the contribution of more than one Eu^{3+} centre (namely 2 centres: Eu1 and MS8/Eu_{2I} – see Table 5-2).

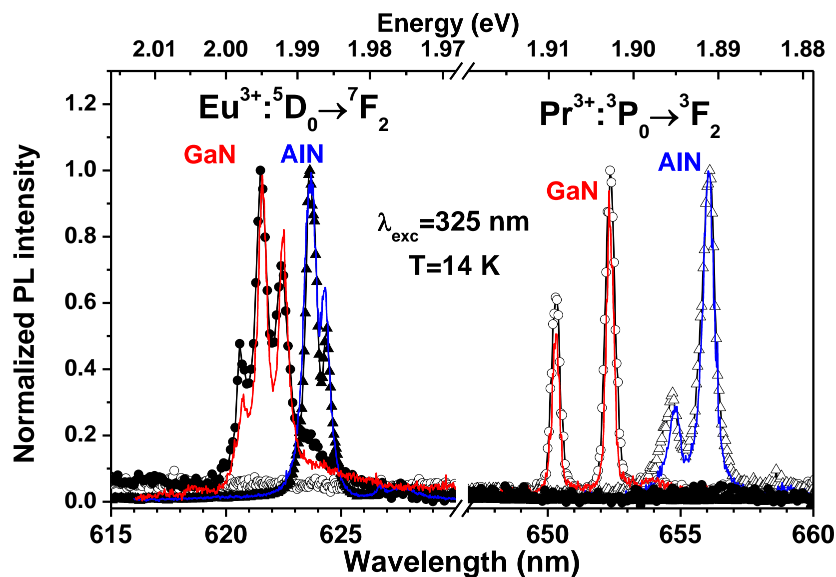

Figure 5-35 – Normalized 14 K PL spectra of Eu^{3+} and Pr^{3+} doped nitride layers obtained with 325 nm excitation. Full and open circles stand for separated GaN layers doped with Eu^{3+} (GaN:Eu) and Pr^{3+}(GaN:Pr), respectively, full and open triangles for separated AlN layers doped with Eu^{3+} (AlN:Eu) and Pr^{3+}(AlN:Pr) respectively. Red and blue lines correspond to the spectra of GaN and AlN samples co-doped with both ions (GaN:Eu,Pr; AlN:Eu,Pr), respectively.

For the Pr^{3+} emission in the GaN:Eu,Pr layer, the $^3P_0 \rightarrow {}^3F_2$ transition occurs at the same energy as the one detected in GaN:Pr layers, with the main lines at ~ 650.3 nm and ~ 652.3 nm (similar to the values reported in Table 5-4) [67,96]. Therefore, despite the stronger lattice damage and reduced substitutional fraction in the co-doped sample, the peak position and spectral shape of

the intraionic luminescence are comparable to samples implanted with only one ion and lower total fluence. In the case of AlN, also a very good match between the co-implanted sample and the ones implanted with only one RE ion is identified in Figure 5-35. The Eu^{3+}-related emission is split into two emission lines, one at 623.7 nm and the other at 624.3 nm, while for the $^3P_0 \rightarrow ^3F_2$ Pr^{3+} transition the lines are placed at 654.8 and 656.1 nm, also in agreement with what was observed in the previous section for the AlN:Pr^{3+} layer. The Pr^{3+} emission lines in both nitrides are compatible with the presence of only one emitting centre.

The temperature dependence of the PL intensity for the $^5D_0 \rightarrow ^7F_2$ (Eu^{3+}) and the $^3P_0 \rightarrow ^3F_2$ (Pr^{3+}) lines for the co-doped nitride layers is depicted in Figure 5-36 and Figure 5-37, respectively. Table 5-6 shows the IQE values for each transition of both samples. For the GaN layers doped with Eu^{3+} and Pr^{3+} ions separately, several reports indicate that the intraionic luminescence decreases gradually with increasing temperature [45,67,96]. As shown in Figure 5-36, for the GaN layer co-doped with Eu^{3+} and Pr^{3+} ions the integrated intensity of the $^5D_0 \rightarrow ^7F_2$ and $^3P_0 \rightarrow ^3F_2$ transitions follow the same trend, both increasing up to ~ 100 K and for higher temperatures a decrease of the luminescence is observed. At RT the PL intensity is about 60% of the one recorded at 14 K for both ions. Such behaviour in the 14 - 100 K temperature range could be explained by a thermal population of both RE ions by thermal detrapping of shallow trap levels. This interpretation is in good agreement with the elevated level of residual implantation defects after annealing in this sample. For higher temperatures, the enhancement of the nonradiative recombination processes leads to a decrease of the intraionic PL intensity. This behaviour is remarkably different from the ones for GaN layers implanted only with Eu^{3+} or Pr^{3+} observed in the two previous sections, where the emission was seen to decrease in all the range between 14 K and RT. This difference can be explained by the presence of different nonradiatiave recombination and thermal detrapping processes probably induced by the co-doping.

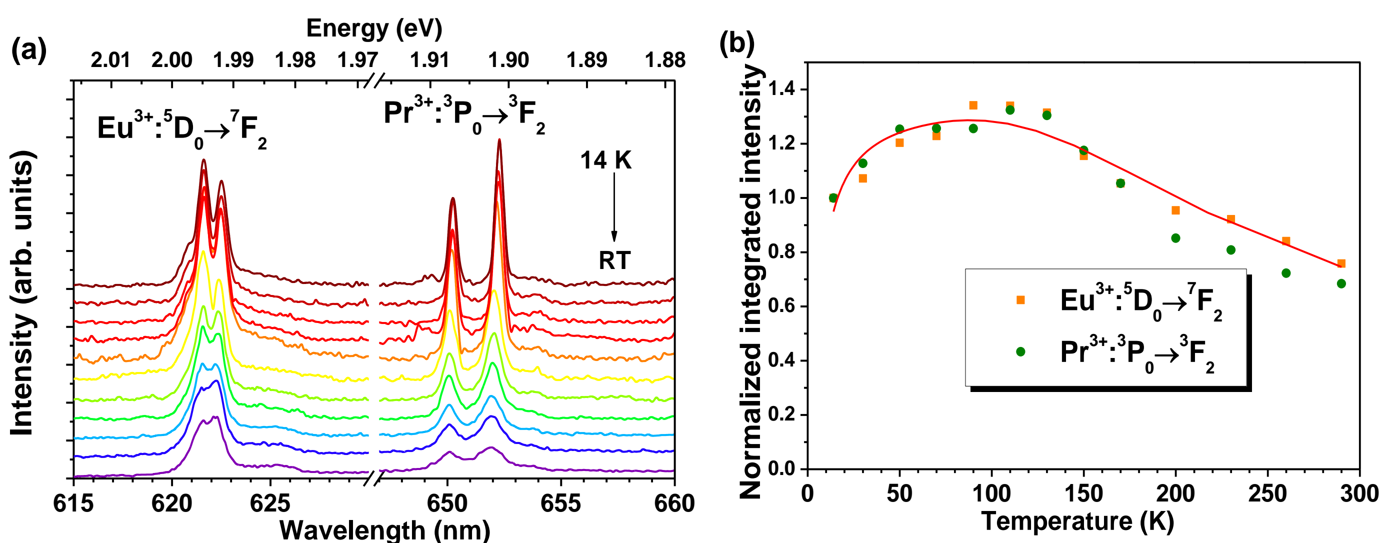

Figure 5-36 – (a) Temperature dependent PL spectra of the Eu^{3+} and Pr^{3+} highest intensity transitions for the co-doped GaN layer. The spectra were obtained with above bandgap excitation and were vertically shifted for clarity. (b) Evolution of the integrated intensity of the $^5D_0 \rightarrow ^7F_2$ (Eu^{3+}) and the $^3P_0 \rightarrow ^7F_2$ (Pr^{3+}) lines with the temperature.

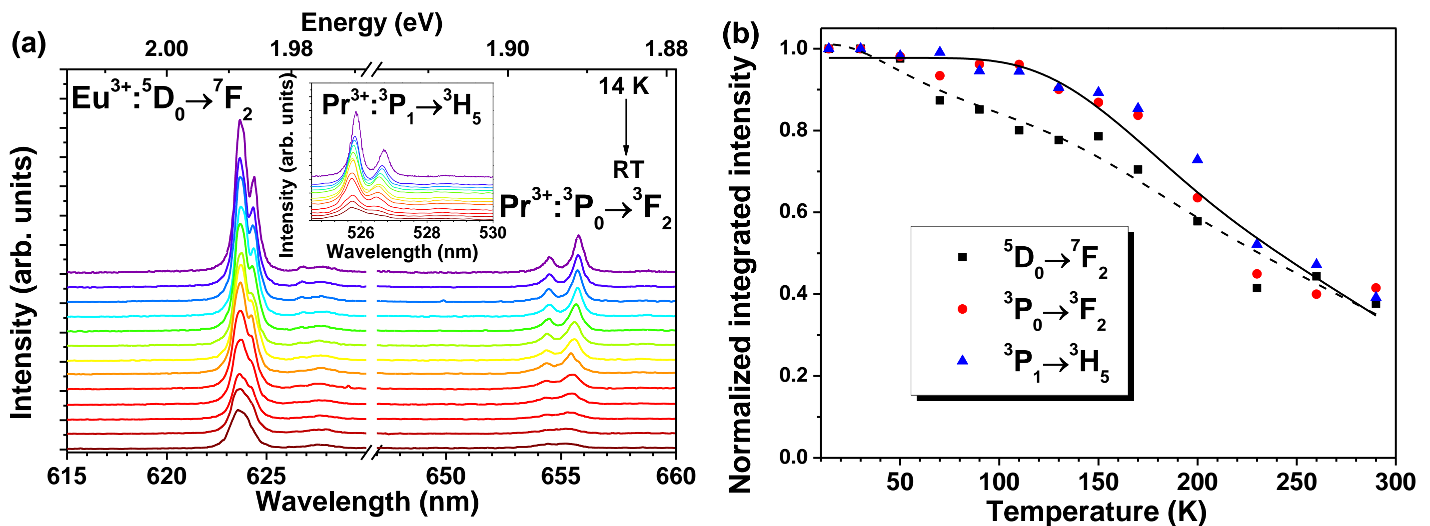

Figure 5-37 – (a) Temperature dependent PL spectra of the Eu^{3+} and Pr^{3+} highest intensity transitions for the co-doped AlN layer. The spectra were obtained with below bandgap excitation and were vertically shifted for clarity. (b) Evolution of the integrated intensity of the $^5D_0\rightarrow^7F_2$ (Eu^{3+}), the $^3P_0\rightarrow^3F_2$ (Pr^{3+}) and $^3P_1\rightarrow^3H_5$ (Pr^{3+}) lines with the temperature.

Table 5-6 – IQE values for the Eu^{3+} and Pr^{3+} multiplet transitions of the co-implanted GaN and AlN layers.

	GaN layers		AlN layers		
Transitions	**Eu^{3+}:$^5D_0\rightarrow^7F_2$**	**Pr^{3+}:$^3P_0\rightarrow^3F_2$**	**Eu^{3+}:$^4D_0\rightarrow^7F_2$**	**Pr^{3+}:$^3P_0\rightarrow^3F_2$**	**Pr^{3+}:$^3P_1\rightarrow^3H_5$**
IQE (%)	76	68	38	42	39

Figure 5-37a and b shows the temperature dependent PL spectra and the behaviour of the integrated intensity for the RE transitions in the AlN:Eu,Pr layer. Additionally, while for the GaN:Eu,Pr layer the temperature dependence of the integrated intensity for the main emission lines of both RE ions follow the same trend, for the case of the AlN:Eu,Pr layer distinct behaviours were observed for both ions (Figure 5-37b). In particular, the decrease in intensity of the Eu^{3+} $^5D_0\rightarrow^7F_2$ transition is described by two nonradiative paths in a fair agreement with previous results for the AlN:Eu layers [96]. On the other hand, the decrease of the intensity for Pr^{3+} luminescence, coming from both the $^3P_0$ and $^3P_1$ multiplets, reveals that the luminescence quenching can be accounted by a single nonradiative extinction mechanism.

In contrast with the GaN:Eu,Pr layer for which the luminescence is obtained upon above GaN bandgap (Figure 5-38a), in the AlN case the luminescence was excited by below bandgap energy, as identified by the RT PLE spectra shown in Figure 5-38b. Eu^{3+} luminescence is excited via the previously reported excitation bands (X2) and (X1) with maxima at ~ 265 nm and 345 nm, respectively [71,86,90,96–98]. By monitoring the $^3P_1\rightarrow^3F_2$ transition of Pr^{3+} ion in the co-doped sample a main broad excitation band peaked near the same peak position of the X2 band and a less intense band at ~ 320 nm can also be recognized in the spectrum. Monitoring at the $^3P_1\rightarrow^3H_5$ transition, mostly the broad excitation X2 band is identified. These peak positions are close to the

energy values earlier stated for Pr^{3+} in AlN layers [90,98]. Additionally, an excitation band in the shortest wavelength range is also known to populate a DAP transition involving Al vacancies in AlN layers, which is responsible for a broad band luminescence the ~ 450 nm region, as can be seen in Figure 5-38c [49].

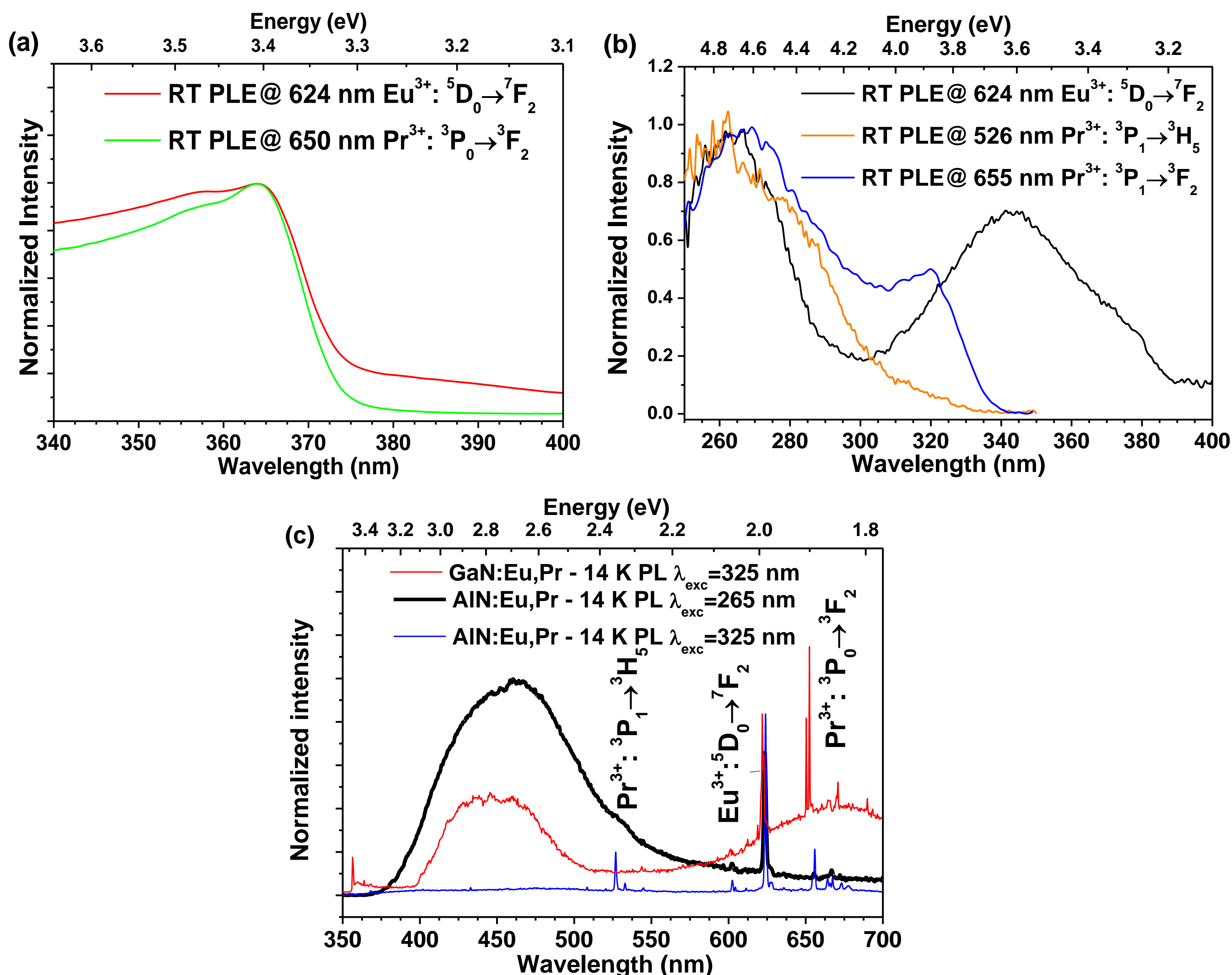

Figure 5-38 –RT PLE spectra for the (a) GaN:Eu,Pr and (b) AlN:Eu,Pr samples monitored at the transitions of the Eu^{3+} and Pr^{3+} ions. (c) Enlarged 14 K PL spectra for co-doped AlN and GaN layers obtained with the 325 nm line of a He-Cd laser (solid lines) and 265 nm excitation (dashed line).

With 325 nm below bandgap excitation the excited levels of both ions in the co-doped sample were being populated simultaneously. Despite the fact that the Pr^{3+} ions could be excited at shorter wavelengths, their emission intensity is mainly hidden by the strong AlN defect band. With 265 nm excitation, besides the violet/blue AlN defect band, only the europium luminescence could be distinguished (Figure 5-38c). While for the GaN:Eu,Pr layer the Eu^{3+} and Pr^{3+} peak intensities are similar at low temperature, for the AlN:Eu,Pr layer the Pr^{3+} emission has a lower intensity than that of Eu^{3+}, as expected from the PLE data (Figure 5-38b). Figure 5-38c also puts in evidence the presence of a broad band in the red spectral region (RL) for the GaN sample, as was previously mentioned. The presence of this red band, which is not in the same spectral position as

the ones observed in the samples analysed in sections 5.3 and 5.4 (YL bands), may also be accounted for the different temperature behaviour verified in the co-doped sample.

RT TRPL measurements were also performed (Figure 5-39) in order to get some insight about the dynamics of the identified transitions. The samples were excited with 325 nm photon excitation and the spectra were obtained with different delay times after the pulse of the lamp, for a fixed time window of 0.5 ms. Despite the fact that the intensity of the Pr^{3+} $^3P_0 \rightarrow {}^3F_2$ transition is very weak when compared with the Eu^{3+} related transition, it is possible to observe that the $^5D_0 \rightarrow {}^7F_2$ Eu^{3+} emission vanishes for higher delays in both samples, indicating a shorter lifetime for the Pr^{3+} $^3P_0 \rightarrow {}^3F_2$ transition, which is compatible with the results of the previous sections and the fact that the Pr^{3+} $^3P_0 \rightarrow {}^3F_2$ is a spin allowed transition. Considering the $^5D_0 \rightarrow {}^7F_2$ Eu^{3+} transition, and comparing the decay profile for both samples, a shorter lifetime was found for the GaN sample. In the case of this sample, the Eu^{3+} emission almost disappears for delays above 0.5 ms, while for the AlN sample the emission vanishes for delays higher than 1.2 ms. This indicates a lifetime in the range of a few hundreds of μs for GaN, as previously found for the GaN layers doped only with Eu^{3+} studied in section 5.3, which is also in line with the literature [48,60,61,70]. For the AlN samples, the lifetime of the same transition is slightly higher, close to the millisecond range.

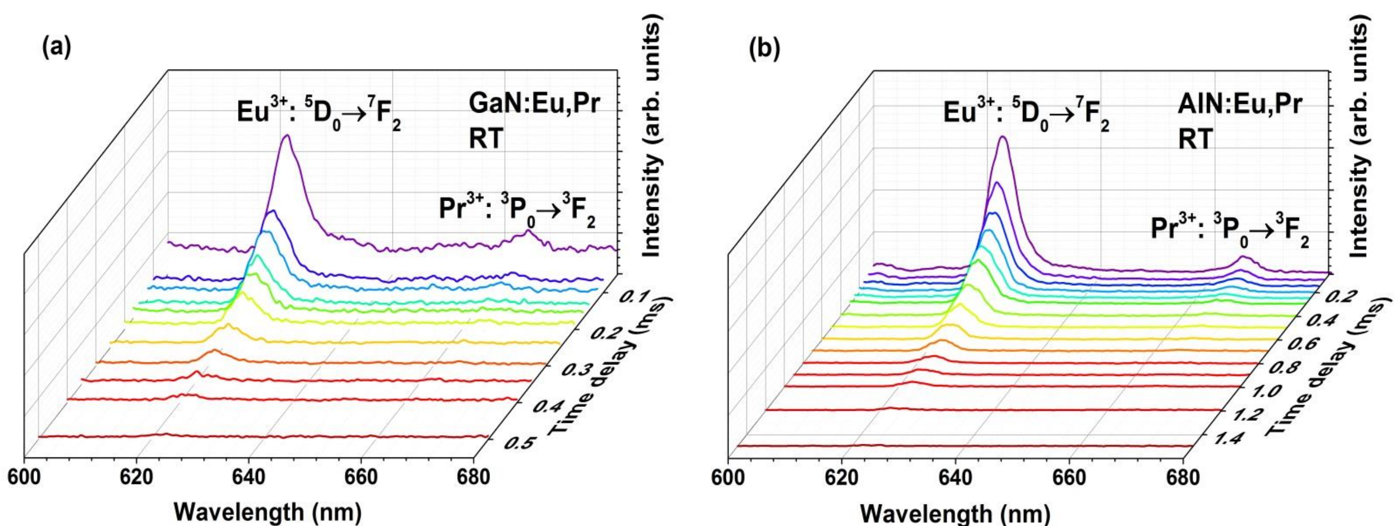

Figure 5-39 – TRPL spectra of the (a) GaN:Eu,Pr and (b) AlN:Eu,Pr samples, obtained under 325 nm excitation of a Xe lamp.

GaN layers co-implanted with other RE ions, namely Tm^{3+}, Er^{3+} and Eu^{3+}, were also studied (not shown). However, despite the fact that both Tm^{3+} and Eu^{3+} ions were successfully optically activated, only the Eu^{3+}-related emission was observed in the visible range, leading only to red emission.

5.6. $Al_xGa_{1-x}N$ layers implanted with Tb^{3+} and Tm^{3+}

5.6.1. Tb^{3+}

For green lighting purposes, besides the optical activation of Er^{3+} [99], Tb^{3+} ions have also been incorporated and optically activated in GaN, AlN and $Al_xGa_{1-x}N$ alloys [48,100–105].

With a $4f^8$ electronic configuration, the green emission provided by Tb^{3+} is known to be due to electronic transitions between the $^5D_4 \rightarrow {}^7F_6$ multiplets occurring at ~ 491 nm [102,106,107]. Additionally, low energy transitions from the $^5D_4 \rightarrow {}^7F_{J(5-0)}$ have been observed, as well as blue light in the 380 - 490 nm region due to $^5D_3 \rightarrow {}^7F_J$ lines [48,102,104–106,108]. Tb^{3+} luminescence in $Al_xGa_{1-x}N$ layers has been reported in photoluminescence and cathodoluminescence studies [48,90,102,104–106,108,109], typically exhibiting the blue and green recombination, with their intensity showing a strong dependence on the alloy composition and temperature.

As mentioned in Chapter 4, the analysis of the excitation paths for the intra-$4f^n$ RE^{3+} emission in nitrides have been subject to different approaches, such as the alignment of the atomic-like levels with the material bandgap [110,111] and the generation of bound exciton with further energy transfer, considering that the RE^{3+} acts as an isoelectronic trap capturing a carrier into a localized state, and subsequent capture of a carrier of opposite charge by Coulomb interaction [98]. The importance of both approaches was recently emphasized by Wang and co-workers [71] in the analysis of the optical features in europium doped $Al_xGa_{1-x}N$ alloys. In particular, the authors propose the creation of core excitonic complexes as the main paths for the Eu^{3+} emission and their model formally equates charge transfer with isoelectronic exciton creation [71].

In this section, the structural and luminescent features of Tb implanted $Al_xGa_{1-x}N$ ($0 \leq x \leq 1$) layers submitted to a rapid thermal annealing (RTA) at 1200 ^oC were analysed. The AlN molar fractions of the analysed samples correspond to x = 0, 0.19, 0.53, 0.77 and 1, as determined by RBS. With exception of the layers with low AlN content, all the implanted and annealed samples exhibit the green $^5D_4 \rightarrow {}^7F_J$ optical activity of the Tb^{3+} ions which can be observed up to RT. Blue light emission from the $^5D_3 \rightarrow {}^7F_J$ transitions was undetectable in all samples covering the entire alloy composition. For the GaN samples, the intraionic luminescence is only observed after a thermal annealing treatment at 1400 ^oC and high pressure. The preferential population paths of the Tb^{3+} ions were identified by PLE measurements at RT. The green emission of the Tb^{3+} ions in samples with lower aluminium content is mainly excited through across bandgap excitation while subgap excitation bands were identified for samples with higher compositions, x. Aiming to contribute to the understanding of the nature of the excitation pathways involved in the Tb^{3+}-doped $Al_xGa_{1-x}N$ alloys within the framework of recently published data [48,71,90,98,101,102,104,105,110] the optical properties of the trivalent ion inside the nitride alloys were fully exploited. The present data strongly suggests an assignment to excitonic features in agreement with the dependence of the Tb^{3+} intra-shell line broadening with increasing composition.

5.6.1.1. Structural characterization

5.6.1.1.1. Raman Spectroscopy

The $Al_xGa_{1-x}N$ samples were analysed by Raman spectroscopy and the results can be seen in Figure 5-40. In the case of GaN and AlN samples, Figure 5-40 shows the typical Raman spectra of the hexagonal wurtzite structure where the A_1 (TO and LO) modes and the two E_2 (high and low) phonons were identified for AlN and only the A_1 (TO and LO) modes and the E_2^H were observed for GaN.

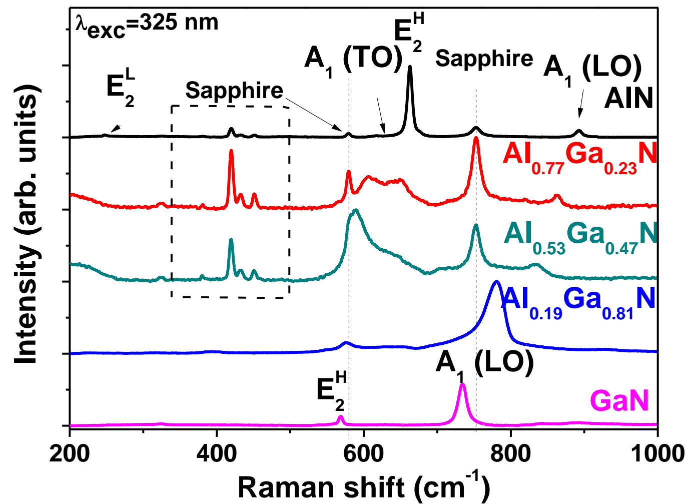

Figure 5-40 – RT Raman spectra obtained in backscattering configuration upon excitation with the 325 nm He–Cd laser line.

For the case of the $Al_xGa_{1-x}N$ alloy, it was observed that the A_1 (LO) phonon shifts smoothly to higher energies with the increasing AlN molar fraction, as reported in the literature [112]. Nevertheless, the presence of free carriers in the samples can lead to a high-frequency shift of the LO-phonon lines since there is the possibility of the formation of mixed plasmon-phonon modes [113]. Davydov *et al*. [113] proposed a set of equations to theoretically calculate an approximate position of the A_1(TO), A_1(LO), E_1(TO) and E_2(low) modes as a function of the AlN molar fraction. The position of the A_1 modes can be predicted using: A_1(LO): $734 + 153\, x + 75\, x\, (1\text{-}x)$ cm^{-1} and A_1(TO): $531.8 + 64.5\, x - 1.9\, x\, (1\text{-}x)$ cm^{-1} while the E_1 mode is predicted by $742 + 170\, x + 65\, x\, (1\text{-}x)$ cm^{-1} and the E_2^L by $172 + 43.5x - 14.5\, x\, (1\text{-}x)$ cm^{-1}. The small bowing parameter (~ 1) for the A_1(TO) mode indicates an approximately linear variation which makes this equation suitable for estimating x from the Raman spectra [33]. In the present samples the A_1(LO) is observed at ~ 780 cm^{-1} for $x = 0.19$, ~ 833 cm^{-1} for $x = 0.53$ and ~ 863 cm^{-1} for $x = 0.77$. Using the above mentioned equation to estimate the position of the modes, values of ~ 775 cm^{-1} for x=0.19, ~ 834 cm^{-1} for x=0.53 and ~ 865 cm^{-1} for x=0.77 were obtained. The last two values are in good agreement with the predicted ones [113]. The higher shift of the A_1 mode for the sample with x=0.19 can be explained by a higher concentration of free carriers. This shift was only clearly observed when the sample was analysed with the 325 nm (3.81 eV) line which corresponds to a resonant excitation in the case of the sample with x = 0.19. Using Vegard's law (Eq. 1-4) to determine the bandgap of this sample a value of ~ 3.78 eV was found taking into account a

bowing parameter listed in Table 1-2 [114]. The resonant excitation could justify the higher intensity of the A_1(LO) mode for this sample. It is known that both the A_1(LO) and E_1(LO) modes show one-mode behaviour, whereas the A_1(TO), E_1(TO), E_2^H, and E_2^L show two-mode behaviour [33] which is in accordance with the results for the present samples. The E_2^H mode shifts to higher energies with increasing Al content and for AlN molar fractions of 0.53 and 0.77 two peaks are observed in agreement with the results reported in the literature [16,18]. The shape of the detected peaks is very similar with the ones reported by Davydov *et al*. [113].

5.6.1.1.2. RBS/C measurements

Figure 5-41a shows the random and aligned RBS/C spectra along the [0001] crystallographic direction measured directly after implantation and after RTA at 1200 °C, for the $Al_{0.77}Ga_{0.23}N$ sample. The aligned spectrum of the as-grown sample is also shown for reference. As mentioned before, the minimum yield, χ_{min} (defined as the ratio of the backscattering yield of the aligned to that of the random spectrum), is a measure of the crystalline quality. A χ_{min} ~ 2% was obtained for the as-grown samples, indicating a good crystalline quality.

After implantation, the backscattering yield for the Ga-signal in the aligned spectrum increases due to implantation damage and slightly decreases again after thermal annealing due to partial recovery of the lattice. This behaviour is observed for all the studied samples. Figure 5-41b presents the comparison of χ_{min} of the pure, implanted and annealed samples for the different AlN molar fraction. The χ_{min} of the as-implanted samples decreases with increasing AlN molar fraction until x = 0.77, revealing the augmented resistance to radiation damage in $Al_xGa_{1-x}N$ alloys with high AlN content, as previously reported [115].

The minimum yields after annealing are similar for all samples. In the inset of Figure 5-41b the substitutional fraction, f_s, representing the fraction of Tb^{3+} ions on substitutional or near-substitutional cation sites, is displayed. In contrast to the GaN sample that presents a strong decrease in f_s (to ~ 0%) after RTA at 1200 °C, this fraction decreases only slightly for most of the samples with x > 0 after RTA.

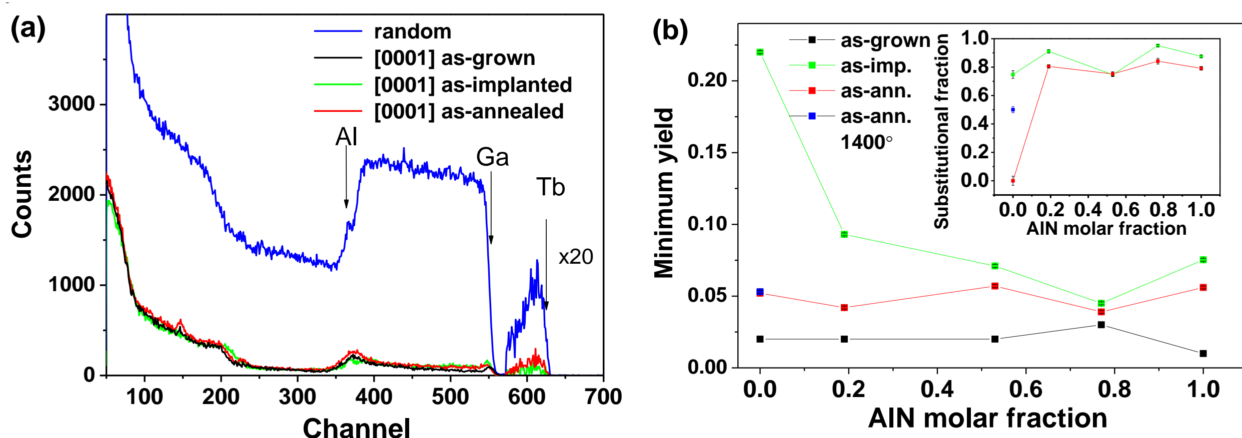

Figure 5-41 – a) Random and aligned RBS/C spectra along the [0001] crystallographic direction, measured directly after implantation and after RTA at 1200 °C, for the $Al_{0.77}Ga_{0.23}N$ sample. b) Comparison of χ_{min} of the pure, implanted and annealed samples for the different $Al_xGa_{1-x}N$ compositions. The inset shows the RE substitutional fraction for all the samples analysed in this sub-section.

Figure 5-42a shows RBS/C spectra for the two GaN samples annealed at 1200 °C and 1400 °C aligned with [0001] and the comparison with the as-implanted sample. Figure 5-42b represents an amplification of the Tb region, revealing that a large fraction of Tb is seen to diffuse towards the GaN surface for the sample annealed at 1200 °C, probably related with the dissociation of GaN at this high temperature when no measures are taken to protect the surface [116]. The GaN sample annealed at 1400 °C (and at high nitrogen pressure effectively protecting the GaN surface from dissociation) shows no significant surface diffusion of Tb ions and presents a higher f_s (50%) as compared to the GaN sample annealed at 1200 °C (0%). The suppression of nitrogen vacancy formation at high N pressures may explain the differences observed in the two samples. Nevertheless, also in the sample annealed at 1400 °C, the aligned spectrum ([0001]) shows an increase in backscattering yield from Tb (decrease of the substitutional fraction) close to the surface.

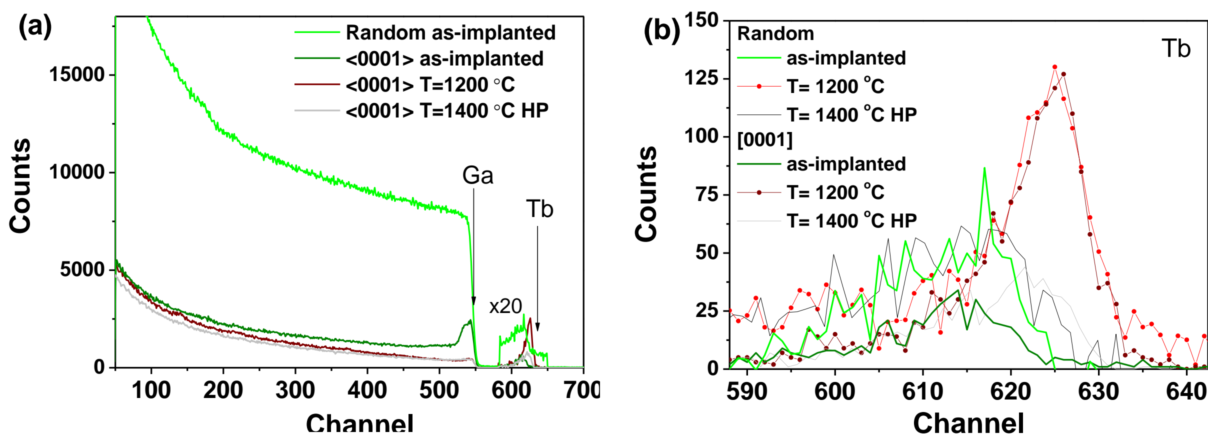

Figure 5-42 – RBS/C spectra for the two GaN:Tb samples annealed at 1200 °C and 1400 °C: (a) the entire spectra and (b) a detailed view of the Tb signal.

5.6.1.2. Optical characterization

5.6.1.2.1. Low temperature PL

Tuning the bandgap between the binaries GaN (~ 3.4 eV) and AlN (~ 6.2 eV) is a common engineering procedure in the development of $Al_xGa_{1-x}N$ ternary alloys by varying the AlN molar fraction between zero and one ($0 \leq x \leq 1$). The present analysis focuses on ion implanted and annealed layers with $x = 0$, 0.19, 0.53, 0.77 and 1, with expected bandgaps of 3.4 eV, 3.78 eV, 4.63 eV, 5.38 eV and 6.2 eV [114], respectively. Therefore, when the 325 nm He-Cd laser line (3.8 eV) is used as excitation source the samples with lower x ($x \leq 0.19$) are still excited above bandgap, while all the other samples are excited below the bandgap.

Figure 5-43a shows the 14 K PL spectra obtained with 325 nm photon excitation for all the implanted and annealed samples. The optical activation of the Tb^{3+} ions was successfully achieved for all the samples, with the exception of the GaN layer annealed at 1200 °C. For this binary compound a higher temperature treatment (1400 °C) was required in order to observe the Tb^{3+}-related transitions. These observations are in agreement with the RBS data, since only for the

higher annealing temperature a high substitutional fraction was found together with the absence of Tb-diffusion towards the surface. Thus, hereafter, the analysis will be focused on this sample and the sample treated at 1200 °C will be discarded. Tb^{3+} $f\rightarrow f$ radiative transitions occur from the $^5D_4$ multiplet, whereas the recombination from the $^5D_3$ state was not observed. Besides the intra-shell luminescence, the whole set of studied samples exhibits host defect-related broad emission bands in the near-UV and visible spectral region, overlapped with the ion emission. The maximum of the broad visible band (between ~ 450 nm and 600 nm; ~ 3.1 eV – 2.07 eV) is seen to shift to higher energy with increasing *x*. Noteworthy, for the AlN sample, the broad host defect band in the visible spectral region is practically absent under the used excitation conditions and a strong near-UV/violet band is identified. As mentioned before, oxygen-related and native defects-assigned emission bands, with maxima in the near-UV (~ 400 nm; ~ 3.1 eV) and blue spectral region (~ 480 nm; ~ 2.58 eV), are commonly observed in the AlN samples [43–45]. Typically, these optically active defects are preferentially observed for UV excitation, namely for wavelengths shorter than ~ 320 nm (~ 3.9 eV). In the case of the GaN sample treated at higher temperature, besides the typical yellow luminescence band [11,55], a well-defined near band edge emission is also observed, attesting the good optical quality of the sample.

Enlarged and high resolution spectra of the 14 K intra-shell Tb^{3+} luminescence are depicted in Figure 5-43b. At this temperature, the highest intensity of the Tb^{3+} emission is observed for the binary samples. In the case of GaN and the alloy with the lower AlN content, *x* = 0.19, the highest peak intensity was observed for the $^5D_4 \rightarrow {^7F_6}$ transition, at ~ 491 nm, and the highest total intensity for the $^5D_4 \rightarrow {^7F_5}$ (~ 545 nm) recombination (obtained from the overall integrated area). Minor intensity lines attributed to $^5D_4 \rightarrow {^7F_4}$ (~ 584 nm) and the $^5D_4 \rightarrow {^7F_3}$ (~ 625 nm [shown in Figure 5-43a]) were also observed. The similarity of the spectral shape of the $^5D_4 \rightarrow {^7F_J}$ transitions between $Al_{0.19}Ga_{0.81}N$ and GaN samples suggests that the Tb^{3+} optically active ions in these two layers have alike local environments. As previously mentioned and according to the channelling data, the RE ions in nitrides preferentially substitute the cations in regular or slightly displaced sites [67,117,118]. For Tb^{3+} ions in a substitutional cation site, corresponding to a C_{3v} coordination symmetry, the degeneracy of the ion multiplets is broken down by the action of the host crystalline field. A state with *J* = 6, 5, 4 will split in a total of nine, seven and six energy levels, respectively (see Table 4-1) [68]. For *J* = 6 five singlets (3 Γ_1+2 Γ_2) and four doublets (4 Γ_3) are expected, while the *J* = 5 state splits into three singlets (1 Γ_1+2 Γ_2) and four doublets (4 Γ_3) and the *J* = 4 unfolds as 2 Γ_1+1 Γ_2+3 Γ_3.

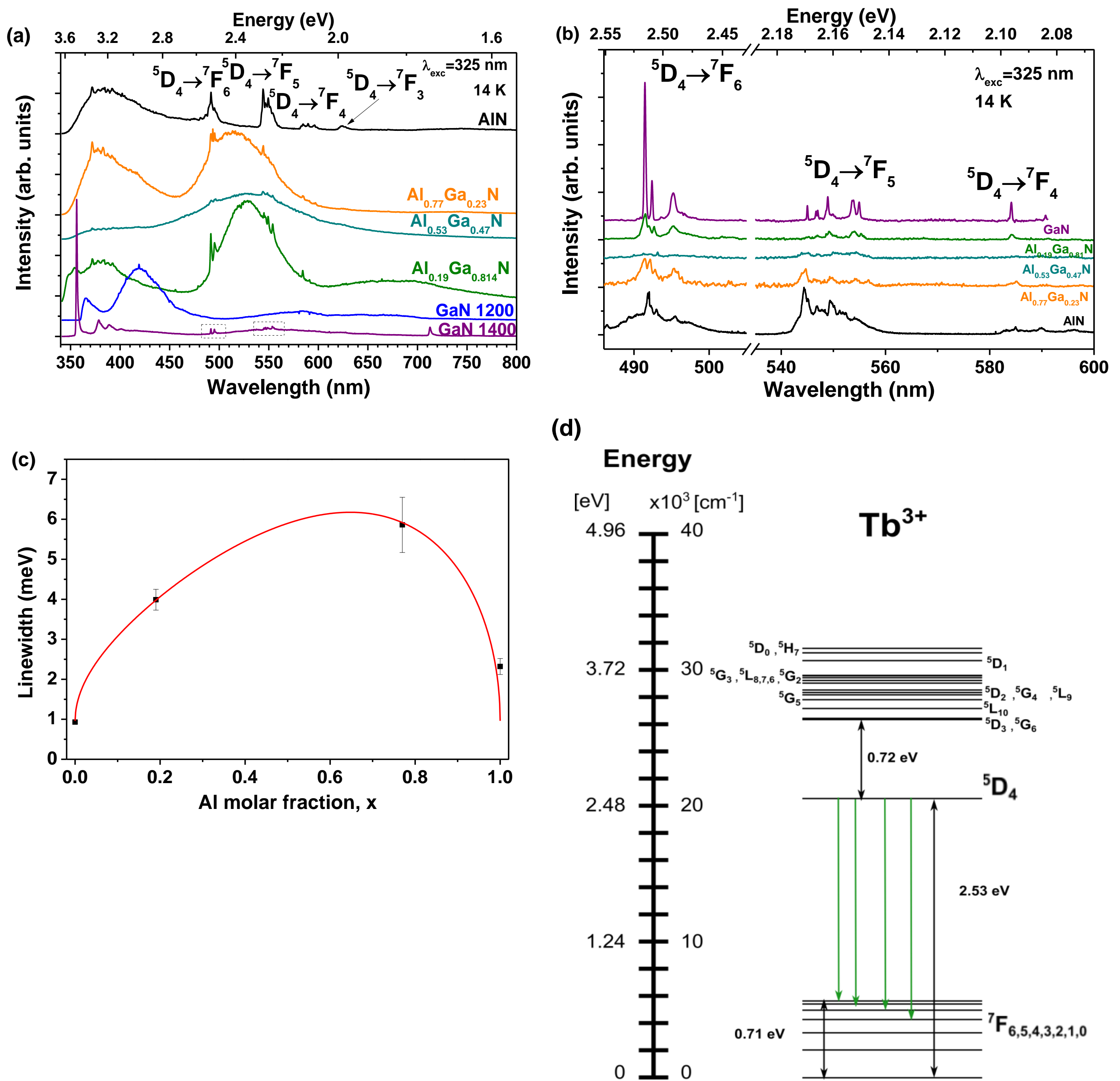

Figure 5-43 – (a) 14 K PL spectra of the $Al_xGa_{1-x}N$:Tb samples (with $0 \leq x \leq 1$) obtained with 325 nm He-Cd laser line excitation. (b) Expanded region of the Tb^{3+} luminescence after baseline subtraction. (c) Linewidth as a function of the alloy composition fitted with Eq. 4-56. The linewidth corresponds to the first Stark level of the $^5D_4 \rightarrow {}^7F_6$ transition after the line deconvolution into Lorentzians. (d) Schematic energy band diagram of the Tb^{3+} free ion. The energy level were constructed based on reference [65]. The arrows indicate the transitions observed in the studied samples.

Well defined narrow transitions, with FWHM varying between ~ 1 to 3 meV, can be resolved for GaN in the low temperature spectrum as shown in Figure 5-43b. A close inspection of each set of transition lines (using high resolution spectra, not shown) allows to identify a total of 9 and 8 lines for the case of the $^5D_4 \rightarrow {}^7F_{6,5}$ transitions at 14 K, respectively. Assuming that only the lowest Stark level from the $^5D_4$ emitting level is populated at this temperature, the number of the

observed lines is higher than those expected for induced electric dipole assisted transitions in C_{3v} symmetry. The $4f \rightarrow 4f$ transitions are known to be parity forbidden for electric dipole interaction, being allowed due to admixture of states of opposite parity and cooperative vibronic transitions [68]. The breakdown of the selection rules promotes, however, the induced electric dipole transitions (*e.g.* $\Delta J = 2$) as well as the magnetic dipole allowed ones (obeying to $\Delta J = \pm 1$). Typically, the intensity of the magnetic dipole assisted transitions is nearly insensitive to the ion environment, whereas the intensity of the transitions induced by electric dipole is quite sensitive [119]. In the case of Tb^{3+} ions embedded in several hosts [119] it has been reported that the $^5D_4 \rightarrow {}^7F_5$ transition possesses the highest intensity among the transitions originated in the $^5D_4$ state, as this emission has the largest transition probability among all the induced electric dipole or magnetic-dipole lines [119]. Figure 5-43b evidences the spectral shape of the $^5D_4 \rightarrow {}^7F_{6,5}$ manifold transitions and their intensity and spectral shape sensitivity with the alloy composition, suggesting an electric dipole induced nature. On the other hand, the experimental data reveal an analogous Stark splitting for the different J levels in the whole set of samples, suggesting that the optically active ions occupy similar site symmetries in the binary and ternary layers.

To obtain more information regarding the observed transitions, their line broadening was analysed by spectral deconvolution into Lorentzians, in order to extract their linewidth. The line broadening and the slight deviations in the line peak positions with increasing x (a total of $\sim$ 2 meV monotonic low energy shift between GaN and AlN) reflects variations in the crystal field intensity and the lattice polarizability effect on the ions' coordination sphere. Moreover, and comparing with the $^5D_4 \rightarrow {}^7F_5$ line, the peak intensity of the $^5D_4 \rightarrow {}^7F_6$ transition is found to decrease for alloys with $x \geq 0.53$, indicating a larger value of the transition probability matrix element for the $^5D_4 \rightarrow {}^7F_5$ transition in samples with higher x. Figure 5-43c displays the experimental data obtained after the deconvolution of the first Stark level of the $^5D_4 \rightarrow {}^7F_6$ transition. The low signal to noise ratio present in the spectrum of the sample with $x = 0.53$ hampered its spectral deconvolution and linewidth determination. As observed in Eu^{3+}-doped alloys by Wang and co-authors [71], the asymmetrical variation in the linewidth with increasing x is very similar to the one observed for bound excitons in semiconductor alloys [71,120,121]. Like so, the data were found to be well fitted by Eq 4-55 [71], where $E_g(x)$ was obtained using Vegard's law (Eq. 1-4), with a bowing parameter as displayed in Table 1-2 [114]. A R_{ex} of 15 $\pm$ 2 Å was obtained which is in line with the values of 27 Å in GaN and 12 Å in AlN reported by Meyer *et al.* [121]. The value for σ_0 was found to be 1.6 $\pm$ 0.5 meV, which is very close to the 1.4 meV obtained for Eu^{3+} by Wang *et al.* [71]. In fact, the linewidth tendency of the Stark levels with increasing composition closely follows the model described for excitonic recombinations (bound excitons) in ternary alloys [45,71,122] and seems to be a general trend in $Al_xGa_{1-x}N$ samples doped with different lanthanides ions (see next section) [71,78,102,123]. A similar linewidth behaviour for terbium doped samples was earlier reported in CL measurements [102]. Thus, the results suggest that excitonic features, sensitive to the alloy disorder, are involved in the excitation processes of the $^5D_4$ Tb^{3+} emitting states for the entire alloy composition, in a similar behaviour to what was found for Eu^{3+}-doping [45,71,122].

Assuming that the ion's levels lay inside the host bandgap, it is expected that the intraionic emission from the $^5D_3$ multiplet of the Tb^{3+} ion could occur for Tb^{3+}-doped $Al_xGa_{1-x}N$ samples,

providing that $x > 0.38$. In this situation, the ion excited state is expected to be located inside the ternary host bandgap. In fact, intraionic emission from the $^5D_3$ to ^7F_J multiplets was recently reported in PL and CL experiments in terbium doped alloys, however this is not the case of the present samples [102,105,109]. The absence of the $^5D_3 \rightarrow ^7F_J$ lines is a common tendency in wide bandgap hosts [124,125] when adjacent Tb^{3+} ions interact with each other, allowing the occurrence of energy transfer by a cross relaxation mechanism via the depopulation of the $^5D_3$ multiplet to the $^5D_4$ level and the $^7F_6 \rightarrow ^7F_{0,1}$ absorption from nearby ions. This process involves an energy difference of ~ 10 meV since the energy separation of the $^5D_3$ and $^5D_4$ and the $^7F_0$ and $^7F_6$ multiplets are ~ 720 meV and ~ 710 meV, respectively [126], as represented in the Tb^{3+} energy level diagram of Figure 5-43d.

5.6.1.2.2. Temperature-dependent PL

The temperature dependence of the $^5D_4 \rightarrow ^7F_{6,5}$ transitions for the GaN sample is shown in Figure 5-44a. For temperatures above 14 K the intra-shell recombination was found to suffer a strong thermal quenching being almost undetectable for temperatures above 70 K. The temperature dependent integrated intensity of the $^5D_4 \rightarrow ^7F_6$ transition shown in Figure 5-44b reveals that the nonradiative competitive processes can be well described by a the classical model of Eq. 4-29, assuming that only one active centre is present in our samples. The best fit to the experimental data was obtained for an activation energy of 9.0 ± 1.2 meV. A similar value (8 meV) was obtained by Wakahara and co-workers [102,105,109], which was assigned to the energy back transfer from the terbium ions to the GaN lattice.

In accordance with the literature reports [98,102,109], a much higher thermal stability of the ion luminescence was observed in the AlN host (Figure 5-44c), with a small decrease of the luminescence intensity between 14 K and the RT. The thermal quenching was well described using an activation energy of ~ 5 meV (Figure 5-44d).

Figure 5-45 shows the PL temperature dependence as well as the integrated intensity of the $^5D_4 \rightarrow ^7F_6$ transition as a function of temperature, obtained after spectral deconvolution, for the $Al_{0.19}Ga_{0.81}N$, $Al_{0.53}Ga_{0.47}N$ and $Al_{0.77}Ga_{0.23}N$ samples. Using above bandgap excitation for the $Al_{0.19}Ga_{0.81}N$ layer, the activation energy for the $^5D_4 \rightarrow ^7F_6$ luminescence thermal quenching was estimated by using the aforesaid classical model, corresponding to 12.3 ± 1.1 meV, taking into account the range of temperatures studied. For temperatures higher than 170 K a very low intensity was observed, hampering the adequate determination of the integrated intensity. The estimated value strongly differs from the 150 meV obtained by Wakahara *et al.* [102] for the deexcitation of thermal depopulation of the $^5D_4$ state in samples with similar composition. For samples $Al_{0.53}Ga_{0.47}N$ and $Al_{0.77}Ga_{0.23}N$, the $^5D_4 \rightarrow ^7F_6$ luminescence thermal quenching was also well fitted to a single activation energy for the radiationless processes, with very close values (~ 26 meV and ~ 24 meV, respectively). The overall results indicate that radiationless pathways of the intra-$4f^8$ Tb^{3+} luminescence are composition dependent, especial in the low x regime.

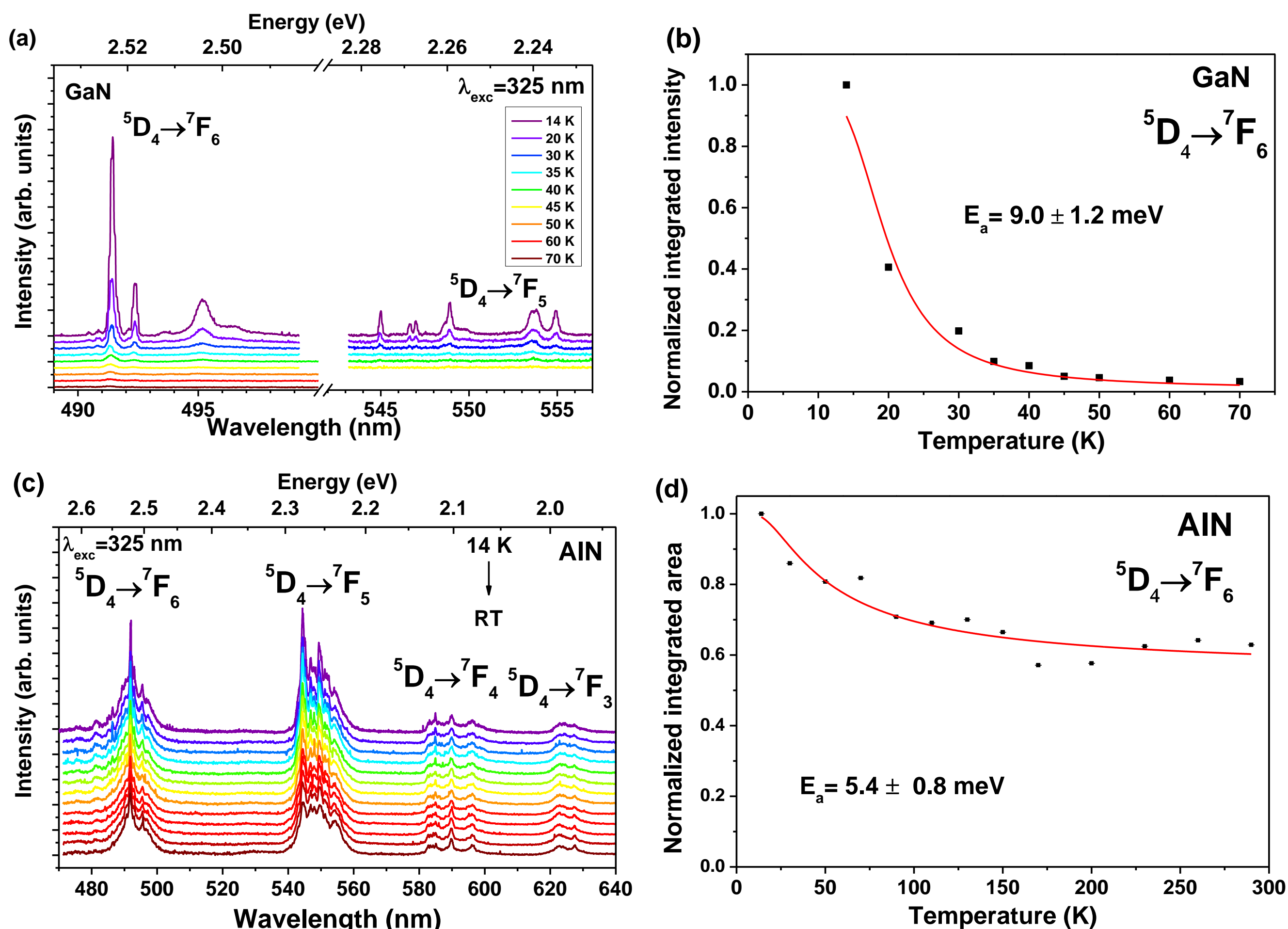

Figure 5-44 – (a) and (c) Temperature dependent Tb^{3+} emission for the GaN and AlN samples, respectively. The spectra are vertically shifted for clarity. (b) and (d) Integrated intensity of the $^5D_4 \rightarrow {}^7F_6$ transition as a function of temperature. The full line corresponds to the theoretical fit to the experimental data as described in the text.

The IQE and activation energy values for the $^5D_4 \rightarrow {}^7F_6$ multiplet transitions of the Tb^{3+} ions for all the $Al_xGa_{1-x}N$ samples are summarized in Table 5-7. With the exception of $Al_{0.77}Ga_{0.23}N$ sample, the IQE value is seen to increase with Al content, and thus, for higher bandgap. This results are in agreement with what was proposed by Favennec [127], who showed that there is a direct correlation between the bandgap of the host and the thermal quenching of the RE ions in a way that when incorporated in hosts with high bandgap, the thermal quenching of the ions tend to decrease with increasing bandgap.

It is important to point out that for the ternary samples ($0 < x < 1$), a dominant broad defect-band was observed overlapped with the Tb^{3+}-related emission, whose excitation/deexcitation processes may affect the ion luminescence.

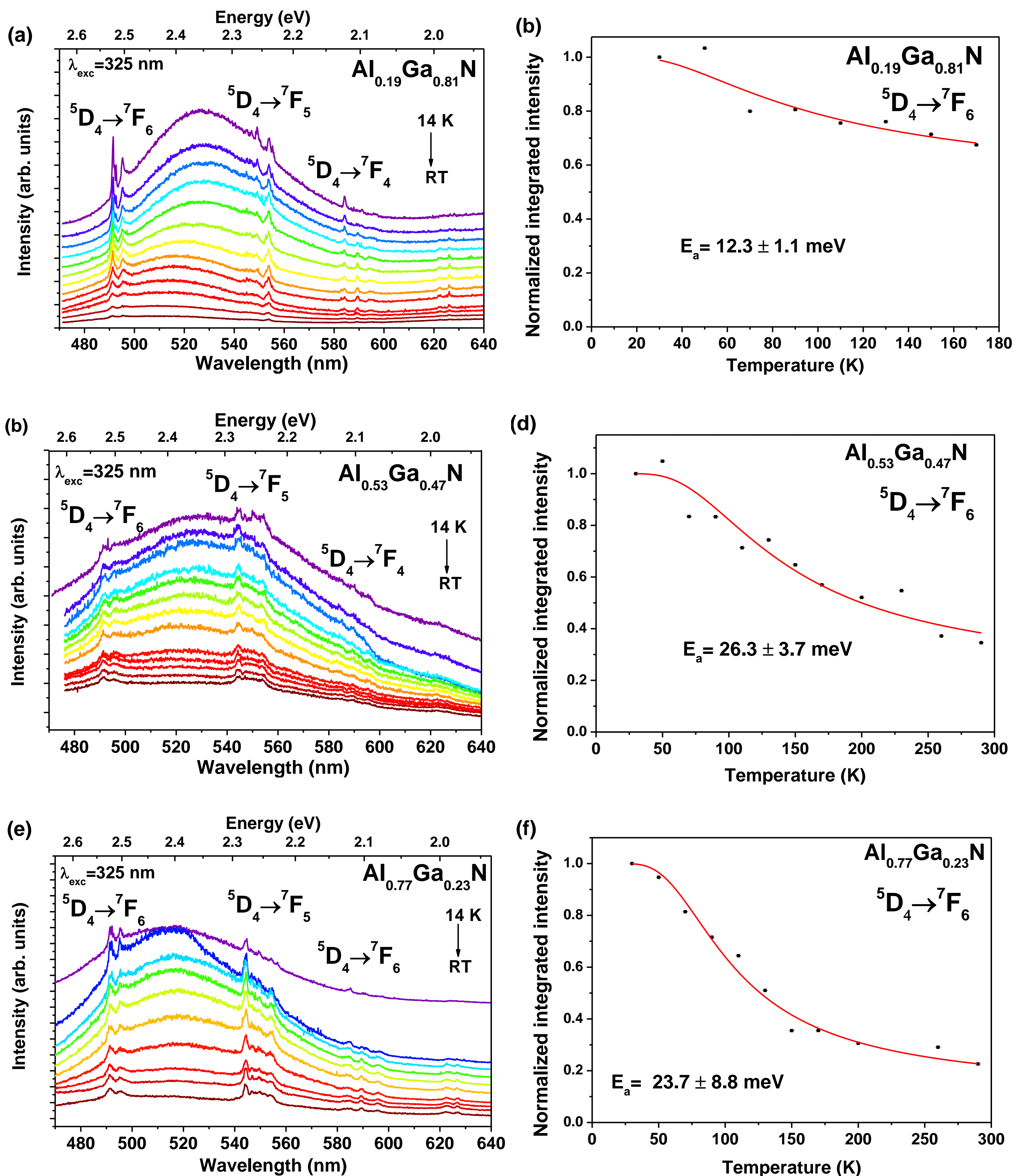

Figure 5-45 – Temperature dependent PL spectra of the Tb^{3+} doped (a) $Al_{0.19}Ga_{0.81}N$, (c) $Al_{0.53}Ga_{0.47}N$, and (e) $Al_{0.77}Ga_{0.23}N$ samples. The spectra were vertically displaced for better clarity. The corresponding integrated intensity of the $^5D_4 \rightarrow {}^7F_6$ transition as a function of temperature obtained after spectral deconvolution are shown in (b), (d) and (f), respectively. The full line corresponds to the theoretical fit to the experimental data using the model $I(T)/I_0=[1+C\exp(-E_a/k_BT)]^{-1}$ (Eq.4-29), as described before.

Table 5-7 – IQE and E_a values for the $^5D_4 \rightarrow ^7F_6$ multiplet transitions in the $Al_xGa_{1-x}N$ samples.

	$Al_xGa_{1-x}N$ layers				
Al content	0	0.19	0.53	0.77	1
IQE (%)	--	14	34	23	63
E_a (meV)	9.0 ± 1.2	12.3 ± 1.1	26.3 ± 3.7	23.7 ± 8.8	5.4 ± 0.8

In these three samples, the intensity of the band is seen to decrease with temperature. Moreover, the three bands shift to higher energies as the temperature increases, as is particularly visible in Figure 5-46a for sample $Al_{0.19}Ga_{0.81}N$. The broad defect bands were well fitted by a Gauss function over all the range of temperatures. The small deviation observed in the high energy region are related to the fact that contributions from the luminescence centres observed in the violet-blue region (Figure 5-43a) are being neglected. For samples $Al_{0.53}Ga_{0.47}N$ and $Al_{0.77}Ga_{0.23}N$ only temperatures up to 200 K were considered since, for higher temperatures, the contribution of these bands becomes relevant and thus, it was not possible to correctly reproduce the shape of the band from the available data. Fitting the data for sample $Al_{0.19}Ga_{0.81}N$ and plotting the peak position *vs* temperature (Figure 5-46b) puts in evidence its atypical red-blueshift behaviour. For temperatures up to 50 K the peak position decreases, while for higher temperatures this value increases with increasing temperature. In the case of sample $Al_{0.53}Ga_{0.47}N$ (Figure 5-46c) only a shift towards higher energies is observed, while sample $Al_{0.77}Ga_{0.23}N$ presents a redshift for temperatures up to 110 K, turning to a blueshift for higher temperatures, in a similar way with what happens for $Al_{0.19}Ga_{0.81}N$, however with different temperature dependence. This kind of behaviour is frequently found in semiconductor alloys, including $Al_xGa_{1-x}N$ and $In_xGa_{1-x}N$ [128–130], and is frequently attributed to inhomogeneous potential fluctuation caused by alloy disorder [121]. Statistical fluctuations in the composition of a random alloy generally lead to potential fluctuations capable of spatially localizing carriers [128].

Regarding the intensity of the luminescence band, the integrated area value decreases with temperature for all samples. The temperature behaviour of the PL broad band of sample $Al_{0.19}Ga_{0.81}N$ was seen to follow the classical model of Eq. 4-29, being necessary two activation energies, as seen in Figure 5-47a. In the case of sample $Al_{0.53}Ga_{0.47}N$ (Figure 5-47b), the behaviour was well accounted for only one activation energy, whereas for sample $Al_{0.77}Ga_{0.23}N$ (Figure 5-47c) also two activation energies were used to describe the intensity decrease of the emission. None of the estimated activation energy values seems to be related with the ones obtained for the Tb^{3+}-related transitions, pointing out distinct nonradiative relaxation phenomena related with the host defect bands associated to one or multiple overlapped optically active centres.

Despite its importance for the adequate understanding of the samples behaviour, a detailed study of the band behaviour falls outside the frame of the present work, where the focus is given to the RE related transitions.

Figure 5-46 – (a) 14 K and RT PL spectra of sample $Al_{0.19}Ga_{0.81}N$ showing the Gauss fit used to calculate the integrated intensity of the defect. Peak position *vs* temperature for the samples (b) $Al_{0.19}Ga_{0.81}N$, (c) $Al_{0.53}Ga_{0.47}N$ and (d) $Al_{0.77}Ga_{0.23}N$.

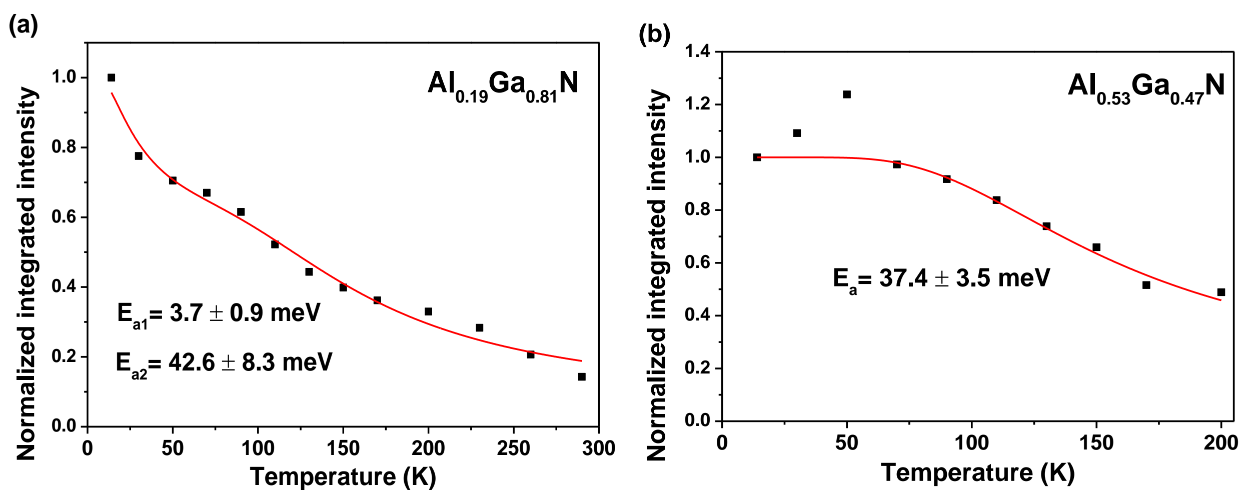

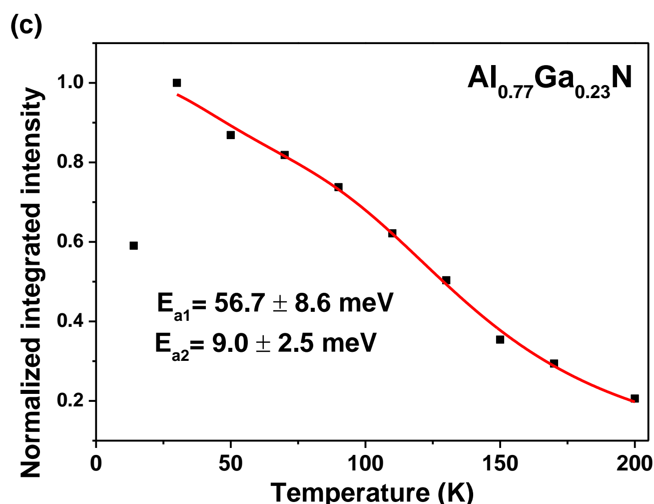

Figure 5-47 – Integrated intensity *vs* temperature for the broad defect band of samples (a) $Al_{0.19}Ga_{0.81}N$, (b) $Al_{0.53}Ga_{0.47}N$ and (c) $Al_{0.77}Ga_{0.23}N$.

5.6.1.2.3. RT PLE studies

In order to acquire in-depth information about the preferential excitation pathways of the trivalent terbium ions, RT PLE spectra were monitored at the $^5D_4 \rightarrow ^7F_6$ and $^5D_4 \rightarrow ^7F_5$ intra-shell transitions for the $Al_{0.53}Ga_{0.47}N$, $Al_{0.77}Ga_{0.23}N$ and AlN samples, as shown in Figure 5-48a. It is important to take into account that, as an overlap of emitting centres occurs for the two first layers with lower AlN molar fraction, the PLE measurements simultaneously assess the excitation population mechanisms of the broad band emitting host defect and the ion luminescence. For GaN and the alloy with x = 0.19 it was not possible to measure the RT PLE since, as previously mentioned, the ion-related emission is very weak or even absent (in the case of the GaN sample) for this temperature.

For the $Al_{0.53}Ga_{0.47}N$ layer (E_g ~ 4.63 eV; 268 nm) the PLE spectrum shown in Figure 5-48a reveals that the excitation of the host defect and the $^5D_4$ Tb^{3+} emitting level is preferentially accomplished via a well-defined excitation band with a maximum at ~270 nm (~ 4.59 eV), showing a tail extending to ~ 365 nm (~ 3.40 eV). The excitation band maximum at ~ 270 nm (~ 4.59 eV) matches well the expected bandgap for this ternary alloy, suggesting that both the defect band and the ion luminescence are favourably excited through above bandgap excitation. However, the excitation with below bandgap photon energies between 3.4 eV (~ 365 nm) and 4.63 eV (~ 268 nm) also leads to the observation of the wide host-defect luminescence and the Tb^{3+} intraionic recombination. Indeed, as seen in Figure 5-48b, which shows the selectively excited RT PL spectra obtained by exciting the samples in the PLE band maxima, for the case of the sample with x = 0.53 the host defect band dominates the spectrum by using above and subgap excitation. A shift of the defect band is observed depending on the excitation energy. Although only one Gauss function was needed to fit this band, it is very likely that different optical centres may be emitting in this spectral region, thus changing the excitation energy leads to different relative intensities of the emitting centres, resulting in a shift of the overall luminescence. The PLE

spectrum monitored in the $Al_{0.77}Ga_{0.23}N$ sample, simultaneously at the $^5D_4 \rightarrow {}^7F_6$ line and the defect band, unveil an additional subgap broad excitation band, together with the rise due to the material bandgap absorption, recognized in the short wavelength region, as shown in Figure 5-48b. The two subgap excitation bands have similar full widths at half maximum (~ 0.4 eV). Figure 5-48b shows the RT PL spectra obtained for this sample when excited with 270 nm and 290 nm (~ 4.28 eV) excitation. Under subgap excitation a higher intensity of the ion emission is reached through 270 nm wavelength photon excitation, while the host defect attains higher intensity when excited via 290 nm. Also in this case, a slightly shift to lower wavelengths of the defect band is observed upon excitation with 270 nm. In the case of the AlN samples (where almost no overlap of the host defect emission occurs when excited with 325 nm), similar subgap excitation bands with maxima at ~ 267 nm (~ 4.64 eV) and ~ 295 nm were observed, a common feature to the $Al_{0.77}Ga_{0.23}N$ sample. These findings are in line with other reported RE^{3+} PLE spectra in nitrides [71,90]. The band at ~ 267 nm is also in agreement with the one observed for the AlN sample co-doped with Eu^{3+} and Pr^{3+} (observed at ~ 265 nm). It is important to note that excitation with ~ 295 nm leads to the observation of a visible broad band peaked at ~ 470 nm, due to host-related defects. According to Lozykowski and co-authors [98,131], the PLE broad bands may originate from the RE^{3+} isovalent trap bound excitons or from direct excitation of the RE^{3+} isovalent trap core electron $4f^{\,n} \rightarrow 4f^{\,n-1}5d$ or other energy transfer mechanisms [90,132]. However, additional excitation mechanisms must be taken into account, as will be discussed in the following section.

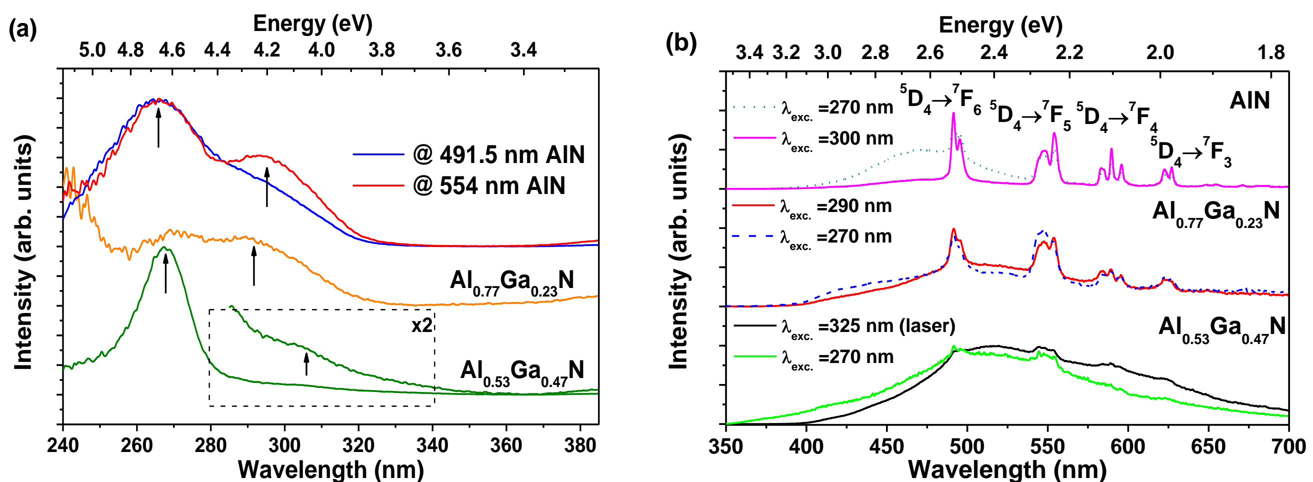

Figure 5-48 – (a) RT PLE spectra for the terbium doped $Al_{0.53}Ga_{0.47}N$, $Al_{0.77}Ga_{0.23}N$ and AlN layers at the $^5D_4 \rightarrow {}^7F_6$ and $^5D_4 \rightarrow {}^7F_5$ transitions of the Tb^{3+} ion (b) RT PL spectra excited in the maxima of the PLE spectra.

5.6.1.2.4. Excitation model

Using an atomic-like model, Dorenbos *et al.* [110,111] positioned energetically the Tb^{3+} $^7F_6$ ground state at 0.9 eV and 1.2 eV above the VB of GaN and AlN, respectively. The same author also located energetically the $^5D_4$ and $^5D_3$ multiplets of the $4f^{\,8}$ electronic configuration for all the $Al_xGa_{1-x}N$ alloy compositions. Furthermore, the $5d_1$ [high (HS) and low spin (LS)] states of the

$4f^7$5d configuration for the entire alloy composition were also identified [110,111]. Figure 5-49 depicts the peak position of the PLE excitation bands observed in the terbium doped samples here studied as a function of the AlN molar fraction, in a similar schematic representation of the Tb^{3+} multiplets and 5d states proposed by Dorenbos *et al.* [110,111]. In the diagram, the $^5D_4$ level was located 0.72 eV below the PLE peak position and the subtraction of the $^5D_4 \rightarrow ^7F_6$ energy transition places the Tb^{3+} ground state. The peaks assigned to PLE1 correspond to the higher wavelength PLE band maximum, while PLE2 stands for the lowest wavelength (high energy) PLE band, located near 270 nm. According to the assignment made by Dorenbos *et al.* [110,111], the band identified as PLE1 corresponds to the position of the $^5D_3$ excited level, which, in the case of the samples with lower AlN content, is well inside the CB. The PLE2 band can be attributed to the $5d_1$ (HS) level. The tendency of the excitation energy bands with increasing *x* follows closely the energy location determined by Dorenbos *et al.* [23, 24] for the Tb^{3+} multiplets and $5d_1$ (HS) state. In both hosts, the Tb divalent ground state is located on the CB. Being so, it is unlikely that an indirect excitation via a charge transfer state could be invoked for the feeding of the $^5D_4$ emitting level of the Tb^{3+} ion. Moreover, and based on experimental evidences, Lozykowski *et al.* stated that the occurrence of a charge transfer model in rare earth doped semiconductors is unexpected [98].

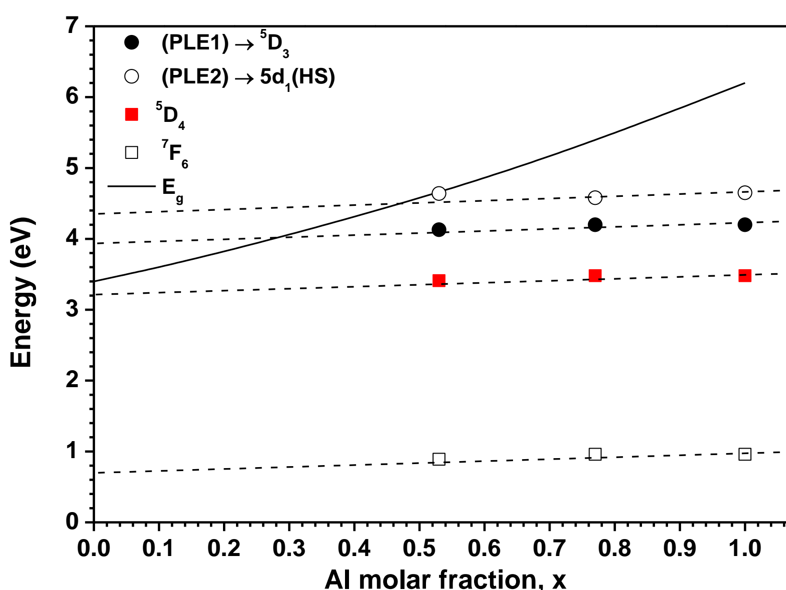

Figure 5-49 – Peak position of the PLE band maxima as a function of the alloy composition in a similar schematic energy diagram proposed by the authors of Ref. [110]. The assignment of the location of the Tb3+ multiplets and 5d states from the same reference was included.

In several wide bandgap hosts direct excitation leading to intraconfigurational parity forbidden $f \rightarrow f$ excitation lines, such as those corresponding to the promotion of the RE^{3+} in the ground state to excited multiplets, is well established [133–135]. Direct excitation was also recently observed in nitrides doped with thulium ions [136]. Assuming that the transitions observed in the PL spectra would result from direct excitation to the ion's levels, transitions from the $^7F_6$ ground state to the excited $^5D_{3-1}$, ^5G_J, ^5L_J, ^5H_J, levels of the Tb^{3+} ions should be visible for wavelengths shorter than 381 nm (3.25 eV), which did not happen in the present Tb^{3+}-doped samples, since only broad bands were identified. On the other hand, interconfigurational $f \rightarrow d$ excitation bands involving a

parity change, associated with the allowed and forbidden low and high spin $5d_1$ levels, are known to be responsible, in several matrixes, for broad excitation bands due to the coupling of the RE ion to the lattice in the UV spectral region [133,134]. Broad excitation bands, similar to the ones observed in this work, are expected considering the model of the RE core excitons, as observed by Wang *et al.* in Eu^{3+} doped $Al_xGa_{1-x}N$ layers [45,71], or bound excitons trapped by a RE structured isoelectronic trap, as mentioned by Lozykovski *et al.* in $Al_xGa_{1-x}N$ samples doped with Pr^{3+}, Eu^{3+}, Tb^{3+} and Tm^{3+} [98]. Subgap excitation bands can also be due to coupling of defects (including the lanthanide itself or complexes) with carriers with further nonradiative energy transfer to the RE ion [45].

In the case of the GaN and $Al_{0.19}Ga_{0.81}N$ samples, the estimated low activation energies are compatible with the Dorenbos' model [110]. This author proposed that, for GaN, the $^5D_3$ level is placed well within the CB and the $^5D_4$ just below the bandgap. As such, he assumed that a small ionization energy for the $^5D_4$ electron explains the low activation energy observed for the thermal quenching of the intra-shell Tb^{3+} PL in GaN obtained by Wakahara and co-workers [105], validating the $^5D_4$ multiplet as the emitting state and the missing of the $^5D_3 \rightarrow {}^7F_J$ lines. The same is valid for the $Al_{0.19}Ga_{0.81}N$ sample, where (in present work) an activation energy much smaller than the one reported by Wakahara *et al.* [105] was found. The value of ~ 12 meV is compatible to the assumption that this value may correspond to the energy difference between the $^5D_4$ level and the bottom of the CB and that the terbium ion can donate an electron to the conduction band. Figure 5-50 shows a schematic diagram of an attempt to place the intraionic recombination and energy levels location for both samples, excited with above bandgap excitation, according to the Dorenbos model [110].

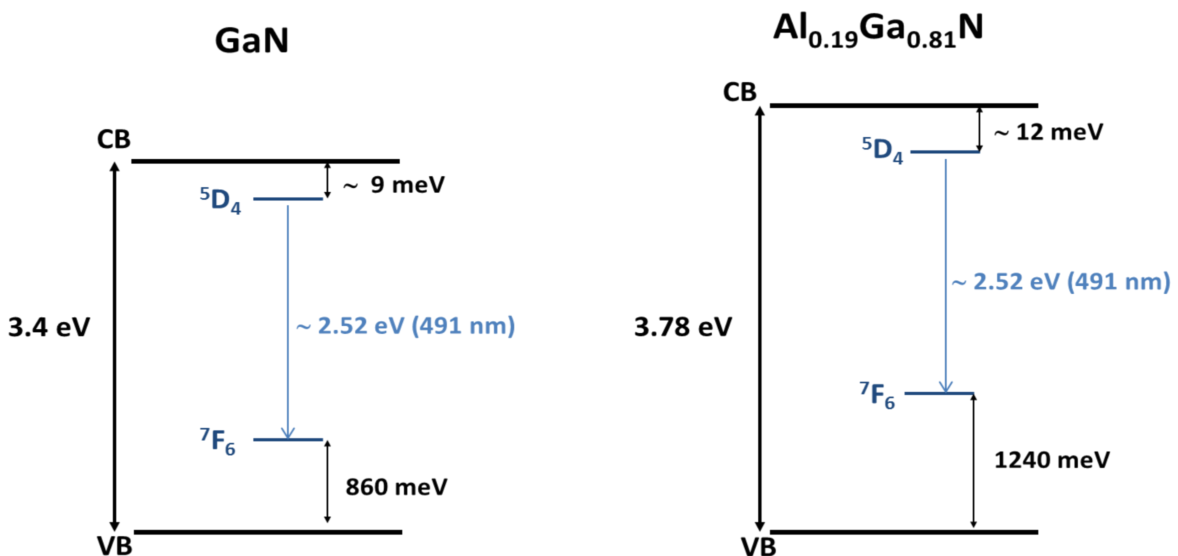

Figure 5-50 – Schematic representation of the possible location of the $^5D_4$ and $^7F_6$ levels of the Tb^{3+} ion relatively to the bottom of the CB and top of the VB for GaN and $Al_{0.19}Ga_{0.81}N$, as placed by the model of Dorenbos [110,111].

With above bandgap excitation free carriers are generated that can be trapped by intrinsic or extrinsic host defects (including the lanthanide ion itself or related complexes) [45,98] or promoting RE core excitons, as identified in the europium doped $Al_xGa_{1-x}N$ alloys [45,71], whose

excess of energy is further transferred to the $4f^n$ configuration levels. Thus, taking into account the model used to describe the linewidth behaviour, excitonic features are assumed to be involved in the ion excitation processes of the present samples, giving a possible explanation for the activation energies found for alloys with $x \geq 0.53$. Unlike the ionization of the $^5D_4$ electron observed for samples with low aluminium content, the measured activation energies for layers with $x \geq 0.53$ should be accounted for a different model. Dorenbos *et al*. [110,111] predicted a quenching energy barrier for the $^5D_4$ state of ~ 1 eV for samples with high Al content, which is a large energy compared to the ones estimated in the present samples, suggesting that a different thermal extinction luminescence model should be considered. Consequently, the deexcitation paths for all the samples are likely to be due to thermal release of a defect mediated bound exciton responsible for the energy transfer feeding of the $^5D_4$ emitting multiplet, leading to the quenching of the Tb^{3+} luminescence. This model explains the ion luminescence quenching over all the alloy composition but further information on the microscopic origin of the defect that binds the exciton (the RE ion itself, RE-complexes with native and other defects or further host defects) is needed.

5.6.1.2.5. RT kinetics: time resolved spectra and decay profiles

The time resolved spectra and decay profile of the $^5D_4$ multiplet of the Tb^{3+} ions were measured at RT for the $Al_{0.53}Ga_{0.47}N$, $Al_{0.77}Ga_{0.23}N$ and AlN samples using the 266 nm pulsed Nd:YAG laser line, as depicted in Figure 5-51. GaN and $Al_{0.19}Ga_{0.81}N$ samples could not be measured due to the weak luminescence intensity at this temperature. The used wavelength excitation corresponds to above bandgap excitation for the $Al_{0.53}Ga_{0.47}N$ and below bandgap excitation for the $Al_{0.77}Ga_{0.23}N$ and AlN layers. In both cases the intraionic Tb^{3+} and host defect band luminescence were observed. Figure 5-51b, d and f show the experimental $^5D_4 \rightarrow {}^7F_6$ luminescence decay obtained after spectral deconvolution of the ion-related emission for each measured samples. The measured experimental lifetimes comprise the radiative and nonradiative transition probabilities involved in the deexcitation processes of the $^5D_4$ state. If the interaction between the optically active ions is insignificant, a single exponential function can be used to fit the experimental data as indicated in the Figure 5-51. The observation of a single exponential decay also corroborates the assumption that only one Tb^{3+} optically active centre is present in the measured samples. Time constants of 207 µs, 322 µs and 385 µs were found for the ions embedded in the $Al_{0.54}Ga_{0.46}N$, $Al_{0.77}Ga_{0.23}N$ and AlN layers, respectively.

Deviations from an exponential law are an indication of the presence of nonradiative phenomena [137] such as multiphonon relaxation and energy transfer. The good agreement between the experimental data and a single time constant suggests that nonradiative decay from the $^5D_4$ level is negligible. The decay times are seen to increase with *x*. The differences in the radiative lifetime for the $^5D_4 \rightarrow {}^7F_6$ transition for samples with different *x* can be explained by a host dependent increase in the transition oscillator strength, which is known to scale with the matrix where the ions are embedded (according to the Judd-Ofelt theory [138,139]).

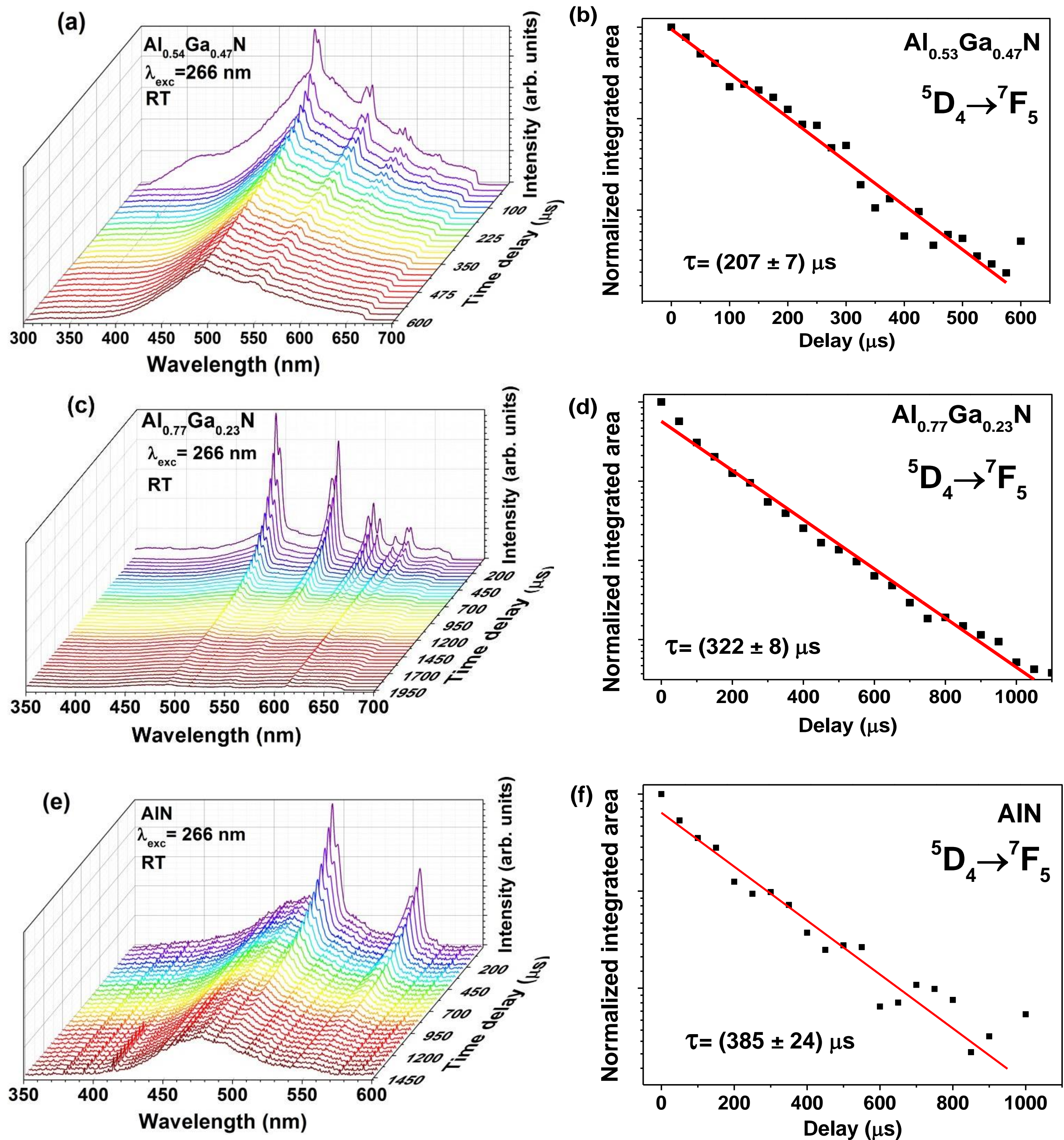

Figure 5-51 – RT TRPL and lifetime measurements (a and b) for $Al_{0.53}Ga_{0.47}N$:Tb, (c and d) $Al_{0.77}Ga_{0.23}N$:Tb and (e and f) AlN:Tb. A 266 nm pulsed laser line excitation was used. The single exponential fits are depicted on the right side figures.

In ternary alloys with similar composition, Wakahara *et al* [102,123] identified a double exponential behaviour at low temperatures with a fast component with few tens of μs and a ~ 200 μs slow component, independently of the alloy composition for samples with low x ($x \leq 0.32$), while for samples with higher x, the decay can be well accounted by a single

exponential. The PL decay time observed in the samples with high *x* is almost the same as the slow component observed in low *x* samples [102]. These authors attributed the fast decay component to a nonradiative recombination and/or energy-back-transfer processes, and the slow component to a radiative transition in the 4*f* energy levels. With increasing temperature, the decay times become dependent on the AlN molar fraction, with the same behaviour identified in the samples studied in the present work and with comparable values. Moreover, Wakahara *et al.* [102,123] identified rise times in their samples, suggesting thermally activated energy transfer processes between $^5D_3$ and $^5D_4$ excited levels [123]. The absence of a rise time in our $^5D_4$ level decay measurements is compatible with the absence of a thermally assisted feeding of the $^5D_4$ multiplet from the $^5D_3$ state, as reported by other authors [98,102,109,123].

5.6.2. Tm^{3+}

The trivalent thulium ions, with a $4f^{12}$ electron configuration, are known to be important activators in lighting devices since they give rise to emissions in the UV, visible and IR spectral ranges [132,140]. Gruber *et al.* [141] reported more than 200 intra-4*f* Tm^{3+} transitions in Tm^{3+}-implanted AlN samples, in the spectral range between 290 and 820 nm, being able to identify approximately 100 lines [132]. Moreover, works performed by Hommerich *et al.* [142] and Nepal *et al*. [132] revealed a strong dependence of the Tm^{3+} emissions on AlN molar fraction of the $Al_xGa_{1-x}N$ alloys, especially in the case of the blue emission. Steckl *et al.* [143] also observed a strong blue electroluminescence in $Al_xGa_{1-x}N$ host, increasing in intensity with the AlN molar fraction, since the increase of the bandgap enabled the excitation of a second blue line that was attributed to the $^1D_2 \rightarrow {}^3F_4$ transition. They also observed that, for high Al content, the blue emission became stronger than the one appearing in NIR [143].

Although the blue Tm^{3+} emission in these alloys has been studied at some extent in the literature, due to its interest in visible light emission, less attention has been paid to the NIR emission. Detailed studies on the NIR lines are scarce even though this is the most commonly found emission in the Tm^{3+}-doped nitrides. In this section, a detailed spectroscopic analysis of the NIR emission of Tm^{3+} in implanted and annealed $Al_xGa_{1-x}N$ assessed by temperature dependent steady-state PL, RT PLE and TRPL is reported.

5.6.2.1. Structural characterization

The Raman spectra of the $Al_xGa_{1-x}N$ samples are shown in Figure 5-52. The results are very similar to the ones observed for the alloys implanted with Tb (sub-section 5.6.1). A_1(TO) and A_1(LO) phonons and the two E_2 (high and low) modes were identified for AlN, while only the A_1(TO) and A_1(LO) phonons and the E_2^H were observed for GaN, in accordance with the assignments reported in the literature [33,112,113]. In addition, sapphire peaks (indicated with "S") could be resolved.

In line with what was obtained for the previous set of samples implanted with Tb^{3+} ions, the measured peak positions are in fairly good agreement with previously reported values for these

materials [33,52]. In the present samples, following the theoretical equations proposed by Davydov *et al.* [113], the A_1(LO) observed at ~ 778 cm^{-1} for x = 0.15 is deviated from the expected ~ 767 cm^{-1} theoretical value, whereas the measured ~ 867 cm^{-1} for x = 0.77 is in good agreement with the predicted and only slightly shifted from the one observed for the Tb-doped sample. This shift can be due to different strain states introduced during the implantation process as well as to the different size of the implanted ions, leading to slightly different distortions. The former shift of the A_1 mode is likely to be related with a higher concentration of free carriers in this particular sample, since the excitation energy (3.8 eV) is very close to the estimated bandgap energy of ~ 3.69 eV, leading to resonant Raman scattering, which is not the case of the sample with x = 0.77 (bandgap ~ 5.76 eV) [114].

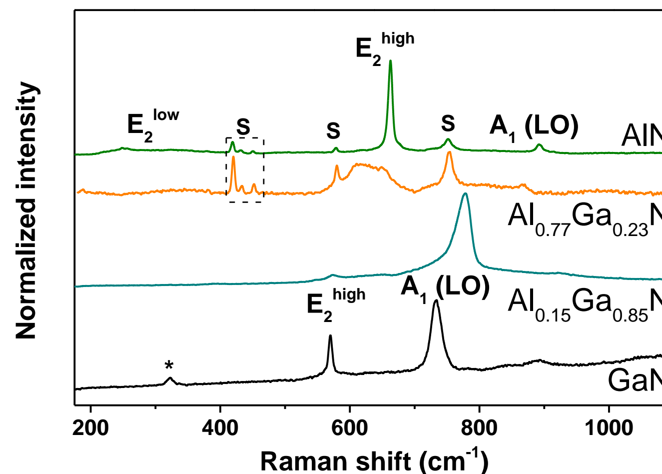

Figure 5-52 – RT Raman spectra for the GaN, $Al_{0.15}Ga_{0.85}N$, $Al_{0.77}Ga_{0.23}N$ and AlN implanted (1×10^{15} Tm^{3+}.cm^{-2}) and annealed samples. The spectra were acquired in backscattering configuration under 325 nm photon excitation. The asterisk denotes an artefact from the system and the peaks labelled with S correspond to the sapphire substrate.

RBS measurements were performed in order to estimate the damage generated by the implantation process and the lattice site location of Tm^{3+} in the nitride matrix. Figure 5-53 depicts the random and aligned RBS/C spectra along the [0001] crystallographic direction for the Tm-implanted GaN sample after annealing. All the obtained results are displayed in Table 5-8. The low χ_{min} ~ 0.1 found for the present samples reveal that the annealing recovers efficiently the lattice damage. It was shown previously that Tm^{3+} implanted into GaN occupies substitutional Ga-sites [144], while in AlGaN this ion was found in two different sites, one substitutional and one site slightly displaced from the substitutional cation site [145,146]. The fraction of the thulium ions in these near-substitutional sites, f_s, can be estimated using Eq. 5-1. After implantation and annealing, values of f_s around 0.8 - 0.9 were obtained for all the samples. As already seen in other RE-implanted III-nitride samples, the substitutional fraction is higher for the as-implanted samples, showing a slight decrease after annealing, possibly due to the formation of RE-defect clusters [49]. A detailed structural analysis and lattice site location discussion for samples $Al_xGa_{1-x}N:Tm^{3+}$ with x = 0.15 and 0.77 was previously reported by Fialho, *et al.* [145]. The authors presented angular scans for Ga and Tm through the <0001> axial direction, as well as using the Monte Carlo code FLUX simulations and found that, for the implanted and annealed samples, the

Tm angular scans and respective simulations show some differences, suggesting that a small fraction of the Tm^{3+} ions may occupy different positions than the substitutional one. The best fit was obtained taking into account three fractions of Tm^{3+} ions in different sites [145].

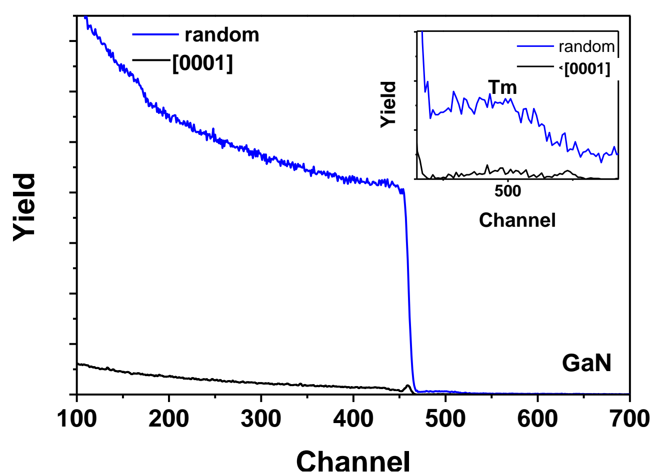

Figure 5-53 – Random and aligned RBS/C spectra along the [0001] crystallographic direction for the Tm-implanted GaN sample after annealing.

Table 5-8 – Minimum yield obtained for Ga/Al and Tm and the fraction of Tm^{3+} ions in near-substitutional sites after the implantation and annealing processes.

Sample	Annealed at 1200 °C		
	χ_{min} (Ga/Al)	χ_{min} (Tm)	f_s [0001]
GaN	0.029 ± 0.001	0.135 ± 0.004	0.891 ± 0.004
$Al_{0.15}Ga_{0.75}N$	0.074 ± 0.009	0.20 ± 0.01	0.87 ± 0.01
$Al_{0.77}Ga_{0.23}N$	0.110 ± 0.001	0.24 ± 0.01	0.86 ± 0.01
AlN	0.098 ± 0.001	0.26 ± 0.01	0.82 ± 0.02

5.6.2.2. Photoluminescence studies

Figure 5-54 shows the 14 K PL spectra of the $Al_xGa_{1-x}N:Tm^{3+}$ ($0 \le x \le 1$) samples. Figure 5-54a displays the PL spectra in the spectral range from 350 to 850 nm. The PL spectra were obtained by using the 325 nm excitation line, which corresponds to an above bandgap excitation for the GaN and $Al_{0.15}Ga_{0.85}N$ samples, and to a below bandgap excitation for the $Al_{0.77}Ga_{0.23}N$ and AlN samples. In all the samples, the PL is dominated by the NIR intraionic emission of the Tm^{3+} ions, corresponding to the overlapping of at least two multiplet optically active transitions of the Tm^{3+} ions, which were tentatively assigned to the $^1G_4 \rightarrow {}^3H_5$ and $^3H_4 \rightarrow {}^3H_6$ transitions. Different transitions have been assigned in this spectral region with some overlapping of the multiplet emission lines, namely $^1G_4 \rightarrow {}^3H_5$, $^3H_4 \rightarrow {}^3H_6$, $^1D_2 \rightarrow {}^3F_3$, $^3F_4 \rightarrow {}^3H_6$ and $^1I_6 \rightarrow {}^1G_4$ [90,136,147]. Therefore, the presence of other overlapped transitions in the present samples cannot be discarded. For the samples with low AlN molar fraction, the observation of transitions from the $^1D_2$ excited state is unlikely, since the energy of this level is very similar to the GaN bandgap energy. However, for samples with high AlN molar fraction ($Al_{0.77}Ga_{0.23}N$ and AlN), the larger bandgap results in the

presence of the $^1D_2$ level well within the host bandgap, allowing to observe transitions from this excited multiplet [142,148]. Even so, this assignment was not considered due to the absence of other transition from the same excited state expected in the visible range. The transition from the $^1I_6$ excited state was also discarded since the employed excitation energy (3.8 eV) is lower than the energy expected for the $^1I_6$ state, taking into account the energy levels' diagram of the Tm^{3+} ion (Figure 5-54b). The mentioned *4f - 4f* inner shell transitions of the Tm^{3+} ion are shown in Figure 5-54b. For the AlN sample, the $^1G_4 \rightarrow {}^3H_6$ Tm^{3+} transition in the blue region was also observed, as indicated in Figure 5-54a.

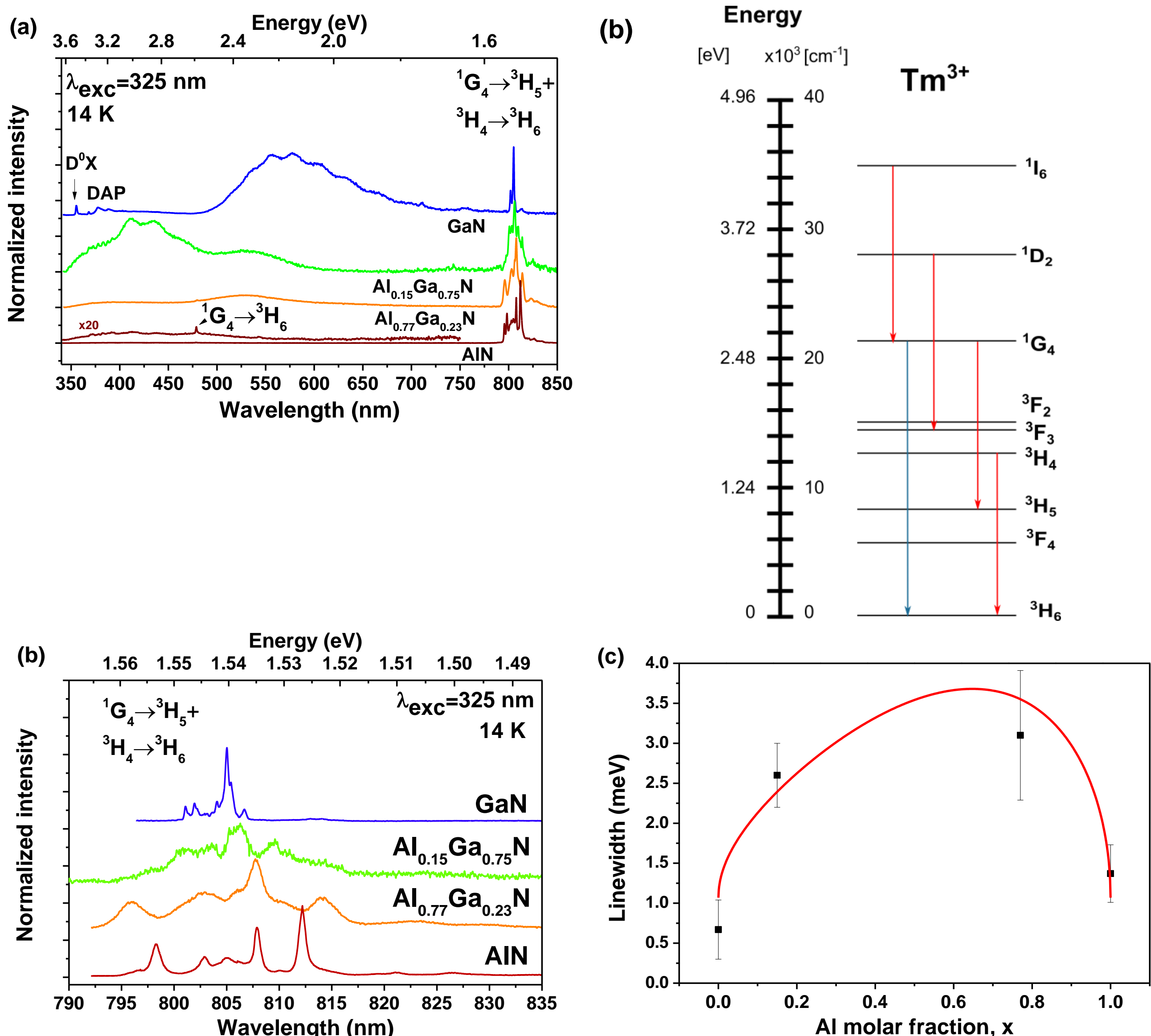

Figure 5-54 – (a) 14 K PL spectra of the $Al_xGa_{1-x}N:Tm^{3+}$ samples (with *x* = 1, 0.77, 0.15 and 0) obtained with 325 nm He-Cd laser line excitation. (b) Schematic energy levels' diagram of the Tm^{3+} free ion. The arrows indicate the transitions observed in the studied samples. (c) Expanded region of the NIR Tm^{3+} luminescence. (d) Linewidth as a function of the alloy composition for the most intense Stark level of the NIR transition (after the line deconvolution into Lorentzians). Full line corresponds to the fit following Eq. 4-56.

Besides the intraionic transitions, other optically active centres were identified. In the case of GaN, D^0X, DAPs and a broad YL were also observed. For the other samples, other broad bands are present both in the UV and visible regions. These bands might be associated with defects in the samples, although a possible contribution of scattered light due to the roughness of the samples' surface has to be considered for those observed in the near-UV region. High resolution spectra of the NIR Tm^{3+} ion-related emission lines are depicted in Figure 5-54c. The lines in the binaries GaN and AlN are much sharper than the ones observed for the ternary alloys due to the Tm^{3+} sensitivity to the disorder in the compounds, as was reported for other RE in $Al_xGa_{1-x}N$ alloys [78,149]. Decrease of the line intensities was also observed for the ternary alloys. A strong decrease in the intraionic intensity is seen in the $Al_{0.15}Ga_{0.75}N$ sample, showing only a very weak emission. The intensity increases with the Al content, giving rise to a strong emission for the sample with $x = 1$. Besides the variation in the linewidths, the strongest emission line is found to shift to higher wavelengths when x increases. According to the RBS measurements, it is known that most of the Tm^{3+} ions are placed in the cation substitutional sites and only a small fraction is displaced from the regular site. Thus, it is fair to assume that the stronger luminescence contribution is given by the substitutional ions. Nevertheless, a minor presence of other emitting centres must be taken into account. Figure 5-54d exhibits the linewidth behaviour with composition in Tm implanted hosts. The linewidth corresponds to the most intense Stark level of the identified transitions after spectral deconvolution into Lorentzians. The asymmetric linewidth behaviour with increasing Al content follows a similar trend as the one observed for the Tb^{3+} implanted samples. This behaviour indicates that excitonic features should be involved in the excitation population processes, as was observed for bound excitons in semiconductor alloys [71,122]. The equation used to fit the experimental data of the linewidth with the alloy composition was Eq. 4-55, as reported in the work of Wang and co-authors [71]. As before, $E_g(x)$ was obtained using Vegard's law (Eq. 1-4), and σ_0 and R_{ex} were used as fitting parameters. A value of 1.1 ± 0.3 meV was obtained for σ_0 which is just slightly lower than the one previously obtained for the Tb^{3+} implanted alloys, with the difference falling within the error range. Moreover, this value is also in fairly good agreement with the value reported by Wang *et al*. [71] for Eu^{3+} implanted AlGaN (1.4 meV). A R_{ex} of 21 ± 4 Å was estimated for the present samples, a slight higher value than the one reported for the samples implanted with Tb^{3+}, nevertheless well within the range of the values for GaN and AlN reported by Meyer *et al*. [121].

Figure 5-55 displays the temperature dependence of PL for all the samples, as well as the temperature dependence of the overall NIR integrated PL intensity. In all cases, the luminescence intensity decreases gradually with temperature due to competitive thermally activated nonradiative processes. It is observed that the thermal stability increases with increasing AlN molar fraction, as summarized in Table 5-9, where the IQE values are shown. Once again, the results are in line with what was proposed by Favennec *et al*. [127] regarding the direct correlation between the bandgap of the host material and the thermal quenching of the RE^{3+} emission. It can be seen that the luminescence thermal quenching decreases with increasing bandgap. The fact that more than one ion emitting centres may be present hampered the determination of the activation energies of the observed emission.

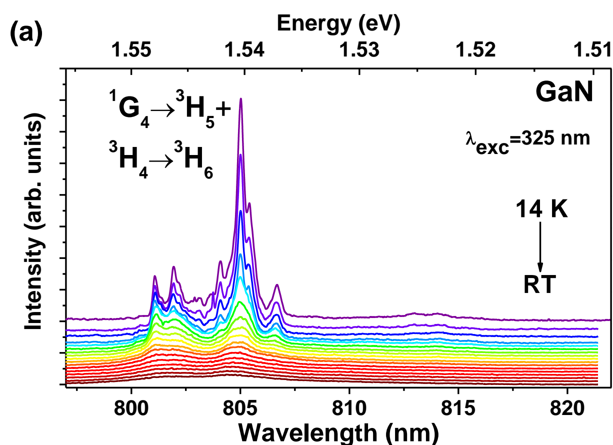
(a)
Energy (eV)
1.55 1.54 1.53 1.52 1.51
$^1G_4 \rightarrow ^3H_5 +$
$^3H_4 \rightarrow ^3H_6$
GaN
λexc=325 nm
14 K
RT
Intensity (arb. units)
800 805 810 815 820
Wavelength (nm)

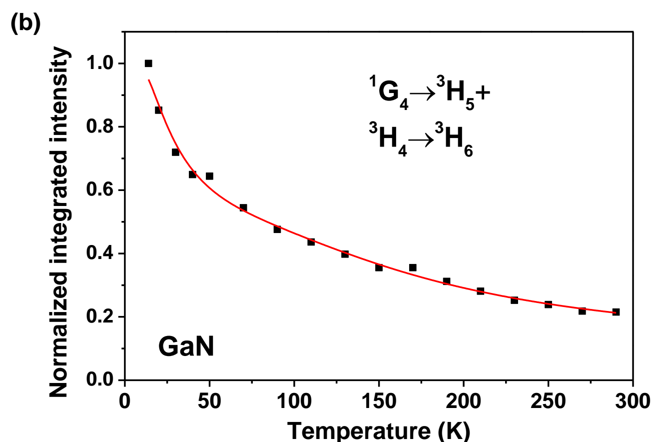
(b)
$^1G_4 \rightarrow ^3H_5 +$
$^3H_4 \rightarrow ^3H_6$
GaN
Normalized integrated intensity
Temperature (K)

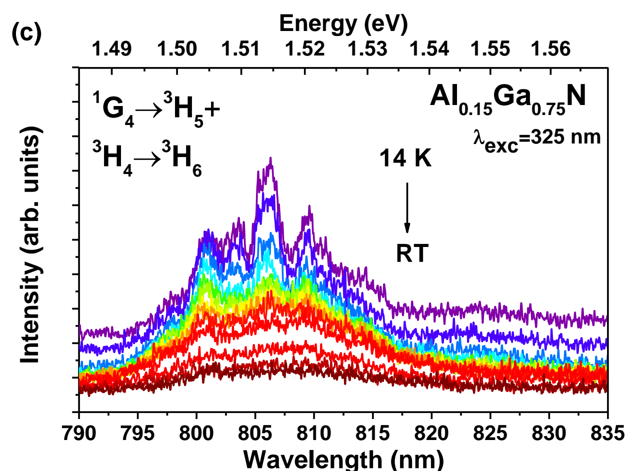
(c)
Energy (eV)
1.49 1.50 1.51 1.52 1.53 1.54 1.55 1.56
$^1G_4 \rightarrow ^3H_5 +$
$^3H_4 \rightarrow ^3H_6$
$Al_{0.15}Ga_{0.75}N$
λexc=325 nm
14 K
RT
Intensity (arb. units)
790 795 800 805 810 815 820 825 830 835
Wavelength (nm)

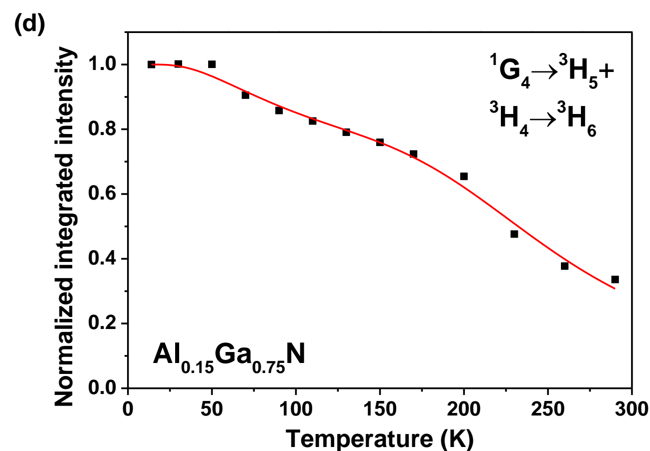
(d)
$^1G_4 \rightarrow ^3H_5 +$
$^3H_4 \rightarrow ^3H_6$
$Al_{0.15}Ga_{0.75}N$
Normalized integrated intensity
Temperature (K)

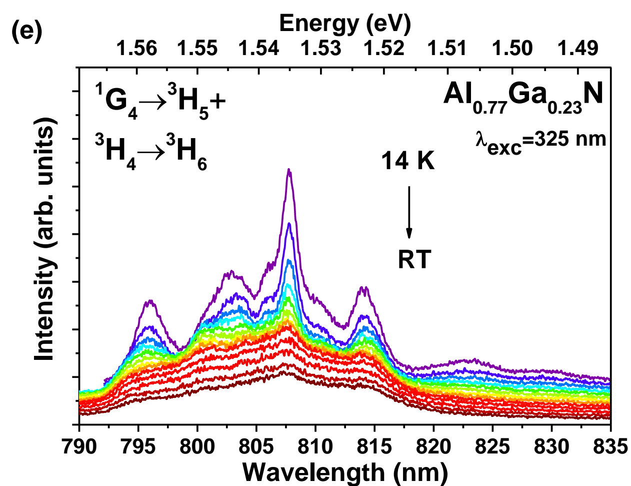
(e)
Energy (eV)
1.56 1.55 1.54 1.53 1.52 1.51 1.50 1.49
$^1G_4 \rightarrow ^3H_5 +$
$^3H_4 \rightarrow ^3H_6$
$Al_{0.77}Ga_{0.23}N$
λexc=325 nm
14 K
RT
Intensity (arb. units)
790 795 800 805 810 815 820 825 830 835
Wavelength (nm)

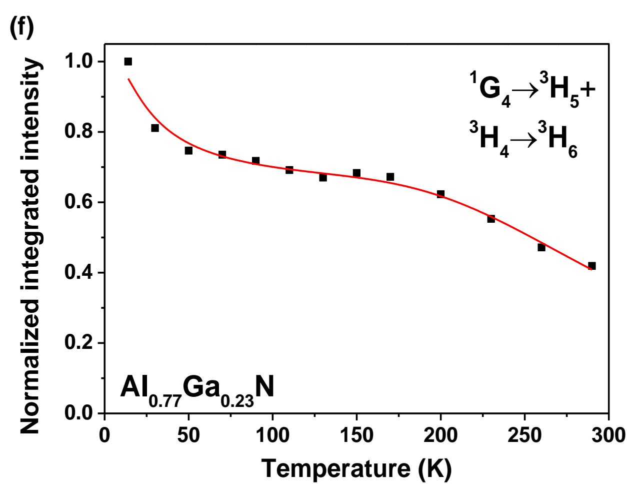
(f)
$^1G_4 \rightarrow ^3H_5 +$
$^3H_4 \rightarrow ^3H_6$
$Al_{0.77}Ga_{0.23}N$
Normalized integrated intensity
Temperature (K)

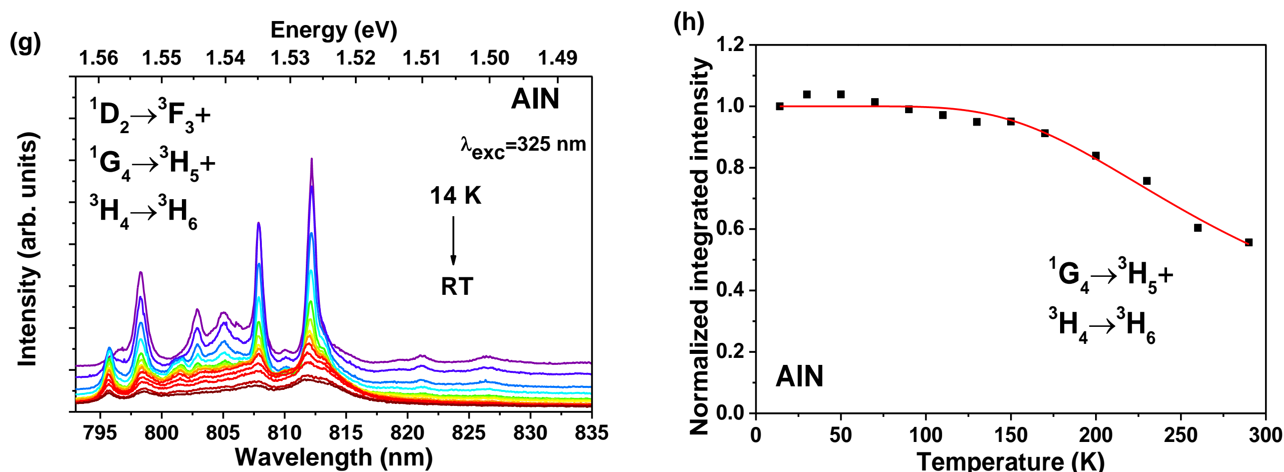

Figure 5-55 – Temperature dependent PL spectra of the thulium doped (a) GaN, (c) $Al_{0.15}Ga_{0.75}N$, (e) $Al_{0.77}Ga_{0.23}N$ and (g) AlN, obtained with 325 nm He-Cd laser line excitation. The spectra were vertically displaced for better clarity. The corresponding NIR overall integrated intensity as a function of temperature is shown in (b), (d), (f) and (h), respectively. Full lines were added as a guide to the eyes for the PL temperature dependence behaviour.

Table 5-9 – IQE values for the identified NIR transitions of the Tm^{3+} ions.

$Al_xGa_{1-x}N$ layers				
Al content	0	0.15	0.77	1
IQE (%)	22	34	42	56

Figure 5-56a shows the PL/PLE spectra of the GaN and AlN samples monitored at 803 nm and 811 nm, respectively. The PLE spectra of the GaN sample revealed that the preferential excitation pathway for the Tm^{3+} luminescence is obtained via above bandgap excitation. In the case of the AlN sample two distinct excitation bands are clearly identified, one with the maximum around ~ 250 nm and the other at ~ 332 nm. These bands have a similar spectral shape as the ones for the Tb^{3+}-implanted samples, however with different peak positions. The spectral shape is also in agreement with the excitation bands identified by Wang *et al.* [71] for Eu^{3+}-doped AlN, even though the present bands evidence a shift to lower wavelengths (higher energies). Lozykowski *et al.* [98] also report the presence of two excitation bands in the PLE spectrum of Tm^{3+}-doped AlN when the emission was monitored at 805 nm and state that the emission observed in this spectral range originates from two Tm^{3+} centres. The presence of analogous excitation bands for samples doped with different RE ions may indicate that the excitation mechanisms are similar for all the RE ions in this host.

As already discussed, according to Lozykowski and co-authors [98,131], these broad bands may originate from the RE^{3+} isovalent trap bound excitons or from direct excitation of the RE^{3+} isovalent trap core electron $4f^{\,n}\rightarrow 4f^{\,n-1}5d$ or other energy transfer mechanisms [90,132]. However, once again, additional excitation mechanisms must be taken into account, namely the Dorenbos' model (that includes charge transfer) [110]. Considering this model, RE ions can be active electron traps when the ground state of the divalent RE is located below the bottom of the conduction band, which in the case of the Tm^{3+} ions happens for high values of *x*, allowing charge

transfer mechanisms. Unfortunately, due to the overlapping of the NIR transitions and the difficulty to associate the observed lines to the respective transition, it was not possible to estimate the activation energy for each transitions, hampering a similar discussion to the one carried out in the previous sub-section regarding the Tb^{3+} ions (5.6.1). Taking into account the excitonic model previously assumed, it is fair to accept that an excited electron from a neighbouring anion is transferred to the RE ion, for instance to the 5*d* shell, leading to the formation of an exciton. The excess energy produced by that exciton can be transferred to the 4*f* core states, giving rise to the observed ion-related luminescence features [71]. The UV bands can be related with the recombination of the mentioned excitons, as proposed by Wang *et al.* [71].

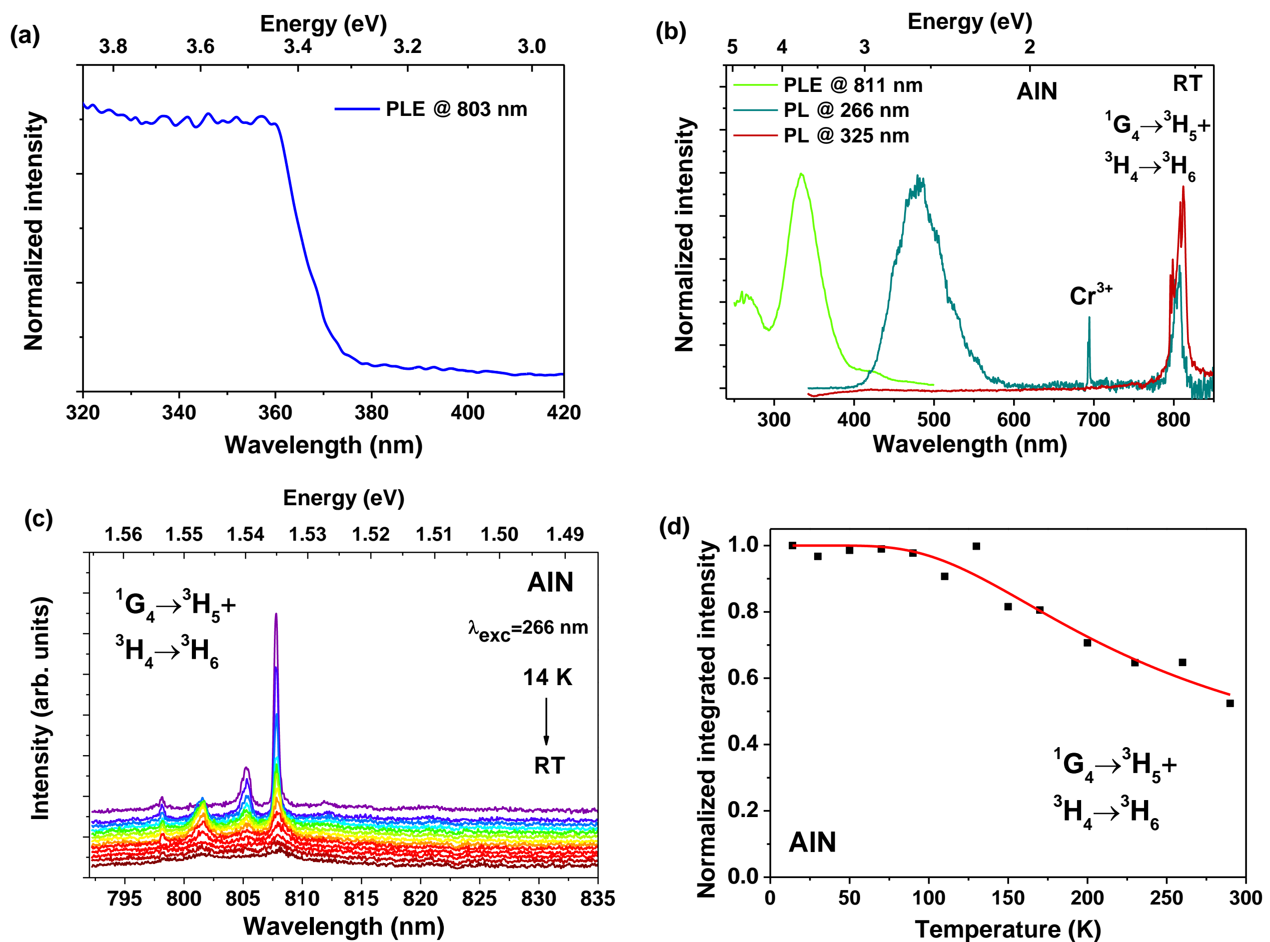

Figure 5-56 – (a) RT PLE spectrum of the GaN and (b) RT PL/PLE spectra of the AlN samples. (c) Temperature dependent PL spectra of the NIR intraionic transitions for the AlN obtained with 266 nm excitation. The spectra are vertically shifted for clarity. The corresponding integrated intensity of the mentioned transition as a function of temperature is shown in (d).

Taking into account the PLE results, the PL features of the AlN sample were also studied by exciting the sample with a 266 nm laser line. Besides the ion-related emission lines, also a broad band centred at ~ 489 nm was observed, probably due to intrinsic defects in the AlN host overlapped with the intraionic lines. The narrow line that appears close to 692 nm is most probably due to the presence of optically active Cr^{3+} contaminants in the sapphire substrate. Figure 5-56b and c depict the temperature dependent PL spectra of the NIR transitions obtained

with 266 nm excitation and the corresponding overall integrated intensity as a function of temperature, respectively. The calculated IQE value is ~ 52 %, which is close to the value obtained when the 325 nm excitation was used.

Figure 5-57 shows the TRPL and the corresponding PL decay profile of the emissions peaked at 803 nm for GaN sample and at 805 nm for the $Al_{0.77}Ga_{0.23}N$ and AlN samples, measured at RT and excited with photons with a wavelength of 325 nm. In the case of the GaN samples, the best fit to the decay profiles was achieved with a bi-exponential equation (Eq. 4-39), where τ_1=150 µs and τ_2=1.31 ms are the measured fast and slow decays and α_1 (79%) and α_2 (21%) correspond to the relative strength of the amplitude of each component which must be normalized, $\alpha_1 + \alpha_2 = 1$ [150,151] (t_0 = 0.05 ms is the initial delay). The bi-exponential behaviour could be explained by the presence of the ion emitter in two different environments. If this is the case, it is fair to assume that the measured decay corresponds to the same multiplet transition in the different centres. However, under such assumption, the presence of fast and slow decays implies a decrease in the transition probability of the intraionic emission in order to explain the longer decay time. This hypothesis also presupposes that the ions environment should be different as, for instance, a slightly distorted site as measured by RBS. Nevertheless, a second hypothesis cannot be discarded: the bi-exponential decay could be due to the different NIR multiplet transitions for a given centre as the measured TRPL line corresponds to the overlap of the $^1G_4 \rightarrow {}^3H_5$ and $^3H_4 \rightarrow {}^3H_6$ transitions (Figure 5-57a). In the latter case the two distinct lifetimes should be due to the different transition probabilities expected for the spin allowed (fast component) and forbidden (slow component) emission lines.

In the case of the $Al_{0.77}Ga_{0.23}N$ and AlN samples the experimental data were well fitted taking into account only one decay constant, τ_1. The presence of a single decay suggests that only one Tm^{3+} emitting centre is observed at RT. In this case, we should assume that the long lived $^1G_4 \rightarrow {}^3H_5$ transition was already thermally quenched and only the fast $^3H_4 \rightarrow {}^3H_6$ emission is detected. The obtained lifetime value for the RT NIR Tm^{3+} emission in the AlN host is in fair agreement with the one reported in the literature for the $^3H_4 \rightarrow {}^3H_6$ transition [142]. For the $Al_{0.15}Ga_{0.85}N$ the extremely low intensity of the ion related emission hampered the measurement of the time dependence.

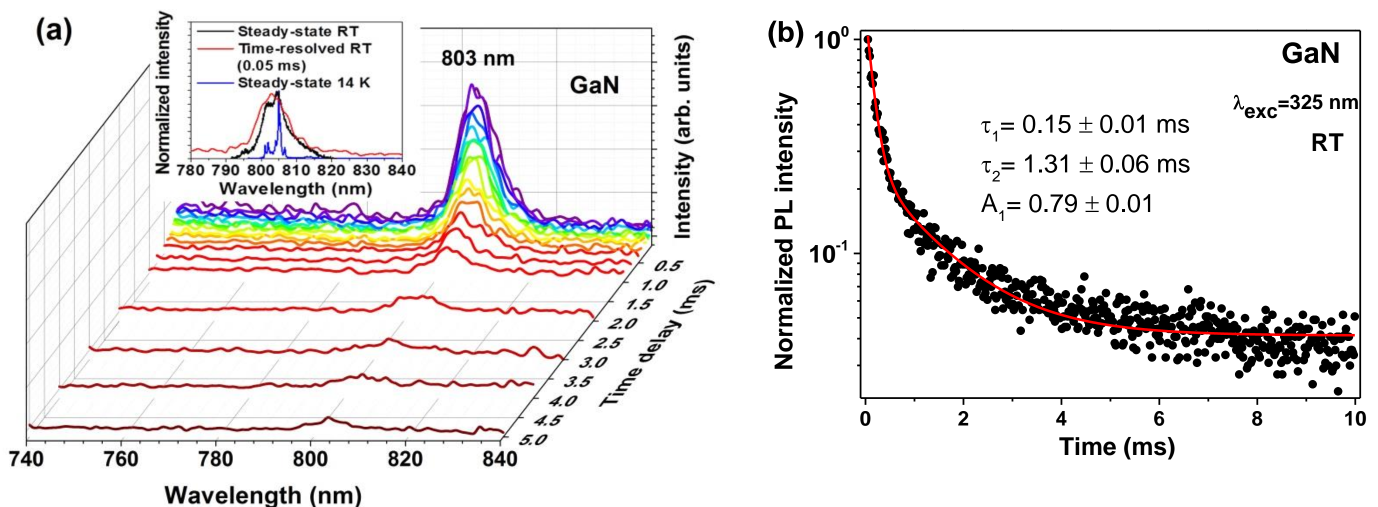

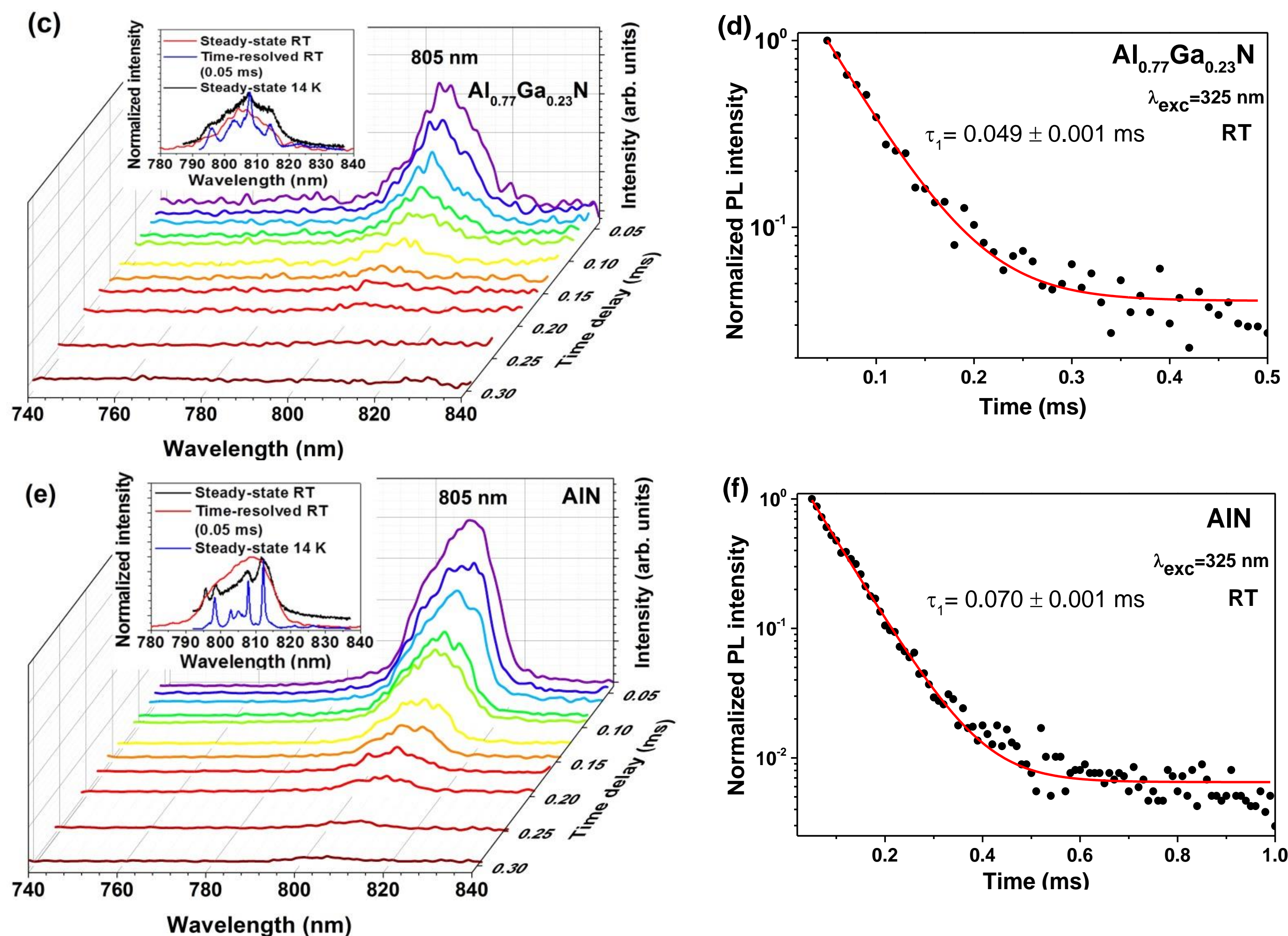

Figure 5-57 – RT TRPL and lifetime measurements spectra of the NIR transitions for the samples (a) and (b) GaN, (c) and (d) $Al_{0.77}Ga_{0.23}N$ and (e) and (f) AlN, obtained with excitation with 325 nm, respectively. The lifetime decay was monitored on the maximum of the emission labelled in the TRPL figures (note the different time scales in the graphs). The insets in the TRPL figures show a comparison between the spectra obtained for steady-state (14 K and RT) and after a time delay of 0.05 ms.

5.7. Conclusions

With the exception of Er^{3+}, for all the others RE^{3+} ions optical activation was achieved in all samples. The measured samples allowed the study of the different ion transitions as well as to gain a better understanding of their behaviour when incorporated in nitride matrixes.

It was demonstrated that it is possible to enhance/induce the YL in NWs structures by ion implantation and thermal annealing. It is worth to mention that, in the analysed wires, the thermal annealing alone was enough to promote the enhancement of the YL band. This band was found to be environment sensitive, strongly suggesting the involvement of surface-mediated defects.The study of different GaN nanostructures highlighted the differences that may be found in the RE luminescence when incorporated in the nanostructured host, namely due to possible distinct ion surroundings or the presence of different intrinsic defects. These finding were

particularly verified in the Eu^{3+}-doped samples where different Eu^{3+} optically active centres were found for layers and NWs. As a general trend, for the same implantation and annealing conditions, the NWs samples revealed a higher luminescence thermal stability along with a higher luminescence intensity, which is in line with the higher light extraction efficiency expected for NWs over the planar structures. The high temperature and high pressure treatment also proved to be very efficient to improve the luminescence of the RE-implanted GaN samples. In fact, an intense RT red emission was observed for the Pr doped GaN layer implanted with high fluence.

In the case of the $Al_xGa_{1-x}N$ alloys, strong evidences of a bound exciton mediated excitation pathway of the RE emission were found, supported by the linewidth behaviour of the ion-related emission lines varying with the AlN molar fraction. Nevertheless, the presence of other mechanisms cannot be discarded. The results were also discussed within the framework of the Dorenbos' model, which places the RE^{3+} ion levels relatively to the CB and VB energy position. This model may be useful to explain some of the observed luminescence features, likely the absence of some RE transitions due to their positioning inside (or not) the bandgap. In fact, a good agreement was found for the location of some multiplets (in the case of the Tb^{3+}-doped GaN and $Al_{0.19}Ga_{0.81}N$ samples) considering the model based on the atomic properties of the lanthanides. However, not all the results can be explained by this model and alternative explanations were proposed.

Also in the alloys, it was found that AlN samples exhibit the highest intensity, as well as the highest thermal stability, as expected for a higher bandgap material, in accordance with the work of Favennec [127]. Although GaN shows the lowest thermal stability, the low temperature PL emission reveals a strong intensity of the RE-related transition, accompanied by well-defined sharp emission lines. The alloys with $0 < x < 1$ show broader transition lines, as expected due to the ion sensitivity to compounds disorder in the ternaries.

Even though the luminescence intensity at RT was weak in most of the studied samples, it was possible to demonstrate that the tuning of the visible light emission can be accomplished by an adequate choice of trivalent RE ions to incorporate in the nitride hosts. Thus, further work is still needed in order to improve the luminescence efficiency. Particularly, lanthanide co-doped nitrides can assume an important role in extending the visible emission to desired wavelengths for lighting devices. For this purpose, it is extremely important to understand the phenomena that may take place during the excitation process, as well as a deep knowledge of the defects' nature (intentionally or non-intentionally incorporated) and their luminescence behaviour.

5.8. References

1. B. Monemar, P. P. Paskov, J. P. Bergman, A. A. Toropov, T. V. Shubina, T. Malinauskas, and A. Usui, Phys. Status Solidi **245**, 1723 (2008).

2. S. J. Pearton, *GaN and Related Materials II* (CRC Press, 2000).

3. J. H. Edgar, *Properties of Group III Nitrides* (EMIS Datareviews Series, n°11, An INSPEC publication, 1994).

4. R. Pässler, E. Griebl, H. Riepl, G. Lautner, S. Bauer, H. Preis, W. Gebhardt, B. Buda, D. J. As, D. Schikora, K. Lischka, K. Papagelis, and S. Ves, J. Appl. Phys. **86**, 4403 (1999).

5. R. Pässler, F. Blaschta, E. Griebl, K. Papagelis, B. Haserer, T. Reisinger, S. Ves, and W. Gebhardt, Phys. Status Solidi **204**, 685 (1997).

6. M. A. Reshchikov, H. Morkoç, S. S. Park, and K. Y. Lee, Appl. Phys. Lett. **81**, 4970 (2002).

7. T. Ogino and M. Aoki, Jpn. J. Appl. Phys. **19**, 2395 (1980).

8. T. Suski, P. Perlin, H. Teisseyre, M. Leszczyński, I. Grzegory, J. Jun, M. Boćkowski, S. Porowski, and T. D. Moustakas, Appl. Phys. Lett. **67**, 2188 (1995).

9. K. Saarinen, T. Laine, S. Kuisma, J. Nissilä, P. Hautojärvi, L. Dobrzynski, J. M. Baranowski, K. Pakula, R. Stepniewski, M. Wojdak, A. Wysmolek, T. Suski, M. Leszczynski, I. Grzegory, and S. Porowski, Phys. Rev. Lett. **79**, 3030 (1997).

10. J. Neugebauer and C. G. Van de Walle, Appl. Phys. Lett. **69**, 503 (1996).

11. M. A. Reshchikov and H. Morkoç, J. Appl. Phys. **97**, 061301 (2005).

12. K. Saarinen, T. Suski, I. Grzegory, and D. C. Look, Phys. Rev. B **64**, 233201 (2001).

13. T. Mattila and R. M. Nieminen, Phys. Rev. B **55**, 9571 (1997).

14. M. A. Reshchikov, D. O. Demchenko, A. Usikov, H. Helava, and Y. Makarov, Phys. Rev. B **90**, 235203 (2014).

15. R. Calarco, T. Stoica, O. Brandt, and L. Geelhaar, J. Mater. Res. **26**, 2157 (2011).

16. L. Polenta, M. Rossi, A. Cavallini, R. Calarco, M. Marso, R. Meijers, T. Richter, T. Stoica, and H. Lüth, ACS Nano **2**, 287 (2008).

17. R. Calarco, M. Marso, T. Richter, A. I. Aykanat, R. Meijers, A. V D Hart, T. Stoica, and H. Lüth, Nano Lett. **5**, 981 (2005).

18. G. T. Wang, A. A. Talin, D. J. Werder, J. R. Creighton, E. Lai, R. J. Anderson, and I. Arslan, Nanotechnology **17**, 5773 (2006).

19. A. Armstrong, Q. Li, K. H. A. Bogart, Y. Lin, G. T. Wang, and A. A. Talin, J. Appl. Phys. **106**, 053712 (2009).

20. S.-J. Cho, S. Doğan, S. Sabuktagin, M. A. Reshchikov, D. K. Johnstone, and H. Morkoç, Appl. Phys. Lett. **84**, 3070 (2004).

21. S. A. Chevtchenko, M. A. Reshchikov, Q. Fan, X. Ni, Y. T. Moon, A. A. Baski, and H. Morkoç, J. Appl. Phys. **101**, 113709 (2007).

22. M. Foussekis, A. A. Baski, and M. A. Reshchikov, Appl. Phys. Lett. **94**, 162116 (2009).

23. E. Calleja, F. J. Sánchez, D. Basak, M. A. Sánchez-García, E. Muñoz, I. Izpura, F. Calle, J. M. G. Tijero, J. L. Sánchez-Rojas, B. Beaumont, P. Lorenzini, and P. Gibart, Phys. Rev. B **55**, 4689 (1997).

24. D. M. Hofmann, D. Kovalev, G. Steude, B. K. Meyer, A. Hoffmann, L. Eckey, R. Heitz, T. Detchprom, H. Amano, and I. Akasaki, Phys. Rev. B **52**, 16702 (1995).

25. M. A. Reshchikov, Phys. Status Solidi **8**, 2136 (2011).

26. J. L. Lyons, A. Janotti, and C. G. Van de Walle, Appl. Phys. Lett. **97**, 152108 (2010).

27. P. Corfdir, P. Lefebvre, J. Ristić, P. Valvin, E. Calleja, A. Trampert, J.-D. Ganière, and B. Deveaud-Plédran, J. Appl. Phys. **105**, 013113 (2009).

28. J. Rodrigues, S. M. C. Miranda, and M. Peres, Nucl. Instruments Methods Phys. Res. Sect. B Beam Interact. with Mater. Atoms **306**, 201 (2013).

29. Q. Li and G. T. Wang, Nano Lett. **10**, 1554 (2010).

30. Z. Wang, J. Li, F. Gao, and W. J. Weber, J. Appl. Phys. **108**, 044305 (2010).

31. G. M. Dalpian and J. R. Chelikowsky, Phys. Rev. Lett. **96**, 226802 (2006).

32. P. Lefebvre, S. Albert, J. Ristić, S. Fernández-Garrido, J. Grandal, M.-A. Sánchez-García, and E. Calleja, Superlattices Microstruct. **52**, 165 (2012).

33. H. Harima, J. Phys. Condens. Matter **14**, R967 (2002).

34. H.-L. Liu, C.-C. Chen, C.-T. Chia, C.-C. Yeh, C.-H. Chen, M.-Y. Yu, S. Keller, and S. P. DenBaars, Chem. Phys. Lett. **345**, 245 (2001).

35. B. Ha, S. H. Seo, J. H. Cho, C. S. Yoon, J. Yoo, G.-C. Yi, C. Y. Park, and C. J. Lee, J. Phys. Chem. B **109**, 11095 (2005).

36. T. Ota, K. Maehashi, and H. Nakashima, Phys. Status Solidi **224**, 169 (2001).

37. B. Sieber, J. Appl. Phys. **98**, 083520 (2005).

38. M. S. Brandt, N. M. Johnson, R. J. Molnar, R. Singh, and T. D. Moustakas, Appl. Phys. Lett. **64**, 2264 (1994).

39. A. Hierro, S. A. Ringel, M. Hansen, J. S. Speck, U. K. Mishra, and S. P. DenBaars, Appl. Phys. Lett. **77**, 1499 (2000).

40. H. W. Choi, S. J. Chua, A. Raman, J. S. Pan, and A. T. S. Wee, Appl. Phys. Lett. **77**, 1795 (2000).

41. T. Hashizume, S. Ootomo, T. Inagaki, and H. Hasegawa, J. Vac. Sci. Technol. B Microelectron. Nanom. Struct. **21**, 1828 (2003).

42. C. Ronning, C. Borschel, S. Geburt, and R. Niepelt, Mater. Sci. Eng. R Reports **70**, 30 (2010).

43. M. V. Fernández-Serra, C. Adessi, and X. Blase, Phys. Rev. Lett. **96**, 166805 (2006).

44. K. Lorenz, E. Nogales, S. M. C. Miranda, N. Franco, B. Méndez, E. Alves, G. Tourbot, and B. Daudin, Acta Mater. **61**, 3278 (2013).

45. K. P. O'Donnell, *Rare-Earth Doped III-Nitrides for Optoelectronic and Spintronic Applications* (Springer, 2009).

46. J. Rodrigues, S. M. C. Miranda, M. Peres, E. Nogales, L. C. Alves, E. Alves, G. Tourbot, B. Daudin, B. Méndez, K. Lorenz, and T. Monteiro, Nucl. Instruments Methods Phys. Res. Sect. B Beam Interact. with Mater. Atoms **306**, 201 (2013).

47. A. Nishikawa, T. Kawasaki, N. Furukawa, Y. Terai, and Y. Fujiwara, Appl. Phys. Express **2**, 1004 (2009).

48. W. M. Jadwisienczak, H. J. Lozykowski, I. Berishev, A. Bensaoula, and I. G. Brown, J. Appl. Phys. **89**, 4384 (2001).

49. J. Rodrigues, S. M. C. Miranda, N. F. Santos, A. J. Neves, E. Alves, K. Lorenz, and T. Monteiro, Mater. Chem. Phys. **134**, 716 (2012).

50. J. F. Ziegler, SRIM-2013 Softw. Packag. Available Online http//www.srim.org (2013).

51. M. W. Ullah, A. Kuronen, A. Stukowski, F. Djurabekova, and K. Nordlund, J. Appl. Phys. **116**, 124313 (2014).

52. V. Y. Davydov, Y. E. Kitaev, I. N. Goncharuk, A. N. Smirnov, J. Graul, O. Semchinova, D. Uffmann, M. B. Smirnov, A. P. Mirgorodsky, and R. A. Evarestov, Phys. Rev. B **58**, 12899 (1998).

53. H. Siegle, G. Kaczmarczyk, L. Filippidis, A. P. Litvinchuk, A. Hoffmann, and C. Thomsen, Phys. Rev. B **55**, 7000 (1997).

54. M. A. Reshchikov, H. Morkoç, S. S. Park, and K. Y. Lee, Appl. Phys. Lett. **78**, 2882 (2001).

55. R. Seitz, C. Gaspar, T. Monteiro, E. Pereira, M. Leroux, B. Beaumont, and P. Gibart, MRS Int. J. Nitride Semicond. Res. **2**, e36 (1997).

56. V. Darakchieva, T. Monteiro, J. Rodrigues, M. T. Son, M.-Y. Xie, N. Ben Sedrine, E. Alves, A. Usui, C. Hemmingson, and B. Monemar, in *Oral Presentation* (ICNS-9, 2011).

57. M. A. Reshchikov, D. O. Demchenko, J. D. McNamara, S. Fernández-Garrido, and R. Calarco, Phys. Rev. B **90**, 035207 (2014).

58. J. Rodrigues, S. M. C. Miranda, A. J. S. Fernandes, E. Nogales, L. C. Alves, E. Alves, G. Tourbot, T. Auzelle, B. Daudin, B. Méndez, T. Trindade, K. Lorenz, F. M. Costa, and T. Monteiro, Phys. Status Solidi **10**, 667 (2013).

59. H. Peng, C.-W. Lee, H. O. Everitt, C. Munasinghe, D. S. Lee, and A. J. Steckl, J. Appl. Phys. **102**, 073520 (2007).

60. L. Bodiou, A. Oussif, A. Braud, J.-L. Doualan, R. Moncorgé, K. Lorenz, and E. Alves, Opt. Mater. (Amst). **28**, 780 (2006).

61. C.-W. Lee, J. Appl. Phys. **95**, 7717 (2004).

62. K. Wang, R. W. Martin, K. P. O'Donnell, V. Katchkanov, E. Nogales, K. Lorenz, E. Alves, S. Ruffenach, and O. Briot, Appl. Phys. Lett. **87**, 112107 (2005).

63. J. Rodrigues, N. Ben Sedrine, M. Felizardo, M. J. Soares, E. Alves, A. J. Neves, V. Fellmann, G. Tourbot, T. Auzelle, B. Daudin, M. Boćkowski, K. Lorenz, and T. Monteiro, RSC Adv. **4**, 62869 (2014).

64. V. Katchkanov, K. P. O'Donnell, S. Dalmasso, R. W. Martin, A. Braud, Y. Nakanishi, A. Wakahara, and A. Yoshida, Phys. Status Solidi **242**, 1491 (2005).

65. W. T. Carnall, J. Chem. Phys. **49**, 4424 (1968).

66. T. Andreev, N. Q. Liem, Y. Hori, M. Tanaka, O. Oda, D. L. S. Dang, and B. Daudin, Phys. Rev. B **73**, 195203 (2006).

67. T. Monteiro, C. Boemare, M. J. Soares, R. A. Sá Ferreira, L. D. Carlos, K. Lorenz, R. Vianden, and E. Alves, Phys. B Condens. Matter **308-310**, 22 (2001).

68. B. G. Wybourne, *Spectroscopic Properties of Rare Earths* (Interscience Publishers, Jonh Wiley & Sons Inc., 1965).

69. L. Bodiou, A. Braud, J.-L. Doualan, R. Moncorgé, J. H. Park, C. Munasinghe, A. J. Steckl, K. Lorenz, E. Alves, and B. Daudin, J. Appl. Phys. **105**, 043104 (2009).

70. I. S. Roqan, K. P. O'Donnell, R. W. Martin, P. R. Edwards, S. F. Song, A. Vantomme, K. Lorenz, E. Alves, and M. Bockowski, Phys. Rev. B **81**, 085209 (2010).

71. K. Wang, K. P. O'Donnell, B. Hourahine, R. W. Martin, I. M. Watson, K. Lorenz, and E. Alves, Phys. Rev. B **80**, 125206 (2009).

72. Z. Fleischman, C. Munasinghe, A. J. Steckl, A. Wakahara, J. Zavada, and V. Dierolf, Appl. Phys. B **97**, 607 (2009).

73. K. P. O'Donnell, I. S. Roqan, K. Wang, K. Lorenz, E. Alves, and M. Boćkowski, Opt. Mater. (Amst). **33**, 1063 (2011).

74. O. Brandt, C. Pfüller, C. Chèze, L. Geelhaar, and H. Riechert, Phys. Rev. B **81**, 045302 (2010).

75. M. A. Reshchikov, J. D. McNamara, A. Behrends, M. S. Mohajerani, A. Bakin, and A. Waag, Phys. Status Solidi **10**, 507 (2013).

76. H. J. Lozykowski, W. M. Jadwisienczak, and I. Brown, J. Appl. Phys. **88**, 210 (2000).

77. R. Birkhahn, M. Garter, and A. J. Steckl, Appl. Phys. Lett. **74**, 2161 (1999).

78. M. Peres, S. Magalhaes, N. Franco, M. Soares, A. Neves, E. Alves, K. Lorenz, and T. Monteiro, Microelectronics J. **40**, 377 (2009).

79. J. M. Zavada, R. A. Mair, C. J. Ellis, J. Y. Lin, H. X. Jiang, R. G. Wilson, P. A. Grudowski, and R. D. Dupuis, Appl. Phys. Lett. **75**, 790 (1999).

80. E. Alves, K. Lorenz, R. Vianden, C. Boemare, M. J. Soares, and T. Monteiro, Mod. Phys. Lett. B **15**, 1281 (2001).

81. E. Schultheiss, A. Scharmann, and D. Schwabe, Phys. Status Solidi **140**, 173 (1987).

82. L. Esterowitz, F. Bartoli, R. Allen, D. Wortman, C. Morrison, and R. Leavitt, Phys. Rev. B **19**, 6442 (1979).

83. B. Daudin, F. Widmann, G. Feuillet, Y. Samson, M. Arlery, and J. Rouvière, Phys. Rev. B **56**, R7069 (1997).

84. M. Arlery, J. L. Rouvière, F. Widmann, B. Daudin, G. Feuillet, and H. Mariette, Appl. Phys. Lett. **74**, 3287 (1999).

85. V. Chamard, T. Schülli, M. Sztucki, T. Metzger, E. Sarigiannidou, J.-L. Rouvière, M. Tolan, C. Adelmann, and B. Daudin, Phys. Rev. B **69**, 125327 (2004).

86. M. Peres, S. Magalhães, J. Rodrigues, M. J. Soares, V. Fellmann, A. J. Neves, E. Alves, B. Daudin, K. Lorenz, and T. Monteiro, Opt. Mater. (Amst). **33**, 1045 (2011).

87. D. Chen, J. Wang, D. Xu, and Y. Zhang, Vacuum **83**, 865 (2009).

88. B. Berzina, L. Trinkler, J. Grabis, and I. Steins, Phys. Status Solidi **4**, 959 (2007).

89. M. Peres, S. Magalhães, V. Fellmann, B. Daudin, A. Neves, E. Alves, K. Lorenz, and T. Monteiro, Nanoscale Res. Lett. **6**, 378 (2011).

90. H. J. Lozykowski, W. M. Jadwisienczak, A. Bensaoula, and O. Monteiro, Microelectronics J. **36**, 453 (2005).

91. A. Redondo-Cubero, K. Lorenz, E. Wendler, D. Carvalho, T. Ben, F. M. Morales, R. García, V. Fellmann, and B. Daudin, Nanotechnology **24**, 505717 (2013).

92. C. Leclere, V. Fellmann, C. Bougerol, D. Cooper, B. Gayral, M. G. Proietti, H. Renevier, and B. Daudin, J. Appl. Phys. **113**, 034311 (2013).

93. B. Damilano, N. Grandjean, F. Semond, J. Massies, and M. Leroux, Appl. Phys. Lett. **75**, 962 (1999).

94. J. Heikenfeld, M. Garter, D. S. Lee, R. Birkhahn, and A. J. Steckl, Appl. Phys. Lett. **75**, 1189 (1999).

95. Y. Q. Wang and A. J. Steckl, Appl. Phys. Lett. **82**, 502 (2003).

96. K. Lorenz, E. Alves, F. Gloux, P. Ruterana, M. Peres, A. J. Neves, and T. Monteiro, J. Appl. Phys. **107**, 023525 (2010).

97. S. Magalhães, M. Peres, V. Fellmann, B. Daudin, A. J. Neves, E. Alves, T. Monteiro, and K. Lorenz, J. Appl. Phys. **108**, 084306 (2010).

98. H. J. Lozykowski and W. M. Jadwisienczak, Phys. Status Solidi **244**, 2109 (2007).

99. A. J. Steckl, J. Heikenfeld, D. S. Lee, and M. Garter, Mater. Sci. Eng. B **81**, 97 (2001).

100. K. Hara, N. Ohtake, and K. Ishii, Phys. Status Solidi **216**, 625 (1999).

101. W. M. Jadwisienczak, H. J. Lozykowski, F. Perjeru, H. Chen, M. Kordesch, and I. G. Brown, Appl. Phys. Lett. **76**, 3376 (2000).

102. A. Wakahara, Y. Nakanishi, T. Fujiwara, A. Yoshida, T. Ohshima, and T. Kamiya, Phys. Status Solidi **202**, 863 (2005).

103. R. Weingärtner, O. Erlenbach, A. Winnacker, A. Welte, I. Brauer, H. Mendel, H. P. Strunk, C. T. M. Ribeiro, and A. R. Zanatta, Opt. Mater. (Amst). **28**, 790 (2006).

104. H. J. Lozykowski, W. M. Jadwisienczak, and I. Brown, Mater. Sci. Eng. B **81**, 140 (2001).

105. Y. Nakanishi, A. Wakahara, H. Okada, A. Yoshida, T. Ohshima, and H. Itoh, Phys. Status Solidi **240**, 372 (2003).

106. F. Lu, R. Carius, A. Alam, M. Heuken, and C. Buchal, J. Appl. Phys. **92**, 2457 (2002).

107. S. Aldabergenova, A. Osvet, G. Frank, H. Strunk, P. Taylor, and A. Andreev, J. Non. Cryst. Solids **299-302**, 709 (2002).

108. Q. L. Liu, T. Tanaka, J. Q. Hu, F. F. Xu, and T. Sekiguchi, Appl. Phys. Lett. **83**, 4939 (2003).

109. A. Wakahara, Opt. Mater. (Amst). **28**, 731 (2006).

110. P. Dorenbos and E. van der Kolk, Opt. Mater. (Amst). **30**, 1052 (2008).

111. P. Dorenbos and E. van der Kolk, in *Proc. SPIE 6473, Gall. Nitride Mater. Devices II*, edited by H. Morkoc and C. W. Litton (International Society for Optics and Photonics, 2007), pp. 647313–647313–10.

112. A. Cros, H. Angerer, O. Ambacher, M. Stutzmann, R. Höpler, and T. Metzger, Solid State Commun. **104**, 35 (1997).

113. V. Davydov, I. Goncharuk, A. Smirnov, A. Nikolaev, W. Lundin, A. Usikov, A. Klochikhin, J. Aderhold, J. Graul, O. Semchinova, and H. Harima, Phys. Rev. B **65**, 125203 (2002).

114. F. Yun, M. A. Reshchikov, L. He, T. King, H. Morkoc, S. W. Novak, and L. Wei, J. Appl. Phys. **92**, 4837 (2002).

115. K. Lorenz, E. Alves, T. Monteiro, A. Cruz, and M. Peres, Nucl. Instruments Methods Phys. Res. Sect. B Beam Interact. with Mater. Atoms **257**, 307 (2007).

116. J. Bartels, K. Freitag, J. G. Marques, J. C. Soares, and R. Vianden, Hyperfine Interact. **120-121**, 397 (1999).

117. U. Wahl, A. Vantomme, G. Langouche, J. P. Araújo, L. Peralta, J. G. Correia, and ISOLDE Collaboration, J. Appl. Phys. **88**, 1319 (2000).

118. K. P. O'Donnell and B. Hourahine, Eur. Phys. J. - Appl. Phys. **36**, 91 (2006).

119. Michael Gaft, R. Reisfeld, and G. Panczer, *Modern Luminescence Spectroscopy of Minerals and Materials* (Springer-Verlag, 2005).

120. A. N. Westmeyer, S. Mahajan, K. K. Bajaj, J. Y. Lin, H. X. Jiang, D. D. Koleske, and R. T. Senger, J. Appl. Phys. **99**, 013705 (2006).

121. G. Steude, B. K. Meyer, A. Göldner, A. Hoffmann, F. Bertram, J. Christen, H. Amano, and I. Akasaki, Appl. Phys. Lett. **74**, 2456 (1999).

122. E. Schubert, E. Göbel, Y. Horikoshi, K. Ploog, and H. Queisser, Phys. Rev. B **30**, 813 (1984).

123. A. Wakahara, K. Takemoto, F. Oikawa, H. Okada, T. Ohshima, and H. Itoh, Phys. Status Solidi **205**, 56 (2008).

124. E. Zych, J. Trojan-Piegza, D. Hreniak, and W. Strek, J. Appl. Phys. **94**, 1318 (2003).

125. B. V. Ratnam, M. Jayasimhadri, G. Bhaskar Kumar, K. Jang, S. S. Kim, Y. I. Lee, J. M. Lim, D. S. Shin, and T. K. Song, J. Alloys Compd. **564**, 100 (2013).

126. W. T. Carnall, J. Chem. Phys. **49**, 4447 (1968).

127. P. Favennec and H. L'haridon, Electron. Lett. Lett. **25**, 718 (1989).

128. A. Bell, J. Appl. Phys. **95**, 4670 (2004).

129. Y.-H. Cho, G. H. Gainer, J. B. Lam, J. J. Song, W. Yang, and W. Jhe, Phys. Rev. B **61**, 7203 (2000).

130. T. Y. Lin, J. C. Fan, and Y. F. Chen, Semicond. Sci. Technol. **14**, 406 (1999).

131. H. Lozykowski, Phys. Rev. B **48**, 17758 (1993).

132. N. Nepal, J. M. Zavada, D. S. Lee, and A. J. Steckl, Appl. Phys. Lett. **93**, 061110 (2008).

133. E. Cavalli, P. Boutinaud, R. Mahiou, M. Bettinelli, and P. Dorenbos, Inorg. Chem. **49**, 4916 (2010).

134. M. R. N. Soares, C. Nico, J. Rodrigues, M. Peres, M. J. Soares, A. J. S. Fernandes, F. M. Costa, and T. Monteiro, Mater. Lett. **65**, 1979 (2011).

135. C. Nico, M. P. F. Graça, M. Elisa, B. A. Sava, R. C. C. Monteiro, L. Rino, and T. Monteiro, Opt. Mater. (Amst). **35**, 2382 (2013).

136. Y. Glinka, H. Everitt, D. Lee, and A. Steckl, Phys. Rev. B **79**, 113202 (2009).

137. M. Inokuti and F. Hirayama, J. Chem. Phys. **43**, 1978 (1965).

138. B. Judd, Phys. Rev. **127**, 750 (1962).

139. G. S. Ofelt, J. Chem. Phys. **37**, 511 (1962).

140. N. Nepal, S. M. Bedair, N. A. El-Masry, D. S. Lee, A. J. Steckl, and J. M. Zavada, Appl. Phys. Lett. **91**, 222503 (2007).

141. J. B. Gruber, B. Zandi, H. J. Lozykowski, and W. M. Jadwisienczak, J. Appl. Phys. **92**, 5127 (2002).

142. U. Hommerich, E. Nyein, and D. Lee, Appl. Phys. Lett. **82**, 4556 (2003).

143. D. Lee and A. Steckl, Appl. Phys. Lett. **83**, 2094 (2003).

144. K. Lorenz, U. Wahl, E. Alves, E. Nogales, S. Dalmasso, R. W. Martin, K. P. O'Donnell, M. Wojdak, A. Braud, T. Monteiro, T. Wojtowicz, P. Ruterana, S. Ruffenach, and O. Briot, Opt. Mater. (Amst). **28**, 750 (2006).

145. M. Fialho, K. Lorenz, S. Magalhães, J. Rodrigues, N. F. Santos, T. Monteiro, and E. Alves, Nucl. Instruments Methods Phys. Res. Sect. B Beam Interact. with Mater. Atoms **307**, 495 (2013).

146. M. Fialho and K. Lorenz, Ion Implant. Technol. 2012, AIP Conf. Proc. **1496**, 63 (2012).

147. J. Gruber, U. Vetter, H. Hofsäss, B. Zandi, and M. Reid, Phys. Rev. B **70**, 245108 (2004).

148. U. Hömmerich, E. E. Nyein, D. S. Lee, J. Heikenfeld, A. J. Steckl, and J. M. Zavada, Mater. Sci. Eng. B **105**, 91 (2003).

149. K. Wang, K. O'Donnell, B. Hourahine, R. Martin, I. Watson, K. Lorenz, and E. Alves, Phys. Rev. B **80**, 125206 (2009).

150. H. Y. Peng, C. W. Lee, H. O. Everitt, D. S. Lee, A. J. Steckl, and J. M. Zavada, Appl. Phys. Lett. **86**, 051110 (2005).

151. J. Lackowicz, *Principles of Fluorescence Spectroscopy* (Plenum Press, 1983).

Chapter 6. Zinc oxide-based materials

This chapter is mostly dedicated to the characterization of ZnO samples grown by the laser assisted flow deposition (LAFD) technique. A description of the morphological, structural and optical properties for each structure is given and a detailed analysis of the influence of the different growth parameters is made. Besides the unintentionally doped micro/nanocrystals, ZnO/Ag and ZnO/CNT composite structures were also investigated. The main properties of these structures, as well as the contribution of the LAFD technique in the composite preparation are highlighted in the present chapter. Additionally, taking into account that a crucial step in designing modern optoelectronic devices is to accomplish bandgap engineering [1], the last section is concerned to the study of the optical properties of the $Cd_xZn_{1-x}O$ alloy (grown by MBE), resulting in the tuning of the ZnO bandgap towards the visible spectral region.

6.1. ZnO produced by laser assisted flow deposition

As explained in Chapter 2, the LAFD technique can produce different ZnO morphologies depending on the region of the growth chamber where the products are formed. Unfortunately, the different morphologies are grown mixed together, essentially because of local fluctuations of the conditions during the growth. Therefore, specific optimizations need to be done to the synthesis process in order to control the production of the different morphologies [2], which is not an easy task. In the case of the LAFD method, even though several morphologies are produced, three different types revealed to be the dominant ones: nanoparticles (NPs), tetrapods (TPs) and microrods (MRs). The NPs constitute the first layer of ZnO grown on the substrate/holder and correspond to the initial heating stage of the growth process. The following layer is comprised mostly by TPs with dimensions from hundreds of nanometers to a few micrometres. These two type of morphologies correspond to the structures that are formed in the low temperature regions, where a holder is placed. On the other hand, the ZnO rods are grown on the tip of the precursor rod. These crystals exhibit a high aspect ratio with hexagonal cross-section and larger dimensions than the structures formed on the sample holder region. The MRs present lengths of several micrometers and diameters in the order of hundreds of nanometers. These different morphologies are formed during the same run of growth. Nonetheless, with an appropriate choice of the growth conditions, namely the laser power and the growth atmosphere, it is possible some control over the morphologies produced. The influence of the growth

parameters in the morphology of the LAFD ZnO structures will be studied in detail in the following sections.

6.1.1. Tetrapods and nanoparticles

The LAFD technique was presented in Chapter 2, together with the most important growth parameters and their influence in the morphology of the produced structures. The study of these parameters allowed a better understanding of the growth process, as well as to infer about the growth mechanisms involved. For this, an intensive study was employed, especially regarding the nanostructures found in the colder regions of the chamber. A great number of samples were produced (as depicted in Table 2-10) varying parameters like laser power (temperature), growth atmosphere, distance between the precursor and the substrate, and growth time. While the later ones were found to have limited influence in the produced structures, the former were found to be crucial. Figure 6-1 summarizes the results obtained using different combinations of these two parameters. For this evaluation, the same distance precursor - substrate (6 mm) and the same growth time (3 min) were employed. It is worth to mention that, besides the N_2 atmosphere, also an Argon atmosphere was used, leading to results similar to the ones obtained under N_2 (at the same pressure). In this sense, only the results for the nitrogen atmosphere are represented in the table. The significant differences found for the controlled atmosphere growths conducted to the conclusion that the oxygen availability and/or the oxygen pressure are of paramount importance in the growth of these ZnO nanostructures, independently on the type of gas that surrounds the precursors.

The effect of increasing laser powers, from 20 to 35 W reveals dramatically changes in the ZnO morphologies. For the lowest power (20 W) only NPs are observed. These NPs present a polyhedral configuration with an average size around 100 nm, even though smaller particles can be found. In most of the cases, the particles appear agglomerated and a slight coalesce between some of them can be observed. Usually, only a very thin layer is deposited on the surface of the substrate, almost invisible to the naked eye. This layer was found to be somehow attached to the substrate, independently of the substrate's nature. It is worth to mention that below this laser power almost no material was deposited in the substrate surface.

Increasing the power by a small amount (25 W) resulted in the formation of small TPs with cylindrical-like/prismatic-like branches and average length lower than 100 nm. As discussed in Chapter 2 (sub-section 2.2.1), one of the accepted mechanisms for the LAFD growth is based on the assumption that in the first stage of heating (lower powers/temperatures), as the Zn vapour goes to colder regions of the growth chamber and condenses, the formation of instable spherical clusters takes place. Then these clusters collapse into crystalline structures in the form of polyhedral NPs with WZ structure. The NPs exposed faces depend on the formation energy of each surface and the interface of the grain boundaries [3]. If the reaction is stopped at low temperatures, the NPs morphology is kept. Further heating results in the TP formation, with the growth directed through the most favourable crystallographic directions. The TP shape is the most energetically favourable since it offers the minimum energy ratio between the area of the grain boundaries and the surface area. The shape and length of the TPs branches is given by the

anisotropy between the growth rate of each direction and the surface energy (surfaces with higher formation energy tend to be more easily supressed), which are temperature dependent [3]. Thus, with further increasing of the laser power (30 W), the TP branches become longer and a decrease of the thickness along the branch starts to occur.

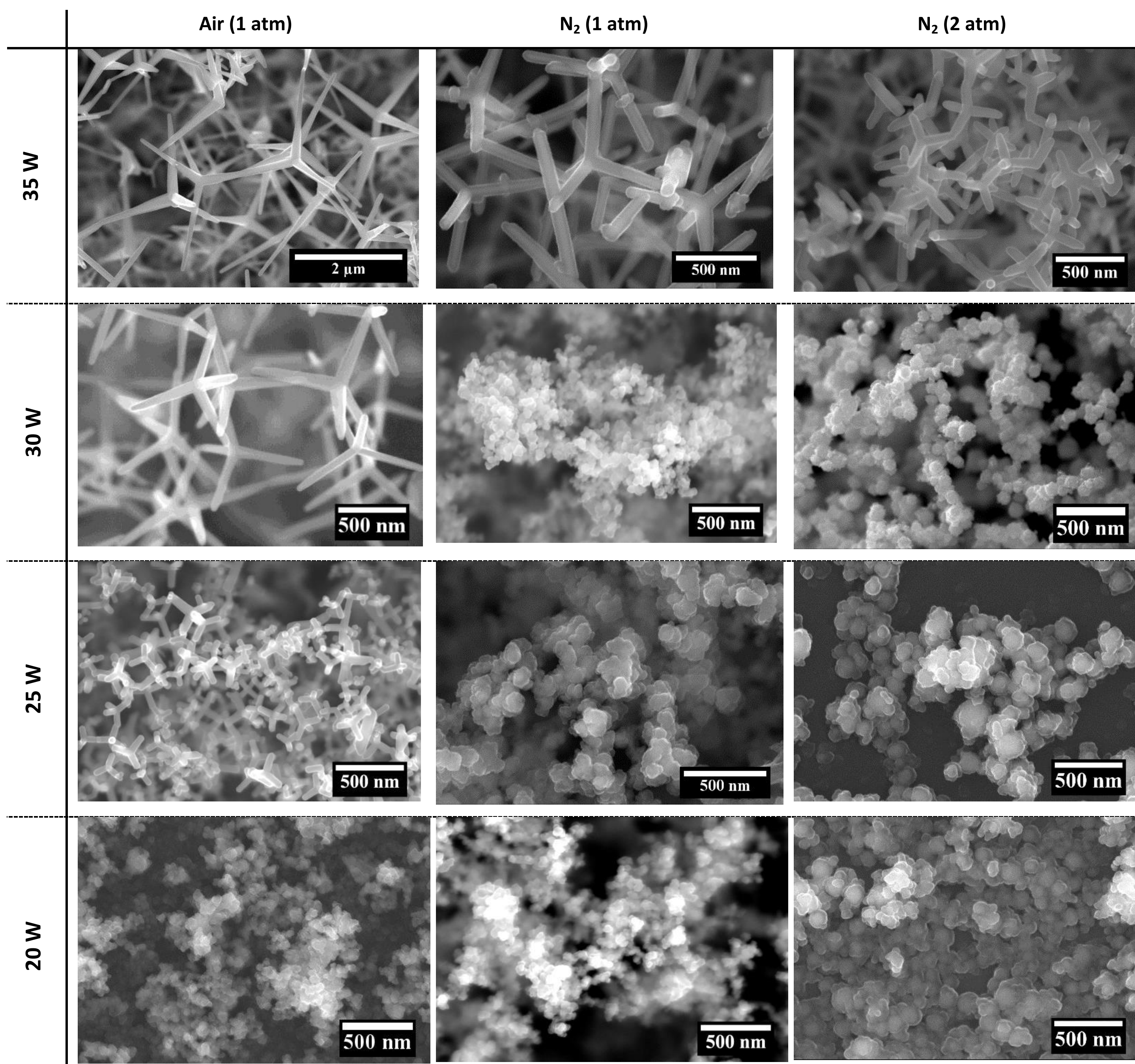

Figure 6-1 – SEM micrographs of the ZnO structures grown by LAFD using different laser powers and growth atmospheres.

Higher powers lead to larger TPs with long branches and sharper tips, as seen in Figure 6-1 for the samples grown with 35 W (in air). Therefore, the dominant morphology for laser powers higher than 25 W is the TP one. However, as mentioned previously, since the NPs correspond to the initial heating stage of the growth process, the first layer of deposited material is always

composed by these nanostructures, and such nanocrystals are always present, even when high laser powers are applied. It is also important to mention that while this first layer of NPs is relatively adherent to the substrate, the sequential "layers" composed mainly by TPs (but also some NPs) were found to detach very easily. The handling of the sample is enough to remove the material from the substrate.

Qiu and Yang [4] found that the size of the TPs is strongly dependent on the local temperature and Zn vapour pressure (for a constant oxygen content). High temperature and Zn vapour pressure (which is promoted by the high temperature) lead to a rapid growth into large TPs, whereas the opposite results in a slow nucleation/growth rate. The TPs formed in higher temperature regions are rapidly transported to lower temperature zones by the flowing stream, thus effectively slowing down the growth rate and ending the process [4]. Moreover, Calestani *et al.* [2] also stated that eventually complete self-inhibition of the growth process is observed due to the continuous decrease in Zn vapour caused by the extremely rapid reaction with the oxygen present in the atmosphere.

In the LAFD method, it was seen that high powers result in a high TPs/NPs ratio. Increasing the power beyond ~ 35 W results in the production of larger size TPs. However, the most important change is not the TP size but size distribution. Figure 6-2a shows a sample grown with 40 W, where one undoubtedly see that a wide size distribution of the TPs can be found. Dimensions from hundreds of nanometers to a few micrometers were measured in the same run of growth. This fact is related to different local growth and kinetic conditions inside the growth chamber. Since it is believed that the TPs formation occurs during the vapour phase and are then transported to the substrate's surface, it can be assumed that the different sizes result from TP formation in different temperature regions: higher temperatures account for the production of larger TPs, while small TPs are formed in lower temperature regions. This becomes more pronounced as the temperature is increased. Low temperatures limit the TPs growth, thus a sample with more uniform TP sizes is produced. When the temperature is increased a higher temperature gradient is present inside the chamber, resulting in a more pronounced difference between thermodynamic and kinetic conditions in the different regions of the chamber, and consequently in more distinct TP sizes.

Figure 6-2b exhibits a high amplification of the TPs structures where is possible to see an entire TP. These structures exhibit a tetrahedral shape with four branches extended from a central part. Most of the TPs branches exhibit a needle-like shape, with the thickness decreasing from the central region to the tip of the branch. Typically, all the branches show similar morphologies. In this case, the branches possess a length around 2 μm and a width at the centre of ~ 200 nm.

When high laser powers are applied, a great amount of material is produced due the higher yield of the evaporation process, forming a thick sample. However, the sample shows a high porosity due to interconnected network formed by TPs with different sizes and a small amount of NPs. In this network of different sized TPs, the NPs and the small TPs can fill the spaces between the larger TPs branches, resulting in a porous sample with a high surface area. Although most of the ZnO material does not show a good adhesion to the substrate, the crystals are somehow connected to each other. For powers higher than ~ 40 W it is possible to produce a free-standing

sample with the visual appearance of foam. This foam is extremely fragile and very difficult to handle without damaging the sample. Since it is a very porous sample it is also very light.

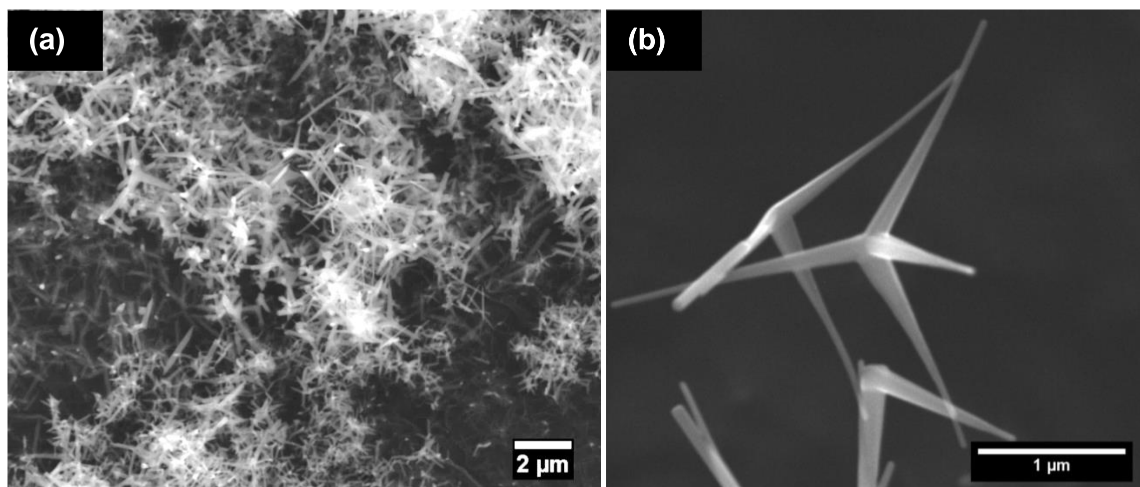

Figure 6-2 – (a) SEM image of the ZnO samples grown with 40 W, showing the large size distribution of the TPs. (b) High amplification image of the TPs, two of them with broken branches.

The changing of the growth atmosphere to one poor in oxygen leads to significant changes in the produced morphologies. While in the case of the samples grown in air TPs start to form for applied laser powers close to 25 W, when grown under N_2 atmosphere and 1 atm, the TP morphology only appears for powers around 35 W and higher, presenting size and shape similar to the TPs grown with 30 W under air conditions. For samples grown under 2 atm of N_2 pressure a similar behaviour was observed, however a reduction of the TPs size using the same power is plainly identified. It was also noted that the produced NPs appear to have a higher degree of coalescence, forming larger structures. This coalescence is likely to be due to the higher pressure inside the growth chamber.

Although the oxygen availability seems to be the dominant factor, as evidenced for the analogous results obtained under argon atmosphere, the pressure inside the growth chamber also plays a role in the control of the size and morphologies obtained. It was seen that reducing the amount of oxygen inside the chamber leads to a decrease of the growth rate of the crystals, allowing the production of NPs up to higher laser powers. Thus, using an oxygen-poor atmosphere it is possible to increase the yield of the NPs production by increasing the laser power. A higher laser power will lead to a higher amount of precursor material being evaporated, while with the low laser powers (~ 20 W) used to produce NPs in air conditions, only the material at the surface of the precursor is being evaporated, thus a small amount of material will be deposited. Since in N_2 or argon atmospheres the only oxygen available to react with the Zn vapour is the one present on the precursor together with some residual amount that exist inside the growth chamber, the growth rate of the ZnO crystals will be significantly reduced, resulting in crystals with smaller dimensions. According to Calestani *et al.* [2], in vapour phase synthesis, usually the introduction of oxygen in the growth system leads to fast Zn oxidation, with a consequent continuous decrease in Zn vapour up to complete self-inhibition of the growth process, as mentioned above. Thus, limiting the amount of oxygen inside the growth chamber limits the Zn consumption and leads to

a reduction in the crystals' growth rate, as observed in the present samples. Qiu and Yang [4] also saw that oxygen concentration has an important role in the TPs growth. They observed that for low oxygen concentration (< 7.5 %) most of the products obtained did not present the TP shape. This shape was only obtained with increasing the concentration of oxygen, becoming the dominant one. Regarding the samples grown at a pressure higher than the ambient one (2 atm), it seems fair to infer that, besides the low oxygen content, the pressure of the gas inside the growth chamber contributes to a reduction in the Zn pressure, with a consequent reduction of the crystals growth rate.

The influence of heat treatments in the morphology of the samples was also evaluated. Figure 6-3 depicts the SEM image of a sample grown in air with an applied laser power of 20 W. As already discussed above, the as-grown sample is comprised by polyhedral NPs and no TP morphology was identified under such low power (Figure 6-3a). After being placed in an oven, at atmospheric pressure during 2 h at 500 ^{o}C (Figure 6-3b), the presence of small TPs is evident. It was observed that, while some NPs remained, most of them undergo a morphology transformation into TPs. The shape of these TPs is similar to the one obtained for the sample grown at 25 W, with bulkier branches with lengths around 100 nm. Thus, one can assume that, in fact, the NPs produced with low laser power correspond to the nuclei from where the TPs growth proceeds. Subject the NPs to high temperature allows the growth process to continue, forming the TPs structures with an analogous shape as the ones produced by LAFD. The same behaviour was observed for the NPs grown under N_2 atmosphere (not shown).

The TPs grown with 25 W (air) were also subject to thermal treatments with three different temperatures (500 ^{o}C, 600 ^{o}C and 700 ^{o}C), during 2 h (Figure 6-4). It was found that the size of the TPs progressively increased with temperature at the same time that the branches acquire a needle-like shape. In this case, where a more uniform heating was applied, the TPs size distribution seems to be more uniform than in the case of the LAFD growth.

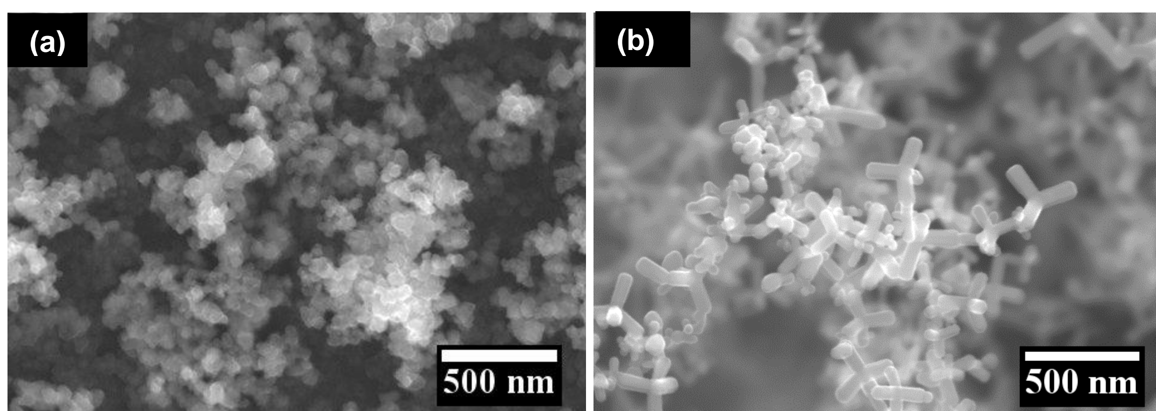

Figure 6-3 – ZnO sample grown with 20 W in air (a) as-grown and (b) thermal annealed in air at 500 ^{o}C during 2 h.

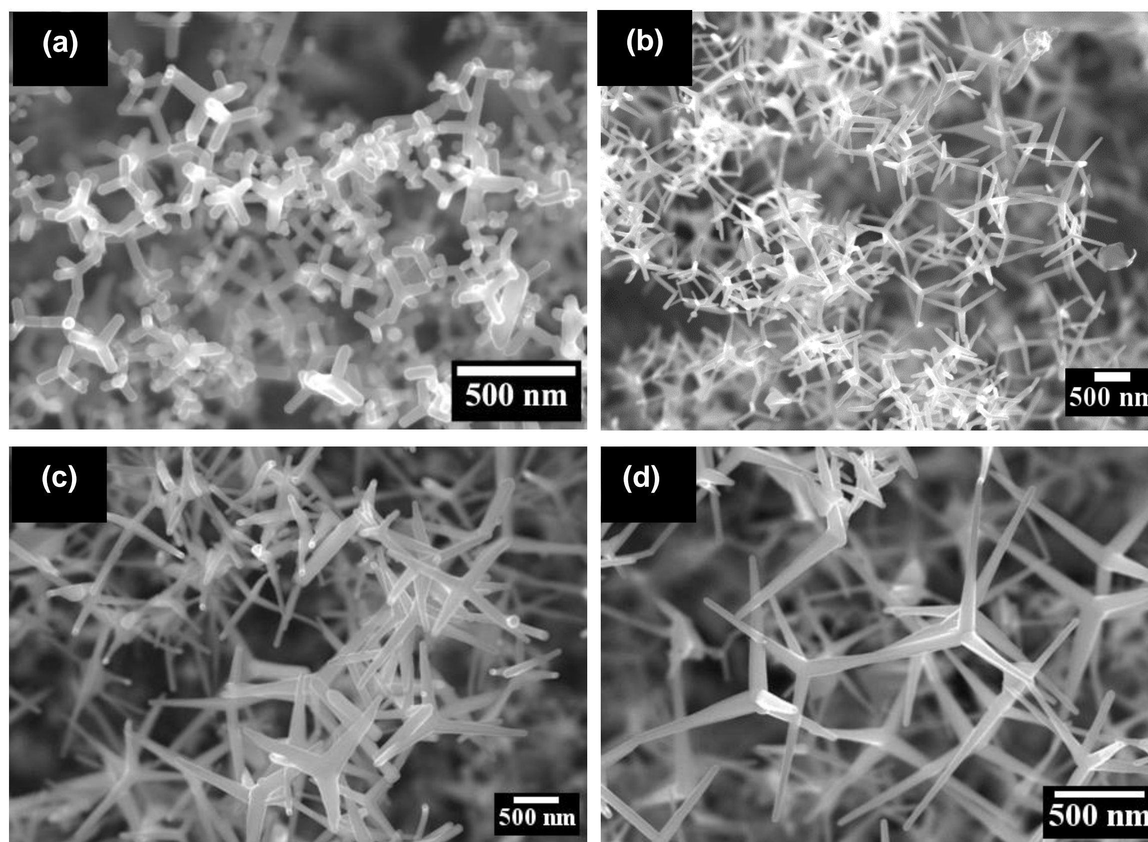

Figure 6-4 – ZnO TPs grown in air atmosphere at 25 W (a) as-grown and thermal annealed in air at (b) 500 ^{o}C, (c) 600 ^{o}C and (d) 700 ^{o}C.

The ZnO samples produced by LAFD at air with a heating power of 35 W were analysed by TEM and some of the results are present in Figure 6-5 and Figure 6-6. As already discussed (Chapter 2), the formation of the interconnected network of NPs and TPs depending on the applied laser power (heating) is in fairly good agreement with the growth mechanism reported by Ronning *et al*. [3]. This mechanism is further corroborated by the presence of a twin relation between the TP branches, as evidenced by TEM analysis (Figure 6-5). These measurements revealed that the four branches of the TPs correspond to single crystals. The interfaces between the neighbouring crystalline domains are fairly sharp, straight and connected with little lattice distortion. Figure 6-6a shows a high angle annular dark field (HAADF-STEM) image of one representative ZnO TP. Based on the present *Z*-contrast image, where the intensities strongly depend on the atomic number *Z*, the composition seems to be uniform along the entire TP, both in longitudinal and transversal directions. Likewise, HRTEM images of the analysed TPs (see an example in Figure 6-5b) showed an excellent crystalline quality and no dislocations or stacking faults were found along the entire nanostructure. The inset of Figure 6-6b corresponds to the FFT recorded from the TP highlighted in Figure 6-6b. The FFT is consistent with the WZ structure of ZnO observed along the [0001] zone axis. Taking into account the orientation of TP branch in the HRTEM image it was concluded that the [$11\bar{2}0$] was the crystallographic direction of the growth for this specific TP branch. However, analysis in different branches of different TPs revealed other growth directions, namely the typical *c*-direction [0001] (Figure 6-6c), which is the dominant one. The differences

found in the growth direction of the branches may be related to the different faces exposed in the nuclei particles from where the TP growth proceeds. It was seen that the NPs exhibit irregular shapes that differ from particle to particle, evidencing the presence of distinct surface faces. As discussed in Chapter 2, the shape of the TPs is given by the anisotropy of the respective growth rates in the different directions, which depend on the surface energy of each crystal face.

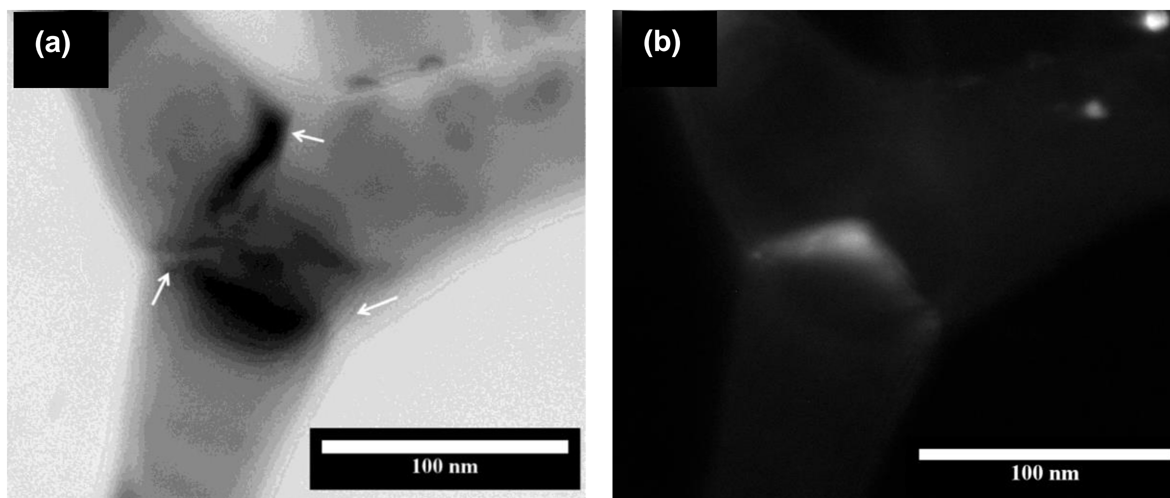

Figure 6-5 – (a) Bright and (d) dark field images of the central part of a ZnO TP, pointing out to the presence of twin boundaries. The forth branch of the TP is perpendicular to the plane of the figure.

Increasing the laser power does not seem to significantly influence the crystallinity of the produced material, as evidenced by the TEM measurements in the TPs grown in air with a power of 60 W (Figure 6-7). HRTEM results proved the high crystalline quality without the presence of defects, even when high laser powers are used in the growth.

The samples grown under N_2 atmosphere (2 atm) and 35 W of applied power were also analysed by TEM and the results are summarized in Figure 6-8. In accordance with the SEM results, it was observed that under these conditions the TPs growth is inhibited, leading to a reduction of their amount and size. A larger number of NPs was obtained, with a quantity comparable to the one found for the TPs (Figure 6-8a), which strongly contrasts with the samples grown in air at the same laser power. The shape and dimensions of the produced TPs are well seen in Figure 6-8b. In this case, the branches do not exhibit the needle-like shape characteristic of the TPs grown in air, presenting bulkier branches instead. According to the work of Ronning *et al.* [3], this type of branches is a result of almost comparable growth rates between the different faces. It was also seen than the length of the branches is around 100 nm, while the average diameter is 50 nm. The NPs are represented in Figure 6-8c, showing a wide size distribution. From this TEM image the polyhedral shape of the NPs is unambiguously identified, though with a number of different shapes. The HRTEM together with the FFT results (Figure 6-8d) proved that the crystalline quality of the crystals grown by the LAFD technique is kept even under poor oxygen atmosphere conditions. No crystalline defects or stacking faults were observed in the analysed nanocrystals. The FFT highlights the WZ nature of the structures.

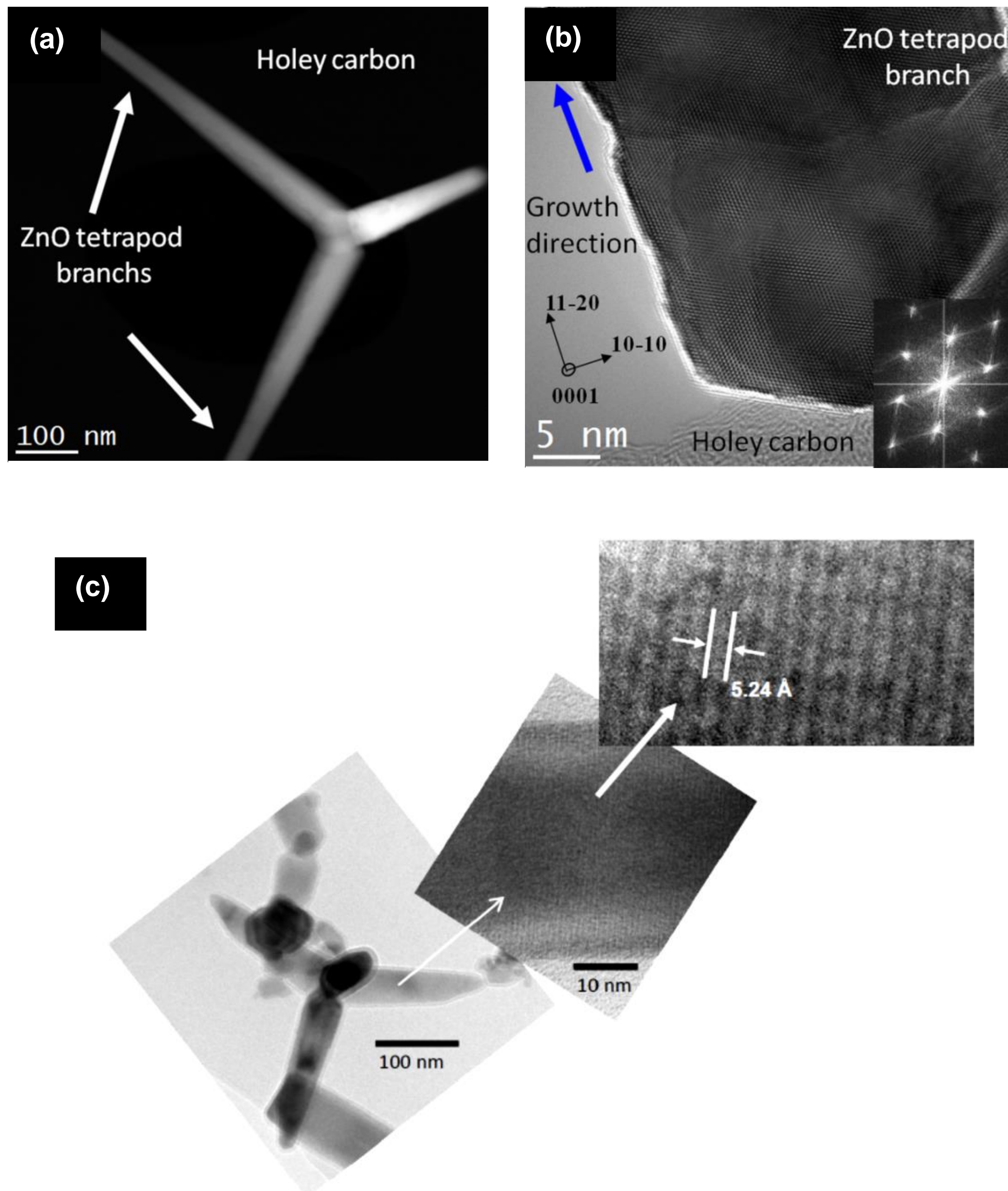

Figure 6-6 – (a) HAADF-STEM image showing one representative ZnO TP scraped from the substrate surface. (b) HRTEM images of a ZnO TP branch. The Fast Fourier Transform of the inset reveals the WZ structure of ZnO along the [0001] zone axis. (c) TEM image of a ZnO tetrapod branch showing the interplanar spacing along the [0001] direction.

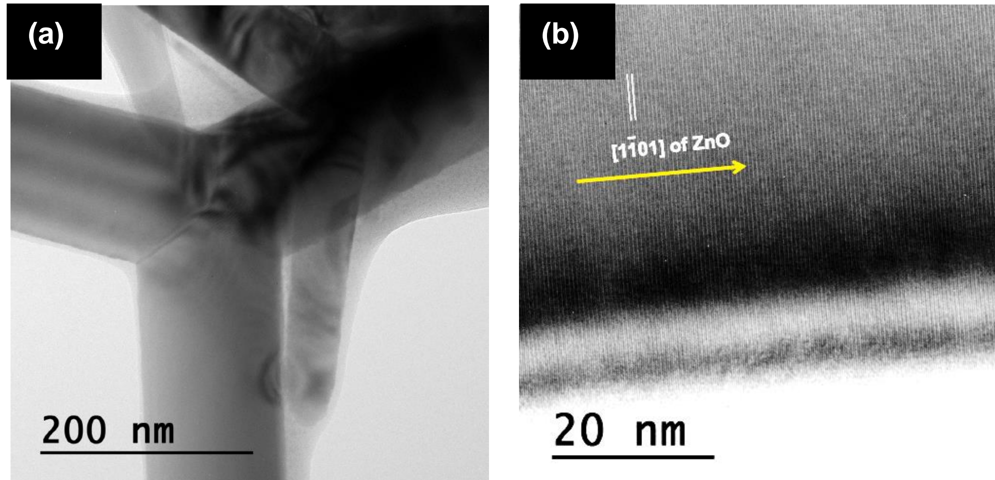

Figure 6-7 – (a) TEM of ZnO TPs grown with high laser power (60 W). (b) HRTEM image of a single ZnO TP branch.

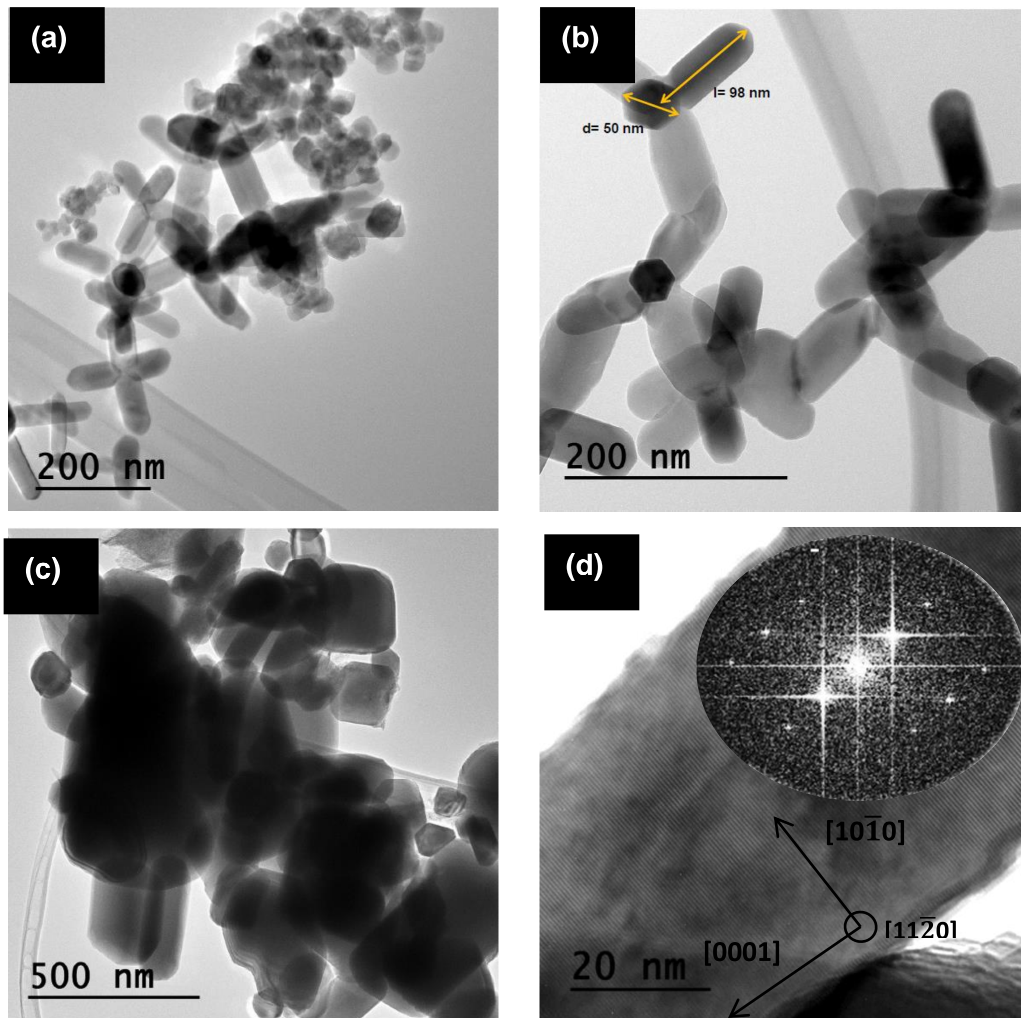

Figure 6-8 – (a), (b) and (c) TEM of ZnO samples growth with 35 W under N_2 atmosphere (2 atm). (d) HRTEM image of a selected ZnO TP branch showing its high crystallinity. The inset corresponds to the FFT pointing to the *c*-axis orientation and WZ crystalline structure.

The TEM results were further corroborated by XRD measurements, where all the planes depicted in the diffraction pattern can be associated to the mentioned crystalline structure (Figure 6-9), emphasizing the single phase nature of the produced samples. Both TEM and XRD results confirm the high crystallinity of the LAFD produced samples independently of the growth conditions, as supported by the narrow FWHM values of the diffraction patterns.

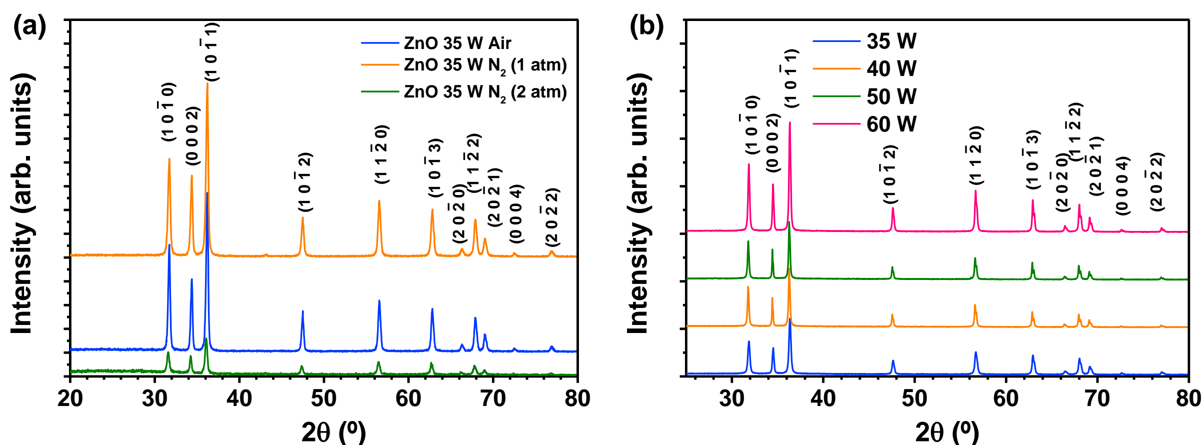

Figure 6-9 – XRD patterns of the deposited ZnO samples (a) grown at the same laser power but different atmospheres and (b) grown in air with high laser powers. The spectra are vertically shifted for clarity.

Figure 6-10 shows the Raman spectra for ZnO NPs and TPs grown under different atmospheres. In this case, the samples were analysed with 325 nm (~ 3.8 eV) photon excitation. This photon energy is slightly higher than the WZ ZnO energy bandgap, so the virtual states in the Raman scattering process are replaced by real electronic states, leading to an enhancement of the scattering cross-section for phonon/electron coupling, considering the large ZnO polaron coupling coefficient. The observed lines result from the contributions of the A_1(LO) symmetry mode and its overtones [5,6]. This wavelength was used in order to assess only the surface of the samples. Since the NPs layer deposited on the substrate is extremely thin, higher wavelength resulted in the observation of mostly the silicon substrate and not the ZnO sample.

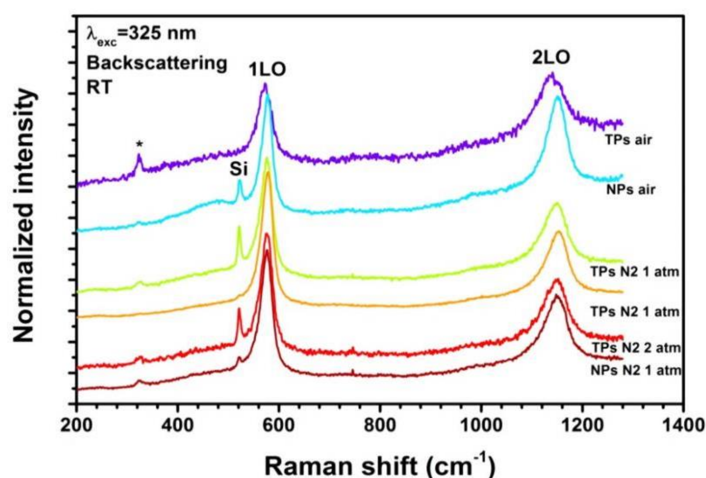

Figure 6-10 – Raman spectra of the ZnO nanostructures obtained with 325 nm (resonant excitation condition) for NPs and TPs grown under different atmospheres. The asterisk denotes an artefact from the measuring system. A peak from the Si substrate is also visible. The spectra are vertically shifted for clarity.

The optical properties of the LAFD samples were studied by low temperature PL, as can be seen in Figure 6-11 and 6-12. While in Figure 6-11 the spectra correspond to samples containing only NPs, Figure 6-12 displays spectra from samples comprised mostly by TPs, even though some NPs are likely to be present, as discussed before. Nevertheless, hereafter, these samples will be designated only as TPs. Therefore, whereas the TPs emission (Figure 6-12) is always dominated by the D^0X [7–9] in the UV region and almost no visible luminescence is observed, for the NPs (Figure 6-11) besides the NBE recombination, also the broad visible bands were identified [10–12], with the exception of the sample grown with 2 atm of N_2, where practically no visible luminescence was observed. The dominant D^0X emission peaked at ~ 3.36 eV is attributed to the overlap of several emitting lines, designated by *I lines* [7,11,13]. These transitions have been previously assigned to different impurities like H (I_4), Al (I_6), Ga (I_8) and In (I_9) (Figure 4-5) [7]. In addition and as reported by Grabowska *et al.* [14], the surface exciton (SX) recombination near ~ 3.366 eV may also be present, as well as the FX transition, that is usually found at ~ 3.376 eV [7,11].

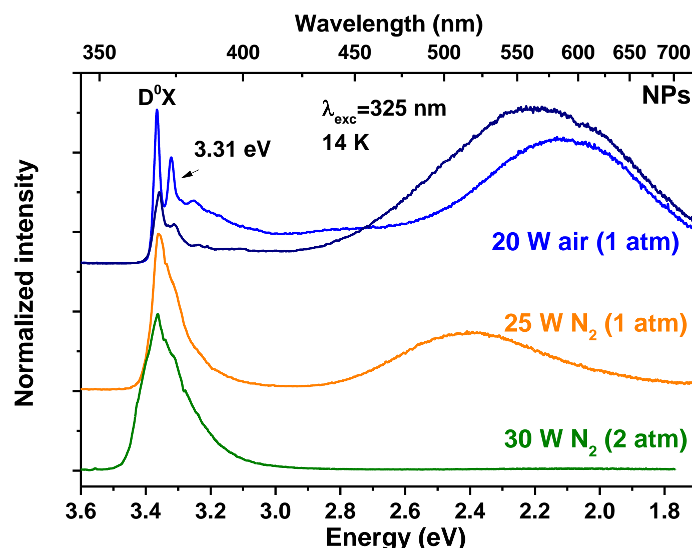

Figure 6-11 – Low temperature PL spectra of the NPs produced under different atmospheres.

Significant changes are identified in the NBE region between the samples grown in different atmospheres. The NPs grown in air show well-defined NBE transitions, with a narrow D^0X emission and other line peaked at ~ 3.31 eV. As already mentioned in Chapter 4, the 3.31 eV line has been widely discussed in the literature and its nature is still under debate. Most of the well-established models to explain the optical properties of the ZnO were developed several decades ago [10,15,16] and plenty of important contributions have been added since then [7,11,17–22]. In particular, in low dimensional structures, SXs have been observed and reported [14,23]. One of the most argued optical centres corresponds to the aforementioned 3.31 eV line, detected in all forms of ZnO structures and assigned to different recombination mechanisms, as recently reported by Thonke *et al*. [19,24,25]. According to this author, the 3.31 eV line is associated with an acceptor level at 0.13 eV above the ZnO VB and the transition is related with the presence of stacking faults in the basal plane. Other hypotheses for the nature of this emission line have been also addressed in the literature [19,26]. In the present laser processed samples the origin of this line will be discussed in detail in the next section concerning the ZnO MRs. Nevertheless, it is

important to mention that this is a reproducible feature in the LAFD NPs since it was observed in more than one sample grown in the same conditions, as can be seen in the upper spectra of Figure 6-11. The same lines are present in the NBE region, however with a distinct relative intensity regarding the visible broad band. The visible band exhibits different broadening depending on the analysed sample (grown in the same conditions). The distinct width of the bands strongly suggests the presence of more than one optically active centre contributing to the broad emission. The distinct spectral positions observed can be accounted for different defect distribution in the samples, resulting in different relative intensities between the emissions of the centres. As discussed in Chapter 4, the broad visible bands are frequently observed in ZnO. The most common ones corresponded to the GL and YL bands. It is known that different types of defects are responsible for these emissions, but the chemical nature of the defects responsible for them have not been conclusively established yet [1,27]. The GL band is probably the most studied one. In early studies, the structured GL was unambiguously attributed to copper impurities, while for the unstructured GL strong evidences were presented in favour of the presence of oxygen or zinc vacancies, although other defects/impurities have been pointed out [10,11,28]. On the other hand, the YL band is commonly associated to oxygen interstitial defects [1,27]. Both of these centres appear to be present in the NPs grown by LAFD. In the case of the sample grown with 1 atm of N_2, the broad visible band corresponds to the typically observed unstructured GL, which, in this case it is fair to assume that could be related to oxygen vacancies, since this sample was grown in an oxygen-poor atmosphere. However, this band did not appear in the sample grown under higher pressure. Regarding the NBE for these two samples, a broader emission than the one observed for the particles grown in air is observed. In both cases the emission is peaked at ~ 3.36 eV. The observed emission is most probably due to the overlapping of different recombination centres that occur in this spectral region, including the ones identified for the samples grown in air, with a strong contribution of the D^0Xs.

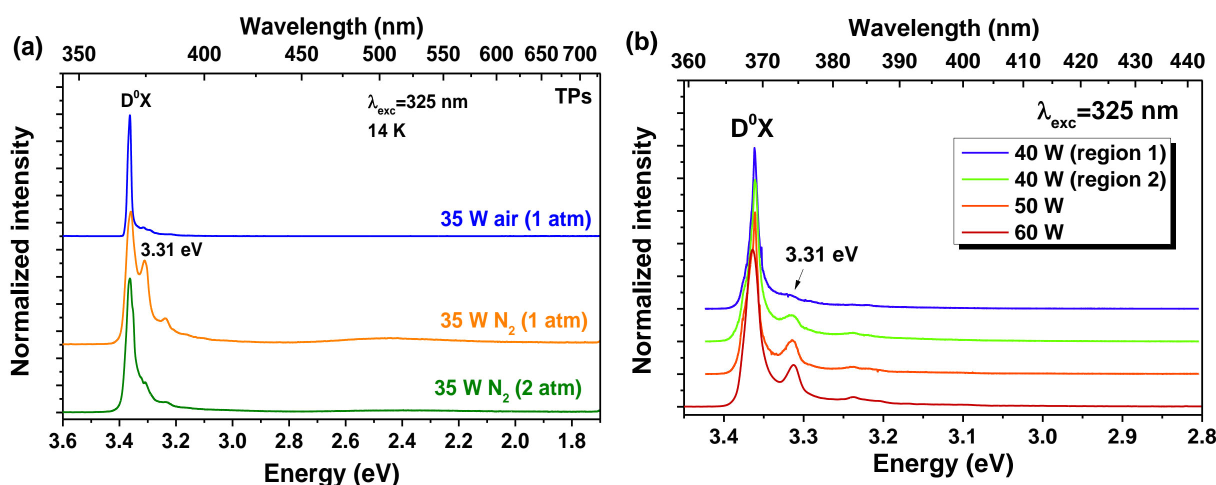

Figure 6-12 – Low temperature PL spectra of the ZnO TPs grown under different (a) atmospheres and (b) laser powers.

Comparing the NBE region of the different TPs samples grown in air one clearly sees that when a higher laser power was used, besides the dominant D^0X emission, the 3.31 eV also starts to appear, increasing its relative intensity as the power is increased. Assuming that this line is related

with surface defects (see a detailed discussion in sub-section 6.1.2), the enhancement of this line with increasing power means that more surface defects are been created due to the higher growth rate. This line is also present for samples grown with N_2 atmosphere. Even though only a shoulder appears for the sample grown under 2 atm, this line is particularly intense in ZnO produced under 1 atm, which may also indicate the creation of more surface defects under this atmosphere.

The low temperature PL of the ZnO structures is usually used as a reference of the samples' optical quality and is generally accounted by a high resolved NBE spectrum, as is the present case both for TPs and the NPs grown in air. Another indication of the optical quality of the samples is the ratio between the NBE recombination and the deep level visible emission, which is clearly the case of all the TPs, where almost no visible emission was detected at low temperature (when compared with the NBE emission), showing their high optical quality.

Figure 6-13 and 6-14 depict a comparison between the spectra measured at 14 K and RT and the NBE temperature dependence for both TPs and NPs samples grown in air, respectively. The decrease in the PL intensity with temperature can be explained by competitive nonradiative processes typically expected for higher temperatures. In the present case, although a very strong PL intensity is measured both at 14 K and RT, the thermal quenching of the NBE is observed when the temperature rises from 14 K to RT following a similar behaviour of bulk ZnO (not shown) [7]. Increasing the temperature promotes the dissociation of the D^0X and, at RT, the emission is dominated by the FX recombination peaked at 3.28 eV, in both cases (Figure 6-13b and 6-14b).

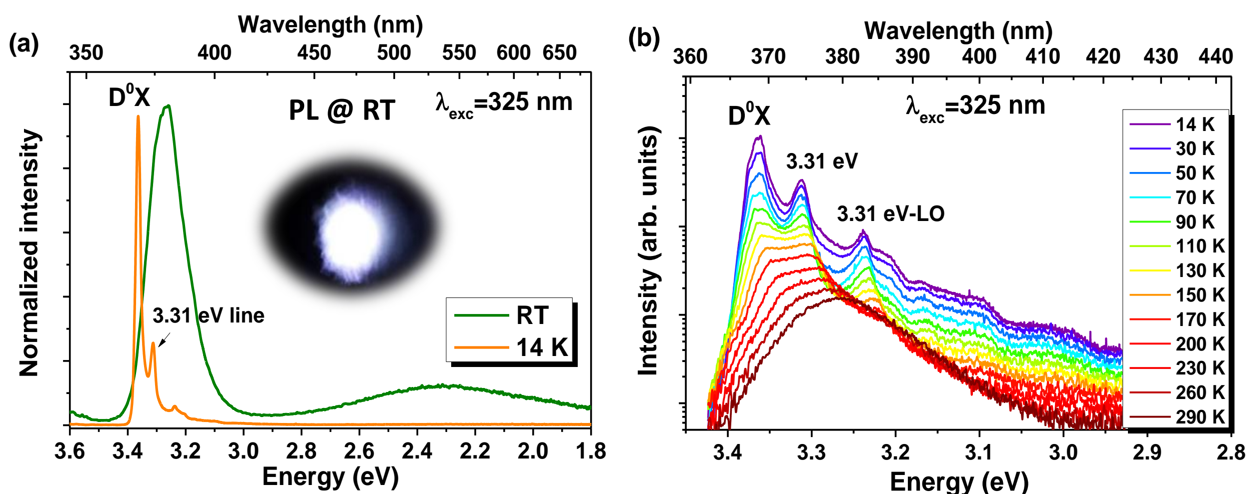

Figure 6-13 – (a) Low temperature and RT PL spectra of the ZnO TPs grown with 60 W of laser power. The inset corresponds to the visual appearance of the ZnO emission at RT. (b) Temperature dependence study of the NBE emission for the same nanostructures. The spectra are vertically shifted for clarity and are represented in a semi-log scale.

In the case of the TPs, and due to the decrease of the NBE/GL intensity ratio, the GL becomes visible with increasing temperature, as can be seen in the RT spectrum. The inset in Figure 6-13a corresponds to the visual appearance of the luminescence at RT, showing a cold-white emission resulting from the overlap of the near-UV and visible emissions. In the case of the NPs (Figure 6-14a), it is seen that at 14 K the visible emission is dominated by the YL. With increasing temperatures an enlargement of the emission is observed accompanied with a shift on the band

maximum to higher energies. This behaviour constitutes an indication that the broad visible band is, in fact, composed by at least to emitting centres (GL and YL) that change their relative intensity with increasing temperature.

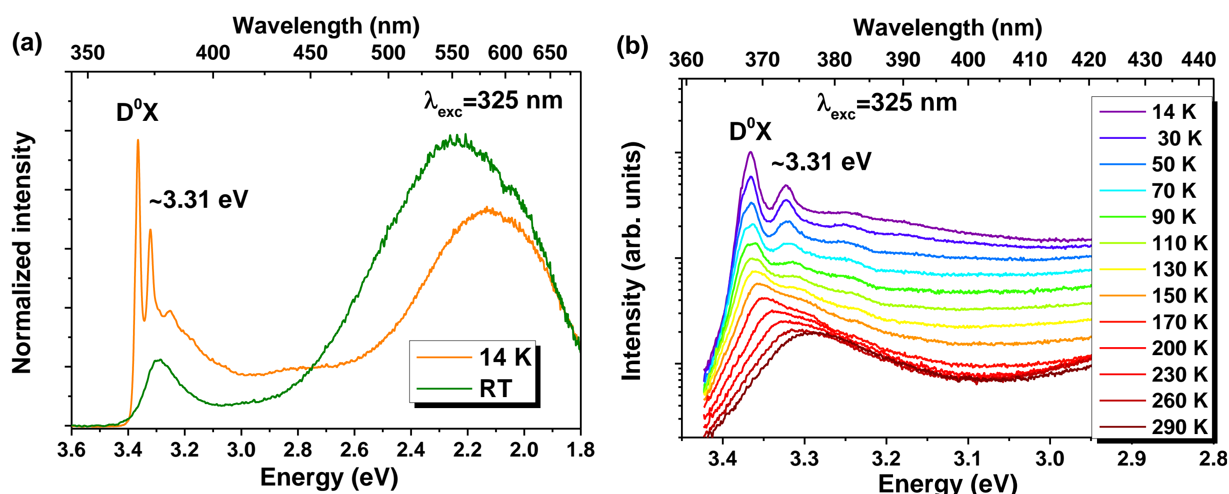

Figure 6-14 – (a) Low temperature and RT PL spectra of the ZnO NPs growth with 20 W of laser power and (b) temperature dependence study of the NBE emission for the same sample. The spectra are vertically shifted for clarity and are represented in a semi-log scale.

RT PLE performed on the broad visible band of the TPs sample (Figure 6-15a) revealed that its population is essentially accomplished via above bandgap excitation. TRPL measurements (Figure 6-15b and c) allowed to verify that also in this case, the broad band is composed by more than one optical emitting centre. This is evident from the band behaviour with increasing time delay. For the delay of 0.05 ms the maximum of the band in placed in the green region (~ 2.39 eV), while for 0.1 ms the band is peaked in the yellow spectral region (~ 2.12 eV). As depicted in Figure 6-15d, the shape of steady-state band matches fairly well the band obtained with a delay of 0.05 ms (taking into account that for the latter a low signal to noise ratio was observed due to low intensity of the band using the flash lamp as excitation source). The small shift to lower energies is most probably due to decrease of the green component with the used delay. Deconvolution of this band can be well described by two Gauss functions (Figure 6-15d) peaked at 2.43 eV (green) and 2.12 eV (yellow). It was seen that the green component lifetime is much shorter than the one observed for the yellow one. In the former case, the emission almost vanishes after only 0.2 ms, indicating a lifetime of a few tens of µs, whereas for the latter, the emission decreased by around 2 orders of magnitude after ~ 1 ms, suggesting a lifetime in the range of some hundreds of µs. In the case of the NPs, the low intensity of the PL emission when excited with the low excitation density of the Xe lamp hampered the PLE and TRPL measurements.

In order to acquire more information regarding the nature of visible band, excitation density dependence studies were performed in both samples (TPs and NPs) at RT. The results can be seen in Figure 6-16 and 6-17. In both cases there is no shift of the broad band, even after spectral deconvolution, ruling out the possibility of a DAP related transition. Also in the case of the NPs, and taking into account the results of the temperature dependence that suggest the presence of more than one centre, two Gauss functions were used to fit the visible luminescence band (Figure 6-17b). The two bands were found to be in the same spectral position as the ones identified for

the TPs sample, although with different relative intensities, indicating that the same defects are present in both samples and are responsible for the observed luminescence, even though with different defect distribution. Log (I/I_0)-log (P/P_0) plots of each band from both samples revealed a slope $m < 1$, which, according to T. Schmidt *et al.* [29], means that the nature of the radiative transitions involves either DAPs or free-to-bound carrier recombination. Since the first hypothesis was already discarded, one may infer that the bands involved in the visible broad band observed at RT in both NPs and TPs should be related with free-to-bound recombination processes.

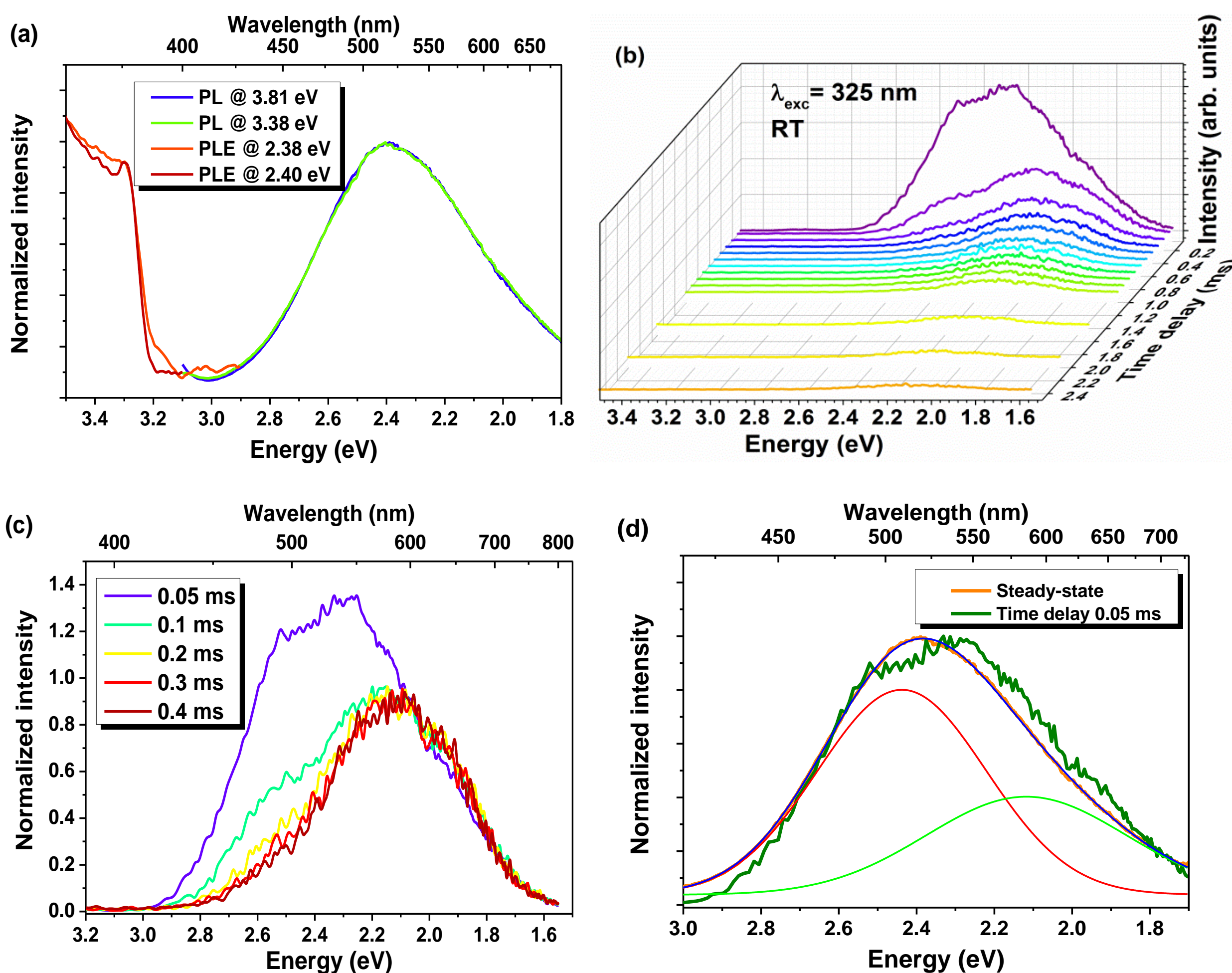

Figure 6-15 –RT (a) PL/PLE and (b) TRPL spectra of the broad band of the ZnO nanostructures grown with 60 W of laser power. (c) Normalized intensity of TRPL spectra for the first time delays. (d) Comparison between the broad visible bands obtained under steady-state and TRPL (delay 0.05 ms) conditions and spectral deconvolution of the broad band into 2 Gauss functions.

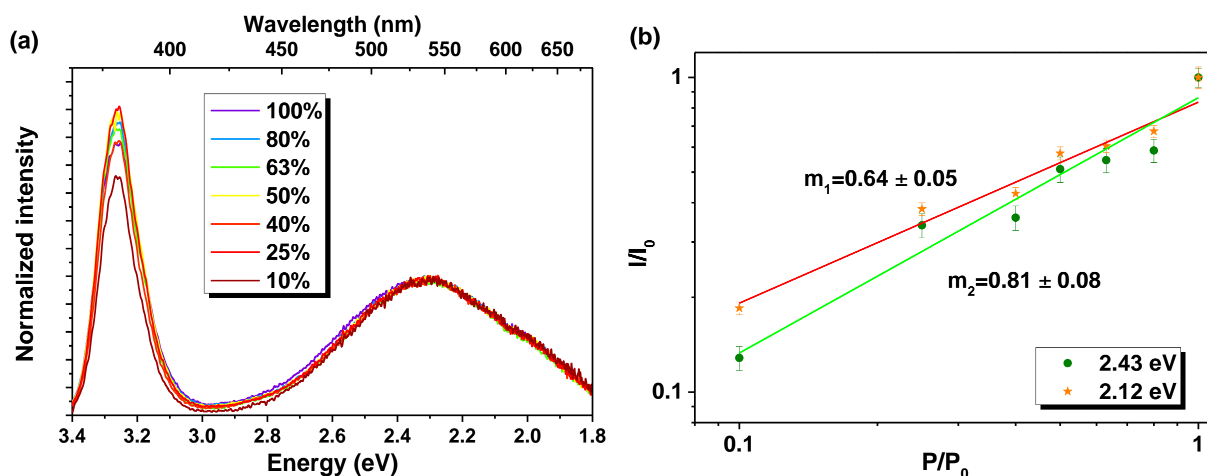

Figure 6-16 – (a) Excitation density dependence of the visible luminescence band at RT for the ZnO TPs grown with 60 W of laser power. (b) Log (I/I_0)-log (P/P_0) plot for each band after spectral decomposition (as seen in Figure 6-15d).

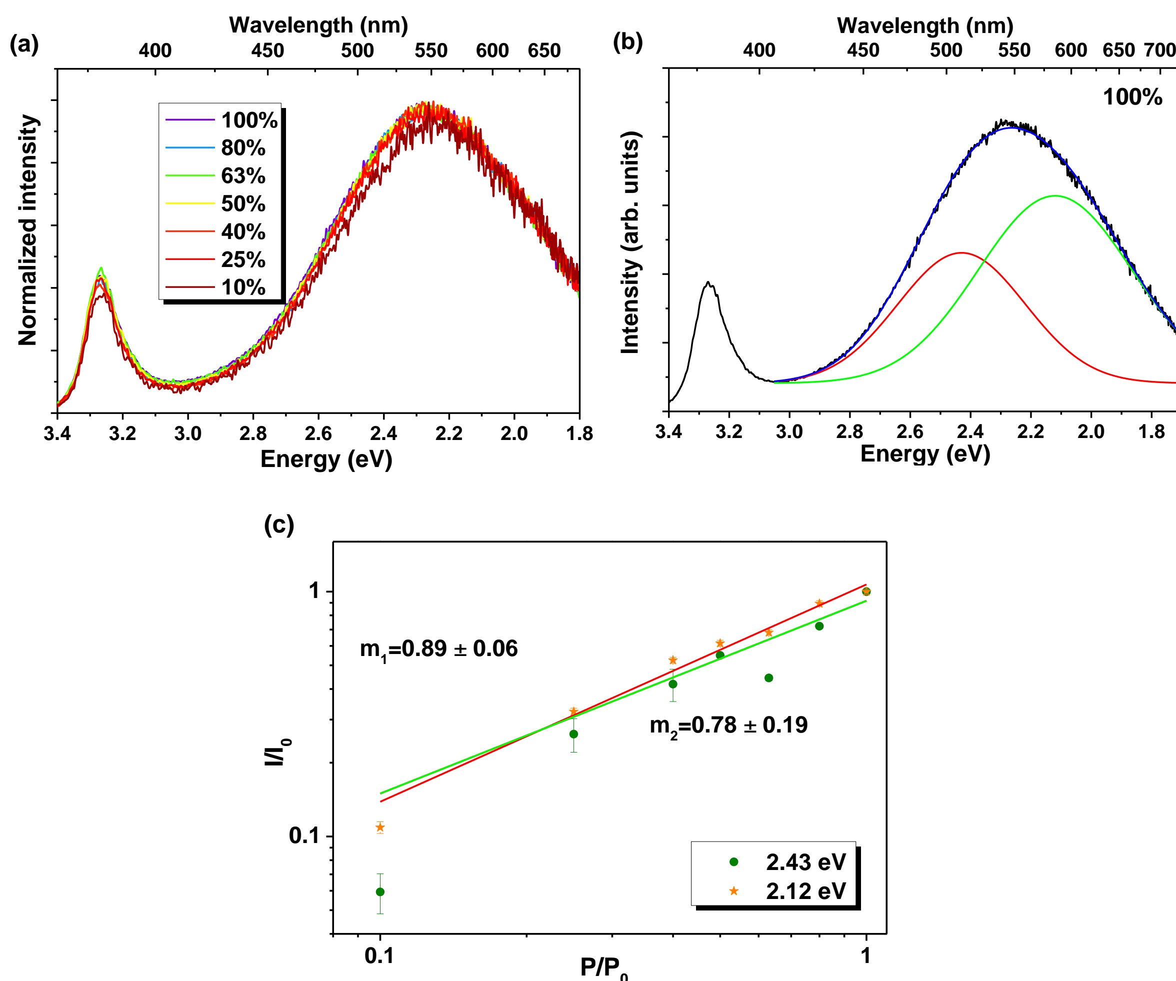

Figure 6-17 – (a) Excitation density dependence of the visible luminescence band at RT for the ZnO NPs grown with 20 W of laser power (in air). (b) Spectral deconvolution of the visible band and (c) log (I/I_0)-log (P/P_0) plot for each band.

To provide additional information about the luminescence features of the ZnO NPs (grown in air and N_2 atmosphere - 1atm), further RT PL measurements were carried out to test the luminescence stability over time (Figure 6-18). The measurements were carried out in air and vacuum with the photon illumination time during almost 4 h. The spectra were acquired at regular intervals (~ 18 min). For the sample produced in air (Figure 6-18a) just a slightly decrease in the visible band and in the NBE intensity was observed when analysed in air, following a similar trend for the vacuum case (not shown). In the case of the N_2 sample (Figure 6-18b), the visible band intensity remained practically constant during the measured time, while distinct behaviours where identified in the NBE recombination for air and vacuum conditions. In the latter case the intensity seems to be constant, however, when the sample was placed in air, the intensity of the NBE emission started to increase with the increasing of the exposure time. These photo-promoted enhancement of the emission as a function of increasing photon illumination time strongly suggests that surface mediated processes may be contributing for the emission observed in this region. As referred above, due to the high surface to volume ratio of the low dimensional structures, optically active surface defects are commonly observed in ZnO [14,30] (and in other semiconductor nanostructures [31–33]) affecting their optical and electrical properties.

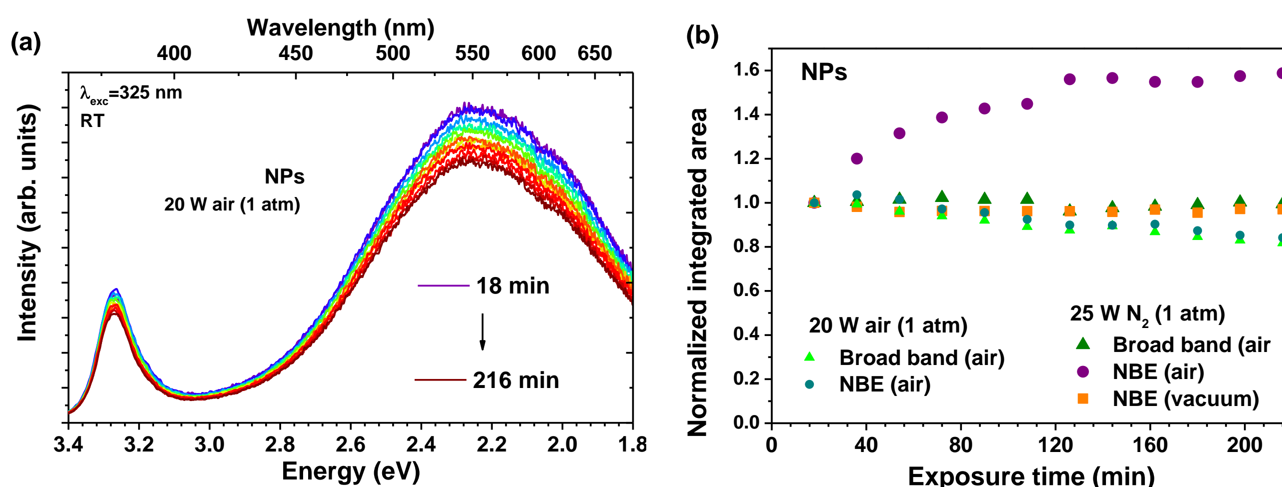

Figure 6-18 – (a) Evolution of the PL emission with the ultraviolet excitation exposure time for measurements performed in air for the NPs samples grown with 20 W at air. (b) Integrated PL intensity of the GL and NBE emission for the same structures grown with 20 W at air and 25 W under N_2 atmosphere (1 atm).

6.1.2. ZnO microrods

Hereafter, the attention will be focused on the MRs grown on the top of the precursor rod. As previously pointed out, these crystals are grown with powers > 25 W and the precursor rod acts as the substrate for the MRs growth. Thus, they have to be scrapped from the precursor in order to be studied or otherwise some contribution from the precursor could be detected. Figure 6-19a depicts an example of the visual appearance of the larger ZnO crystals when removed from the precursor rod, while Figure 6-19b evidences their high transparency. The inset shows the crystals

formed on the top of the precursor and corresponding RT PL emission with above bandgap excitation.

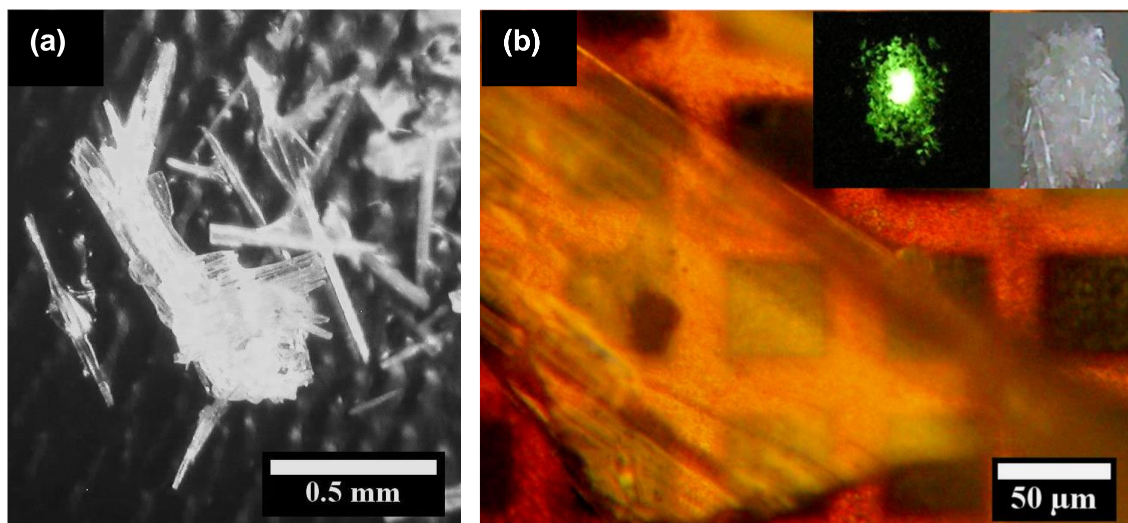

Figure 6-19 – (a) Micrograph of an agglomerate of large ZnO crystals produced by LAFD. (b) Micrograph of one of that ZnO crystals showing its transparency on a TEM Cu grid. Inset: crystals formed on the top of the precursor and their corresponding RT PL emission with above bandgap excitation (325 nm He-Cd laser line).

Different laser powers were used to grow these microstructures. It was seen that the growth of the MRs takes place for laser powers higher than ~ 25 W up to ~ 50 W. For higher laser powers, these structures are formed but are rapidly detached from the precursor or decomposed by the laser beam (unless the heated spot is quickly removed from the region near the beam). MRs grown in the different conditions were evaluated by SEM, XRD, Raman and PL spectroscopy and no significant changes in the morphological, structural or optical properties were found. Even the dimensions of the rods are in the same range for all laser powers.

Despite the fact that large crystals, as the ones represented in Figure 6-19, are produced, the ZnO grown in the precursor tip is dominated by structures at the micrometer scale. Figure 6-20 shows representative SEM images of the produced ZnO crystals (40 W). As can be seen in Figure 6-20a, a great number of rods seem to be grown from a common core, most probably the precursor rod. The rods are randomly oriented and their density depends on the region of the sample. A wide size distribution was also observed, showing rods with lengths ranging from hundreds of μm to hundreds of nm. Unfortunately, the studied growth conditions were not sufficient to find the ideal conditions to obtain rods with comparable lengths in a reproducible way. Higher magnification SEM images (Figure 6-20b) reveals that these samples exhibit a high aspect ratio with a hexagonal cross-section. A study of a significant number of MRs was carried out by TEM techniques (see an example in Figure 6-21a). The analyses showed that most of the lengths of the analysed MRs are in the range of several μm with diameters ranging from 200 - 500 nm to a few μm. In addition, HAADF-STEM imaging (Figure 6-21a) revealed a lack of intensity contrasts inside the ZnO MRs and pointed to a homogenous composition along the growth and radial directions. In order to analyse the crystal structure and the presence of extended defects by TEM, the MRs were tilted to align the electron beam with their $[2\bar{1}\bar{1}0]$

crystallographic direction. HRTEM analysis and the corresponding FFT (see an example in Figure 6-21c) confirmed that all of the studied MRs grew along the [0001] direction. No dislocations or basal stacking faults perpendicular to the general [0001] growth direction were found along the entire MR length, even in the apex. Moreover, the lateral walls of the MRs appear almost atomically flat without roughness or a shell structure.

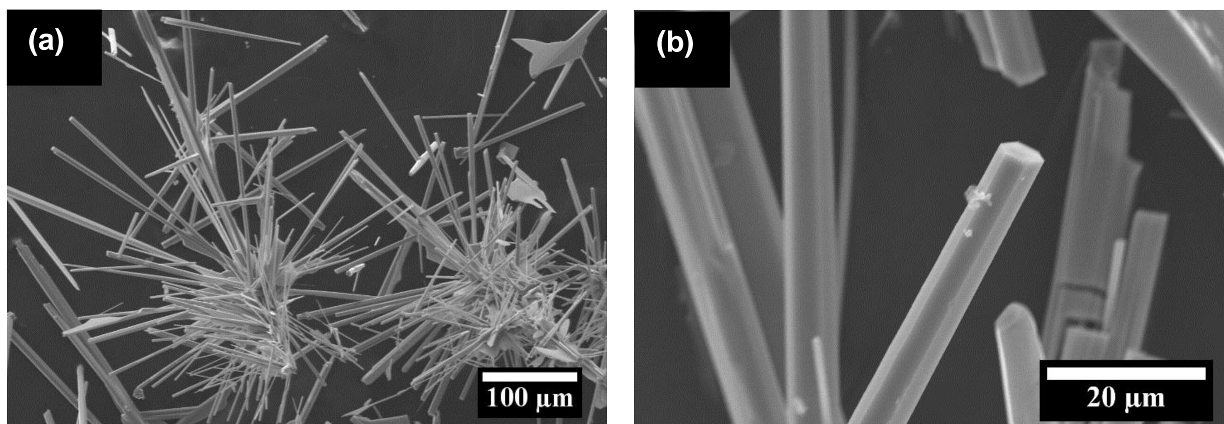

Figure 6-20 – SEM micrographs of the LAFD as-grown ZnO MRs.

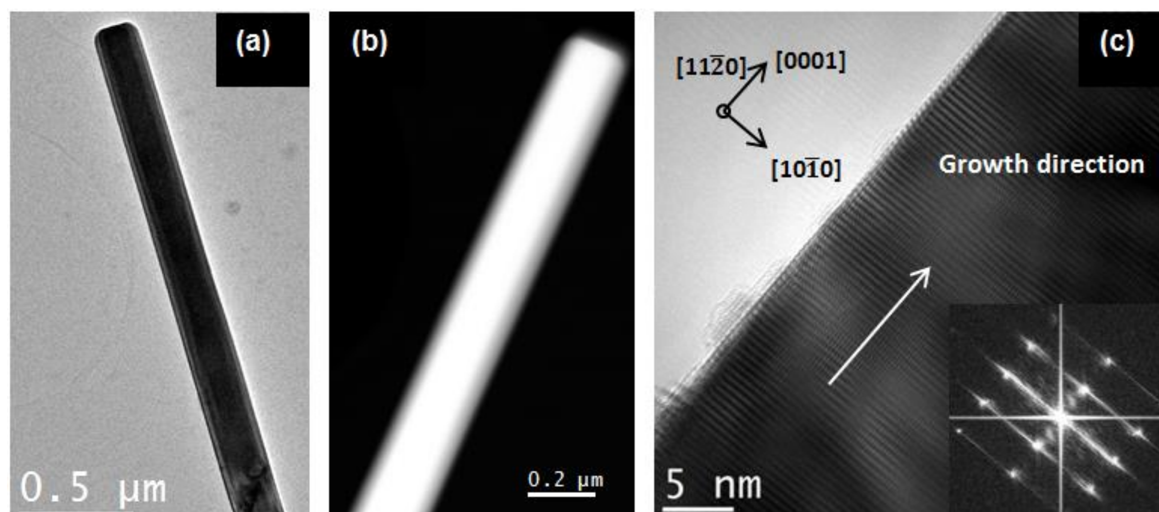

Figure 6-21 – (a) TEM and (b) HAADF-STEM of a ZnO rod scraped from the precursor rod and dispersed on a TEM grid. (c) HRTEM image and the corresponding FFT of a single ZnO rod confirming *c*-axis orientation and WZ crystalline structure.

As mentioned in Chapter 2, under oxygen-poor atmosphere the production of MRs is strongly reduced, thus the study of the samples grown in this type of atmosphere was mainly focused on the material deposited (NPs and TPs) on the substrate/holder. Nevertheless, the crystallinity of the MRs grown under N_2 atmosphere (2 atm) was also evaluated by TEM analysis, as represented in Figure 6-22. Figure 6-22a depicts one representative rod. The TEM analysis evidenced that the dimensions of the MRs produced in these conditions are very similar to the ones grown at air. HRTEM micrographs show that, also in this case, no structural defects have been found in the analysed rods. High crystalline quality was proved by the FFT image acquired from the HRTEM

micrographs. This leads to the conclusion that growing in an oxygen-poor atmosphere does not seem to significantly affect the crystallinity of the LAFD produced MRs.

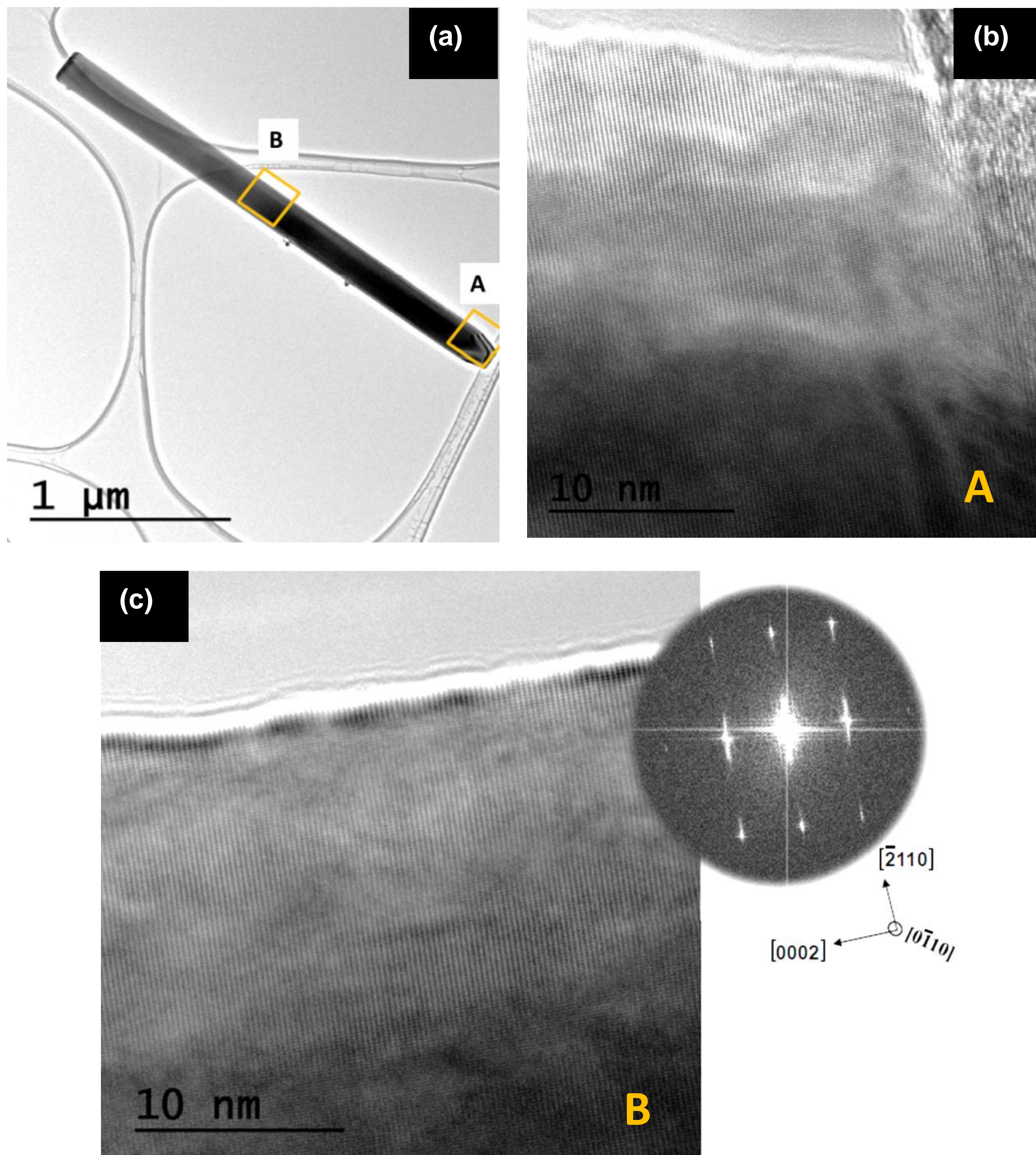

Figure 6-22 – (a) TEM image of a ZnO rod grown under N_2 atmosphere. (b) and (c) HRTEM images acquired from the regions marked in (a). The inset corresponds to the FFT confirming *c*-axis orientation and WZ crystalline structure.

The XRD pattern (Figure 6-23) of the ZnO MRs produced by the LAFD technique was acquired in a monocrystal X-ray spectrometer during several hours. As in the case of the TPs and NPs, all the planes depicted in the diffraction pattern can be associated to the hexagonal WZ crystalline structure of ZnO, highlighting the single phase nature of the produced samples. The XRD results emphasize the high crystallinity of the samples, corroborating the TEM results. From the XRD maxima it was possible to calculate the lattice constants $a = b = 3.25$ Å and $c = 5.21$ Å as well as

the angles of the WZ structure, α = β = 90° and Υ = 120°, which are in good agreement with the values reported for the bulk material [34].

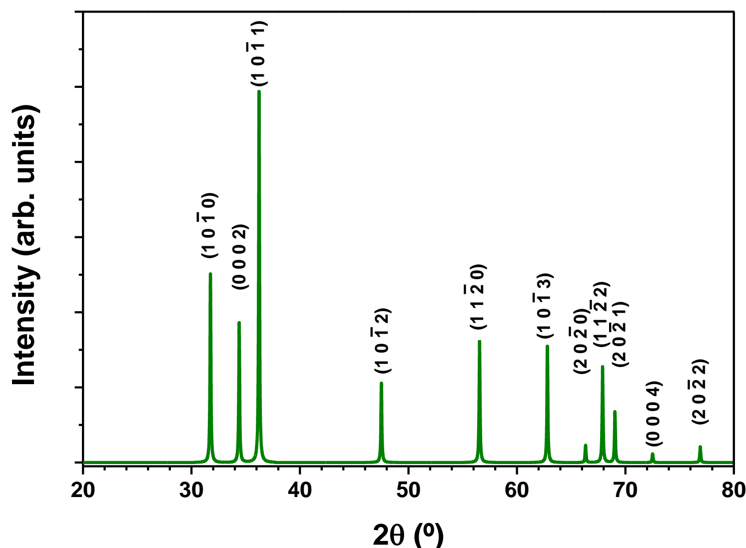

Figure 6-23 – XRD patterns of the ZnO MRs grown by LAFD.

Figure 6-24 shows typical UV excited Raman spectra of the as-grown MRs. For the spectrum recorded with 325 nm (resonant Raman scattering) three major vibrational bands, due to the A_1(LO) phonon mode and its overtones, are observed at 576, 1151 and 1732 cm^{-1} with FWHM of 26, 51 and 63 cm^{-1}, respectively, similarly to the case of the NPs and TPs samples shown above. The Raman spectrum recorded with the 532 nm line displayed all the typical vibrational modes of the ZnO WZ structure that are Raman active, A_1, E_1 and E_2, as well as its combined modes [35,36].

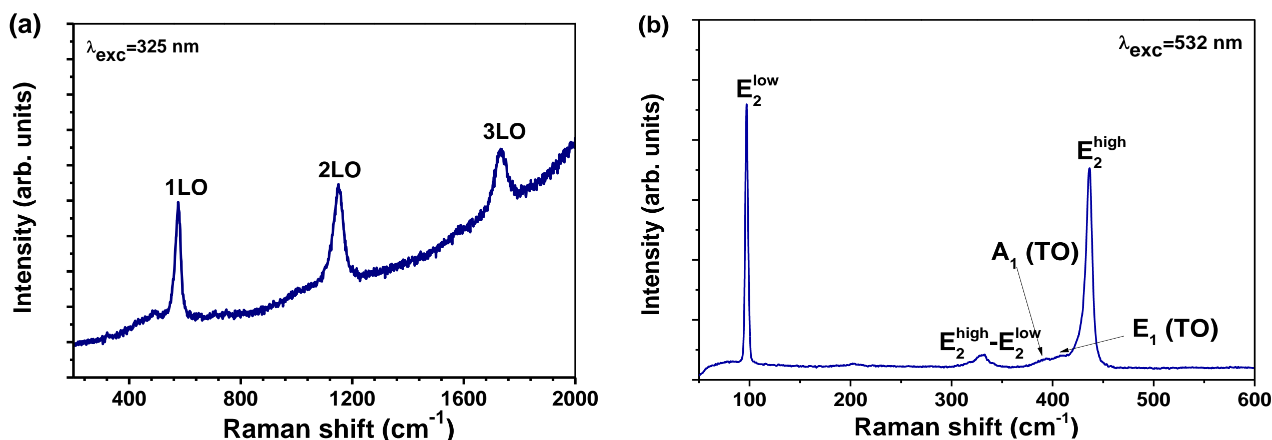

Figure 6-24 – Raman spectra of the ZnO MRs obtained with (a) 325 nm and (b) 532 nm photon excitation.

Macro-PL provides global information over the whole sample, illuminating a great number of MRs during the experimental acquisition. Since these rods are randomly oriented regarding the illumination, the luminescence was collected from both top and side planes of the ZnO rods. In all the cases, approximately the same amount of MRs was used for the PL measurements. For each sample, different laser spots were recorded in order to check the homogeneity of the samples.

PL measurements performed at 14 K (Figure 6-25a) revealed the presence of an intense broad band in the green spectral region related to deep level defects [37–39]. In the NBE region the emission is dominated by a line at ~ 3.31 eV, as observed by its highest intensity when compared with the other emission lines. The emission due to the FX can be found at ~ 3.37 eV and the D^0X lines are also present at ~ 3.36 eV. The energy separation between the FX and the 3.31 eV emission is ~ 64 meV, which is in close agreement with the values reported in the literature [40–42]. The emission observed at ~ 3.24 eV is most likely due to the first LO phonon replica of the 3.31 eV line, and a second phonon replica can also be observed at ~ 3.16 eV, each with an energy separation of ~ 70 meV.

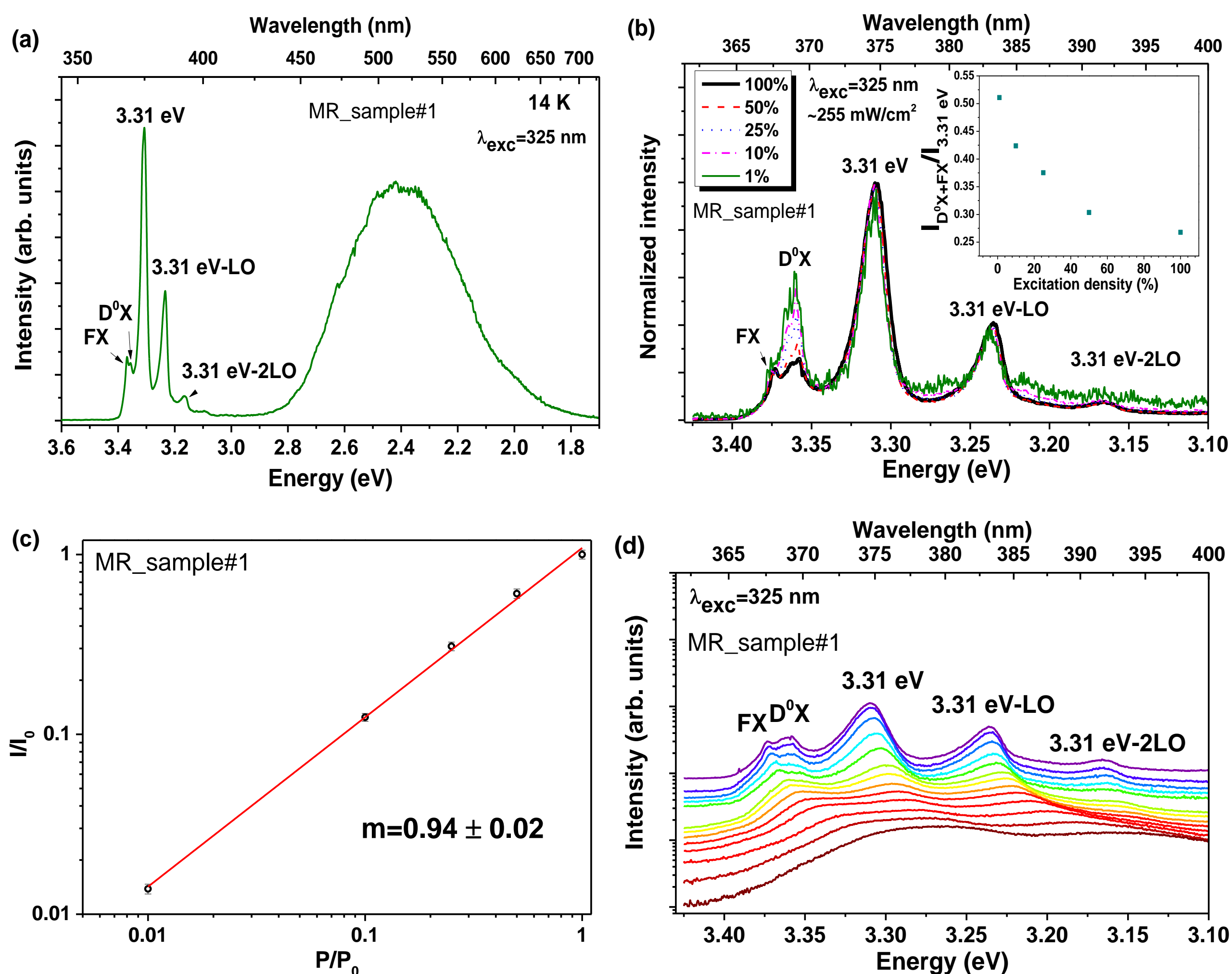

Figure 6-25 – a) PL of the near band edge emission of the ZnO MRs grown by LAFD (MR_sample#1) at low temperature. b) Excitation density dependence of the near band edge emission at 14 K. The inset depicts the ratio between the D^0X+FX and 3.31 eV emission intensity as a function of excitation power. c) Log (I/I_0)-log (P/P_0) plot for the 3.31 eV emission. d) Temperature dependence of the NBE emission. The spectra are vertically shifted for clarity and are represented in a semi-log scale.

The emission observed around 3.31 eV was many times associated to an unknown acceptor responsible for the non-reproducible *p*-type conductivity in the material [18]. However, the fact that this band also appears in nominally undoped *n*-type samples requires a more careful analysis. As previously reported, the 3.31 eV emission has been extensively studied in bulk [43], thin films

[19] and nanostructures [44], and has been associated to distinct recombination mechanisms such as donor-valence band transitions, electron-hole recombination from DAP transitions, electron-acceptor transitions, excitons bound to deep neutral acceptors, TES of D^0X, LO replicas of the D^0X, among others [19,26]. Nowadays, the most accepted hypotheses for the nature of this band are the surface excitonic contribution [44,45] or structural defects-related transitions [19,25,26,46]. Thonke and co-workers [19,24,25] made an extensive investigation of the 3.31 eV emission in ZnO films and pillars and, using space resolved CL, proved that in the case of their samples, this emission only appears in well-defined defect lines. Monochromatic CL images recorded at 3.31 eV allowed identifying basal plane stacking faults as the origin of this emission [19,24,25].

A recent work published by Khranovskyy *et al.* [47] reported the presence of basal plane stacking faults in WZ ZnO nanowires that act like ZB QWs in a type II band alignment. These authors state that a emission observed at 3.329 eV (at 4 K) is a result of an indirect excitation transition from electrons in the CB of the QW, which recombine with holes confined at the interface of the basal plane stacking faults. Similar results were observed for other semiconductors like in GaN [48] or GaAs[49] nanowires with WZ/ZB heterostructures.

Another widely discussed hypothesis is the presence of surface states and excitons bound to surface defects [44,45]. This argument is supported by the fact that this emission is frequently observed in samples with a high surface/volume ratio [41]. Fallert *et al*. [44] reported a study where ZnO nanoparticles with different diameters were analysed by PL. Those samples also exhibited a strong luminescence band around 3.31 eV and the exact position of this band was slightly changed from sample to sample. The authors showed that decreasing the size of the NPs, the intensity of the emission around 3.31 eV increased in comparison with the D^0X emission [44]. Considering that the 3.31eV/D^0X intensities ratio depends on the surface/volume ratio and it is proportional to the inverse of the particle size, they conclude that the luminescence was associated mainly with states present at the particle's surface, suggesting a bound-exciton-like transition model for the recombination [44]. In the works performed by Tainoff *et al.* [26,46], the authors studied different types of samples (single crystals, nanorods and NPs) and concluded that the 3.31 eV emission is composed by an overlap of different processes, namely the LO replicas of the FX and a defect-related transition, since the 3.31 eV appeared in the PL spectra of the nanorods even when the FX emission was not observed.

As aforementioned, a well-accepted origin for the 3.31 eV optical centre was related with the presence of basal plane stacking faults [19,24,25]. However in the case of the samples produced by LAFD, the TEM analysis showed that the as-grown MRs did not reveal any evidence of dislocations or stacking faults, regardless of the emission visible at 3.31 eV. Thus, a different origin should be responsible for this emission.

As in the case of previous works reported by other authors [41], in the present samples excitation density studies revealed a strong dependence of the emission intensity with the excitation power (Figure 6-25b). The relative intensity of the emission related with the D^0X increases in comparison with the 3.31 eV when the excitation density decreases, as shown in the inset of Figure 6-25b. A study of the PL emission as a function of the illumination time was carried out during 3 hours to understand the effect of the local heating caused by the laser beam in the sample (not shown). No changes in the relative intensity between the 3.31 eV and D^0X lines were

observed, evidencing that the behaviour observed is not related with local heating. The presence of defects caused by photon irradiation can be ruled out since the emission intensity is reversible. Similar behaviour was attributed to the saturation of the D^0X recombination with increasing excitation density [41]. It is important to note that no shift was observed in the peak position of the 3.31 eV emission with decreasing excitation density, eliminating the possibility of a DAP recombination. The assumption of having a localized state is compatible with the dependence on the excitation intensity also observed by Schneider *et al.*[41]. As a function of the excitation density, the PL intensity of the 3.31 eV line (Figure 6-25c) can be well fitted to a power law, $I \propto P^m$ (Eq. 4-34). The 3.31 eV line was well fitted by a Lorentzian expression. The analysis reveals a slope just below the unity (0.94 ± 0.02). As already mentioned, following T. Schmidt *et al.* [29], DAPs or free-to-bound carrier recombination models can be estimated based on the m value. Therefore, the present data is consistent with a free-to-bound transition explaining the 3.31 eV emission. Temperature dependence of the NBE is depicted in Figure 6-25d. Increasing the temperature results in the dissociation of the bound excitons and leads to a redshift of the FX and 3.31 eV line emission and its replicas, due to the bandgap shrinkage. This behaviour is similar to the one observed by Schirra *et al*. [19] where the authors associated the 3.31 eV emission with a free-to-bound transition involving the recombination of an electron from the CB with a hole bound to an acceptor state (e-A).

The influence of the surface becomes important when dealing with samples having high surface to volume ratio as is the case of the MRs produced in this work. The presence of surface states due to dangling bonds, point defects or surface adsorbed species must be considered as potential influencers on the material optical properties [50].

In order to understand the nature of the 3.31 eV emission, hydrogen and nitrogen plasma passivation treatments were performed in the ZnO MRs. The spectra recorded before and after the treatments are shown in Figure 6-26. After the first hydrogenation treatment (MR_sample#2) the intensity of the 3.31 eV line decreased regarding to the D^0X line, and the latter became the dominant emission in the NBE region. Since a decrease in the intensity of the line in question was observed, a higher plasma power was used (MR_sample#3) with the purpose of further reduction. In the case of the sample labelled MR_sample#3, the line observed at 3.31 eV was suppressed, as well as its phonon replicas at ~ 3.24 eV and ~ 3.16 eV. Instead, MR_sample #3 clearly evidences the TES lines at ~ 3.32 eV and the phonon replicas of the D^0X transitions ~ 70 meV apart from the main transition at ~ 3.36 eV. The PL spectrum of MR_sample #3 resembles the one obtained for a bulk sample, as can be observed in the Figure 6-26. Therefore, passivation with H_2 plasma leads to a luminescence emission similar to the one obtained for ZnO bulk sample. As H_2 is known to be a fast interstitial diffuser in ZnO (0.2 cm^2s^{-1} [34]), even at low temperatures (100 ^oC) [51], the performed H_2 plasma treatments should promote the incorporation of hydrogen throughout entire volume of the ZnO MRs, leading to an increase in intensity of the H-related D^0X, the I_4 line [7] peaked at ~ 3.362 eV, as identified in Figure 6-26a. It is worth to mention that at the present plasma conditions a temperature around 900 ^oC is expected inside the reactor. Several works reported the enhancement of the NBE emission of ZnO after the treatment with H_2 plasma [52–54]. Therefore, the incorporation of hydrogen as a dopant into the ZnO matrix must be also taken into account to explain the increasing of the D^0X emission intensity after the passivation. All the

incorporated hydrogen by the plasma treatment is expected to be removed after a thermal treatment with temperatures higher than 500 – 600 °C [51]. MR_sample #3 was further submitted to a thermal annealing at 700 °C in air during 5 hours. As evidenced in Figure 6-26a, after this treatment (MR_sample#4) the D^0X emission is reduced and the emission around 3.31 eV became dominant again, despite of a slight shift to lower energies, which could be related with the thermal expansion of the lattice with the annealing treatment. The recovering of the emission is an indication that the H_2 concentration after the annealing was reduced, as identified by the strong decrease of the D^0X line intensity. As previously reported [52], the H_2 plasma treatment leads to a reversible process.

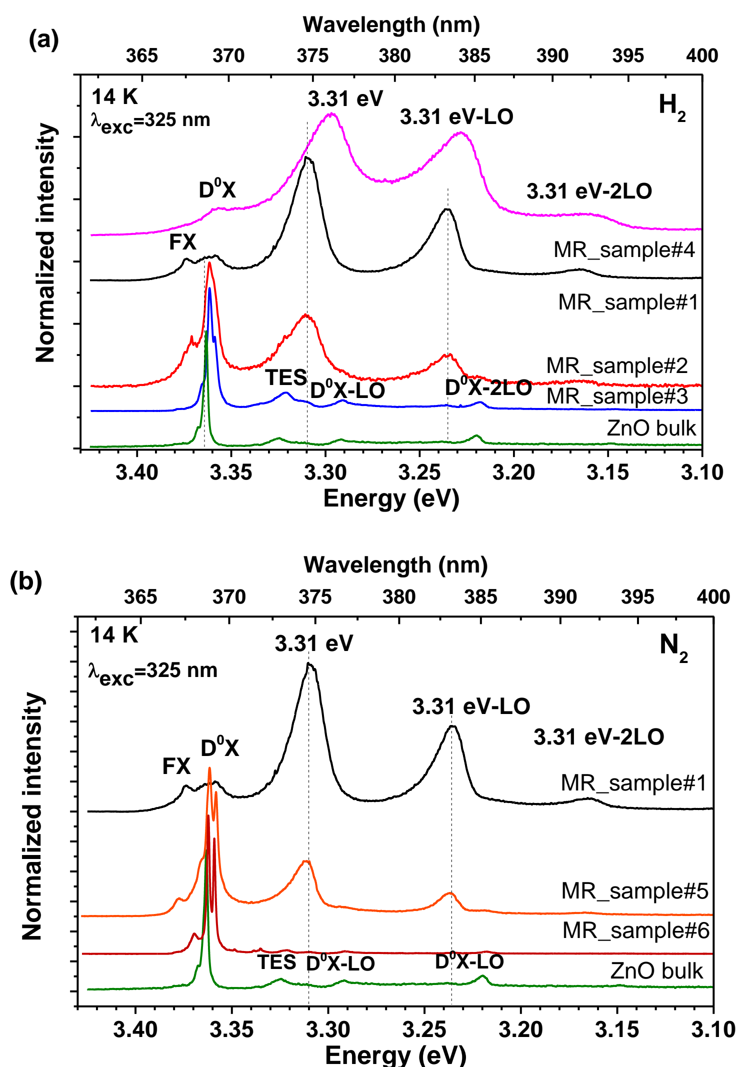

Figure 6-26 – Comparison between the PL emission before and after the treatment with the (a) H_2 and (b) N_2 plasmas.

As nitrogen is a slow diffuser in ZnO [55], surface treatments with N_2 plasma were attempted in the ZnO MRs in order to infer about the presence of surface states and their relationship with the 3.31 eV emission. Børseth *et al*. [55] estimated a diffusivity up to 10^{-15} cm^2s^{-1} based on an estimated maximum diffusion length of 10 nm after 1 h annealing at 1000 °C. As in the case of the hydrogenation, the estimated temperature inside the reactor chamber is higher than 700 °C, so it

is expected that most of the nitrogen remains at the surface of the ZnO MRs. Figure 6-26b depicts the spectra of the N_2 treated samples. A decrease of the relative intensity of the 3.31 eV line regarding the D^0X emission is clearly observed after the first treatment (MR_sample#5). The treatment carried out with higher N_2 plasma power (MR_sample#6) revealed a complete suppression of the 3.31 eV emission. In both samples a high resolution of the split D^0X lines is observed. Since the passivation with nitrogen acts on the surface states, the suppression of the band observed at 3.31 eV after the second plasma treatment (MR_sample#6) suggests that the surface states are in the origin of the mentioned emission.

Figure 6-27 depicts a schematic representation of a proposed model for the energy band diagram of the surface of the ZnO MRs before and after passivation. The presence of surface states due to dangling bonds, point defects or surface adsorbed species at the ZnO surface causes a band bending of the energy bands near the ZnO surface, which leads to the capture of charged carriers near the surface and the generation of a surface charge [56]. The formation of this depletion region will lead to modifications in the recombination processes, which becomes particularly important for samples with a high surface to volume ratio. If these defects are optically active, new emission may arise, dominating over the bulk luminescence. When the surfaces are passivated, eliminating dangling bonds or surface adsorbed species, a strong reduction of these surface states occurs, the bending of the bands can be almost neglected and the bulk's recombination processes dominate.

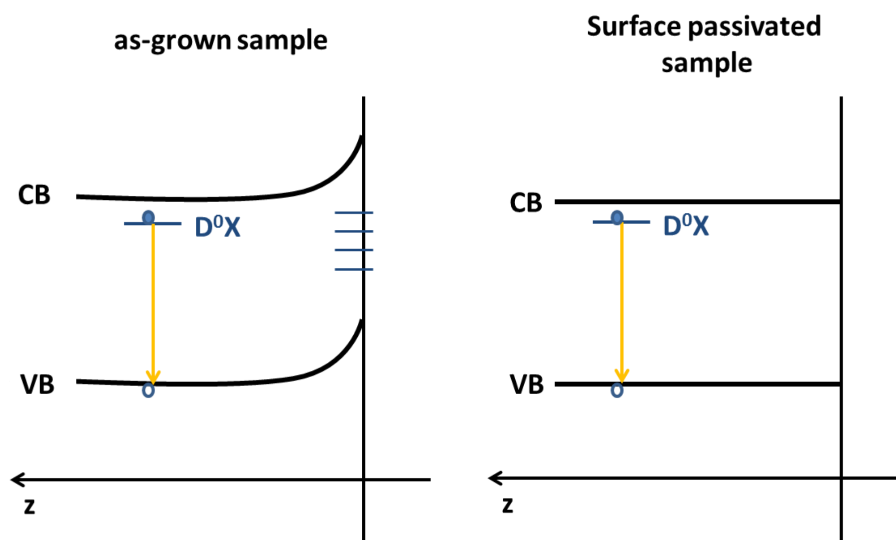

Figure 6-27 – Schematic representation of the proposed energy band diagram of the surface of the ZnO MRs before and after passivation.

Excitation density studies were performed in all the treated samples (Figure 6-28) revealing an accentuated reduction of the 3.31 eV PL intensity with decreasing excitation density as observed for the case of the MR_samples #2 (Figure 6-28a), #5 (Figure 6-28b) and #4 (Figure 6-28c). For the lowest excitation power, the mentioned band is decomposed into two emission lines, one at ~ 3.32 eV due to the TES recombination and another at ~ 3.31 eV. In MR_samples #3 and #6 the stated emission was almost suppressed and consequently no significant changes with the decreasing of the excitation density were observed (not shown). This observed dependence on

the excitation density of the intensity of the dominant PL lines (3.31 eV versus D^0X) indicates that, as for the case of MR_sample #1, a saturation effect of the D^0X recombination occurs, leading to the change in the relative intensity of both lines. Comparing the ratio between the intensities of the D^0X+FX and 3.31 eV line emissions as a function of the excitation density for the plasma treated samples, a ratio decrease with increasing excitation power is observed. In the case of the sample treated with H_2 plasma the decrease was about 56 % while for the sample treated with N_2 a decrease of 52 % was found. These values point to an analogous behaviour for both treatments, which can indicate that the phenomena involved in the passivation are similar and most of the hydrogen is located at the surface of the MRs instead of the bulk. However, this small difference can imply that the N_2 plasma is more efficient in the passivation of the surface defects.

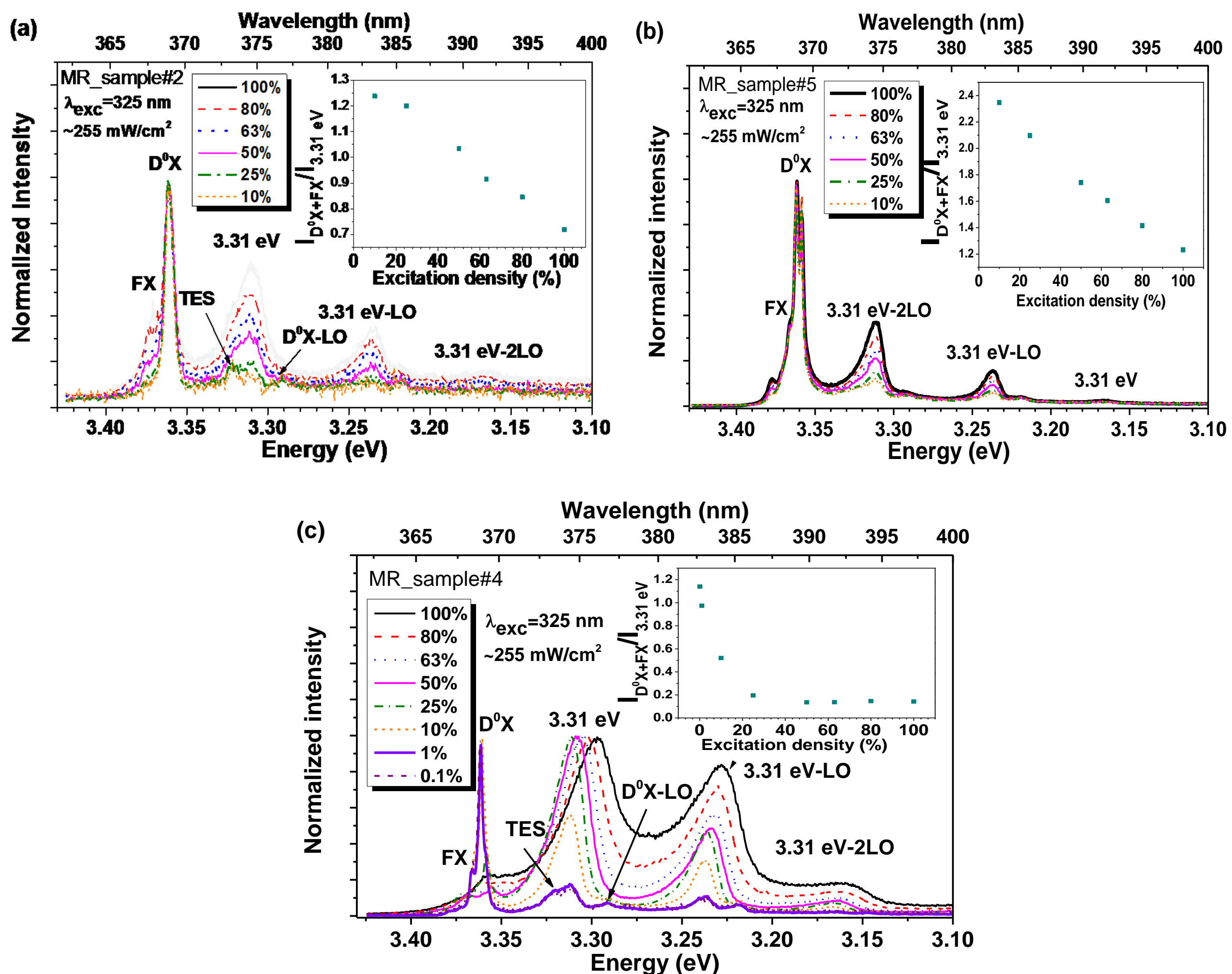

Figure 6-28 – Excitation density dependence of the PL for (a) MR_sample#2, (b) MR_sample#5 and (c) MR_sample#4. The insets correspond to the ratio between the integrated intensity of the D^0X+FX and the 3.31 eV emission lines for each sample.

For MR_sample #4 a red shift of the 3.31 eV line with increasing excitation density is observed. This behaviour can be attributed to possible changes at the surface charge density after the annealing at high temperature (700 °C), due to the presence of different species adsorbed at surface. It is well known that after annealing at this kind of temperatures re-adsorption of species

(like the case of OH-groups) is expected when the samples are exposed to the ambient atmosphere [56]. This fact associated with the number of charge carriers that are being generated under the different excitation powers can conduct to modifications in the band bending. It is likely that a decrease in the band bending energy promotes the observed red shift. It is also convenient to mention that for low excitation powers an inversion of the D^0X and 3.31eV line emissions relative intensities is observed, which did not occurred for the as-grown sample. This fact can be explained by the incorporation of H ions inside the ZnO matrix promoted by both passivation and annealing treatments, leading to an increase of the D^0X emission when compared with the as-grown case.

Despite the unknown nature of the defects that generate the 3.31 eV band in the studied samples, the performed passivation treatments suggest that surface defects must be considered on the band recombination model. The excitation density dependence of the luminescence data clearly evidences that for the highest excitation densities the generated free carriers are predominantly captured by the defects from where the 3.31 eV emission arises, as inferred from the passivation studies. An effective control of the 3.31 eV PL relative intensity can be obtained by controlling the excitation density.

Regarding the green broad band emission, the luminescence is centred at ~ 2.39 eV and exhibits a structured shape with a FWHM close to ~ 0.43 eV. Although no zero phonon lines where found, the shape of the band resembles a vibronic band with an energy separation of each peak around 72 meV, close to a LO-phonon mode of the ZnO crystal [1]. As aforementioned, this structured GL is frequently associated to the presence of Cu impurities, as reported by Dingle and other authors [1,10,12]. According to Garces *et al.* [57], Cu impurities can be responsible for two distinct mechanisms giving rise to GL, depending on the Cu charge state. In their work, two different GL bands were observed: one unstructured band peaked near 2.48 eV (500 nm), arising from the as-grown samples (with Cu^+ present), and another peaked at ~ 2.43 eV (510 nm) with the characteristic vibronic structure reported by Dingle [10], present in thermally annealed samples (with Cu^{2+}). The charge state of the copper ions was assessed by EPR measurements. Thus, the structured GL accounts for a Cu^{2+}-related emission which corresponds to a neutral acceptor (A^0) centre, i.e., a neutral copper acceptor, since a Cu^{2+} ion refers to a copper ion in a $3d^9$ $4s^2$ configuration. The authors claim that when Cu^+ ions ($3d^{10}$ $4s^2$ configuration) are present they are singly ionized acceptor (A^-) centres. This means that a portion of the shallow donors must also be singly ionized (D^+) centres. When these two centres (A^- and D^+) are present, the classic situation to observe DAP recombination occurs, if the sample is pumped with either above bandgap or near bandgap excitation. Therefore, the authors suggest that the unstructured emission peaked at ~ 2.48 eV is due to DAP recombination involving shallow donors and copper acceptors [57]. On the other hand, the recombination model for the structured Cu-related emission is usually attributed to a transition of an acceptor-type bound exciton [$Cu^+(d^9$+e),h] to the ground state ($^2T_2$) of $Cu^{2+}(d^9)$ ion. This state acts as an electron-trapping level located ~ 200 meV below the bottom of the CB [58–60]. To explore the possible presence of copper and its charge state EPR measurements were performed in the LAFD ZnO MRs, however no conclusive results were found. It is important to stress out that even very low impurity/defect concentrations (trace impurities) can be accounted for emissions observed in PL measurements, since this is a

very sensitive technique. In fact, Dahan *et al.* [60] observed this structured GL band in high-quality unintentionally doped ZnO crystals where copper intensities as low as 10 - 250 ppm were found.

Even though the GL in the different ZnO structures appear in the same spectral region, the fact that a structureless band is observed for the NPs at low temperature, while a band with a well-defined structure is identified for the MRs, strongly points to the distinct origin of the defect responsible for the GL, in accordance with what has been reported in the literature (concerning unstructured and structured band). Moreover, the shape of the band is not the same in the different LAFD structures, being wider in the case of the NPs, due to an overlap of different luminescence centres, as pointed out by its spectral deconvolution. In order to investigate the nature of the transitions involved in the GL of the MRs, density excitation studies were performed, as displayed in Figure 6-29. The spectral shape and peak position does not change with decreasing excitation density (Figure 6-29a), excluding the hypothesis of the presence of a DAP related emission. Fitting the PL intensity as a function of the excitation density (Figure 6-29b) in accordance with the power law, $I \propto P^m$, proposed by T. Schmidt *et al.* [29], a value of 0.84 ± 0.03 was obtained for the slope, *m*, indicating a free-to-bound carrier recombination, in agreement with what was expected for the donor-hole recombination suggested by Garces *et al.* [57].

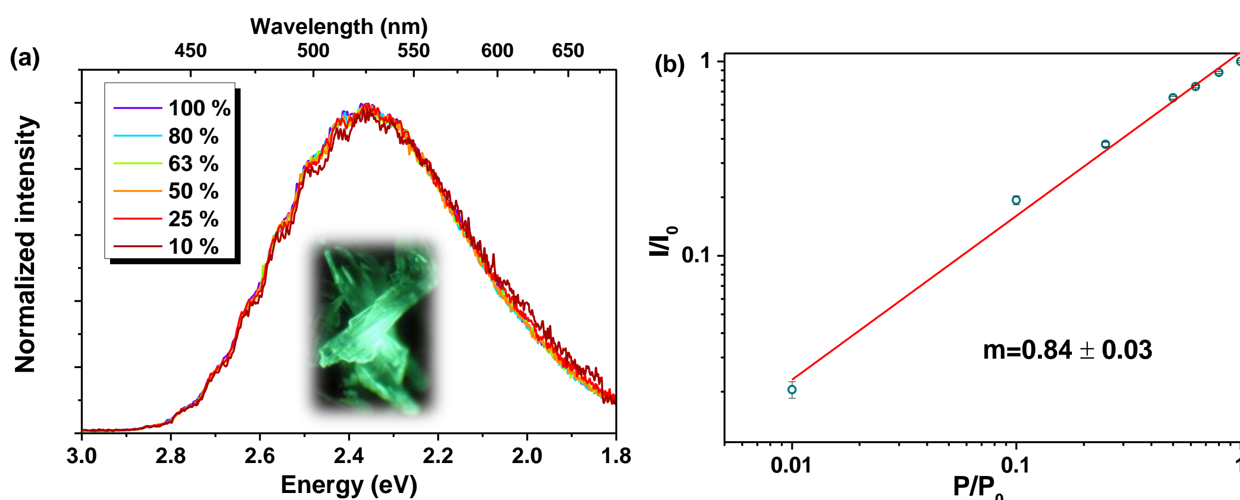

Figure 6-29 – (a) Excitation density dependence of the green emission at 14 K. (b) Log (I/I_0)-log (P/P_0) plot for the same emission. The inset in figure (a) corresponds to the RT visual appearance of the green emission with 325 nm photon excitation.

RT PLE measurements (Figure 6-30) performed on the GL showed that the preferential pathway for the population of this centre is via above bandgap excitation, as in the case of the TPs sample. This band was also analysed by RT TRPL (Figure 6-31), revealing that after only 0.2 ms the band almost completely vanishes, indicating a lifetime in the order of tens of µs. This value is significantly smaller than the one reported by Dingle [10], where a fast exponential decay, with a lifetime close to 440 ns (at 1.6 K), was identified. However, it is important to bear in mind that these values were obtained at different temperatures, thus differences are expected. Comparing this result with the one obtained for the nanostructures grown with 60 W (mostly TPs), it is clearly observed that the broad visible emission of the MRs possess a much shorter lifetime, comparable

with the one obtained for the green component of the TPs' emission. Thus, taking into account both TRPL results for MRs and TPs, the possibility that the green centre has the same nature in the two samples cannot be discarded.

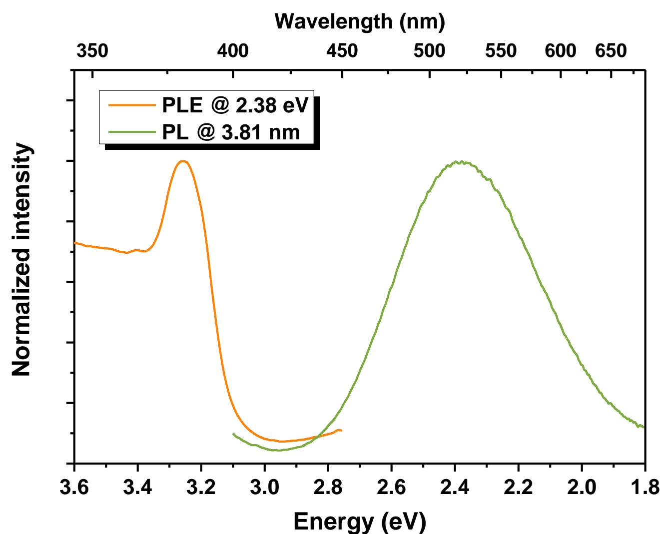

Figure 6-30 – RT PL/PLE of the green emission in the ZnO MRs.

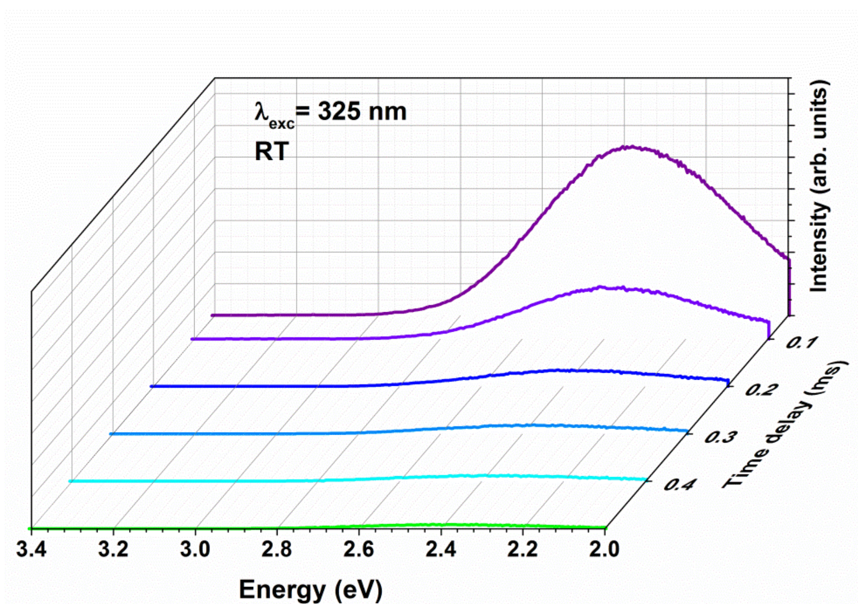

Figure 6-31 – RT TRPL of the green band acquired under 325 nm photon excitation.

It is worth to mention that the plasma treatments performed in the studies of the 3.31 eV does not seem to affect the shape or spectral position of the GL. This may suggest that the recombination responsible for this luminescence is mainly dominated by the bulk and not from the surface.

6.2. ZnO grown in the presence of silver

A great number of attempts to incorporate elements like RE or transition metal ions into the ZnO structures by *in-situ* doping during the LAFD growth were performed. With this purpose, different compounds were mixed with the ZnO powders during the preparation of the rod precursors. However, this task revealed to be very challenging and extremely difficult to accomplish. The most probable explanation is related to the fact that for a material to be grown by the LAFD technique, the melting and ebullition temperatures must be closer. Therefore, this technique can only be applied to a very limited number of compounds. Nevertheless, it was found that it is possible to form complex structures in a single step, as demonstrated for samples grown in the presence of Ag [61].

The ZnO potential for some applications can also be improved by forming complex structures with other materials. For instance, the synergetic combination of ZnO with metallic NPs [62] has been intensively investigated due to the possibility to modulate their properties [63]. The research on the modification of semiconductors with noble metal ions, as is the case of silver or gold, has gained a significant interest in different technological fields like photocatalysis, sensing, or biomedicine [63–65]. Among the different metals, Ag has demonstrated a great potential in different areas such as photocatalysis [62] or antibacterial [66,67] applications, especially when combined with ZnO structures. This semiconductor also demonstrates photacaltalytic and antibacterial activities by itself, so an enhancement on its performance in such applications is expected when combined with silver. One of the most important limitations of the ZnO nanostructures to achieve high photocaltalytic efficiency is the high recombination rate of photoinduced charge carriers. One efficient method to overcome this problem is to deposit noble metals (as silver) on the surface of the semiconductor [66]. The photogenerated electrons are then transferred from the CB to the metal particle while the holes remain in the semiconductor surface, improving the charge separation and thus the photocatalytic efficiency [66]. Furthermore, since Ag is a group 11 (I-b) element, Ag doping has been reported as a possible way to form acceptor energetic states in ZnO, if the Ag ion occupies a substitutional Zn site (Ag_{Zn}), therefore achieving *p*-type conductivity [68–71]. However, Ag is considered to have a low solubility in ZnO at equilibrium conditions, since the Ag ion has a different valence state than Zn and a larger ionic radius, so diffusion of the Ag to the surface of the ZnO is frequently observed [72]. The production of this type of ZnO/metal structures usually involves procedures as calcination, sputter or electrophoretic deposition of metals in the ZnO surfaces [65]. In most of these cases several steps are needed in order to produce the materials. The LAFD method offers the advantage of synthesizing the silver NPs directly on the surface of the ZnO in a single and short step [61]. The addition of silver to the ZnO precursors aimed mainly to the study of the samples' morphology that may have a great influence on possible catalysis applications, and bio and/or toxicity studies. Moreover, the determination of the silver incorporation on the ZnO host as a potential acceptor element was also explored.

Figure 6-32 and Figure 6-33 show the SEM images of the ZnO microcrystals grown in the presence of silver for two different laser powers, 25 W and 35 W, respectively. As in the case of the samples analysed in the previous section, randomly oriented ZnO hexagonal rods are

observed in all cases. Spherical droplets could be seen deposited over the surface of these rods. These particles correspond to metallic aggregates of Ag, as confirmed by EDS map observation on Figure 6-34, as well as the presence of diffraction peaks associated with Ag (Figure 6-35). These droplets tend to accumulate predominantly on the top of the crystals. It was observed that, especially for the samples grown with higher power, increasing the nominal Ag concentration, the metal particles assume a catalyst role promoting re-nucleation and growth. This is particularly evident on the SEM image of the sample grown at 35 W with nominal 2 mol% of silver in Figure 6-33, were the tips of the larger rods are covered with new ZnO crystals. It is clearly seen that the silver distribution is not uniform all over the samples, some regions show silver droplets along all the length of a ZnO rods, while there are rods without any silver on them. This may be due to some inhomogeneity on the silver distribution in the precursor rods as well as to the evaporation properties of the Ag compound (silver nitrate) added to the ZnO precursor. As reported for the samples without silver, increasing the power does not seem to affect significantly the morphology of the rods, however, it seems to promote the re-nucleation of ZnO crystals in the regions where the silver droplets accumulate.

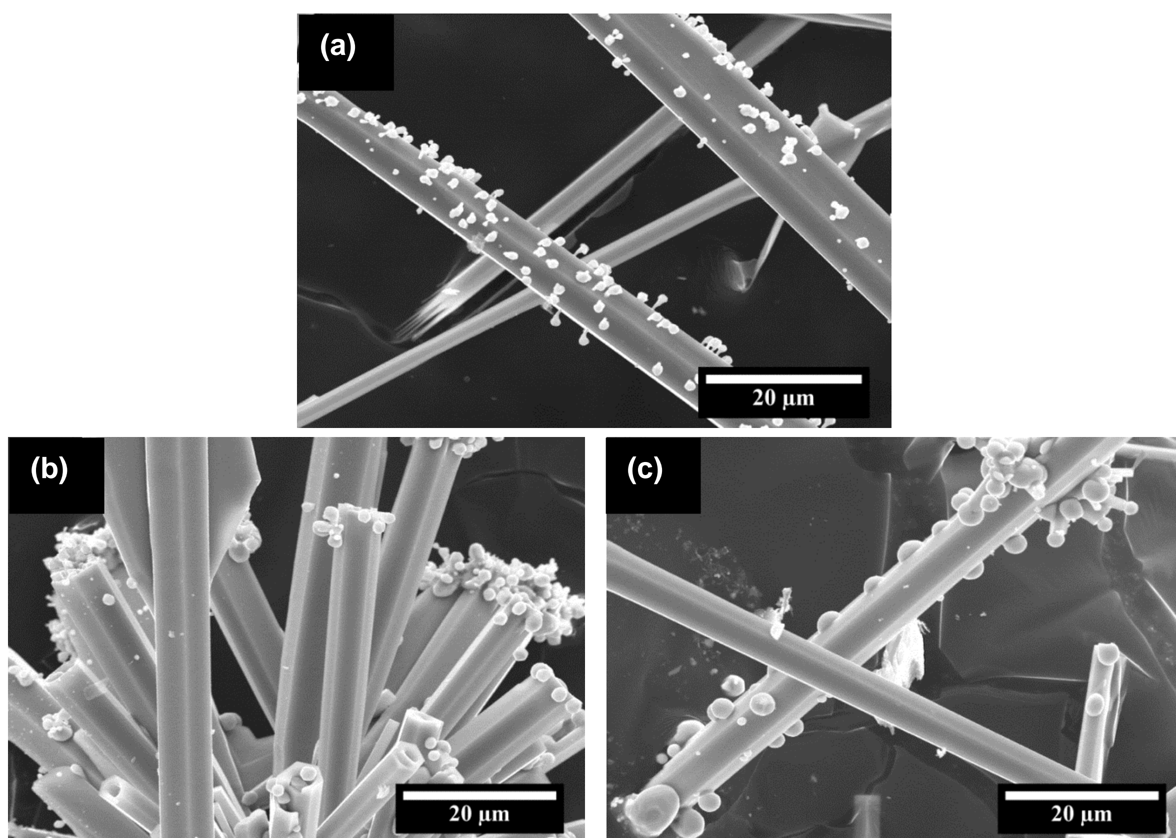

Figure 6-32 – SEM images of the ZnO rods grown using a laser power of 25 W in the presence of (a) 0.8, (b) 1.0 and (c) 2.0 mol% of Ag.

As in the case of the as-grown ZnO structures highlighted in the previous subsection, XRD (Figure 6-35) measurements demonstrate the hexagonal wurtzite crystalline structure for the ZnO rods in the ZnO/Ag system. All the samples lead to a similar X-ray diffraction patterns with narrow diffraction lines. Besides the ZnO crystalline structure, the XRD pattern (Figure 6-35) shows a small contribution of Ag related diffraction maxima. While the peak at $\sim 44.3^{\circ}$ is clearly attributed to

the metallic Ag (200), the peak at ~ 38.1° can be associated either with Ag (111) or Ag_2O (200) [73], suggesting that silver oxide phase can be promoted under the used growth conditions. A more detailed observation of the XRD patterns from the ZnO crystals reveals a shift of the diffraction peaks positions, a decrease of the peaks intensity and an increase of their FWHM (Figure 6-35b). These observations suggest an incorporation of Ag^+ ions into the ZnO lattice sites. In fact, the lattice parameters calculated for undoped (c = 5.210 Å, a = 3.252 Å) and 2.0 mol% Ag doped samples ($c_{2mol\%}$ = 5.181 Å, $a_{2mol\%}$ = 3.237 Å) allows to conclude that the contraction of the crystal lattice comes from the introduction of Ag^+ ions in the ZnO lattice.

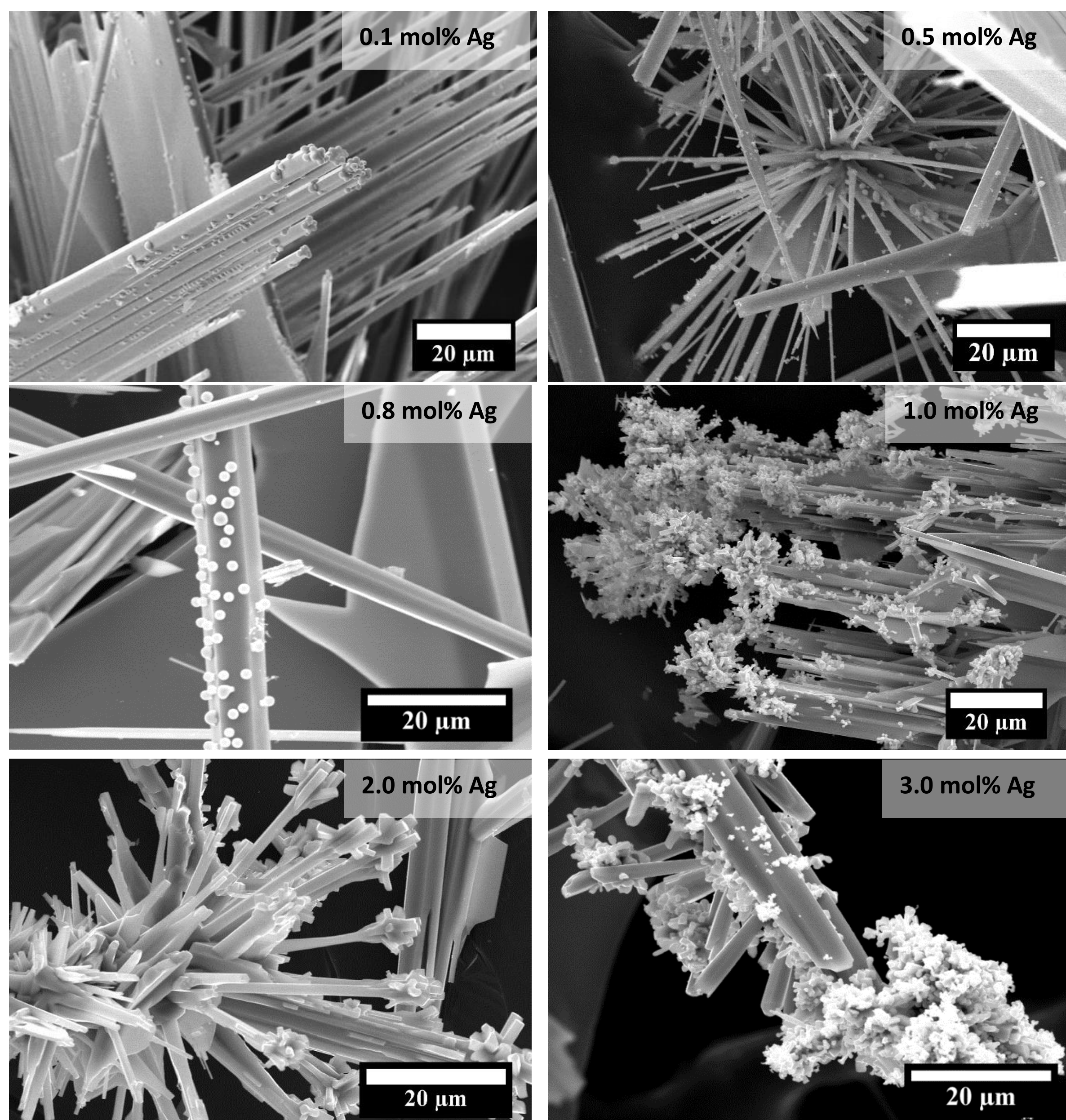

Figure 6-33 – SEM micrographs of the ZnO rods grown in the presence of different amounts of silver. Spherical droplets of metallic silver are observed at the surface of the rods, causing the re-nucleation of the ZnO crystals when a higher silver concentration was used. These samples were grown with 35 W of laser power.

Raman spectra measured with the 532 nm line as excitation source (Figure 6-36) are very similar to the one obtained for the ZnO MRs without silver (also shown in the Figure for comparison) and no changes were introduced by the presence of silver, even in the high wavenumbers region. The differences observed in the relative intensity of the vibrational modes can be attributed to polarization effects due to the different orientations of the ZnO crystals regarding the incidence of the laser wavevector.

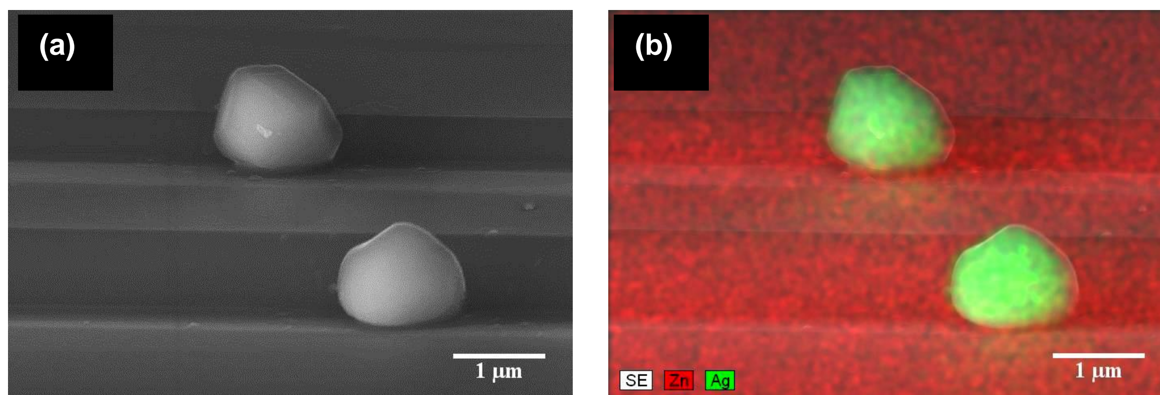

Figure 6-34 – (a) SEM image of Ag particles in the surface of the ZnO MRs. (b) EDS elemental map of the same region, evidencing that the particles are indeed composed by silver.

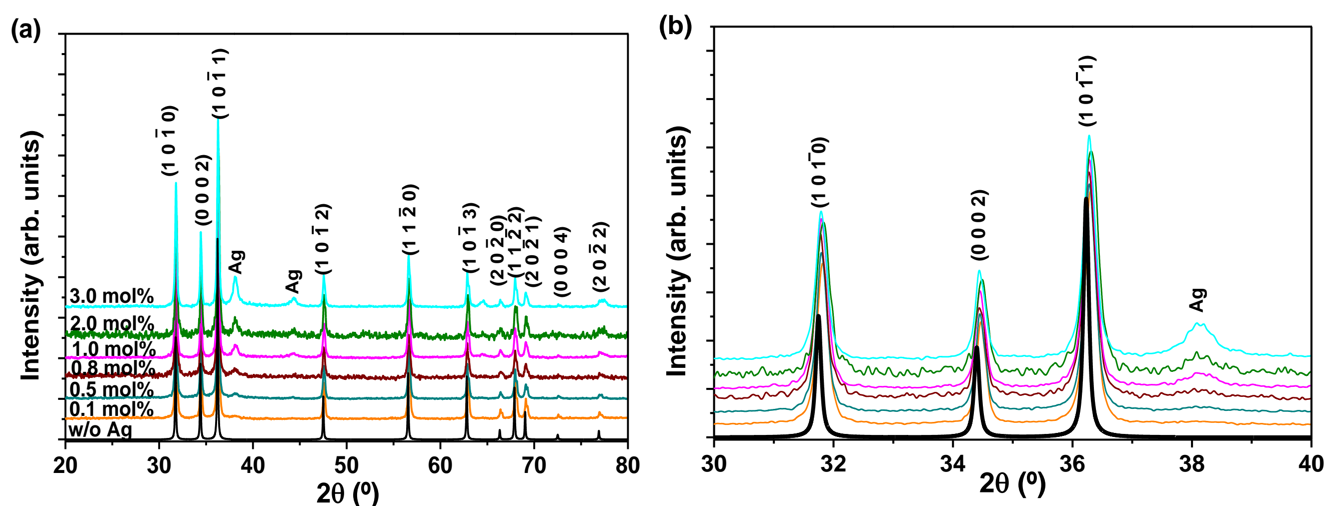

Figure 6-35 – (a) XRD patterns of the ZnO MRs showing the typical WZ diffraction maxima. Additional Ag-related peaks were also identified. (b) Magnification of the XRD patterns in the region 30 - 40°, showing a shift of the diffraction peaks positions and an increase of their full width at half maximum when silver was added. The spectra are vertically shifted for clarity.

The sample grown with 2.0 mol% of Ag was further analysed by TEM. As previously evidenced by the SEM micrographs, some ZnO rods appear without silver droplets at its surface. In some of that "free-particle" ZnO rods, compositional analysis by EDS reveal low (around 2%) Ag signals, which are likely to be related with silver located inside the ZnO lattice, in line with the XRD results. However, measurements errors cannot be completely excluded.

In the case of ZnO rods with Ag particles, two particle's types could be differentiated by their dimensions, as it can be seen in Figure 6-37. The larger particles, with dimensions around 500 nm,

can be found mainly in the larger rods. It seems that they could be the origin of the promotion of the lateral ZnO growth, as showed before from the SEM results. The secondary nucleation of the ZnO rods on the Ag particles is particularly evident in Figure 6-37b where an Ag particle appears on the top of a small growing rod. These particles were analysed by EDS (far from the ZnO rods) and showed Ag and O signals with a stoichiometry close to the one of Ag_2O phase. Along the re-nucleated rod the particle has left a footprint of silver where the percentage of Ag decreases from the top of the rod (were the Ag_2O particle is placed) to the bottom. Besides these big particles, small Ag particles appear attached to the rod surface with sizes ranging between 15 - 25 nm (Figure 6-37c and d). Though due to the proximity of the ZnO matrix it is difficult to obtain reliable compositional analysis of these particles, the atomic percentage of Ag never overcomes the 60% of content. Nevertheless, the interplanar distances measured in FFT corresponding to the particle did not correspond to ZnO or silver oxide phases, so further analyses are required to ascertain about its nature.

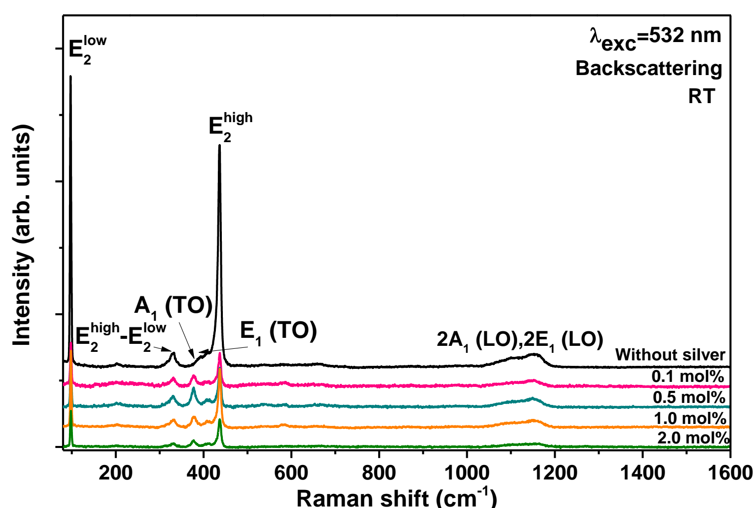

Figure 6-36 – Raman spectra of the ZnO rods acquired with 532 nm excitation showing their WZ structure. The spectra are vertically shifted for clarity.

Additional compositional measurements were accomplished by particle induced X-ray emission (PIXE) maps as shown in Figure 6-38. PIXE analysis corroborate the SEM and TEM results, showing that also at a macroscopic scale the Ag is not homogeneously distributed in the ZnO rods, revealing some points with pure ZnO (point 1) and others with a higher content of silver than the nominal one (point 3 with ~ 16 mol% Ag). Some rods with hollow core were also detected (point 2). The average Ag content in the maps scales with the nominal values added to the precursor rods. In the case of the samples with 0.5, 1.0 and 2.0 mol% Ag nominal values average amounts of 0.7, 1.9 and 2.7 mol% Ag were measured.

Regarding the low temperature PL spectra of the ZnO/Ag structures (Figure 6-39), no additional lines were observed when compared with the as-grown MRs. Despite the fact that EDS and XRD measurements suggest that a fraction of the silver is incorporated in the ZnO rods no new luminescence lines or bands were observed, suggesting that with the used conditions Ag does not create optically active defects in the UV-visible range. The only visible difference is related with the relative intensity between the NBE emission and the broad GL, between the

samples grown with and without silver. The latter is seen to have a higher intensity of the NBE emission when compared to the visible one. However, no trend was identified among the samples with silver.

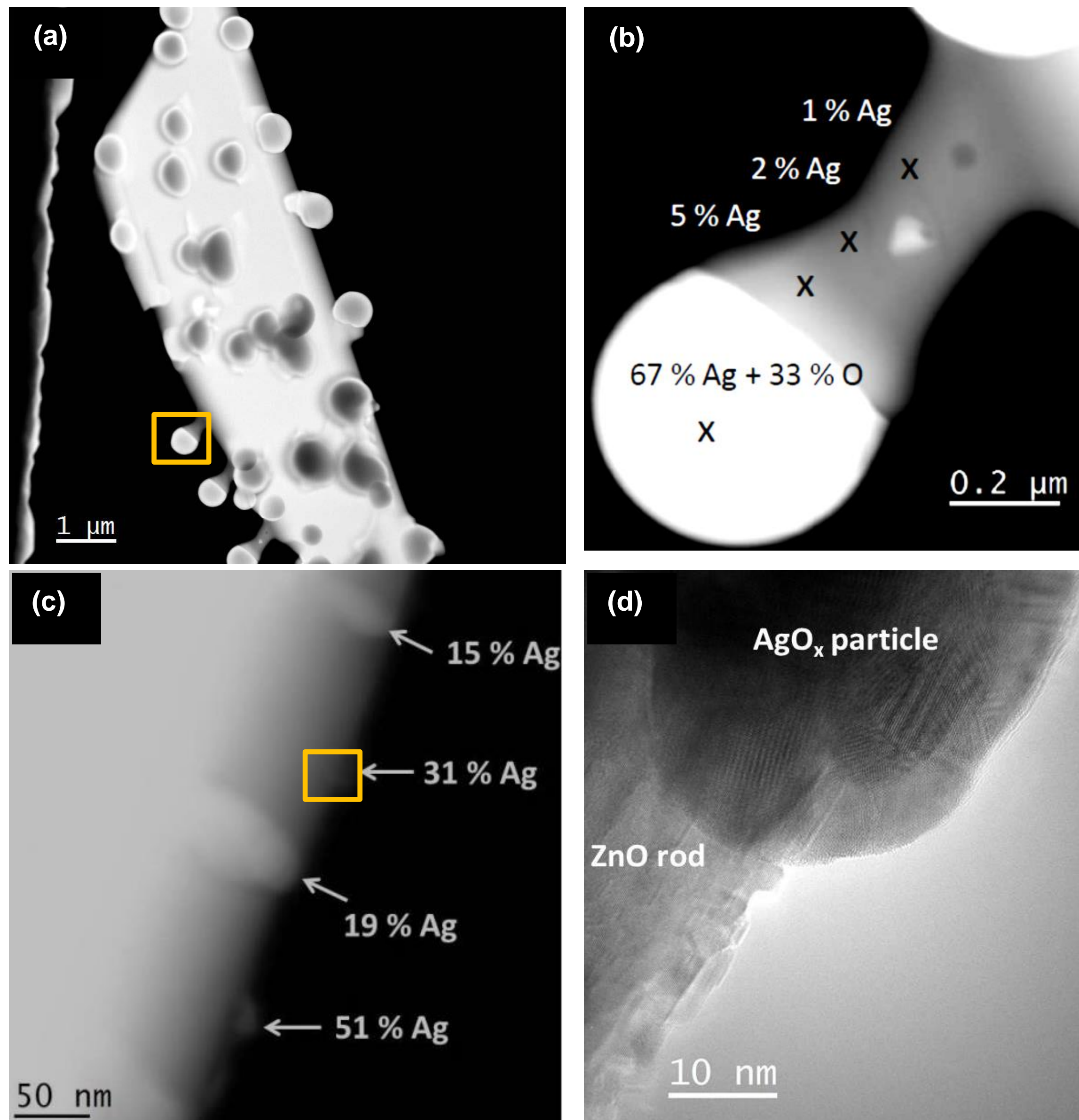

Figure 6-37 – (a) HAADF-STEM image showing silver particles and re-nucleated nanorods covering the surface of a ZnO MR. (b) Higher magnification image of the squared area in (a) highlighting the formation of new nanorods from the MR side walls. The compositional analysis carried out by EDS spectroscopy confirmed that the large particles present at the nanorod tip were made up of Ag_2O. (c) HAADF-STEM image showing smallest particles containing different amounts of Ag deposited on the surface of a ZnO MR. (d) HRTEM image showing the side wall of the ZnO MR of the squared area in (c).

Thin films of ZnO intentionally implanted with Ag (fluences ranging from 10^{13} and 10^{15} ions.cm^{-2}) and thermally annealed were also analysed (not shown here) in order to compare their PL signal with the samples grown with LAFD. Also in the former case no other transitions

besides the FX, D^0X, 3.31 eV and green band were found to occur in the UV-visible spectral region, as observed in the LAFD grown samples.

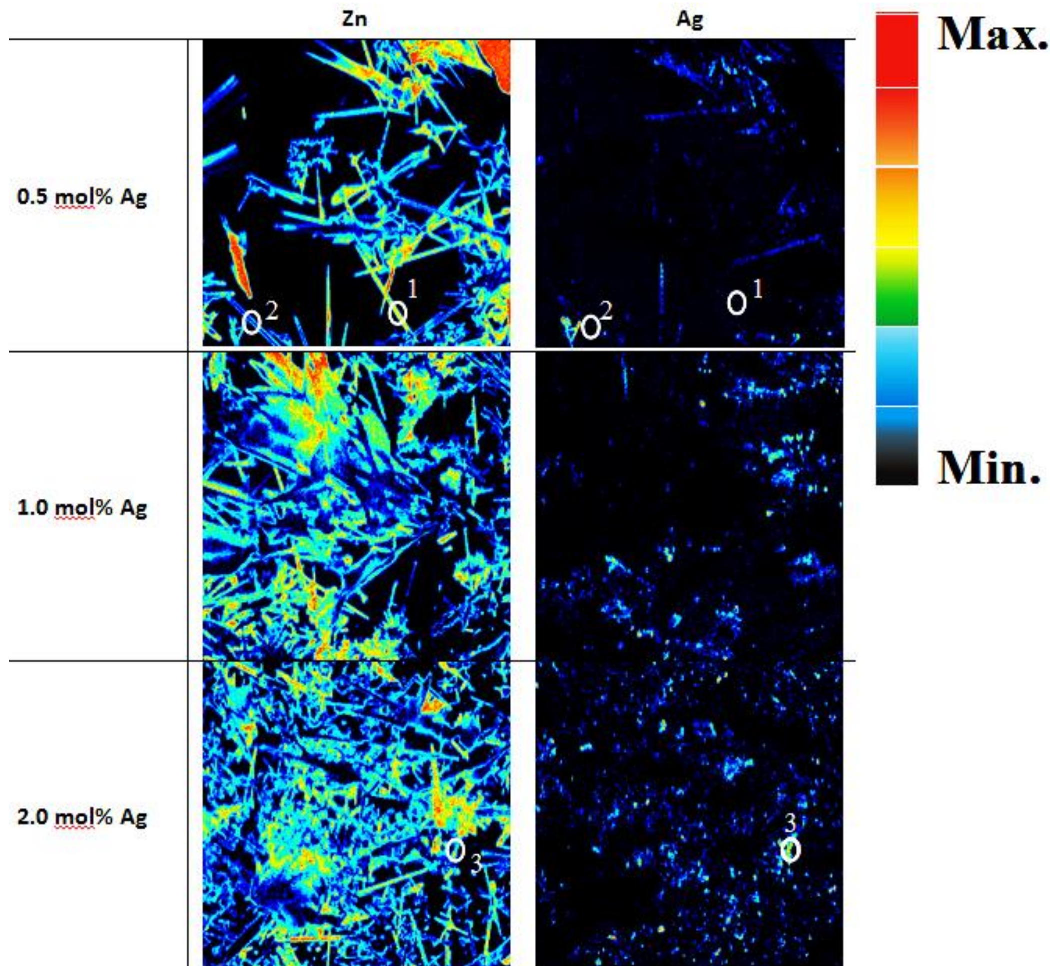

Figure 6-38 – PIXE analysis of the samples grown with 0.5, 1.0 and 2.0 mol% Ag acquired within a 1320 × 1320 μm² area and using a ~ 3 - 4 μm diameter beam spot. Point 1 corresponds to a pure ZnO rod, point 2 to a hollow rod and point 3 to a rod with higher Ag concentration.

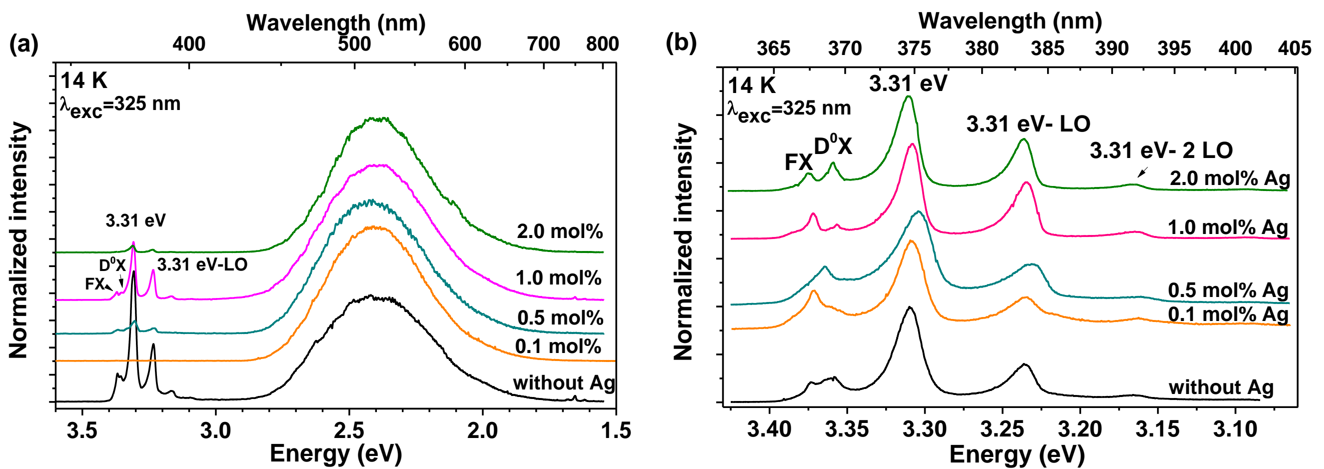

Figure 6-39 – Low temperature PL spectra of ZnO crystals grown by LAFD with different amounts of silver measured with above bandgap excitation (He–Cd, 325 nm). (a) Spectra acquired in UV-visible region and (b) NBE emission of the different samples.

6.3. ZnO/CNTs composites

CNTs are promising materials for nanoscale devices due to their hollow geometry, structural integrity [74], high chemical stability, high tensile strength, and unique electrical properties [75]. CNTs contain only conjugated carbon atoms and therefore they are chemically inert, and this is reflected in their properties such as insolubility in all solvents and low chemical reactivity [76]. This chemical inertness supports its relatively high oxidation stability [74]. The inert nature of CNTs limits the available identification and characterization tools, and hinders their manipulation and application. It has been demonstrated that CNTs can interact with different classes of compounds [77], therefore chemical functionalization of CNTs is a useful tool for addressing these problems, and functionalized CNTs have found wide range of technological applications at nanoscale, including composite materials, sensors, and biomaterials [76]. Functionalization of CNTs remains one of the most studied areas in the CNTs research field [74]. The formation of supramolecular complexes allows a better processing of CNTs towards the fabrication of ground-breaking nanodevices [77]. As such, CNTs are auspicious materials for the development of functional hybrid materials and nanocomposites [78]. CNTs can preserve their morphology and structure even when mixed with a high amount of other nanostructures, due to their great mechanical properties. In this sense, different semiconductor nanostructures have been used to produce CNTs composites by several methods [79].

In the last few years, ZnO nanostructures have received a lot of attention due to their ability to tune the optical properties by hybridizing them with different materials [80]. The assembly of isotropic nanoparticles on the top of 1D architectures represents an important step in the direction of the integration of NPs into nanodevices [81]. At nanoscale, hybridization of ZnO with other materials alters the properties of both components which may give rise to functional materials with advantageous properties [80]. Among these hybrid structures, an interesting class of CNTs derivatives results from depositing semiconducting NPs/nanoclusters on the CNTs surface [82]. Thus, an assembly of ZnO NPs on the surface of CNTs may exhibit physical properties which are different from CNTs and ZnO alone [83].

Gupta *et al*. [80] reported that ZnO/multi-walled CNTs (MWCNTs) have higher luminescence characteristics than other carbon nanovariants, such as graphite or carbon wool. According with these authors [80] one possible reason that explains the strong luminescence of this hybrid system is the higher interfacial area provided by MWCNTs to ZnO, which leads to a higher exposure of the ZnO surface. Also Zhang *et al.* [84] affirmed that the growth of ZnO nanowires on vertically aligned MWCNTs improves the active surface area, which enhances the effective absorption of photons. In one of the earliest works on ZnO/CNT hybrids, MWCNTs were heat-treated with zinc at various temperatures leading to ZnO growth on their surface with several morphologies (ultrathin films, quantum dots, nanowires, nanorods) without the presence of a metal catalyst [85]. ZnO/CNT hybrid structures are also achievable by a two-step growth by thermal CVD [86]. Vapour phase transport is also on the basis of the growth of ZnO nanowires on regular pyramid-like CNT micropatterns [87], or ZnO multipods [88], leading to field emission enhancement factor when compared to pristine CNTs. A thermal evaporation method involving the carbothermal reduction of ZnO powders and subsequent reoxidation on a MWCNT template

produced various ZnO nanostructures [89]. Plasma assisted sputtering can be also used to deposit a Zn film on a MWCNT template [81]. A different dry via to synthesize ZnO/CNT hybrids is co-sintering of MWCNTs and ZnO powder [80]. ZnO/CNT hybrids were alternatively obtained by wet processes [90–92] but these engage with many chemicals which may lead to contamination problems.

The various strategies for CNT-inorganic hybrids can be divided as *ex-situ* and *in-situ* techniques. The first approach begins with the production of the inorganic component in the desired dimensions and morphology; this component is then modified and attached to the surface of the CNTs via covalent, noncovalent or electrostatic interactions. The *in situ* methods carry out the synthesis of the inorganic components in the presence of the CNTs, onto which the inorganic material grows as particles, nanowires or thin films [74]. The LAFD method developed during this thesis can be included in the *in-situ* category.

6.3.1. Vertically aligned CNTs decorated with ZnO

In this part of the work it is reported the morphological, structural, optical and electrical characterization of ZnO nano/microstructures grown on an array of vertically aligned 1-D CNTs (VACNTs) by the LAFD method. The high optical quality of the as-produced crystals is evidenced by the low temperature PL and its dependence with temperature. ZnO nano/microstructures were also grown simultaneously (in the same run of the growth) on silicon substrates in order to compare the PL emission of the samples with and without a VACNT substrate grown in exactly the same conditions. Electrical measurements indicate that the system ZnO/VACNTs exhibits an I-V characteristic curve with a rectifying behaviour.

The strategy of ZnO/CNTs synthesis supported by a high yield ZnO deposition LAFD technique constitutes the main novelty of this approach. This method possesses crucial advantages compared to other dry techniques. It offers very high yield at atmospheric pressure (at moderate laser powers), thus preserving the CNTs structure and alignment, avoiding the collapse of the VACNT structures. Also, it is catalyst-free, easily scalable, allowing the ZnO synthesis in a single step.

Figure 6-40 shows representative SEM micrographs of distinct morphological regions of the ZnO/VACNTs composite material. The pristine VACNTs array before deposition is shown in Figure 6-40a. A general overview of the composite material after deposition (Figure 6-40b) shows that the VACNTs array is coated by a ZnO layer. This coating comprises two layers: a thin layer of ZnO NPs directly attached to the CNTs, on the top of which a thick powdery ZnO layer is deposited. These two layers can be observed simultaneously in Figure 6-40b where the peeled-off left region puts in evidence the bottom thin layer, while in the right region the total coating is preserved. This thin NPs layer is better seen in Figure 6-40c, where a lower laser power (20 W) was used to grow the ZnO, resulting in the deposition of only NPs. Figure 6-40d correspond to a region where a hole in the VACNTs array was present, enabling the introduction of the NPs inside the CNTs forest. In this case, the NPs are seen to attach through all the length of the tubes. However, in most of the cases, the high density of the CNTs array (Figure 6-40a and Figure 6-41a) hinders the

ZnO particles penetration into the forest of CNTs. However, it is expected that the accessibility of the ZnO to the forest inner regions could be tailored using different approaches, namely i) by controlling the VACNTs nucleation density by laser patterning of the alumina diffusion barrier layer or changing the catalyst cluster size or ii) by *in-situ* “combing” of the VACNTs template during growth. These approaches were not yet tried due to the lack of necessary equipment.

The ZnO nanoparticles (with sizes of ~ 100 nm) are in direct contact with the VACNTs (Figure 6-41b) leading to a relatively dense first coating. TPs with a micrometer size are found on the top layer. These loose crystals constitute the top powdery layer and detached very easy from the sample (as also seen for the silicon substrate), in opposition to the NPs layer that seems to be very well attached to the CNTs. The same morphologies were found when ZnO is deposited directly on Si reference substrates, as previously mentioned.

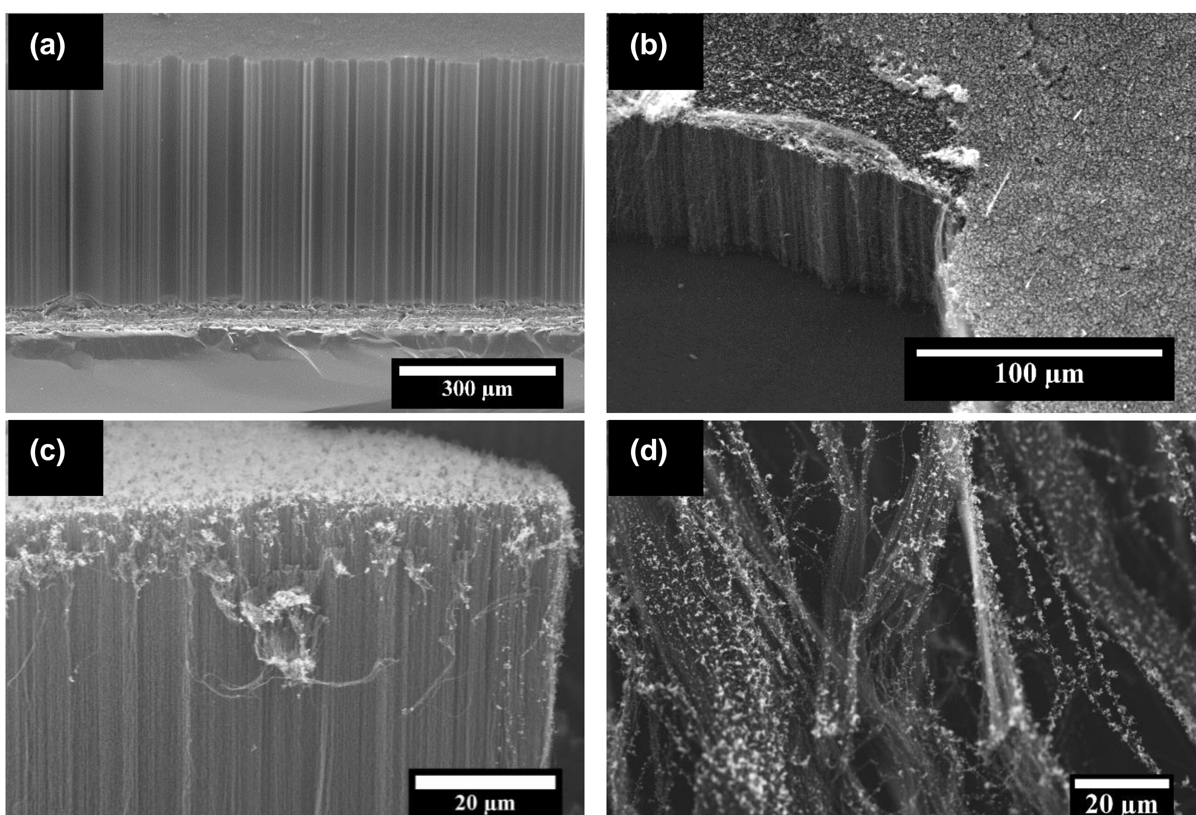

Figure 6-40 – SEM micrographs of: (a) a cross-section of a VACNTs array, (b) an overview and (c) a cross-section of a ZnO/VACNTs sample prepared by LAFD, showing that the nanoparticles are only deposited on the top of the VACNTs array. (d) ZnO NPs attached through all the length of the CNTs in a region where a hole in the VACNT array was present.

The assessment of the structural quality of these structures was achieved by XRD and Raman spectroscopy. Figure 6-42a shows typical X-ray diffraction patterns of the first ZnO nanocystalline layer deposited on CNTs and on silicon substrates. Both samples have similar XRD spectra with narrow FWHM values, indicating the high crystallinity of the coating with a ZnO-WZ structure. Raman spectra of the analysed samples are shown in Figure 6-42b. The ZnO A_1(LO) vibrational mode is observed at 562 cm^{-1}, with overtones at 1132 and 1712 cm^{-1}. Although the first mode should appear at 574 cm^{-1}, local heating by the laser radiation due to high absorption is accounted for the shift to lower wavenumbers [93]. Two extra vibrational bands appear in the hybrid

ZnO/VACNTs samples located at 1403 and 1580 cm^{-1}, the D and G bands typical of CNTs, respectively. The dispersive D band is disorder induced, usually centred at ~ 1350 cm^{-1} (with visible excitation) and shifting to higher wavenumbers with increasing excitation energy [94]. The G band corresponds to the E_{2g} vibration mode, analogous to the one found in graphite [95]. The peak observed at 320 cm^{-1} corresponds to an artefact of the system. The signal to noise ratio of the ZnO Raman modes was slightly enhanced by the presence of CNTs.

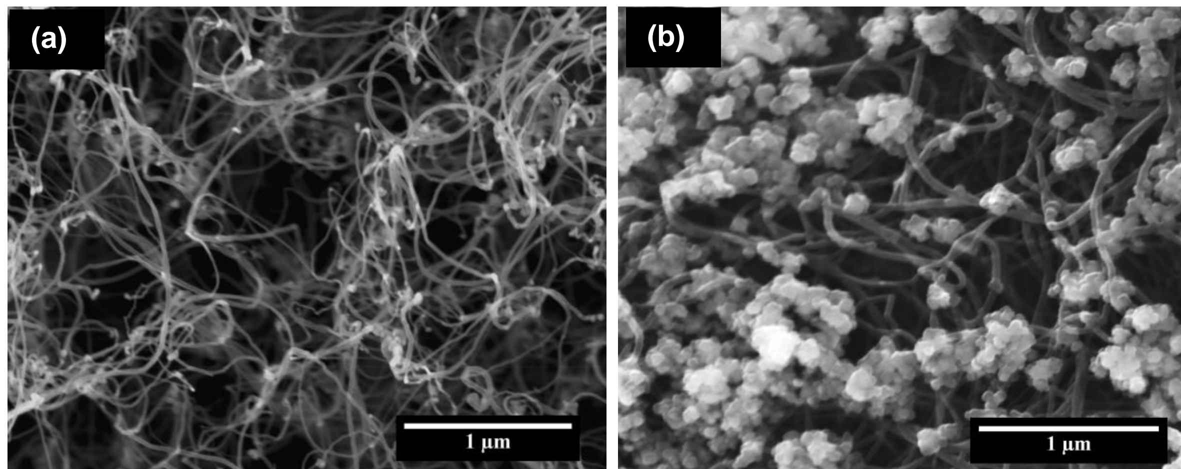

Figure 6-41 – SEM images of the top of (a) CNT array and (b) nanoparticles coating carbon nanotubes.

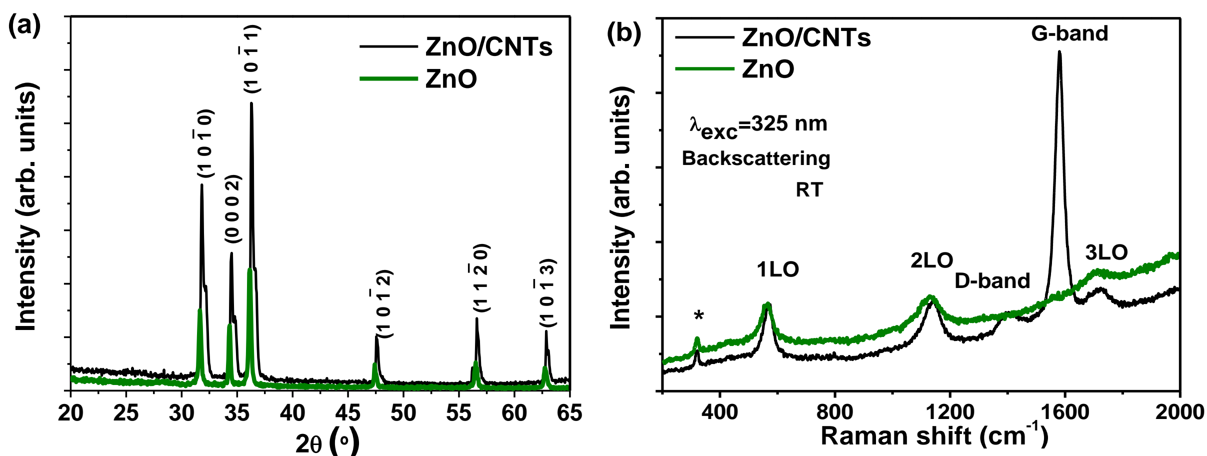

Figure 6-42 – (a) Typical XRD patterns of the ZnO nano/microstructures and (b) RT Raman spectra obtained in backscattering configuration with the 325 nm He-Cd laser line.

Figure 6-43a shows the room temperature PL spectra of the ZnO nanostructures and ZnO/VACNTs composites processed in the same run of the growth and thus grown with exactly the same conditions. In both cases, and as similarly observed for the ZnO TPs/NPs, the emission is dominated by the NBE recombination although deep level luminescence is also observed. The spectra, measured under the same conditions, indicate that an enhancement of the PL intensity occurs for the ZnO/VACNTs samples when compared with the one detected for the ZnO system. In fact, despite the fact that the intensity ratio of the UV to visible band keeps nearly constant in both samples, an enhancement of the overall luminescence was detected when the ZnO coats the

VACNTs. An increase of the overall intensity could be explained if the optical centres concentration from where the luminescence occurs is higher and for a higher exposure of the ZnO material to the laser incidence due to the higher surface area provided by the VACNT array. The data are in line with the one reported by Zhang *et al.* [84] suggesting that for the samples with CNTs an enhancement of the intrinsic carriers is promoted with above bandgap excitation photon energy, leading to a higher intensity of both free exciton recombination and green band.

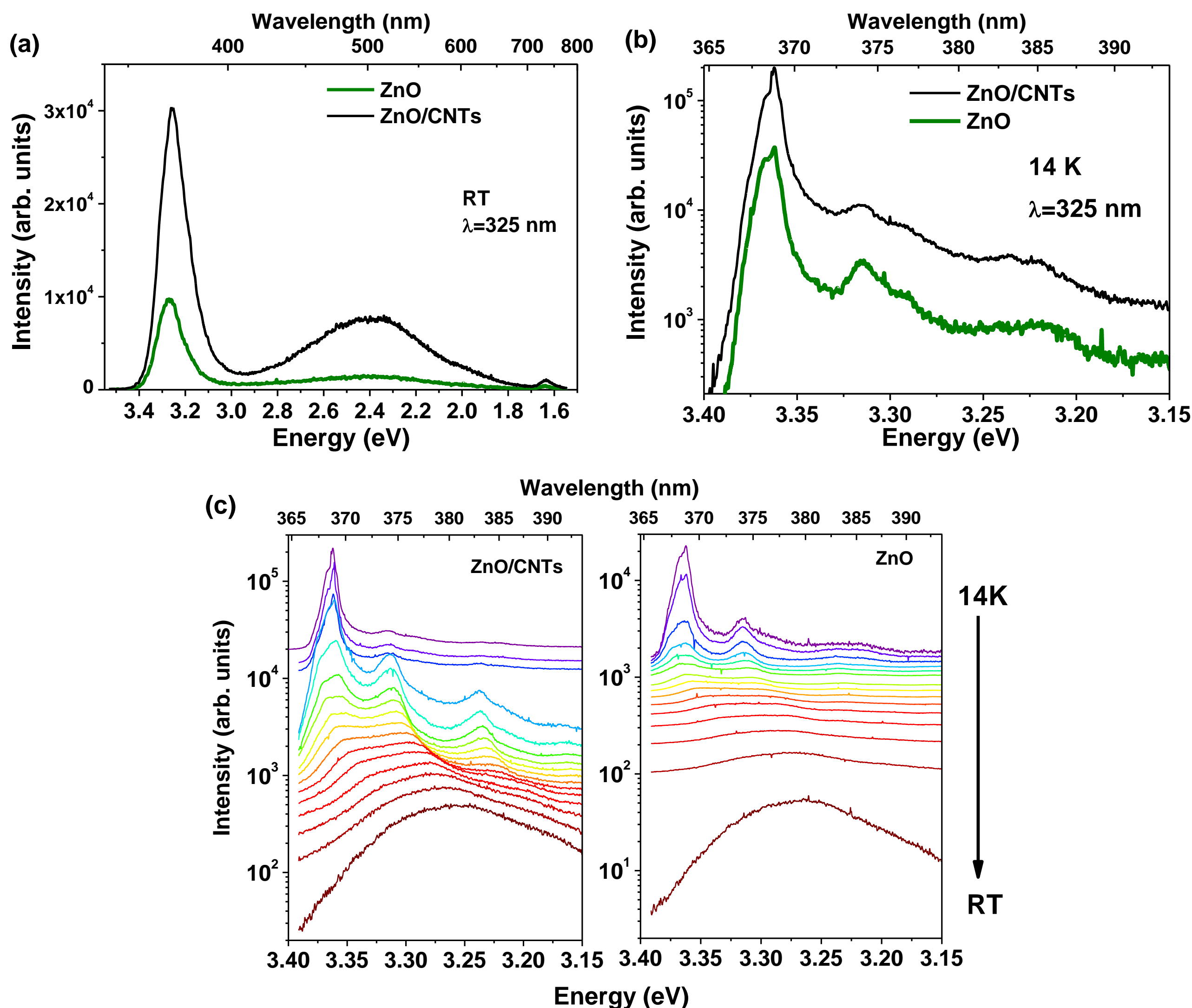

Figure 6-43 – (a) RT and (b) low temperature PL spectra of the ZnO nano/microstructures and the ZnO/VACNTs hybrids. Comparison between two samples grown at the same time with the same growth parameters, one deposited on an array of MWCNTs and the other deposited on a silicon substrate. (c) Dependence with temperature of the ZnO/MWCNTs and ZnO samples. The spectra are vertically shifted for clarity and are represented in a semi-log scale.

As previously mentioned, the low temperature PL of the ZnO nanostructures is usually used as a reference to determine the samples optical quality. Figure 6-43b shows the high resolved NBE spectra for the ZnO/VACNTs and ZnO systems at low temperature, as well as its temperature dependence (Figure 6-43c). At low temperatures the ultraviolet emission is peaked at ~ 3.36 eV and, as mentioned before, is due to the overlap of several emitting D^0X (I_i lines) [7,13]. The

observation of the structure in this spectral region corroborates the high optical quality of the ZnO nano/microstructures. On the low energy side of the D^0X transitions the 3.31 eV line [19,25,45] as well as their LO phonon replicas were also detected. The temperature behaviour is analogous to the one reported for these ZnO nanostructures: increasing the temperature promotes the dissociation of the bound excitons and at RT the emission is dominated by a transition peaked at ~ 3.28 eV, due to an overlap of the FX recombination and the 3.31 eV line. In contrast with recent published data [80,96,97], in the LAFD produced ZnO/CNTs systems the intensity of the NBE is always higher than the deep level emission, proving the samples superior optical quality.

Electrical measurements were performed at the centre of the samples in air and at RT by a two-wire homemade probe apparatus. For each sample the ground wire was fixed to the silicon substrate with silver glue ($\rho < 0.001\ \Omega$.cm) whereas the bias electrode was mechanically attached to a tungsten (W) wire (250 μm thick). Afterwards, a XYZ positioning stage was used to place the W wire in contact with the samples' top surface. Plots of the current versus voltage (I-V) were obtained for all samples using a computer-controlled 16-bit-high speed acquisition board (National Instruments DAQPad-6015) and adapted electronics. The applied voltage was varied in steps of 0.5 V from -10 V to 10 V with 1 s time interval. To prevent current overflow during data acquisition a 4.7 kΩ resistor was placed in series. The measured I-V characteristic curves of VACNTs, ZnO and ZnO/VACNTs samples can be seen in Figure 6-44. The VACNTs sample is highly conductive ($\sigma \sim 2.9\times10^2$ S.m^{-1}) and the linearity of the *I-V* curve demonstrates an Ohmic behaviour. Measurements were made on a small range of voltages due to high conductivity of the VACNTs. Higher voltages lead to currents well above the limits of the detection system. In the case of the ZnO sample, the characteristic curve exhibits a strong nonlinear behaviour, suggesting a turn-on voltage of ~ 1 V. This diode-like conduction mode was previously observed on ZnO nanorod arrays [98,99]. The current *I* of a Schottky barrier diode is described by

$$I = I_s\left(e^{\frac{qV}{nk_BT}} - 1\right) \quad \textbf{Eq. 6-1}$$

where I_s is the saturation current, V is the voltage across the sample, k_B is the Boltzmann constant, T is the operating temperature (in K) and n is the ideality factor, close to unity for dominant thermoionic emission of conventional Schottky diodes [99]. The best fit of the experimental data using this equation (Eq. 6-1) was obtained for $n \sim 60$, which is a large deviation from the ideal case. Deviations of this order were reported previously in aligned ZnO nanorods [98] and in Schottky diodes made from GaN nanowires [100]. A large n could be related to an insulating interfacial layer between the W metal electrode and the semiconductor surface [98]. The *I-V* characteristic curve for the ZnO/VACNTs sample reveals a rectifying behaviour. The sample shows a turn-on voltage close to 0.5 V for the forward bias and a reverse bias breakdown voltage of -1 V.

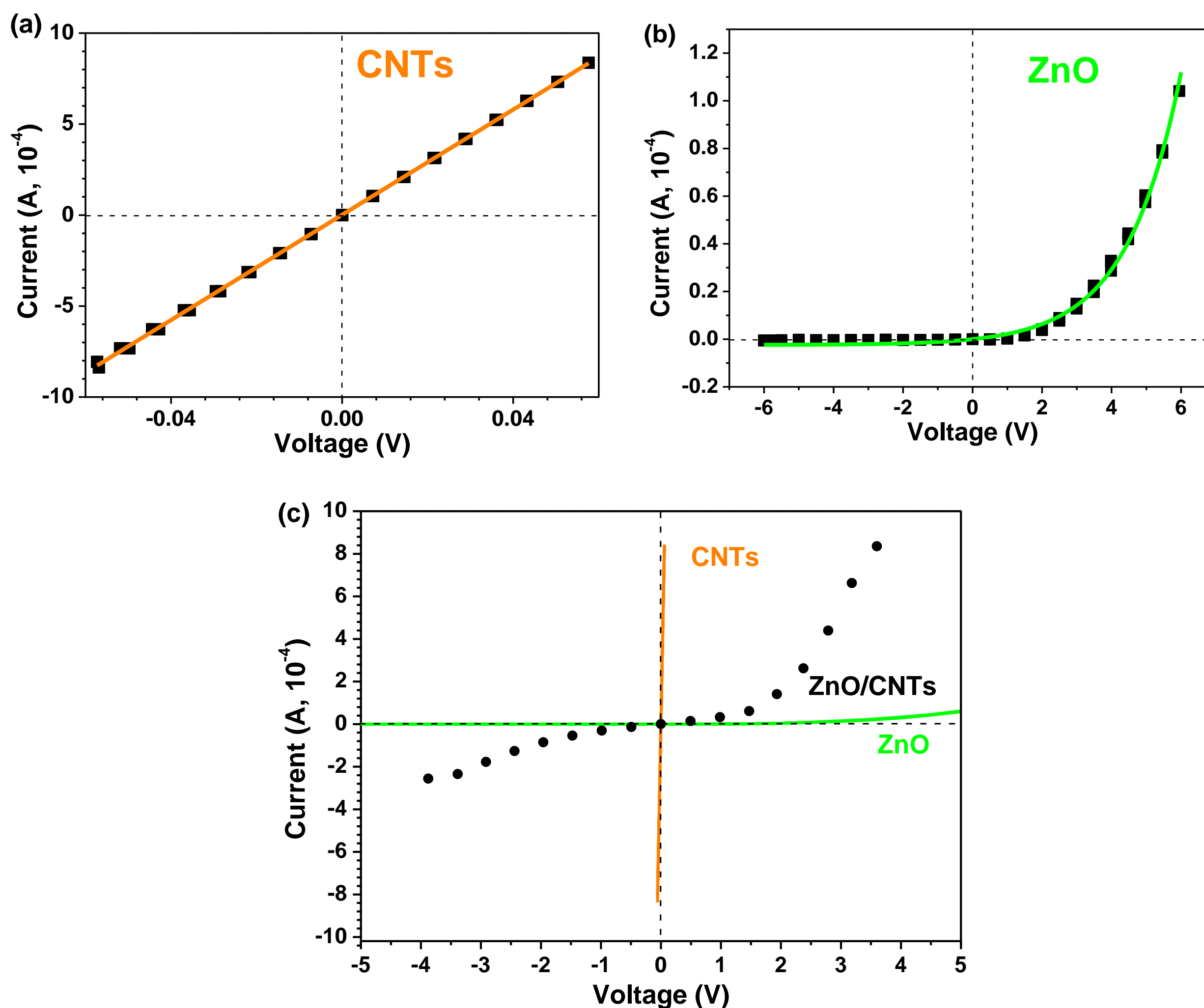

Figure 6-44 – Current–voltage characteristics for (a) CNT, (b) ZnO and (c) a comparison of the CNT, ZnO and ZnO/CNT samples measured at RT.

6.3.2. ZnO/CNTs buckypapers

A CNTs buckypaper is a self-supported membrane with entangled CNTs forming a flexible structure with chemical-physical stability and similar properties to those seen in nanotubes alone [101], offering the advantage of easy application as flexible electronic devices [102]. Constituting a functional component in various applications, buckypapers can be used as permeable membranes, capacitors, electrodes for fuel cells, reinforcement in composite materials, among others [103–107]. This approach could be used as an effective method to create composites of CNTs with metal oxide nanoparticles with suitable properties to give rise to new materials with tailoring properties [80,102]. ZnO appears as a good candidate to be incorporated in CNT buckypapers since this material enlarges the photon absorption region, increasing the photoconversion efficiency of the generated photocurrent [102].

As an extension of the preliminary work performed in the VACNTs, now the focus is given to the production of ZnO/CNT buckypapers composites to explore their fundamental properties for

optical and electrical applications. For some applications, as it is the case of dye-sensitized solar cells, during the device construction the introduction of a liquid electrolyte destroys the CNTs alignment, compromising the integrity of the composite samples [108]. In this sense, using disordered CNTs in the form of buckypapers constitute an advantage relative to the VACNTs. The combining semiconductor nature of the ZnO nanostructures with the excellent electric properties of CNTs in a flexible sample shows a great potential for application as an electrode for this type of solar cells.

Following this approach, the morphological, structural, optical and electrical properties of the synthesised ZnO/CNT buckypaper composites were analysed and discussed. Since in composites the particles size and morphology constitute important parameters for the resulting material properties, the effect of ZnO morphologies (TPs and NPs) on the CNT buckypapers' properties were studied.

The micrographs of the three different types of composites prepared are shown in Figure 6-45: (a, b) buckypapers containing only COOH functionalized CNTs; a mixture of COOH functionalized CNTs with (c, d) ZnO TPs and (e, f) ZnO NPs. In the case of the samples prepared with TPs, a good dispersion in the composite was observed. It is worth noting that the TPs maintained their shape during the preparation of the buckypaper, highlighting the mechanical properties of these structures produced by LAFD. Notwithstanding, the aggressiveness of the composites production process, the excellent mechanical strength of TPs due to predominantly ionic bonds in ZnO enables to preserve the shape intact. On the other hand, NPs tend to remain agglomerated during the solvent extraction step of the composite preparation process. Despite some aggregation observed in NPs, the EDS analysis attested the homogeneous distribution of ZnO within the composites network, as shown in Figure 6-46.

Even after their incorporation into the buckypaper composite, the structures (TPs and NPs) present good crystallinity**,** as evidenced by the X-ray diffractograms of the composite samples (Figure 6-47a)**.** The XRD pattern of the sample containing only CNTs revealed the presence of one diffraction maxima at 25.8^{o} corresponding to the (002) reflection and revealing an interlayer spacing of 0.34 nm, which is in good agreement with the literature [109]. The composites of CNTs with ZnO TPs and NPs present similar diffraction patterns with maxima that can be fully indexed to the hexagonal WZ ZnO structure with lattice constant of a = 3.3 Å and c = 5.2 Å, which is in accordance with the literature [34,110] and the values already reported in this work. Raman measurements using the 632.8 nm laser line in these ZnO/CNTs buckypapers (Figure 6-47b) revealed the expected vibrational modes for the wurtzite structure of ZnO along with those typically associated with sp^2 coordinated carbon (D, G and D' bands at 1325, 1580 and 1610 cm^{-1}, respectively), as previously observed in the VACNTs samples. However, the D/G band intensity ratio showed to be higher for the buckypaper material compared to the VACNTs, denoting lower defect density of the later. This is due to the lower quality of the commercial raw materials used to produce the buckypaper.

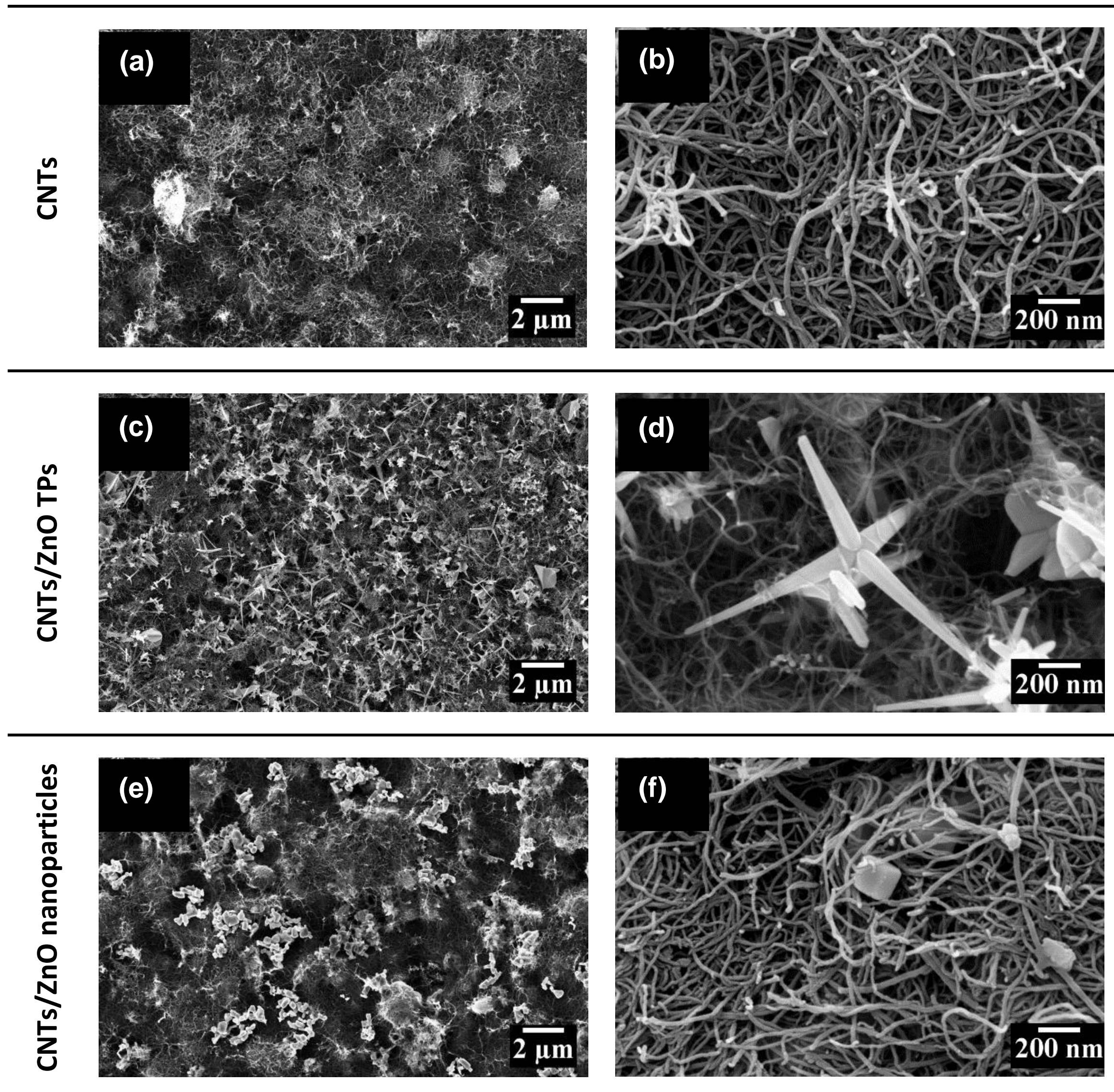

Figure 6-45 – SEM micrographs of (a) and (b) CNTs buckypaper, (c) and (d) ZnO TPs/CNTs buckypapers and (e) and (f) ZnO NPs/CNTs buckypapers.

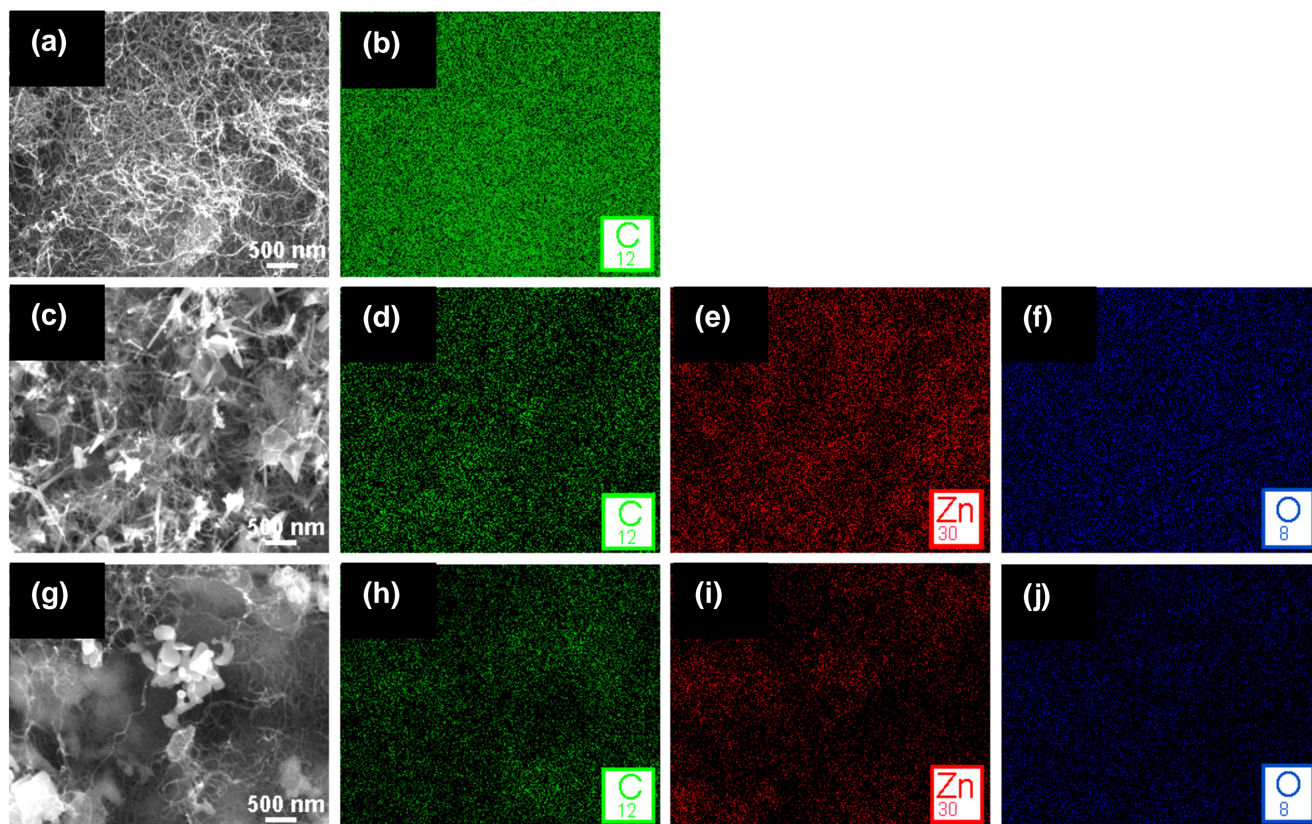

Figure 6-46 – SEM images of (a) CNTs, (c) ZnO TPs/CNTs and (g) ZnO NPs/CNTs buckypapers; the respective EDS maps corresponding to C are presented in (b), (d) and (h), and the ones related to Zn are presented in (e) and (i) and to O in (f) and (j).

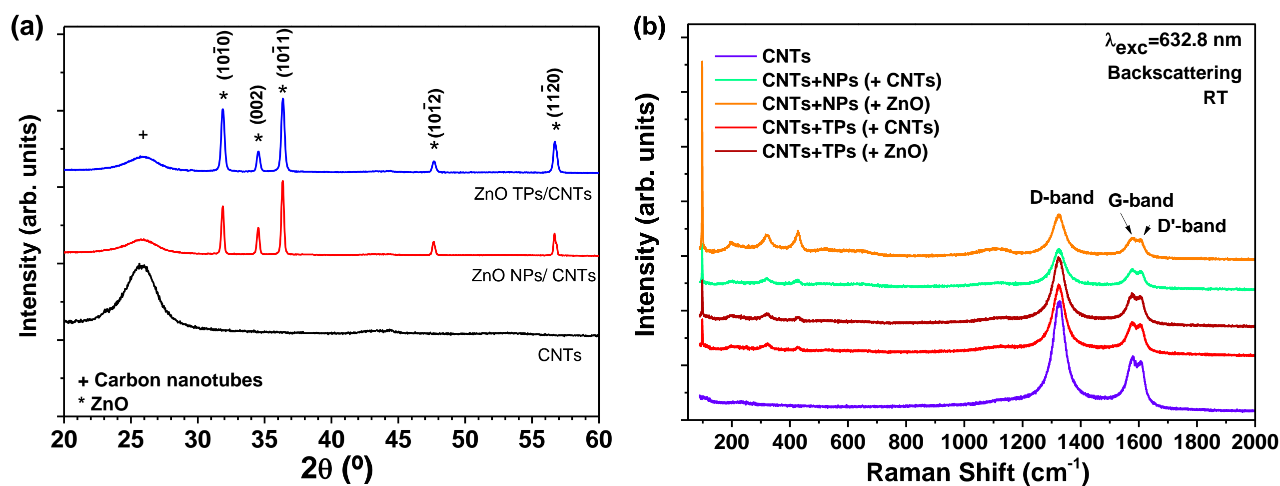

Figure 6-47 – (a) XRD patterns and (b) Raman spectra of the buckypapers samples.

The 14 K PL spectra for the ZnO TPs and NPs and their composites with CNTs is shown Figure 6-48. It is important to point out that no luminescence is observed in the case of the CNTs alone, only when ZnO is incorporated. Either as nanostructures or embedded in the CNT composites, the ZnO luminescence is dominated by a well-structured NBE recombination and almost no visible emission was detected, attesting again the high optical quality of the LAFD grown material. In the ZnO TPs, NPs and ZnO TPs, NPs/CNTs composites the NBE emission is constituted by three main

lines, one located at ~ 3.36 eV due to the overlap of several D^0X transitions and the 3.31 eV line together with its LO replica (at ~ 3.24 eV), as observed and discussed in section 6.1. The inset depicts an enlargement of the high energy region of the PL spectra. In the case of the TPs, after the incorporation in the CNT composite it was possible to de-convolute the high energy line into two components. The shoulder at ~ 3.37 eV is likely due to the FX recombination. Noteworthy, in low dimensional structures, SXs have been observed and reported in the same region [14,23], so the presence of these luminescence centres should also be taken into account. The mentioned shoulder is also present in the TPs samples without CNTs but with a lower definition, as can be better seen in Figure 6-49, where higher resolution spectra are shown. For the TPs samples, the emission is dominated by the D^0X transitions, while for the NPs samples the emission in the 3.31 eV region is the dominant one. As seen in the ZnO rods grown by the same method, a strong correlation of the 3.31 eV emission line with the presence of surface states is suggested. As such, the incorporation of TPs in the CNTs composite associated with higher defect concentration on ZnO surface yielded an enhanced 3.31 eV line intensity. This fact constitutes another indication that the emission is affected by surface states. When incorporated in the CNTs composite, the surface of the TPs is in direct contact with the functionalized CNTs, which could lead to a higher concentration of electron-hole pairs in the surface of the TPs. The enhancement of the PL intensity in ZnO/CNTs composites was previously reported in the literature [80,111], and also in the ZnO/VACNTs samples analysed in the previous sub-section, due to the generation of a higher concentration of optically active defects in the mentioned spectral region, namely improving surface and excitonic related recombination.

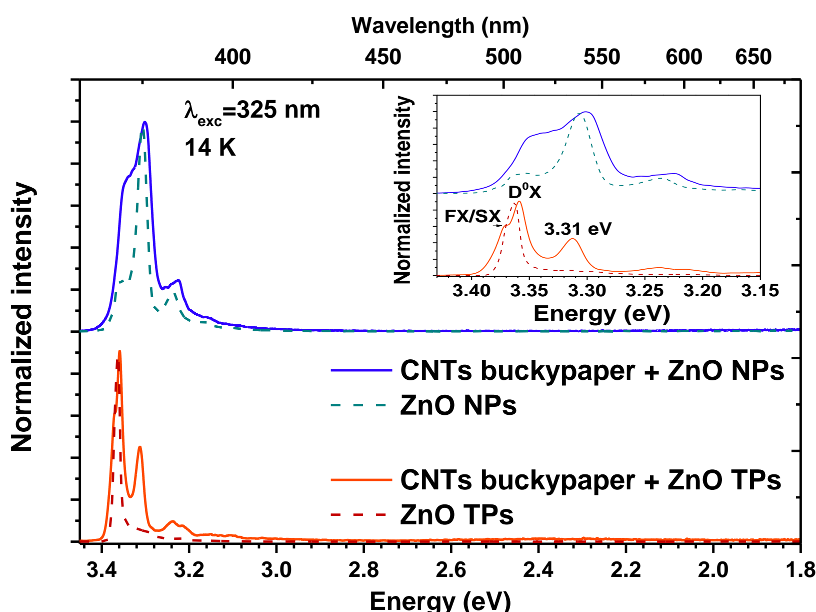

Figure 6-48 – Comparison between the low temperature PL spectra of the ZnO TPs and NPs and ZnO/CNTs buckypapers.

The temperature dependent PL spectra of the NBE for the ZnO TPs/CNTs and NPs/CNTs composite samples are shown in Figure 6-49 and Figure 6-50, respectively. Additionally, the temperature dependence of the NBE integrated intensity in the 14 K - RT interval is also displayed, including the one for the TPs and NPs alone. In the case of the TPs, a strong thermal quenching of

the NBE is observed when the temperature raises from 14 K to RT, following a similar behaviour of bulk ZnO [7]. The overall integrated intensity reveals that only approximately 10% of the emission observed at 14 K remains at RT. A similar trend was observed for the ZnO TPs/CNT composite, whereas a lower thermal quenching was identified in the 14 K - 50 K region (Figure 6-49). For the ZnO NPs a strong decrease of the NBE emission with increasing temperature is also observed. At RT only ~ 20% of the 14 K intensity is present. On the other hand, the ZnO NPs/CNTs composite reveals a higher PL thermal stability, showing that more than 50% of the 14 K luminescence intensity is still observed at RT (Figure 6-50). The identified behaviour highlights the role of the feeding and de-excitation paths on both kinds on ZnO nanostructures and ZnO/CNTs composites, revealing that for the ZnO NPs/CNTs a suppression of additional nonradiative paths results in higher thermal stability of the NBE recombination. Particularly, while in the case of TPs nonradiative routes strongly influence the radiative recombination either with or without the CNTs composite, for the smaller ZnO structures embedded in the CNTs the data evidence that the nonradiative channels, which compete with the ZnO luminescence, are much suppressed. Since the surface area is in the same order of magnitude for both structures, the identified behaviour in the ZnO (NPs, TPs) and ZnO NPs, TPs/CNTs is likely due to the differences in the samples morphology. The data suggest a different ability for the terminated surfaces of the nanostructures to spatial capture defects, which in turn are optically active.

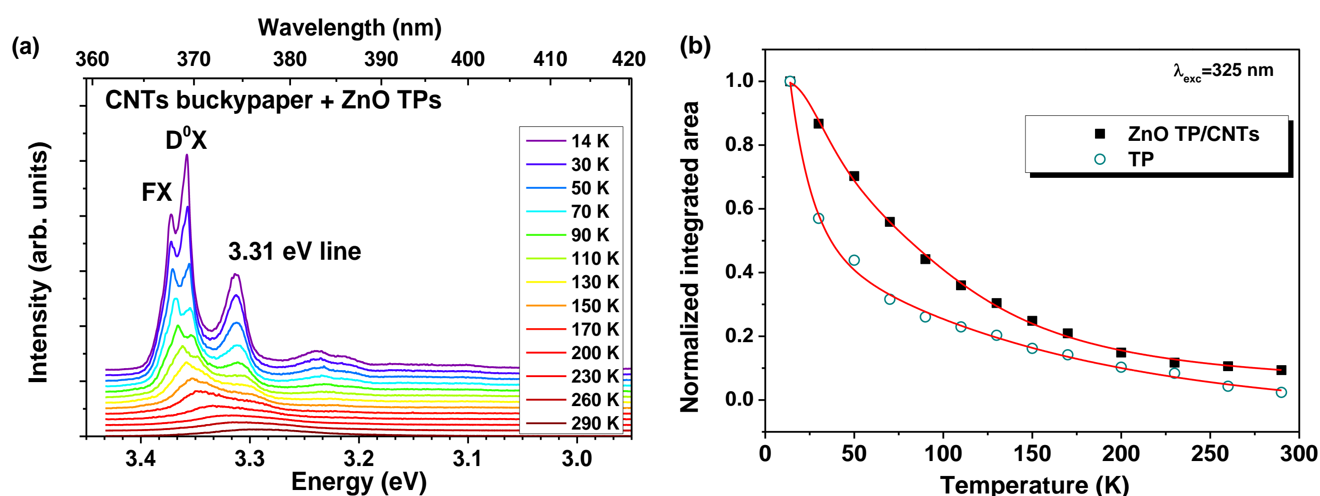

Figure 6-49 – (a) Temperature dependence PL emission and (b) evolution of the integrated intensity as a function of temperature for the ZnO TPs/CNTs buckypapers, as well as for the TPs before the incorporation in the composite. The spectra were acquired with above bandgap excitation (325 nm).

Electrical measurements revealed in plane resistivity values in the same order of magnitude for the CNTs and prepared ZnO/CNTs composites (Table 6-1). A metallic behaviour was found for all the samples, as is expected for MWCNTs [112]. These results suggest that the addition of ZnO TPs or NPs to the CNTs does not change significantly the electrical resistivity, showing that the main contribution for this quantity comes from the CNTs. Highly dense CNT mats of individual tubes with an average length size of 1.5 µm can easily touch each other to form a high electrical conductive 3D-network where embedded semiconductive ZnO particles of shorter length sizes (typically between 100 to 500 nm) are not expected to affect significantly the electrical percolation of the CNT mat. The obtained values are consistent with those reported in the

literature for CNTs buckypapers [78,112,113] with the dependence of the electrical conductivity mainly due on two factors: the conductivity of the nanotubes themselves and the ability of the charge carriers to tunnel between neighbouring nanotubes, which, in turn, depends on the number of contact points or conductive channels between the CNTs. If the CNTs network increase, more conductive pathways for the charge carriers are available, increasing the film conductivity [103].

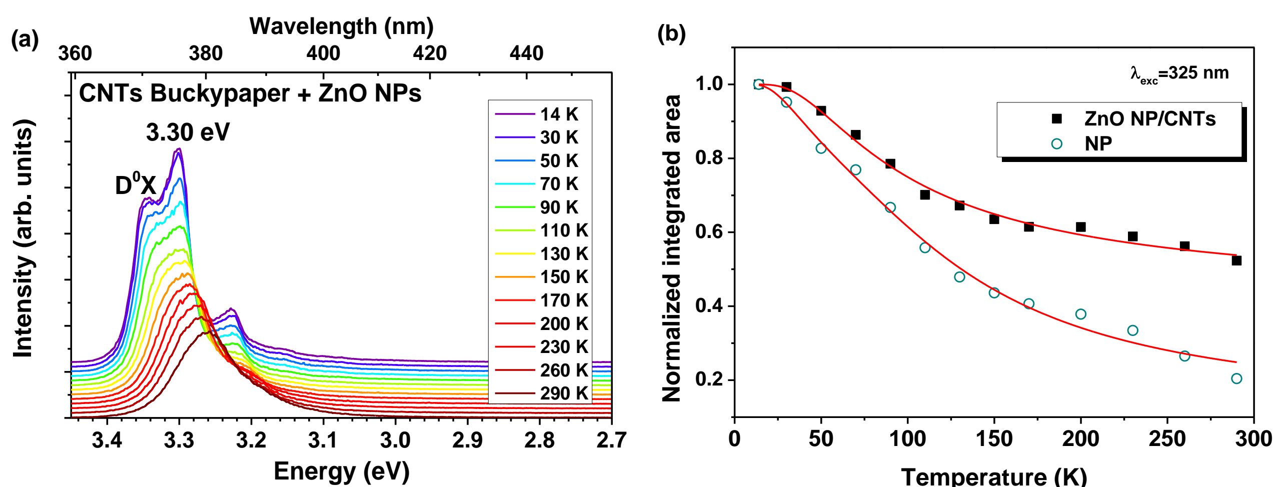

Figure 6-50 – (a) Temperature dependent PL emission and (b) evolution of the integrated intensity as a function of temperature for the ZnO NsP/CNTs buckypapers, as well as for the NPs before the incorporation in the composite The spectra were acquired with above bandgap excitation (325 nm).

Table 6-1 also evidences that distinct carrier mobilities occur for the CNTs and composites. Particularly, ZnO TPs/CNTs exhibits slightly low electron mobility. It is well established that the conductivity/resistivity depends on the carrier concentration and scattering time which in turn is dependent on backscattering carrier phenomena at surfaces and grain boundaries. The lowest mobility found for the ZnO TPs/CNTs indicates smaller carrier collision times in this composite. Since the composites resistivity is similar, a higher carrier concentration is expected for the ZnO TPs/CNT sample, as was experimentally confirmed and shown in Table 6-1.

The obtained results suggest that a good combination of the ZnO optical and CNTs electrical properties can be achieved by an appropriate choice and dispersion of the ZnO nanostructures, which is of potential importance for technological applications.

Table 6-1 – Electrical properties of the prepared composites obtained from Hall measurements.

	CNTs	ZnO TPs/CNT composites	ZnO NPs/ CNT composites
In plane resistivity ($\Omega \cdot$ cm)	7.59×10^{-2}	8.01×10^{-2}	9.13×10^{-2}
Electron mobility ($cm^2\ V^{-1} \cdot s^{-1}$)	6.30×10^{-2}	2.15×10^{-2}	8.17×10^{-2}
Carrier concentration (cm^{-3})	1.23×10^{21}	3.67×10^{21}	8.37×10^{20}

6.4. $Cd_xZn_{1-x}O/Mg_yZn_{1-y}O$ heterostructures

After a detailed studied of the LAFD produced ZnO structures and their potential to form composites with other materials capable of tailor the semiconductor's properties, it is important to make a small remark concerning the alloying of ZnO with other semiconductors (namely CdO) envisaging the tuning of the bandgap and, consequently, of its luminescence properties. As discussed in Chapter 1, alloying ZnO with CdO is known to promote a shift of the bandgap to the visible region with increasing CdO molar fraction [1,114,115]. In this section, the effect of the incorporation of different Cd contents (x_{Cd}) on the optical properties of the $Cd_xZn_{1-x}O$ alloy is studied by PL. As mentioned in Chapter 2, these samples were grown by MBE and are composed by a layered structure of $Cd_xZn_{1-x}O$ grown on top of a buffer layer of $Mg_yZn_{1-y}O$ deposited on sapphire. The structural characterization of the present samples was also carried out, and part of the results are reported in the reference [116] by Redondo-Cubero and co-workers. Even though in here only the optical properties will be discussed, it is important to highlight that RBS measurements allowed to assess the composition of the film, which is slightly different from the nominal one for samples 936 and 938 (Table 2-13). In these two cases the x_{Cd} was found to be 0.17 and 0.38, instead of 0.15 and 0.31. Moreover, RBS depth profiles allowed to rule out the presence of compositional phase separation with depth and showed that the compositional gradient has a maximum at the surface [116].

Figure 6-51 depicts the transmittance spectra for the $Cd_xZn_{1-x}O$ sample with different Cd composition, x_{Cd} = 0, 0.12, 0.17, 0.25 and 0.38 (corresponding to samples 934, 935a, 936, 937 and 938, respectively, as mentioned in Chapter 2, Table 2-13). The shifting of the bandgap towards lower energies is clearly observed with the increasing of the Cd amount. In the case of the ZnO sample, the transmittance behaviour is in line with what is expected for a direct bandgap material, while for the remaining samples, a band tail is observed, due to the presence of disorder in these ternary alloys. Thus an exponential tail of the density of states caused by localized states is present [117,118]. The structured features observed in the transmittance plateaus are due to optical interference effects. A closer inspection of the figure allows the identification of more than one bandgap for the ternary alloys, which is associated with the presence of the $Mg_yZn_{1-y}O$ buffer layer. Figure 6-51b corresponds to an enlargement of the marked area on Figure 6-51a, showing the different transmittance plateaus and onset absorption (black arrows) for the $Mg_yZn_{1-y}O$ buffer layer of each sample. The differences observed reveal that the Mg content is not the same in all the samples. In fact, for the sample with x = 0.12, the curve of the buffer layer resembles the one of the ZnO, with the same onset absorption, suggesting that in this case an extremely low Mg content (most probably y = 0) is present. Figure 6-51c shows the evolution of the onset absorption with increasing x_{Cd}. The values follow closely the trend expected for the bandgap energy described by Eq.1-4. Taking into account the values of 3.3 eV and 2.3 eV for the RT bandgap energy of ZnO and CdO, respectively [1], the expression can be written as

$$E_g(x)^{\mathrm{Cd}_x\mathrm{Zn}_{1-x}\mathrm{O}} = 3.3 - (1+b)x + bx^2. \qquad \textbf{Eq. 6-2}$$

As described in Chapter 1, b is the bowing parameter, which depends on the difference in electronegativities of the end binaries ZnO and CdO. An adequate determination of this parameter is very important for the accuracy of bandgap engineering [1,119]. Different values

have been reported in the literature [120–123], usually between 8.14 [120] and 1.21 eV [124], and no consensus was yet found. For the present data a value of b = 2.1 $\pm$ 0.1 eV was obtained, which is well within the reported range.

Figure 6-51 – (a) Transmittance spectra of the ZnO and $Cd_xZn_{1-x}O$ samples. (b) Amplification of the region marked in (a). A decrease in the bandgap of the samples with increasing Cd content is observed. (c) Position of the onset of absorption. The solid red line corresponds to the fitting using Eq. 6-2.

When irradiated with a 325 nm He–Cd laser at 14 K, the samples exhibit a strong and homogeneous visible emission that ranges from dark blue to orange, with increasing x_{Cd}, as can be seen in Figure 6-52.

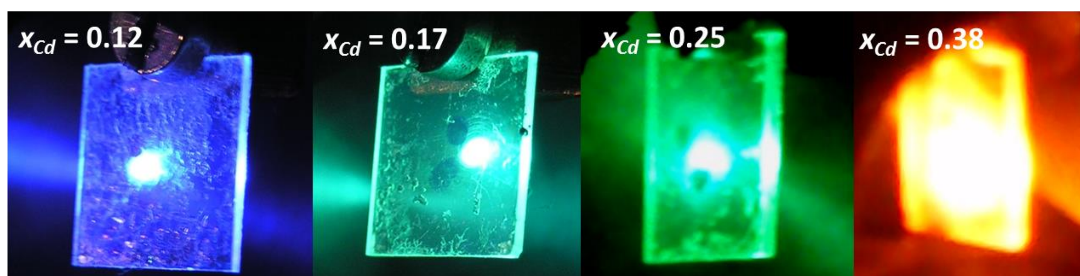

Figure 6-52 – Visual appearance of the emission at low temperature for all the alloy samples.

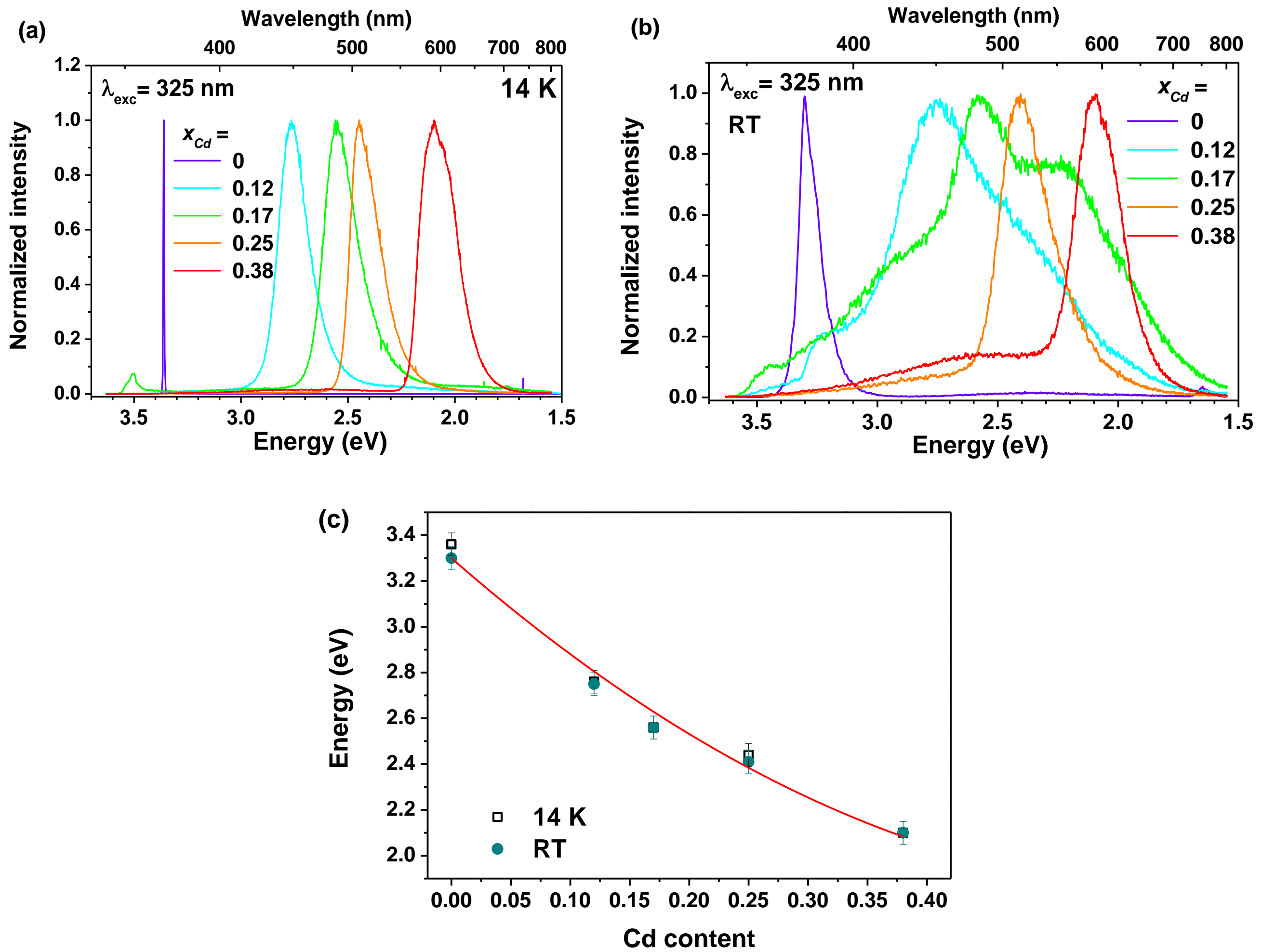

Figure 6-53 – PL spectra of the ZnO and $Cd_xZn_{1-x}O$ samples with different Cd content obtained at (a) 14 K and (b) RT. The shift of the NBE emission to lower energies with increasing Cd content is clearly seen. (c) Position of the maximum of the PL. The solid red line corresponds to the fitting using Eq. 6-2.

The samples were also analysed by PL, as represented in Figure 6-53. The PL spectra have been normalized for clarity. Both 14 K (Figure 6-53a) and RT (Figure 6-53b) spectra evidence a redshift of the emission from the UV to orange spectral region, going from 0 to 0.38 of x_{Cd}, as expected due to the Cd-induced decrease in the bandgap energy. At 14 K, well-defined PL lines, associated with the NBE emission are seen to shift from ~ 3.35 eV (x = 0) to ~ 2.10 (x = 0.38), covering almost whole visible range. A very narrow (~ 5 meV) and well-defined NBE (mainly due to D^0X recombination [7]) was observed for the sample corresponding to the ZnO binary, evidencing its high optical quality. The NBE emission for samples with $x > 0$ is rather broad, between ~ 160 and ~ 190 meV, with a tendency to increase with x_{Cd}. This increase of broadening can be explained by the increase of disorder in the semiconductor alloy, which leads to the appearance of localized carrier states [117,118,125,126]. Disorder and potential fluctuation generated in alloyed and heavily extrinsic doped semiconductors may cause an increase in the number of localized states [118].

At RT, an additional broadening of the emission is observed for all the samples, which is particularly visible in the ZnO sample. The PL peak position data was also well fitted using Eq. 6-2 , obtaining a b = 3.6 $\pm$ 0.2 eV. A close inspection of Figure 6-51c and Figure 6-53c reveals a substantial Stokes' shift between the PL emission and absorption edges, with values that vary between ~ 240 meV and ~ 300 eV, once again with a tendency to increase with increasing x_{Cd}. This behaviour was previously reported by many authors [118,125,127–129] including Buyanova *et al.* [127], which obtained a Stokes' shift value in agreement with the one found for the present samples. These authors considered the mentioned shift as an indicative of the participation of band tail states in the radiative transitions [127]. Moreover, their findings, based on temperature dependence TRPL studies, suggest that the alloys' NBE emission is governed by the recombination of excitons localized within the band tail states which are likely caused by nonuniformity in Cd distribution [127,130]. They observed that, at RT, the PL spectra shifted toward lower photon energies with increasing time after the excitation pulse due to the faster PL decay monitored at higher emission energies. This spectral dependence of the decay time was pointed as an indication that the RT PL emissions from the alloys might result primarily from localized exciton recombination [127]. As stated by Kang *et al.* [118,131], the increase of localized states with increasing Cd content results in the enhancement of the Stokes' shift and broadening of the emission and absorption edges [118,131].

It is also important to mention that there is a clear influence of broad bands associated to defects (normally in the green region), even though the edge emission remains the dominant one. Since, as will be seen later, a strong thermal quenching is observed for the NBE emission of all the $Cd_xZn_{1-x}O$ alloy samples. Additionally, the contributions of emission coming from the $Mg_yZn_{1-y}O$ buffer layer cannot be discarded. With the purpose to explore that hypothesis, PL measurements where performed in the substrate face. The results for samples 935a, 936 and 938 are summarized in Figure 6-54. In fact, broad bands are present in the spectra recorded from the substrate face in the same spectral range as the ones identified in the film face, even though with different maxima positions. These bands appear overlapped with the emission originated from the $Cd_xZn_{1-x}O$ layer, as corroborated by the well match between the spectra from both faces. Besides the broad bands, also the NBE emission of the $Mg_yZn_{1-y}O$ alloy was observed in the case of samples 936 and 938, being the dominant emission in both. For sample 936 (Figure 6-54b), this emission is even visible when the sample is excited through the film face. Sample 935a evidences a narrow peak near ~ 3.35 eV, the same position of the one identified for ZnO, supporting the results obtained by transmittance were the buffer layer was found to be composed of only ZnO.

In order to rule out the contribution of the $Mg_yZn_{1-y}O$ emission to the one identified for the $Cd_xZn_{1-x}O$ alloy film face, samples with $x \geq 0.17$ were also excited with 442 nm (~ 2.80 eV) photons (Figure 6-55), corresponding also to above bandgap excitation for these x_{Cd}, but not for the alloy with Mg. As seen in Figure 6-55, the emission matches almost perfectly for both excitations, suggesting the involvement of the same emitting centres and no buffer layer contribution in the observed emission.

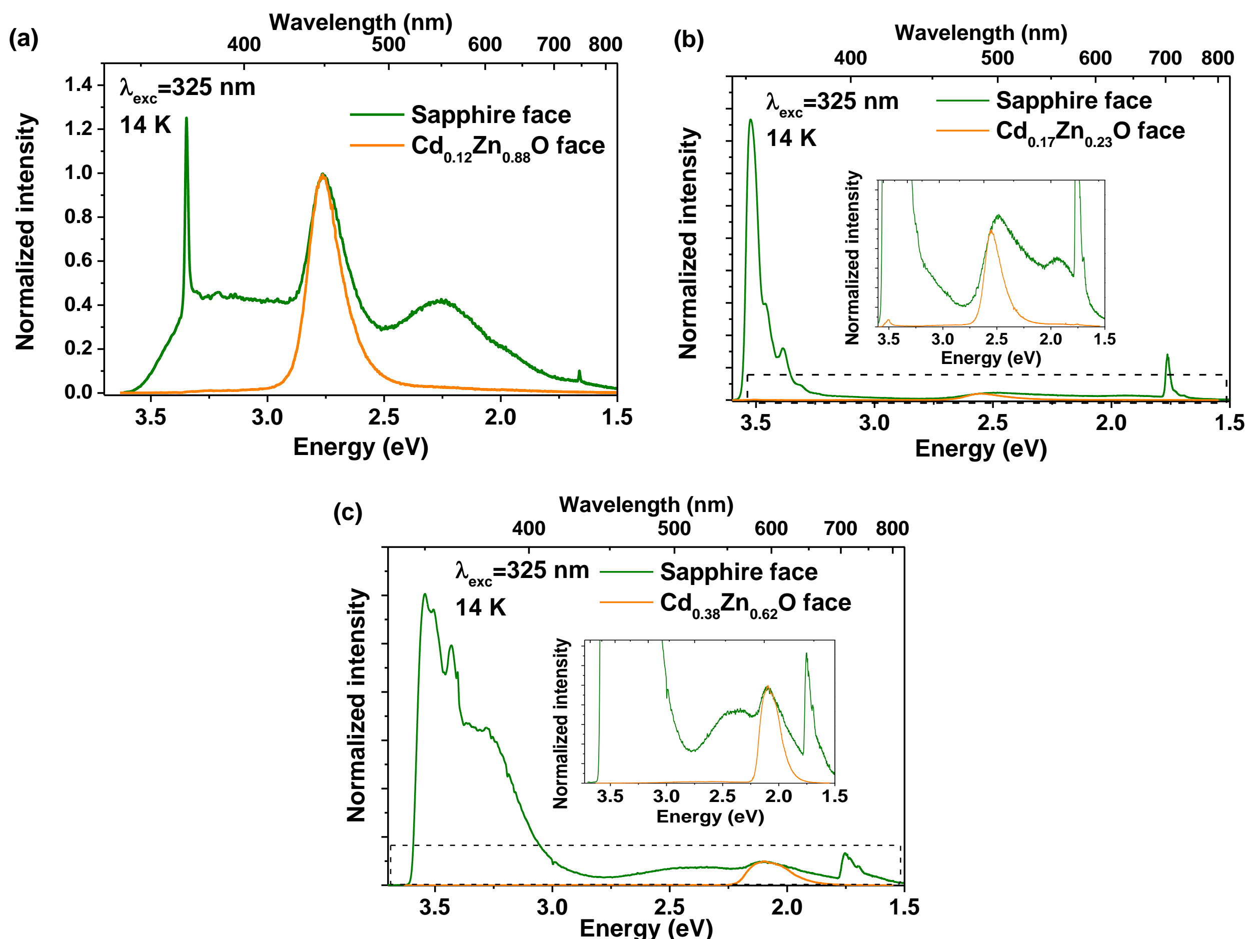

Figure 6-54 – Low temperature PL emission obtained when excited in both film and substrate faces with 325 nm, for samples with (a) x_{Cd} = 0.12, (b) x_{Cd} = 0.17 and (c) x_{Cd} = 0.38.

Figure 6-56 shows the temperature dependent PL spectra for the ternary samples (with $x > 0$). In all the cases a strong thermal quenching is observed and the intensity at RT is about two orders of magnitude lower that the one observed at 14 K. The value of integrated intensity versus temperature (Figure 6-56b, d, f, h and j) were fitted by the classical model described in Eq. 4-29, well accounted by only one activation energy. Similar values were found for all the samples, vary between ~ 29 and ~ 26 meV for 325 nm excitation. A slightly smaller value (~ 23 meV) was estimated for sample 938 under 442 nm. This difference is small and falls between the error range. The estimated activation energies are in line with the ones obtained by Yang *et al.* [132], for samples also grown by MBE and with comparable x_{Cd}. These authors reported values of ~ 25 meV for all the samples, independently of the Cd content. Mohana *et al.* [133] also reported a value (~ 22 meV) close to the ones here calculated. The fact that approximately the same activation energy values were obtained for all the samples suggests the involvement of the same type of recombination processes. The value found for the activation energy in the alloys are about 2 times higher than the values typically reported for the D^0X in ZnO, which ranges around ~ 10 - 15 meV [7,134].

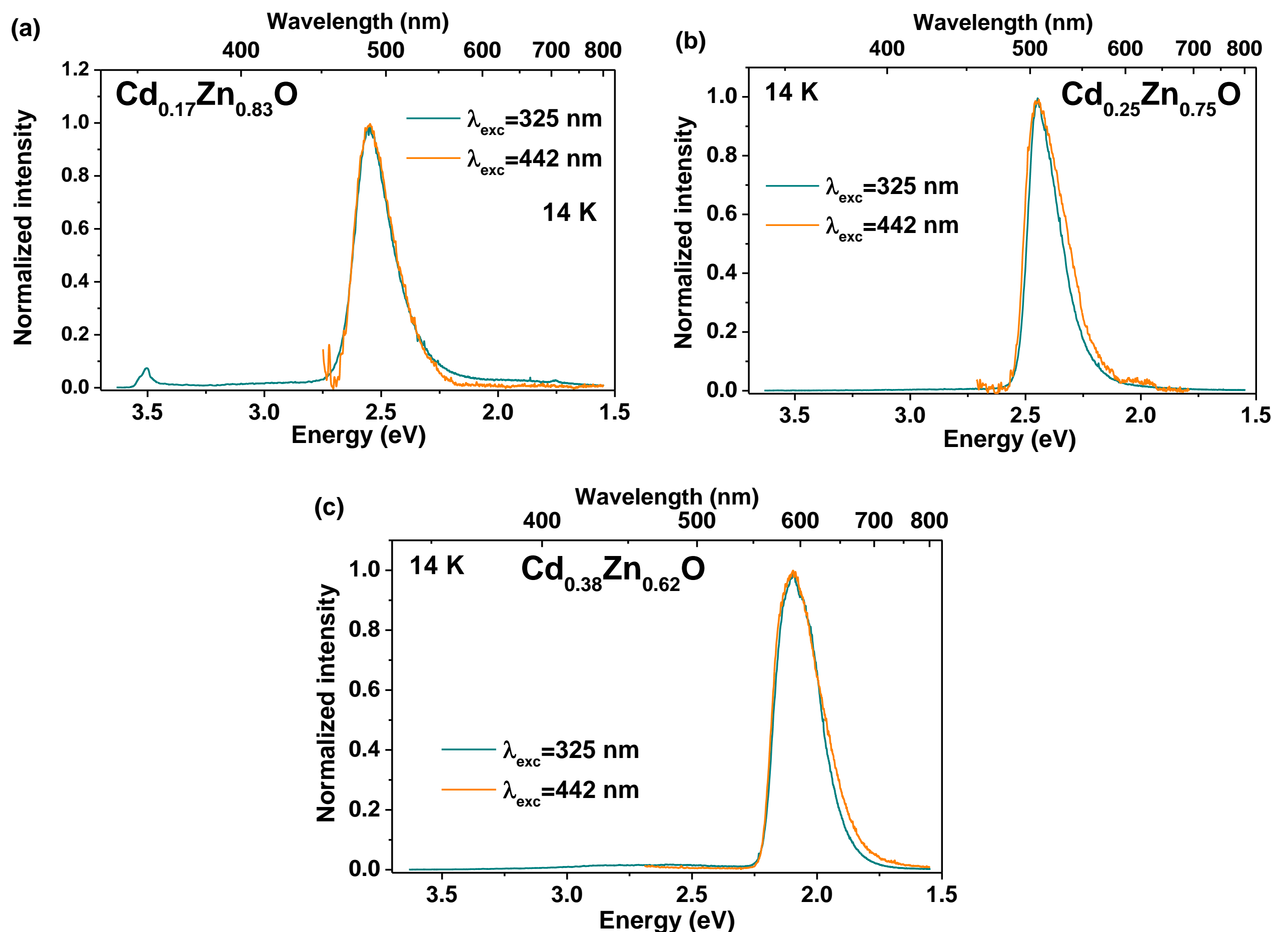

Figure 6-55 – Low temperature PL emission obtained when excited with 325 nm and 442 nm for samples with (a) x_{Cd} = 0.17, (b) x_{Cd} = 0.25 and (c) x_{Cd} = 0.38.

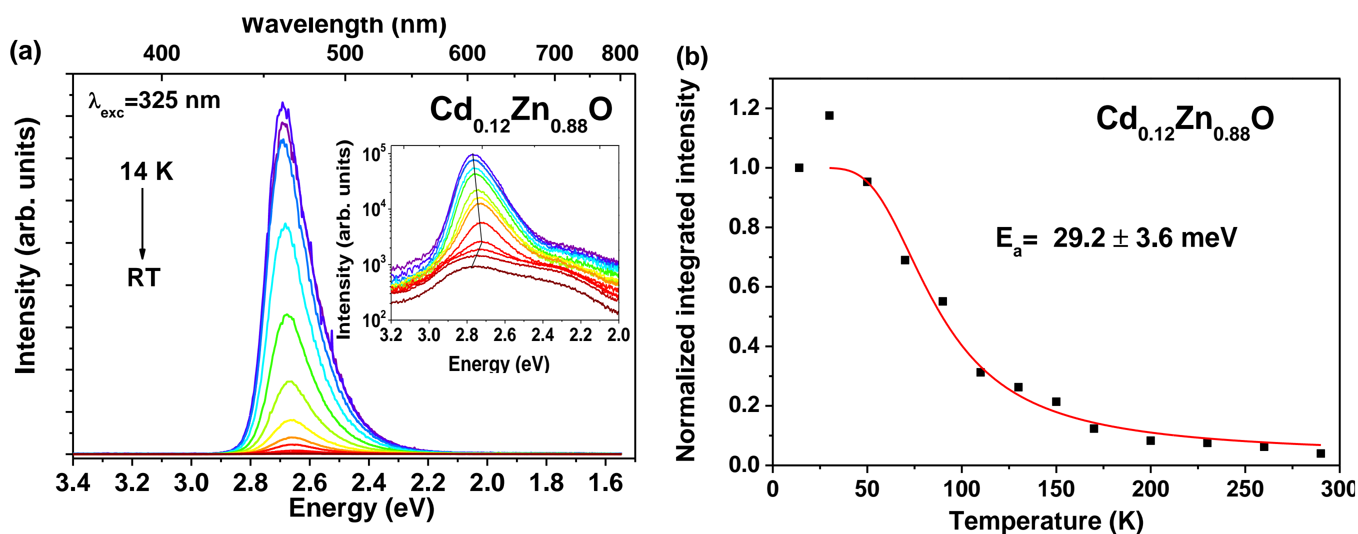

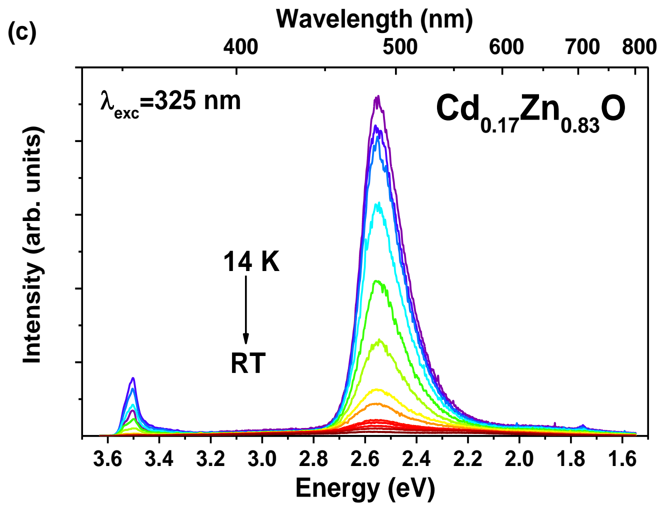
(c)
Wavelength (nm)
400
500
600
700
800
λ_{exc}=325 nm
$Cd_{0.17}Zn_{0.83}O$
14 K
RT
Intensity (arb. units)
3.6 3.4 3.2 3.0 2.8 2.6 2.4 2.2 2.0 1.8 1.6
Energy (eV)

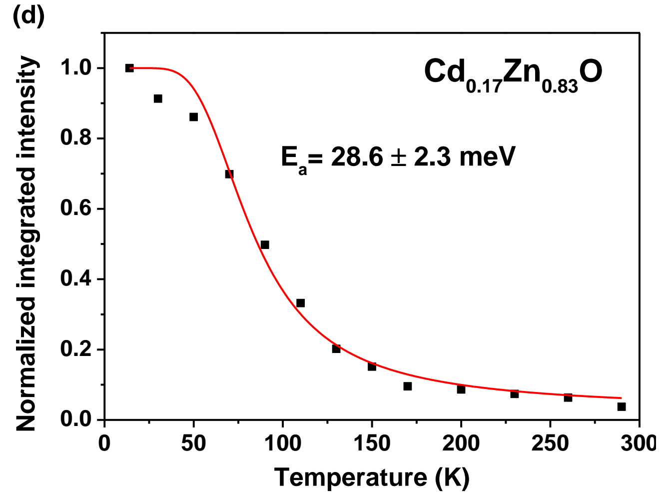
(d)
$Cd_{0.17}Zn_{0.83}O$
E_a= 28.6 ± 2.3 meV
Normalized integrated intensity
1.0 0.8 0.6 0.4 0.2 0.0
0 50 100 150 200 250 300
Temperature (K)

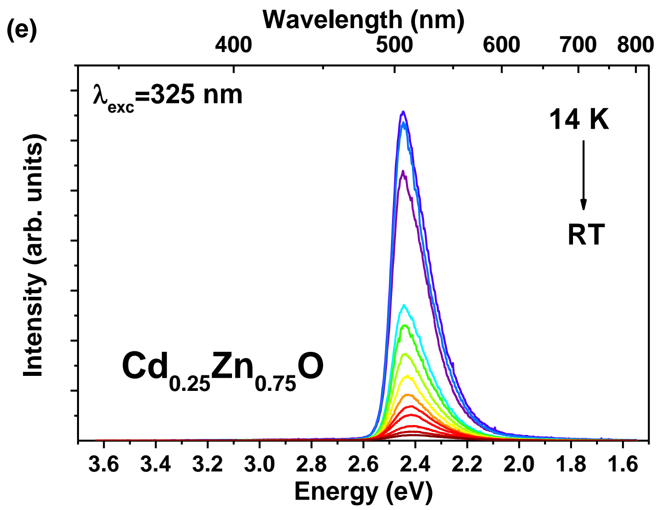
(e)
Wavelength (nm)
400
500
600
700
800
λ_{exc}=325 nm
14 K
RT
$Cd_{0.25}Zn_{0.75}O$
Intensity (arb. units)
3.6 3.4 3.2 3.0 2.8 2.6 2.4 2.2 2.0 1.8 1.6
Energy (eV)

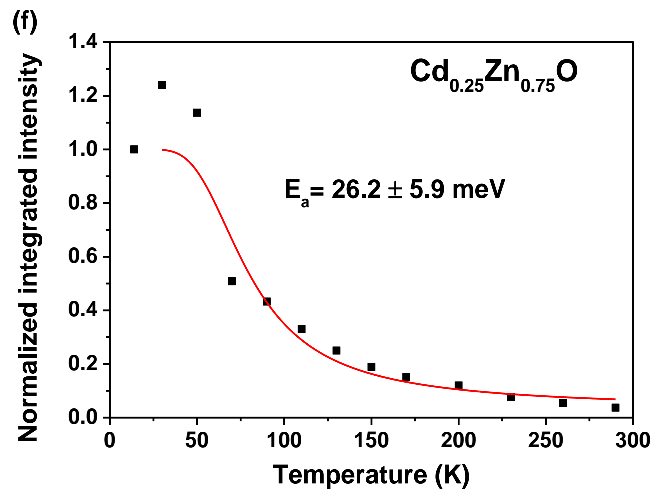
(f)
$Cd_{0.25}Zn_{0.75}O$
E_a= 26.2 ± 5.9 meV
Normalized integrated intensity
1.4 1.2 1.0 0.8 0.6 0.4 0.2 0.0
0 50 100 150 200 250 300
Temperature (K)

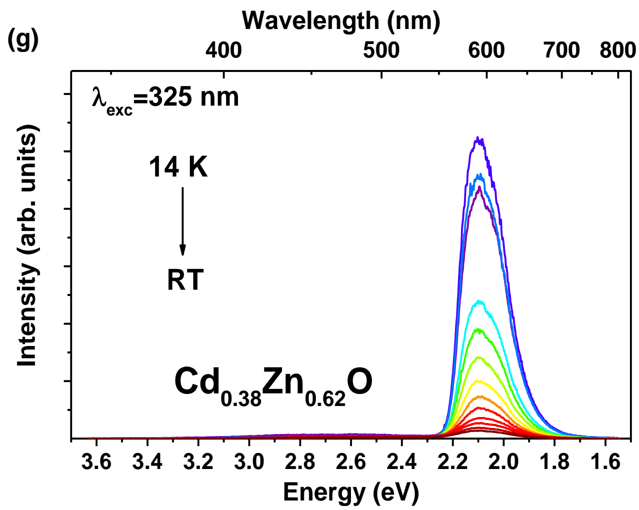
(g)
Wavelength (nm)
400
500
600
700
800
λ_{exc}=325 nm
14 K
RT
$Cd_{0.38}Zn_{0.62}O$
Intensity (arb. units)
3.6 3.4 3.2 3.0 2.8 2.6 2.4 2.2 2.0 1.8 1.6
Energy (eV)

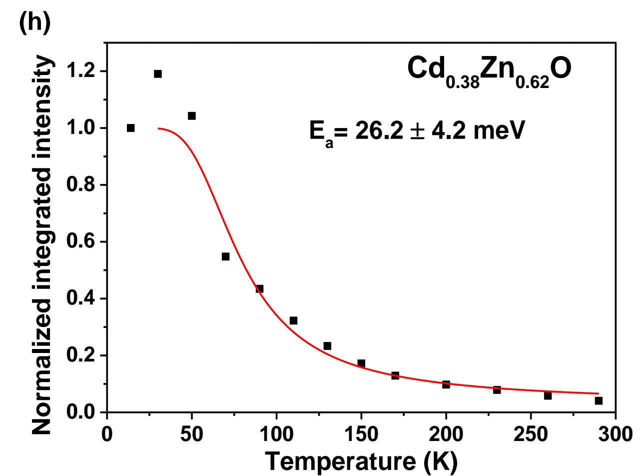
(h)
$Cd_{0.38}Zn_{0.62}O$
E_a= 26.2 ± 4.2 meV
Normalized integrated intensity
1.2 1.0 0.8 0.6 0.4 0.2 0.0
0 50 100 150 200 250 300
Temperature (K)

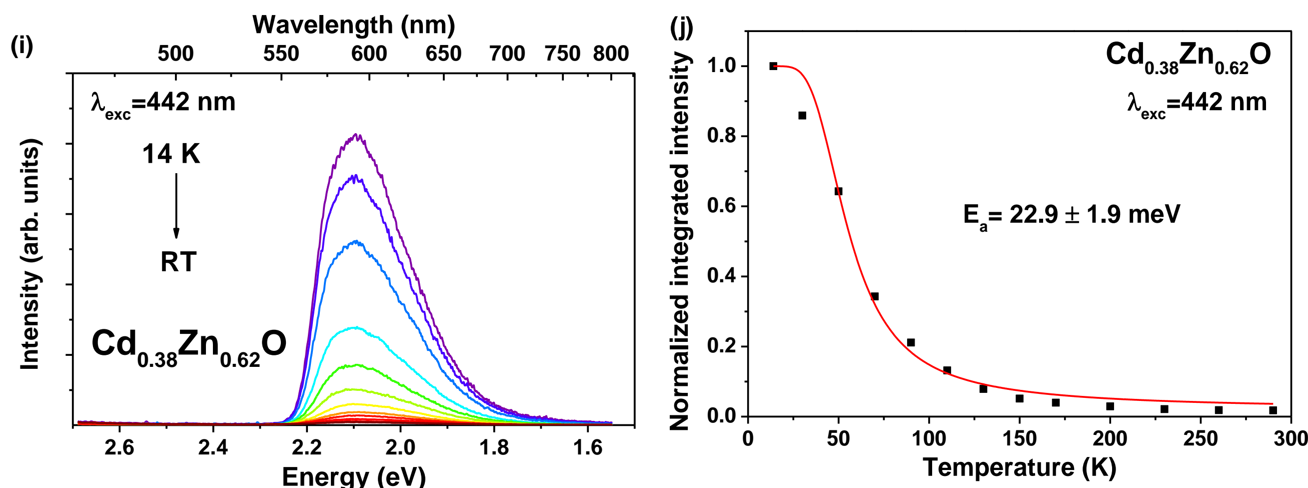

Figure 6-56 – Temperature dependence PL emission for samples with (a) x_{Cd} = 0.12, (c) x_{Cd} = 0.17, (e) x_{Cd} = 0.25 and (g) x_{Cd} = 0.38 excited with 325 nm. (b), (d), (e) and (f) Evolution of the overall integrated intensity with increasing temperature for the same samples. (i) Temperature dependence PL emission for the sample with x_{Cd} = 0.38, when excited with 442 nm photons and (j) respective integrated intensity as a function of the temperature. The inset in (a) shows the temperature dependence PL emission in semi-log scale to highlight the abnormal shift of the peak position with increasing temperature.

It is interesting to note that for sample 935a (Figure 6-56a) the temperature-dependent PL shows an abnormal red-blueshift with increasing temperature, as represented in Figure 6-57. This behaviour resembles the one observed by Mohanta *et al.* [135] in ZnCdO alloys, although with different temperature dependence. Similar results were also identified for ZnCdO/ZnO single quantum wells [136] and in other semiconductor alloys as $GaInP_2$ [137] and in InGaN/GaN multiple quantum wells [138], as well as the $Al_xGa_{1-x}N$ layers analysed in Chapter 5. Once again, carriers in localized states, caused by potential fluctuation in the alloys, are pointed out as the most probable responsible for the observed shifts in the peak position [135,136]. The potential fluctuations are ascribed to the inhomogeneous alloy composition and rough interface [136]. According to Mohanta *et al.* [133,135], as the temperature increases localized carries in lower lying localized states are thermalized to occupying higher energy states, which leads to a blueshift in the emission peal position. This phenomena competes with the redshift due to the typical bandgap shrinkage with increasing temperature [132,135]. In the case of sample with x_{Cd} = 0.12, as the temperature increases from 14 to 170 K the peak shows the usual redshift, probably due to the fact that the random distributed carriers do not have sufficient thermal energy to overcome the localization potential. A further increasing in the temperature ($T >$ 170 K) leads to a thermalization of the localized carriers to occupy higher-energy level states, thus the blueshift in the peak position [133]. The spacing between the states depends on the Cd concentration and structural disorder [135], which may explain the different temperature-dependent behaviours found for the different alloys, as evidenced in Figure 6-57. As can be seen, the S-shaped behaviour can be also identified in sample 936 (x_{Cd} = 0.17), but with smaller differences in the peak position energies. For the sample with x_{Cd} = 0.25 only a small redshift is observed while for the sample with x_{Cd} = 0.38 the peak position is kept constant for all the temperatures. In the first case, the temperature-induced bandgap shrinkage is the dominant contribution, whereas in the latter both

phenomena are likely compensating with each other, maintaining the peak position constant through all the temperatures.

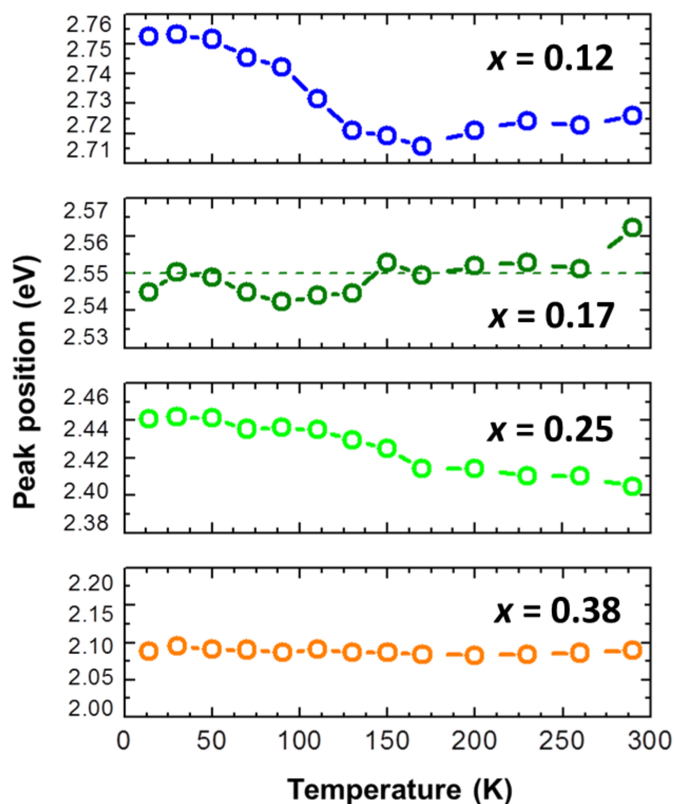

Figure 6-57 – Temperature-dependent peak position of the PL maxima in the $Cd_xZn_{1-x}O$ alloys.

Power excitation depend PL measurements were also carried out in order to gain more insight about the recombination processes involved in the observed luminescence. For that purpose sample 937 was chosen. The results are displayed in Figure 6-58. Figure 6-58a shows the PL spectra for different excitation powers vary up to 4 orders of magnitude. As is clearly seen in the figure, no shift of the peak position or change in the emission spectral shape were observed with decreasing excitation power, which allows to rule out the possible contribution of DAP recombination. The fitting of the emission was accomplished by the use of 3 Gauss functions, as shown in Figure 6-58b. The spectral deconvolution was performed for all the powers and a log(I/I_0)-log (P/P_0) graph was plotted for each one (Figure 6-58c). As a function of the excitation density the PL intensity for all the components can be well fitted to a power law over four decades of excitation density, in accordance with Eq. 4-34 and with an exponent close to unity for all of them. As already mentioned, T. Schmidt *et al.*[29] reported a PL power dependence described by an exponent m between $1 < m < 2$ for free and bound-excitons, supporting a recombination model where localized excitons are involved.

RT PLE experiments were also conducted to evaluate the preferential excitation pathways in the alloy samples. Unfortunately, due to the strong thermal quenching and consequent low RT PL intensity, only samples 937 and 938 were possible to measure (Figure 6-59). When monitored in the maximum of the NBE emission, it is clearly seen that the preferential population of the involved states is made via above bandgap excitation in both cases. Moreover, for samples 938,

monitoring in the broad band (~ 2.87 eV) reveals that this band is preferentially excited through the MgZnO bandgap, which corroborates the hypothesis previously discussed, attributing the presence of the broad bands to the buffer layer.

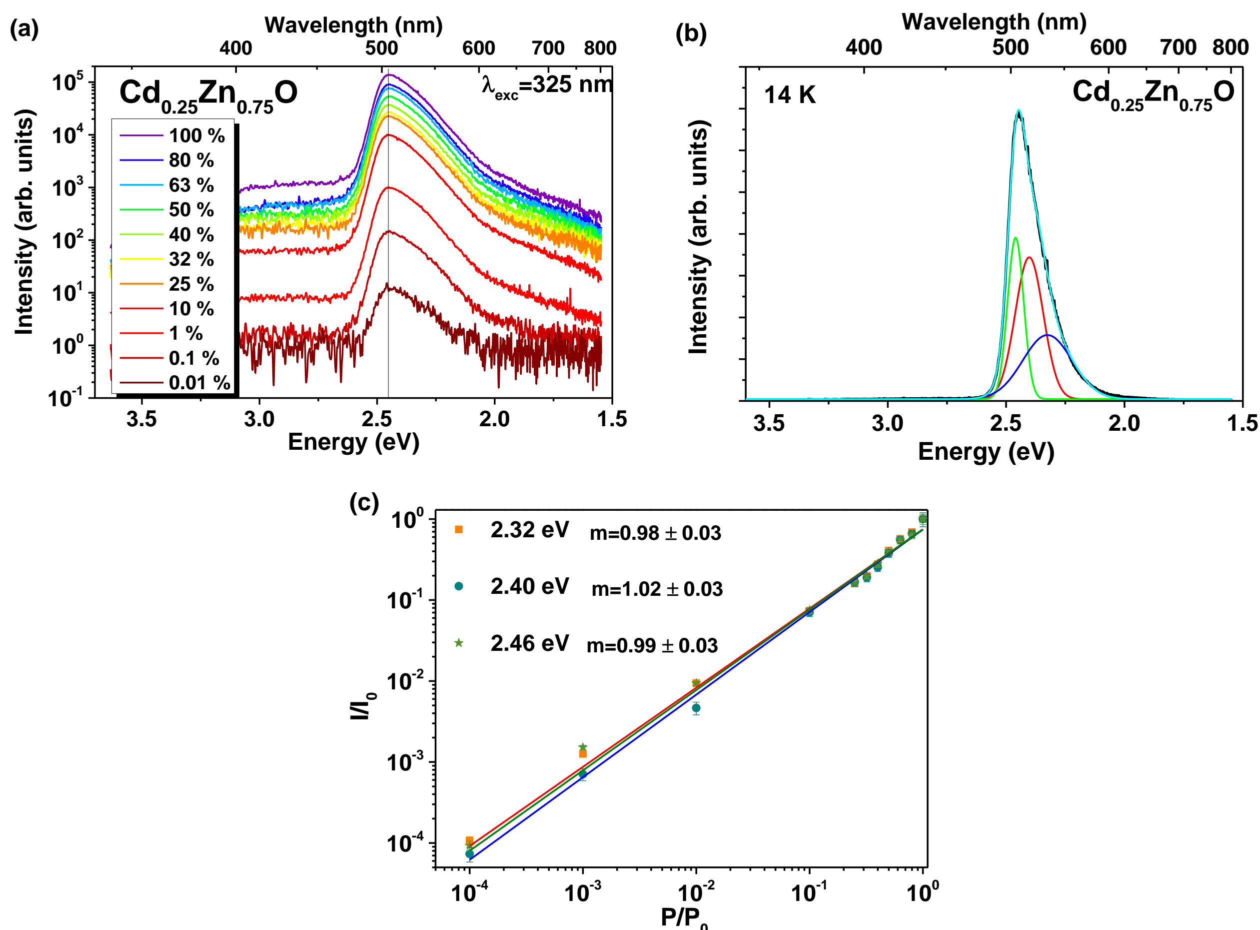

Figure 6-58 – (a) Density excitation PL dependence at 14 K for the sample with x_{Cd} = 0.25, excited with 325nm. (b) Spectral deconvolution of the sample's emission into 3 Gauss functions. (c) Log (I/I_0)-log (P/P_0) plot for the different lines after spectral deconvolution.

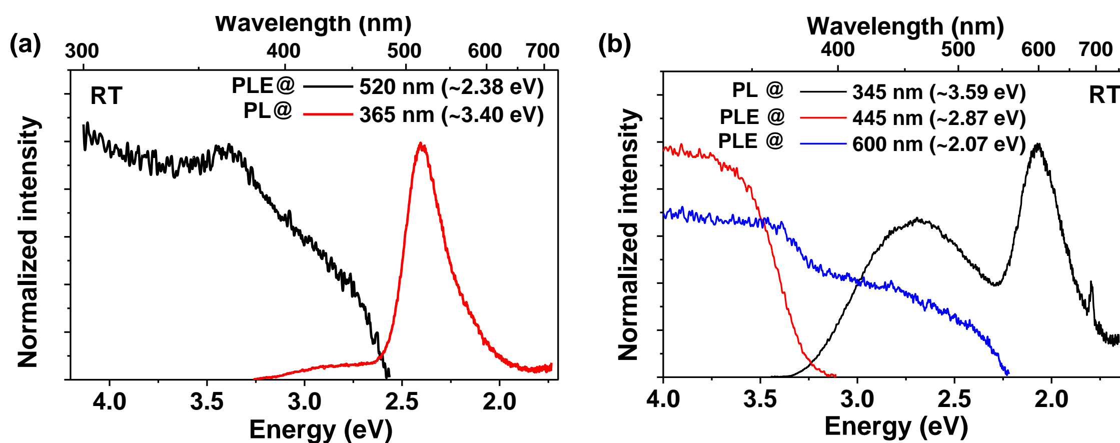

Figure 6-59 – RT PL/PLE spectra for samples with (a) x_{Cd} = 0.25 and (b) x_{Cd} = 0.38.

6.5. Conclusions

A new method to produce ZnO nano and micro crystals was developed: the laser assisted flow deposition. It was successfully demonstrated that this method exhibits a very high yield, being only necessary a few tens of seconds to cover the substrate area with highly crystalline ZnO nano/microstructures (when moderate laser powers are used). A self-catalytic vapour-solid mechanism was accounted for the nucleation and growth process of the ZnO material. Different types of morphologies can be produced depending on the thermodynamic and kinetic conditions inside the growth chamber. Although several morphologies can be found in the produced samples, the dominant ones include NPs, TPs and MRs. The latter are essentially produced on the top of the precursor rod, while the former are deposited in a substrate/holder. The morphologies of the deposited material can be controlled at some extent by an adequate choice of the growth parameters, where the most important ones were found to be the laser power (temperature) and the growth atmosphere (oxygen availability). TEM measurements confirmed the high crystallinity for all the produced structures and the absence of dislocations or stacking faults. Luminescence studies revealed a structured NBE emission which is an indication of the high optical quality of the samples. While in the case of TPs and NPs this emission is dominated by the D^0Xs, for the MRs the emission in this region is dominated by the 3.31 eV band. Plasma treatments (H_2 and N_2) were performed in order to study the nature of the defects associated with this emission and it was observed that after the treatments significant changes occurred in the PL intensity in this spectral region. The 3.31 eV band was suppressed for the samples treated with a higher power for both plasmas. The suppression observed with the N_2 plasma indicates that the emission is probably related with the presence of surface states in nature, since nitrogen has a low diffusivity in ZnO at the temperature present inside the reactor and it is expect that most of it remains at the surface. Furthermore, it was found that an effective control of the PL intensity of the 3.31 eV versus D^0X lines can be reached by considering the effects of the excitation intensity on the free exciton capture. The MRs also present a higher green band/NBE ratio than the TPs, where, at low temperature, the deep-defect broad visible band is almost negligible when compared to the intensity of the D^0X.

For the samples grown in the presence of Ag, it was seen that the metal is mainly present in small particles attached to the surface of the rods. The presence of higher concentration of Ag promotes the catalytic growth of ZnO rods on top of the previously grown ones. EDS and PIXE revealed the inhomogeneous distribution of Ag in the ZnO crystals. No significant difference was found between the PL features observed for the crystals grown with and without Ag.

ZnO/CNTs composite samples were produced in the form of buckypapers and ZnO nanostructures deposited on top VACNTs arrays. It was observed that the LAFD technique preserves the CNTs structure and avoids the collapse of the VACNTs array, which is a major advantage of the method. Different features in the Raman and PL spectra were observed for the two sets of samples. In the case of the ZnO/VACNTs an enhancement in the overall luminescence was observed when the ZnO was deposited on top of the CNTs and no change in the shape of the spectra was detected. On the other hand, for the buckypaper samples a change in the shape of the NBE emission was observed when the ZnO was mixed with the CNTs, especially in the case of

the TPs samples, where a significantly increase of the 3.31 eV line was verified. Moreover, while in the case of the ZnO deposited on the VACNTs forest the temperature behaviour does not seem to differ from the one observed in the sample deposited in silicon, for the buckypapers a ~ 90 % of the luminescence was extinguished between 14 K and the RT in the case of the ZnO TPs/CNTs composite, while an higher thermal stability (~ 50%) was found for the ZnO NPs/CNTs composite. In both cases, embedding the ZnO in the CNTs yields to an enhanced PL intensity, with a smaller drop of the luminescence intensity in the composites compared with those observed in ZnO NPs and TPs alone. The electrical properties of the ZnO/VACNTs hybrid samples reveal a rectifying behaviour which is different from the one obtained for the ZnO sample. Electrical measurements in the VACNTs samples show an ohmic response. In the case of the buckypapers, the samples resistivity was shown to be of the order of ~ 10^{-1} $\Omega \cdot$cm for all set of samples, with a carrier mobility dependent on the ZnO morphology. The lower mobility was found to occur for the ZnO TPs/CNTs composite where a high carrier concentration was measured. Since no significant changes were found for the electrical properties between the three types of samples, the obtained results suggest that a good combination of the ZnO optical and CNTs electrical properties can be achieved by an appropriate choice and dispersion of the ZnO nanostructures, which is of potential importance for technological applications. This kind of structures exhibit interesting properties for applications in photovoltaic devices due to their co-operative behaviour. CNTs offer extremely large surface areas which are important for building nanoscale heterojunctions between conductive and semiconductor materials for energy conversion devices.

$Cd_xZn_{1-x}O$ samples grown by MBE with different x_{Cd} were studied by optical techniques, evidencing the possibility to tune the ZnO bandgap to the visible region by alloying this semiconductor with CdO. As expected, the NBE emission was seen to shift from the UV to the orange spectral region by increasing the Cd content up to 0.38. The thermal stability was assessed by temperature-dependent PL measurements, revealing a strong thermal quenching, with a decrease of the intensity around two orders of magnitude between 14 K and RT. Similar activation energy values were estimated for all the samples, suggesting the presence of the same recombination mechanisms. Power dependence studies on the sample with x_{Cd} = 0.25 pointed for the excitonic nature of the identified transitions. Although more detailed studies and more reliable information is need regarding the properties of the $Cd_xZn_{1-x}O$ alloys, this ternary is immerging as an excellent candidate for optical applications in the visible range and it is a possible competitor for the more conventional and well-known $In_xGa_{1-x}N$ alloys.

6.6. References

1. C. Jagadish and S. J. Pearton, *Zinc Oxide Bulk, Thin Films and Nanostructures: Processing, Properties and Applications* (Elsevier, 2006).

2. D. Calestani, M. Zha, R. Mosca, A. Zappettini, M. C. Carotta, V. Di Natale, and L. Zanotti, Sensors Actuators B Chem. **144**, 472 (2010).

3. C. Ronning, N. G. Shang, I. Gerhards, H. Hofsäss, and M. Seibt, J. Appl. Phys. **98**, 034307 (2005).

4. Y. Qiu and S. Yang, Adv. Funct. Mater. **17**, 1345 (2007).

5. J. Scott, Phys. Rev. B **2**, 1209 (1970).

6. X. Zhu, H.-Z. Wu, D.-J. Qiu, Z. Yuan, G. Jin, J. Kong, and W. Shen, Opt. Commun. **283**, 2695 (2010).

7. B. K. Meyer, H. Alves, D. M. Hofmann, W. Kriegseis, D. Forster, F. Bertram, J. Christen, A. Hoffmann, M. Straßburg, M. Dworzak, U. Haboeck, and A. V. Rodina, Phys. Status Solidi **241**, 231 (2004).

8. A. Teke, Ü. Özgür, S. Doğan, X. Gu, H. Morkoç, B. Nemeth, J. Nause, and H. Everitt, Phys. Rev. B **70**, 195207 (2004).

9. K. Lischka, A. Waag, H. Mariette, J. Neugebauer, M. R. Wagner, H. W. Kunert, A. G. J. Machatine, A. Hoffmann, P. Niyongabo, J. Malherbe, and J. Barnas, Microelectronics J. **40**, 289 (2009).

10. R. Dingle, Phys. Rev. Lett. **23**, 579 (1969).

11. Ü. Özgür, Y. I. Alivov, C. Liu, A. Teke, M. A. Reshchikov, S. Doğan, V. Avrutin, S.-J. Cho, and H. Morkoç, J. Appl. Phys. **98**, 041301 (2005).

12. D. Byrne, F. Herklotz, M. O. Henry, and E. McGlynn, J. Phys. Condens. Matter **24**, 215802 (2012).

13. T. Monteiro, A. J. Neves, M. C. Carmo, M. J. Soares, M. Peres, J. Wang, E. Alves, E. Rita, and U. Wahl, J. Appl. Phys. **98**, 013502 (2005).

14. J. Grabowska, A. Meaney, K. K. Nanda, J.-P. Mosnier, M. O. Henry, J.-R. Duclère, and E. McGlynn, Phys. Rev. B **71**, 115439 (2005).

15. D. Reynolds, C. Litton, and T. Collins, Phys. Rev. **140**, A1726 (1965).

16. C. Klingshirn, R. Lévy, J. B. Grun, and B. Hönerlage, Solid State Commun. **20**, 413 (1976).

17. K. Thonke, T. Gruber, N. Teofilov, R. Schönfelder, A. Waag, and R. Sauer, Phys. B Condens. Matter **308**, 945 (2001).

18. D. C. Look, D. C. Reynolds, C. W. Litton, R. L. Jones, D. B. Eason, and G. Cantwell, Appl. Phys. Lett. **81**, 1830 (2002).

19. M. Schirra, R. Schneider, A. Reiser, G. M. Prinz, M. Feneberg, J. Biskupek, U. Kaiser, C. E. Krill, K. Thonke, and R. Sauer, Phys. Rev. B **77**, 125215 (2008).

20. Ü. Özgür, D. Hofstetter, and H. Morkoç, Proc. IEEE **98**, 1255 (2010).

21. M. Brandt, H. von Wenckstern, G. Benndorf, M. Lange, C. P. Dietrich, C. Kranert, C. Sturm, R. Schmidt–Grund, H. Hochmuth, M. Lorenz, M. Grundmann, M. R. Wagner, M. Alic, C. Nenstiel, and A. Hoffmann, Phys. Rev. B **81**, 073306 (2010).

22. L. Wang and N. C. Giles, J. Appl. Phys. **94**, 973 (2003).

23. L. Wischmeier, T. Voss, I. Rückmann, J. Gutowski, A. Mofor, A. Bakin, and A. Waag, Phys. Rev. B **74**, 195333 (2006).

24. M. Schirra, R. Schneider, A. Reiser, G. M. Prinz, M. Feneberg, J. Biskupek, U. Kaiser, C. E. Krill, R. Sauer, and K. Thonke, Phys. B Condens. Matter **401-402**, 362 (2007).

25. K. Thonke, M. Schirra, R. Schneider, A. Reiser, G. M. Prinz, M. Feneberg, J. Biskupek, U. Kaiser, and R. Sauer, Microelectronics J. **40**, 210 (2009).

26. D. Tainoff, B. Masenelli, P. Melinon, A. Belsky, G. Ledoux, D. Amans, C. Dujardin, N. Fedorov, and P. Martin, J. Lumin. **129**, 1798 (2009).

27. A. B. Djurišić, Y. H. Leung, K. H. Tam, Y. F. Hsu, L. Ding, W. K. Ge, Y. C. Zhong, K. S. Wong, W. K. Chan, H. L. Tam, K. W. Cheah, W. M. Kwok, and D. L. Phillips, Nanotechnology **18**, 095702 (2007).

28. A. F. Kohan, G. Ceder, D. Morgan, and C. G. Van De Walle, Phys. Rev. B **61**, 19 (2000).

29. T. Schmidt, K. Lischka, and W. Zulehner, Phys. Rev. B **45**, 8989 (1992).

30. Z.-M. Liao, H.-Z. Zhang, Y.-B. Zhou, J. Xu, J.-M. Zhang, and D.-P. Yu, Phys. Lett. A **372**, 4505 (2008).

31. Q. Li and G. T. Wang, Nano Lett. **10**, 1554 (2010).

32. J. Rodrigues, S. M. C. Miranda, A. J. S. Fernandes, E. Nogales, L. C. Alves, E. Alves, G. Tourbot, T. Auzelle, B. Daudin, B. Méndez, T. Trindade, K. Lorenz, F. M. Costa, and T. Monteiro, Phys. Status Solidi **10**, 667 (2013).

33. X. T. Zhou, F. Heigl, M. W. Murphy, T. K. Sham, T. Regier, I. Coulthard, and R. I. R. Blyth, Appl. Phys. Lett. **89**, 213109 (2006).

34. H. Landolt, R. Börnstein, H. Fischer, O. Madelung, and G. Deuschle, *Landolt-Bornstein: Numerical Data and Functional Relationships in Science and Technology, Volume 17* (Springer Verlag, 1987).

35. R. Cuscó, E. Alarcón-Lladó, J. Ibáñez, L. Artús, J. Jiménez, B. Wang, and M. Callahan, Phys. Rev. B **75**, 165202 (2007).

36. H. Siegle, G. Kaczmarczyk, L. Filippidis, A. P. Litvinchuk, A. Hoffmann, and C. Thomsen, Phys. Rev. B **55**, 7000 (1997).

37. X. L. Wu, G. G. Siu, C. L. Fu, and H. C. Ong, Appl. Phys. Lett. **78**, 2285 (2001).

38. F. K. Shan, G. X. Liu, W. J. Lee, and B. C. Shin, J. Appl. Phys. **101**, 053106 (2007).

39. S. A. Studenikin and M. Cocivera, J. Appl. Phys. **91**, 5060 (2002).

40. Q. X. Zhao, M. Willander, R. E. Morjan, Q.-H. Hu, and E. E. B. Campbell, Appl. Phys. Lett. **83**, 165 (2003).

41. L. Schneider, S. V. Zaitsev, G. Bacher, W. Jin, and M. Winterer, J. Appl. Phys. **102**, 023524 (2007).

42. M. A. M. Al-Suleiman, A. Bakin, and A. Waag, J. Appl. Phys. **106**, 063111 (2009).

43. M. R. Wagner, P. Zimmer, A. Hoffmann, and C. Thomsen, Phys. Status Solidi – Rapid Res. Lett. **1**, 169 (2007).

44. J. Fallert, R. Hauschild, F. Stelzl, A. Urban, M. Wissinger, H. Zhou, C. Klingshirn, and H. Kalt, J. Appl. Phys. **101**, 073506 (2007).

45. S. S. Kurbanov and T. W. Kang, J. Lumin. **130**, 767 (2010).

46. D. Tainoff, B. Masenelli, P. Mélinon, A. Belsky, G. Ledoux, D. Amans, C. Dujardin, N. Fedorov, and P. Martin, Phys. Rev. B **81**, 115304 (2010).

47. V. Khranovskyy, A. M. Glushenkov, Y. Chen, A. Khalid, H. Zhang, L. Hultman, B. Monemar, and R. Yakimova, Nanotechnology **24**, 215202 (2013).

48. G. Jacopin, L. Rigutti, L. Largeau, F. Fortuna, F. Furtmayr, F. H. Julien, M. Eickhoff, and M. Tchernycheva, J. Appl. Phys. **110**, 064313 (2011).

49. B. P. Falcão, J. P. Leitão, M. R. Correia, M. R. Soares, F. M. Morales, J. M. Mánuel, R. Garcia, A. Gustafsson, M. V. B. Moreira, A. G. de Oliveira, and J. C. González, J. Appl. Phys. **114**, 183508 (2013).

50. T. Gfroerer, Encycl. Anal. Chem. 9209 (2000).

51. K. Ip, M. E. Overberg, Y. W. Heo, D. P. Norton, S. J. Pearton, C. E. Stutz, S. O. Kucheyev, C. Jagadish, J. S. Williams, B. Luo, F. Ren, D. C. Look, and J. M. Zavada, Solid. State. Electron. **47**, 2255 (2003).

52. C.-C. Lin, H.-P. Chen, H.-C. Liao, and S.-Y. Chen, Appl. Phys. Lett. **86**, 183103 (2005).

53. A. Dev, R. Niepelt, and J. Richters, Nanotechnology **21**, 065709 (2010).

54. C. Chen, H. He, Y. Lu, K. Wu, and Z. Ye, ACS Appl. Mater. Interfaces **5**, 6354 (2013).

55. T. Børseth, F. Tuomisto, J. Christensen, E. Monakhov, B. Svensson, and A. Kuznetsov, Phys. Rev. B **77**, 045204 (2008).

56. Z. N. Urgessa, J. R. Botha, M. O. Eriksson, C. M. Mbulanga, S. R. Dobson, S. R. Tankio Djiokap, K. F. Karlsson, V. Khranovskyy, R. Yakimova, and P.-O. Holtz, J. Appl. Phys. **116**, 123506 (2014).

57. N. Y. Garces, L. Wang, L. Bai, N. C. Giles, L. E. Halliburton, and G. Cantwell, Appl. Phys. Lett. **81**, 622 (2002).

58. P. J. Dean, D. J. Robbins, S. G. Bishopt, J. A. Savage, and P. Porteous, J. Phys. C Solid State Phys. **14**, 2847 (1981).

59. T. Monteiro, C. Boemare, M. J. Soares, E. Rita, and E. Alves, J. Appl. Phys. **93**, 8995 (2003).

60. P. Dahan, V. Fleurov, and P. Thurian, J. Phys. Condens. Matter **10**, 2007 (1998).

61. J. Rodrigues, M. R. N. Soares, R. G. Carvalho, A. J. S. Fernandes, M. R. Correia, T. Monteiro, and F. M. Costa, Thin Solid Films **520**, 4717 (2012).

62. Q. Simon, D. Barreca, D. Bekermann, A. Gasparotto, C. Maccato, E. Comini, V. Gombac, P. Fornasiero, O. I. Lebedev, S. Turner, A. Devi, R. A. Fischer, and G. Van Tendeloo, Int. J. Hydrogen Energy **36**, 15527 (2011).

63. Y. Zheng, L. Zheng, Y. Zhan, X. Lin, Q. Zheng, and K. Wei, Inorg. Chem. **46**, 6980 (2007).

64. R. Georgekutty, M. K. Seery, and S. C. Pillai, J. Phys. Chem. C **112**, 13563 (2008).

65. J. Im, J. Singh, J. W. Soares, D. M. Steeves, and J. E. Whitten, J. Phys. Chem. C **115**, 10518 (2011).

66. W. Lu, G. Liu, S. Gao, S. Xing, and J. Wang, Nanotechnology **19**, 445711 (2008).

67. C. Karunakaran, V. Rajeswari, and P. Gomathisankar, J. Alloys Compd. **508**, 587 (2010).

68. Y. Zhang, Z. Zhang, B. Lin, Z. Fu, and J. Xu, J. Phys. Chem. B **109**, 19200 (2005).

69. Y. Yan, M. M. Al-Jassim, and S.-H. Wei, Appl. Phys. Lett. **89**, 181912 (2006).

70. H. S. Kang, B. Du Ahn, J. H. Kim, G. H. Kim, S. H. Lim, H. W. Chang, and S. Y. Lee, Appl. Phys. Lett. **88**, 202108 (2006).

71. Q. Wan, Z. Xiong, J. Dai, J. Rao, and F. Jiang, Opt. Mater. (Amst). **30**, 817 (2008).

72. I. Sakaguchi and K. Watanabe, J. Ceram. Soc. Japan **118**, 217 (2010).

73. F. X. Bock, T. M. Christensen, S. B. Rivers, L. D. Doucette, and R. J. Lad, Thin Solid Films **468**, 57 (2004).

74. D. Eder, Chem. Rev. **110**, 1348 (2010).

75. D. J. Yang, S. G. Wang, Q. Zhang, P. J. Sellin, and G. Chen, Phys. Lett. A **329**, 207 (2004).

76. B. Zhao, H. Hu, E. Bekyarova, M. E. Itkis, S. Niyogi, and R. C. Haddon, in *Dekker Encycl. Nanosci. Nanotechnology, Second Ed.* (2009).

77. D. Tasis, N. Tagmatarchis, A. Bianco, and M. Prato, Chem. Rev. **106**, 1105 (2006).

78. M. D. Rein, O. Breuer, and H. D. Wagner, Compos. Sci. Technol. **71**, 373 (2011).

79. L.-P. Zhu, G.-H. Liao, W.-Y. Huang, L.-L. Ma, Y. Yang, Y. Yu, and S.-Y. Fu, Mater. Sci. Eng. B **163**, 194 (2009).

80. B. K. Gupta, V. Grover, G. Gupta, and V. Shanker, Nanotechnology **21**, 475701 (2010).

81. Y. Zhu, H. I. Elim, Y.-L. Foo, T. Yu, Y. Liu, W. Ji, J.-Y. Lee, Z. Shen, A. T. S. Wee, J. T. L. Thong, and C. H. Sow, Adv. Mater. **18**, 587 (2006).

82. I. Sameera, R. Bhatia, and V. Prasad, Phys. B Condens. Matter **405**, 1709 (2010).

83. J. Khanderi, R. C. Hoffmann, A. Gurlo, and J. J. Schneider, J. Mater. Chem. **19**, 5039 (2009).

84. W.-D. Zhang, L.-C. Jiang, and J.-S. Ye, J. Phys. Chem. C **113**, 16247 (2009).

85. H. Kim and W. Sigmund, Appl. Phys. Lett. **81**, 2085 (2002).

86. J. G. Ok, S. H. Tawfick, K. A. Juggernauth, K. Sun, Y. Zhang, and A. J. Hart, Adv. Funct. Mater. **20**, 2470 (2010).

87. X. Yan, B.-K. Tay, and P. Miele, Carbon N. Y. **46**, 753 (2008).

88. C. S. Chen, X. H. Chen, B. Yi, T. G. Liu, W. H. Li, L. S. Xu, Z. Yang, H. Zhang, and Y. G. Wang, Acta Mater. **54**, 5401 (2006).

89. A. Chrissanthopoulos, S. Baskoutas, N. Bouropoulos, V. Dracopoulos, D. Tasis, and S. N. Yannopoulos, Thin Solid Films **515**, 8524 (2007).

90. C. Zhang, G. Wang, M. Liu, Y. Feng, Z. Zhang, and B. Fang, Electrochim. Acta **55**, 2835 (2010).

91. G.-Q. Mo, J.-S. Ye, and W.-D. Zhang, Electrochim. Acta **55**, 511 (2009).

92. J. Klanwan, N. Akrapattangkul, V. Pavarajarn, T. Seto, Y. Otani, and T. Charinpanitkul, Mater. Lett. **64**, 80 (2010).

93. K. A. Alim, V. A. Fonoberov, M. Shamsa, and A. A. Balandin, J. Appl. Phys. **97**, 124313 (2005).

94. H.-B. Zhang, G.-D. Lin, Z.-H. Zhou, X. Dong, and T. Chen, Carbon N. Y. **40**, 2429 (2002).

95. S. Reich and C. Thomsen, Philos. Trans. A. Math. Phys. Eng. Sci. **362**, 2271 (2004).

96. M. Baibarac, I. Baltog, S. Lefrant, J. Y. Mevellec, and M. Husanu, Phys. E Low-Dimensional Syst. Nanostructures **40**, 2556 (2008).

97. M. Baibarac, I. Baltog, T. Velula, I. Pasuk, S. Lefrant, and N. Gautier, J. Phys. Condens. Matter **21**, 445801 (2009).

98. O. Harnack, C. Pacholski, H. Weller, A. Yasuda, and J. M. Wessels, Nano Lett. **3**, 1097 (2003).

99. W. I. Park, G.-C. Yi, J.-W. Kim, and S.-M. Park, Appl. Phys. Lett. **82**, 4358 (2003).

100. J.-R. Kim, H. Oh, H. M. So, J.-J. Kim, J. Kim, C. J. Lee, and S. C. Lyu, Nanotechnology **13**, 701 (2002).

101. X. Yang, J. Lee, L. Yuan, S.-R. Chae, V. K. Peterson, A. I. Minett, Y. Yin, and A. T. Harris, Carbon N. Y. **59**, 160 (2013).

102. J.-H. Liu, L. Saravanan, and H.-Y. Miao, Mater. Lett. **134**, 30 (2014).

103. G. Trakakis, D. Tasis, J. Parthenios, C. Galiotis, and K. Papagelis, Materials (Basel). **6**, 2360 (2013).

104. S. M. Cooper, H. F. Chuang, M. Cinke, B. A. Cruden, and M. Meyyappan, Nano Lett. **3**, 189 (2003).

105. C. Zhou, S. Kumar, C. D. Doyle, and J. M. Tour, Chem. Mater. **17**, 1997 (2005).

106. S. Sfaelou, M. Antoniadou, G. Trakakis, V. Dracopoulos, D. Tasis, J. Parthenios, C. Galiotis, K. Papagelis, and P. Lianos, Electrochim. Acta **80**, 399 (2012).

107. G. Trakakis, D. Tasis, C. Aggelopoulos, J. Parthenios, C. Galiotis, and K. Papagelis, Compos. Sci. Technol. **77**, 52 (2013).

108. G.-Y. Zeng, K.-S. Nian, and K.-Y. Lee, Diam. Relat. Mater. **19**, 1457 (2010).

109. C. Pirlot, I. Willems, and A. Fonseca, Adv. Eng. Mater. **4**, C 183 (2002).

110. S. Baruah and J. Dutta, Sci. Technol. Adv. Mater. **10**, 013001 (2009).

111. J. Rodrigues, D. Mata, A. J. S. Fernandes, M. A. Neto, R. F. Silva, T. Monteiro, and F. M. Costa, Acta Mater. **60**, 5143 (2012).

112. T. Holz, D. Mata, N. F. Santos, I. Bdikin, A. J. S. Fernandes, and F. M. Costa, ACS Appl. Mater. Interfaces **6**, 22649 (2014).

113. P. Slobodian, P. Riha, A. Lengalova, P. Svoboda, and P. Saha, Carbon N. Y. **49**, 2499 (2011).

114. D. V Sathish, C. Rama Krishna, C. Venkata Reddy, U. S. Udayachandran Thampy, and R. V. S. S. N. Ravikumar, Phys. Scr. **86**, 035708 (2012).

115. H. Morkoç and Ü. Özgür, *Zinc Oxide: Fundamentals, Materials and Device Technology* (John Wiley & Sons, 2008).

116. A. Redondo-Cubero, J. Rodrigues, M. Brandt, P. Schäfer, F. Henneberger, M. R. Correia, T. Monteiro, E. Alves, and K. Lorenz, in *SPIE OPTO*, edited by F. H. Teherani, D. C. Look, and D. J. Rogers (International Society for Optics and Photonics, 2013), p. 86260N.

117. C. F. Klingshirn, *Semiconductor Optics* (Springer, 2007).

118. H. Kang, J. Kim, J. Kim, and S. Lee, J. Appl. Phys. **99**, 066113 (2006).

119. J. Jiang, L. Zhu, Y. Li, Y. Guo, W. Zhou, L. Cao, H. He, and Z. Ye, J. Alloys Compd. **547**, 59 (2013).

120. T. Gruber, C. Kirchner, R. Kling, F. Reuss, A. Waag, F. Bertram, D. Forster, J. Christen, and M. Schreck, Appl. Phys. Lett. **83**, 3290 (2003).

121. T. Makino, Y. Segawa, M. Kawasaki, A. Ohtomo, R. Shiroki, K. Tamura, T. Yasuda, and H. Koinuma, Appl. Phys. Lett. **78**, 1237 (2001).

122. X. Ma, P. Chen, R. Zhang, and D. Yang, J. Alloys Compd. **509**, 6599 (2011).

123. W. F. Yang, B. Liu, R. Chen, L. M. Wong, S. J. Wang, and H. D. Sun, Appl. Phys. Lett. **97**, 061911 (2010).

124. X. D. Zhang, M. L. Guo, W. X. Li, and C. L. Liu, J. Appl. Phys. **103**, 063721 (2008).

125. H. S. Kang, S. H. Lim, J. W. Kim, H. W. Chang, G. H. Kim, J.-H. Kim, S. Y. Lee, Y. Li, J.-S. Lee, J. K. Lee, M. A. Nastasi, S. A. Crooker, and Q. X. Jia, J. Cryst. Growth **287**, 70 (2006).

126. R. W. Martin, P. G. Middleton, K. P. O'Donnell, and W. Van der Stricht, Appl. Phys. Lett. **74**, 263 (1999).

127. I. A. Buyanova, J. P. Bergman, G. Pozina, W. M. Chen, S. Rawal, D. P. Norton, S. J. Pearton, A. Osinsky, and J. W. Dong, Appl. Phys. Lett. **90**, 261907 (2007).

128. M. Lange, C. P. Dietrich, K. Brachwitz, T. Böntgen, M. Lorenz, and M. Grundmann, J. Appl. Phys. **112**, 103517 (2012).

129. J. Ishihara, A. Nakamura, S. Shigemori, T. Aoki, and J. Temmyo, Appl. Phys. Lett. **89**, 091914 (2006).

130. S. Kalusniak, S. Sadofev, J. Puls, and F. Henneberger, Laser Photonics Rev. **3**, 233 (2009).

131. K. P. O'Donnell, R. W. Martin, and P. G. Middleton, Phys. Rev. Lett. **82**, 237 (1999).

132. Z. Yang, L. Li, Z. Zuo, and J. L. Liu, J. Cryst. Growth **312**, 68 (2009).

133. A. Mohanta and R. K. Thareja, J. Appl. Phys. **103**, 024901 (2008).

134. D. W. Hamby, D. A. Lucca, M. J. Klopfstein, and G. Cantwell, J. Appl. Phys. **93**, 3214 (2003).

135. A. Mohanta and R. K. Thareja, J. Appl. Phys. **107**, 084904 (2010).

136. W. F. Yang, L. M. Wong, S. J. Wang, H. D. Sun, C. H. Ge, A. Y. S. Lee, and H. Gong, Appl. Phys. Lett. **98**, 121903 (2011).

137. F. A. J. M. Driessen, G. J. Bauhuis, S. M. Olsthoorn, and L. J. Giling, Phys. Rev. B **48**, 7889 (1993).

138. Y.-H. Cho, G. H. Gainer, A. J. Fischer, J. J. Song, S. Keller, U. K. Mishra, and S. P. DenBaars, Appl. Phys. Lett. **73**, 1370 (1998).

Chapter 7. Applications of LAFD grown ZnO

ZnO is a very attractive semiconductor for applications in different areas due its abundance, low cost, nontoxicity, high electron mobility, easy synthesis, among other properties [1–4]. In this sense, the potential application of the LADF produced ZnO structures in the photocatalysis and photovoltaic fields was tested. The preliminary results obtained are discussed in the present chapter, showing interesting prospects in both fields. Notwithstanding, much more work must be done to improve the LAFD grown ZnO structures for the mentioned applications.

7.1. Solar cells

As worldwide energy demand increases, conventional energy resources, as the natural fossil fuels like oil or coal, are expected to reach an end in a near future if the energy consumption continues to increase [5]. In this sense, intensive research has been devoted to find alternatives for energy production. Photovoltaic cells constitute ideal devices, capable to provide clean electrical energy (since the solar energy is directly converted into electrical energy) without any other fuel sources or realising sub-products pollutants to the environment [5,6]. Moreover, the solar energy is unlimited, is free of charge, and abundant in many parts of the world [6,7].

The energy supply for a solar cell corresponds to the photons coming from the sun. The solar output spectra reaching the planet is distributed in ways that depend on variables like latitude, time of the day, and atmospheric conditions [8]. Solar radiation is partially absorbed during its passage through the atmosphere, which depends on the mass of air through which the radiation passes [9]. The photons path length is called the air mass (AM) and can be approximated by AM = 1/cos ϕ, where ϕ is the angle of elevation of the sun relatively to the normal to the earth's surface [9,10]. Figure 7-1 displays the solar spectra at various AM conditions, resembling the blackbody radiation spectrum (T ~ 5800 K). As can be seen, the sun emits light with a range of wavelengths from the UV to far IR, with its maximum in the visible spectral region [5,10]. Outside the atmosphere, the solar spectrum is designated by AM0, and the one that reaches the surface of the earth is AM1 (for normal incidence) [9]. The AM1.5 G (global) spectrum is the standard for terrestrial applications and the one used for efficiency measurements of solar cells [5,8,10]. In this spectrum $\phi \sim 42^{o}$-45° and the intensity is normalized so that the integrated irradiance[1] is

[1] Amount of radiant energy received from the sun per unit area per unit time.

1000 W m^{-2} [10]. Standard spectra are needed in solar cell research, development, and marketing since the actual spectrum reaching a cell in operation can vary due to weather, season, time of day, and location. In this way, the performance of a given solar cell can be readily compared to that of other devices and evaluated properly [8].

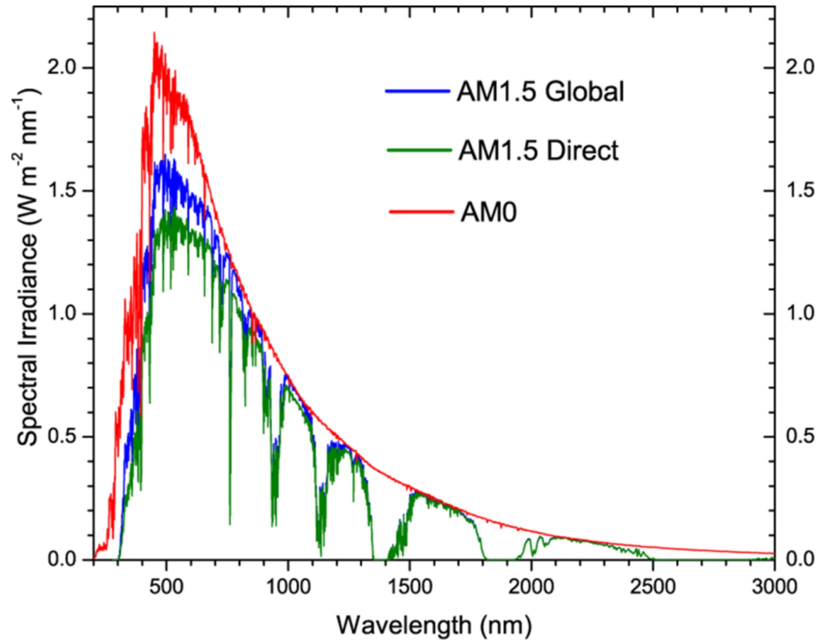

Figure 7-1 – Solar spectra at different air-mass (AM) conditions, resembling the one of blackbody radiation. Image reproduced from [13].

The total power of incident light, P_{in}, per area impinging on the cell for a given photon spectrum, $\Phi_0(\lambda)$, is given by the integral of the incoming energy per time, per area, per bandwidth, Δλ, over the entire spectrum [8]:

$$P_{in} = \int_{\lambda} \frac{hc}{\lambda} \Phi_0(\lambda) \mathrm{d}\lambda. \qquad \textbf{Eq. 7-1}$$

Photovoltaic devices are based on the concept of charge separation at an interface of two materials with distinct conduction mechanism [11]. The solar cells are typically made with semiconductor materials, as Si or titanium dioxide (TiO_2). It converts a fraction of the energy contained in sunlight directly to electrical energy at a voltage and current level determined by the properties of the semiconductor, the solar cell design and construction techniques [12]. The energy conversion consists of absorption of light energy, leading to the formation of electron-hole pairs in the absorber material [6]. The charge carriers are then separated in the interface of the hole and electron transport materials, working as a *p-n* junction. Charge carriers collected by two electrodes give rise to a photocurrent when the two terminals are connected externally [6,8].

7.1.1. Theoretical principles of an ideal solar cell

During a long time the photovoltaic field was dominated by solid-state *p-n* junction like devices based on silicon, which took advantage of its availability, technological integration and

knowledge, provided by the (micro-) electronic industry. Nowadays, the designated "3rd generation" solar cells (based, for instance, on nanostructures or polymeric materials) have established a competitive role [11].

Since the solar cells based on nanocrystalline materials exhibit a more complex structure when compared to the conventional *p-n* junction solar cell, the fundamental phenomena occurring in the cell will be described based in the latter [6]. In this case, the solar cell is assumed to have ideal diode *I-V* characteristics [5]. Under illumination, these characteristics corresponds to the summation of the dark current and the photocurrent and is given by [5,14]

$$I = I_s \left[e^{\frac{eV}{k_B T}} - 1 \right] - I_L, \qquad \textbf{Eq. 7-2}$$

where I_s is the saturation current and I_L is the current due to generation of excess carriers by the absorption of the sunlight. V stands for the applied bias and e, k_B and T assume the standard description taken through the manuscript. For a typical *p-n* junction, the saturation current density is a function of I_s and can be defined as [5,14]

$$J_s = \frac{I_s}{A} = eN_c N_v \left(\frac{1}{N_A} \sqrt{\frac{D_n}{\tau_n}} + \frac{1}{N_D} \sqrt{\frac{D_p}{\tau_p}} \right) e^{\frac{-E_g}{k_B T}}, \qquad \textbf{Eq. 7-3}$$

where A is the cell area, N_c and N_v are the CB and VB effective density of states, respectively, N_A and N_D the acceptor and donor concentration, respectively, and, finally, τ_n and τ_p correspond to the carrier lifetime for electrons and holes, respectively. From this expression it readily follows that I_s decreases exponentially with the bandgap energy, E_g [5].

When $I = 0$, the voltage of the system is designated by *open-circuit voltage* and is written as [5,14]

$$V_{oc} = \frac{k_B T}{e} ln\left(\frac{I_L}{I_s} + 1\right) \approx \frac{k_B T}{e} ln\left(\frac{I_L}{I_s}\right). \qquad \textbf{Eq. 7-4}$$

Thus, for a given photocurrent I_L, V_{oc} increases logarithmically as the saturation current I_s decreases. In this sense, taking the two previous expressions into consideration, one can conclude that to obtain a large V_{oc} value a large bandgap energy is needed[2] [5].

Conversely, when $V = 0$, the current is termed *short-circuit current* and $I_{sc} = I_L$. Figure 7-2 illustrates a characteristic *I-V* curve (Eq. 7-2) from a solar cell, where all the above mentioned quantities are identified. The shaded area corresponds to the maximum power output, P_M, defined as [5]

$$P_M = V_m I_m. \qquad \textbf{Eq. 7-5}$$

Here, V_m corresponds to the maximum voltage that leads to the maximum power output, while I_m is the current when $V = V_m$ (as seen in Figure 7-2).

Considering that the output power is given by [5]

$$P = IV = I_s V \left[e^{\frac{eV}{k_B T}} - 1 \right] - I_L V, \qquad \textbf{Eq. 7-6}$$

[2] V_{oc} is equivalent to the built-in potential of a junction, which has its maximum close to E_g.

the maximum power can be obtained when *dP/dV=0*, and thus

$$P_M = FF\, I_{sc}\, V_{oc}\ . \qquad \text{Eq. 7-7}$$

Here, *FF* is the fill factor which describes the shape of the *I-V* curve. From combining Eqs. 7-5 and 7-7, the *FF* can be written as

$$FF = \frac{V_m I_m}{I_{sc}\, V_{oc}}, \qquad \text{Eq. 7-8}$$

which, in the ideal case, is equal to unity [8].

The overall energy conversion efficiency, η, is given by the photocurrent measured at short-circuit, the open-circuit voltage, the fill factor of the cell and the power of the incident light [5,10]:

$$\eta = \frac{FF\, I_{sc}\, V_{oc}}{P_{in}} (\times\ 100\%). \qquad \text{Eq. 7-9}$$

Another fundamental measurement of the performance of a solar cell is the *external quantum efficiency* (*EQE*) or *incident photon to current conversion efficiency* (*IPCE*). The *IPCE* value gives practical information regarding the monochromatic quantum efficiencies of a cell [10]. This parameter is defined as the photocurrent density produced in the external circuit under monochromatic illumination of the cell divided by the photon flux that reaches the cell [10]

$$IPCE = \frac{J_{sc}(\lambda)}{e\Phi(\lambda)} = 1240\frac{J_{sc}(\lambda)[A \cdot cm^{-2}]}{\lambda\ [nm] P_{in}(\lambda)[W \cdot cm^{-2}]}, \qquad \text{Eq. 7-10}$$

with $J_{sc} = I_{sc}/A$.

In a real solar cell, the effect of parallel resistance, also known as shunt resistance, R_{sh}, (due to leakage current, *e.g.* by local shorts of the solar cell) and serial resistance R_s (due to ohmic loss) should also be considered [14]. In practice, the shunt resistance has much less effect than the serial resistance and the effect of the latter can be simply obtained by replacing *V* by $(V-IR_S)$ in Eq. 7-2 [5]. The main impact of these parameter is seen on the FF value, which is lowered [5,14].

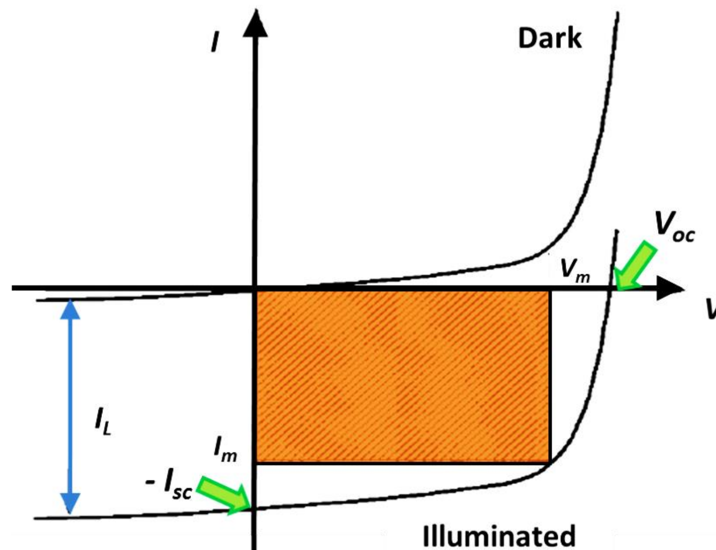

Figure 7-2 – *I-V* characteristics of a solar cell under illumination. Image adapted from [5].

7.1.2. Dye-sensitized solar cells (DSSC)

As mentioned above, a new generation of solar cells based on nanostructured materials have been increasingly dominating the nowadays photovoltaic exploration. Among this new generation photovoltaic devices, dye-sensitized solar cells (DSSCs) have been subject of an intense research worldwide. Since the innovative work conducted by O'Regan and Grätzel [15,16], more than three decades ago, exhaustive work has been devoted to improve the DSSCs performance [10,15,17,18]. This type of solar cells offers low cost and reasonably high light-to-electricity conversion efficiency [19], as well as innovative design opportunities, such as transparency and multicolour options, flexibility and lightweight [10].

DSSCs differ substantially from conventional semiconductor devices in the way that the function of light absorption is separated from charge carrier transport. Contrarily to what happens in a typical cell, where the semiconductor play both the roles of light absorber and charge transporter, in a DSSC these functions are carried out by different components. The absorption of the incident light is made by the dye sensitizer that provides electron transfer to the semiconductor. In comparison to the conventional Si-based photovoltaics (*p*-*n* junction), DSSCs present several advantages, namely the fact that photon absorption has a lower sensitivity to the defects in the semiconductor; the semiconductor-electrolyte interface is easy to form and it is cost effective for production [20].

Figure 7-3 illustrates a typical DSSC based on nanostructured oxide as the active area of the cell. In a simple way, the DSSCs are characterized by the presence of a semiconductor oxide layer, usually mesoporous, which forms a network where electronic conduction can take place. This layer is usually deposited on a transparent conducting oxide coated substrate. A monolayer of the charge transfer dye (the sensitizer) is then attached to the surface of the nanocrystalline layer. Upon photoexcitation, the dye injects an electron into the CB of the semiconductor. This electron-transfer results in an oxidation state of the dye that is further restored to its ground state by electron transfer from the electrolyte. This electron transfer minimizes the undesirable regeneration of the sensitizer via recapture of the electron in the CB of the semiconductor. The charge state of the electrolyte (frequently an organic solvent containing redox system such as the iodide/triiodide couple) is regenerated in the cathode (counter-electrode), usually comprised by a platinum-coated glass substrate, placed parallel to the working electrode with a face-to-face configuration and with the space between the two electrodes filled with the electrolyte. The working circuit is completed via electron migration through the external load. Thus, there is a strong and complex interaction between all the components, especially in the semiconductor/dye/electrolyte interfaces. The voltage generated under illumination corresponds to the difference between the Fermi level of the electron in the semiconductor and the redox potential of the electrolyte. In summary, the device generates electric power from light without suffering any permanent chemical transformation [10,11,21].

An important benefit of employing nanostructures in DSSCs is that the photoelectrode films, formed by nanostructures, are highly porous. These films offer a larger surface area for dye adsorption, which enhances the optical absorption and leads to the improvement of the solar cell efficiency [21].

The most widely used semiconductor oxide for this type of photovoltaic devices is TiO_2, since it is the one that exhibits higher efficiencies, up to now [22,23]. Other metal oxides have been used as photoelectrodes, as is the case of tin oxide (SnO_2), niobium pentoxide (Nb_2O_5) or ZnO, among others [10,24–26]. In fact, ZnO was one of the first metal oxide materials applied in sensitization studies [18,27,28]. Besides its low cost and non-toxicity, ZnO is supposed to be a potential substitute for TiO_2 owning to their similar bandgap and electron affinities [17,29]. The main advantages of ZnO over TiO_2 are its higher electron mobility (see Table 1-4), and as seen before, the ability to be easily produced in a great variety of nanostructured morphologies. It is estimated that the former property may lead to an improvement of the electron transport, while the later one is expected to offer a wide range of photoelectrode architectures/networks, enabling the design of surface areas that maximize the dye absorption [10,17,29–31]. Moreover, an adequate choice of morphology may result in a significant improvement of the efficient charge transport, a crucial aspect to obtain a good photovoltaic efficiency [17].

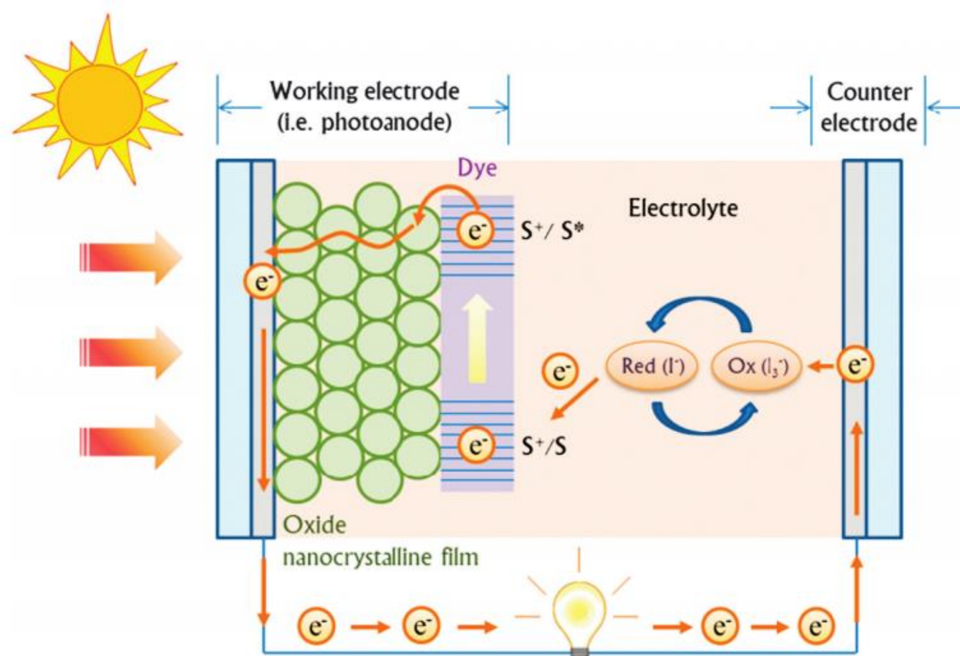

Figure 7-3 – Scheme of a typical dye-sensitized solar cell, and its principles of operation. The working cycle starts with the photoexcitation of the sensitizer (S), followed by electron injection into the CB of the oxide semiconductor. Then, the dye molecule is regenerated by the redox system, which regenerates itself at the counter-electrode with the electrons travelling through the external circuit [16]. Image reprinted from [32].

A great amount of work in ZnO DSSCs has been done using different morphologies and aiming its optimization for the incorporation in the cell active area [17,19,21,24,30,33]. To the best of our knowledge, the best efficiency reported in ZnO-based DSSCs is around ~ 7.5 % for a cell composed by hierarchical aggregates of ZnO nanocrystallites and using the N719 dye as sensitizer [34]. However, the majority of DSSCs using this semiconductor report values mostly between 0.4–5.8 % [31]. Even though the energy conversion efficiency of ZnO based DSSCs remains lower than the values found for TiO_2-based DSSCs, mostly due to the poor chemically stability of ZnO under acidic

dye solutions [18,29], increasingly research has been devoted to this material in order to overcome these limitations.

As pointed out, the dye molecules adsorbed in the semiconductor play a role of ‘’antenna’’ for photon harvesting in DSSCs. For this reason, an appropriate choice of dye is important. Intensive research has been employed aiming to increase the extinction coefficient and widen the optical absorption spectrum [21]. Photosensitizers must gather several essential characteristics: spectral absorption must cover a wide spectral range in the visible and NIR regions; anchoring groups should be present in order to provide a strong bind of the dye onto the semiconductor surface; the excited level of the sensitizer should be higher in energy than the CB edge of semiconductor (in the case of *n*-type DSSCs) so that an efficient electron transfer process between the excited dye and the CB of the semiconductor can occur; the oxidized state level of the dye must be more positive than the redox potential of the electrolyte in order to achieve an efficient dye regeneration; dye aggregation should be avoided; and, finally, the photosensitizer should be photo- electrochemical and thermally stable [10].

7.1.3. ZnO-based DSSCs fabrication

In the current dissertation the production of ZnO TPs and NPs by the LAFD technique were explored for the incorporation in the active area of DSSCs. The growth of the ZnO nanostructures was carried out in air with a laser power of 60 W. As mentioned in the previous chapter, with this power mostly TPs are produced, although some nanoparticles can also be found in the same run of growth due to the initial heating stage of the process. In order to compare the results obtained with nanostructures produced by LAFD and infer about their advantages over other structures, hydrothermal prepared ZnO nano/microflowers [1] (courtesy of *CENIMAT/I3N*) and colloidal NPs [35,36](courtesy of *CICECO*) were also evaluated.

A schematic representation of the cell’s structure is depicted in Figure 7-4. The cell is comprised by two electrodes made of fluorine-doped tin oxide (FTO) coated glass. For the counter-electrode, a small area is also coated with platinum, while the other one is coated with a ZnO blocking layer, prior to the ZnO active area deposition. The blocking layer is used in order to avoid direct contact between the electrolyte and the conducting FTO, which could result in undesirable recombination of electrons between the FTO and the oxidized species in the electrolyte. The cells were assembled by sandwiching all parts together and introducing the electrolyte solution between the electrodes (Figure 7-4).

The ZnO structures produced by the LAFD method were mixed with ethyl cellulose, terpineol and ethanol to form the photoelectrode. This results in a viscous paste. Details of the paste preparation are as follows: 100 mg of ZnO were dispersed in 0.4 ml of ethanol where 50 mg of ethyl cellulose and 405 mg of terpineol were added. The mixture was ultrasonicated during 1 h to obtain a homogeneous paste. FTO coated glasses with a dense ZnO blocking layer (~ 50 nm) were used as substrates. The FTO coating was performed by spray pyrolysis at 500 ^{o}C using a solution consisting of 40 ml ethanol, 4 ml of deionized water, 0.48 g of ammonium fluoride (NH_4F) and 2.81 g of tin chloride pentahydrate ($SnCl_4.{\cdot}5H_2O$).The ZnO blocking layer was deposited by

RF-magnetron sputtering, using a ZnO target with a 99.999 % purity. The working pressure was 1.6×10^{-2} Torr, the substrate was kept at RT and the processing gas was a mixture of argon and oxygen obtained by injecting pure Ar at 18 sccm and 97% Ar + 3% O_2 at 7 sccm. The RF power was 100 W during the sputtering process. A portion of the glass/FTO substrate was left un-coated by the blocking layer to provide the electric contact.

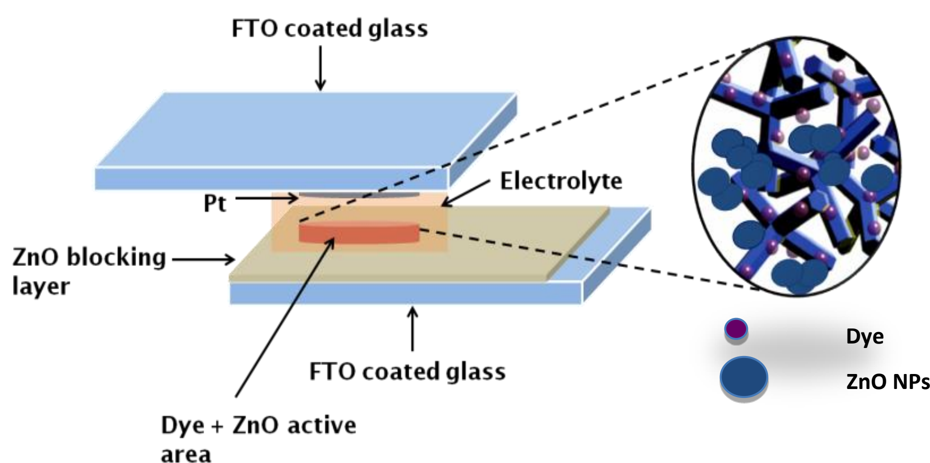

Figure 7-4 – Illustration of the structure of the DSSCs fabricated in this work.

ZnO films for the dye deposition were prepared on the produced substrates via the doctor blade technique and then left to dry in air. The films were deposited in a circular area with 5 mm of diameter using a mask. The thickness was kept nearly constant for all the samples, as defined by the thickness of the used mask. The mask was composed by two layers of scotch tape with a hole of the desired area. To increase the adhesion of the ZnO structures to the substrate and to form a porous ZnO film, the photoelectrodes were then subject to a thermal treatment at 400 ^{o}C for 20 min with a plateau at 100 ^{o}C for 10 min to remove all the organic compounds. The visual appearance of the ZnO electrode is depicted in Figure 7-5a.

The sensitization was performed by immersing the electrodes in a dye solution of 1.7×10^{-4} mol L^{-1} of *cis*-bis(isothiocyanato) bis(2,2-bipyridyl-4,4'-dicarboxylato) ruthenium (II) bis-tetrabutylammonium (N719) dispersed in ethanol, or 3.0×10^{-4}/3.0×10^{-3} mol L^{-1} of the 4,5,6,7-Tetrachloro-2',4',5',7'-tetraiodofluorescein disodium salt (Rose Bengal [RB]) also dispersed in ethanol (Figure 7-5b). The immersion was kept at RT during different loading times. Afterward, the samples were rinsed in ethanol to remove the excess dye on the surface, and dried gently. A platinum-coated FTO/glass was used as counter-electrode. The platinum was deposited using a solution of 2 mg of chloroplatinic acid solution (8 wt% water) in 1 ml of ethanol. The solution was deposited in an area equal to the one of the ZnO electrode (diameter ~ 5 mm), using a similar mask. Six to seven drops of the solution were added to the glass/FTO substrate, and the solution was left to dry between each drop. After the preparation, the counter-electrode was treated at 470 ^{o}C for 20 min. A redox iodide/tri-iodide Iodolyte R150 was used as electrolyte. Figure 7-5c shows the assembled DSSCs.

The solar cells' performance was studied by *J–V* measurements using a solar light simulator with a tungsten-halogen lamp, combined with an infrared filter for spectrum conditioning, resulting in an illumination of 1000 W m^{-2} (AM 1.5). The short circuit density current, open circuit voltage, fill factor, and efficiency were calculated from the *J–V* curves, taking into account a cell active area of ~ 0.196 cm^2 (assuming an active area with a diameter of ~ 5 mm).

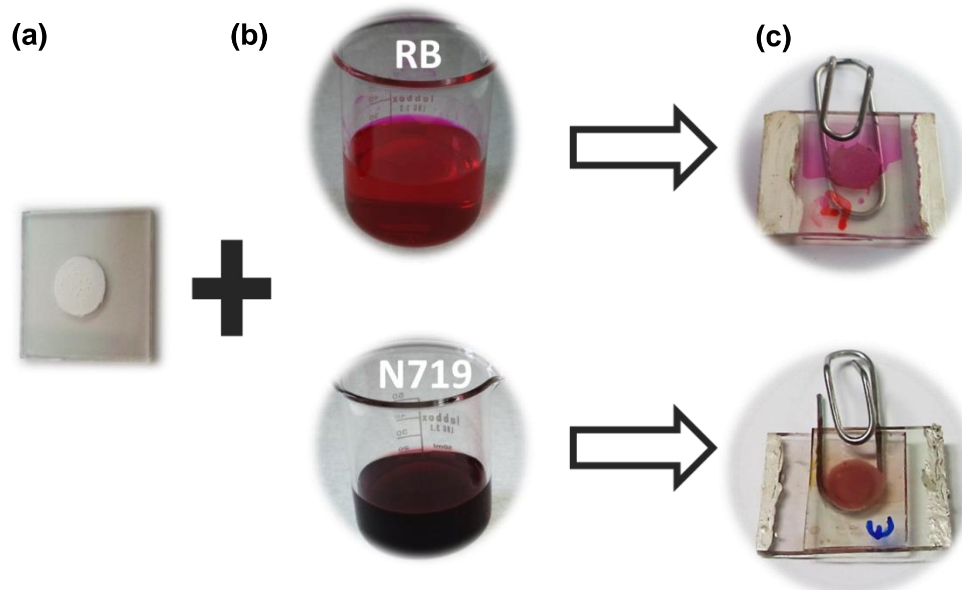

Figure 7-5 – Schematic diagram of the DSSCs sensitization process: the ZnO electrode (a) is immersed in the dye solution (b) during a specific time. Finally, the cell is assembled after drying (c).

Figure 7-6 shows SEM images of the active layer of DSSCs prepared with the ZnO structures produced by the LAFD technique. It is possible to observe that a porous layer was formed by the interconnected network of TPs with different sizes and a small amount of NPs. The porous network is formed by TPs connected to each other, as already observed in similar samples [17]. From the cross-section view (Figure 7-6a) one can estimate a thickness of the active layer of ~ 17 µm. Similar thicknesses were found for all the cells and this parameter was kept fixed during all the studies.

As mentioned in the preparation part, two different dyes (Rose Bengal and N719) were used to evaluate the potential of the LAFD produced nanostructures in ZnO-based DSSCs. These dyes were chosen taking into account the results reported in the literature, indicating an adequate DSSCs performance [2,18,37–39], and the positioning of their energy levels regarding the ZnO and all the components in the cell. Energy level diagrams for Rose Bengal and N719 dyes (and considering all the components) are represented in Figure 7-7a and b, respectively. As was described above, the working principle of a DSSCs can be understood, shortly, as follows: the incident light excites the dye so that it donates electrons from its excited state (LUMO) to the CB of ZnO. Consequently, the electron is then transferred to the FTO electrode [37]. The redox electrolyte regenerates the dye by transferring electrons to the lower energy state (HOMO).

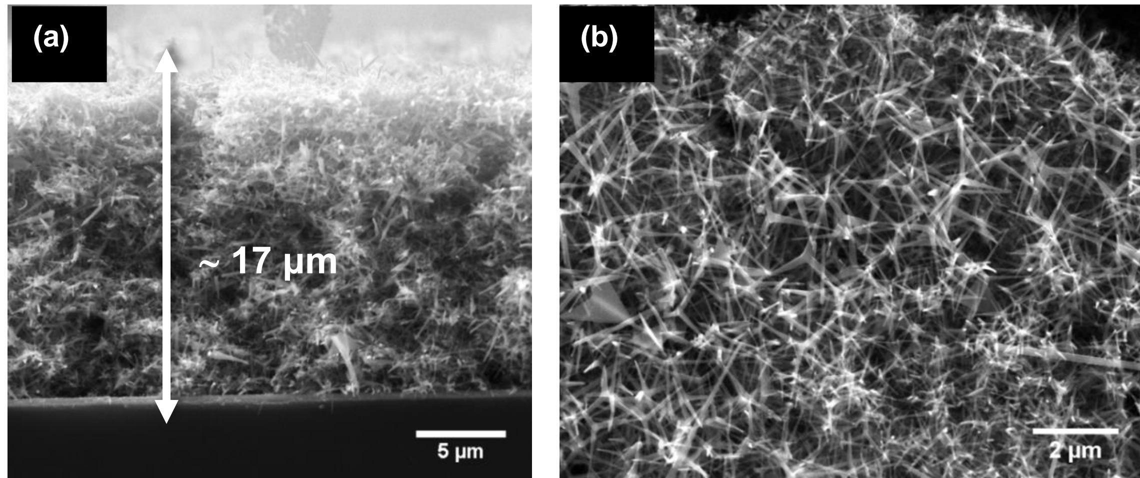

Figure 7-6 – (a) Cross-section and (b) top view SEM images of the DSSCs active area composed by LAFD TPs and a small amount of NPs, prior to immersion in the dye.

Table 7-1 summarizes the best DSSCs parameters that describe the performance of all the tested fabrication conditions. At least three DSSCs devices per test were assembled and some of the tests were repeated more than once due to reproducibility problems. It is important to note that, due to the number of steps involved in the cell's preparation, lack of reproducibility was a constant in the first test attempts, which was fairly overcome by the optimization of the cell preparation procedure.

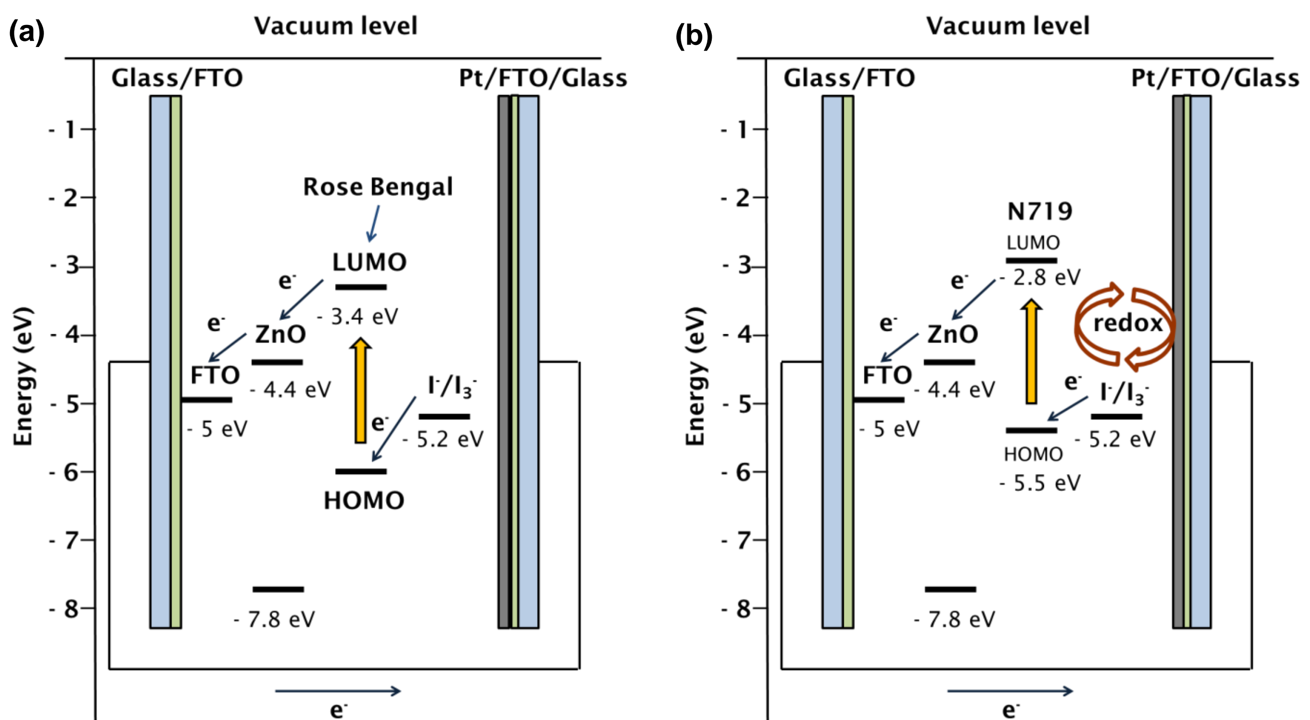

Figure 7-7 – Schematic representation of the energy levels diagram for the DSSC prepared with the (a) Rose Bengal dye and (b) N719 dye, both of them with the iodide-triiodide redox couple electrolyte. Band alignment according to references [37,40,41].

Table 7-1 – V_{oc}, I_{sc}, FF and efficiency values for the ZnO-based DSSCs prepared in this work. The listed values refer to the DSSCs with the highest performance obtained for each set of fabrication conditions. The measurement errors for these parameters are 0.01 (mV, $mA.cm^{-2}$ or %, accordingly). (*No photovoltaic effect was measured for the cells constructed under these conditions.)

Cell	Dye (mol L^{-1})	Time in the dye	Electrode	V_{oc} (mV)	J_{sc} ($mA.cm^{-2}$)	FF (%)	Eff (%)
A	RB: 3.0×10^{-4}	24 h	TPs+NPs	505.86	0.98	68.03	0.34
B	RB: 3.0×10^{-4}	24 h	TPs+NPs + 18 nm ALD layer	504.62	0.40	55.695	0.11
C	RB: 3.0×10^{-4}	48 h	TPs+NPs	327.88	1.68	33.82	0.19
D	RB: 3.0×10^{-4}	16 h	TPs+NPs	515.87	0.70	61.59	0.22
E	RB: 3.0×10^{-4}	12 h	TPs+NPs	503.97	0.65	68.80	0.23
F	RB: 3.0×10^{-4}	6 h	TPs+NPs	486.90	0.39	58.86	0.11
G	RB: 3.0×10^{-4}	1 h	TPs+NPs	329.97	0.28	34.46	0.03
H	RB: 3.0×10^{-3}	24 h	TPs+NPs	354.35	1.92	36.18	0.25
I*	N719: 3.0×10^{-4}	24 h	TPs+NPs	-	-	-	-
J	N719: 3.0×10^{-4}	4 h	TPs+NPs	653.00	0.87	60.19	2.31
K	N719: 3.0×10^{-4}	2 h	TPs+NPs	626.29	0.06	68.20	1.73
L	N719: 3.0×10^{-4}	1 h 30 min	TPs+NPs	655.23	6.17	65.52	2.65
M	**N719: 3.0×10^{-4}**	**1 h**	**TPs+NPs**	**666.15**	**6.43**	**67.80**	**2.90**
N	N719: 3.0×10^{-4}	1 h	TPs+NPs (commercial FTO)	655.23	6.17	65.52	2.65
O	N719: 3.0×10^{-4}	30 min	TPs+NPs	660.99	6.38	66.76	2.82
P	N719: 3.0×10^{-4}	20 min	TPs+NPs	662.82	6.02	61.65	2.46
Q	N719: 3.0×10^{-4}	1 h	Nano/ microflowers	631.67	3.63	55.97	1.28
R	N719: 3.0×10^{-4}	1 h	Colloidal NPs	587.56	1.75	65.48	0.67

The first cell's tests were carried out using the Rose Bengal dye as sensitizer. Experimental parameters like dye concentration and immersion time in the dye solution were evaluated. Additionally, a thin layer of ZnO deposited by atomic layer deposition (ALD) was added to the ZnO electrode with the purpose of improving the connection between the ZnO TPs and NPs network which was expected to enhance the cell efficiency. However, no improvement was observed when this layer was added. In fact, a slight decrease of the efficiency was measured, which could be due to the lower crystallinity of the ALD produced ZnO. Thus, the use of this layer was abandoned for the tests that followed. In general, the efficiency values obtained using Rose Bengal dye were very low (around 0.2%) and considerably different from the ones found in the literature [2,37]. In fact, early in 2015, Mahmoud *et al.* [2] reported one of the highest efficiencies

obtained in a ZnO-based DSSC. A value of 6.74% was measured in a cell composed by ZnO TP-like structures with dimensions on the micrometer range, sensitized during 24 h. The samples were prepared by heating well-mixed powders of ZnO with carbon powders at temperatures ranging from 1000 to 1200 °C.

Even though the cells' performance was not nearly as high as those reported by Mahmoud *et al.* [2], several attempts to improve the results were carried out. Different immersion times in the dye were tested, however with no significant changes. The dye loading time is known to be an extremely important parameter to optimize the cell performance, since not enough sensitization time may result in insufficient dye absorption from the semiconductor, lowering the photon absorption, while leaving the samples for a very long time in the dye solution may lead to the formation of aggregates between the dye molecules, which reduces the photogenerated current [39].The same happen for the dye concentration. The value was chosen taking into consideration the values found in the literature [37]. Since the initial dye concentration gave rise to DSSCs with a low efficiency (especially due to the low J_{sc}), a more concentrated solution was used. Though, it was seen that increasing the dye concentration over an order of magnitude resulted in an increasing of the J_{sc} but in a decrease of the V_{oc} and *FF*, leading to a lower efficiency. The best efficiency value obtained with this dye was ~ 0.34% for a loading time of 24 h and a dye concentration of 3.0×10^{-4} mol L^{-1} (Cell A). The *J-V* characteristics for this cell is shown in Figure 7-8a. The experimental data were well fitted using the diode characteristics of Eq. 7-2, with an ideality factor n close to 2 (± 0.2) and a $J_L \sim 1.01$ (± 0.04) mA.cm^{-2}. In this case, a V_{oc} of 505.86 mV and a J_{sc} of 0.98 mA.cm^{-2} were obtained.

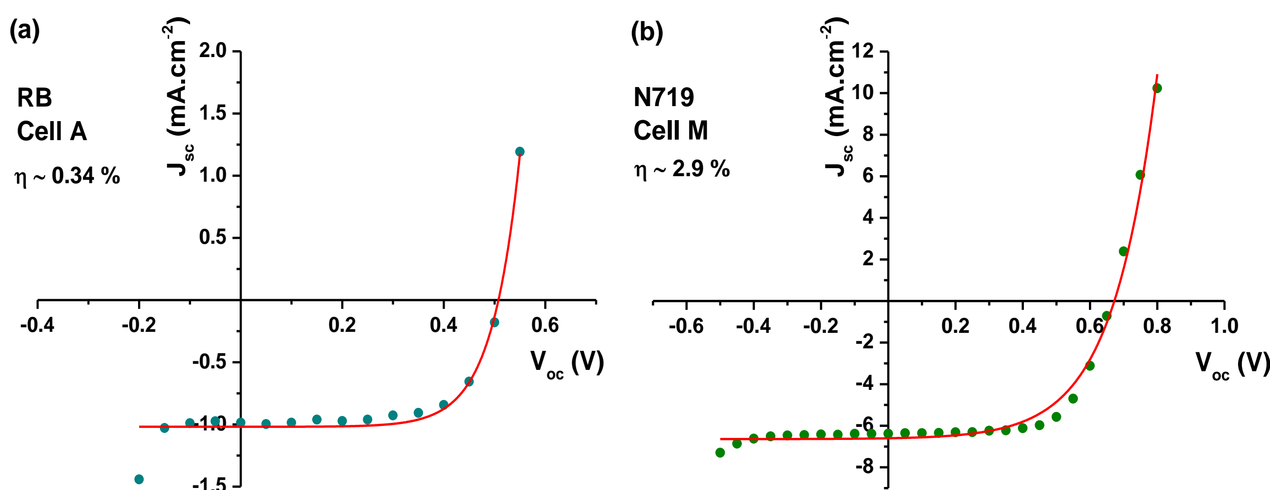

Figure 7-8 – *J-V* curves for the overall best performing cells obtained for each dye: (a) Rose Bengal and (b) N719. The experimental results were fitted by the Eq. 7-2.

Since no promising results were obtained with the Rose Bengal dye, the tests were continued using the Ru-based N719, very common in the fabrication of the TiO_2-base DSSCs. Among the dyes based on metal complexes, the Ru complexes have among the best photovoltaic properties: a broad absorption spectrum, suitable excited and ground state energy levels, relatively long excited-state lifetime, and good (electro) chemical stability [10]. In the case of the cells produced

with the N719 dye, different loading times were also employed. Moreover, a comparison for the different ZnO morphologies was also performed, namely using ZnO nano/microflowers produced by the hydrothermal method assisted by microwave radiation and colloidal NPs. Inspection of the Table 7-1 shows that the best J_{sc} (6.43 mA.cm^{-2}) and V_{oc} (666.15 mV) performance was obtained for a loading time of 1 h (cell M), being achieved a maximum efficiency of 2.9%. The *J-V* characteristic of this cell is represented in Figure 7-8b, showing a diode-like behaviour well fitted by Eq. 7-2. In this case, J_L was found to be ~ 6.60 (± 0.09) mA.cm^{-2} and a slightly higher ideality factor (5 ± 0.2) than the one verified for cell A was obtained. This factor is a measure of how closely the cell follows the ideal diode equation (n = 1).

Using the same conditions, and applying exactly the same procedure for the cells' preparation, a lower efficiency was obtained when the nano/microflowers were used, mainly due to a pronounced reduction of the J_{sc}. These results may be explained taking into account the surface area of the different morphologies, since TPs present a higher surface area than the nano/microflowers (see reference [1]) and the use of a network of different sized TPs and NPs results in a further increase of that area, with the NPs and the small TPs filling the spaces between the bigger TPs branches. Thus, higher surface area allows higher dye adsorption, leading to an increase of the J_{sc}. Additionally, ZnO colloidal NPs with diameters around 10 nm were tested. These samples exhibited significantly lower efficiency values than the ones obtained for the other structures. Once again, a noticeable reduction of the J_{sc} was observed. The colloidal NPs tend to agglomerate resulting in a strong reduction of the surface area available to sensitization and, consequently, decreasing the generated photocurrent. Another factor that may contribute for the differences in the cells performance is the presence of different defects, namely surface states, or chemical species adsorbed at surface of the ZnO structures, which are known to affect the photovoltaic parameters [30]. The presence of surface states, identified in the PL study mentioned in Chapter 6, can constitute one of the limiting factors in the cell performance. It was already stated in previous chapters that the presence of surface states may lead to the pinning of the Fermi level, with band bending and the formation of energy barriers [30], causing the trapping of the carriers. This affects the charge transfer to the electrode, which results in a decrease of the generated current. In this sense, surface/passivation treatments of the ZnO structures prior to their introduction in the device may lead to an enhancement of the cell efficiency. Furthermore, it is known that the presence of a large concentration of nonradiative defects (as shown by PL measurements) decreases the performance of photovoltaic devices [30]. Although the correlation between the PL results and the DSSCs performance may be rather complex and requires a careful analysis, some studies indicate that ZnO samples with lower PL emission tend to result in a performance lower than those exhibiting higher luminescence intensity [42].

It must be mentioned that a dye loading time of 24 h was also used, resulting in no photovoltaic response. This finding may be explained by the formation of aggregates between dissolved Zn^{2+} ions in the ZnO surface and the dye molecules [17,18,39]. As mentioned previously, the immersion time in the dye solution is a crucial parameter to achieve high performance DSSCs, as pointed by Keis *et al.* [39]. The photocurrent generated by the cells decreases significantly for long loading times. In the works of Chou *et al.* [43] and Keis *et al.* [39], it was found that shorter dye immersion times are preferred for ZnO. The dye concentration is also an important aspect to

take into account in the evaluation of the ideal dye immersion times, since more concentrated solutions result to a faster sensitization but also to a quicker decrease of the generated current [18]. This can be justified by several reasons, including the aggregation of dye molecules in the ZnO surface, hampering an efficient electron injection, or the instability of this semiconductor in acidic solution, which leads to the formation of Zn^{2+}/dye complexes. This complexes tend to form a thick layer covering the ZnO surface and can also fill the pores of the ZnO active layer [17,18,30,31]. The molecules of the Ru-based dyes possess carboxyl groups that attach easily to the TiO_2 surface. However, in the case of ZnO, the surface structure of the ZnO crystals may be destroyed when they are soaked in such an acidic solution for an extended period of time. This happens due to the dissolution of surface Zn atoms by the protons released from the dye molecules in an ethanol solution [31]. This deterioration of the surface of the ZnO structures inhibits the charge separation, since the Zn^{2+}/dye complexes are not able to efficiently inject electrons into the semiconductor CB [18]. This instability of ZnO in acidic solutions is a characteristic of the surface properties of this semiconductor. Its isoelectronic point is close to 9, while in the sensitization solution the pH is around 5, which is considerably lower than the isoelectronic point. This means that the ZnO surface is positively charged and the protons adsorbed on the ZnO surface will dissolve the ZnO, thereby explaining its poor chemical stability in this dye [18,31]. Thus, shorter sensitization times should be chosen in order to avoid the formation of Zn^{2+}/dye complexes. Though, the formation of these complexes is very difficult to avoid completely and is also very sensitive to the experimental conditions. This results in a considerable difference in the optimization of the dye loading time depending on the active area thickness and ZnO morphology, among other parameters [31,39]. Adding an unprotonated dye or using a neutral dye solution could be good alternatives to supress this undesired complex formation, as was already demonstrated by Keis *et al.* [39].

After proving the viability of the LAFD produced nanostructures into photovoltaic applications, and in order to improve the connection between the ZnO nanostructures and the anode substrate VACNTs were incorporation in the active area of the cell. With this approach it is expected that aligned CNTs can provide more landing sites for the growth of ZnO nanostructures, resulting in a higher contact area between the ZnO and the dye, and an increase of photon absorption. This anode structure was expected to lead to a greatly reduced recombination at the interface with the dye ionized molecules and the iodine ions, through a reduction of the charge carrier collection time. This is possible due to the high mobility of electrons in ZnO and the high surface area of the interface between ZnO and the highly conductive VACNT forest template. In fact, in 2010 Zeng and co-authors [44] reported the fabrication of DSSCs with such configuration. The ZnO nanostructures were attached to the VACNTs array using CVD technique, which allowed an uniform coating on each CNT in the array. An enhancement of the cell efficiency from 0.49 % up to 1.94 % (depending on the dye loading time) was obtained when the CNTs were used. However, as seen in the previous chapter, the LAFD technique was unable to completely cover the CNTs (just the top of the forest) due to the size of the produced particles, which are larger than the spaces between CNTs. Direct contact of the CNTs with the dye solution led to the collapse of the CNT aligned array. Furthermore, a poor attachment was found between the ZnO NPs and the CNTs, causing the detachment of part of the ZnO NPs from the electrode structure during the

sensitization bath. All these drawbacks, in combination with the time limitation, hampered the fabrication of DSSCs using VACNTs in useful time for the compilation of this thesis. Even so, CNT buckypapers/ZnO composites were also produced, avoiding the problem with the loss of alignment during the immersion in the dye. Despite its successful fabrication, other problems arose with this configuration, namely the high permeability of the membrane (even with the blocking layer coating) which resulted in the direct contact between the electrolyte and the electrode. This brings another challenge in the use of the CNTs in the DSSCs.

7.2. Photocatalysis

In the last decades an increasing interest has been devoted to the research of solutions to treat the wastewaters that are highly contaminated with residual dyes from textile, paper and other industries, constituting an environmental problem [45]. The use of photoactive oxides as catalysts have been subject to considerable interest, due to their ability to induce the indirect transformations of pollutants in water [46,47]. Among these photoactive oxides, TiO_2 is by far the most popular, transforming organic pollutants to mineralization by an efficient electron transfer process [46]. However, a growing interest in ZnO has been verified. ZnO structures have been used in a photocatalytic degradation of organic pollutants due to their non-toxic and high photocatalytic efficiency with good sensing behaviour [47–49]. This semiconductor appears as an alternative to TiO_2 due its high photosensitivity, stability and similar bandgap [45]. Moreover, ZnO is known to possess a very high surface reactivity [50,51], which is beneficial for an efficient visible light photocatalyst [50]. In fact, larger photocatalytic efficiencies have been reported for this material when compared with TiO_2 [46,52,53].

As widely discussed in this thesis, when semiconductor structures are illuminated with light with energy equal or higher than its E_g, electrons are excited from the VB to the CB, leaving positively charged holes in the VB [45,54]. If the charge separation is maintained, the electron and hole may migrate to the catalyst surface where they participate in redox reactions with adsorbed species on the semiconductor surface such as hydroxyl groups (OH^-), water molecules, dissolved oxygen molecules, organic species or metal ions [45,54]. Holes may react with surface-bounded H_2O or OH^- to produce the hydroxyl radical (OH), while free electrons can be captured by oxygen to generate superoxide radical anions (O_2^-), which are the active species for oxidation [45]. However, before these processes occur, holes and electrons may recombine making them unavailable to participate in useful redox reactions [54,55]. A high rate of charge carrier recombination inevitably decreases the number of free electrons and holes that are available to react with adsorbed molecules and thereby generate free radicals [56]. Thus, electron-hole recombination constitutes a limiting factor of the photocatalytic reaction [55], together with the limited absorption capability of the photocatalyst material [54].

The photodegradation mechanisms for ZnO have been proven to be similar to that of TiO_2 [46] and may be described as presented below [1,2,57,58]:

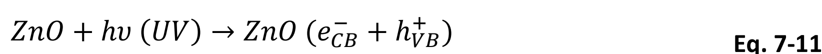

$$ZnO + h\upsilon\ (UV) \rightarrow ZnO\ (e_{CB}^{-} + h_{VB}^{+}) \quad \textbf{Eq. 7-11}$$

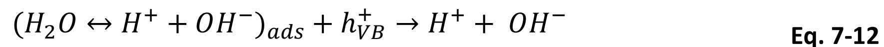

$$(H_2O \leftrightarrow H^+ + OH^-)_{ads} + h^+_{VB} \rightarrow H^+ + OH^- \quad \textbf{Eq. 7-12}$$

$$h^+_{VB} + OH^- \rightarrow OH \quad \textbf{Eq. 7-13}$$

$$e^- + O_2(ads) \rightarrow O_2^- \quad \textbf{Eq. 7-14}$$

$$O_2^- + HO_2 + H^+ \rightarrow H_2O_2 + O_2 \quad \textbf{Eq. 7-15}$$

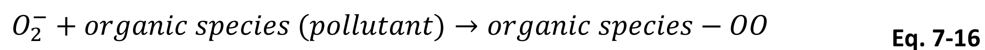

$$O_2^- + organic\ species\ (pollutant) \rightarrow organic\ species - OO \quad \textbf{Eq. 7-16}$$

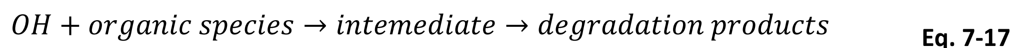

$$OH + organic\ species \rightarrow intemediate \rightarrow degradation\ products \quad \textbf{Eq. 7-17}$$

$$h^+_{VB} + organic\ species^+ \rightarrow degradation\ products \quad \textbf{Eq. 7-18}$$

After the formation of the superoxide radical anions, this radical may form organic peroxides or hydrogen peroxide in the presence of organic pollutants (Eq. 7-15 and Eq. 7-16). The hydroxyl radical is a powerful oxidizing agent and capable of oxidizing most of the organic compounds and form intermediate products [2,56]. These intermediate products may react again with hydroxyl radicals, leading to the final degradation of the pollutant products (Eq. 7-17) [2]. It has also been suggested that direct oxidation of the substrate by positive hole (h^+) may efficiently occur (Eq. 7-18) [47,58].

Visible light photocatalysis is activated in the metal oxide semiconductors like TiO_2 or ZnO through the presence of their defect states. These defects may be intrinsic, as the case of oxygen vacancies, or due to impurity incorporation, either intentional or unintentional. Moreover, they can be created through doping with appropriate activators to promote the photon absorption in the region of interest [1,50]. Furthermore, hybridization with other materials, as noble metals may be advantageous [59]. Surface and bulk defects are known to play a vital role in photocatalysis reactions and, as mentioned before, ZnO offers a multiplicity of defects-levels, some deriving from residual impurities, some from oxygen deficiency, and others related to topographical irregularities [50,51]. The surface-defects are very important in ZnO and the photocatalytic activity of this semiconductor has been attributed to a high concentration of surface donor defects, that may include oxygen vacancies and/or zinc interstitials [60].

The main disadvantage of ZnO as a photocatalyst is its instability in acidic and basic media, as already mentioned in the case of the DSSCs. Sometimes photocorrosion under UV illumination is observed, which is considered to be one of the main reasons for the decrease in ZnO photocatalytic activity over time. Therefore, ZnO is only suitable for photocatalytic applications in neutral environments [47,61].

In this section, the photocatalytic activity of the ZnO TPs and MRs synthesised by LAFD is explored. Moreover, the addition of silver (~ 3 mol% added to the precursor rods) was also studied. Both TPs (with and without silver) were grown in air with a laser power of 60 W, while the MRs were grown with 35 W. It is important to bear in mind that, as evidenced in Chapter 6, the silver distribution in the samples it is not homogeneous. The amount of 3 mol % of silver was chosen taking into account the results reported in the literature, where the authors claimed that this value was the one that led to the best results [45,62].

Figure 7-9 shows the SEM images of the samples used for the photocatalytic tests and Figure 7-10 depict the EDS spectra acquired in the samples grown in the presence of silver, confirming that silver is indeed present in the tested samples.

The UV photocatalytic activities of ZnO structures grown by LAFD were evaluated at RT from the degradation of methylene blue (MB) as model dye. In a typical experiment, 30 mg of each ZnO structures were dispersed in 50 ml of aqueous MB (2 mg L^{-1}) solutions. The reaction mixture was mixed thoroughly in an ultrasonic water bath for 10 min and then stirred for 30 min in the dark to establish absorption-desorption equilibrium. The solutions were exposed to UV irradiation using a deuterium lamp (model L11798 from Hamamatsu) with its maximum intensity peak at 160 nm (7.75 eV). 4 ml of samples were collected before and at regular intervals (10 min) during irradiation and analysed by UV-Vis spectrophotometry, after centrifugation, using a UV/VIS/NIR spectrophotometer, as reported in [1]. The absorbance was obtained from 350 nm (~ 3.54 eV) to 800 nm (~ 1.55 eV). The photocatalysis measurements were performed in *CENIMAT/I3N* laboratory.

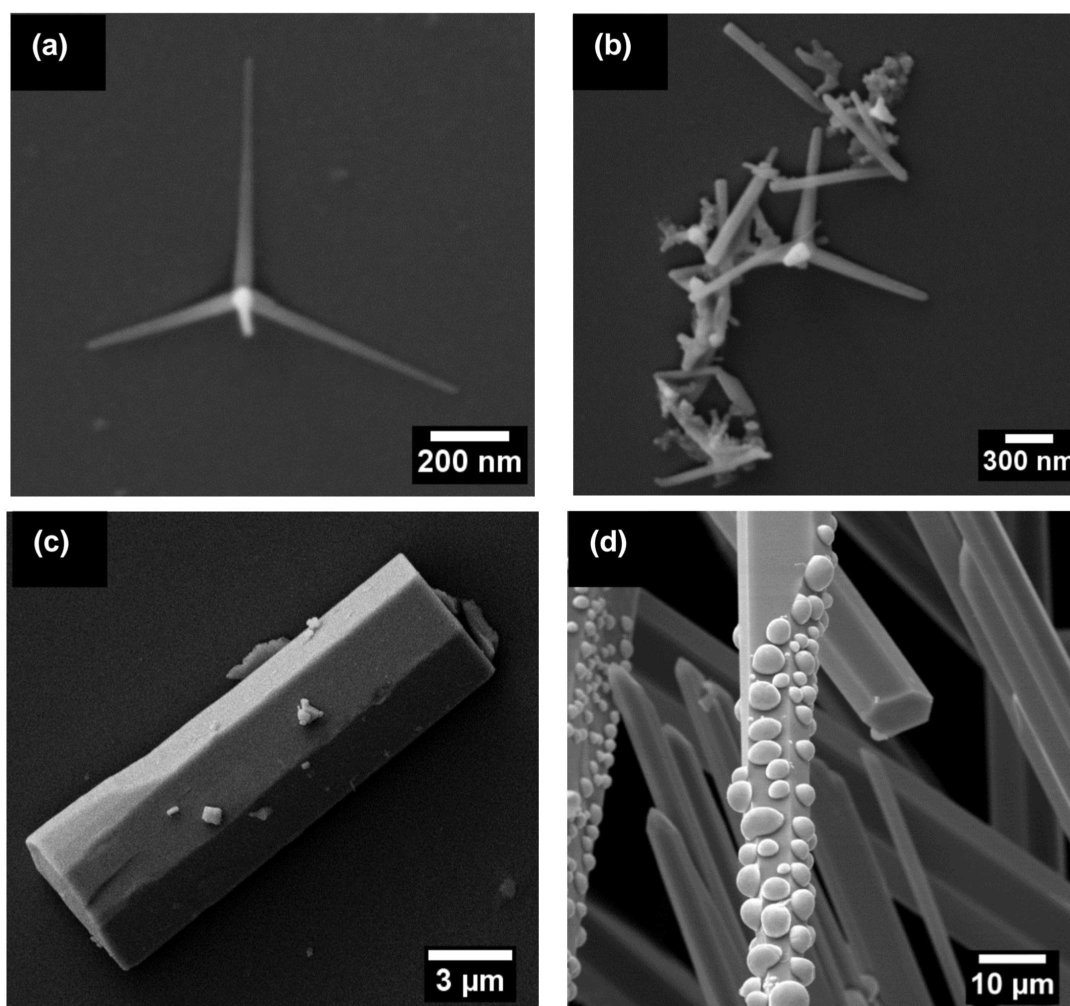

Figure 7-9 – SEM images of ZnO nanostructures: (a) TPs, (b) TPs with silver, (c) MRs and (d) MRs with silver.

MB is considered as a model-test contaminant and indicator due to its photocatalytic activity and absorption peaks in the visible range. Therefore, its degradation can be easily monitored by optical absorption spectroscopy. The visible spectra of dilute solutions contain a band associated with monomeric MB at 665 nm (~ 1.86 eV) with a shoulder attributed to the 0-1 vibronic transition of monomers at 605 nm (~ 2.05 eV). The cationic dimers that are frequently formed in aqueous solutions for concentration higher than 2.5×10^{-6} mol L^{-1} (~ 8.0×10^{-4} g L^{-1}) also absorb near 605 nm [1,63,64]. This compound is an electroactive substance with the ability to accept electrons that lead to its further degradation into leucomethylene blue, resulting in a colourless solution [1,50]. Thus, the addition of ZnO structures into MB solution promotes charge transfer between the semiconductor and the MB molecules when irradiated with UV light, conducting to the MB degradation [1]. Details regarding the MB degradation can be found in reference [58].

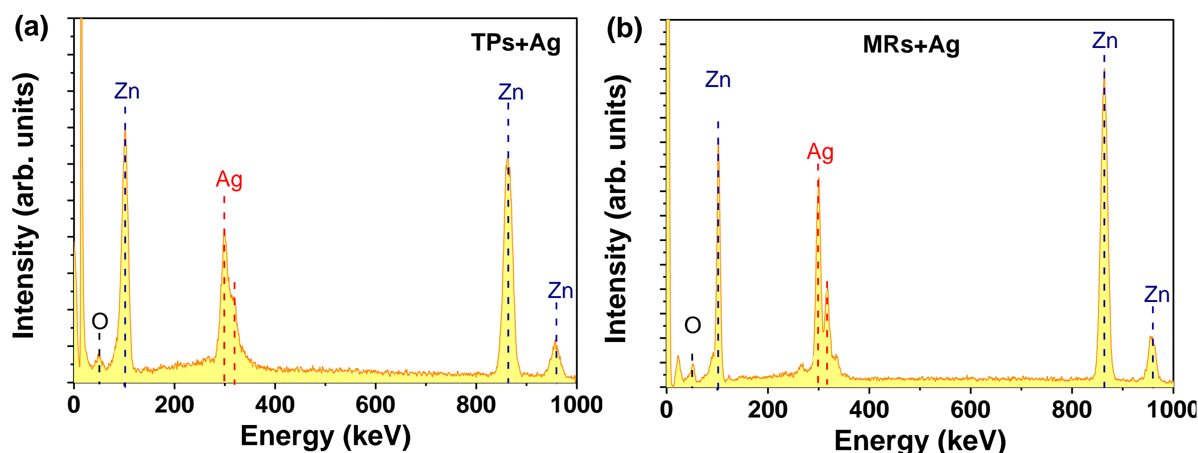

Figure 7-10 – EDS spectra of the samples grown in the presence of silver: (a) TPs and (b) MRs.

Figure 7-11 and Figure 7-12 show the results obtained for the MB photodegradation in the presence of ZnO structures grown by LAFD, TPs and MRs with and without the presence of silver, respectively. The MB photodegradation was observed by monitoring the evolution of the MB absorption band intensity at 665 nm upon continued exposure of UV radiation, as already reported for other ZnO structures grown by the hydrothermal method [1]. As in the work reported by Pimentel *et al.* [1], the photodegradation was found to be dependent on the type of nanostructure used. A much faster degradation was seen to occur when TPs were used (Figure 7-11a) than in the case of the MRs (Figure 7-12a). The MB concentration was reduced 50% in ~ 60 minutes using TPs as photocatalytic agent (Figure 7-13). This time was decreased by more than a half by adding silver to these nanostructures (Figure 7-11b), which was anticipated due to the excellent catalytic properties of silver [65,66]. In this case only 24 minutes were necessary to reduce the MB concentration to half of the initial one. A reduction in the degradation time of the contaminates with the addition of silver was also reported for TiO_2 particles [54].

In the case of the MRs (Figure 7-12a), only after ~ 150 minutes the reduction to the MB concentration to half of the initial one was verified (Figure 7-13). Also in this case, the growth in the presence of silver conducted to a reduction in the photodegradation time to ~ 130 minutes. This decrease was less pronounced than in the TPs case. These results show not only the improvement on the photocatalytic activity due to the silver addition, but also the strong

influence of the morphology on the photocatalytic properties. This arises from differences in surface areas, polar planes, or even the type and concentration of oxygen vacancies on the surface [49]. It is fair to assume that a high specific surface area has beneficial effect on the activity of catalysts, since the photocatalytic reaction occurs at the surfaces [49,61]. Thus, it is estimated that structures with nanoscale dimensions would increase the decomposition rate due to the increase in their surface area [61]. Increasing specific surface area consequently increases the number of active surface sites where the photogenerated charge carriers are able to react with adsorbed molecules to form hydroxyl and superoxide radicals [56]. However, it is important to take into account that the photocatalytic activity does not increase linearly with a decreasing of crystal size, due to the increasing probability of surface recombination which will compete with the photocatalyst effect [1,56].

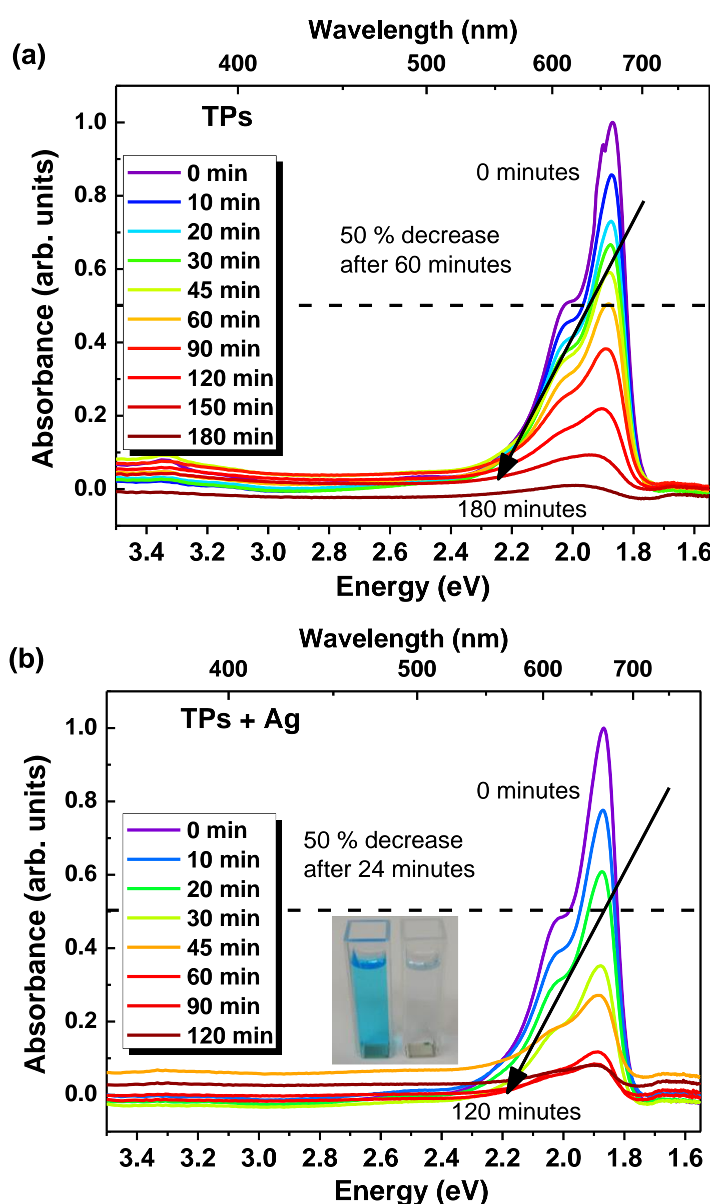

Figure 7-11 – Photocatalytic degradation of MB over time in the presence of the ZnO (a) TPs, and (b) TPs with silver, at RT and under an UV radiation of 160 nm. The inset corresponds to a photo of the MB blue degradation in the presence of ZnO TPs with silver.

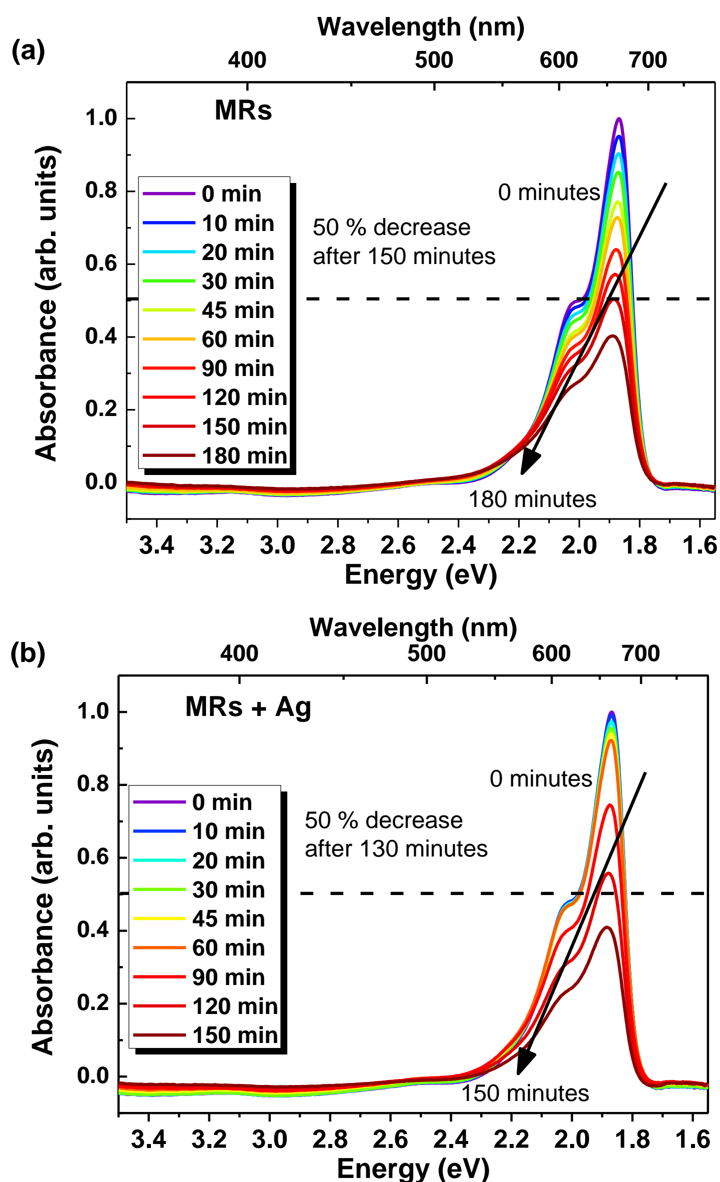

Figure 7-12 – Photocatalytic degradation of MB over time in the presence of the ZnO (a) MRs and (b) MRs with silver, at RT and under an UV radiation of 160 nm.

The high surface to volume ratio exhibited by the TPs structures may account for the better photocatalytic response when compared to the MRs. Moreover, the TP configuration avoids easy aggregation, which is a problem frequently encountered in NPs. Their shape/size, the low tendency for particle aggregation, together with the highly open and porous network structure formed for the TPs constitutes an important advantage when a high specific surface area is needed (as is also the case of the DSSCs). Guo *et al*. [60] reported a work where the phocatalytic properties of ZnO TPs and NPs were studied and observed that TPs exhibited a higher photocatalytic activity, compared to the different NPs and independently on the NPs size, for all the dyes investigated (which included MB). The TPs used in their work show similar dimensions to the ones produced in this thesis by LAFD. These authors also conclude that native defects

constituted a critical factor in the photocatalytic efficiency of ZnO TPs, since lower concentration of nonradiative defects would result in lower losses of photogenerated carriers and low nonradiative defects/recombination centres concentration would enhance photocatalytic activity [60]. From the PL studies performed in the LAFD samples it is known that both TPs and MRs present a strong thermal quenching of their NBE emission, which is an indication of the presence of nonradiative channels. However, the thermal quenching was found to be comparable in both cases, so it cannot be accounted for the different degradation behaviour observed.

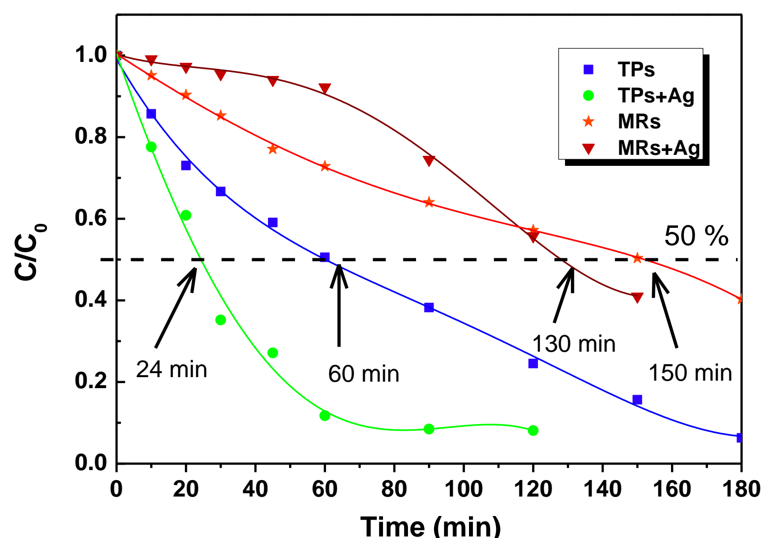

Figure 7-13 – MB concentration versus exposure time for the different photocatalysts. Full lines were added as a guide to the eyes.

Another critical factor in the phocatalytic activity is the polarity of the exposed surfaces. It is widely accepted that catalytic properties are dependent on specific crystal facets, since different crystal facets have different dangling bond configurations and preferential adsorption [47]. Reported data suggests that exposure of a greater proportion of polar faces leads to greater photocatalytic activity [48]. The higher activity of the polar basal planes is attributed to the intrinsically high surface energy of {0001}, favouring the reactant molecule adsorption. The OH^- ions could preferentially adsorb onto these faces due to the positive charge, which could lead to a greater rate of OH radicals production and hence degradation of MB during the photocatalysis [1,48]. Li *et al.* [67] used photoluminescence spectroscopy studies to establish a positive correlation between the proportion of polar faces exposed and the surface oxygen vacancy density [47,48]. They showed that samples with a large fraction of polar planes contain more oxygen vacancies, suggesting that oxygen vacancies may be preferably formed on the polar planes of ZnO [67]. Therefore, a higher amount of oxygen vacancies will trap more electrons, assisting the charge separation and increasing the photocatalytic activity [47,48]. As shown in the TEM results, the LAFD MRs were preferentially grown along the [0001] direction, which mean that the basal faces are placed on the extremities of the rods, corresponding to the smallest surface area. This fact may explain the lower photocatalytic response obtained for these structures.

In nominal undoped ZnO structures, the defects, as oxygen deficiencies, may act as trap centres that capture photogenerated electrons, restraining them from recombining with the holes

(with the emission of visible photons), while surface hydroxyl groups act as the drivers of the photocatalytic reaction. The holes attack the surface hydroxyl, attaching OH groups to the semiconductor surface [68]. The interfacial electron transfer takes place predominantly between the surface donor states and the MB molecules [51,60]. Being a cationic dye, MB receives electrons from the excited donor states, these electrons interact with the molecular structure of MB leading to its complete decomposition [1,51]. On the other hand, and as mentioned in the previous chapter, with the addition of silver particles to the ZnO surface it is expected that the electrons photogenerated in the CB can be transferred to the metal particles due to the Schottky barrier formed at the metal-semiconductor interface, while the holes remain in the semiconductor surface. Thus, the silver particles are expected to act as electron sinks, leading to an enhancement in the charge separation and consequently the photocatalytic efficiency [45,59], as verified in the present samples. Figure 7-14a shows an illustration of the most probable band structures of the Schottky junction between metallic silver and ZnO, including the Fermi energy level at equilibrium (E_f). Since the Fermi energy level of ZnO (denoted in the Figure by E_{fs}) has a lower energy than that of Ag (E_{fm}), due to the larger work function of ZnO, there is a spontaneous transfer of electrons from silver to ZnO until the equilibrium is reached and a new Fermi level is established (E_f) [59,69]. Upon UV-illumination (Figure 7-14b) the electrons excited to the CB tend to be transferred to the metallic silver, owning to the higher energy of the ZnO CB, subsequently inhibiting the electron-hole recombination and extending the lifetime of the photogenerated electron-hole pairs. In this way, the electrons in the metal can be trapped by the chemisorbed O_2 and the hole can be captured by the surface OH groups, both resulting in the formation of hydroxyl radical species (·OH) [59,62].

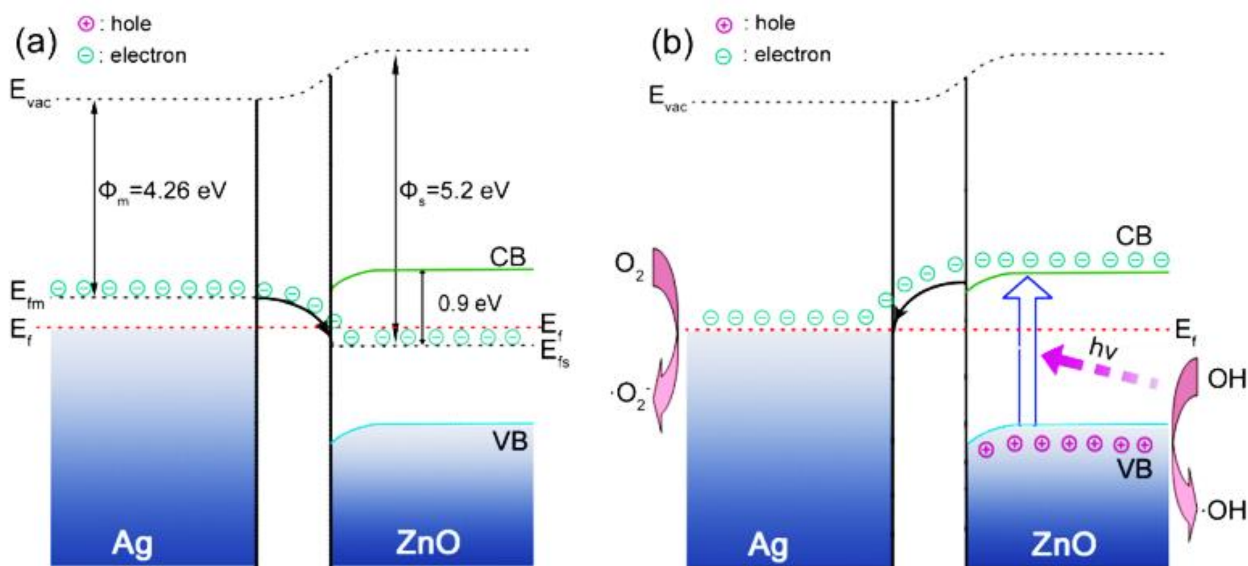

Figure 7-14 – (a) Schematic representation of the band structures for Ag and ZnO junction and the Fermi energy level at equilibrium. (b) Proposed charge separation process and photocatalytic mechanism of the Ag/ZnO samples under UV illumination. Image reproduced from reference [59].

Based on what was previously discussed for the pure ZnO and taking into account the silver interaction, the possible photocatalysis mechanism of the silver/ZnO samples in the degradation of the MB solution may be described as follows [59]:

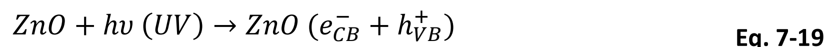

$$ZnO + h\upsilon\ (UV) \rightarrow ZnO\ (e_{CB}^{-} + h_{VB}^{+})$$ **Eq. 7-19**

$$Ag \rightarrow Ag^{+} + e^{-}$$ **Eq. 7-20**

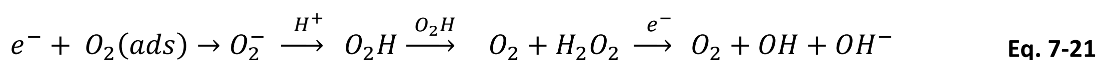

$$e^{-} + O_2(ads) \rightarrow O_2^{-} \xrightarrow{H^{+}} O_2H \xrightarrow{O_2H} O_2 + H_2O_2 \xrightarrow{e^{-}} O_2 + OH + OH^{-}$$ **Eq. 7-21**

$$Ag^{+} + e^{-} \rightarrow Ag$$ **Eq. 7-22**

$$h_{VB}^{+} + OH^{-} \rightarrow OH$$ **Eq. 7-23**

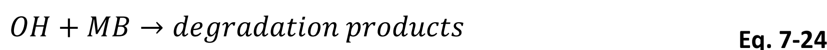

$$OH + MB \rightarrow degradation\ products$$ **Eq. 7-24**

Further studies are needed, specifically the influence of the silver amount on the ZnO structures, in order to optimize the photocatalytic performance of the LAFD produced material, since this was seen to be a crucial parameter [45,59,62]. Another parameter that will require attention is the homogeneity in the distribution of metallic silver on the ZnO surface, since it was shown to affect the photocatalytic activity [70].

Tests using the CNT buckypaper composites with ZnO TPs and ZnO TPs grown with silver are scheduled to be conducted soon.

7.3. Conclusions

The LAFD produced ZnO interconnected network of TPs and NPs was used to form a porous ZnO layer that worked as active area for the assembling of DSSCs. Two different dyes were used: Rose Bengal and N719. A better performance was obtained with N719. For this dye different loading times were employed and a maximum efficiency of 2.9 % was achieved for a residence time in the dye of 1 h. A comparison with other morphologies was also carried out, showing that, for the present cell fabrication conditions, the cells where LAFD produced ZnO structures were used resulted in a better performance. Further optimization in the DSSCs fabrication process is needed in order to improve device performance, such as ZnO layer thickness, ZnO passivation and sensitization conditions (namely the type of dye solution and concentration). To accomplish this purpose, an intensive and detailed study must be conducted. Notwithstanding, this work proved that LAFD is a suitable technique to produce high quality ZnO nanostructures that are suitable to be incorporated in the fabrication of DSSCs.

Concerning the introduction of the CNTs, several challenges in the cell preparation must be overcome before its successful incorporation into the devices.

Regarding the photocatalysis studies, the preliminary results evidenced the strong morphology dependence in the pollutant degradation. TPs exhibited a much faster MB photodegradation when compared with the MRs. The higher surface area of the former is expected to increase the interfacial charge transfer rate. The reactivity of the exposed surfaces may also play a role in the obtained results. Adding silver to the ZnO structures revealed an enhancement of the

photocatalytic performance, due to a more efficient charge separation. Overall, the results obtained are in line with what is found in the literature for similar samples (size and morphology).

7.4. References

1. A. Pimentel, J. Rodrigues, P. Duarte, D. Nunes, F. M. Costa, T. Monteiro, R. Martins, and E. Fortunato, J. Mater. Sci. **50**, 5777 (2015).

2. S. A. Mahmoud and O. A. Fouad, Sol. Energy Mater. Sol. Cells **136**, 38 (2015).

3. C. Jagadish and S. J. Pearton, *Zinc Oxide Bulk, Thin Films and Nanostructures: Processing, Properties and Applications* (Elsevier, 2006).

4. H. Morkoç and Ü. Özgür, *Zinc Oxide: Fundamentals, Materials and Device Technology* (John Wiley & Sons, 2008).

5. S. M. Sze, *Physics of Semiconductor Devices* (Wiley, 1981).

6. T. Sog, *Nanostructured Materials for Solar Energy Conversion* (Elsevier, 2006).

7. X. Huang, S. Han, W. Huang, and X. Liu, Chem. Soc. Rev. **42**, 173 (2013).

8. S. J. Fonash, *Solar Cell Device Physics* (Elsevier, 2010).

9. P. Wurfel, *Physics of Solar Cells* (Wiley-VCH Verlag GmbH, 2005).

10. A. Hagfeldt, G. Boschloo, L. Sun, L. Kloo, and H. Pettersson, Chem. Rev. **110**, 6595 (2010).

11. M. Grätzel and G. Michael, J. Photochem. Photobiol. C Photochem. Rev. **4**, 145 (2003).

12. R. C. Neville, *Solar Energy Conversion: The Solar Cell* (Elsevier Scientific Publishing Co., 1978).

13. C. Honsberg and S. Bowden, PVEducation.org (2013).

14. M. Grundmann, *The Physics of Semiconductors: An Introduction Including Devices and Nanophysics* (Springer Science & Business Media, 2006).

15. B. O'Regan and M. Grätzel, Nature **353**, 737 (1991).

16. Grätzel M, Curr. Opin. Colloid Interface Sci. **4**, 314 (1999).

17. Y. F. Hsu, Y. Y. Xi, C. T. Yip, A. B. Djurišić, and W. K. Chan, J. Appl. Phys. **103**, 083114 (2008).

18. J. A. Anta, E. Guillén, and R. Tena-Zaera, J. Phys. Chem. C **116**, 11413 (2012).

19. J. Xu, K. Fan, W. Shi, K. Li, and T. Peng, Sol. Energy **101**, 150 (2014).

20. D. Wei, Int. J. Mol. Sci. **11**, 1103 (2010).

21. Q. Zhang and G. Cao, Nano Today **6**, 91 (2011).

22. S. Mathew, A. Yella, P. Gao, R. Humphry-Baker, B. F. E. Curchod, N. Ashari-Astani, I. Tavernelli, U. Rothlisberger, M. K. Nazeeruddin, and M. Grätzel, Nat. Chem. **6**, 242 (2014).

23. A. Yella, H.-W. Lee, H. N. Tsao, C. Yi, A. K. Chandiran, M. K. Nazeeruddin, E. W.-G. Diau, C.-Y. Yeh, S. M. Zakeeruddin, and M. Grätzel, Science **334**, 629 (2011).

24. C.-H. Lee, W.-H. Chiu, K.-M. Lee, W.-H. Yen, H.-F. Lin, W.-F. Hsieh, and J.-M. Wu, Electrochim. Acta **55**, 8422 (2010).

25. S. Gubbala, V. Chakrapani, V. Kumar, and M. K. Sunkara, Adv. Funct. Mater. **18**, 2411 (2008).

26. F. Lenzmann, J. Krueger, S. Burnside, K. Brooks, M. Grätzel, D. Gal, S. Rühle, and D. Cahen, J. Phys. Chem. B **105**, 6347 (2001).

27. H. Gerischer, Photochem. Photobiol. **16**, 243 (2008).

28. H. Tributsch and M. Calvin, Photochem. Photobiol. **14**, 95 (1971).

29. C.-P. Lee, C.-Y. Chou, C.-Y. Chen, M.-H. Yeh, L.-Y. Lin, R. Vittal, C.-G. Wu, and K.-C. Ho, J. Power Sources **246**, 1 (2014).

30. A. B. Djurišić, X. Liu, and Y. H. Leung, Phys. Status Solidi - Rapid Res. Lett. **8**, 123 (2014).

31. Q. Zhang, C. S. Dandeneau, X. Zhou, and G. Cao, Adv. Mater. **21**, 4087 (2009).

32. Q. Zhang, D. Myers, J. Lan, S. A. Jenekhe, and G. Cao, Phys. Chem. Chem. Phys. **14**, 14982 (2012).

33. R. R. Bacsa, J. Dexpert-Ghys, M. Verelst, A. Falqui, B. Machado, W. S. Bacsa, P. Chen, S. M. Zakeeruddin, M. Graetzel, and P. Serp, Adv. Funct. Mater. **19**, 875 (2009).

34. N. Memarian, I. Concina, A. Braga, S. M. Rozati, A. Vomiero, and G. Sberveglieri, Angew. Chem. Int. Ed. Engl. **50**, 12321 (2011).

35. A. S. Pereira, M. Peres, M. J. Soares, E. Alves, A. Neves, T. Monteiro, and T. Trindade, Nanotechnology **17**, 834 (2006).

36. T. Monteiro, M. J. Soares, A. Neves, S. Pereira, M. R. Correia, M. Peres, E. Alves, D. Rogers, F. Teherani, V. Munoz-SanJose, T. Trindade, and A. Pereira, J. Non. Cryst. Solids **352**, 1453 (2006).

37. S. Rani and R. M. Mehra, J. Renew. Sustain. Energy **1**, 033109 (2009).

38. B. Pradhan, S. K. Batabyal, and A. J. Pal, Sol. Energy Mater. Sol. Cells **91**, 769 (2007).

39. K. Keis, E. Magnusson, H. Lindström, S.-E. Lindquist, and A. Hagfeldt, Sol. Energy Mater. Sol. Cells **73**, 51 (2002).

40. F. De Angelis, S. Fantacci, and A. Selloni, Nanotechnology **19**, 424002 (2008).

41. M. G. Helander, M. T. Greiner, Z. B. Wang, W. M. Tang, and Z. H. Lu, J. Vac. Sci. Technol. A Vacuum, Surfaces, Film. **29**, 011019 (2011).

42. K. K. Wong, A. Ng, X. Y. Chen, Y. H. Ng, Y. H. Leung, K. H. Ho, A. B. Djurišić, A. M. C. Ng, W. K. Chan, L. Yu, and D. L. Phillips, ACS Appl. Mater. Interfaces **4**, 1254 (2012).

43. T. Chou, Q. Zhang, and G. Cao, J. Phys. Chem. C **111**, 18804 (2007).

44. G.-Y. Zeng, K.-S. Nian, and K.-Y. Lee, Diam. Relat. Mater. **19**, 1457 (2010).

45. M. J. Height, S. E. Pratsinis, O. Mekasuwandumrong, and P. Praserthdam, Appl. Catal. B Environ. **63**, 305 (2006).

46. B. Dindar and S. Içli, J. Photochem. Photobiol. A Chem. **140**, 263 (2001).

47. S. Xu and Z. L. Wang, Nano Res. **4**, 1013 (2011).

48. A. McLaren, T. Valdes-Solis, G. Li, and S. C. Tsang, J. Am. Chem. Soc. **131**, 12540 (2009).

49. M. Rezapour and N. Talebian, Mater. Chem. Phys. **129**, 249 (2011).

50. S. Baruah, S. S. Sinha, B. Ghosh, S. K. Pal, A. K. Raychaudhuri, and J. Dutta, J. Appl. Phys. **105**, 074308 (2009).

51. R. Ullah and J. Dutta, J. Hazard. Mater. **156**, 194 (2008).

52. I. Poulios and I. Tsachpinis, J. Chem. Technol. Biotechnol. **74**, 349 (1999).

53. A. A. Khodja, T. Sehili, J.-F. Pilichowski, and P. Boule, J. Photochem. Photobiol. A Chem. **141**, 231 (2001).

54. V. Vamathevan, R. Amal, D. Beydoun, G. Low, and S. McEvoy, J. Photochem. Photobiol. A Chem. **148**, 233 (2002).

55. H. Gerischer and A. Heller, J. Phys. Chem. **95**, 5261 (1991).

56. A. C. Dodd, A. J. McKinley, M. Saunders, and T. Tsuzuki, J. Nanoparticle Res. **8**, 43 (2006).

57. M. Pera-Titus, V. García-Molina, M. A. Baños, J. Giménez, and S. Esplugas, Appl. Catal. B Environ. **47**, 219 (2004).

58. A. Houas, Appl. Catal. B Environ. **31**, 145 (2001).

59. W. Lu, G. Liu, S. Gao, S. Xing, and J. Wang, Nanotechnology **19**, 445711 (2008).

60. M. Y. Guo, A. M. C. Ng, F. Liu, A. B. Djurišić, W. K. Chan, H. Su, and K. S. Wong, J. Phys. Chem. C **115**, 11095 (2011).

61. F. Lu, W. Cai, and Y. Zhang, Adv. Funct. Mater. **18**, 1047 (2008).

62. R. Georgekutty, M. K. Seery, and S. C. Pillai, J. Phys. Chem. C **112**, 13563 (2008).

63. J. Bujdák and P. Komadel, J. Phys. Chem. B **101**, 9065 (1997).

64. K. Bergmann and C. T. O'Konski, J. Phys. Chem. **67**, 2169 (1963).

65. Q. Simon, D. Barreca, D. Bekermann, A. Gasparotto, C. Maccato, E. Comini, V. Gombac, P. Fornasiero, O. I. Lebedev, S. Turner, A. Devi, R. A. Fischer, and G. Van Tendeloo, Int. J. Hydrogen Energy **36**, 15527 (2011).

66. A. Roucoux, J. Schulz, and H. Patin, Chem. Rev. **102**, 3757 (2002).

67. G. Li, T. Hu, G. Pan, and T. Yan, J. Phys. Chem. B **112**, 11859 (2008).

68. L. Jing, Z. Xu, X. Sun, J. Shang, and W. Cai, Appl. Surf. Sci. **180**, 308 (2001).

69. H. Han, N. D. Theodore, and T. L. Alford, J. Appl. Phys. **103**, 013708 (2008).

70. Y. Zheng, C. Chen, Y. Zhan, X. Lin, Q. Zheng, K. Wei, and J. Zhu, J. Phys. Chem. C **112**, 10773 (2008).

Conclusions and future work

This thesis was devoted to the study of GaN and ZnO based samples evaluating their potential application in optoelectronic devices. One of the fundamental aims was the optical characterization of GaN structures implanted with RE^{3+} ions, as a means to optimize this type of luminescence emitters and contribute to the development of GaN: RE^{3+}-based solid state lighting devices. The analysis of the nitride samples was focused on the luminescence characteristics of the $4f^n$-intraionic transitions of the RE^{3+} ions, although some studies were also performed in the intrinsic optical centres of the semiconductors, as is the case of the broad bands and the NBE emission. Different types of nitride structures were characterized, namely layers, NWs, QWs and QDs, with an especial focus in the firsts two types.

The RE implanted and annealed nitride samples were studied by Raman, PL, PLE, and TRPL. It was shown that Eu, Pr, Tb and Tm ions implanted in GaN and its alloys with AlN ($Al_xGa_{1-x}N$) could be activated as luminescent centres after post-implantation annealing. This annealing not only led to the optical activation of the ions but also contributed for the lattice recovery after the damaging by ion implantation, as confirmed by Raman measurements. The optical activation of these ions led to the observation of the sharp characteristic emission lines corresponding to RE^{3+} transitions from the intra $4f^n$-shell both in the visible and NIR spectral regions, depending on the chosen ion.

Regarding the YL band, this optical centre was found to exhibit a distinct behaviour with the illumination/irradiation time in the NWs, when compared with the one usually observed in both GaN bulk crystals and layers. The luminescence degradation depends on the environment media meaning that surface adsorbed species (as revealed from the in-vacuum and in-air PL spectra) must be considered has potential sources of luminescence killers. In order to gain a better understanding of this behaviour, the YL was intentionally induced/enhanced in GaN NWs by using post-growth ion implantation and annealing. The yellow emitting GaN NWs ensembles were exposed to different surface treatments, namely hydrogen plasma etching, wet chemical acid bath and amorphous silica coating. PL studies after these surface modifications revealed the sensitivity of the YL intensity to the GaN NWs surface properties. In particular, the YL was strongly enhanced after hydroxylation. The stability of the YL in untreated and surface treated samples was studied during 4 h as a function of illumination/irradiation time in air and vacuum. The data allowed to conclude that photodegradation mechanisms occurred always for samples analysed in air and for the untreated samples analysed in vacuum. For the surface treated samples a nearly constant YL intensity was found when the samples were probed in vacuum, meaning that under

this atmosphere, the nonradiative paths competing with the YL could be suppressed by using samples' surface modification processes. The treatment with hydrogen plasma revealed to be an efficient process to control and improve the YL stability in both environments.

In the case of the Eu^{3+} implanted NWs and layers, independently of the used implantation angle and fluence, all the samples exhibit Eu^{3+} emission dominated by the $^5D_0 \rightarrow {}^7F_2$ transition. NWs showed higher intensity of the ion emitting lines than the layers implanted in the same conditions. A slightly higher thermal stability of the intraionic emission (~ 50%) was found for the implanted and annealed NWs. The intraionic emission was discussed in the basis of a dominant Eu^{3+} centre in the GaN samples, with a contribution from minority centres that differ in the layers and NWs, as suggested by the identified number of Stark lines. With above bandgap excitation, a lifetime in the range of hundreds of microseconds was found for the Eu^{3+} $^5D_0 \rightarrow {}^7F_2$ transition for both layers and NWs, as expected for transitions between energy levels with different spin multiplicities. Besides the intraionic emission the implanted and annealed NWs and layers exhibit YL bands with distinct characteristics. The YL in GaN layers follows the typical behaviour of the commonly assigned e−A and DAP recombination models in GaN samples. Contrarily, the YL identified in the NWs with a faster decay than the intraionic emission puts in evidence a distinct recombination model supporting a surface state mediated recombination process, likely present in these NWs with high surface/volume ratio.

Pr^{3+} implanted and annealed GaN samples revealed that the optical activation of the ions was achieved in all GaN structures (layers, QWs, NWs and QDs) after thermal annealing. For all the samples, the Pr^{3+} ion-related emission is dominated by the $^3P_0 \rightarrow {}^3F_2$ transition. The layer with high Pr content showed a strong red emission even at RT, suggesting that high dopant concentration is necessary to reach intense emission and the luminescence efficiency can be improved by annealing at high temperatures and high N_2-pressures, which minimizes the nonradiative processes. For the NWs the peak position and spectral shape were in good agreement with the layers, which proves the effective incorporation of the ion inside the GaN NWs. However, in the case of GaN QDs the intraionic emission appears to be mostly originated in the AlN layers used as spacers in the superlattice structure. In the QWs the sharp lines of the intraionic emission was found to be superimposed to a broad band likely due to the overlap of multiple Pr^{3+} centres caused by disorder-related effects after the implantation, while the formation of intermixed AlGaN regions may give rise to additional centres with broad emission. The highest thermal stability of the emission intensity was obtained for the layer implanted with the higher fluence and also for the NWs implanted with both fluences. This higher thermal stability observed for the NWs is in line with the results obtained for the Eu^{3+}-implanted samples.

Despite the fact that several works have been conducted concerning single RE^{3+} luminescence in nitrides, much less attention has been paid to the co-doping effects with different lanthanide ions in order to improve the potentialities of the RE emitters in the nitride systems. In this sense, GaN and AlN were co-implanted with Eu^{3+} and Pr^{3+} ions in order to widen the contribution of the red spectral range light provided by both ions, which is of interest for nitrides-based lighting systems. It was found that the emission properties of both samples are comparable to the ones implanted only with one ion and lower total fluence. Nevertheless, temperature dependent PL measurements showed different behaviours of the integrated intensity for the RE^{3+} transitions

when compared to the ones verified for the single implanted samples. Different behaviours were also observed for the two binary nitrides. In the case of the GaN sample the integrated intensity of the $^5D_0 \rightarrow {}^7F_2$ and $^3P_0 \rightarrow {}^3F_2$ transitions follow the same trend, both increasing up to ~ 100 K and decreasing for higher temperatures. In the AlN sample two distinct nonradiative paths described the decrease of the Eu^{3+} transition and only one nonradiative extinction mechanism was associated with the Pr^{3+} ions. These differences might be explained by the presence of different nonradiatiave recombination and thermal detrapping processes probably induced by the co-doping.

$Al_xGa_{1-x}N$ alloys implanted with Tb^{3+} and Tm^{3+} ions were also subject to extensive spectroscopic analysis. AlN samples were found to exhibit the highest intensity, as well as the highest thermal stability, while the alloys with $0 < x < 1$ showed broader transition lines, as expected due to the ion sensitivity to compounds disorder in the ternaries. In this case, an investigation of the RE^{3+} centre's excitation mechanisms was also performed. The outer electron configurations of RE^{3+} ions are the same ($5s^2$ $5p^6$). If the RE^{3+} ions replace the element from column III (Ga^{3+}, Al^{3+}) in III-nitride semiconductors that are isovalent concerning outer electrons of RE^{3+} ions, these ions tend to create isoelectronic traps. This is one of the most accepted models to describe the optical activity of RE in the III-nitride, where the REs are treated as isoelectronic impurities and energy transfer mechanisms take place in the RE excitation. Notwithstanding, another model based on the atomic properties of RE ions extensively developed by Dorenbos, should be considered. For the Tb^{3+}-implanted samples, a detailed discussion regarding these excitation models was conducted. Analysing the linewidth behaviour of both Tb^{3+} and Tm^{3+} ions in the $Al_xGa_{1-x}N$ alloys evidenced that with increasing AlN molar fraction both ions followed a similar trend. This trend was also observed in other RE^{3+} doped samples and it is compatible with the model involving excitonic features for the excitation population processes of the ions luminescence.

It is important to mention that, in the case of the Tb-implanted $Al_xGa_{1-x}N$ samples, the maxima of the broad luminescence bands were seen to shift to lower wavelengths as the temperature increased, most probably as a result of potential fluctuations in the ternary alloys. Still, a more detailed study is needed to fully understand the involved processes.

In summary, it was possible to demonstrate that the tuning of the visible light emission can be accomplished by an adequate choice of trivalent RE ions incorporated in the nitride hosts. Nevertheless, focus should be given to the optimization of doping and co-doping conditions, as well as further improvement of thermal annealing conditions. The next step should be devoted to the incorporation of these RE ions in nitride-based *p-n* junction devices and to test their electroluminescence properties, envisaging further development into commercial lighting devices.

The other major goal of the present work was the growth and characterization of ZnO structures. With this purpose in mind, a new growth technique was developed, designated by laser assisted flow deposition (LAFD). ZnO is known to decompose into its atomic components at its melting temperature and at atmospheric pressure. This fact, associated with its high vapour pressure, favours the ZnO growth by flux methods, as is the case of LAFD technique that proved to be a very efficient method to grow ZnO with high crystallinity and optical quality. This method combines local heating generated by the high power laser focused on the precursor with the thermal decomposition of ZnO at its melting temperature. The generated gases are transferred to

the low temperature regions, after the reaction of the zinc with the oxygen to form ZnO products. Different ZnO morphologies can be obtained for the as-grown samples as a result of different kinetics/thermodynamics local conditions verified in different regions of the growth chamber. Although several morphologies can be found in the produced samples, the dominant ones include nanoparticles, tetrapods and microrods. Micrometer scale crystals are observed on the top of the precursor, while nanoparticles and tetrapods tend to form in the holder region. The former are promoted by the high temperature verified in the precursor region where the laser hits, together with the permanent air convection. In the holder region the temperature is lower, resulting in structures with smaller dimensions, some of them at the nanoscale. Advantages of this growth technique include being catalyst-free, it is highly versatile to grow ZnO nano/microstructures at relatively high synthesis rates (depending on the applied laser power), avoiding time consuming operations and thus being easily up scalable to large area deposition. Furthermore, this is a simple single-step method that prevents contamination, since no crucibles or additional reagents are used. It was seen that the morphologies produced on the substrate region can be controlled to some extent by monitoring the growth parameters, namely the laser power/temperature and the growth atmosphere/oxygen availability. At atmospheric conditions, the production of only nanoparticles can be achieved when lower powers (~ 20 W) are applied. For higher powers, tetrapods become the dominant morphology, although some nanoparticles can also be found in the same run of growth due to the initial heating stage, hampering the production of only tetrapods. However, the ratio tetrapods/nanoparticles can be increased by using high heating powers during the growth. High laser power results also in an increasing of the growth yield. The morphologies can also be controlled by an adequate combination between laser power and growth atmosphere, enabling the dominant production of nanoparticles at higher laser powers (~ 30 W). Structural characterization revealed that even the crystals grown under low oxygen availability preserve the high crystalline quality, evidencing no stacking faults or other structural defects.

Low temperature PL analysis of the ZnO nano/microstructures showed an intense NBE emission for all the morphologies, usually an indication of high optical quality of ZnO crystals. Broad bands in the visible region were also identified. The ultraviolet PL recombination of the nanoscale crystals is dominated by the D^0X transition lines, while for the microrods the emission in this region is dominated by the 3.31 eV line. In order to gain a better understanding of the nature of the defects associated with this emission, plasma treatments (H_2 and N_2) were performed. These experiments leaded to significant changes, suggesting that the emission could be related with the presence of surface states in nature, since the 3.31 eV band was suppressed for the samples treated with both plasmas (applying and adequate plasma power). Additionally, an effective control of the PL intensity of the 3.31 eV versus D^0X lines was accomplished by considering the effects of the excitation intensity on the FX capture.

Samples grown in the presence of silver revealed that the metal tend to segregate to the surface of the ZnO crystals, being present essentially in the form of small particles attached to the rods. A secondary nucleation was observed from the termination of these rods as the silver amount increased on the precursor rod. The re-nucleation and sequential growth of crystals led to a complex three-dimensional ZnO hierarchical architecture. The silver droplets are responsible for

the re-nucleation process since they act as a catalyst for the ZnO growth. The distribution of these particles revealed to be inhomogeneous. Although most of the silver was seen to segregate to the surface, XRD and EDS-TEM results suggested that some incorporation of silver in ZnO crystals was indeed achieved by this growth process.

ZnO/CNTs samples were produced in the form of buckypapers and ZnO nanoparticles deposited on top of arrays of VACNTs. Different features in the Raman and PL spectra were observed for the two sets of samples. In the case of the ZnO/VACNTs it was observed that ZnO nanoparticles constituted the first layer, directly coating the CNTs. Photoluminescence studies enabled the identification of an enhancement of the ZnO emission when the particles are deposited on the VACNTs substrates and no changes in the shape of the spectra were identified. At low temperature, the NBE recombination was found to be structured and due to the overlap of D^0X recombination lines. Furthermore, in all samples the presence of the 3.31 eV transition was detected and deep level emission was found in the green spectral region. The samples optical quality was measured by the intensity ratio of the near band edge recombination and deep level emission. An intensity ratio of $\sim$ 4 was found at RT showing the good optical quality of the produced ZnO structures. The electrical properties of the ZnO/VACNTs sample revealed a rectifying behaviour which was different from the one obtained for the ZnO sample. Electrical measurements in the VACNTs samples showed an ohmic response.

For the buckypaper samples, SEM images evidence that the produced ZnO tetrapods were well dispersed in the composite while the nanoparticles showed some agglomerates. The morphology was kept for both structures before and after the composite preparation. The samples resistivity was shown to be of the order of $\sim 10^{-1}\ \Omega \cdot cm$ for all sets of samples and the carrier mobility was found to be dependent on the ZnO morphology. The lower mobility was found to occur for the ZnO composite with tetrapods where a high carrier concentration was measured, as expected for higher scattering rates. Regarding the luminescence properties, and in opposition to what happen in the ZnO/VACNTs samples, in this case slight changes in the shape of the NBE emission were observed for the composite structures, especially in the case of the tetrapods samples. A strong increase of the 3.31 eV line was observed when the tetrapods were mixed with the CNTs. Moreover, the temperature dependence of the NBE emission exhibits different behaviours before and after the incorporation of the ZnO nanostructures into the CNTs membrane. For both structures a smaller drop of the luminescence intensity was measured in the composites compared with those observed in ZnO nanoparticles and tetrapods alone. The observed combination of ZnO optical and CNTs electrical properties highlights the potential importance of this type of composite materials for technological applications.

The optical properties of $Cd_xZn_{1-x}O$ samples grown by MBE with different x_{Cd} were also studied. By alloying ZnO with CdO it is possible to tune its bandgap towards the visible region, as experimentally verified. NBE emission was seen to shift from the UV (for ZnO) to the orange spectral region by increasing the Cd content up to 0.38. Temperature dependence studies revealed a strong thermal quenching, with a decrease of the intensity around two orders of magnitude between 14 K and RT (for all the samples). Similar activation energies were estimated for the different samples, suggesting the presence of the similar recombination mechanisms. In addition, the temperature dependent PL puts in evidence the presence of potential fluctuations,

as in the case of the $Al_xGa_{1-x}N$ alloys. However, further studies are needed, namely to understand and minimize the competing nonradiative defects responsible for the strong thermal quenching observed.

Finally, the potential applications of the LADF produced ZnO structures in the photocatalysis and photovoltaic fields were tested. An interconnected network of both tetrapods and nanoparticles was used as the semiconductor active area for the assembling of DSSCs. A maximum efficiency of 2.9 % was accomplished, indicating the adequacy of the LAFD structures in the fabrication of this type of devices. This constitutes only the starting point, where the objective was solely to make a proof of concept regarding the application of the ZnO produced by this new growth technique. Further optimization in the DSSCs fabrication process is of paramount importance and there is much room for improvement. Similarly, photocatalysis preliminary results were obtained for both microrods and tetrapods, revealing strong morphology dependence in the pollutant degradation. Adding silver to the ZnO structures conducted to an enhancement of the photocatalytic performance, due to a more efficient charge separation. Overall, the results obtained are in line with what is found in the literature for similar samples (size and morphology).

As future research lines involving the ZnO-based structures, it is important to point out a further optimization of the LAFD technique, not only for ZnO but also for other material with close ebullition and melting points. As accurate knowledge and control of the temperature inside the growth chamber, especially in the top of the precursor and in the substrate regions is crucial for a reproducible growth. Moreover, a well isolated chamber that can support higher vapour pressures would be advantageous and would also lead to a better atmosphere control.

Subject the LAFD produced samples to different surface and heat treatments, including in different and controlled atmospheres, may bring more information about the optical centres present in these samples that were found to emit in the visible region, even enabling a correlation between the luminescence and the defects that originate them, as observed for the 3.31 eV emission.

Regarding the DSSCs, the next steps towards the improvement of their performance will comprise the study of different thicknesses of the semiconductor active layers, the test of different dyes and their best sensitization conditions (namely concentration and dye loading time). Since the photovoltaic response is known to be strongly dependent of the semiconductor surface states, surface passivation should be performed in the as-grown ZnO samples prior to their incorporation into the device. The optimization of all the steps/processes that compose the DSSCs fabrication and assembling also constitutes a critical factor.

Concerning the photocatalytic applications, as mentioned in Chapter 7, tests using the CNTs buckypaper composites with ZnO tetrapods (with and without silver) are scheduled to be conducted soon. It would be advantageous to have a free-standing membrane to perform this type of studies, since one of the issues that arise often in the use of nanoparticles in wastewater treatment is to ensure that after the treatment all the nanostructures are effectively eliminated from the solution. Moreover, it is important to study the influence of the silver amount on the ZnO structures, in order to find the ideal amount that lead to the best photocatalytic response. Another parameter that will require attention is the homogeneity in the distribution of metallic

silver on the ZnO surface, since literature reports suggested its strong influence in the photocatalytic activity.